INTEGRATED POINT-OF-CARE TESTING (POCT) SYSTEMS: RECENT PROGRESS AND APPLICATIONS

EDITED BY: Tailin Xu and Yunlu Pan

PUBLISHED IN: Frontiers in Bioengineering and Biotechnology

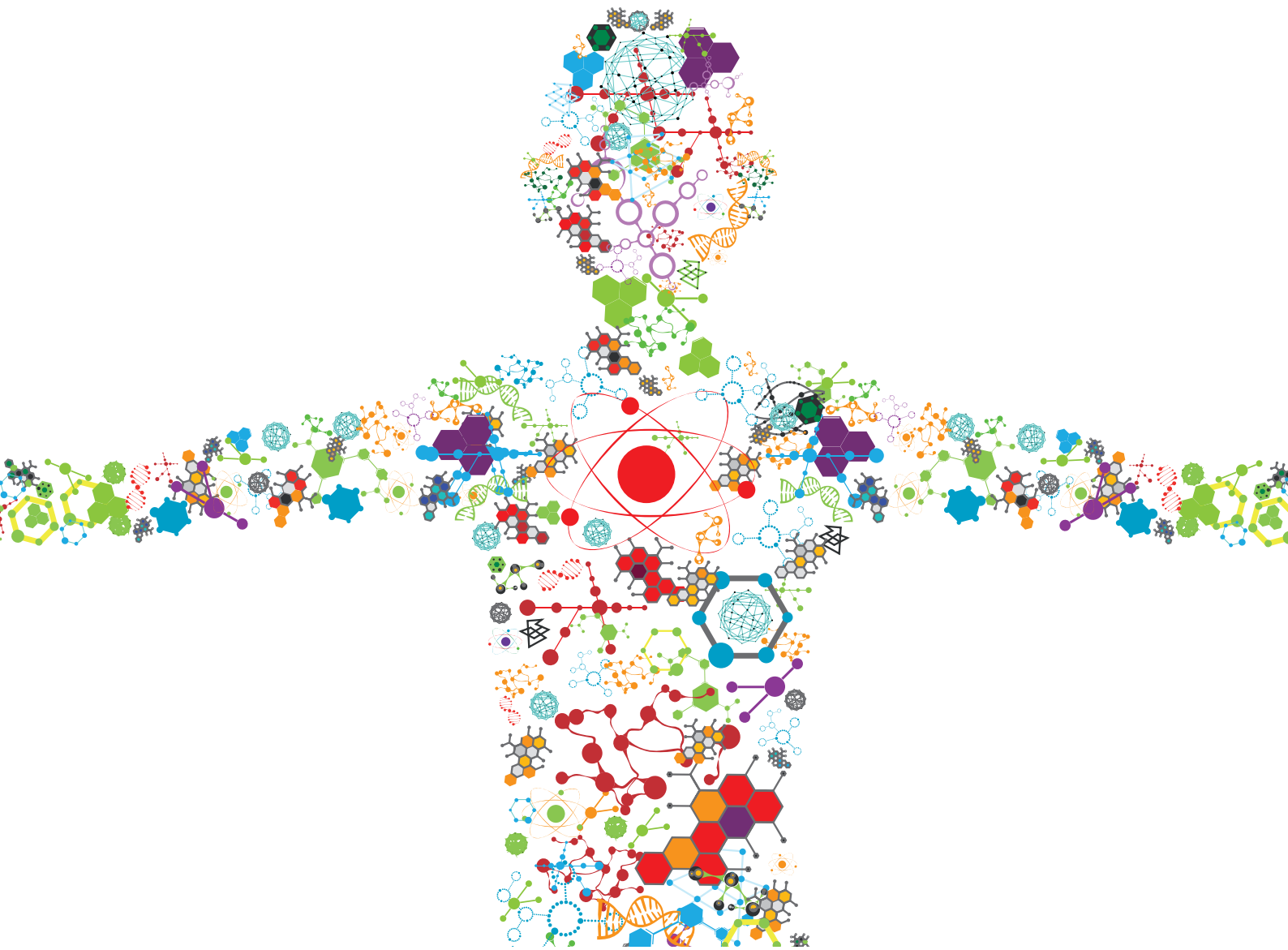

frontiers Research Topics

ISSN 1664-8714
ISBN 978-2-88974-739-9
DOI 10.3389/978-2-88974-739-9

About Frontiers

Frontiers is more than just an open-access publisher of scholarly articles: it is a pioneering approach to the world of academia, radically improving the way scholarly research is managed. The grand vision of Frontiers is a world where all people have an equal opportunity to seek, share and generate knowledge. Frontiers provides immediate and permanent online open access to all its publications, but this alone is not enough to realize our grand goals.

Frontiers Journal Series

The Frontiers Journal Series is a multi-tier and interdisciplinary set of open-access, online journals, promising a paradigm shift from the current review, selection and dissemination processes in academic publishing. All Frontiers journals are driven by researchers for researchers; therefore, they constitute a service to the scholarly community. At the same time, the Frontiers Journal Series operates on a revolutionary invention, the tiered publishing system, initially addressing specific communities of scholars, and gradually climbing up to broader public understanding, thus serving the interests of the lay society, too.

Dedication to Quality

Each Frontiers article is a landmark of the highest quality, thanks to genuinely collaborative interactions between authors and review editors, who include some of the world's best academicians. Research must be certified by peers before entering a stream of knowledge that may eventually reach the public - and shape society; therefore, Frontiers only applies the most rigorous and unbiased reviews.
Frontiers revolutionizes research publishing by freely delivering the most outstanding research, evaluated with no bias from both the academic and social point of view. By applying the most advanced information technologies, Frontiers is catapulting scholarly publishing into a new generation.

What are Frontiers Research Topics?

Frontiers Research Topics are very popular trademarks of the Frontiers Journals Series: they are collections of at least ten articles, all centered on a particular subject. With their unique mix of varied contributions from Original Research to Review Articles, Frontiers Research Topics unify the most influential researchers, the latest key findings and historical advances in a hot research area! Find out more on how to host your own Frontiers Research Topic or contribute to one as an author by contacting the Frontiers Editorial Office: frontiersin.org/about/contact

INTEGRATED POINT-OF-CARE TESTING (POCT) SYSTEMS: RECENT PROGRESS AND APPLICATIONS

Topic Editors:
Tailin Xu, Shenzhen University, China
Yunlu Pan, Harbin Institute of Technology, China

Citation: Xu, T., Pan, Y., eds. (2022). Integrated Point-of-care Testing (POCT) Systems: Recent Progress and Applications. Lausanne: Frontiers Media SA. doi: 10.3389/978-2-88974-739-9

Table of Contents

frontiers in Bioengineering and Biotechnology

EDITORIAL
published: 01 March 2022
doi: 10.3389/fbioe.2022.851675

Editorial: Integrated Point-of-Care Testing (POCT) Systems: Recent Progress and Applications

Lirong Wang[1,2] *and Tailin Xu*[1,2]*

[1]School of Biomedical Engineering, Health Science Center, Shenzhen University, Shenzhen, China, [2]Research Center for Bioengineering and Sensing Technology, University of Science and Technology Beijing, Beijing, China

Keywords: wearables, POCT, flexible biomaterials, bioelectronics, biosensors, portable devices, disease diagnostics, healthy monitoring

Editorial on the Research Topic

Integrated Point-of-Care Testing (POCT) Systems: Recent Progress and Applications

Traditional diagnostic methods for various biomarkers and biochemical parameters are normally carried out in specialized laboratories with professional workers, which leads to long assay times, high reagent consuming, and low efficiency (Shrivastava et al., 2020). Nowadays, point-of-care testing (POCT) technology with miniaturization of diagnostic tools has been successfully commercialized for health monitoring and disease diagnostics (Kim et al., 2019; Yang and Gao, 2019). Compared with traditional laboratory testing, POCT technology exhibits the attractive properties of small batches of samples, less reagent usage, user-friendliness, easy-to-use format, compact appearance, and fast turnaround time (Ray et al., 2019; Liu et al., 2020; Qiao et al., 2020). Recently, with emerging technological innovations in chemical and biochemical sensors, bioelectronics, and wearable electronics, the development of integrated POCT systems has an unprecedented opportunity to achieve personal healthcare and precision medicine (Gao et al., 2016; Luo et al., 2020; Ates et al., 2021; Sempionatto et al., 2021; Wang et al., 2021).

In this special topic issue, 14 papers have been included, with a mixture of 10 original research articles, 4 reviews. This research topic aims at discussing recent progress and applications of integrated POCT systems, including user-friendly, portable and simple monitoring platforms; immediate clinical assessment technology; flexible wearable sensors based on nanomaterials; and highly sensitive and specific biosensors. In addition, these integrated POCT systems are also widely applied in clinical diagnosis, disease control and other fields through the detection of various biomarkers.

For example, large-scale rapid POCT systems for infectious diseases are urgently needed during the COVID-19 pandemic. Wang et al. reported a novel diagnostic testing platform based on the principle of real-time reverse transcription loop-mediated isothermal amplification for the diagnosis of COVID-19, which can complete the entire testing process from sample Research Topic to result interpretation within 55 min. In addition, research progress in developing paper-based POC devices for SARS-CoV-2 detection was reviewed by Jia et al., including the detection principle, analysis performance, advantages and disadvantages of existing methods and equipment.

Recently, wearable sensors capable of continuously monitoring human physiological signals in real-time have attracted a lot of research interest with the emergence of flexible bioelectronics and biomaterials. Therefore, Cheng et al. comprehensively reviewed the research progress of intelligent wearable sensors for detecting various biological fluids, including sweat, blood, interstitial fluid, tears and wound fluid, and made concluding comments to guide their better development in

OPEN ACCESS

Edited and reviewed by:
Guozhen Liu,
The Chinese University of Hong Kong, Hong Kong SAR, China

***Correspondence:**
Tailin Xu
xutailin@szu.edu.cn

Specialty section:
This article was submitted to Biosensors and Biomolecular Electronics, a section of the journal Frontiers in Bioengineering and Biotechnology

Received: *10 January 2022*
Accepted: *03 February 2022*
Published: *01 March 2022*

Citation:
Wang L and Xu T (2022) Editorial: Integrated Point-of-Care Testing (POCT) Systems: Recent Progress and Applications. Front. Bioeng. Biotechnol. 10:851675. doi: 10.3389/fbioe.2022.851675

commercialization and practicability. Yan et al. summarized the application of flexible biosensors in POCT and classified them according to substrate materials (polymers, paper, and textiles) to help readers gain a comprehensive understanding of the development trends in the field. Moreover, Raza et al. also introduced the research progress of wearable electrochemical biosensors to readers from the perspective of conductive nanomaterials. Furthermore, a flexible sensor for simultaneous detection of ascorbic acid, dopamine, and uric acid is fabricated by growing 3D graphene nanosheets on flexible carbon cloth through thermal chemical vapor deposition, with linear monitoring ranges of 0.02–0.1, 0.0005–0.02, and 0.0005–0.02 mM, respectively, (Meng et al.). Fu et al. proposed a strategy that can not only effectively inhibit bacterial adhesion (the antibacterial efficiency remains above 66%), but also capture and detect nickel ions through chelation reaction (the capture efficiency is about 57% at 5 days), which can be used in implantable biomedical materials and equipment in the future.

More importantly, the combination of POCT with nano-diagnostics technology has become the latest trend in the development of fully integrated POCT systems in the field of personal healthcare. A novel approach for the visual detection of the Hepatitis B virus in the clinical application was first developed by Chen et al. by integrating loop-mediated isothermal amplification with a gold nanoparticle-based lateral flow biosensor, and the entire detection process includes genomic DNA extraction (~10 min), preamplification (~40 min), and LFB readout (~2 min) can be completed in 60 min. Similarly, Wang et al. (2021) developed a novel detection method called "CRISPR-HBV" for Hepatitis B virus diagnosis, which can detect 10 copies of genomic DNA with 100% specificity. He et al. provide a promising point-of-care biosensor for a biomarker of Alzheimer's disease (Amyloid-β protein) in which ZnO@polydopamine/Au nanocomposites has excellent visible-light activity, possessing a wide Linear range (1 pg/ml to 100 ng/ml) and low detection limit (0.26 pg/ml). An intelligent multi-modal point-of-care system combining clinical indicators with CT images was developed to predict transarterial chemoembolization response in hepatocellular carcinoma with 98% accuracy (Sun et al.). A point-of-care testing system based on a magnetically propelled microdimer was reported for the quantification analysis of plasma glucose, cholesterol, and triglyceride concentrations (Yu et al.). Hwang et al. presented a magnetic force-assisted electrochemical sandwich immunoassay for the quantitative analysis of carcinoembryonic antigen, which showed a linear relationship of 0.5–200 ng/ml and a detection limit of 0.50 ng/ml. Sun et al. developed a method for the timely diagnosis of B. pertussis infections that combines loop-mediated isothermal amplification and a nanoparticle-based lateral flow biosensor with a sensitivity of 50 fg per reaction. Notably, these works require further follow-up and provide more clinical data to confirm their practicability and accuracy.

In conclusion, we have included recent advances and applications of integrated point-of-care testing (POCT) systems in this topic. We hope to bring readers a timely and interesting overview to inspire future attention to multidisciplinary research in materials science, chemistry and biotechnology to address the remaining challenges of integrated POCT systems for personal healthcare. For example, a powerful wearable sensing system integrating new materials, sensing technology and a seamless system is lacking, which can accurately and continuously collect and output data from the human body. Miniaturization and integration of signal processing systems need to be explored to fully exploit the potential of flexible electronics. Considering the complexity of the human body, future research work should also focus on human comfort studies, especially friendly sampling methods and flexible systems that mechanically match the skin interface. Further research in these directions could accelerate the commercialization of such integrated POCT systems, which will have a significant impact on personalized healthcare.

AUTHOR CONTRIBUTIONS

LW wrote the draft. TX revised and approved the final version for publication.

ACKNOWLEDGMENTS

The topic editors would like to acknowledge all the authors, reviewers, and scientists who participated in this research topic.

REFERENCES

Ates, H. C., Yetisen, A. K., Güder, F., and Dincer, C. (2021). Wearable Devices for the Detection of COVID-19. *Nat. Electron.* 4, 13–14. doi:10.1038/s41928-020-00533-1

Gao, W., Emaminejad, S., Nyein, H. Y. Y., Challa, S., Chen, K., Peck, A., et al. (2016). Fully Integrated Wearable Sensor Arrays for Multiplexed *In Situ* Perspiration Analysis. *Nature* 529, 509–514. doi:10.1038/nature16521

Kim, J., Campbell, A. S., de Ávila, B. E.-F., and Wang, J. (2019). Wearable Biosensors for Healthcare Monitoring. *Nat. Biotechnol.* 37, 389–406. doi:10.1038/s41587-019-0045-y

Liu, C., Xu, T., Wang, D., and Zhang, X. (2020). The Role of Sampling in Wearable Sweat Sensors. *Talanta* 212, 120801. doi:10.1016/j.talanta.2020.120801

Luo, Z., Lv, T., Zhu, K., Li, Y., Wang, L., Gooding, J. J., et al. (2020). Paper-Based Ratiometric Fluorescence Analytical Devices towards Point-of-Care Testing of Human Serum Albumin. *Angew. Chem. Int. Ed.* 59, 3131–3136. doi:10.1002/anie.201915046

Qiao, L., Benzigar, M. R., Subramony, J. A., Lovell, N. H., and Liu, G. (2020). Advances in Sweat Wearables: Sample Extraction, Real-Time Biosensing, and Flexible Platforms. *ACS Appl. Mater. Inter.* 12, 34337–34361. doi:10.1021/acsami.0c07614

Ray, T. R., Choi, J., Bandodkar, A. J., Krishnan, S., Gutruf, P., Tian, L., et al. (2019). Bio-Integrated Wearable Systems: A Comprehensive Review. *Chem. Rev.* 119, 5461–5533. doi:10.1021/acs.chemrev.8b00573

Sempionatto, J. R., Lin, M., Yin, L., De La Paz, E., Pei, K., Sonsa-Ard, T., et al. (2021). An Epidermal Patch for the Simultaneous Monitoring of Haemodynamic and Metabolic Biomarkers. *Nat. Biomed. Eng.* 5, 737–748. doi:10.1038/s41551-021-00685-1

Shrivastava, S., Trung, T. Q., and Lee, N.-E. (2020). Recent Progress, Challenges, and Prospects of Fully Integrated mobile and Wearable point-of-care Testing Systems for Self-Testing. *Chem. Soc. Rev.* 49, 1812–1866. doi:10.1039/c9cs00319c

Wang, L., Xu, T., He, X., and Zhang, X. (2021). Flexible, Self-Healable, Adhesive and Wearable Hydrogel Patch for Colorimetric Sweat Detection. *J. Mater. Chem. C* 9, 14938–14945. doi:10.1039/d1tc03905a

Yang, Y., and Gao, W. (2019). Wearable and Flexible Electronics for Continuous Molecular Monitoring. *Chem. Soc. Rev.* 48, 1465–1491. doi:10.1039/c7cs00730b

Conflict of Interest: The authors declare that the research was conducted in the absence of any commercial or financial relationships that could be construed as a potential conflict of interest.

Publisher's Note: All claims expressed in this article are solely those of the authors and do not necessarily represent those of their affiliated organizations, or those of the publisher, the editors and the reviewers. Any product that may be evaluated in this article, or claim that may be made by its manufacturer, is not guaranteed or endorsed by the publisher.

frontiers in Bioengineering and Biotechnology

BRIEF RESEARCH REPORT
published: 24 June 2021
doi: 10.3389/fbioe.2021.698745

Nickel-Catcher-Doped Zwitterionic Hydrogel Coating on Nickel–Titanium Alloy Toward Capture and Detection of Nickel Ions

Xiaoyi Fu[1†], Xi Liu[2,3†], Dezhao Hao[2,3], Wuyi Xiao[2,3], Qiong Nie[1] and Jingxin Meng[2,3*]*

[1] National Center of Stomatology, National Clinical Research Center for Oral Diseases, National Engineering Laboratory for Digital and Material Technology of Stomatology, Department of Orthodontics, Peking University School and Hospital of Stomatology, Beijing, China, [2] CAS Key Laboratory of Bio-Inspired Materials and Interfacial Science, CAS Center for Excellence in Nanoscience, Technical Institute of Physics and Chemistry, Chinese Academy of Sciences, Beijing, China, [3] University of Chinese Academy of Sciences, Beijing, China

OPEN ACCESS

Edited by:
Tailin Xu,
Shenzhen University, China

Reviewed by:
Feilong Zhang,
Nanyang Technological University, Singapore
Zhen Gu,
University of Science and Technology Beijing, China
Li Huizeng,
Institute of Chemistry (CAS), China

***Correspondence:**
Qiong Nie
nieqiong@bjmu.edu.cn
Jingxin Meng
mengjx628@mail.ipc.ac.cn

[†] These authors have contributed equally to this work and share first authorship

Specialty section:
This article was submitted to Biosensors and Biomolecular Electronics, a section of the journal Frontiers in Bioengineering and Biotechnology

Received: 22 April 2021
Accepted: 25 May 2021
Published: 24 June 2021

Citation:
Fu X, Liu X, Hao D, Xiao W, Nie Q and Meng J (2021) Nickel-Catcher-Doped Zwitterionic Hydrogel Coating on Nickel–Titanium Alloy Toward Capture and Detection of Nickel Ions. Front. Bioeng. Biotechnol. 9:698745. doi: 10.3389/fbioe.2021.698745

Nickel–titanium (NiTi) alloys show broad applicability in biomedical fields. However, the unexpected aggregation of bacteria and the corrosion of body fluid on NiTi-based medical devices often lead to the leakage of nickel ions, resulting in inevitable allergic and cytotoxic activities. Therefore, the capture and detection of nickel ions are important to avoid serious adverse reactions caused by NiTi-based medical devices. Herein, we presented a nickel ion capture strategy by the combination of zwitterionic hydrogels as anti-bacteria layers and carbon disulfide (CS_2) components as nickel-catchers (Ni-catchers). On the one hand, the hydration layer of zwitterionic hydrogel can efficiently inhibit bacteria adhesion and reduce nickel ions leakage from NiTi corrosion. On the other hand, Ni-catchers can capture leaked nickel ions from NiTi alloy actively by chelation reaction. Therefore, this strategy shows great capabilities in resisting bacteria adhesion and capturing nickel ions, providing the potential possibility for the detection of nickel ion leakage for implantable biomedical materials and devices.

Keywords: nickel ion capture, anti-bacteria adhesion, zwitterionic hydrogel, surface modification, nickel–titanium alloy

INTRODUCTION

With the rapid development of biomedicine, implantable materials have been widely used in diagnosis, treatment, and prosthesis (Sylvestre et al., 2020). As one of the most popular biomaterials, nickel–titanium (NiTi) alloys have been applied in orthodontic archwires (Liu et al., 2019), bone implants (Raphel et al., 2016), and vascular stents (Robertson and Ritchie, 2007), due to their unique superelasticity and good biocompatibility. However, the leakage of nickel ions (Ni^{2+} ions) from NiTi alloys often leads to adverse reactions such as allergic signs (e.g., contact mucositis and eczematic and urticarial reactions; Huang et al., 2003; Kolokitha and Chatzistavrou, 2008) and cytotoxic responses (Jia et al., 1999). In addition, the unexpected adhesion of bacteria and acidic oral environment corrode NiTi alloys, aggravating the leakage of Ni^{2+} ions (Huang et al., 2003). Therefore, a novel strategy for capturing and detecting leaked Ni^{2+} ions is urgently needed for potential biomedical applications.

In recent years, many passive strategies have been developed to avoid the leakage of Ni^{2+} ions, including growing oxide films [e.g., TiO_2 layer (Gu et al., 2005) and $NiTiO_3$ nanosheet (Hang et al., 2019)], depositing coatings [e.g., diamond-like carbon coating (Hang et al., 2012) and 1*H*,1*H*,2*H*,2*H*-perfluorodecyltrimethoxysilane (FAS) deposited layer (Liu et al., 2019)], and implanting barrier elements [e.g., carbon (Poon et al., 2005) and oxygen (Wu et al., 2006) plasma immersion ion implantation]. However, most of them can not prohibit long-term leakage of Ni^{2+} ions because of the low stability of hydrophobic surface in acidic oral environment (Liu et al., 2019) and the corrosion of adhered bacteria (Gu et al., 2005). Moreover, there are many anti-bacteria methods including zwitterionic hydrogels (Li et al., 2008; Shivapooja et al., 2015; Lin et al., 2020), polyethylene glycol (Peng et al., 2017), quaternary ammonium salt groups (Wei et al., 2016, 2017), protein-based surfaces (Liu et al., 2018), and multiwalled carbon nanotubes (Hartono et al., 2018). Thus, combining anti-bacteria and Ni^{2+} ion capture may be a promising strategy for the new generation of NiTi-based medical devices. As a conventional medical treatment for acute carbonyl nickel poisoning, carbon disulfide (CS_2) derivates can serve as Ni-catchers by chelation reaction (Sunderman, 1990). Therefore, we believe that introducing Ni-catchers into anti-bacteria layer can achieve long-term Ni^{2+} ion capture and detection.

Herein, we present a Ni-catcher-doped zwitterionic hydrogel coating on the surface of NiTi alloy, showing robust anti-bacteria and long-term Ni^{2+} ion capture (**Figure 1**). In brief, zwitterionic hydrogel was firstly prepared on the surface of NiTi alloy (H-NiTi) by the copolymerization of 2-hydroxyethyl methacrylate (HEMA), 3-dimethyl(methacryloyloxyethyl)ammonium propane-sulfonate (DMAPS), and methyl methacrylate (MMA; Su et al., 2020). Then, the CS_2 as a Ni-catcher was grafted into zwitterionic hydrogel by immersing H-NiTi in the mixture of CS_2 and triethylamine (TEA) to obtain CS-NiTi (**Figure 1A** and **Supplementary Figure 1**). The zwitterionic hydrogel can prevent the adhesion of bacteria by the hydration layer on the surface of CS-NiTi. Moreover, the Ni-catcher endows this coating with Ni^{2+} ion capture through chelation reaction. Therefore, this work provides a promising avenue to capture and detect Ni^{2+} ions, which could be used for implantable biomedical materials and devices.

MATERIALS AND METHODS

Chemicals and Materials

Nickel–titanium alloy was purchased from Sunway Technology Co. Ltd. (Guangdong, China). Brain heart infusion (BHI) was obtained from Oxoid Co. (Hampshire, United Kingdom). Dulbecco's modified Eagle medium (DMEM) was bought from Thermo Fisher Biochemical Products Co. Ltd. (Beijing, China). Tris–HCl buffer was purchased from Coolaber Science Technology (Beijing, China). Phosphate-buffered saline (PBS) was bought from HyClone Laboratories Inc. (Logan, UT, United States). Acetone (>99.5%, AR) and alcohol (≥99.8%, GR) were obtained from the Beijing Chemical Co. (Beijing, China). Bis(2-methacryloxyethyl)phosphate (bis-HEMAP) and 2,2-diethoxyacetophenone (DEAP) were bought from J&K Scientific (Beijing, China). HEMA and DMAPS were purchased from Aladdin Ltd. (Shanghai, China). MMA and poly(ethylene glycol)dimethacrylate (PEGDMA) were purchased from Alfa Aesar (Haverhill, MA, United States). CS_2 and TEA were obtained from Macklin Inc. (Shanghai, China). Deionized water (>1.82 MΩ cm, Milli-Q system, Merck & Co., Kenilworth, NJ, United States) was used. All reagents were used as received.

Preparation of CS-NiTi

The CS-NiTi was fabricated according to previous literature, with some modifications (Su et al., 2020). Firstly, pristine NiTi alloy was immersed in bis-HEMAP (5% ethanol solution) for 24 h and washed with deionized water for three times. Then, the 0.5 wt% of the photoinitiator DEAP was coated on the surface of NiTi alloy. The hydrogel precursor solution was obtained by mixing the crosslinker of PEGDMA (2 wt%) with the hydrogel monomers solution, including DMAPS (5 wt%), HEMA (40 wt%), and MMA (5 wt%). Then, it was degassed for 20 min by KQ5200DE ultrasonic cleaner (Kun Shan Ultrasonic Instruments Co. Ltd., Shanghai, China). The degassed precursor solution was poured on the surface of NiTi alloy and exposed to UV irradiation (wavelength ≈ 365 nm) in a dark chamber for 600 s by a UV LED curing system (Beijing NBET Technology Co. Ltd., Beijing, China), to obtain H-NiTi. To graft Ni-catchers on H-NiTi, H-NiTi was immersed into a mixture for 24 h containing CS_2, TEA, and deionized water. LCS-NiTi, MCS-NiTi, and HCS-NiTi were obtained by regulating the concentration of CS_2 (0.2, 0.6, and 1.0 mol/L), respectively.

Characterizations

The morphology of pristine NiTi, H-NiTi, and CS-NiTi were observed with S-4800 scanning electron microscope (SEM; Hitachi, Tokyo, Japan) and Single Lens Reflex camera (SLR camera; Nikon D80, Tokyo, Japan). Water contact angles (WCAs) were measured by dropping 2 μl of water on the surface of pristine NiTi, H-NiTi, and CS-NiTi by the Dataphysics OCA 20 Contact-Angle System (Filderstadt, Germany). The S element analysis was performed on ESCALAB 250Xi X-ray photoelectron spectroscopy analysis (XPS; Thermo Fisher Scientific, Waltham, MA, United States). The transmittance was measured by UV-2600 UV-VIS spectrophotometer (SHIMADZU, Kyoto, Japan) with wavelength from 450 to 700 nm.

Cell Culture and Cellular Toxicity Test

Cell Counting Kit-8 (CCK-8) assay was performed to investigate the cell viability (Xiao et al., 2020). And the cytotoxicity of materials including pristine NiTi, H-NiTi, and CS-NiTi was evaluated with HepG2 cells. HepG2 cells with the density of 1×10^5 cells per well were seeded into the 24-well plates in DMEM containing 10% fetal bovine serum (FBS) and 1% antibiotic solution (penicillin and streptomycin) and then cultured at 37 C in a humidified atmosphere with 5% CO_2 for 36 h. Pristine NiTi, H-NiTi, and CS-NiTi were added to each well, and the cells were incubated for 12 h. Subsequently, CCK-8 solutions were added to the wells followed by 2-h incubation at

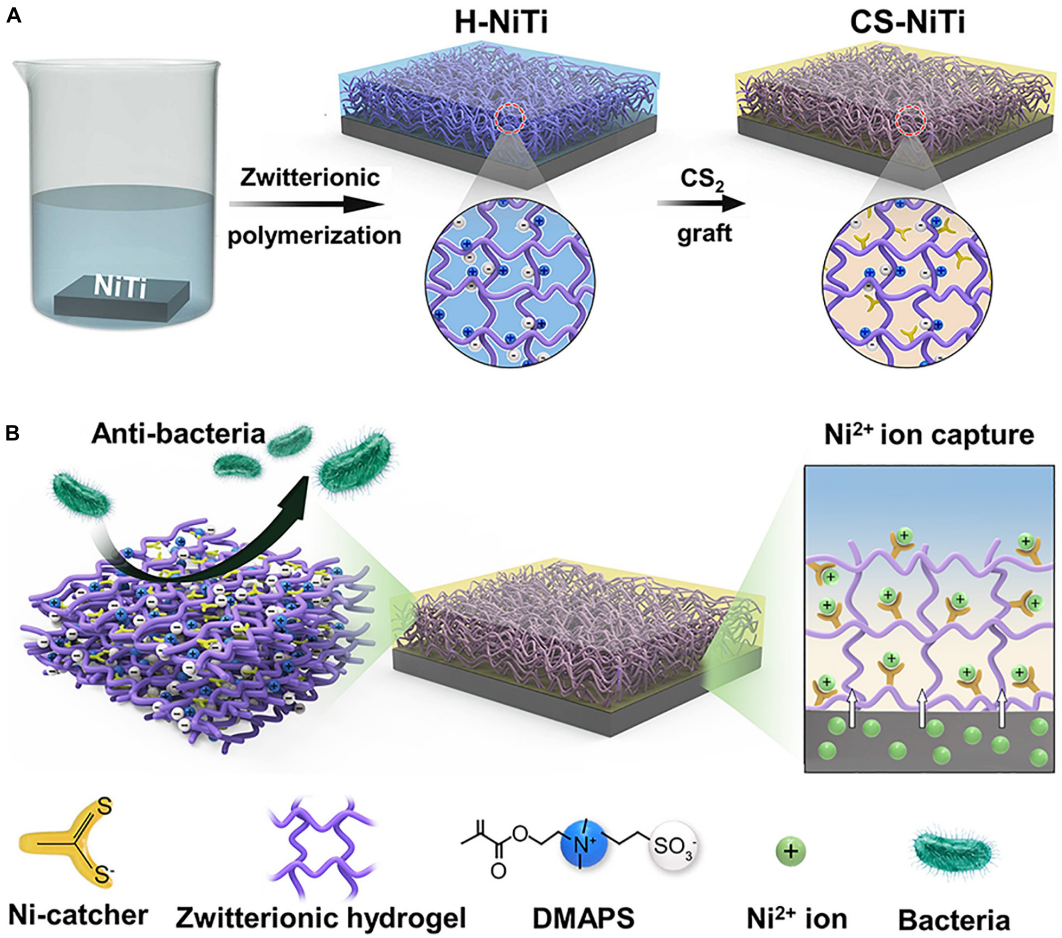

FIGURE 1 | Design principle of CS-NiTi for long-term Ni^{2+} ion capture. **(A)** Schematic of the fabrication process of CS-NiTi. **(B)** The as-prepared CS-NiTi shows dual functions of anti-bacteria and Ni^{2+} ion capture.

37°C. And then the supernatant was obtained and added to 96-well plates. Finally, microplate reader was used to measure the absorbance values per well at a test wavelength of 450 nm and a reference wavelength of 690 nm to analyze the cell viability. Control experiments were done under the same condition with PBS. Eq. (1) was used to calculate the cell viability rate:

$$\text{Cell viability} = As/Ac \times 100\% \quad (1)$$

where *As* represents the absorbance of the treatments of different groups and *Ac* represents the absorbance of the control treatments with PBS. All the experiments were performed in triplicate.

Bacteria Cultivation

Streptococcus mutans (UA159) was used as the model bacteria. *S. mutans* was revived by incubating its freezing solution with 1 ml of BHI at 37°C for 48 h. Then the suspension of *S. mutans* was centrifugated at 2,000 rpm for 10 min at room temperature to discard the supernatant. Then, the *S. mutans* aggregation was resuspended in another 1 ml of BHI and incubation at 37°C for another 48 h. After the logarithmic phase was reached, the bacteria were harvested by centrifugation at 2,000 rpm for 10 min at room temperature and washed with Tris–HCl buffer three times. Subsequently, the bacteria were suspended in 50 ml of Tris–HCl buffer at a final concentration of 1×10^8 CFU/ml (Liu et al., 2018).

Anti-bacteria Property

To test anti-bacteria ability, the pristine NiTi, H-NiTi, and CS-NiTi were incubated in the as-prepared bacteria suspensions for 1, 3, 6, 12, 18, and 24 h at 37°C. After the incubation, they were taken out and fixed in 2.5% glutaraldehyde for 1 h at room temperature, followed by immersing in a graded series of alcohol concentrations (30, 50, 70, 80, 90, and 100%) for 10 min to dehydrate the adhered bacteria. SEM was used to observe bacteria adhesion performance. The quantitative evaluation of the adhered bacteria was obtained by Cell Profiler 4.0.7. The anti-bacteria efficiency ($E_{anti-bacteria}$) could be calculated by Eq. (2):

$$E_{anti-bacteria} = (1 - D_{CS-NiTi}/D_{NiTi}) \times 100\% \quad (2)$$

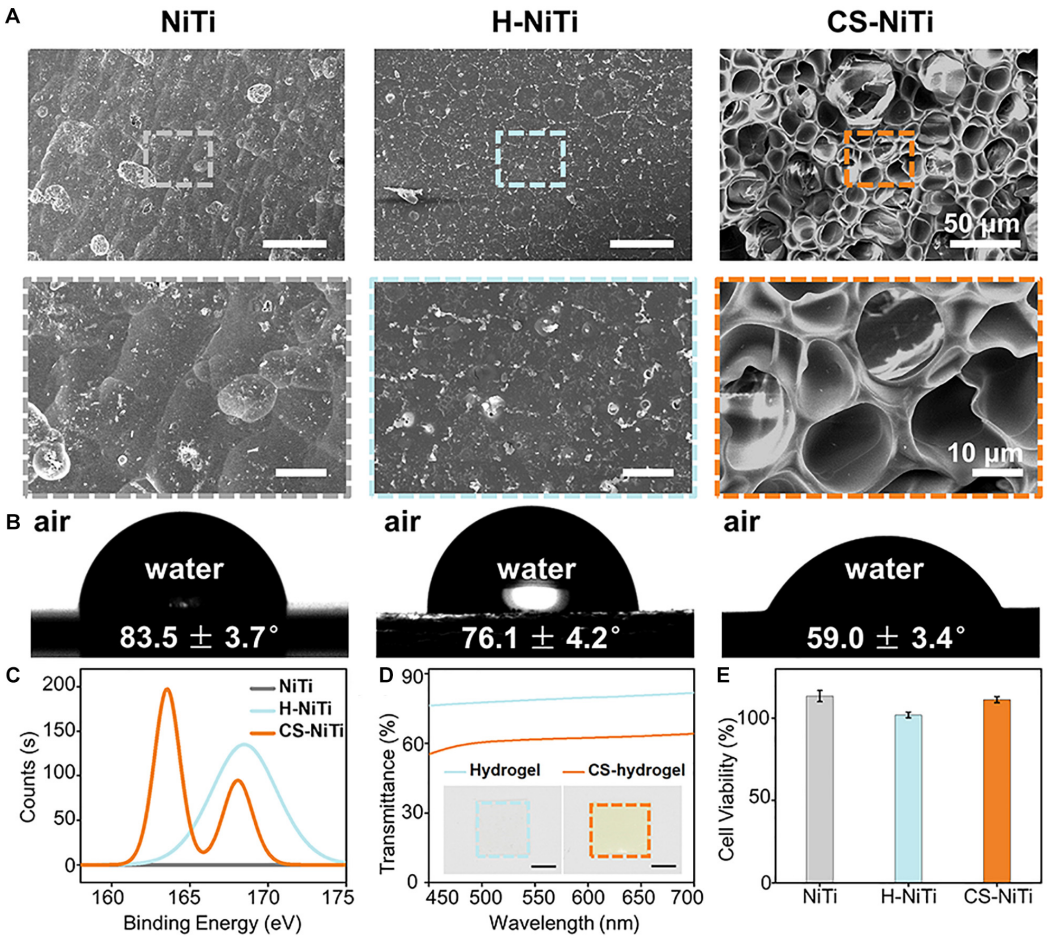

FIGURE 2 | Characterizations of CS-NiTi. SEM images **(A)**, water contact angles (WCAs; **B)**, X-ray photoelectron spectroscopy (XPS) spectra **(C)**, transmittance, **(D)** and biocompatibility **(E)** of pristine NiTi, H-NiTi, and CS-NiTi. The insets in **(D)** show the optical images of zwitterionic hydrogel and CS-hydrogel. Scale bar, 5 mm for **(D)**.

where $D_{CS-NiTi}$ and D_{NiTi} refer to the bacteria density on the surface of CS-NiTi and pristine NiTi, respectively.

Performance of Ni^{2+} Ion Capture

The performance of Ni^{2+} ion capture was investigated on 710-OES inductively coupled plasma emission spectrometer (ICP; Varian, Palo Alto, CA, United States) by detecting the concentration of nickel ions in the supernatant of the remaining bacteria suspension incubated with pristine NiTi, H-NiTi, LCS-NiTi, MCS-NiTi, and HCS-NiTi for different times at 37°C. The capture efficiency of Ni^{2+} ions ($E_{capture}$) could be calculated by Eq. (3):

$$E_{capture} = (1 - C_{CS-NiTi}/C_{H-NiTi}) \times 100\% \quad (3)$$

where $C_{CS-NiTi}$ and C_{H-NiTi} refer to the concentration of Ni^{2+} ions in the supernatant of remaining bacteria suspension incubated with CS-NiTi and H-NiTi, respectively.

RESULTS

Characterizations of CS-NiTi

To verify the introduction of Ni-catchers, we compared the pristine NiTi, H-NiTi, and CS-NiTi from surface morphology, WCAs, XPS spectra, transmittance, optical images, and biocompatibility. As shown in **Figure 2A**, the introduction of Ni-catchers resulted in the porous morphology of CS-NiTi, compared with the flat morphology of H-NiTi, probably because of the phase separation (Su et al., 2020). Furthermore, the WCAs decreased from 83.5 ± 3.7° (NiTi) to 59.0 ± 3.4° (CS-NiTi), indicating the hydrophilicity of CS-NiTi (**Figure 2B**). The change of wettability might be attributed to the formation of hydrophilic xanthates in the presence of TEA (Weißl et al., 2018) and the porous morphology of CS-NiTi. More hydrophilic surface was beneficial to the formation of the hydration layer, enhancing the anti-bacteria adhesion ability of NiTi alloys (Lin et al., 2020). XPS was further employed to verify the presence of Ni-catchers in CS-NiTi. As shown in **Figure 2C** and **Supplementary Figure 2**, two S 2p peaks at 163 and 168 eV were observed in the XPS spectrum

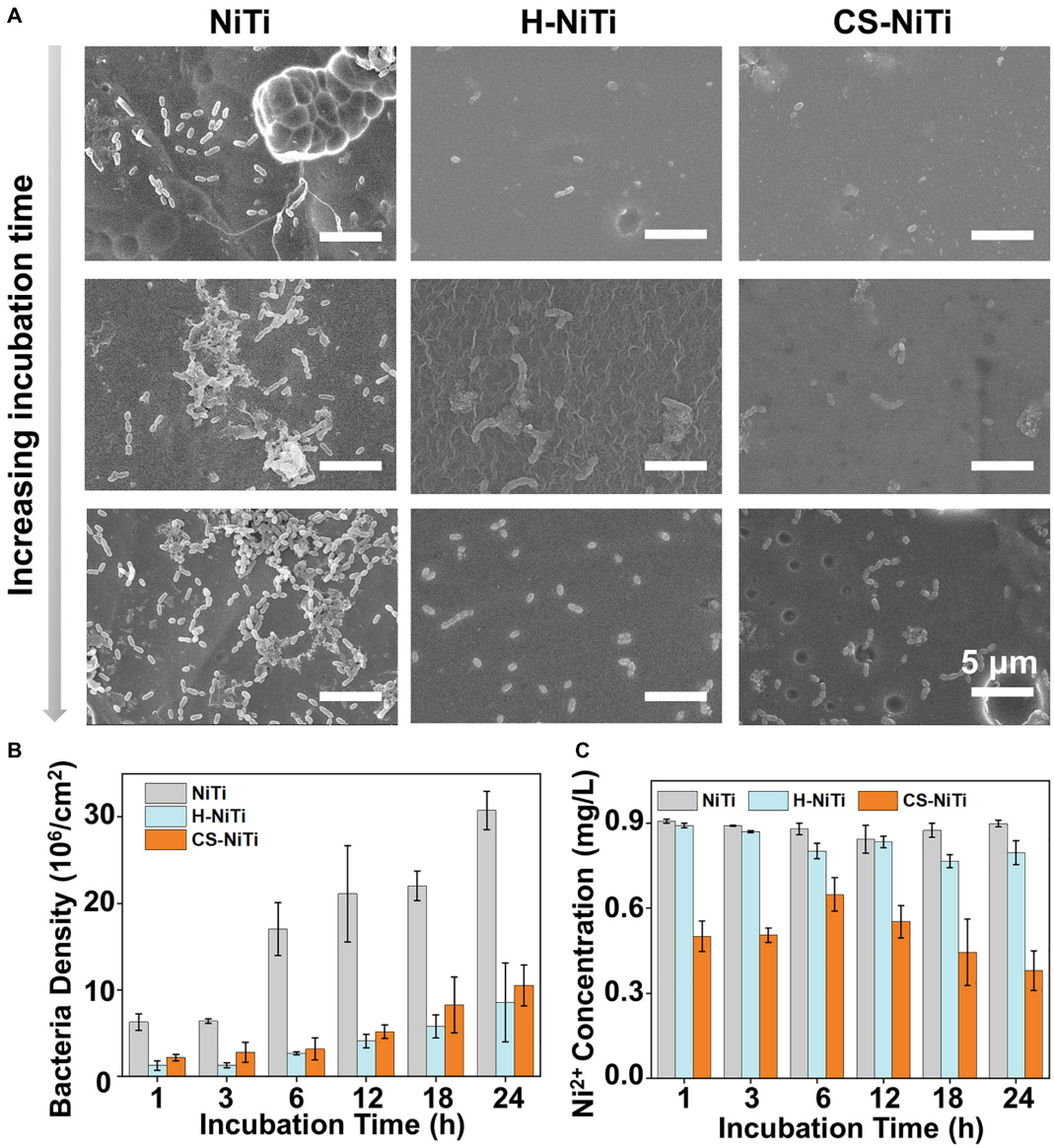

FIGURE 3 | The anti-bacteria property of CS-NiTi. **(A)** SEM images of pristine NiTi, H-NiTi, and CS-NiTi after being incubated with bacteria suspension for different times (1, 12, and 24 h). The quantitative analysis of bacteria adhesion **(B)** and Ni^{2+} ion capture performance **(C)** on the surface of pristine NiTi, H-NiTi, and CS-NiTi at different incubation times.

of CS-NiTi, compared with the single S 2p peak at 168 eV for H-NiTi and no S 2p peak for NiTi. The S 2p peak at 168 eV shown in H-NiTi represented the S element in zwitterionic hydrogel network. The new S 2p peak at 163 eV indicated the successful introduction of Ni-catchers in CS-NiTi (Deng et al., 2013). Moreover, the appearance of zwitterionic hydrogels changed from colorless to yellow with lower transmittance after Ni-catcher (CS_2) graft (**Figure 2D**), for xanthates always appear as a series of yellow compounds. The transmittance of Ni-catcher-doped zwitterionic hydrogel coating was higher than 60%, which has an insignificant impact on the appearance of NiTi alloys and would not affect the application of NiTi alloys in the implantable biomedical field. Furthermore, we tested the biocompatibility of CS-NiTi using CCK-8 test (Xiao et al., 2020). Higher HepG2 cell viability in **Figure 2E** indicated the excellent biocompatibility of CS-NiTi, showing promising applicability in biomedical field. Therefore, we successfully fabricated CS-NiTi with good biocompatibility.

Anti-bacteria Property of CS-NiTi

As a kind of widely used orthodontic material, NiTi alloys are often exposed to the oral environment. However, cleaning teeth is difficult during orthodontic treatment, leading to the adhesion of bacteria and causing caries and periodontitis. To investigate the anti-bacteria property in the oral environment, CS-NiTi was incubated in 1×10^8 CFU/ml bacteria suspension (*S. mutans*, the

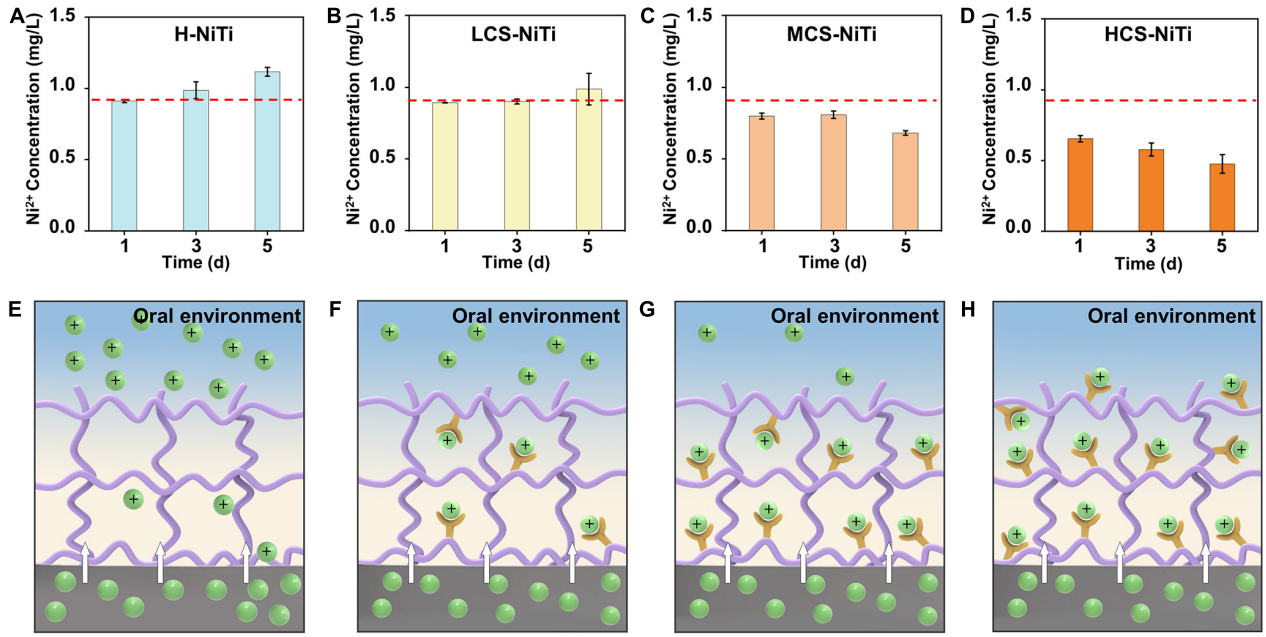

FIGURE 4 | The mechanism of Ni^{2+} ion capture of CS-NiTi. **(A–D)** The quantitative analysis of Ni^{2+} ion capture performance of H-NiTi, LCS-NiTi, MCS-NiTi, and HCS-NiTi. **(E–H)** Schematic of Ni^{2+} ion capture property of CS-NiTi with different concentrations of Ni-catchers.

largest proportion of bacteria in oral environment) for different times, taking pristine NiTi and H-NiTi as controls. As shown in **Figure 3A** and **Supplementary Figure 3**, many bacteria adhered on the surface of pristine NiTi after being incubated for 1 h. In contrast, there were a few bacteria on the surfaces of H-NiTi and CS-NiTi, indicating their good anti-bacteria properties. By prolonging incubation time, a growing number of bacteria adhered on the surface of pristine NiTi and formed a biofilm at 12 h. In contrast, the bacteria density was still very low on the surfaces of H-NiTi and CS-NiTi. The quantitative analysis in **Figure 3B** revealed a good anti-bacteria efficiency in H-NiTi and CS-NiTi at 6 h, showing the highest efficiency of ca. 84% for H-NiTi and ca. 81% for CS-NiTi. By prolonging the incubation time to 24 h, the anti-bacteria efficiency maintained higher than 72% for H-NiTi and 66% for CS-NiTi. These results indicated that CS-NiTi had excellent long-term anti-bacteria property. Moreover, ICP was employed for exploring the performance of Ni^{2+} ion capture by monitoring the concentration of Ni^{2+} ions in bacteria suspension (1×10^8 CFU/ml). As shown in **Figure 3C**, the concentration of Ni^{2+} ions in CS-NiTi was significantly lower than that of NiTi and H-NiTi. Even though it was incubated for 24 h, the concentration of Ni^{2+} ions for CS-NiTi was still as low as 0.38 ± 0.07 mg/L, indicating the excellent ability of Ni^{2+} ion capture of CS-NiTi. Therefore, CS-NiTi showed dual properties of anti-bacteria and Ni^{2+} ion capture at the same time.

Mechanism of Ni^{2+} Ion Capture

To further investigate the performance of Ni^{2+} ion capture, a series of CS-NiTi were fabricated by regulating the CS_2 concentration in the mixed solution, that is, 0.2 mol/L of CS_2 for low concentration (denoted as LCS-NiTi), 0.6 mol/L of CS_2 for medium concentration (MCS-NiTi), and 1.0 mol/L of CS_2 for high concentration (HCS-NiTi). With the increasing concentration of Ni-catchers, the surface became more hydrophilic, revealing by the WCAs changing from $73.0 \pm 2.8°$ to $59.0 \pm 3.4°$, along with the increased pore size (**Supplementary Figures 4A,B**). Furthermore, the appearance of CS-hydrogel changed from colorless with high transparency to yellow with reduced transparency (**Supplementary Figure 4C**). To verify the long-term ability of Ni^{2+} ion capture, we incubated H-NiTi, LCS-NiTi, MCS-NiTi, and HCS-NiTi with *S. mutans* suspensions for different days. After the incubation, the concentration of leaked Ni^{2+} ions from NiTi alloy was reduced from 0.91 ± 0.01 mg/L (H-NiTi) to 0.65 ± 0.02 mg/L (HCS-NiTi) with the incubation time of 1 day (**Figures 4A–D**). By prolonging the incubation time to 5 days, the concentration of leaked Ni^{2+} ions increased to 1.12 ± 0.03 mg/L for H-NiTi gradually. On the contrary, the concentration of leaked Ni^{2+} ions in HCS-NiTi reduced from 0.65 ± 0.02 to 0.48 ± 0.07 mg/L dramatically, indicating its excellent long-term property of Ni^{2+} ion capture.

The possible mechanism of Ni^{2+} ion capture is proposed in **Figures 4E–H**. Due to the corrosion of the adhered bacteria and acidic oral microenvironment, Ni^{2+} ions are released slowly and persistently from NiTi alloy (Huang et al., 2003). Briefly, the leaked Ni^{2+} ions can pass through the zwitterionic hydrogel coating on the surface of NiTi alloy and be released to oral environment easily (**Figure 4E**), as the diffusion of Ni^{2+} ions is not efficiently restricted in single zwitterionic hydrogel. In contrast, the concentration of Ni^{2+} ions is dramatically decreased after introducing Ni-catchers because grafted CS_2 can capture free Ni^{2+} ions and restrain their diffusion to oral environment (**Figures 4F–H**). Moreover, the long-term capture efficiency of

Ni^{2+} ions is improved with the increasing concentration of Ni-catchers. Therefore, the introduction of Ni-catchers endows CS-NiTi with robust Ni^{2+} ion capture property.

DISCUSSION

In summary, we demonstrate a long-term Ni^{2+} ion capture coating on the surface of NiTi alloy. The zwitterionic hydrogels and Ni-catchers endow CS-NiTi with excellent anti-bacteria and Ni^{2+} ion capture properties. The CS-NiTi exhibited long-term anti-bacteria efficiency of ca. 66% at 24 h and Ni^{2+} ion capture efficiency of ca. 57% at 5 days. Furthermore, by integrating chelation reaction and introducing color change, this coating may apply to Ni^{2+} ion capture and detection. Therefore, this coating provides a new clue to design the next generation of biomaterials and devices with capture and detection of Ni^{2+} ions.

DATA AVAILABILITY STATEMENT

The raw data supporting the conclusions of this article will be made available by the authors, without undue reservation.

AUTHOR CONTRIBUTIONS

QN and JM conceived the idea. DH and XF contributed the fabrication process. XF and WX performed the experiments. XF and XL analyzed the results. XF, XL, QN, and JM wrote the manuscript. All authors contributed to the article and approved the submitted version.

FUNDING

This research is supported by the National Natural Science Foundation of China (Nos. 51973003, 21875269, and 21988102), National Key R&D Program of China (Nos. 2019YFA0709300 and 2018YFC1105301), and Youth Innovation Promotion Association, CAS (No. 2017036).

SUPPLEMENTARY MATERIAL

The Supplementary Material for this article can be found online at: https://www.frontiersin.org/articles/10.3389/fbioe.2021.698745/full#supplementary-material

REFERENCES

Deng, M., Karpuzov, D., Liu, Q., and Xu, Z. (2013). Cryo-XPS study of xanthate adsorption on pyrite. *Surf. Interface Anal.* 45, 805–810. doi: 10.1002/sia.5165

Gu, Y. W., Tay, B. Y., Lim, C. S., and Yong, M. S. (2005). Characterization of bioactive surface oxidation layer on NiTi alloy. *Appl. Surf. Sci.* 252, 2038–2049. doi: 10.1016/j.apsusc.2005.03.207

Hang, R., Liu, S., Liu, Y., Zhao, Y., Bai, L., Jin, M., et al. (2019). Preparation, characterization, corrosion behavior and cytocompatibility of $NiTiO_3$ nanosheets hydrothermally synthesized on biomedical NiTi alloy. *Mater. Sci. Eng. C* 97, 715–722. doi: 10.1016/j.msec.2018.12.124

Hang, R., Ma, S., and Chu, P. K. (2012). Effects of diamond-like carbon coatings with different thickness on mechanical properties and corrosion behavior of biomedical NiTi alloy. *Rare Metal Mater. Eng.* 41, 1505–1510. doi: 10.1016/s1875-5372(13)60001-6

Hartono, M. R., Kushmaro, A., Chen, X., and Marks, R. S. (2018). Probing the toxicity mechanism of multiwalled carbon nanotubes on bacteria. *Environ. Sci. Pollut. Res.* 25, 5003–5012. doi: 10.1007/s11356-017-0782-8

Huang, H. H., Chiu, Y. H., Lee, T. H., Wu, S. C., Yang, H. W., Su, K. H., et al. (2003). Ion release from NiTi orthodontic wires in artificial saliva with various acidities. *Biomaterials* 24, 3585–3592. doi: 10.1016/s0142-9612(03)00188-1

Jia, W., Beatty, M. W., Reinhardt, R. A., Petro, T. M., Cohen, D. M., Maze, C. R., et al. (1999). Nickel release from orthodontic arch wires and cellular immune response to various nickel concentrations. *J. Biomed. Mater. Res.* 48, 488–495. doi: 10.1002/(sici)1097-4636(1999)48:4<488::aid-jbm14<3.0.co;2-d

Kolokitha, O. E. G., and Chatzistavrou, E. (2008). Allergic reactions to nickel-containing orthodontic appliances: clinical signs and treatment alternatives. *World J. Orthod.* 9, 399–406.

Li, G., Cheng, G., Xue, H., Chen, S., Zhang, F., and Jiang, S. (2008). Ultra low fouling zwitterionic polymers with a biomimetic adhesive group. *Biomaterials* 29, 4592–4597. doi: 10.1016/j.biomaterials.2008.08.021

Lin, X., Wu, K., Zhou, Q., Jain, P., Boit, M. O., Li, B., et al. (2020). Photoreactive carboxybetaine copolymers impart biocompatibility and inhibit plasticizer leaching on polyvinyl chloride. *ACS Appl. Mater. Interfaces* 12, 41026–41037. doi: 10.1021/acsami.0c09457

Liu, R., Liu, X., Zhou, J., Nie, Q., Meng, J., Lin, J., et al. (2019). Bioinspired superhydrophobic Ni-Ti archwires with resistance to bacterial adhesion and nickel ion release. *Adv. Mater. Interfaces* 6:1801569. doi: 10.1002/admi.201801569

Liu, X., Peng, L., Meng, J., Zhu, Z., Han, B., and Wang, S. (2018). Protein-mediated anti-adhesion surface against oral bacteria. *Nanoscale* 10, 2711–2714. doi: 10.1039/c7nr08844b

Peng, L., Chang, L., Liu, X., Lin, J., Liu, H., Han, B., et al. (2017). Antibacterial property of a polyethylene glycol-grafted dental material. *ACS Appl. Mater. Interfaces* 9, 17688–17692. doi: 10.1021/acsami.7b05284

Poon, R. W. Y., Yeung, K. W. K., Liu, X. Y., Chu, P. K., Chung, C. Y., Lu, W. W., et al. (2005). Carbon plasma immersion ion implantation of nickel-titanium shape memory alloys. *Biomaterials* 26, 2265–2272. doi: 10.1016/j.biomaterials.2004.07.056

Raphel, J., Holodniy, M., Goodman, S. B., and Heilshorn, S. C. (2016). Multifunctional coatings to simultaneously promote osseointegration and prevent infection of orthopaedic implants. *Biomaterials* 84, 301–314. doi: 10.1016/j.biomaterials.2016.01.016

Robertson, S. W., and Ritchie, R. O. (2007). In vitro fatigue-crack growth and fracture toughness behavior of thin-walled superelastic Nitinol tube for endovascular stents: a basis for defining the effect of crack-like defects. *Biomaterials* 28, 700–709. doi: 10.1016/j.biomaterials.2006.09.034

Shivapooja, P., Yu, Q., Orihuela, B., Mays, R., Rittschof, D., Genzer, J., et al. (2015). Modification of silicone elastomer surfaces with zwitterionic polymers: short-term fouling resistance and triggered biofouling release. *ACS Appl. Mater. Interfaces* 7, 25586–25591. doi: 10.1021/acsami.5b09199

Su, X., Hao, D., Xu, X., Guo, X., Li, Z., and Jiang, L. (2020). Hydrophilic/hydrophobic heterogeneity anti-biofouling hydrogels with well-regulated rehydration. *ACS Appl. Mater. Interfaces* 12, 25316–25323. doi: 10.1021/acsami.0c05406

Sunderman, F. W. (1990). Use of sodium diethyldithiocarbamate in the treatment of nickel carbonyl poisoning. *Ann. Clin. Lab. Sci.* 20, 12–21.

Sylvestre, M., Crane, C. A., and Pun, S. H. (2020). Progress on modulating tumor-associated macrophages with biomaterials. *Adv. Mater.* 32:1902007. doi: 10.1002/adma.201902007

Wei, T., Zhan, W., Cao, L., Hu, C., Qu, Y., Yu, Q., et al. (2016). Multifunctional and regenerable antibacterial surfaces fabricated by a universal strategy. *ACS Appl. Mater. Interfaces* 8, 30048–30057. doi: 10.1021/acsami.6b11187

Wei, T., Zhan, W., Yu, Q., and Chen, H. (2017). Smart biointerface with photoswitched functions between bactericidal activity and bacteria-releasing

ability. *ACS Appl. Mater. Interfaces* 9, 25767–25774. doi: 10.1021/acsami.7b06483

Weißl, M., Niegelhell, K., Reishofer, D., Zankel, A., Innerlohinger, J., and Spirk, S. (2018). Homogeneous cellulose thin films by regeneration of cellulose xanthate: properties and characterization. *Cellulose* 25, 711–721. doi: 10.1007/s10570-017-1576-3

Wu, S. L., Chu, P. K., Liu, X. M., Chung, C. Y., Ho, J. P. Y., Chu, C. L., et al. (2006). Surface characteristics, mechanical properties, and cytocompatibility of oxygen plasma-implanted porous nickel titanium shape memory alloy. *J. Biomed. Mater. Res. A* 79A, 139–146. doi: 10.1002/jbm.a.30705

Xiao, W. Y., Wang, Y., An, H. W., Hou, D., Mamuti, M., Wang, M. D., et al. (2020). Click reaction-assisted peptide immune checkpoint blockade for solid tumor treatment. *ACS Appl. Mater. Interfaces* 12, 40042–40051. doi: 10.1021/acsami.0c10166

Conflict of Interest: The authors declare that the research was conducted in the absence of any commercial or financial relationships that could be construed as a potential conflict of interest.

frontiers in Bioengineering and Biotechnology

ORIGINAL RESEARCH
published: 14 September 2021
doi: 10.3389/fbioe.2021.731415

Nanoparticle-Based Lateral Flow Biosensors Integrated With Loop-Mediated Isothermal Amplification for the Rapid and Visual Diagnosis of Hepatitis B Virus in Clinical Application

Xu Chen[1,2†], Shoshi Wang[2†], Yan Tan[3†], Junfei Huang[4], Xingui Yang[4] and Shijun Li[4*]*

[1]The Second Clinical College, Guizhou University of Traditional Chinese Medicine, Guiyang, China, [2]Central Laboratory of the Second Affiliated Hospital, Guizhou University of Traditional Chinese Medicine, Guiyang, China, [3]Guizhou Provincial Center for Clinical Laboratory, Guiyang, China, [4]Laboratory of Bacterial Infectious Disease of Experimental Centre, Guizhou Provincial Centre for Disease Control and Prevention, Guiyang, China

Hepatitis B virus (HBV) infection remains one of the major public health issues worldwide. Developing a rapid, sensitive, specific, easy-to-operate, and cost-saving approach for the diagnosis of HBV is essential for its therapy and prevention. Here, we first devised a novel approach, termed "loop-mediated isothermal amplification integrated with a nanoparticle-based lateral flow biosensor (LAMP-LFB)," for the detection of HBV in clinical application. The results indicated that a set of LAMP primers based on the *S* gene were valid for the establishment of HBV-LAMP-LFB. The optimal HBV-LAMP can be carried out at a constant temperature of 65°C for 40 min. The whole detection process, including HBV genomic DNA preparation (~10 min), LAMP (40 min), and LFB reading (within 2 min), can be accomplished within 60 min. The limit of detection of the HBV-LAMP-LFB assay was 7.5 IU per test. The specificity of this assay was one hundred percent, and there was no cross-reactivity with other pathogens. Hence, these results indicated that the HBV-LAMP-LFB assay established in the current study is a sensitive, rapid, specific, visual, simple, and cost-saving method for the screening of HBV agents. More importantly, the HBV-LAMP-LFB has remarkable potential to develop a point-of-care testing in clinical application, especially in resource-scarce regions.

Keywords: hepatitis B virus, loop-mediated isothermal amplification, lateral flow biosensor, rapid of detection, limit of detection

Abbreviations: BC, blank control; CL, control line; DW, distilled water; FAM, 6-carboxy-fluorescein; GZCDC, Guizhou Provincial Center for Disease Control and Prevention; HBV, hepatitis B virus; HCV, hepatitis C virus; HIV, human immunodeficiency virus; mer, monomeric unit; MG, malachite green; NC, negative control; NCBI, National Centre for Biotechnology Information; nt, nucleotide; POCT, point-of-care testing; second GZUTCM, Second Affiliated Hospital, Guizhou University of Traditional Chinese Medicine; TL, test line; WHO, World Health Organization.

OPEN ACCESS

Edited by:
Tailin Xu,
Shenzhen University, China

Reviewed by:
Yan Huang,
University of Science and Technology Beijing, China
Yongqiang Wen,
University of Science and Technology Beijing, China
Yibiao Liu,
Shenzhen University, China

***Correspondence:**
Xu Chen
xuchen1220@com
Shijun Li
zjumedjun@163.com

†These authors have contributed equally to this work

Specialty section:
This article was submitted to Biosensors and Biomolecular Electronics, a section of the journal Frontiers in Bioengineering and Biotechnology

Received: *27 June 2021*
Accepted: *28 July 2021*
Published: *14 September 2021*

Citation:
Chen X, Wang S, Tan Y, Huang J, Yang X and Li S (2021) Nanoparticle-Based Lateral Flow Biosensors Integrated With Loop-Mediated Isothermal Amplification for the Rapid and Visual Diagnosis of Hepatitis B Virus in Clinical Application. Front. Bioeng. Biotechnol. 9:731415. doi: 10.3389/fbioe.2021.731415

INTRODUCTION

Hepatitis B virus (HBV) is a life-threatening pathogen that can cause acute and chronic infection and puts people at high risk of death from cirrhosis and liver cancer (Bollinger et al., 2020; Liaw, 2019). Generally, HBV spreads through blood or blood-related products from HBV-infected patients. Most people do not experience any symptoms when newly infected with HBV. When the disease progresses, some people show jaundice, extreme fatigue, nausea, acute liver failure, hepatitis, liver cirrhosis, and hepatocellular carcinoma (Blackard and Sherman, 2018; Revill et al., 2019). It is hard to detect HBV-infected cases, owing to the absence of hepatitis B surface antigen and a low amount of HBV-DNA in blood at the early stage of HBV infection (Liang, 2009; Tong and Revill, 2016). The problem mainly compounded by the lack of advanced diagnostic methods and medical services for donor screening or routine testing of patients. Hence, developing a rapid, sensitive, specific, easy-to-use assay is critical for addressing the burden of HBV infection.

Traditionally, enzyme-linked immunosorbent assay (ELISA) and real-time quantitative polymerase chain reaction (qPCR) have been widely used to probe HBV based on HBsAg and HBV-DNA (Mallika, 2015; Villar et al., 2015). However, the sensitivity of the ELISA was remarkably low, especially in the early stage of HBV infection (Sara, 2011). In recent decades, nucleic acid amplification technologies (NAATs), including polymerase chain reaction (PCR) and real-time quantitative PCR were considered as good alternative methods for the diagnosis of HVB infection owing to being more sensitive than ELISA (Jain et al., 2018; Coffin et al., 2019). Nevertheless, these methods need special laboratory layout and expensive instruments that may not be readily available in many resource-shortage settings. Moreover, it is time-consuming (approximately 130 min). Herein, developing a cost-effective, rapid, simple, sensitive, and specific assay for identification of HBV is necessary for the diagnosis of blood donors and HBV-infected patients.

To address the shortcomings of these approaches, loop-mediated isothermal amplification (LAMP), a rapid and simple NAAT, has been devised and gradually applied to the diagnosis of many pathogens, such as human papillomavirus, influenza virus, and severe acute respiratory syndrome coronavirus 2 (Zhu et al., 2020; Landaverde et al., 2020; Le Thi et al., 2020), which can robust amplify the target sequence at a fixed temperature (58–69°C) for 30–60 min. The primer set includes a pair of outer primers (F3 and B3), loop primers (LF and LB), and inner primers (FIP and BIP) (Seki et al., 2018). Then, analysis of the LAMP reactions has become another major concern. Conventionally, agarose gel electrophoresis, fluorescent agents, real-time turbidimetry, and colorimetric indicators (MG reagent) have been widely used to read out LAMP products (Romero and Cook, 2018; Kubota and Jenkins, 2015; Notomi et al., 2000). However, these methods require special facilities and reagents. To overcome these drawbacks, the gold nanoparticle-based lateral flow biosensor (LFB) with easy accessibility, good robustness, visualization, low limits of detection, and specificity features has been reported for the detection of nucleic acid and protein molecules in recent years (Quesada-Gonzá lez and Merkoçi, 2015; Huang et al., 2021).

In this study, the loop-mediated isothermal amplification integrated with the gold nanoparticle-based lateral flow biosensor (LAMP-LFB) was devised first for rapid, visual, simple, specific, and sensitive identification of HBV by targeting on the *S* gene (Nyan et al., 2014). The principle of the HBV-LAMP-LFB is illustrated in **Figure 1**, and its feasibility was validated with clinical samples.

MATERIALS AND METHODS

Standard Panels and Clinical Samples Preparation

HBV, hepatitis C virus (HCV), and human immunodeficiency virus (HIV) nucleic acid standard substances were obtained from the Chinese Academy of Metrology (Code No. GBW09150, GBW(E)090118, and GBW(E)090272, respectively). 115 clinical serum specimens were collected from patients with suspected HBV infection at the Second Affiliated Hospital, Guizhou University of Traditional Chinese Medicine (Guizhou, China), during June 2019 to May 2020 and stored at −80°C until use; other non-HBV pathogens used in the current study are shown in **Table 1**. The genomic DNA templates were extracted using nucleic acid-releasing agents (Sansure Biotech, Changsha, China) in accordance with the manufacturer's instructions and stored at −20°C before use. The concentrations were measured using NanoDrop ND-2000 (Beijing, China) at A260/280.

MATERIALS AND INSTRUMENTS

Microbial nucleic acid-releasing agents were obtained from Sansure Biotech (Changsha, China). The colorimetric indicator (malachite green, MG), isothermal amplification kits, and gold nanoparticle-based LFB were obtained from HuiDeXin Biotechnique (Tianjin, China). The dye streptavidin-coated gold nanoparticles (streptavidin-GNPs) were obtained from HuiDeXing Biotech Co., Ltd. (Tianjing, China); the size of GNPs is 34.46 ± 4.34 nm, and the extinction coefficient of GNPs is $6.0 \times 10^9\ M^{-1}\ cm^{-1}$ at 506 nm. Biotin-BSA (biotinylated bovine serum albumin) and anti-FAM (rabbit anti-fluorescein antibody) were purchased from Abcam Co., Ltd. (Shanghai, China). The real-time turbidimeter (LA-500) was obtained from Eiken Chemical Co., Ltd. (Japan). The HBV real-time quantification PCR diagnosis kit was obtained from DaAn Gene Co., Ltd. (Guangzhou, China).

Construction of the Gold Nanoparticle-Based Lateral Flow Biosensor

The gold nanoparticle-based LFB (60 mm × 4 mm) used in the current study is devised and elaborated in **Figure 2**. In brief, the biosensor consists of four sections, including sample pad, conjugate pad, nitrocellulose (NC) membrane, and absorbent

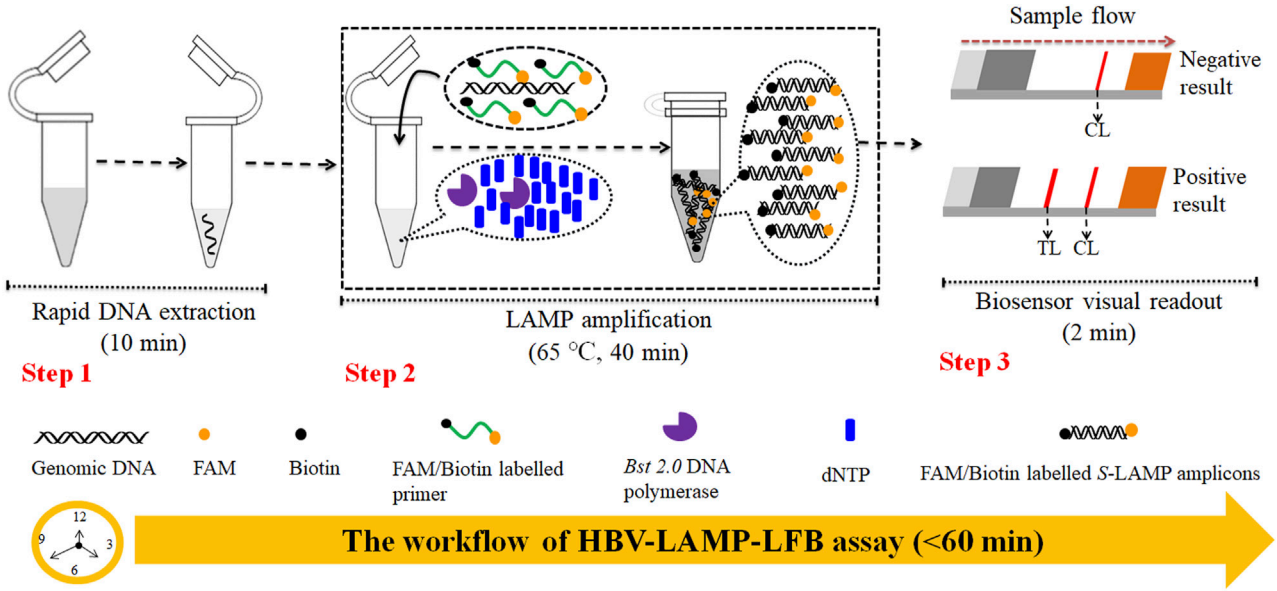

FIGURE 1 | Outline of the HVB-LAMP-LFB workflow. The HVB-LAMP-LFB assay system contains three closely linked steps: DNA extraction (step 1), LAMP (step 2), and gold nanoparticle-based LFB readout (step 4). The whole detection process can be completed within 60 min.

TABLE 1 | Pathogens used in this study.

No.	Pathogen	Pathogen no. (source of pathogens)[a]	No. of strains	LAMP-LFB result[b]
1	HBV (standard substance)	The Chinese Academy of Metrology	1	P
2	HBV(clinical samples)	2nd GZUTCM	13	P
3	HCV (standard substance)	The Chinese Academy of Metrology	1	N
4	HIV (standard substance)	The Chinese Academy of Metrology	1	N
5	H1N1 (nucleic acid samples)	GZCDC	1	N
6	Influenza B	GZCDC	1	N
7	Respiratory syncytial virus type A	GZCDC	1	N
5	Human rhinovirus	GZCDC	1	N
7	Adenoviruses	GZCDC	1	N
8	*Mycobacterium tuberculosis*	GZCDC	1	N
9	*Pseudomonas aeruginosa*	2nd GZUTCM	1	N
10	*Mycoplasma pneumoniae*	2nd GZUTCM	1	N
11	*Streptococcus pneumoniae*	2nd GZUTCM	1	N
12	*Mycoplasma pneumonia* M129/FH	2nd GZUTCM	1	N
13	*Haemophilus influenzae*	ATCC49247	1	N
14	*Streptococcus pyogenes*	2nd GZUTCM	1	N
15	*Staphylococcus aureus*	2nd GZUTCM	1	N
16	*Acinetobacter baumannii*	2nd GZUTCM	1	N
17	*Leptospira interrogans*	GZCDC	1	N
18	*Shigella flexneri*	2nd GZUTCM	1	N
19	*Bacillus cereus*	GZCDC	1	N
20	*Bordetella parapertussis*	GZCDC	1	N
21	*Bordetella pertussis*	GZCDC	1	N
22	Enteropathogenic *Escherichia coli*	GZCDC	1	N
23	*Candida glabrata*	2nd GZUTCM	1	N
24	*Cryptococcus neoformans*	ATCC14053	1	N
25	*Hemophililus parainfluenzae*	GZCDC	1	N

[a]*2nd GZUTCM, The Second Affiliated Hospital, Guizhou University of Traditional Chinese Medicine; GZCDC, Guizhou Provincial Center for Disease Control and Prevention; ATCC, American Type Culture Collection.*
[b]*P, Positive; N, Negative.*

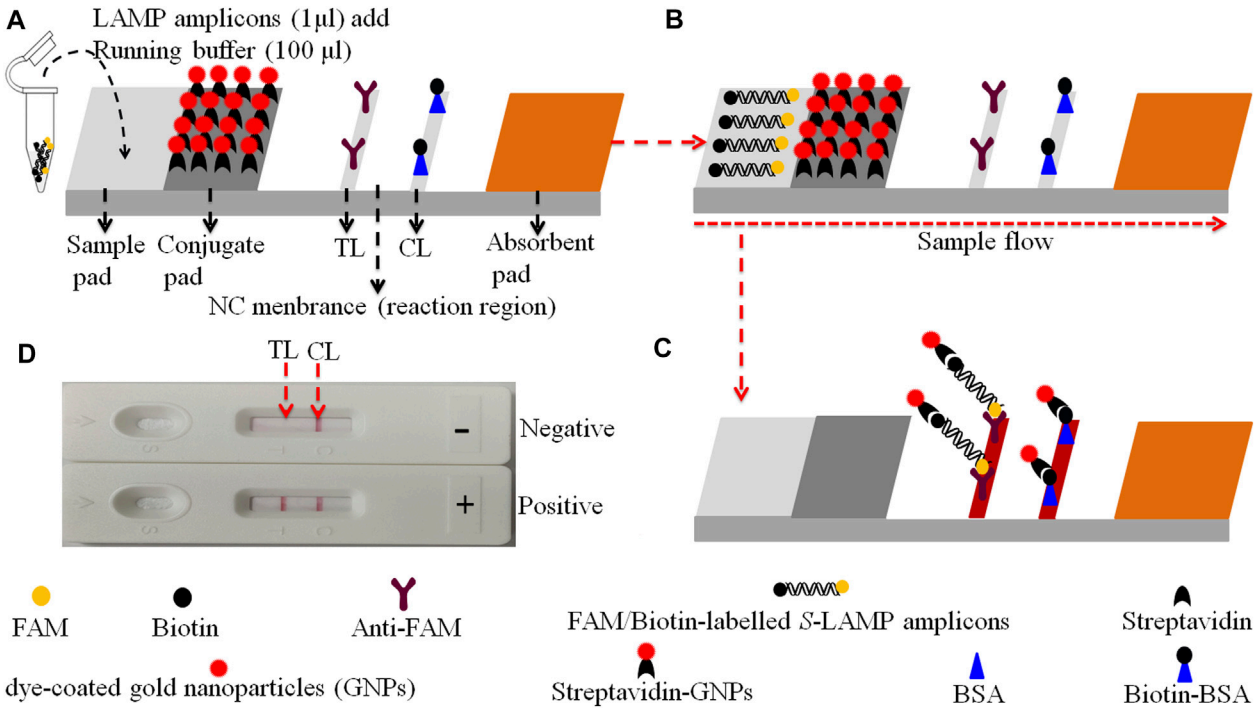

FIGURE 2 | The schematic of the gold nanoparticle-based LFB for the visualization of HVB-LAMP-LFB products. **(A)** The biotin/FAM-labeled HBV-LAMP amplicons (1.0 μL) and the running buffer (100 μL) were added to the sample pad. **(B)** The running buffer containing LAMP products will be moved along the LFB owing to capillary action; meanwhile, the dye streptavidin-coated gold nanoparticles (streptavidin-GNPs) were rehydrated on the conjugate region. **(C)** In the positive sample, the biotin/FAM-labeled HBV-LAMP amplicons were captured by the anti-FAM at the TL and the streptavidin-GNPs were captured by the biotin-BSA at the CL, respectively. However, in negative results, only the streptavidin-GNPs were captured by biotin-BSA at the CL. **(D)** Interpretation of the HBV-LAMP-LFB assay results. For positive results, CL and TL appear on the biosensor, whereas only the CL was observed on the biosensor, indicating negative outcomes.

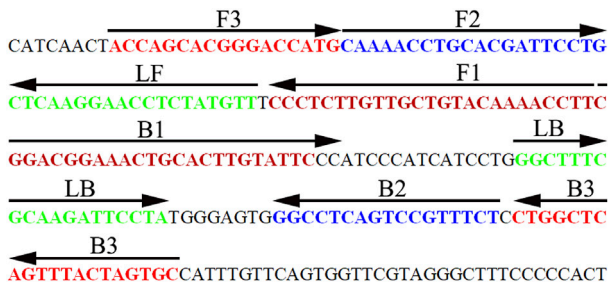

FIGURE 3 | Sequence and location of the HBV-specific *S* gene used to design HBV-LAMP-LFB primers. The nucleotide sequence of the sense strand of the HBV *S* gene is shown in the diagram. Right arrows and left arrows indicate sense and complementary sequences, respectively.

pad (HuiDeXing Biotech Co., Ltd. (Tianjing, China) (Code No. HT100003). The detector reagents (dye streptavidin-coated gold nanoparticles (streptavidin-GNPs), 129 nm, 10 mg·ml^{-1}; 100 mM borate, pH 8.5 with 0.05% Tween 20; 0.1% BSA; and 10 mM EDTA) were laminated onto the conjugate pad. Biotin-BSA (4 mg·ml^{-1}; Abcam) and rabbit anti-FAM (0.25 mg·mL^{-1}; Abcam) were coupled onto the NC membrane for the control line (CL) and test line (TL), respectively. Each band was separated by 5 mm. In the end, the assembled biosensor was preserved in a plastic box and conserved with a silica gel desiccant at room temperature.

Design and Synthesis of Hepatitis B Virus–Loop-Mediated Isothermal Amplification Primers

Three pairs of HBV-LAMP special primers based on the *S* gene (GenBank Accession No. AB809557.1) were designed through Primer Explorer V5 and PRIMER PREMIER 5.0 software (Eiken Chemical, Japan). The HBV-LAMP primers were analyzed with the basic local alignment search tool (BLAST) for the primer sets to validate sequence specificity. The position of each primer is shown in **Figure 3**, and the sequences and modifications are shown in **Table 2**. All of the oligomers were synthesized and purified by TsingKe Biotech Co., Ltd. (Beijing, China) at an HPLC purification grade.

The Standard Hepatitis B Virus–Loop-Mediated Isothermal Amplification Reaction

The HBV-LAMP was carried out in a 25 μL reaction system, including 12.5 μL of 2 × reaction buffer (40 mM Tris-HCl (pH 8.8), 40 mM KCl, 16 mM $MgSO_4$, 20 mM $(NH_4)_2SO_4$, 2 M

TABLE 2 | The primers used in the present study.

Primer name	Sequence and modifications	Length	Gene
F3	5′-ACCAGCACGGGACCATG-3′	17 nt	*S*
B3	5′-GCACTAGTAAACTGAGCCAG-3′	20 nt	
FIP*	5′-FAM-AAGGTTTTGTACAGCAACAAGAGGG-CAAAACCTGCACGATTCCTG-3′	45 mer	
BIP	5′-CGGACGGAAACTGCACTTGTATTC-AGAAACGGACTGAGGCC-3′	41 nt	
LF*	5′-Biotin-AACATAGAGGTTCCTTGAG-3′	19 nt	
LB	5′-GGCTTTCGCAAGATTCCTA-3′	19 nt	

FIP, 5′-labeled with FAM when used in the HBV-LAMP-LFB assay; LF*, 5′-labeled with biotin when used in the HBV-LAMP-LFB assay; FAM, 6-carboxy-fluorescein; nt, nucleotide; mer, monomeric unit.*

betaine, and 0.2% Tween-20), 1 μL genomic template, 0.4 μM each of outer primer F3 and B3, 1.6 μM each of inner primer FIP* and BIP, 0.8 μM each of loop primer LF* and LB, 1 μL (8U) of *Bst 2.0* DNA polymerase, 1 μL (10U) of AMV reverse transcriptase (for RNA virus only), and 1 μl colorimetric indicator (MG), along with addition of double distilled water to 25 μL. The LAMP was performed at 64°C for 1 h. HCV and HIV were used as negative controls (NCs), and double distilled water (DW) was used as the template in blank control (BC).

Detection of Hepatitis B Virus–Loop-Mediated Isothermal Amplification Products

Four monitoring techniques, including 2% agarose gel electrophoresis, colorimetric indicator (MG), real-time turbidimeter, and gold nanoparticle-based LFB, were used for the detection and confirmation of the LAMP products. For positive results, the agarose gel presented ladder-like bands and the color changed from colorless to light green in the reaction system. However, there were no bands in gel electrophoresis and it was colorless in NC and BC. For real-time turbidity measurement, turbidity >0.1 is considered as the positive result. With LFB detection, two visible red lines (CL and TL) appeared simultaneously indicating a positive result, and only the CL was observed for a negative outcome.

Temperature Optimization of the Hepatitis B Virus–Loop-Mediated Isothermal Amplification Assay

Reaction temperature is of vital importance to LAMP. In this study, the reaction temperature was tested in a range from 60 to 67°C with 1°C interval for 60 min. The LAMP products were monitored using real-time turbidity (LA-500). Each temperature was tested independently at least thrice.

Sensitivity of the Hepatitis B Virus–Loop-Mediated Isothermal Amplification-Lateral Flow Biosensor Assay

To identify the limit of detection (LoD) of the HBV-LAMP-LFB assay, HBV nucleic acid standard substances (Chinese Academy of Metrology) were serially diluted 10-fold from 1.0×10^4 to 1.0×10^{-1} IU. The HBV-LAMP operation is as described above, and the LAMP products were analyzed simultaneously with MG and LFB. The sensitivity of HBV-LAMP-LFB was confirmed as the last dilution of each positive test. All examinations were confirmed in triplicate.

Optimization of Amplification Time for the Hepatitis B Virus–Loop-Mediated Isothermal Amplification–Lateral Flow Biosensor Assay

In order to optimize the reaction time for preamplification of the assay, four reaction time periods ranging from 20 to 50 min with 10 min interval were tested at the optimal amplification temperature. The HBV-LAMP products were analyzed with the MG reagent and LFB. Each of the reaction time was tested independently in triplicate.

Analytical Specificity of the Hepatitis B Virus–Loop-Mediated Isothermal Amplification-Lateral Flow Biosensor Assay

The HBV nucleic acid standard substance, 13 HBV-positive clinical samples, and 25 non-HBV pathogens (**Table 1**) were employed for testing the specificity of HBV-LAMP-LFB. The operation was performed as described above. All of the LAMP amplicons were analyzed through the LFB. Each sample was identified at least three times.

Confirming the Feasibility of the Hepatitis B Virus–Loop-Mediated Isothermal Amplification–Lateral Flow Biosensor Assay Using Clinical Samples

In order to confirm the applicability of HBV-LAMP-LFB assay in clinical setting, 115 serum samples with suspected HBV infection were collected from the Second Affiliated Hospital of Guizhou University of Traditional Chinese Medicine. All of the clinical specimens were evaluated simultaneously using qPCR and HBV-LAMP-LFB. The qPCR diagnosis was carried out using a commercial real-time TaqMan PCR kit (DaAn Gene Co., Ltd. China), and the detection was carried out with the Applied Biosystems™ 7,500 Real-Time PCR system (Life Technologies, Singapore). The concentrations of HBV less than 30 IU will be considered as the negative result according to the manufacturer's instructions. The HBV-LAMP-LFB operation is as described above.

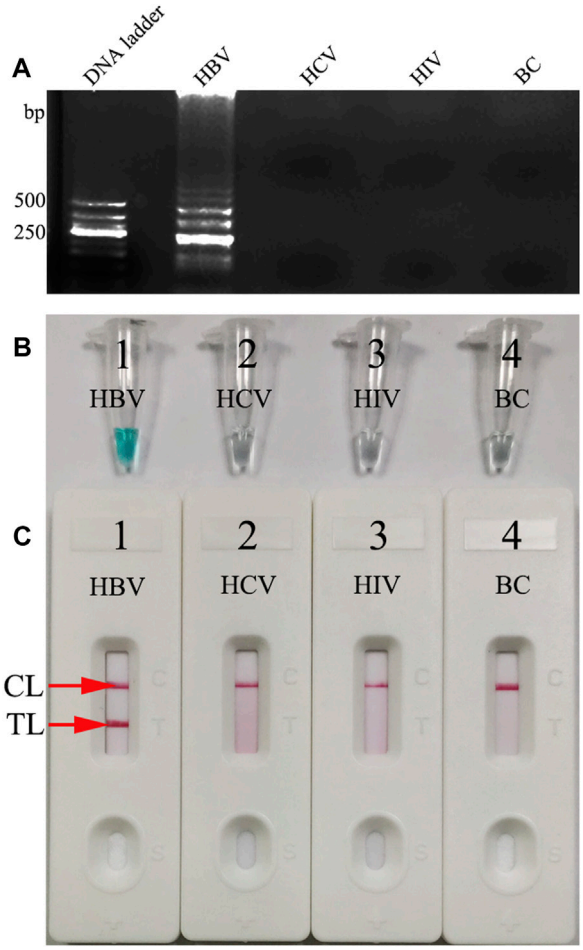

FIGURE 4 | Determination and confirmation of HBV-LAMP products. The HBV-LAMP products were analyzed by 2% agarose gel electrophoresis **(A)** with the MG reagent **(B)** and LFB **(C)**. Lane DNA ladder: 500-bp DNA ladder; the ladder-like bands indicate positive LAMPs **(A)**. The color change from colorlessness to bright green indicates positive nucleic acid amplifications **(B)**. Two visible red lines (CL and TL) appeared for positive results **(C)**. However, there was no band in gel electrophoresis **(A)**, the color remains colorless **(B)**, and only the CL was observed **(C)** in NC and BC.

In the current study, each test was repeated at least three times for repeatability.

RESULTS

Overview of the Hepatitis B Virus–Loop-Mediated Isothermal Amplification–Lateral Flow Biosensor Assay System

The principle of HBV-LAMP-LFB assay is illustrated in **Figure 1**. In brief, the HBV genomic DNA was extracted using nucleic acid–releasing agents within 10 min, and then, preamplification was carried out at a fixed temperature (65°C) for 40 min. We modified the LAMP primers LF and FIP at 5'-end with biotin and FAM, respectively. The HBV-LAMP amplicons were labeled with biotin and FAM; finally, the LAMPs were read out with LFB (**Figure 1**). For biosensor detection, the dye streptavidin-coated gold nanoparticles (streptavidin-GNPs) were laminated onto the conjugate pad, by adding 1.0 μL of HBV-LAMP products and 100 μL of running buffer (100 mM PBS, pH 7.4 with 1% Tween 20) (Zhu et al., 2021) to the sample pad. The running buffer containing HBV-LAMP products were absorbed, and the detection results were read out visually on the NC membrane (red line) within 2 min. In the positive sample, the biotin/FAM-labeled HBV-LAMP amplicons were captured by anti-FAM at the TL and streptavidin-GNPs were captured by biotin-BSA at the CL. However, in negative results, only the streptavidin-GNPs were captured the biotin-BSA at the CL (**Figure 2**).

Confirmation and Verification of Hepatitis B Virus–Loop-Mediated Isothermal Amplification Assay

In order to identify the availability of the set of LAMP primers for the HBV assay, the LAMP reactions were performed in the presence and absence of HBV DNA (Chinese Academy of Metrology) as the template at a constant temperature of 64°C for 1 h. Then, the LAMP products were monitored simultaneously by 2% agarose gel electrophoresis, with a colorimetric indicator (MG) and LFB. The results showed that the positive outcomes appeared with the nucleic acid from HBV, but not from HCV, HIV, and BC (**Figures 4A–C**). Therefore, these results suggested that the set of HBV-LAMP primers for *S* gene designed here was valid for the development of the HBV-LAMP-LFB assay.

Optimal Reaction Temperature for Hepatitis B Virus–Loop-Mediated Isothermal Amplification Assay

To determine the optimal reaction temperature at the preamplification stage, a HBV-LAMP reaction was carried out at a range from 60 to 67°C (with 1°C interval) with 100 IU of HBV nucleic acid as the template per test. The results were monitored by real-time turbidity (LA-500). The kinetic data showed that the robust reactions of HBV-LAMP were obtained at the reaction temperature range from 65 to 67°C (**Figure 5**). Hence, 65°C was selected as the optimal amplification temperature for the HBV-LAMP-LFB assay.

Sensitivity of the Hepatitis B Virus–Loop-Mediated Isothermal Amplification–Lateral Flow Biosensor Assay

The sensitivity of the HBV-LAMP-LFB assay was verified with serial dilutions of the HBV DNA standard substance (ranging from 1.0×10^4 to 1.0×10^{-1} IU) as the template, and the LAMP products were visually read out with the MG reagent and LFB,

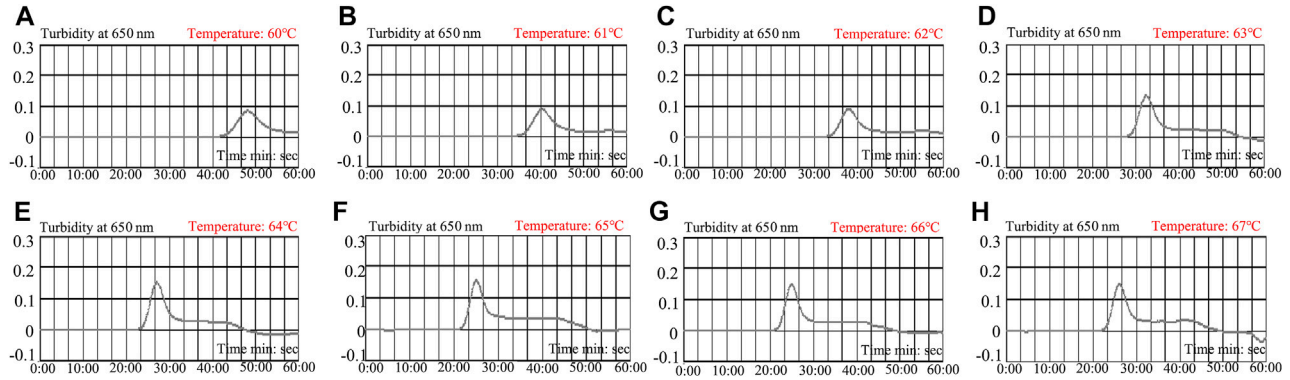

FIGURE 5 | Optimization of amplification temperature for the HBV-LAMP primer set. The LAMP reactions for the detection of HBV were monitored through real-time turbidity (LA-500), and the corresponding curves of DNA concentrations are displayed in the graph. The threshold value > 0.1 was considered as the positive result. 8 kinetic graphs were obtained at different temperatures (60–67°C; 1°C interval) with 100 IU target genomic DNA per reaction. The graphs from e to h show robust amplification. The optimal amplification temperature was 65°C.

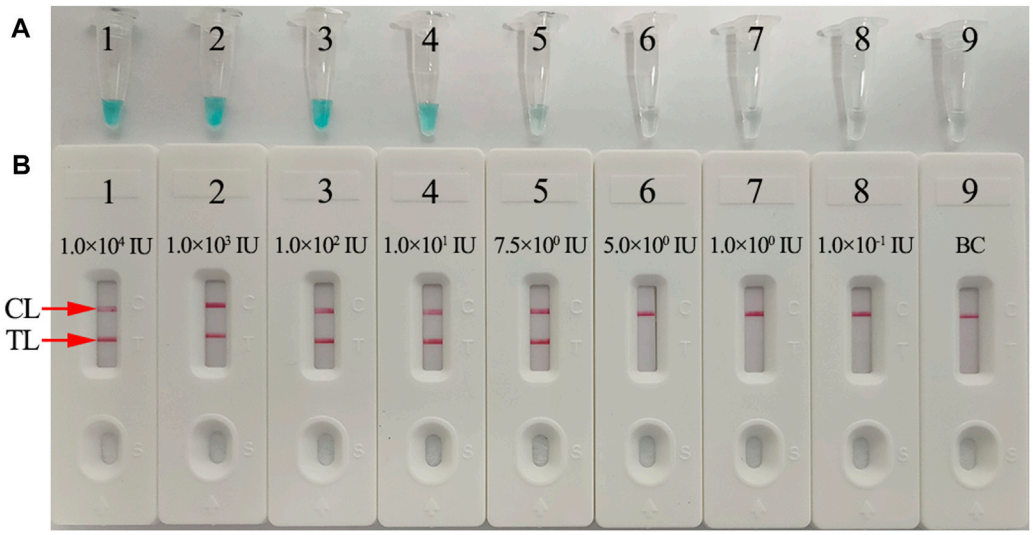

FIGURE 6 | Sensitivity analysis of the HBV-LAMP-LFB assay with serial dilutions of HBV genomic DNA concentrations. Two detection techniques, including colorimetric indicator (MG) **(A)** and LFB **(B)**, were used to analyze HBV-LAMP products. Tubes A1–A9 (Biosensors B1–B9) represent the genomic DNA amounts of 1×10^4 IU, 1×10^3 IU, 1×10^2 IU, 10 IU, 7.5 IU, 5 IU, 1 IU, and 0.1 IU per reaction and BC (DW), respectively. The LoD of the HBV-LAMP-LFB assay for *S* gene detection was 7.5 IU of the genomic template per reaction.

respectively. As shown in **Figures 6A,B**, the LoD of the HBV-LAMP assay was 7.5 IU obtained by both detection methods.

Optimal Amplification Time for the Hepatitis B Virus–Loop-Mediated Isothermal Amplification–Lateral Flow Biosensor Assay

To further optimize the reaction time for the HBV-LAMP-LFB assay at the preamplification stage, four reaction time intervals (20, 30, 40, and 50 min) were tested at 65°C, respectively. The LAMP products were identified through MG and LFB methods, respectively. The results confirmed that the limit level of genomic DNA (7.5 IU per reaction) was tested when the reaction lasted 40 and 50 min (**Figure 7**). Hence, 40 min was recommended as the optimal reaction time for the preamplification stage of the HBV-LAMP assay. Hence, the whole detection procedure, including genomic DNA extraction (~10 min), preamplification (40 min), and LFB reading (~2 min), can be accomplished within 60 min.

Specificity of the Hepatitis B Virus–Loop-Mediated Isothermal Amplification–Lateral Flow Biosensor Assay

For evaluation of HBV-LAMP-LFB assay specificity, the HBV nucleic acid standard substance (Chinese Academy of Metrology), 13 HBV-positive clinical samples, and 25 non-

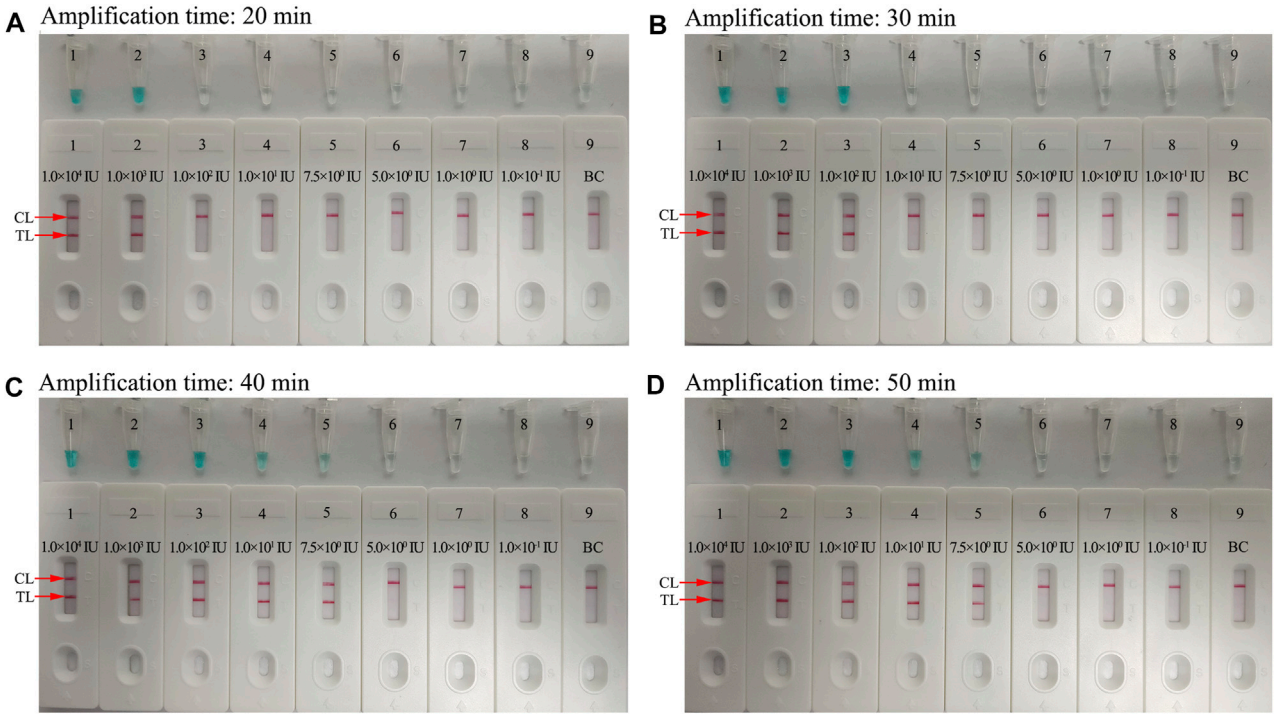

FIGURE 7 | Optimization of the amplification time for HBV-LAMP-LFB detection. Different amplification time intervals, **(A)** 20 min, **(B)** 30 min, **(C)** 40 min, and **(D)** 50 min, were tested at 65°C. Tubes 1–7 (Biosensors 1–7) represent HBV genomic DNA levels of 1×10^4 IU, 1×10^3 IU, 1×10^2 IU, 10 IU, 7.5 IU, 5 IU, 1 IU, and 0.1 IU per reaction and BC (DW), respectively. The best sensitivity was observed when the amplification lasted for 40 min.

HBV pathogens (**Table 1**) were used in the current study. The process of HBV-LAMP-LFB assay was as described above. The results showed that only genomic DNA extracted from HBV samples presented positive results and there was no cross-reactivity with other pathogens (**Figure 8**). Hence, these results indicated that the HBV-LAMP-LFB assay can accurately differentiate an HBV agent from other microbes.

Evaluation of the Feasibility of the Hepatitis B Virus–Loop-Mediated Isothermal Amplification–Lateral Flow Biosensor Assay With Clinical Samples

To further demonstrate the feasibility of HBV-LAMP-LFB assay as a valuable method for the detection of HBV agents, 115 clinical serum samples were collected from patients and tested simultaneously using the HBV-LAMP-LFB and qPCR assay. Among them, 76 of 115 clinical samples were confirmed as positive results through qPCR (>30 IU), which have also been verified as positive results through the HBV-LAMP-LFB assay. More importantly, 2 of the 39 "negative samples" (approximately 20 IU) were tested as positive outcomes using the HBV-LAMP-LFB assay (**Table 3** and **Supplementary Table S1**). These results suggested that the HBV-LAMP-LFB assay devised here shows more sensitivity in detecting HBV-infected patients, especially for those at the early stage of HBV infection.

DISCUSSION

HBV infection remains one of the main public health issues worldwide (Nguyen et al., 2020; Coffin et al., 2019). It can lead to a wide spectrum of liver diseases, such as acute hepatitis, chronic hepatitis, cirrhosis, and hepatocellular carcinoma (Nelson et al., 2016; Loomba and Liang, 2017). Besides, HBV, HCV, and HIV co-infections become increasingly frequent owing to shared routes of transmission and resulting in serious public health burden, especially in underprivileged regions of the world (Sarmati and Malagnino, 2019; Leoni et al., 2018). Screening and diagnosis of HBV remain a considerable challenge in many resource-limited settings with cost and equipment limitations (Mallika, 2015). In these regions, screening of HBsAg in blood with ELISA is the main approach for detecting HBV. However, this assay often poses a serious threat of misdiagnosis and transmission of HBV with low sensitivity (Coffin et al., 2019). In recent years, NAATs have become the primary tests for the identification of HBV in clinical application (Zhao et al., 2005; Li et al., 2018). Nevertheless, their use in resource-limited regions is not readily affordable, owing to requiring special facilities and trained experts. Here, the novel HBV-LAMP-LFB assay, integrating the gold nanoparticle-based LFB with preamplification, was devised first for the detection of HBV agents. Achieving this assay just requires exceedingly simple facilities, such as heating block and water bath that can hold a fixed reaction temperature of 65°C for 40 min. In addition, the

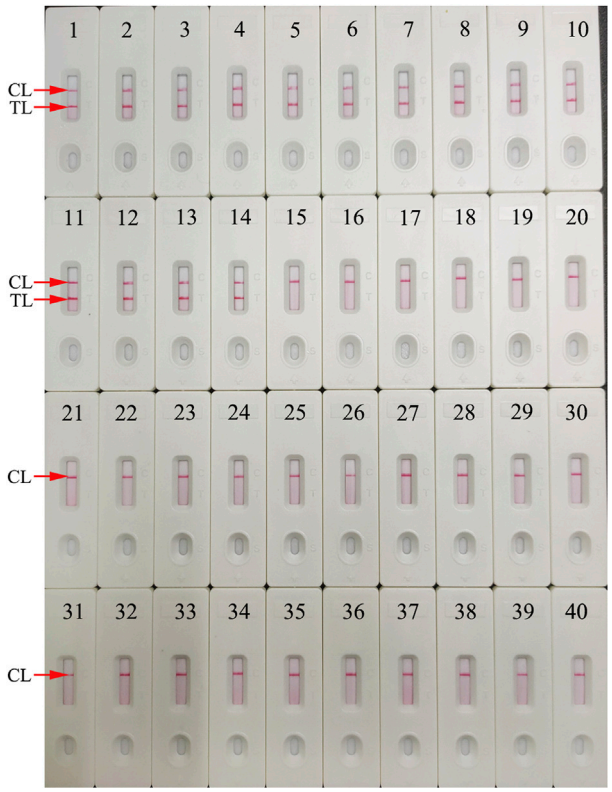

FIGURE 8 | Specificity analysis of the HBV-LAMP-LFB assay using different pathogens. The LAMP reactions were carried out with different genomic RNA/DNA as templates, and each of the amplification products was determined by means of the visual LFB method. Biosensor 1, HBV (standard substance); Biosensors 2–14, HBV (clinical samples); Biosensor 15, HCV (standard substance); Biosensor 16, HIV (standard substance); Biosensor 17, H1N1 (nucleic acid samples); Biosensor 18, influenza B; Biosensor 19, respiratory syncytial virus type A; Biosensor 20, human rhinovirus; Biosensor 21, adenoviruses; Biosensor 22, *Mycobacterium tuberculosis*; Biosensor 23, *Pseudomonas aeruginosa*; Biosensor 24, *Mycoplasma pneumonia*; Biosensor 25, *Streptococcus pneumonia*; Biosensor 26, *Mycoplasma pneumonia* M129/FH; Biosensor 27, *Haemophilus influenzae;* Biosensor 28, *Streptococcus pyogenes*; Biosensor 29, *Staphylococcus aureus*; Biosensor 30, *Acinetobacter baumannii*; Biosensor 31, *Leptospira interrogans*; Biosensor 32, *Shigella flexneri*; Biosensor 33, *Bacillus cereus*; Biosensor 34, *Bordetella parapertussis*; Biosensor 35, *Bordetella pertussis*; Biosensor 36, Enteropathogenic *Escherichia coli*; Biosensor 37, *Candida glabrata*; Biosensor 38, *Cryptococcus neoformans*; Biosensor 39, *Hemophililus parainfluenzae*; Biosensor 40, BC (DW).

gold nanoparticle-based LFB provides an easy-to-operate detection platform, which can rapidly and visually read out the HBV-LAMP outcomes. The whole HBV-LAMP-LFB detection process, including genomic DNA extraction (approximately 10 min), preamplification (40 min), and LFB reading (approximately 2 min), can be accomplished within 60 min.

LAMP, as a rapid, sensitive, low equipment–cost assay, was devised first in 2000 by Notomi et al. (2000), and it has been extensively used to detect various pathogens (Dolka et al., 2019; Huang et al., 2017; Kanitkar et al., 2016). The isothermal amplification of the target gene is completed by using a set of four (or six) specific primers spanning six (or eight) distinct regions of the special sequence with *Bst* DNA polymerase at a fixed reaction temperature (between 58 and 69°C) (Notomi et al., 2000). In the current study, three pairs of HBV-LAMP primers were successfully designed and they specifically identified eight regions of the target gene *S* (**Figure 3**). The specificity of the HBV-LAMP-LFB assay was strongly verified using the nucleic acid extracted from HBV clinical samples and other various pathogens. The positive results only appeared in the positive control and HBV clinical samples and there was no cross-reactivity with other pathogens (**Figure 8**). Apart from its remarkable specificity, the newly devised HBV-LAMP-LFB assay was able to detect the concentration as low as 7.5 IU (**Figure 6**), which is sufficient for the diagnosis of HBV agents in clinical application. Moreover, 2 of the 39 clinical "negative samples" (HBV concentrations below 30 IU) were tested as positive outcomes with the HBV-LAMP-LFB. The results indicated that our HBV-LAMP-LFB assay has higher sensitivity than that of qPCR (**Table 3** and **Supplementary Table S1**).

In the current study, the gold nanoparticle-based LFB was successfully designed and used to read out the HBV LAMP reactions. Gold nanoparticles are the most appropriate materials for making a biosensor, owing to their high adsorption, high surface-to-volume ratio, good biocompatible, and easy-to-manipulate features (Aldewachi et al., 2017; Fuentes et al., 2016; Quesada-Gonzá lez and Merkoçi, 2015). The LFBs have been powerfully proven and widely applied for rapid and sensitivity detection of disease, drug abuse, and food safety in resource-limited areas (Huang et al., 2019; Jiang et al., 2021; Huang et al., 2021). Here, the LFB can visually read out HBV-LAMP reactions for labeling with biotin-BSA and anti-FAM

TABLE 3 | Comparison of qPCR and LAMP-LFB methods to identify HBV in clinical samples.

Detection method	Clinical samples (n = 115)		
	Positive	Negative	Time consumption
qPCR	76 (>30 IU)	39 (37, <7.5 IU; 2, approximately 20 IU)	Approximately 130 min
LAMP-LFB	78	37	Within 60 min

Note. *The qPCR diagnosis was carried out using the commercial real-time TaqMan PCR kit (DaAn Gene Co., Ltd., China). The concentrations of HBV less than 30 IU will be considered as negative results according to the manufacturer's instructions.*

probes on the biosensor pads. For positive outcomes, the two crimson red bands (CL and TL) appeared simultaneously on the LFB strip, while only the CL was presented on the LFB, indicating negative results. Although the real-time turbidity and colorimetric indicator could be used for detecting HBV-LAMP amplicons, the former assay requires a high cost for specific facility and the latter method is ambiguous when the concentration of the amplicons was low (**Figure 6**). The biosensor with high sensitivity, easy-to-operate, and cost-saving (~€1.7 euros) advantages was considered as the appropriate method to readout the HBV LAMP products. The total cost of each test, including genomic DNA extraction (~€ 0.9 euros), preamplification (~€2.9 euros), and LFB reading (~€1.7 euros), is estimated to be € 5.5 euros, which is cheaper than the qPCR technique. By reason of the foregoing, the HVB-LAMP-LFB assay has significant potential to develop a point-of-care (POC) testing for detecting HBV-suspected patients in clinical setting, especially in resource-impoverished regions of the world.

CONCLUSION

In the current study, a rapid, visual, sensitive, simple, and cost-saving HBV-LAMP-LFB assay based on the *S* gene was successfully devised for identifying HBV agents. The results demonstrated that the HBV-LAMP-LFB is a highly specific and sensitive diagnostic tool for the diagnosis of HBV in clinical application. It does not require expensive facilities and reagents, and the whole detection process can be achieved within 60 min. Hence, the HBV-LAMP-LFB assay has remarkable potential to establish a POC testing for the reliable and rapid detection of HBV in clinical setting, especially in resource-limited countries of the world.

DATA AVAILABILITY STATEMENT

The original contributions presented in the study are included in the article/**Supplementary Material**; further inquiries can be directed to the corresponding authors.

ETHICS STATEMENT

The study was approved by the Human Ethics Committee of the Second Affiliated Hospital of Guizhou University of Traditional Chinese Medicine (Approval No. TYH2020011) and complied with the Declaration of Helsinki. Before our team obtained the samples/isolates and conducted the study, any personal identifiers of the suspected HBV-infected patients had been removed by the monitoring stations. So, the patient informed consent was waived by the Human Ethics Committee of the Second Affiliated Hospital of Guizhou University of Traditional Chinese Medicine.

AUTHOR CONTRIBUTIONS

XC and SL conceived and designed the study. XC, SW, and YT participated in primers design. XC, SW, YT, JH, and XY contributed to all the laboratory works. SW, YT, and JH contributed to the data collection. XC, JH, and XY performed statistical analysis. XC wrote the initial draft of the manuscript, and SL revised the manuscript. All the authors read and approved the final manuscript.

FUNDING

This work was supported by the Program of Scientific and Technological Project in Guizhou Province (Grant No. Qian Ke He (2020)4Y184), the Scientific and Technological Project in Guiyang City (Grant No. Zhu Ke He (2020)-10-5), the Program of Scientific and Technological Innovation Team of Guizhou Province (Grant No. Qian Ke He Platform Talent (2018)5606), and the Public Welfare Technology Research Program in Zhejiang Province (Grant No. LGF21H190001). The funders had no role in study design, data collection, and analysis, decision to publish, or preparation of the manuscript.

ACKNOWLEDGMENTS

The authors would like to express their sincere appreciation to the medical workers in the second GZUTCM and GZCDC for their contribution to the current study.

SUPPLEMENTARY MATERIAL

The Supplementary Material for this article can be found online at https://www.frontiersin.org/articles/10.3389/fbioe.2021.731415/full#supplementary-material

REFERENCES

Aldewachi, H., Chalati, T., Woodroofe, M. N., Bricklebank, N., Sharrack, B., and Gardiner, P. (2017). Gold Nanoparticle-Based Colorimetric Biosensors. *Nanoscale* 10 (1), 18–33. doi:10.1039/c7nr06367a

Blackard, J. T., and Sherman, K. E. (2018). Hepatitis B Virus (HBV) Reactivation-The Potential Role of Direct-Acting Agents for Hepatitis C Virus (HCV). *Rev. Med. Virol.* 28 (4), e1984. doi:10.1002/rmv.1984

Bollinger, R. C., Thio, C. L., Sulkowski, M. S., McKenzie-White, J., Thomas, D. L., and Flexner, C. (2020). Addressing the Global burden of Hepatitis B Virus while Developing Long-Acting Injectables for the Prevention and Treatment of HIV. *The Lancet HIV* 7 (6), e443–e448. doi:10.1016/S2352-3018(19)30342-X

Coffin, C. S., Zhou, K., and Terrault, N. A. (2019). New and Old Biomarkers for Diagnosis and Management of Chronic Hepatitis B Virus Infection. *Gastroenterology* 156 (2), 355–368. doi:10.1053/j.gastro.2018.11.037

Dolka, B., Cisek, A. A., and Szeleszczuk, P. (2019). The Application of the Loop-Mediated Isothermal Amplification (LAMP) Method for Diagnosing

Enterococcus Hirae-Associated Endocarditis Outbreaks in Chickens. *BMC Microbiol.* 19 (1), 48. doi:10.1186/s12866-019-1420-z

Fuentes, M., Díez, P., and Casado-Vela, J. (2016). Nanotechnology in the Fabrication of Protein Microarrays. *Methods Mol. Biol.* 1368, 197–208. doi:10.1007/978-1-4939-3136-1_14

Huang, W., Zhang, H., Xu, J., Wang, S., Kong, X., Ding, W., et al. (2017). Loop-Mediated Isothermal Amplification Method for the Rapid Detection of Ralstonia Solanacearum Phylotype I Mulberry Strains in China. *Front. Plant Sci.* 8, 76. doi:10.3389/fpls.2017.00076

Huang, Y., Xu, T., Luo, Y., Liu, C., Gao, X., Cheng, Z., et al. (2021). Ultra-Trace Protein Detection by Integrating Lateral Flow Biosensor with Ultrasound Enrichment. *Anal. Chem.* 93 (5), 2996–3001. doi:10.1021/acs.analchem.0c05032

Huang, Y., Xu, T., Wang, W., Wen, Y., Li, K., Qian, L., et al. (2019). Lateral Flow Biosensors Based on the Use of Micro- and Nanomaterials: A Review on Recent Developments. *Microchim Acta* 187 (1), 70. doi:10.1007/s00604-019-3822-x

Jain, S., Su, Y.-H., Su, Y.-P., McCloud, S., Xue, R., Lee, T.-J., et al. (2018). Characterization of the Hepatitis B Virus DNA Detected in Urine of Chronic Hepatitis B Patients. *BMC Gastroenterol.* 18 (1), 40. doi:10.1186/s12876-018-0767-1

Jiang, T., Huang, Y., Cheng, W., Sun, Y., Wei, W., Wu, K., et al. (2021). Multiple Single-Nucleotide Polymorphism Detection for Antimalarial Pyrimethamine Resistance via Allele-specific PCR Coupled with Gold Nanoparticle-Based Lateral Flow Biosensor. *Antimicrob. Agents Chemother.* 65 (3). doi:10.1128/AAC.01063-20

Kanitkar, Y. H., Stedtfeld, R. D., Steffan, R. J., Hashsham, S. A., and Cupples, A. M. (2016). Loop-Mediated Isothermal Amplification (LAMP) for Rapid Detection and Quantification of Dehalococcoides Biomarker Genes in Commercial Reductive Dechlorinating Cultures KB-1 and SDC-9. *Appl. Environ. Microbiol.* 82 (6), 1799–1806. doi:10.1128/AEM.03660-15

Kubota, R., and Jenkins, D. (2015). Real-Time Duplex Applications of Loop-Mediated AMPlification (LAMP) by Assimilating Probes. *Ijms* 16 (3), 4786–4799. doi:10.3390/ijms16034786

Landaverde, L., Wong, W., Hernandez, G., Fan, A., and Klapperich, C. (2020). Method for the Elucidation of LAMP Products Captured on Lateral Flow Strips in a point of Care Test for HPV 16. *Anal. Bioanal. Chem.* 412 (24), 6199–6209. doi:10.1007/s00216-020-02702-9

Le Thi, N., Ikuyo, T., Nguyen Gia, B., Truong Thai, P., Vu Thi, T. V., Bui Minh, V., et al. (2020). A Clinic-Based Direct Real-Time Fluorescent Reverse Transcription Loop-Mediated Isothermal Amplification Assay for Influenza Virus. *J. Virol. Methods* 277, 113801. doi:10.1016/j.jviromet.2019.113801

Leoni, M. C., Ustianowski, A., Farooq, H., and Arends, J. E. (2018). HIV, HCV and HBV: A Review of Parallels and Differences. *Infect. Dis. Ther.* 7 (4), 407–419. doi:10.1007/s40121-018-0210-5

Li, M., Sohn, J. A., Seeger, C., and Ou, J. H. J. (2018). Distribution of Hepatitis B Virus Nuclear DNA. *J. Virol.* 92 (1). doi:10.1128/JVI.01391-17

Liang, T. J. (2009). Hepatitis B: The Virus and Disease. *Hepatology* 49 (5 Suppl. l), S13–S21. doi:10.1002/hep.22881

Liaw, Y.-F. (2019). Clinical utility of HBV surface antigen quantification in HBV e antigen-negative chronic HBV infection. *Nat. Rev. Gastroenterol. Hepatol.* 16 (10), 631–641. doi:10.1038/s41575-019-0197-8

Loomba, R., and Liang, T. J. (2017). Hepatitis B Reactivation Associated with Immune Suppressive and Biological Modifier Therapies: Current Concepts, Management Strategies, and Future Directions. *Gastroenterology* 152 (6), 1297–1309. doi:10.1053/j.gastro.2017.02.009

Mallika, G. S. N. S. (2015). Detection of Hepatitis B Virus Infection: A Systematic Review. *World J. Hepatol.* 7 (23), 2482–2491. doi:10.4254/wjh.v7.i23.2482

Nelson, N. P., Easterbrook, P. J., and McMahon, B. J. (2016). Epidemiology of Hepatitis B Virus Infection and Impact of Vaccination on Disease. *Clin. Liver Dis.* 20 (4), 607–628. doi:10.1016/j.cld.2016.06.006

Nguyen, M. H., Wong, G., Gane, E., Kao, J.-H., and Dusheiko, G. (2020). Hepatitis B Virus: Advances in Prevention, Diagnosis, and Therapy. *Clin. Microbiol. Rev.* 33 (2). doi:10.1128/CMR.00046-19

Notomi, T., Okayama, H., Masubuchi, H., Yonekawa, T., Watanabe, K., Amino, N., et al. (2000). Loop-Mediated Isothermal Amplification of DNA. *Nucleic Acids Res.* 28 (12), 63e–63. doi:10.1093/nar/28.12.e63

Nyan, D.-C., Ulitzky, L. E., Cehan, N., Williamson, P., Winkelman, V., Rios, M., et al. (2014). Rapid Detection of Hepatitis B Virus in Blood Plasma by a Specific and Sensitive Loop-Mediated Isothermal Amplification Assay. *Clin. Infect. Dis.* 59 (1), 16–23. doi:10.1093/cid/ciu210

Quesada-González, D., and Merkoçi, A. (2015). Nanoparticle-Based Lateral Flow Biosensors. *Biosens. Bioelectron.* 73, 47–63. doi:10.1016/j.bios.2015.05.050

Revill, P. A., Penicaud, C., Brechot, C., and Zoulim, F. (2019). Meeting the Challenge of Eliminating Chronic Hepatitis B Infection. *Genes* 10 (4), 260. doi:10.3390/genes10040260

Romero, M. R., and Cook, N. (2018). A Rapid LAMP-Based Method for Screening Poultry Samples for Campylobacter without Enrichment. *Front. Microbiol.* 9. doi:10.3389/fmicb.2018.02401

Sara, O. M. L. C. (2011). Diagnostic Strategy for Occult Hepatitis B Virus Infection. *World J. Gastroenterol. : WJG* 17 (12), 1553–1557. doi:10.3748/wjg.v17.i12.1553

Sarmati, L., and Malagnino, V. (2019). HBV Infection in HIV-Driven Immune Suppression. *Viruses* 11 (11), 1077. doi:10.3390/v11111077

Seki, M., Kilgore, P. E., Kim, E. J., Ohnishi, M., Hayakawa, S., and Kim, D. W. (2018). Loop-Mediated Isothermal Amplification Methods for Diagnosis of Bacterial Meningitis. *Front. Pediatr.* 6. doi:10.3389/fped.2018.00057

Tong, S., and Revill, P. (2016). Overview of Hepatitis B Viral Replication and Genetic Variability. *J. Hepatol.* 64 (1 Suppl. l), S4–S16. doi:10.1016/j.jhep.2016.01.027

Villar, L. M., Cruz, H. M., Barbosa, J. R., Bezerra, C. S., Portilho, M. M., and Scalioni, L. D. P. (2015). Update on Hepatitis B and C Virus Diagnosis. *Wjv* 4 (4), 323. doi:10.5501/wjv.v4.i4.323

Zhao, J.-R., Bai, Y. J., Zhang, Q. H., Wan, Y., Li, D., and Yan, X. J. (2005). Detection of Hepatitis B Virus DNA by Real-Time PCR Using TaqMan-MGB Probe Technology. *Wjg* 11 (4), 508–510. doi:10.3748/wjg.v11.i4.508

Zhu, X., Wang, X., Han, L., Chen, T., Wang, L., Li, H., et al. (2020). Multiplex Reverse Transcription Loop-Mediated Isothermal Amplification Combined with Nanoparticle-Based Lateral Flow Biosensor for the Diagnosis of COVID-19. *Biosens. Bioelectron.* 166, 112437. doi:10.1016/j.bios.2020.112437

Zhu, X., Wang, X., Li, S., Luo, W., Zhang, X., Wang, C., et al. (2021). Rapid, Ultrasensitive, and Highly Specific Diagnosis of COVID-19 by CRISPR-Based Detection. *ACS Sens.* 6 (3), 881–888. doi:10.1021/acssensors.0c01984

Conflict of Interest: The authors declare that the research was conducted in the absence of any commercial or financial relationships that could be construed as a potential conflict of interest.

Publisher's Note: All claims expressed in this article are solely those of the authors and do not necessarily represent those of their affiliated organizations, or those of the publisher, the editors, and the reviewers. Any product that may be evaluated in this article, or claim that may be made by its manufacturer, is not guaranteed or endorsed by the publisher.

frontiers in Bioengineering and Biotechnology

ORIGINAL RESEARCH
published: 20 September 2021
doi: 10.3389/fbioe.2021.726071

Graphene-Based Flexible Sensors for Simultaneous Detection of Ascorbic Acid, Dopamine, and Uric Acid

Shuaishuai Meng[1†], Yaming Liu[1†], Li Wang[1†], Xixi Ji[2], Yun Chen[3], Tingting Zheng[3], Jie Yu[2] and Huanhuan Feng[1]*

[1]Sauvage Laboratory for Smart Materials, Flexible Printed Electronic Technology Center, School of Materials Science and Engineering, Harbin Institute of Technology (Shenzhen), Shenzhen, China, [2]School of Materials Science and Engineering, Harbin Institute of Technology (Shenzhen), Shenzhen, China, [3]Peking University Shenzhen Hospital & Biomedical Research Institute, Shenzhen-PKU-HKUST Medical Center, Shenzhen, China

Many diseases are closely related to abnormal concentrations of ascorbic acid (AA), dopamine (DA), and uric acid (UA). Therefore, the detection of these small molecules is significant for monitoring life metabolism and healthy states. Electrochemical detection has been widely used to detect small molecules due to its good selectivity, high sensitivity, and good economics. Fabrication and application are two sides of the coin, and we cannot give up one for the other. Graphene (GN) is a very suitable material for electrochemical sensing due to its excellent catalytic performance and large specific surface area. It possesses many excellent properties but cannot hold itself alone due to its nanoscale thickness. Herein, we have fabricated three-dimensional (3D) GN nanosheets (GNSs) on flexible carbon cloth (CC) by thermal chemical vapor deposition (CVD). The GNSs/CC can successfully detect AA, DA, and UA simultaneously. We find that these GNSs/CC sensors show good performance with 7 h CVD modification. The linear ranges of AA, DA, and UA are 0.02–0.1, 0.0005–0.02, and 0.0005–0.02 mM, respectively. The detection sensitivity rates of AA, DA, and UA are 5,470, 60,500, and 64,000 $\mu A\,mM^{-1}\,cm^{-2}$, respectively. Our GNSs/CC flexible sensors can be successfully applied in the human serum for UA detection. The result matches with commercial sensors very well.

Keywords: 3D graphene, flexible sensing, simultaneous detecting, biological small molecules detection, biochemical detection

OPEN ACCESS

Edited by:
Tailin Xu,
Shenzhen University, China

Reviewed by:
Yueming Zhai,
Wuhan University, China
Junyou Wang,
East China University of Science and Technology, China
Bin Dong,
Soochow University, China

****Correspondence:***
Huanhuan Feng
fenghuanhuan@hit.edu.cn

[†]These authors have contributed equally to this work.

Specialty section:
This article was submitted to Biosensors and Biomolecular Electronics, a section of the journal Frontiers in Bioengineering and Biotechnology

Received: *16 June 2021*
Accepted: *28 July 2021*
Published: *20 September 2021*

Citation:
Meng S, Liu Y, Wang L, Ji X, Chen Y, Zheng T, Yu J and Feng H (2021) Graphene-Based Flexible Sensors for Simultaneous Detection of Ascorbic Acid, Dopamine, and Uric Acid. Front. Bioeng. Biotechnol. 9:726071. doi: 10.3389/fbioe.2021.726071

INTRODUCTION

Clinical medicine research has found that chronic diseases such as scurvy, Parkinson's disease, and gout are highly correlated with abnormal concentrations of ascorbic acid (AA), dopamine (DA), and uric acid (UA) (Masliah et al., 2000; Sansuk et al., 2013; Du et al., 2014; Liao et al., 2014). The coexistence of AA, DA, and UA is very common in the extracellular fluid, serum, and central nervous system. They are important signals of the state of human physiological processes (Wightman et al., 1988; Tukimin et al., 2018). Therefore, the fabrication of selective sensors which can simultaneously detect these biological small molecules in real time is of substantial significance for the normal life activities of human beings and the early diagnosis of related diseases. Nowadays, there are various methods for detecting these small biological molecules: ultraviolet-visible spectroscopy (Han et al., 2014), fluorescence measurement (Hortigon-Vinagre et al., 2016; Tarabova et al., 2019), chemiluminescence (Nalewajko et al., 2004), gas chromatography–mass spectrometry (Xie, 2001;

Lu et al., 2020), and high-performance liquid chromatography (Mesbah et al., 1989; Ianni et al., 2019; Qi et al., 2020). However, these methods require a long detection cycle and professional operation and are of high cost, which limit their efficient detection of these small biological molecules. As these three substances all contain special functional groups, they will be oxidized at a certain potential and exhibit electrochemical activity, which can be measured by current. Therefore, electrochemical methods can be used to monitor the concentrations of these small molecules (Hubbard et al., 2010). Electrochemical sensors have become research hotspots due to their low cost, short detection cycle, high sensitivity, and simple operation (Bakker and Telting-Diaz, 2002; Privett et al., 2010; Li et al., 2019; Karimi-Maleh et al., 2020). Zhu fabricated a novel electrochemical sensor based on carbon nanotube arrays for selective detection of DA or UA (Yang et al., 2019). Wu designed a heteroatom-doped carbon nanoparticle–ionic liquid composite as the electrochemical sensor for UA (Abbas et al., 2020).

The single detection of these small molecules using electrochemical sensors is quite mature, but there are relatively few reports of sensors involved in the simultaneous detection of these three small molecules. The main reason is that the oxidation potentials of these substances on the conventional bare electrodes overlap each other and often suffer from a pronounced fouling effect, which result in rather poor selectivity and reproducibility (Gao and Huang, 1998; Kumar et al., 2005; Premkumar and Khoo, 2005; Zare et al., 2005). In order to overcome the difficulty, new electrode materials must be developed to reduce the oxidation potentials of various substances and to improve the electrode properties. In addition, the sensing materials used in the sensors are mostly inorganic nonmetallic materials such as silicon, zinc oxide, or gallium arsenide. The single-crystal materials are rigid and brittle but not flexible, thus being limited in the fields of application such as irregular surfaces and large deformation (Kim et al., 2008; You et al., 2020). Graphene (GN) electrodes stand out among many modified materials due to their excellent conductivity, high ductility, high thermal conductivity, and large specific surface area (Stankovich et al., 2007; Wu and Drzal, 2012; Yang et al., 2017). Although the GN electrode possesses numerous excellent properties, it cannot hold itself alone due to its nanoscale thickness. Carbon cloth (CC) is a very good electronic substrate, which can integrate with flexible electronics and realize the sensing and detection of biochemical signals (Polovina et al., 1997; Ezzeddine et al., 2015; Hou et al., 2015).

Herein, we report a GNSs/CC flexible sensor using thermal chemical vapor deposition (CVD) to grow three-dimensional (3D) GN nanosheets (GNSs) on the CC substrate for the simultaneous detection of AA, DA, and UA. The GN is directly grown on the CC and firmly combined with the CC fiber and does not fall off easily compared with other physical adsorption techniques. The GNSs/CC sensor has combined the advantages of the flexibility of CC with the high chemical activity and large specific surface area of 3D GN. It possesses excellent catalytic activity for AA, DA, and UA and has the advantages of high sensitivity and a wide linear range. We found that the GNSs/CC sensors show good detection performance when the GN growth time is 7 h. The 7 h GNSs/CC electrodes have sufficient chemical active sites with high chemical reactivity, which can separate the redox peaks of these small molecules without forming dense GN layers to enter the diffusion control stage. In addition, the sensor has good anti-interference performance with regard to common ions and molecules in blood and has been successfully used to detect UA in the human serum, with a recovery rate of 104–124%. This work provides a simple and efficient tool for the simultaneous detection of multiple biochemical signals.

MATERIALS AND METHODS

Fabrication of the GNSs/CC Flexible Sensor

Since carbon materials were hydrophobic, hydrophilic pretreatments were required prior to use. The specific operations were as follows: the samples were immersed in acetone solution and maintained at room temperature for 30 min to dissolve the organic matter on the surface of these samples. The samples were taken out of the acetone solution, then put into deionized water, and maintained for 30 min. The samples were removed from the deionized water, then put into 0.5 M sulfuric acid solution, and maintained for 30 min to oxidize the surface of the carbon materials, so that the oxygen-containing groups can be modified on the samples' surface. The carbon materials were converted from hydrophobic to hydrophilic attribute, and then, they were naturally air-dried in air under room temperature for further detection.

To fabricate our GNSs/CC flexible sensor (**Figure 1**), we put a certain specification of CC into a tube furnace, introduced the protective gas argon (Ar) at a rate of 200 sccm, and heated the tube furnace to 1,100 °C to complete the carbonization of the CC fiber in Ar atmosphere. After some time, Ar was stopped and a mixture of hydrogen (H_2) and carbon source (CH_4) was introduced at a rate of 160 and 6 sccm, respectively, for 10 h (H_2 was introduced to aid in the cleavage of CH_4). On the basis of carbon fiber carbonization, GN with the 3D structure was generated *in situ* on the CC substrate by CH_4 thermal decomposition reaction and the vertical growth of GN was completed. Finally, Ar was introduced to stabilize the GN and drain the mixture of H_2 and CH_4, and the tube furnace was cooled to room temperature to obtain the 10 h GNSs/CC electrode material.

In order to investigate the effect of the thickness of GN grown on CC on the electrochemical performance of the sensor, the GNSs/CC electrodes at different growth periods were fabricated by adjusting the introduction time of the carbon source to 0–10 h, which were 1 h GNSs/CC, 5 h GNSs/CC, 7 h GNSs/CC, and 10 h GNSs/CC electrodes, respectively. The fabricated GNSs/CC electrodes were quenched into 1 cm × 2 cm pieces with liquid nitrogen for further use. After use, they were washed repeatedly with anhydrous ethanol and ultrapure water to remove the residual substances on the surface to obtain good reproducibility.

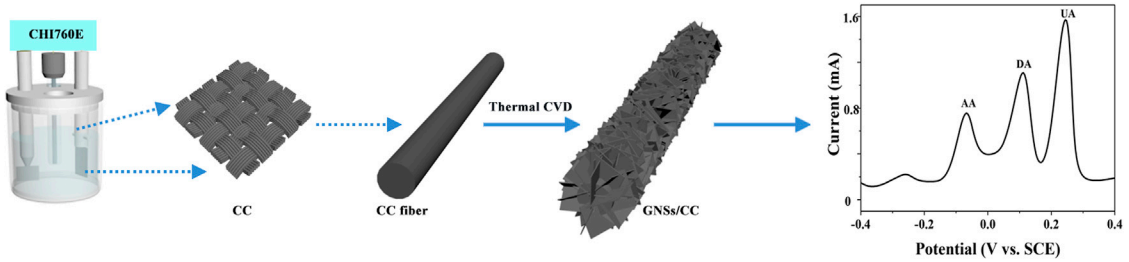

FIGURE 1 | Schematic diagram of the fabrication process of the GNSs/CC sensor and the simultaneous detection of three small molecules (AA, DA, and UA).

Basic Characterization of Materials

Scanning electron microscopy characterization: the cross sections of the samples were obtained by liquid nitrogen quenching. SEM using S-4700 was performed to observe their morphology, structure, and thickness under 15 kV and in the secondary electron mode.

Raman characterization: the samples fabricated in the experiment were characterized by Horiba microconfocal Raman spectroscopy. Selection of test parameters: the detection range was from 1,000 to 3,000 cm^{-1}, the integration time was 3 min, the number of integrations was 20, and the selected laser wavelength was 625 nm. All tests were performed at room temperature.

BET: we carried out nitrogen adsorption and desorption experiments on GNSs/CC materials and calculated the specific surface area of GNSs/CC materials by measuring the saturation adsorption capacity of the nitrogen monolayer.

Electrochemical Testing

Electrochemical impedance spectroscopy (EIS) is commonly used to examine the interface properties of modified electrodes, and potassium ferricyanide/potassium ferrocyanide is often used as an electron transfer redox probe (Pajkossy and Jurczakowski, 2017; Ciucci, 2019). Cyclic voltammetry (CV) scanning includes a pair of reversible redox peaks. In forward scanning, $[Fe(CN)_6]^{4-}$ loses electrons and becomes $[Fe(CN)_6]^{3-}$ through the oxidation reaction, while in reverse scanning, $[Fe(CN)_6]^{3-}$ gains electrons and becomes $[Fe(CN)_6]^{4-}$ through the reduction reaction. We measured the electrochemical impedance of various electrodes with 0.01 mM potassium ferricyanide/potassium ferricyanide solution at 0.1 Hz to 100 kHz with an amplitude of 0.05 V and a standing time of 2 s.

CV (Elgrishi et al., 2018) was used to investigate the electrochemical properties of GNSs/CC electrodes at different growth periods. The experiment was carried out on a CHI 760 E electrochemical workstation using the traditional three-electrode system, in which the GNSs/CC electrode was used as the working electrode, the counter electrode was a platinum plate, and the saturated calomel electrode (SCE) was used as the reference electrode. All potentials given were referred to SCE, and all electrochemical tests were performed at room temperature. 0.1 M phosphate-buffered saline (PBS) at pH 7.4 was used as the electrolyte solution for the performance test with a scan voltage of -0.6 to 0.4 V.

Differential pulse voltammetry (DPV) (Lin et al., 2006) was used to separately detect these small molecules (AA, DA, and UA), and the respective working linear range and sensitivity were obtained when the GNSs/CC electrode was used as the working electrode. Then, DPV was used to simultaneously detect these small molecules and obtain the working linear range and sensitivity of simultaneous detection.

Detection in Real Blood Samples

In order to explore the performance and feasibility of our GNSs/CC sensor in the analysis of real blood samples, fresh human serum samples were analyzed with the sensor and the dry chemical analysis method was adopted by the hospital. Fresh blood samples were collected from Shenzhen Hospital of Peking University and analyzed within 1 hour after sampling. Collection of the samples was approved by the ethical committee of the hospital, and informed consent was obtained from each volunteer. This study was approved by the Medical Ethical Committee of Shenzhen Hospital of Peking University.

RESULTS AND DISCUSSION

Characterization of Carbon Cloth and Graphene Nanosheets/Carbon Cloth

Figure 2A shows the SEM of CC. The surface of the bare CC fiber is relatively smooth, and the fiber is woven to form the CC. **Figure 2B** shows the SEM of GNSs/CC at different growth periods of GN. After growing GN on the CC for 1 hour, GN flakes appeared on the CC like shredded paper. The thickness of the GN layer increases with the growth time. As the growth time of GN increases, it can be seen that not only the thickness and density of GN increase significantly but also a 3D structure is gradually formed. This 3D network structure effectively increases its specific surface area and the contact area with small molecule substances, which provides more chemical active sites. It can be seen from the SEM of GNSs/CC cross sections (**Figure 2C**) that only after as long as 5 h of growth time can the full GN be grown and the thickness of GN coating on the outer layer of the CC fiber is 122 nm. With the increase in growth time, the density of GN and the diameter of the CC fiber gradually increase. The thickness of GN is 134 nm when it grows for 7 h. When the growth time is increased to 10 h, the GN on the CC touches each other, filling the space in the entire CC fiber and forming a unique porous 3D GN

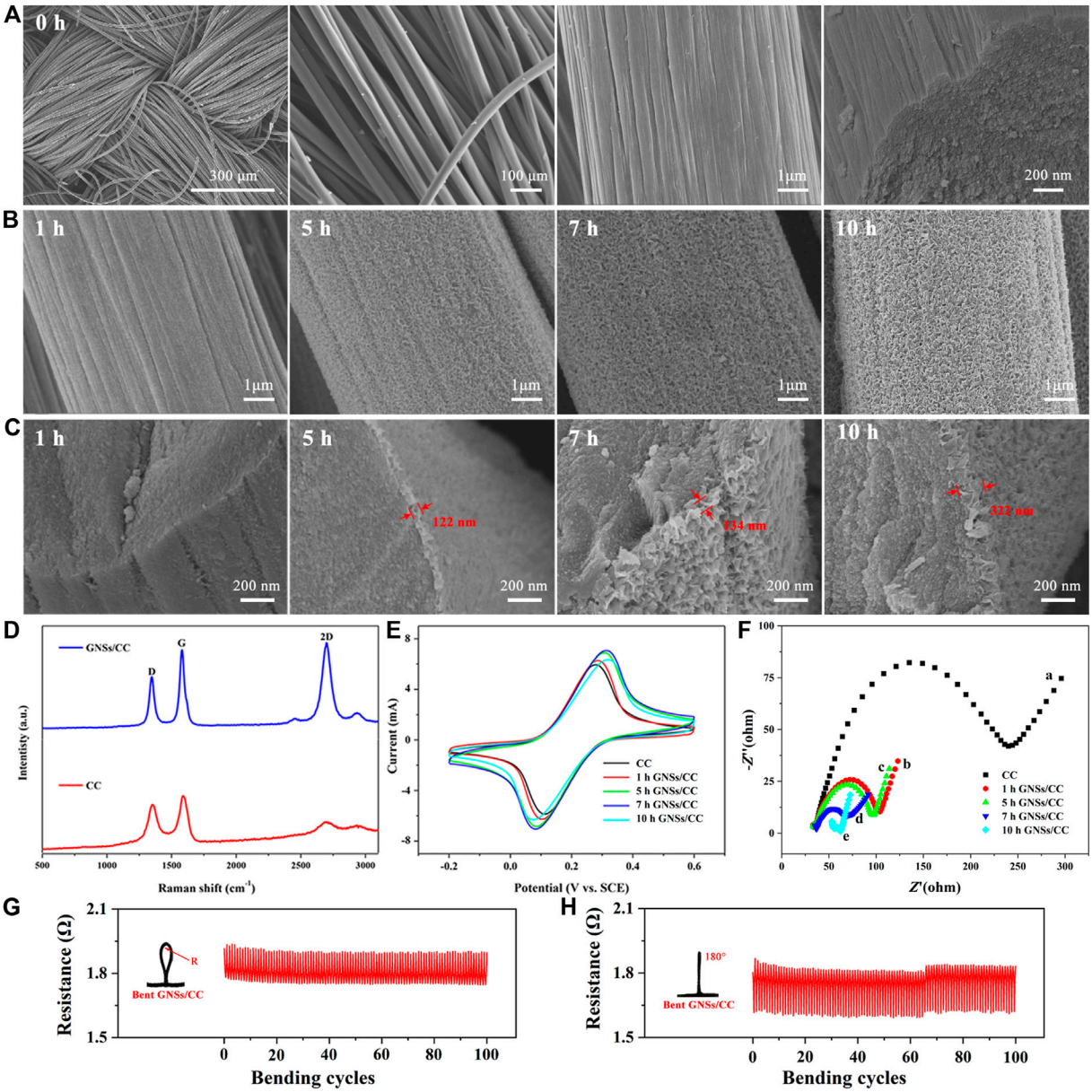

FIGURE 2 | Relevant characterization of CC and GNSs/CC. **(A)** SEM of CC morphology and its cross section. **(B)** SEM of GNSs/CC with different growth periods of GN. **(C)** SEM of GNSs/CC cross sections with different growth periods. **(D)** Raman spectra of CC and GNSs/CC. **(E)** Cyclic voltammograms of CC and GNSs/CC. **(F)** EIS of different electrodes in 0.01 mM $[Fe(CN)_6]^{3-/4-}$ and 0.1 M KCl solutions. **(G)** Resistance of the GNSs/CC flexible sensor bent for 100 times at a radius R = 3 mm. **(H)** Resistance of the GNSs/CC flexible sensor bent for 100 times at 180°.

structure. At this point, the thickness of GN is around 320 nm. This special structure has a large specific surface area, which can further provide sites for the loaded active molecules.

We measure the specific surface area of GNSs/CC at different growth periods of GN. The specific surface area of the CC is not obtained, but after the growth of GN on the CC, the specific surface area increases significantly; the specific surface area of 1 h GNSs/CC is 1.3 $cm^{-2}\,g^{-1}$. As the growth time of GN increases, its specific surface area gradually increases. This is because with the increase in growth time, the GN gradually becomes thicker and denser and forms a 3D structure. The special 3D structure increases the specific surface area of the composite material. Notably, the specific surface area of 5 h GNSs/CC is significantly increased (1.7 $cm^{-2}\,g^{-1}$ at 5 h, 1.9 $cm^{-2}\,g^{-1}$ at 7 h, and 2.0 $cm^{-2}\,g^{-1}$ at 10 h). On the one hand, GN itself has a large specific surface area, and on the other hand, 5 h GNSs/CC forms a complete 3D structure. With the gradual formation of the 3D structure of GN, its specific surface area increases significantly, which is very consistent with the SEM images.

Raman spectra of CC and GNSs/CC show two characteristic peaks, which are the D peak at 1,346 cm^{-1} and G peak at 1,588 cm^{-1} (**Figure 2D**) (Sasaki et al., 2013). In the experiment, the I_D/I_G ratios of CC and GNSs/CC are 0.8 and 0.7, respectively, indicating that the grown GN reduces the defects of the composite. **Figure 2D** shows that the 2D peak appears near 2,700 cm^{-1}. Compared with CC, GNSs/CC has an obvious 2D peak, which can be used to judge that GN has been successfully fabricated. The peak strength ratio of I_G/I_{2D} is used to assist in the analysis of the number of GN layers. In our work, the ratio of I_G/I_{2D} is 0.88, which indicates that the grown GN has fewer layers. This result confirms the statement of 3D GNSs and indicates that the results measured by Raman spectroscopy are consistent with the results of SEM images.

We can judge whether the electrodes are modified and their conductivity is good or bad by comparing the peak currents on different modified electrodes (Zhang et al., 2019). **Figure 2E** shows the cyclic voltammograms of CC and GNSs/CC electrodes in 0.01 mM $[Fe(CN)_6]^{3-/4-}$ and 0.1 M KCl solutions. Compared with CC, the response current of GNSs/CC to $[Fe(CN)_6]^{3-/4-}$ increases obviously, and the larger the peak current, the larger the effective area of the electrode will be. Therefore, GN with the 3D structure fabricated by the thermal CVD method significantly increases the specific surface area of electrodes and provides more chemical active sites. In addition, it shows that the electron transfer ability of GNSs/CC electrodes is good and the excellent conductivity of GN plays an important role. **Figure 2E** also shows that the peak current gradually increases with an increase in the thickness of the GN layer and the maximum current value is obtained in 7 h GNSs/CC electrodes.

Figure 2F is the EIS of different electrodes. In the high-frequency part of EIS representing the resistance, CC electrodes present a large semicircle (curve a) with an impedance value of approximately 245 Ω. The impedance value decreases sharply to 82 Ω (curve b) when GN is modified on the CC fiber for 1 hour, indicating that the GNSs/CC electrodes have better electron transport capacity and electrochemical activity. Curves c, d, and e are the impedance curves of 5 h GNSs/CC, 7 h GNSs/CC, and 10 h GNSs/CC, respectively. The resistance values corresponding to the semicircles are 75, 47, and 11 Ω, respectively. With the prolongation in growth time of GN, the thickness of GN on CC increases gradually and the electron transfer resistance gradually decreases which indicates that the GNSs/CC electrodes can improve the transfer rate of electrons. **Figures 2G,H** show the resistance measurement of our sensor under different bending degrees. The results show that the resistance of the GNSs/CC flexible sensor remains stable during and after bending for 100 times, indicating that our sensor has the advantages of flexibility and performance stability. The reason is that CC is a very good electronic substrate with excellent flexibility, which can maintain its electrochemical performance under tough repeated bending.

Cyclic Voltammetry for the Detection of Small Biological Molecules (Ascorbic Acid, Dopamine, and Uric Acid)

CV is used to investigate the catalytic performance of GNSs/CC electrodes in the detection of AA, DA, and UA. These small molecules are oxidized and lose electrons during the detection process, which generate electric current through electron transfer with the electrode (Ensafi et al., 2010; Zhou et al., 2014). The magnitude of the electric current is positively correlated with the concentrations of small molecules. Therefore, we can test the concentrations of a series of small molecules and their corresponding current values and find the linear range of these analytes.

Figure 3A shows the cyclic voltammograms of 7 h GNSs/CC electrodes from -0.6 to 0.4 V at a rate of 50 mV s^{-1} in 0.01–4.0 mM AA and 0.1 M PBS solutions. The oxidation peak potential of AA on the electrode is −68 mV, and the oxidation peak potential and peak type of AA do not change much at different modified electrodes. In addition, the peak current of AA increases linearly with an increase in the AA concentration. **Figure 3D** shows the fitting results of the relationship between the current and concentration obtained by detecting AA with 1 h GNSs/CC, 5 h GNSs/CC, 7 h GNSs/CC, and 10 h GNSs/CC electrodes. The results show that the electrochemical response and sensitivity of GNSs/CC to AA are gradually enhanced with the increase in the thickness of GN. The maximum sensitivity of 244.3 μA mM^{-1} cm^{-2} and the minimum detectable concentration of 0.001 mM are obtained at 7 h GNSs/CC electrodes. The reason is that the presence of GN can improve the catalytic performance of AA when the growth time of GN is 1 h. Once the 3D structure of GN is formed, its ability to collect reaction electrons is further improved, and with the continuous improvement of this 3D structure, the active sites are further increased. The adsorption enrichment and catalytic capacity of small molecules reach the maximum when the growth time of GN is 7 h, so the response to AA is further improved and the sensitivity reaches the maximum. However, the detection sensitivity and response current of AA decrease when the growth time of GN increases to 10 h. It is possible that the GN coated on the surface of the CC is very thick; only the outer layer of GN participates in the reaction, while the inner layer of GN does not participate in the reaction, which becomes the invalid active site. Subsequently, we use our GNSs/CC electrodes to detect DA and UA by CV, respectively. **Figures 3B,E** show that the electrochemical response of GNSs/CC to DA gradually increases with an increase in the thickness of GN. The maximum sensitivity of 380 μA mM^{-1} cm^{-2} and the minimum detectable concentration of 0.0001 mM are obtained on the 7 h GNSs/CC electrodes. **Figures 3C,F** show that the electrochemical response of 5 h GNSs/CC electrodes to UA reaches the maximum. The sensitivity for detecting UA is 1872 μA mM^{-1} cm^{-2}, and the minimum detectable concentration is 0.001 mM.

In order to verify the feasibility of our GNSs/CC electrodes for the simultaneous detection of three small biomolecules (AA, DA, and UA), we detect them simultaneously by CV using CC electrodes and GNSs/CC electrodes, respectively. In this experiment, the scan voltage range is −0.4–0.6 V, the scan rate is 0.5 mV s^{-1}, and the scan time is 15 turns. An oxidation reaction will occur on the electrode when scanning occurs from the positive electrode to the negative electrode, and an oxidation peak will be obtained; when scanning occurs from the negative electrode to the positive electrode, a reduction reaction occurs, resulting in a reduction peak. The solution used is 0.1 M PBS solution with pH 7.4, and the concentrations of AA, DA, and UA target analytes are 0.8, 0.01, and 0.1 mM, respectively.

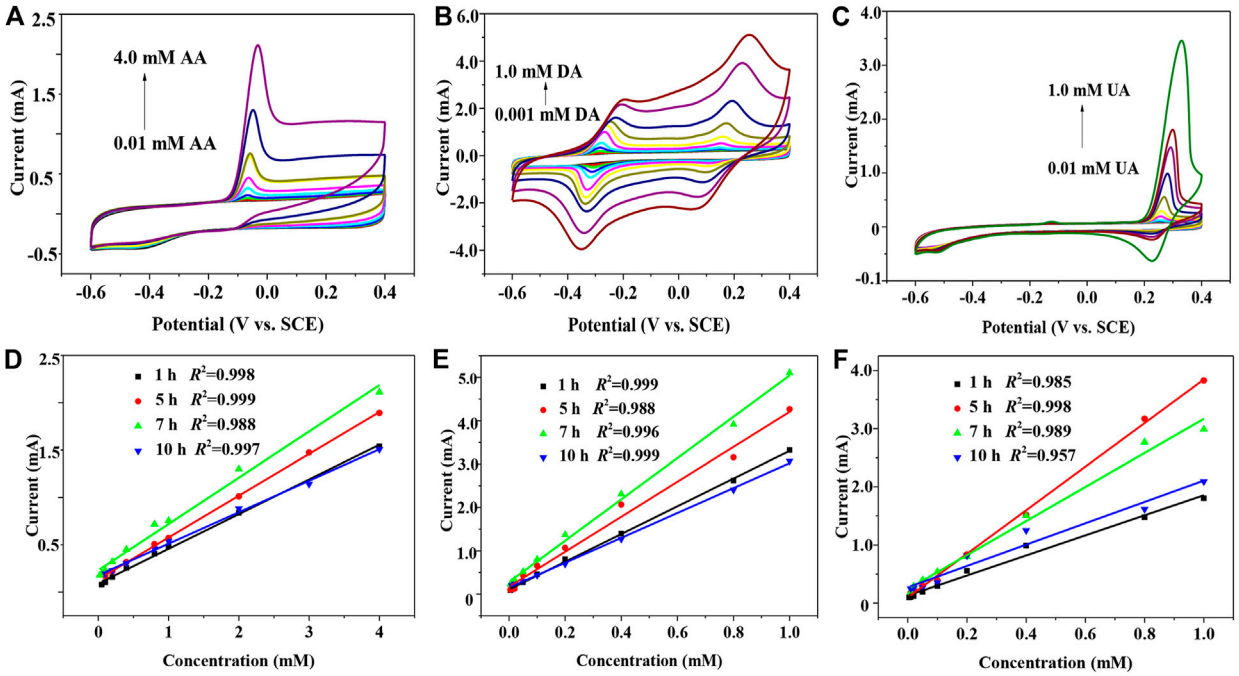

FIGURE 3 | GNSs/CC electrodes with different GN growth periods are used to separately detect AA, DA, and UA by CV. **(A)** CV detecting AA alone. **(B)** CV detecting DA alone. **(C)** CV detecting UA alone. **(D)** Fitting results of the relationship between the current and concentration are obtained by detecting AA using GNSs/CC. **(E)** Fitting results of the relationship between the current and concentration are obtained by detecting DA using GNSs/CC. **(F)** Fitting results of the relationship between the current and concentration are obtained by detecting UA using GNSs/CC.

Supplementary Figure S1 shows the cyclic voltammograms of different electrodes for the simultaneous detection of AA, DA, and UA. The results show that only two oxidation peaks of these three small molecules appear on the CC electrodes and the peak widths are larger, indicating that the oxidation peaks of the bare CC electrodes overlap each other in the detection of these substances. Therefore, the CC electrodes cannot be used to detect AA, DA, and UA simultaneously. On the contrary, the oxidation peaks of these three small molecules are obviously displayed on the GNSs/CC electrodes, the position and shape of the oxidation peaks are changed, and the width of the peaks is narrow. The three oxidation peaks that are initially close to each other are negatively shifted to different degrees, which realizes the separation of the three small molecular oxidation peaks. **Supplementary Figure S1** also shows that the oxidation peak potentials of AA, DA, and UA is at −76, 190, and 327 mV, respectively, and the peak potential difference (ΔE_p) between the two is 266 and 137 mV, respectively. A large ΔE_p is the prerequisite for achieving the separation of the oxidation peaks of the three substances, which is attributed to the excellent catalytic capacity of GN and the large specific surface area of 3D GN. In addition, the peak current corresponding to the oxidation peak on the GNSs/CC electrodes is larger than that on the CC electrodes, which indicates that GN has high electron transfer ability and can improve the response of the electrode to substances with the same concentration.

The GNSs/CC electrodes can distinguish the redox peaks of these three small molecules by CV, detecting them simultaneously. However, CV often presents large non-Faradaic current, which often leads to the extreme drift of peak current (**Figure 4A**). By contrast, DPV can reduce the limit of voltammetry measurement by significantly reducing the ratio of non-Faradaic current to Faradaic current, thus showing a low detection limit and high sensitivity. As shown in **Figure 4B**, the oxidation potentials of the three substances detected by DPV are -60 mV (AA), 116 mV (DA), and 244 mV (UA). The ΔE_p between the two pairs is very large, 176 and 128 mV, respectively. Therefore, the GNSs/CC electrode can meet the requirements of individual and simultaneous detection of these three small molecules. Next, we use DPV to detect the electrochemical properties of electrode materials.

Differential Pulse Voltammetry for the Detection of Three Small Biomolecules

Figure 5A is the pulsed Volt–Ampere characteristic curves obtained by the simultaneous detection of AA, DA, and UA using 7 h GNSs/CC electrodes by DPV. **Figure 5D** shows the fitting result of the relationship between the peak current and concentration of AA. In the three mixtures, the concentration of AA varies from 0.02 to 0.8 mM, while the concentrations of DA and UA remain unchanged, which are 0.01 and 0.1 mM, respectively. The results show that the oxidation peak potential of AA is around −60 mV, that of DA is around 116 mV, and that of UA is around 244 mV. There is a large distance between the oxidation peaks of these three substances, and they are completely

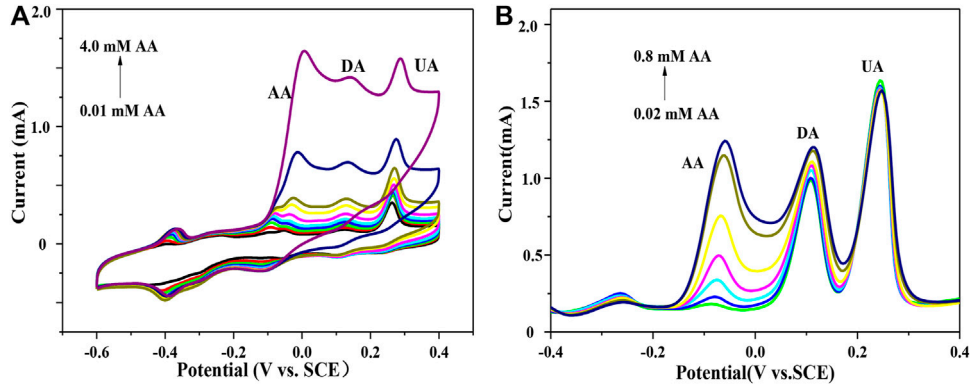

FIGURE 4 | 7 h GNSs/CC electrode detects AA in the presence of DA and UA. **(A)** CV. **(B)** DPV.

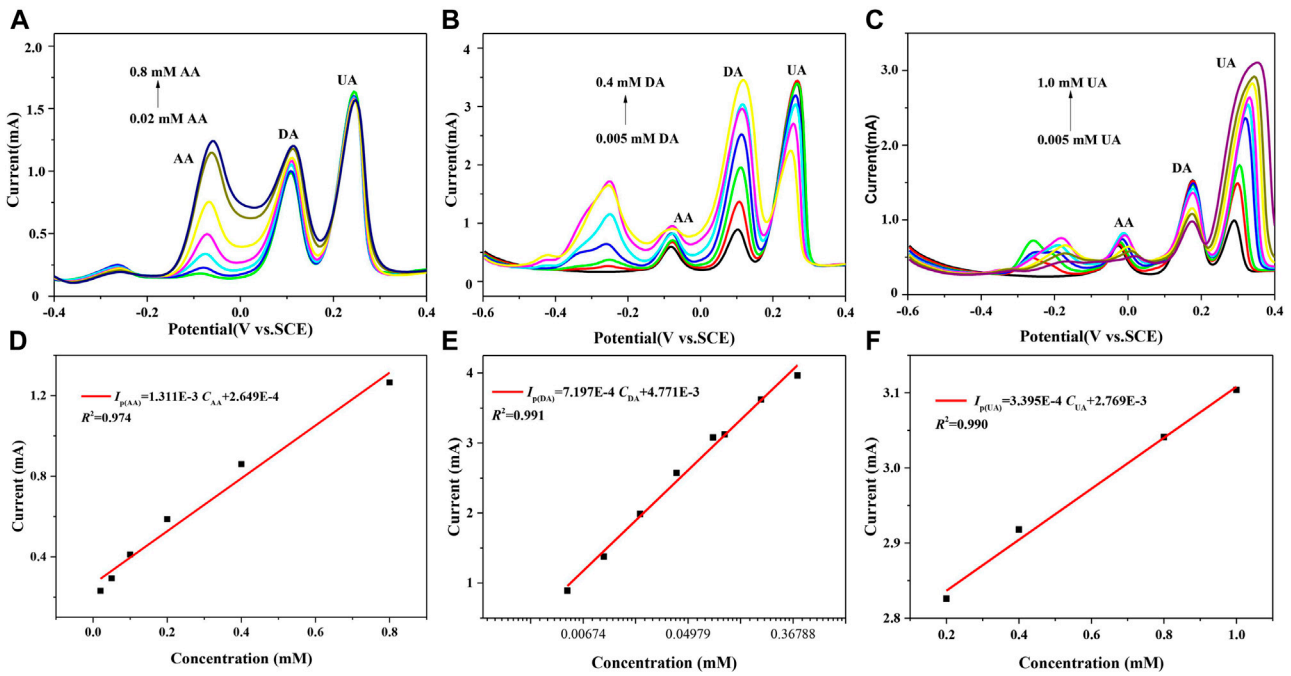

FIGURE 5 | 7 h GNSs/CC electrodes are used to detect AA, DA, and UA by DPV. **(A)** AA concentration changes, whereas DA and UA concentrations remain unchanged. **(B)** DA concentration changes, whereas AA and UA concentrations remain unchanged. **(C)** UA concentration changes, whereas AA and DA concentrations remain unchanged. **(D)** The fitting curve of peak current and concentration of AA. **(E)** The fitting curve of peak current and concentration of DA. **(F)** The fitting curve of peak current and concentration of UA.

undisturbed. The peak current of AA increases linearly with an increase in its concentration, while the corresponding peak current of DA and UA almost remain unchanged. In the presence of high concentrations of UA and DA, the sensitivity of 7 h GNSs/CC electrodes for AA detection is 655.5 μA mM^{-1} cm^{-2} and the linear equation is $I_P(\mu A) = 1311C_{AA} + 264.9$ (R^2 = 0.974). **Figures 5B,E** show the experimental results of detecting DA using 7 h GNSs/CC electrodes by DPV under the condition of constant AA and UA concentrations. The concentration of DA varies in the range of 0.05–0.4 mM, the concentration of AA is 0.1 mM, and the concentration of UA is 0.1 mM. The results show that the oxidation peak potentials of DA, AA, and UA are 116, −76, and 268 mV, respectively. The distance between the oxidation peaks of these three substances is larger, and there is no interference between them. The peak current of DA gradually increases with an increase in its concentration, while the corresponding peak currents of AA and UA almost remain unchanged. In addition, the sensitivity of 7 h GNSs/CC electrodes to detect DA is 359.9 μA mM^{-1} cm^{-2} and the linear equation is $I_P(\mu A) = 719.7C_{DA} + 4{,}711$ (R^2 = 0.991). **Figure 5C**

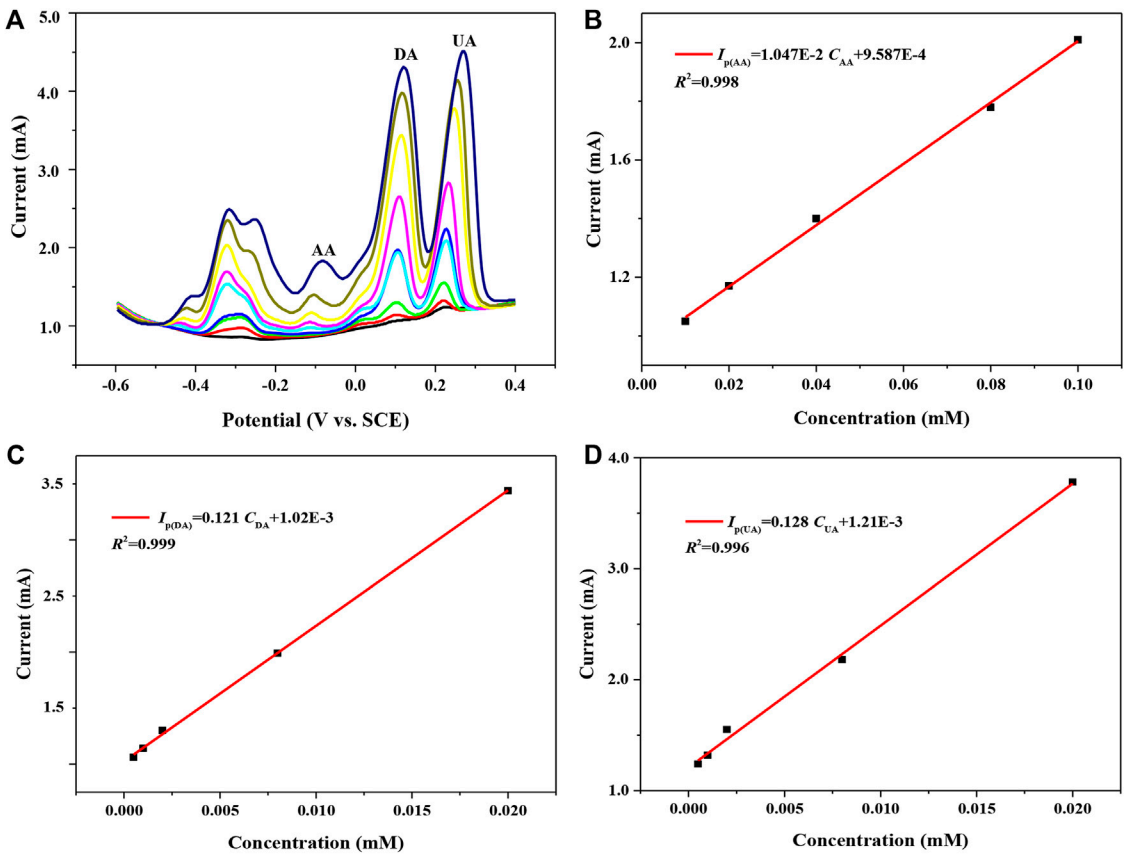

FIGURE 6 | 7 h GNSs/CC electrodes are used to detect AA, DA, and UA by DPV simultaneously. **(A)** Pulsed Volt–Ampere characteristic curves of AA, DA, and UA. **(B)** The fitting curve of peak current and concentration of AA. **(C)** The fitting curve of peak current and concentration of DA. **(D)** The fitting curve of peak current and concentration of UA.

TABLE 1 | Detection of UA in real blood samples.

Serum sample	Results from commercial measurements (mM)	Results of our sensor measurements (mM)	Recovery (%)
1	0.723	0.750	104
2	0.497	0.521	105
3	0.203	0.251	124

TABLE 2 | Performance comparison of sensors for small molecule detection.

Sensor	Linear range (μM)			Detection limit (μM)			References
	AA	DA	UA	AA	DA	UA	
PrGO/MnO_2	1–800	0.03–45	0.3–80	1.00	0.02	0.05	Tukimin et al. (2018)
Pd_3Pt_1/PDDA-RGO	40–1,200	4–200	4–400	0.61	0.04	0.10	Yan et al. (2013)
Au@Pd-RGO	1–800	0.1–100	0.1–350	0.28	0.024	0.02	Jiang and Du, (2014)
rGO-CNT/ITO	10–200	0.2–8.0	0.2–16.0	5.31	0.04	0.17	Zhang et al. (2015)
AuNPs/P(PDA)/GO	6.0–2,400	0.05–100	0.5–150	1.76	0.017	0.16	Tig et al. (2017)
ErGO/CFE	8–2016.45	1.5–224.82	6–899.3	4.5	0.77	2.23	Yang et al. (2014)
GNSs/CC	20–1,000	0.5–20	0.5–20	0.31	0.01	0.03	Our work

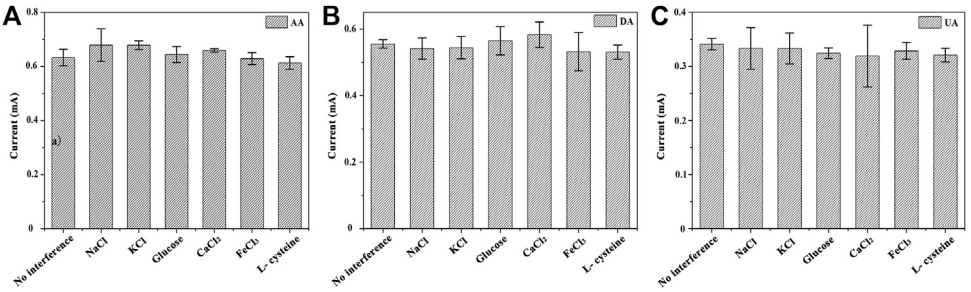

FIGURE 7 | Test results of electrode anti-interference performance of 7 h GNSs/CC electrodes in PBS buffer with pH 7.4. (A) Influence of interfering substances on AA; (B) Influence of interfering substances on DA; (C) Influence of interfering substances on UA.

shows the pulsed Volt–Ampere characteristic curves of UA detected by DPV using 7 h GNSs/CC electrodes under the condition of constant AA and DA concentrations. The concentration of UA ranges from 0.2 to 1.0 mM, with 0.1 mM for AA and 0.01 mM for DA. The results show that the oxidation peaks of these three substances are also spaced far apart and are not disturbed by each other at all. As UA concentration gradually increases, its peak current also increases linearly between 0.2 and 1.0 mM (**Figure 5F**). The sensitivity of 7 h GNSs/CC electrodes while detecting UA in the presence of high concentrations of AA and DA is 169.75 μA mM^{-1} cm^{-2}, and the linear equation is $I_P(\mu A) = 339.5C_{UA} + 2{,}769$ ($R^2 = 0.990$).

Figure 6A shows the pulsed Volt–Ampere characteristic curves of 7 h GNSs/CC electrodes in PBS solution containing AA (concentration is 0.02–0.1 mM), DA (0.0005–0.02 mM), and UA (0.0005–0.02 mM) from −0.6 to 0.4 V potential at a rate of 50 mV s^{-1}. The redox process of these three substances can be simply summarized as follows when they are simultaneously detected using 7 h GNSs/CC electrodes: the three small molecules synchronously diffuse to the nearest electrode surface through mass transfer due to the existence of concentration difference, the small molecules diffused to the electrode surface are electrocatalyzed to undergo a redox reaction, and the oxidation products diffuse away from the electrode surface due to the concentration difference. During this process, the 3D-structured GN can not only add the chemical active sites for the oxidation reaction but also serve as an electrolyte reservoir to store more small molecules and improve the electron transfer rate. As shown in **Figure 6A**, the oxidation peak potentials of AA, DA, and UA are about -84, 120, and 272 mV, respectively. The oxidation peak potential differences of AA and DA and DA and UA are 204 and 152 mV, respectively, indicating that they will not interfere with each other. Moreover, the peak currents of these three substances also gradually increase with the increase in their concentrations. **Figures 6B–D** show the fitting results of peak currents versus concentration for AA, DA, and UA, respectively. The peak current of AA in the three mixtures is proportional to the concentration in the range of 0.02–0.1 mM, giving a detection sensitivity of 5,470 μA mM^{-1} cm^{-2}, and the linear equation is $I_P(\mu A) = 10470C_{AA} + 95{,}870$ ($R^2 = 0.998$). The peak current of DA is proportional to the concentration over the range of 0.0005–0.02 mM, with a detection sensitivity of 60,500 μA mM^{-1} cm^{-2}, and the linear equation is $I_P(\mu A) = 121000C_{DA} + 1{,}020$ ($R^2 = 0.999$). The peak current of UA is proportional to the concentration in the range of 0.0005–0.02 mM, with a detection sensitivity of 64,000 μA mM^{-1} cm^{-2}, and the linear equation is $I_P(\mu A) = 128000C_{UA} + 1{,}210$ ($R^2 = 0.996$). Compared with the single detection of small molecules, the 7 h GNSs/CC electrodes can obtain ultrahigh sensitivity in the low-concentration region when detecting AA, DA, and UA simultaneously. Additionally, the electron transfer of these three small molecules has a synergistic effect during simultaneous detection.

Detection of Stability and Anti-Interference

Research on anti-interference: the anti-interference capability of the GNSs/CC electrodes is very important since the environment of the blood sample is much more complex than the standard solution we prepared. In order to further detect real blood samples and investigate the anti-interference and selectivity of the sensor, we carried out the anti-interference experiment. Some common ions and small molecules coexisting in blood are selected as the research subjects, and the possible ions and molecules are as follows: Na^+, K^+, Ca^{2+}, Cl^-, L-cysteine, and glucose. We use 7 h GNSs/CC electrodes to detect the solution (5 mM) containing the above ions and molecules. When three substances (50 μM AA, 5 μM UA, and 5 μM DA) are detected at a certain concentration in the PBS solution at pH 7.4, we judge the effect of the interfering substance on the detection target analyte by recording the current in the presence and absence of the interfering substance (**Figure 7**). The results show that the current deviation of KCl and $CaCl_2$ is relatively larger, which has a certain influence on AA, while the influence of other substances can be basically ignored. NaCl and $FeCl_3$ have the greatest influence on DA, while $FeCl_3$ and L-cysteine are the most influential substances for UA. On the whole, the common ions and molecules coexisting with AA, DA, and UA have little effect on them, which means that the GNSs/CC biosensor has very good anti-interference ability against potential interfering substances, including ions and small chemical molecules.

Research on repeatability and stability: subsequently, we conducted the repeatability and stability research on the fabricated GNSs/CC sensor. The sensor is sealed in deionized water and stored at room temperature. After 7 days of storage, the same concentrations of AA, DA, and UA are detected again by DPV. The results show that their current values do not change significantly and the responses of AA, DA, and UA are 88.2, 92.5,

and 94.2% to the initial current, respectively. In addition, we fabricate three electrodes under the same conditions, on which the three small molecules of AA, DA, and UA are detected by DPV. The results show that the relative deviation of the peak currents of the three small molecules is 2.23% (AA), 2.34% (DA), and 1.35% (UA). The above results demonstrate that the GNSs/CC sensor has good repeatability and stability.

Detection of Uric Acid in Human Serum Samples

Based on the above discussion, we further apply the GNSs/CC sensor in the detection of real blood samples to explore its practicality. A serum sample with known UA concentration is added to the PBS solution, and the peak current of DPV response is measured. The obtained current value is brought into the fitting relationship between the current and concentration obtained in **Supplementary Figure S2**, $I_p(\mu A) = 3750\ C_{UA} + 763.6$, to calculate the concentration of UA in the serum samples. Then, the concentration of UA in raw serum is calculated according to the volume of the dropwise-added serum. **Table 1** shows the detection results of UA in the human serum with our GNSs/CC sensor and measurements obtained at Shenzhen Hospital of Peking University. The recovery rate is between 104 and 124% compared with the results measured by dry chemical analysis in the hospital, indicating that the GNSs/CC flexible sensor has good recovery and accuracy in the detection of UA in real blood samples.

Table 2 lists six GN-based sensors and their detection performance. It can be seen that GN and its derivatives are very suitable as the substrate materials for sensors since they can prove their high catalytic performance and excellent electrochemical activity. They can provide similar detection and boosting performance after functional material doping. Compared with all of those sensors, our GNSs/CC sensor offers a good linear range (AA: 20–1,000 μM, DA: 0.5–20 μM, and UA: 0.5–20 μM) and low detection limit (AA: 0.31 μM, DA: 0.01 μM, and UA: 0.03 μM; S/N = 3) without further functional material doping. The sensor still holds remarkable potential in performance boosting of biomedical detection. In addition, our sensor is fabricated on the substrate of CC, which can be integrated with flexible electronics to fit many biomedical detection and sensoring scenarios.

CONCLUSION

In summary, we have successfully fabricated a GNSs/CC flexible sensor via thermal CVD that can detect AA, DA, and UA simultaneously. The GNSs/CC electrodes show good electrocatalytic activity in the detection of DA, AA, and UA, and the optimized performance is obtained when the GN growth time is 7 h. The ultrasensitive simultaneous detection of these three small molecules is realized by DPV using 7 h GNSs/CC electrodes, which can reduce the non-Faradaic current drift. The working linear range and sensitivity of the sensor are obtained. The linear ranges for the detection of AA, DA, and UA are 0.02–0.1, 0.0005–0.02, and 0.0005–0.02 mM, respectively, and their sensitivity rates are 5,470, 60,500, and 64,000 $\mu A\ mM^{-1}\ cm^{-2}$, respectively. The flexible sensor has good performance in terms of reproducibility, stability, and anti-interference against common interfering substances in the blood. Moreover, it has successfully detected UA in the human serum with the recovery rate between 104 and 124%, indicating that the GNSs/CC sensor holds remarkable potential in the commercial detection of real biomedical samples. This work provides an ultrasensitive detection tool and method for the simultaneous detection of the basic substances AA, DA, and UA that sustain the metabolic activities of living organisms.

DATA AVAILABILITY STATEMENT

The original contributions presented in the study are included in the article/**Supplementary Material**; further inquiries can be directed to the corresponding author.

AUTHOR CONTRIBUTIONS

SM, YL, and LW analyzed the results and wrote the manuscript under the guidance of HF. SM, LW, XJ, and YC performed the experiments. HF, TZ, and JY conceived the idea for the project and wrote the manuscript. All authors read and approved the final manuscript.

FUNDING

This research was funded by the Shenzhen Science and Technology Planning Project (JCYJ20180507183224565) and the Shenzhen Peacock Group (KQTD20170809110344233).

SUPPLEMENTARY MATERIAL

The Supplementary Material for this article can be found online at: https://www.frontiersin.org/articles/10.3389/fbioe.2021.726071/full#supplementary-material

REFERENCES

Abbas, Y., Ali, S., Basharat, M., Zou, W., Yang, F., Liu, W., et al. (2020). Heteroatom-Doped Carbon Nanoparticle-Ionic Liquid Composites as Electrochemical Sensors for Uric Acid. *ACS Appl. Nano Mater.* 3, 11383–11390. doi:10.1021/acsanm.0c02466

Bakker, E., and Telting-Diaz, M. (2002). Electrochemical Sensors. *Anal. Chem.* 74, 2781–2800. doi:10.1021/ac0202278

Ciucci, F. (2019). Modeling Electrochemical Impedance Spectroscopy. *Curr. Opin. Electrochemistry.* 13, 132–139. doi:10.1016/j.coelec.2018.12.003

Du, J., Yue, R., Ren, F., Yao, Z., Jiang, F., Yang, P., et al. (2014). Novel Graphene Flowers Modified Carbon Fibers for Simultaneous Determination of Ascorbic Acid, Dopamine and Uric Acid. *Biosens. Bioelectron.* 53, 220–224. doi:10.1016/j.bios.2013.09.064

Elgrishi, N., Rountree, K. J., McCarthy, B. D., Rountree, E. S., Eisenhart, T. T., and Dempsey, J. L. (2018). A Practical Beginner's Guide to Cyclic Voltammetry. *J. Chem. Educ.* 95, 197–206. doi:10.1021/acs.jchemed.7b00361

Ensafi, A. A., Taei, M., and Khayamian, T. (2010). Simultaneous Determination of Ascorbic Acid, Dopamine, and Uric Acid by Differential Pulse Voltammetry Using Tiron Modified Glassy Carbon Electrode. *Int. J. Electrochem. Sci.* 5, 116–130.

Ezzeddine, A., Chen, Z., Schanze, K. S., and Khashab, N. M. (2015). Surface Modification of Multiwalled Carbon Nanotubes With Cationic Conjugated Polyelectrolytes: Fundamental Interactions and Intercalation Into Conductive Poly(methyl Methacrylate) Composites. *ACS Appl. Mater. Inter.* 7, 12903–12913. doi:10.1021/acsami.5b02540

Gao, Z., and Huang, H. (1998). Simultaneous Determination of Dopamine, Uric Acid and Ascorbic Acid at an Ultrathin Film Modified Gold Electrode. *Chem. Commun.* 2107–2108. doi:10.1039/a805915b

Han, H. S., Seol, H., Kang, D. H., Ahmed, M. S., You, J.-M., and Jeon, S. (2014). Electrochemical Oxidation and Determination of Dopamine in the Presence of AA Using Ferulic Acid Functionalized Electrochemically Reduced Graphene. *Sensors Actuators B: Chem.* 204, 289–296. doi:10.1016/j.snb.2014.07.075

Hortigon-Vinagre, M. P., Zamora, V., Burton, F. L., Green, J., Gintant, G. A., and Smith, G. L. (2016). The Use of Ratiometric Fluorescence Measurements of the Voltage Sensitive Dye Di-4-ANEPPS to Examine Action Potential Characteristics and Drug Effects on Human Induced Pluripotent Stem Cell-Derived Cardiomyocytes. *Toxicol. Sci.* 154, 320–331. doi:10.1093/toxsci/kfw171

Hou, J., Liu, Z., Li, Y., Yang, S., and Zhou, Y. (2015). A Comparative Study of Graphene-Coated Stainless Steel Fiber Felt and Carbon Cloth as Anodes in MFCs. *Bioproc. Biosyst. Eng.* 38, 881–888. doi:10.1007/s00449-014-1332-0

Hubbard, K. E., Wells, A., Owens, T. S., Tagen, M., Fraga, C. H., and Stewart, C. F. (2009). Determination of Dopamine, Serotonin, and Their Metabolites in Pediatric Cerebrospinal Fluid by Isocratic High Performance Liquid Chromatography Coupled with Electrochemical Detection. *Biomed. Chromatogr.* 24, a–n. doi:10.1002/bmc.1338

Ianni, F., Saluti, G., Galarini, R., Fiorito, S., Sardella, R., and Natalini, B. (2019). Enantioselective High-Performance Liquid Chromatography Analysis of Oxygenated Polyunsaturated Fatty Acids. *Free Radic. Biol. Med.* 144, 35–54. doi:10.1016/j.freeradbiomed.2019.04.038

Jiang, J., and Du, X. (2014). Sensitive Electrochemical Sensors for Simultaneous Determination of Ascorbic Acid, Dopamine, and Uric Acid Based on Au@Pd-Reduced Graphene Oxide Nanocomposites. *Nanoscale.* 6, 11303–11309. doi:10.1039/c4nr01774a

Karimi-Maleh, H., Karimi, F., Alizadeh, M., and Sanati, A. L. (2020). Electrochemical Sensors, a Bright Future in the Fabrication of Portable Kits in Analytical Systems. *Chem. Rec.* 20, 682–692. doi:10.1002/tcr.201900092

Kim, D.-H., Ahn, J.-H., Choi, W. M., Kim, H.-S., Kim, T.-H., Song, J., et al. (2008). Stretchable and Foldable Silicon Integrated Circuits. *Science.* 320, 507–511. doi:10.1126/science.1154367

Kumar, S. S., Mathiyarasu, J., and Phani, K. L. (2005). Exploration of Synergism between a Polymer Matrix and Gold Nanoparticles for Selective Determination of Dopamine. *J. Electroanalytical Chem.* 578, 95–103. doi:10.1016/j.jelechem.2004.12.023

Li, G., Xia, Y., Tian, Y., Wu, Y., Liu, J., He, Q., et al. (2019). Review-Recent Developments on Graphene-Based Electrochemical Sensors Toward Nitrite. *J. Electrochem. Soc.* 166, B881–B895. doi:10.1149/2.0171912jes

Liao, C., Zhang, M., Niu, L., Zheng, Z., and Yan, F. (2014). Organic Electrochemical Transistors With Graphene-Modified Gate Electrodes for Highly Sensitive and Selective Dopamine Sensors. *J. Mater. Chem. B.* 2, 191–200. doi:10.1039/c3tb21079k

Lin, X.-Q., He, J.-B., and Zha, Z.-G. (2006). Simultaneous Determination of Quercetin and Rutin at a Multi-Wall Carbon-Nanotube Paste Electrodes by Reversing Differential Pulse Voltammetry. *Sensors Actuators B: Chem.* 119, 608–614. doi:10.1016/j.snb.2006.01.016

Lu, Q., Lin, R., Du, C., Meng, Y., Yang, M., Zenobi, R., et al. (2020). Metal Probe Microextraction Coupled to Dielectric Barrier Discharge Ionization-Mass Spectrometry for Detecting Drug Residues in Organisms. *Anal. Chem.* 92, 5921–5928. doi:10.1021/acs.analchem.0c00004

Masliah, E., Rockenstein, E., Veinbergs, I., Mallory, M., Hashimoto, M., Takeda, A., et al. (2000). Dopaminergic Loss and Inclusion Body Formation in -Synuclein Mice: Implications for Neurodegenerative Disorders. *Science.* 287, 1265–1269. doi:10.1126/science.287.5456.1265

Mesbah, M., Premachandran, U., and Whitman, W. B. (1989). Precise Measurement of the G+C Content of Deoxyribonucleic Acid by High-Performance Liquid Chromatography. *Int. J. Syst. Bacteriol.* 39, 159–167. doi:10.1099/00207713-39-2-159

Nalewajko, E., Bort Ramı´rez, R., and Kojło, A. (2004). Determination of Dopamine by Flow-Injection Analysis Coupled with luminol-Hexacyanoferrate(III) Chemiluminescence Detection. *J. Pharm. Biomed. Anal.* 36, 219–223. doi:10.1016/j.jpba.2004.05.009

Pajkossy, T., and Jurczakowski, R. (2017). Electrochemical Impedance Spectroscopy in Interfacial Studies. *Curr. Opin. Electrochemistry.* 1, 53–58. doi:10.1016/j.coelec.2017.01.006

Polovina, M., Babić, B., Kaluderović, B., and Dekanski, A. (1997). Surface Characterization of Oxidized Activated Carbon Cloth. *Carbon.* 35, 1047–1052. doi:10.1016/S0008-6223(97)00057-2

Premkumar, J., and Khoo, S. B. (2005). Electrocatalytic Oxidations of Biological Molecules (Ascorbic Acid and Uric Acids) at Highly Oxidized Electrodes. *J. Electroanalytical Chem.* 576, 105–112. doi:10.1016/j.jelechem.2004.09.030

Privett, B. J., Shin, J. H., and Schoenfisch, M. H. (2010). Electrochemical Sensors. *Anal. Chem.* 82, 4723–4741. doi:10.1021/ac101075n

Qi, T., Song, C., He, J., Shen, W., Kong, D., Shi, H., et al. (2020). Highly Sensitive Detection of Multiple MicroRNAs by High-Performance Liquid Chromatography Coupled with Long and Short Probe-Based Recycling Amplification. *Anal. Chem.* 92, 5033–5040. doi:10.1021/acs.analchem.9b05301

Sansuk, S., Bitziou, E., Joseph, M. B., Covington, J. A., Boutelle, M. G., Unwin, P. R., et al. (2013). Ultrasensitive Detection of Dopamine Using a Carbon Nanotube Network Microfluidic Flow Electrode. *Anal. Chem.* 85, 163–169. doi:10.1021/ac3023586

Sasaki, K.-i., Tokura, Y., and Sogawa, T. (2013). The Origin of Raman D Band: Bonding and Antibonding Orbitals in Graphene. *Crystals.* 3, 120–140. doi:10.3390/cryst3010120

Stankovich, S., Dikin, D. A., Piner, R. D., Kohlhaas, K. A., Kleinhammes, A., Jia, Y., et al. (2007). Synthesis of Graphene-Based Nanosheets via Chemical Reduction of Exfoliated Graphite Oxide. *Carbon.* 45, 1558–1565. doi:10.1016/j.carbon.2007.02.034

Tarabová, B., Lukeš, P., Hammer, M. U., Jablonowski, H., von Woedtke, T., Reuter, S., et al. (2019). Fluorescence Measurements of Peroxynitrite/peroxynitrous Acid in Cold Air Plasma Treated Aqueous Solutions. *Phys. Chem. Chem. Phys.* 21, 8883–8896. doi:10.1039/c9cp00871c

Tig, G. A., Gunendi, G., and Pekyardimci, S. (2017). A Selective Sensor Based on Au Nanoparticles-Graphene Oxide-Poly(2,6-Pyridinedicarboxylic Acid) Composite for Simultaneous Electrochemical Determination of Ascorbic Acid, Dopamine, and Uric Acid. *J. Appl. Electrochem.* 47, 607–618. doi:10.1007/s10800-017-1060-7

Tukimin, N., Abdullah, J., and Sulaiman, Y. (2018). Electrodeposition of Poly(3,4-Ethylenedioxythiophene)/Reduced Graphene Oxide/manganese Dioxide for Simultaneous Detection of Uric Acid, Dopamine and Ascorbic Acid. *J. Electroanalytical Chem.* 820, 74–81. doi:10.1016/j.jelechem.2018.04.065

Wightman, R. M., May, L. J., and Michael, A. C. (1988). Detection of Dopamine Dynamics in the Brain. *Anal. Chem.* 60, 769A–779A. doi:10.1021/ac00164a001

Wu, H., and Drzal, L. T. (2012). Graphene Nanoplatelet Paper as a Light-Weight Composite With Excellent Electrical and Thermal Conductivity and Good Gas Barrier Properties. *Carbon.* 50, 1135–1145. doi:10.1016/j.carbon.2011.10.026

Xie, Y. (2001). Analyzing Haloacetic Acids Using Gas Chromatography/Mass Spectrometry. *Water Res.* 35, 1599–1602. doi:10.1016/S0043-1354(00)00397-3

Yan, J., Liu, S., Zhang, Z., He, G., Zhou, P., Liang, H., et al. (2013). Simultaneous Electrochemical Detection of Ascorbic Acid, Dopamine and Uric Acid Based on Graphene Anchored with Pd-Pt Nanoparticles. *Colloids Surf. B: Biointerfaces.* 111, 392–397. doi:10.1016/j.colsurfb.2013.06.030

Yang, B., Wang, H., Du, J., Fu, Y., Yang, P., and Du, Y. (2014). Direct Electrodeposition of Reduced Graphene Oxide on Carbon Fiber Electrode for Simultaneous Determination of Ascorbic Acid, Dopamine and Uric Acid. *Colloids Surf. A: Physicochemical Eng. Aspects.* 456, 146–152. doi:10.1016/j.colsurfa.2014.05.029

Yang, M., Weng, L., Zhu, H., Fan, T., and Zhang, D. (2017). Simultaneously Enhancing the Strength, Ductility and Conductivity of Copper Matrix Composites with Graphene Nanoribbons. *Carbon.* 118, 250–260. doi:10.1016/j.carbon.2017.03.055

Yang, Y., Li, M., and Zhu, Z. (2019). A Novel Electrochemical Sensor Based on Carbon Nanotubes Array for Selective Detection of Dopamine or Uric Acid. *Talanta.* 201, 295–300. doi:10.1016/j.talanta.2019.03.096

You, K., Yan, G., Luo, X., Gilchrist, M. D., and Fang, F. (2020). Advances in Laser Assisted Machining of Hard and Brittle Materials. *J. Manufacturing Process.* 58, 677–692. doi:10.1016/j.jmapro.2020.08.034

Zare, H. R., Nasirizadeh, N., and Mazloum Ardakani, M. (2005). Electrochemical Properties of a Tetrabromo-P-Benzoquinone Modified Carbon Paste Electrode. Application to the Simultaneous Determination of Ascorbic Acid, Dopamine and Uric Acid. *J. Electroanalytical Chem.* 577, 25–33. doi:10.1016/j.jelechem.2004.11.010

Zhang, Y., Ji, Y., Wang, Z., Liu, S., and Zhang, T. (2015). Electrodeposition Synthesis of Reduced Graphene Oxide-Carbon Nanotube Hybrids on Indium Tin Oxide Electrode for Simultaneous Electrochemical Detection of Ascorbic Acid, Dopamine and Uric Acid. *RSC Adv.* 5, 106307–106314. doi:10.1039/c5ra24727f

Zhang, Y., Jiang, X., Zhang, J., Zhang, H., and Li, Y. (2019). Simultaneous Voltammetric Determination of Acetaminophen and Isoniazid Using MXene Modified Screen-Printed Electrode. *Biosens. Bioelectron.* 130, 315–321. doi:10.1016/j.bios.2019.01.043

Zhou, Y., Tang, W., Wang, J., Zhang, G., Chai, S., Zhang, L., et al. (2014). Selective Determination of Dopamine and Uric Acid Using Electrochemical Sensor Based on Poly(alizarin Yellow R) Film-Modified Electrode. *Anal. Methods.* 6, 3474–3481. doi:10.1039/c3ay42216j

Conflict of Interest: The authors declare that the research was conducted in the absence of any commercial or financial relationships that could be construed as a potential conflict of interest.

Publisher's Note: All claims expressed in this article are solely those of the authors and do not necessarily represent those of their affiliated organizations, or those of the publisher, the editors, and the reviewers. Any product that may be evaluated in this article, or claim that may be made by its manufacturer, is not guaranteed or endorsed by the publisher.

frontiers in Bioengineering and Biotechnology

REVIEW
published: 28 September 2021
doi: 10.3389/fbioe.2021.753692

Flexible Biosensors Based on Colorimetry, Fluorescence, and Electrochemistry for Point-of-Care Testing

Tingyi Yan[1†], Guangyao Zhang[1†], Huining Chai[2], Lijun Qu[1*] and Xueji Zhang[3]*

[1]State Key Laboratory of Bio-Fibers and Eco-Textiles, Intelligent Wearable Engineering Research Center of Qingdao, Research Center for Intelligent and Wearable Technology, College of Textiles and Clothing, Qingdao, China, [2]School of Environmental and Municipal Engineering, Qingdao University of Technology, Qingdao, China, [3]School of Biomedical Engineering, Health Science Center, Shenzhen University, Shenzhen, China

OPEN ACCESS

Edited by:
Yunlu Pan,
Harbin Institute of Technology, China

Reviewed by:
Zhen Gu,
University of Science and Technology Beijing, China
Yan Huang,
University of Science and Technology Beijing, China
Ye Tian,
Northeastern University, China
Dan Wen,
Northwestern Polytechnical University, China

***Correspondence:**
Guangyao Zhang
gyzhang@qdu.edu.cn
Lijun Qu
lijunqu@qdu.edu.cn

[†]These authors have contributed equally to this work

Specialty section:
This article was submitted to Biosensors and Biomolecular Electronics, a section of the journal Frontiers in Bioengineering and Biotechnology

Received: *05 August 2021*
Accepted: *13 September 2021*
Published: *28 September 2021*

Citation:
Yan T, Zhang G, Chai H, Qu L and Zhang X (2021) Flexible Biosensors Based on Colorimetry, Fluorescence, and Electrochemistry for Point-of-Care Testing. Front. Bioeng. Biotechnol. 9:753692. doi: 10.3389/fbioe.2021.753692

With the outbreak and pandemic of COVID-19, point-of-care testing (POCT) systems have been attracted much attention due to their significant advantages of small batches of samples, user-friendliness, easy-to-use and simple detection. Among them, flexible biosensors show practical significance as their outstanding properties in terms of flexibility, portability, and high efficiency, which provide great convenience for users. To construct highly functional flexible biosensors, abundant kinds of polymers substrates have been modified with sufficient properties to address certain needs. Paper-based biosensors gain considerable attention as well, owing to their foldability, lightweight and adaptability. The other important flexible biosensor employs textiles as substrate materials, which has a promising prospect in the area of intelligent wearable devices. In this feature article, we performed a comprehensive review about the applications of flexible biosensors based on the classification of substrate materials (polymers, paper and textiles), and illustrated the strategies to design effective and artificial sensing platforms, including colorimetry, fluorescence, and electrochemistry. It is demonstrated that flexible biosensors play a prominent role in medical diagnosis, prognosis, and healthcare.

Keywords: flexible biosensor, point-of-care testing, polymer, paper, textile

INTRODUCTION

COVID-19 is a human infectious disease caused by novel coronavirus, which has posed a serious threat to the public health of more than 200 countries and regions around the world. Therefore, it is important to seek a rapid and accurate method to contain COVID-19 (Udugama et al., 2020). In general, traditional lab-based testing method requires not only bulky analyzers but also professionally operators. Furthermore, patients need to wait several days to get the test results due to the time-consuming preparation of reagents and samples. Point-of-care testing (POCT) allows medics to detect diseases at the patient site, faster than traditional lab-based testing, and plays an important part in the difficult times of the COVID-19 pandemic (Choi, 2020; Nelson et al., 2020; Sachdeva et al., 2020; Zhao et al., 2021a). Among the various devices of POCT, portable sensors with flexible substrates are the most attractive one (Economou et al., 2018).

Portable flexible biosensors represent an increasingly important and rapidly growing area of research (Guo et al., 2019; Manjakkal et al., 2020; Patil et al., 2020). There are some significant

FIGURE 1 | Schematic diagram of flexible biosensors based on colorimetry, fluorescence, and electrochemistry for point-of-care testing.

advantages of portable flexible biosensors: 1) more user-friendly, less affected by external conditions; 2) the test results can be obtained in time without waiting for a long time; 3) the production cost is low and it is beneficial to the resource-limited areas; 4) more suitable for wear, can be fitted to the skin to achieve more real-time sampling. At present, the vast majority of substrate materials come from polymers, perfect fabrication technology and abundant kinds of polymers provide strong support for the development of portable flexible sensors (Spychalska et al., 2020). Paper-based biosensors have received considerable interest in recent years owing to their advantages such as foldability, portability and accessibility (Lee et al., 2018a). Moreover, the surface of paper-based biosensors can be easily and quickly modified with biomolecules and nanomaterials, which is of great help to improve the sensing performance. The other important flexible biosensors use textiles as substrate materials, which have a promising prospect in the area of wearable sensors due to the knittable nature of the fabric (Farajikhah et al., 2019).

Here, as shown in **Figure 1**, we performed a comprehensive review of the applications of flexible biosensors in POCT based on the classification of substrate materials (polymers, paper and textiles). In addition, we also introduce the mainstream sensing strategies of flexible biosensors in detail, including colorimetric, fluorescent, electrochemical technology, etc. Finally, we summarized current problems and discussed the future development of the portable flexible biosensor. This review focuses on the important applications of flexible biosensors in POCT over the past 3 years and in order to help readers understand the future trends in this field.

POLYMER-BASED FLEXIBLE BIOSENSORS FOR POCT

Polymer substrates have been used in the printed electronics for a long time, such as polyethylene naphthalene (PEN), polyethylene terephthalate (PET), polyimide (PI), polytetrafluoroethylene (PTFE), polymethyl methacrylate (PMMA), polydimethylsiloxane (PDMS), polyaniline (PANI), polycarbonate and so on. Because of their inherent plasticity, wide availability, low cost, good insulative properties, and excellent elasticity, a variety of biosensors made of these carrier materials have been introduced one after another (Andrysiewicz et al., 2020; Lee et al., 2020; Wang et al., 2021).

Colorimetric Test

Colorimetry is a common biochemical detection method, which is mainly used to evaluate the change of absorbance or reflectance of analytical reagents (Priye et al., 2018; Wang et al., 2019a). The basic requirement of colorimetric analysis is that the color reaction should have high sensitivity and selectivity, the colored compound generated by the reaction needs to maintain a relatively stable state. Therefore, providing a suitable reaction site and controlling the appropriate reaction conditions are the key to colorimetric analysis. These problems can be solved by emerging microfluidic technologies. Due to the difference of fluid performance between micro-scale and macro-scale, using micron pipes to control fluid can achieve a series of processing and treatment which are difficult to be completed by conventional methods. In recent years, microfluidic based POCT devices are widely used in the fields of chemical (Guo et al., 2018a), molecular biology (Yang et al., 2020) and biochemical analysis (Choi et al., 2018; Xu et al., 2018), while polymer substrates provide a broad stage for research and development of microfluidic technology.

Sweat is an important metabolite, the physiological information contained therein can be easily monitored in a continuous and non-invasive way (Bariya et al., 2018). Xiao et al. (2019) reported on a wearable colorimetric sensor based on microfluidic chip made of PDMS that be used to detect glucose in sweat. The chip consisted of five microfluidic channels branching out from the center, and each of them can lead sweat from the epidermis to the detection microchambers (**Figure 2A**). Pre-embedded reagent in the microchamber will react with glucose in sweat and cause color change. Accordingly, this sensor can perform five parallel tests at the same time, greatly improving the detection efficiency. Due to the low modulus and high elasticity of the PDMS materials, the chip is flexible and can be stretched, twisted, and compressed without damage. Also based on PDMS materials, Bandodkar et al. designed a wearable sensing platform that combines advantages of electrochemical and colorimetric analysis (**Figure 2B**). The resulting sensor can monitor sweat rate, pH, lactate, glucose, and chloride at the same time (Bandodkar et al., 2019). Compared with the conventional sensors that only detect one single sample, this result provides a more comprehensive overview of physiological state.

Tear fluid is a complex fluid composed of lipids, electrolytes, proteins, peptides, glucose, and amino acids, sharing many

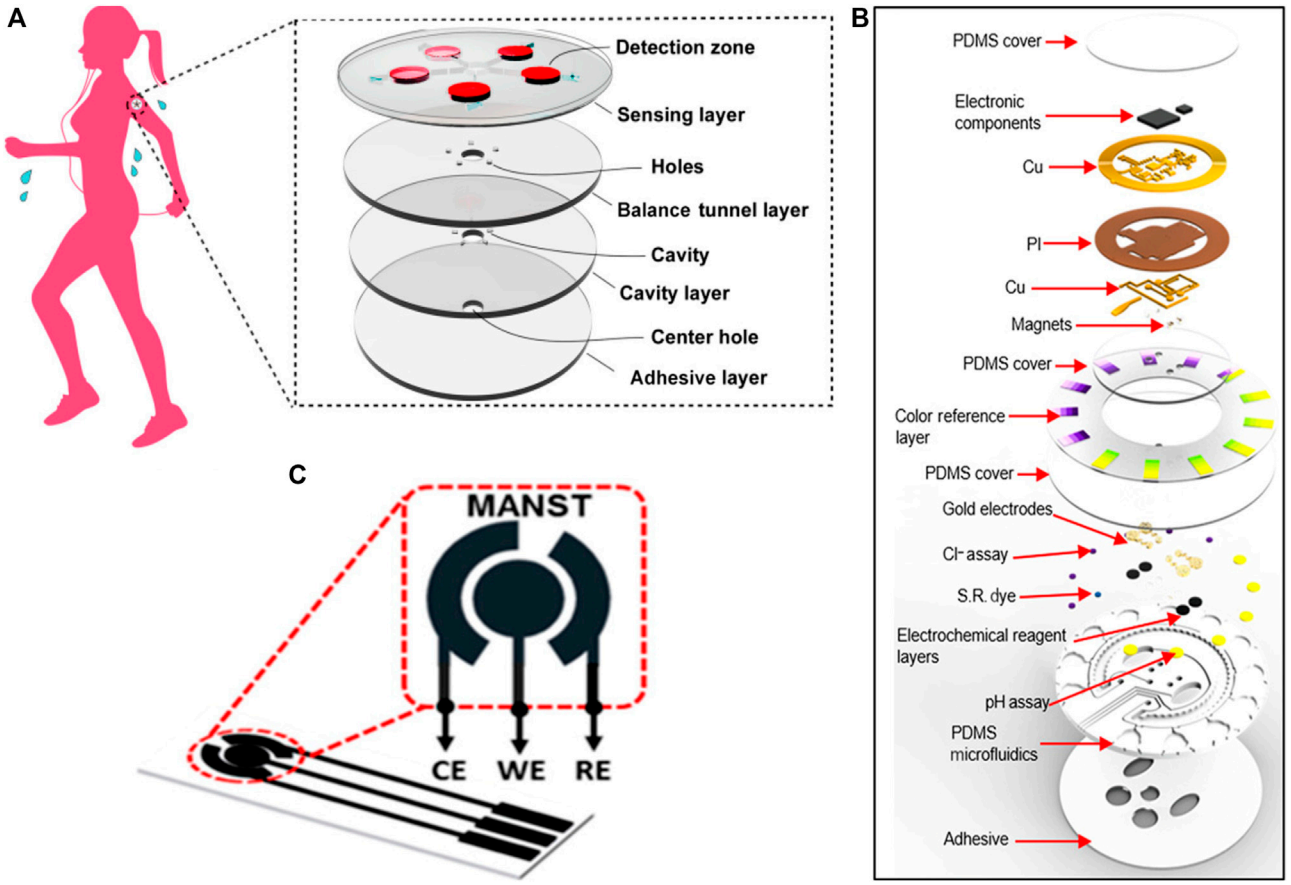

FIGURE 2 | Biosensors based on polymer substrates. **(A)** The microfluidic substrate manufactured by PDMS consists of four layers that facilitate the flow of sweat from the skin surface to the top layer containing five assay chambers with pre-embedded colorimetric reagents (Xiao et al., 2019). **(B)** Exploded view of the complete PDMS-based hybrid battery-free platform (Bandodkar et al., 2019). **(C)** Electrodes printed on PET flexible substrates, contains working, counter and reference electrodes (Shaikh et al., 2019).

similarities in composition with blood (Liu et al., 2019a). For example, the correlation between tear glucose and capillary blood glucose allows to determine the diabetic status of a subject using tear glucose values (Lin et al., 2018). POCT for tears has attracted great interest in recent years, but there are some difficulties in collection. Therefore, designing a device that can collect and analyze tear fluid in a timely manner is of great significance. Smart contact lenses have gained widespread interest for their ability to directly monitor physiological information in tears, and the primary concern in producing them is a suitable selection of flexible substrates. Acrylates can be self-polymerized or copolymerized with other monomers and are often used to make adhesives, rubber and plastics. Rosalia et al. have developed a sensor comes in the form of microfluidic contact lenses made of acrylate materials that can detect pH, glucose, protein and nitrite ions in tears (Moreddu et al., 2020a). In order to obtain accurate results, colorimetric readouts were performed using a smartphone-MATLAB algorithm based on the nearest neighbor model. Tested with artificial tears showed that the sensing device was able to respond within 15 s. An extension of this work by the same group has resulted in a new sensing platform by integrating paper microfluidics within laser-inscribed commercial contact lenses (Moreddu et al., 2020b), the device realized multiplex detection of clinically relevant analytes including proteins, glucose, nitrites, hydrogen ions and L-ascorbic acid.

Fluorescence Test

Fluorescence analysis has a wide range of applications in biomedical research because of its high sensitivity, simple operation and strong specificity (Hou et al., 2019; Sun et al., 2021). Sekine et al. (2018) proposed a wearable sweat-analysis system for *in situ* quantitative analysis of sweat chemistry. The system includes a thin, soft microfluidic device and a smartphone-based optical module. The microfluidic device patterned on the PDMS consists of microchannel networks and microcontainers pre-filled with fluorescent probes. These probes react selectively with target analytes (chloride, sodium and zinc) in the sweat. Fluorescence intensity is detected by a smartphone, ultimately enabling quantitative and rapid analysis. According to experimental results in human subjects, the accuracy is equivalent to traditional laboratory technologies.

Hemophilia and albinism are both serious threats to human health. With the development of molecular biology, it is gradually recognized that these diseases are genetically related, so the application of DNA sensors in genetic testing is extremely valuable. DNA sensors can convert the information of target DNA into detectable electrical signals, which were developed on the basis of the interpenetration of various disciplines such as biology, chemistry, electronics technology and medicine (Srisomwat et al., 2021). Immobilization of the DNA probe is an important step in making a DNA sensor and determines its performance and quality (Huang et al., 2016; Huang et al., 2019). Daniso's group modified the Polyethylene (PE) film surface using corona treatment, followed by the attachment of three different organo-silanes (Daniso et al., 2021). The results show that better adhesion of the DNA probe on the functionalized PE substrate significantly improved the biosensor's limit of detection (LOD) to a value lower than 0.1 ng μl^{-1}. Movilli et al. reported an effective method for selective modification of PDMS substrates utilizing modified poly-$_L$-lysine (PLL) to enhance biomolecular adhesion (Movilli et al., 2019). By utilizing the electrostatic interactions between the positively charged modified PLL and the negatively charged polymer surface, a self-assembled layer is formed, bestowing the possibility of bio-orthogonal anchoring of various biomolecules. Three different peptide nucleic acid (PNA) probes printed as microarrays were able to selectively detect DNA from a mixture of DNA analytes, demonstrating the potential of the modified PLL approach for multiplexed detection of DNA sequences.

Electrochemical Test

Electrochemical sensors achieve sensing by converting the chemical signal of the measured object into an electrical signal. Owing to their inherent miniaturization, low-power consumption, rapidity and low cost, POCT device with the electrochemical sensor meet the requirements of wearable sensing system (Christodouleas et al., 2018; Kanchi et al., 2018; Song et al., 2020). The flexible electrochemical biosensors can be directly attached to the skin surface and can maintain stable performance while undergoing mechanical deformation, which has been favored by researchers in recent years (Lee et al., 2018b; Kim et al., 2019; Seshadri et al., 2019). Preparation of electrodes is the foremost priority in the fabrication of electrochemical testing devices. A glucose sensor was fabricated by drawing gold electrode patterns on the surface of PET substrate via a chemical plating method. The sensitivity of the presented sensor was 22.05 $\mu A\ mM^{-1}\ cm^{-2}$ in linear range of 0.02–1.11 mM and the LOD was 2.7 μM (Wang et al., 2019b). It exhibits good selectivity under the interference of lactic acid, uric acid, dopamine and ascorbic acid. Besides, it also shows excellent reproducibility and long-term stability for more than 1 month. Nanocomposites of graphene nanosheets with diblock copolymers and gold electrodes are proposed for the detection of prostate specific antigen (PSA) in saliva, and this sensing device demonstrated a wide range of PSA detection from 0.1 $pgmL^{-1}$ to 100 $ngmL^{-1}$ with LOD of 40 $fgmL^{-1}$ (Khan et al., 2018). A screen-printed carbon electrode (SPCE) based on PET was reported for the assay of serum albumin (**Figure 2C**) (Shaikh et al., 2019). PANI/gold nanocrystals (AuNCs) nanocomposite films were modified on the surface of carbon electrodes, and the nanostructure of the PANI matrix provided a scaffold for the uniform distribution of AuNCs, resulting in an improved electrochemical response.

Electronic skin is a network of electronic sensors with mechanical deformation capabilities that are able to sense a variety of external stimuli like chemical, mechanical and thermal stimuli (Heikenfeld et al., 2018; Xu et al., 2019; Yang and Gao, 2019). Lee's group presented an electronic skin capable of converting mechanical stimuli into visual readouts (Lee et al., 2021). The material layer of the electronic skin is made of a physically cross-linked polymer matrix with a mixture of ionic transition metal complexes (ITMC) and ionic liquids (IL) encapsulated in it. There is a visco-poroelastic response of the material platform to mechanical stress that causes a change in the distribution of ionic luminophore in the film, which enables the visualization of the stresses applied to the electronic skin.

Molecularly imprinted polymer (MIP) is a special type of polymers with specific recognition and selective adsorption that is synthesized using molecular imprinting technology (MIT). MIT was developed on the basis of bio-nanotechnology by simulating enzyme-substrate and receptor-antibody interactions, and chemists commonly use this technology for molecular recognition studies (Tricoli and Neri, 2018; Ahmad et al., 2019; Lowdon et al., 2020). An ultrasensitive MIP based on carbon screen printed electrodes (C-SPE) was presented for the first time to detect interleukin-6 (IL-6), the Alzheimer's disease (AD) biomarker (Gonçalves et al., 2021). The polymer was electro-synthesized from pyrrole and carboxyl pyrrole under near physiological conditions. IL-6 was trapped in the polymer matrix and subsequently removed by acid cleavage to generate the imprinted sites. This biosensing material showed promising results for POCT of neuroinflammatory biomarkers, which is valuable for the development of AD prevention.

PAPER-BASED FLEXIBLE BIOSENSORS FOR POCT

Paper, composed primarily of cellulose, is ubiquitous in our society and widely used for writing and drawing. However, they hold an equally promising research value in the emerging field of flexible sensors (Wang et al., 2018; Aydindogan et al., 2020). Compared with traditional substrate materials like silicon, glass and rigid polymers, paper has many significant advantages for the fabrication of bioanalytical devices, such as excellent flexibility, low price, and light weight. In addition, the most attractive aspect of cellulose is from its porosity, which provides the paper with good hydrophilicity and allows it to be used as a natural microfluidic system.

Colorimetric Test

Deficiency of glucose-6-phosphate dehydrogenase (G6PD) in red blood cells is one of the causes of neonatal jaundice. White et al. proposed a paper-based biosensor for visual detection of G6PD, which is quite simple to fabricate and does not require any

complex instrumentation (White et al., 2020). The paper biosensor performs G6PD detection through the chromogenic effect generated by the catalysis of dehydrogenase. In addition, the sensor has an ingenious design with all critical reagents contained on the paper or in the diluent buffer, thus reducing the operation steps by users. Similarly, for the prevention of neonatal jaundice, a tape-paper-based sensing device designed and manufactured by Tan et al., which is able to separate plasma from whole blood samples and measure total bilirubin using a colorimetric diazotization method (Tan et al., 2020). The tape-paper sensing method overcomes non-homogeneous color distribution caused by the deposition of analyte, indicator and reaction product at the edge of the reaction zone, and improves the accuracy of colorimetric evaluation of paper-based analytical equipment.

The development of nanomaterials (carbon nanotubes, metal nanoparticles, graphene and quantum dots) for biosensors has been broadly reported in recent years (Lim et al., 2015; Nguyen and Kim, 2020; Wang et al., 2020). Nanomaterials can be used as signal markers or carriers of signal markers for sensitive and specific detection of biomolecules, in addition, a number of nanomaterials with excellent optical properties have been widely applied in colorimetric analysis (Aydindogan et al., 2018). The conjunction of nanomaterials and portable biosensors have acquired numerous applications (Hui et al., 2018; Ji et al., 2018; Faham et al., 2019), an interesting example is the gold nanoparticle-based paper sensor capable of detecting 11 benzimidazoles simultaneously, proposed by Guo's group (Guo et al., 2018b). The immunochromatographic strip is assembled and labeled with gold nanoparticles, and detection results are available in just 15 min. Polydiacetylene (PDA) is a commonly used conjugated polymer with unique chromatographic properties for sensitive optical transduction. PDA nanovesicles with particle size below 100 nm facilitate higher sensitivity owing to their larger surface area for reaction. In addition, a PDA vesicle-based paper strip was recently described, and smartphone was used for image analysis, enabling rapid and quantitative analysis of influenza A (pH1N1) virus at low concentrations (Son et al., 2019). It was confirmed that the LOD of PDA paper strip is from 5×10^3 to 10^4 TCID50 (50% tissue culture infective dose). Metal-organic framework (MOF) materials are coordination polymers with a three-dimensional pore structure, normally connected by metal ions and supported from organic ligands, which have been developed rapidly in the last decade and shown wide applications in catalysis, energy storage and sensing. ZIF-8 is a nano-scale MOF material, Kou et al. demonstrated a portable, user-friendly smartphone-assisted biomimetic MOF nanoreactor colorimetric paper (SBMCP) for POCT of endogenous biomolecules (Kou et al., 2020). Inspired by intracellular cascade signal transduction, the enzyme component trapped in the ZIF-8 exoskeleton allowed for selective and sensitive recognition of target analytes via micropores, followed by conversion of the recognition information into a visual color signal through the cascade reaction. Additionally, the ZIF-8 frameworks can significantly improve the stability of enzyme.

Fluorescence Test

Three-dimensional (3D)-printing technology is actually an additive manufacturing method based on light-curing and paper lamination technology that can turn blueprints in a computer into physical objects in an easy way. Nowadays, 3D-printing is commonly used to manufacture prototypes and gradually gaining prominence in industrial design, aerospace, and medical fields (Scordo et al., 2018). Combined with 3D-printing, Chu et al. (2020) introduced a portable smartphone-based quantitative fluorescence sensing paper strip, capable of accomplishing rapid, real-time, reliable and on-site determination of glutathione (GSH) in human serum, which shows great significance for early disease diagnosis. The sensitive fluorescent nanoprobe was constructed through the mixture of blue carbon dots (CDs) and orange gold nanoclusters (AuNCs). The blue fluorescence remained stable in the presence of copper ions, while the AuNCs with orange fluorescence were quenched (**Figure 3A**). Upon the addition of GSH, the quenched orange fluorescence could be quickly restored, displaying a visible color change from blue to orange, due to the stronger affinity between copper ions and GSH. It was verified that the LOD was 1.84 μM, which is far below the lowest level of GSH in serum.

The fluorescent intensity change that occurs when the spectra of donor and acceptor fluorescent molecules overlap is called fluorescence resonance energy transfer (FRET). Bioluminescence resonance energy transfer (BRET) is one of the FRET, which donor luminophore is a bioluminescent molecule and its electrons are excited by a bioluminescent chemical reaction (Tomimuro et al., 2020). This section will present several interesting applications of BRET in portable paper-based sensors. Yu et al. (2018) created a semi-synthetic luminescent sensor protein that can accurately quantify metabolites in blood by paper-based analysis. The device consists of test paper containing the lyophilized sensor, a cardboard box that provides dark environment, and a digital camera used to capture the fluorescent signal. The metabolite is oxidized by the nicotinamide adenine dinucleotide phosphate (NADPH) on the test paper and the sensor changes color, realizing metabolite quantification. Phenylalanine levels in the blood of patients can be obtained in minutes with this sensor, and the difference is less than 15% compared to conventional assays. Tenda et al.'s work reported on microfluidic paper-based assay devices (μPADs) that rely on BRET-based antibody-sensing proteins for analyte recognition and colorimetric signal generation, which achieved simultaneous detection of three antibodies in whole blood (Tenda et al., 2018). The enclosed space created by vertically assembled and fully laminated paper layers can limit sample volume absorbed by the paper, allowing for sample volume-independent measures. In view of its simplicity, this device is well suited for POCT in resource-limited areas.

Electrochemical Test

Among the paper-based sensor signal readout schemes, electrochemical strategies are more attractive compared to optical methods because of better quantitative and interference immunity.

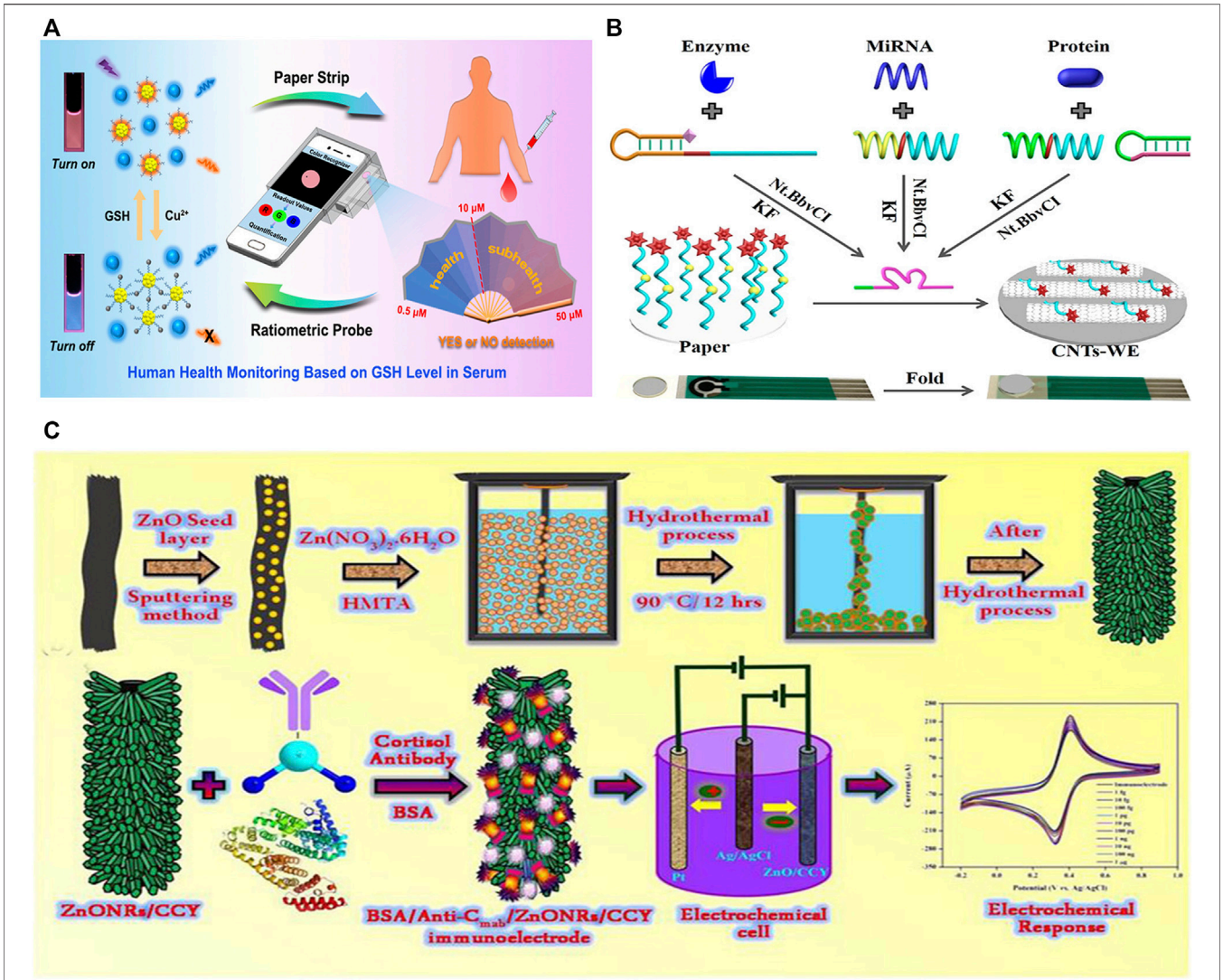

FIGURE 3 | Biosensors based on paper and textile substrates. **(A)** Schematic diagram of a fluorescent paper strip integrated with a portable smartphone platform for monitoring glutathione in human serum (Chu et al., 2020). **(B)** Specially designed universal paper-based electrochemical sensor (Liu et al., 2019b). **(C)** Schematic diagram of a zinc oxide nanorod electrochemical sensing electrode integrated with flexible carbon fibers for sweat cortisol detection (Madhu et al., 2020).

However, high background currents have been a persistent problem faced by electrochemical methods, which results in a loss of sensitivity. To solve this problem, Liu et al. tried to immobilize signal molecules on paper separated from the working electrode, which cannot diffuse or adsorb to the electrode surface non-specifically without target induction (**Figure 3B**) (Liu et al., 2019b). With that in mind, a paper-based electrochemical sensor was fabricated, which can be used for highly sensitive analysis of various different biomarkers. An electrode was designed for the detection of 3-nitrotyrosine (3-NT) in urine (Martins et al., 2020). The MIP for 3-NT was modified on a paper platform and conducted with carbon ink. After condition optimization, the linear detection range of the label-free sensor for 3-NT is 500 nM–1 mM, and the detection limit is evaluated to be 22.3 nM. Mohammadifar et al. (2019) demonstrated a multi-threshold glucose detection test strip that can detect five different glucose concentration levels. The five electrodes integrated in the paper strip were modified with glucose oxidase, and the indicator circuitry will generate a reliable visual signal when a predetermined glucose concentration is reached.

Pencil and paper are wonderful partners in writing and drawing. However, their applications extend beyond that, as the pencil-paper-based on-skin electronic devices designed by Xu et al. (2020) explored applications in emerging skin interface health monitoring and interventions. In this work, a commercial 9B pencil and commonly available office copy paper are the main elements that make up this biosensor. Pencil-drawn graphite patterns are used as conductive traces and sensing electrodes, and paper acts as flexible substrates. Various on-skin electronic sensors were designed by drawing different pencil patterns, including biophysical sensors and sweat biochemical (pH, uric acid, glucose) sensors. Notably, the pencil-paper-based uric acid (UA) sensor has a high sensitivity of 21.9 $nA\mu M^{-1}$ in the

0–600 μM concentration range, exhibiting comparable performance to conventional sensors based on carbon materials.

Foldability is a unique feature of paper, some paper-based sensors take advantage of foldability to achieve highly integrated, which makes it easy to reduce the sensor size. Li et al. (2021) designed a sensing paper for wearable electrochemical sweat analysis utilizing 2D $Ti_3C_2T_x$ as the active materials and foldable paper substrates as sweat analysis patches. Four functional layers are printed on different areas of the paper substrate to facilitate the decoration of enzymes and electrochemical materials, and then fold into 3D structure. The unique 3D structure boosts sweat absorption, improves the accuracy of detecting sweat components, and reduces discomfort caused by sweat accumulation at the human-machine interface. Such a wonderful structure was utilized to prepare a dual-channel sensor, which can detect glucose and lactate simultaneously with a sensitivity of 2.4 nA μM^{-1} and 0.49 μA mM^{-1}, respectively. A portable, robust and user-friendly cobalt-MOF modified carbon cloth/paper (Co-MOF/CC/Paper) electrochemical sensor was fabricated for non-enzymatic quantitative glucose detection (Wei et al., 2021). Co-MOF was crystallized on CC to successfully manufacture a highly integrated electrochemical analytical chip that effectively increased the specific surface area compared to conventional planar electrodes. The chip assembled with patterned paper electrodes and finally folded into a fabulous Co-MOF/CC/paper hybrid button-sensor. The introduced button structure allows easy separation of the working electrode from the sample region and facilitates sample replacement.

TEXTILE-BASED FLEXIBLE BIOSENSORS FOR POCT

Textiles are a fascinating material. Countless individual fibres are interlaced in different manufacturing steps, culminating in a complex structure with quite decent properties. No other material combines drapability, lightness, robustness and decorative properties. However, textiles have been discovered to possess more than just these properties, and recently high-performance textiles have demonstrated amazing examples in military and aerospace applications, such as carbon fibre, aramid and other materials applied to soldiers' protective clothing, which not only improve defensive performance, but also increase warfare efficiency. (Kirstein, 2013). If textiles are capable of such high-tech capabilities, it is logical to consider them for portable wearable sensing applications (Hu et al., 2020).

Colorimetric Test

Urine is a liquid excretion that includes haemoglobin, enzymes, and electrolytes in its composition. In the medical field, urine is a frequently used sample and urinalysis could help physicians diagnose many diseases. To further exploit the advantages of non-invasiveness and accessibility, various POCT devices for urine testing have emerged in recent years (Alves and Reis, 2019; Michael et al., 2020). Integrating a tape-based sensor with a diaper, He et al. (2020) introduce a wearable biosensor for fast multiplex urinalysis. The micro-sensing array was arranged on a flexible waterproof tape through physical punching and textile filling processes, and then adhered to the diaper. One of the major advantages of this tape-based sensor is that urine can be sampled and detected directly through the diaper, without any additional operations in the whole process. This device enables the detection of urinary markers such as glucose, nitrite, protein and phenylpyruvate, which are important for the early warning of some diseases, representing an ideal POCT solution for infants and urinary incontinence patients. A similar example of wearable biosensors could also be seen in sweat detection, Zhao et al. (2021b) prepared a wearable microfluidic thread/fabric-based analytical device (μTFAD) for perspiration sensing. Hydrophilic patterns and a hydrophobic surface were delineated by embroidering cotton threads on a hydrophobic treated cotton cloth. In this case, the hydrophilic parts served as channels and detection zones, which were treated with colorimetric indicators. Smartphone assisted readings showed LOD was 10 μM for glucose concentration, 10 mM for chloride concentration and 4.0–9.0 for pH.

Nanozymes provide not only the high catalytic activity of native enzymes, but also the stability and cost-effectiveness of model enzymes, which are widely accepted in medical, chemical, food and agricultural fields. Reliable glucose testing in the urine is essential for the prevention of diabetes, Karim's team, for the first time, demonstrated silver (Ag) nanoparticles embedded in cotton fabric as free-standing nanozymes for the rapid assay of glucose in urine (Karim et al., 2018). Using cotton as a substrate provides a large number of catalytic active sites for the catalytic reaction, and the excellent absorption characteristic of cotton fibres also facilitates the rapid absorption of glucose. Following the similar principle, Karim et al. also attempted to embed catalytically active copper (Cu) nanoparticles into cotton fabrics to develop a glucose monitoring system (Naveen Prasad et al., 2021). The sensor could operate in the 0.5–15 mM glucose concentration range and provides minimal sample matrix effects, allowing almost direct detection of glucose from urine without complex sample processing.

Electrochemical Test

Mechanical flexibility is critical for a wearable biosensing platform because it is related to the stability and accuracy of the biosensor in real use. In this sense, the importance of designing electrodes with stable tensile performance under mechanical deformation can hardly be overemphasized. An example of a wearable electrochemical biosensor on the basis of flexible zinc-oxide nanowires (ZnO NWs) electrodes is described, which could be applied to the detection of lactate and sodium in sweat during exercise (Zhao et al., 2021c). Thread-based carbon electrodes were fabricated from cotton thread, PDMS, carbon ink, silver and silver chloride (Ag/AgCl) ink, while ZnO-NWs were grown *in situ* on the electrodes by a hydrothermal process. Cotton threads were wrapped around the lactic acid sensing electrode and sodium sensing electrode, in order to assist in sweat absorbing, thus providing reaction reservoirs and transfer routes for lactic acid and sodium ions.

Due to the special structure of graphite microcrystals, carbon fibers possess high strength and modulus along the fiber axis direction. In addition, carbon fibers possess favorable conductivity and have a promising future in the field of textile-based sensors. Madhu's group proposed a flexible yarn-based electrochemical immunosensing method for the analysis of sweat cortisol (Madhu et al., 2020). As shown in **Figure 3C**, ZnO nanorods (ZnONRs) were coated onto flexible carbon yarns using a hydrothermal treatment to facilitate the immobilization of specific anti-cortisol antibodies. The network structure of carbon fibers offers a larger surface area for electrocatalytic reactions, enabling highly sensitive and selective sensing, and making them the prime substrates in biosensor platforms. The sensor showed a range of linear detection from 1 fg ml^{-1} to 1 μg ml^{-1}, and the LOD was between 0.45 and 0.098 fg ml^{-1} obtained by Cyclic Voltammetry (CV) and Differential pulse voltammetry (DPV) techniques.

CONCLUSION AND OUTLOOK

In the past decades, POCT has brought constant surprises. In this review, we systematically review the application of various biosensors in POCT in recent years, categorized by different substrates, in combination with the corresponding sensing methods. These sensing devices overcome the limitations of traditional laboratory tests effectively and present significant potential, especially in resource-limited areas. Polymers as the most commonly used substrate materials in flexible sensors currently, have driven the advancement of microfluidic technology in POCT. Microfluidic-based POCT aims to obtain results faster in order to improve the efficiency of disease detection and the accuracy of diagnosis. Furthermore, using small sample volumes greatly saves the expense of reagent consumption. However, contamination may occur from the production of polymers, which is the most criticized problem. Paper-based sensors have recently become the focus in the construction of portable flexible biosensing platforms. The foldable behavior of paper allows for many marvelous ideas in sensor fabrication, for example, light weight cellulose paper with excellent porosity can be designed as a template for highly integrated microfluidic sensors just by simple folding. The simplicity of fabrication steps is another attractive advantage, which also leads to the low cost of paper-based sensors. But as an emerging technology, paper-based sensors suffer from lack of stability and poor sensitivity. Although integrating sensors with textiles is cumbersome and subject to the problems of short service life and poor robustness, it is undeniable that manufacturing sensors on textiles can improve the user-friendliness of wearable sensors, because they are constantly and intimately in contact with the human body in daily life. The wicking property of fabrics is important which provides a pathway for capturing and transporting target biomolecules to the sensor surface, and it is believed that textile-based sensors will play a key role in detecting biomarkers within body fluids.

Although there are still gaps in the accuracy and stability of POCT compared with traditional laboratory-based tests, the COVID-19 pandemic underscores the importance of more rapid testing platforms. Overall, the opportunities and challenges facing POCT are enormous, making early commercialization still pending the concerted efforts of researchers.

AUTHOR CONTRIBUTIONS

TY: conceptualization and writing—original draft. GZ: conceptualization and writing—original draft, supervision, project administration, and funding acquisition. HC: writing—review and editing, and funding acquisition. LQ: conceptualization, resources, project administration, writing—review and editing, supervision. XZ: project administration, and funding acquisition. All authors contributed to the article and approved the submitted version.

FUNDING

The authors appreciatively acknowledge financial support of the Natural Science Foundation of Shandong Province (No. ZR2020QB092), the China Postdoctoral Science Foundation (No. 2021M691689), National Natural Science Foundation of China (Nos 21801158, 21727815), State Key Laboratory of Bio-Fibers and Eco-Textiles (Qingdao University, Nos ZKT23, KF2020201, GZRC202025).

REFERENCES

Ahmad, O. S., Bedwell, T. S., Esen, C., Garcia-Cruz, A., and Piletsky, S. A. (2019). Molecularly Imprinted Polymers in Electrochemical and Optical Sensors. *Trends Biotechnol.* 37, 294–309. doi:10.1016/j.tibtech.2018.08.009

Alves, I. P., and Reis, N. M. (2019). Microfluidic Smartphone Quantitation of Escherichia Coli in Synthetic Urine. *Biosens. Bioelectron.* 145, 111624. doi:10.1016/j.bios.2019.111624

Andrysiewicz, W., Krzeminski, J., Skarżynski, K., Marszalek, K., Sloma, M., and Rydosz, A. (2020). Flexible Gas Sensor Printed on a Polymer Substrate for Sub-ppm Acetone Detection. *Electron. Mater. Lett.* 16, 146–155. doi:10.1007/s13391-020-00199-z

Aydindogan, E., Ceylan, A. E., and Timur, S. (2020). Paper-Based Colorimetric Spot Test Utilizing Smartphone Sensing for Detection of Biomarkers. *Talanta* 208, 120446. doi:10.1016/j.talanta.2019.120446

Aydindogan, E., Guler Celik, E., and Timur, S. (2018). Paper-Based Analytical Methods for Smartphone Sensing with Functional Nanoparticles: Bridges from Smart Surfaces to Global Health. *Anal. Chem.* 90, 12325–12333. doi:10.1021/acs.analchem.8b03120

Bandodkar, A. J., Gutruf, P., Choi, J., Lee, K., Sekine, Y., Reeder, J. T., et al. (2019). Battery-Free, Skin-Interfaced Microfluidic/Electronic Systems for Simultaneous Electrochemical, Colorimetric, and Volumetric Analysis of Sweat. *Sci. Adv.* 5, eaav3294. doi:10.1126/sciadv.aav3294

Bariya, M., Nyein, H. Y. Y., and Javey, A. (2018). Wearable Sweat Sensors. *Nat. Electron.* 1, 160–171. doi:10.1038/s41928-018-0043-y

Choi, J., Ghaffari, R., Baker, L. B., and Rogers, J. A. (2018). Skin-Interfaced Systems for Sweat Collection and Analytics. *Sci. Adv.* 4, eaar3921. doi:10.1126/sciadv.aar3921

Choi, J. R. (2020). Development of Point-of-Care Biosensors for COVID-19. *Front. Chem.* 8, 517. doi:10.3389/fchem.2020.00517

Christodouleas, D. C., Kaur, B., and Chorti, P. (2018). From Point-of-Care Testing to eHealth Diagnostic Devices (eDiagnostics). *ACS Cent. Sci.* 4, 1600–1616. doi:10.1021/acscentsci.8b00625

Chu, S., Wang, H., Du, Y., Yang, F., Yang, L., and Jiang, C. (2020). Portable Smartphone Platform Integrated with a Nanoprobe-Based Fluorescent Paper Strip: Visual Monitoring of Glutathione in Human Serum for Health Prognosis. *ACS Sustain. Chem. Eng.* 8, 8175–8183. doi:10.1021/acssuschemeng.0c00690

Daniso, E., Maroh, B., Feldbacher, S., Mühlbacher, I., Schlögl, S., and Melpignano, P. (2021). Tailoring the Chemical Functionalization of a Transparent Polyethylene Foil for its Application in an OLED-Based DNA Biosensor. *Appl. Surf. Sci.* 552, 149408. doi:10.1016/j.apsusc.2021.149408

Economou, A., Kokkinos, C., and Prodromidis, M. (2018). Flexible Plastic, Paper and Textile Lab-on-a Chip Platforms for Electrochemical Biosensing. *Lab. Chip* 18, 1812–1830. doi:10.1039/c8lc00025e

Faham, S., Golmohammadi, H., Ghavami, R., and Khayatian, G. (2019). A Nanocellulose-Based Colorimetric Assay Kit for Smartphone Sensing of Iron and Iron-Chelating Deferoxamine Drug in Biofluids. *Analytica Chim. Acta* 1087, 104–112. doi:10.1016/j.aca.2019.08.056

Farajikhah, S., Cabot, J. M., Innis, P. C., Paull, B., and Wallace, G. (2019). Life-Saving Threads: Advances in Textile-Based Analytical Devices. *ACS Comb. Sci.* 21, 229–240. doi:10.1021/acscombsci.8b00126

Gonçalves, M. d. L., Truta, L. A. N., Sales, M. G. F., and Moreira, F. T. C. (2021). Electrochemical Point-of Care (PoC) Determination of Interleukin-6 (IL-6) Using a Pyrrole (Py) Molecularly Imprinted Polymer (MIP) on a Carbon-Screen Printed Electrode (C-SPE). *Anal. Lett.* 54, 2611–2623. doi:10.1080/00032719.2021.1879108

Guo, J., Yang, C., Dai, Q., and Kong, L. (2019). Soft and Stretchable Polymeric Optical Waveguide-Based Sensors for Wearable and Biomedical Applications. *Sensors* 19, 3771. doi:10.3390/s19173771

Guo, L., Wu, X., Liu, L., Kuang, H., and Xu, C. (2018b). Gold Nanoparticle-Based Paper Sensor for Simultaneous Detection of 11 Benzimidazoles by One Monoclonal Antibody. *Small* 14, 1701782. doi:10.1002/smll.201701782

Guo, X.-L., Chen, Y., Jiang, H.-L., Qiu, X.-B., and Yu, D.-L. (2018a). Smartphone-Based Microfluidic Colorimetric Sensor for Gaseous Formaldehyde Determination with High Sensitivity and Selectivity. *Sensors* 18, 3141. doi:10.3390/s18093141

He, X., Pei, Q., Xu, T., and Zhang, X. (2020). Smartphone-Based Tape Sensors for Multiplexed Rapid Urinalysis. *Sensors Actuators B: Chem.* 304, 127415. doi:10.1016/j.snb.2019.127415

Heikenfeld, J., Jajack, A., Rogers, J., Gutruf, P., Tian, L., Pan, T., et al. (2018). Wearable Sensors: Modalities, Challenges, and Prospects. *Lab. Chip* 18, 217–248. doi:10.1039/c7lc00914c

Hou, L., Qin, Y., Li, J., Qin, S., Huang, Y., Lin, T., et al. (2019). A Ratiometric Multicolor Fluorescence Biosensor for Visual Detection of Alkaline Phosphatase Activity via a Smartphone. *Biosens. Bioelectron.* 143, 111605. doi:10.1016/j.bios.2019.111605

Hu, X., Tian, M., Xu, T., Sun, X., Sun, B., Sun, C., et al. (2020). Multiscale Disordered Porous Fibers for Self-Sensing and Self-Cooling Integrated Smart Sportswear. *ACS Nano* 14, 559–567. doi:10.1021/acsnano.9b06899

Huang, Y., Wang, W., Wu, T., Xu, L.-P., Wen, Y., and Zhang, X. (2016). A Three-Line Lateral Flow Biosensor for Logic Detection of microRNA Based on Y-Shaped Junction DNA and Target Recycling Amplification. *Anal. Bioanal. Chem.* 408, 8195–8202. doi:10.1007/s00216-016-9925-x

Huang, Y., Xu, T., Wang, W., Wen, Y., Li, K., Qian, L., et al. (2019). Lateral Flow Biosensors Based on the Use of Micro- and Nanomaterials: A Review on Recent Developments. *Microchim Acta* 187, 70. doi:10.1007/s00604-019-3822-x

Hui, C. Y., Liu, M., Li, Y., and Brennan, J. D. (2018). A Paper Sensor Printed with Multifunctional Bio/Nano Materials. *Angew. Chem. Int. Ed.* 57, 4549–4553. doi:10.1002/anie.201712903

Ji, D., Liu, Z., Liu, L., Low, S. S., Lu, Y., Yu, X., et al. (2018). Smartphone-Based Integrated Voltammetry System for Simultaneous Detection of Ascorbic Acid, Dopamine, and Uric Acid with Graphene and Gold Nanoparticles Modified Screen-Printed Electrodes. *Biosens. Bioelectron.* 119, 55–62. doi:10.1016/j.bios.2018.07.074

Kanchi, S., Sabela, M. I., Mdluli, P. S., Inamuddin, and Bisetty, K. (2018). Smartphone Based Bioanalytical and Diagnosis Applications: a Review. *Biosens. Bioelectron.* 102, 136–149. doi:10.1016/j.bios.2017.11.021

Karim, M. N., Anderson, S. R., Singh, S., Ramanathan, R., and Bansal, V. (2018). Nanostructured Silver Fabric as a Free-Standing Nanozyme for Colorimetric Detection of Glucose in Urine. *Biosens. Bioelectron.* 110, 8–15. doi:10.1016/j.bios.2018.03.025

Khan, M. S., Dighe, K., Wang, Z., Srivastava, I., Daza, E., Schwartz-Dual, A. S., et al. (2018). Detection of Prostate Specific Antigen (PSA) in Human Saliva Using an Ultra-Sensitive Nanocomposite of Graphene Nanoplatelets with Diblock-Co-Polymers and Au Electrodes. *Analyst* 143, 1094–1103. doi:10.1039/c7an01932g

Kim, J., Campbell, A. S., de Ávila, B. E.-F., and Wang, J. (2019). Wearable Biosensors for Healthcare Monitoring. *Nat. Biotechnol.* 37, 389–406. doi:10.1038/s41587-019-0045-y

Kirstein, T. (2013). The Future of Smart-Textiles Development: New Enabling Technologies, Commercialization and Market Trends. *Multidisciplinary Know-How for Smart-Textiles Developers*, 1–25. doi:10.1533/9780857093530.1

Kou, X., Tong, L., Shen, Y., Zhu, W., Yin, L., Huang, S., et al. (2020). Smartphone-Assisted Robust Enzymes@MOFs-Based Paper Biosensor for Point-of-Care Detection. *Biosens. Bioelectron.* 156, 112095. doi:10.1016/j.bios.2020.112095

Lee, E. J., Kim, B.-K., and Lee, K. K. (2020). Finger-Powered, Capillary-Driven Blood Diagnostic Chip for Point-of-Care Technology. *Sensors Actuators A: Phys.* 312, 112153. doi:10.1016/j.sna.2020.112153

Lee, H., Hong, Y. J., Baik, S., Hyeon, T., and Kim, D. H. (2018b). Enzyme-Based Glucose Sensor: From Invasive to Wearable Device. *Adv. Healthc. Mater.* 7, 1701150. doi:10.1002/adhm.201701150

Lee, J. I., Choi, H., Kong, S. H., Park, S., Park, D., Kim, J. S., et al. (2021). Visco-Poroelastic Electrochemiluminescence Skin with Piezo-Ionic Effect. *Adv. Mater.* 33, 2100321. doi:10.1002/adma.202100321

Lee, V. B. C., Mohd-Naim, N. F., Tamiya, E., and Ahmed, M. U. (2018a). Trends in Paper-Based Electrochemical Biosensors: From Design to Application. *Anal. Sci.* 34, 7–18. doi:10.2116/analsci.34.7

Li, M., Wang, L., Liu, R., Li, J., Zhang, Q., Shi, G., et al. (2021). A Highly Integrated Sensing Paper for Wearable Electrochemical Sweat Analysis. *Biosens. Bioelectron.* 174, 112828. doi:10.1016/j.bios.2020.112828

Lim, J. W., Ha, D., Lee, J., Lee, S. K., and Kim, T. (2015). Review of Micro/Nanotechnologies for Microbial Biosensors. *Front. Bioeng. Biotechnol.* 3, 61. doi:10.3389/fbioe.2015.00061

Lin, Y.-R., Hung, C.-C., Chiu, H.-Y., Chang, B.-H., Li, B.-R., Cheng, S.-J., et al. (2018). Noninvasive Glucose Monitoring with a Contact Lens and Smartphone. *Sensors* 18, 3208. doi:10.3390/s18103208

Liu, J., Geng, Z., Fan, Z., Liu, J., and Chen, H. (2019a). Point-of-Care Testing Based on Smartphone: The Current State-of-the-Art (2017-2018). *Biosens. Bioelectron.* 132, 17–37. doi:10.1016/j.bios.2019.01.068

Liu, X., Li, X., Gao, X., Ge, L., Sun, X., and Li, F. (2019b). A Universal Paper-Based Electrochemical Sensor for Zero-Background Assay of Diverse Biomarkers. *ACS Appl. Mater. Inter.* 11, 15381–15388. doi:10.1021/acsami.9b03860

Lowdon, J. W., Diliën, H., Singla, P., Peeters, M., Cleij, T. J., Van Grinsven, B., et al. (2020). MIPs for Commercial Application in Low-Cost Sensors and Assays - an Overview of the Current Status Quo. *Sensors Actuators B: Chem.* 325, 128973. doi:10.1016/j.snb.2020.128973

Madhu, S., Anthuuvan, A. J., Ramasamy, S., Manickam, P., Bhansali, S., Nagamony, P., et al. (2020). ZnO Nanorod Integrated Flexible Carbon Fibers for Sweat Cortisol Detection. *ACS Appl. Electron. Mater.* 2, 499–509. doi:10.1021/acsaelm.9b00730

Manjakkal, L., Dervin, S., and Dahiya, R. (2020). Flexible Potentiometric pH Sensors for Wearable Systems. *RSC Adv.* 10, 8594–8617. doi:10.1039/d0ra00016g

Martins, G. V., Marques, A. C., Fortunato, E., and Sales, M. G. F. (2020). Paper-Based (Bio)sensor for Label-free Detection of 3-nitrotyrosine in Human Urine Samples Using Molecular Imprinted Polymer. *Sensing Bio-Sensing Res.* 28, 100333. doi:10.1016/j.sbsr.2020.100333

Michael, I., Kim, D., Gulenko, O., Kumar, S., Kumar, S., Clara, J., et al. (2020). A Fidget Spinner for the Point-of-Care Diagnosis of Urinary Tract Infection. *Nat. Biomed. Eng.* 4, 591–600. doi:10.1038/s41551-020-0557-2

Mohammadifar, M., Tahernia, M., and Choi, S. (2019). An Equipment-free, Paper-Based Electrochemical Sensor for Visual Monitoring of Glucose Levels in Urine. *SLAS TECHNOLOGY: Translating Life Sci. Innovation* 24, 499–505. doi:10.1177/2472630319846876

Moreddu, R., Elsherif, M., Adams, H., Moschou, D., Cordeiro, M. F., Wolffsohn, J. S., et al. (2020b). Integration of Paper Microfluidic Sensors into Contact

Lenses for Tear Fluid Analysis. *Lab. Chip* 20, 3970–3979. doi:10.1039/d0lc00438c

Moreddu, R., Wolffsohn, J. S., Vigolo, D., and Yetisen, A. K. (2020a). Laser-Inscribed Contact Lens Sensors for the Detection of Analytes in the Tear Fluid. *Sensors Actuators B: Chem.* 317, 128183. doi:10.1016/j.snb.2020.128183

Movilli, J., Di Iorio, D., Rozzi, A., Hiltunen, J., Corradini, R., and Huskens, J. (2019). "Plug-n-Play" Polymer Substrates: Surface Patterning with Reactive-Group-Appended Poly-L-Lysine for Biomolecule Adhesion. *ACS Appl. Polym. Mater.* 1, 3165–3173. doi:10.1021/acsapm.9b00814

Naveen Prasad, S., Weerathunge, P., Karim, M. N., Anderson, S., Hashmi, S., Mariathomas, P. D., et al. (2021). Non-invasive Detection of Glucose in Human Urine Using a Color-Generating Copper Nanozyme. *Anal. Bioanal. Chem.* 413, 1279–1291. doi:10.1007/s00216-020-03090-w

Nelson, P. P., Rath, B. A., Fragkou, P. C., Antalis, E., Tsiodras, S., and Skevaki, C. (2020). Current and Future Point-of-Care Tests for Emerging and New Respiratory Viruses and Future Perspectives. *Front. Cel. Infect. Microbiol.* 10, 181. doi:10.3389/fcimb.2020.00181

Nguyen, Q. H., and Kim, M. I. (2020). Nanomaterial-Mediated Paper-Based Biosensors for Colorimetric Pathogen Detection. *Trac Trends Anal. Chem.* 132, 116038. doi:10.1016/j.trac.2020.116038

Patil, A. B., Meng, Z., Wu, R., Ma, L., Xu, Z., Shi, C., et al. (2020). Tailoring the Meso-Structure of Gold Nanoparticles in Keratin-Based Activated Carbon Toward High-Performance Flexible Sensor. *Nano-micro Lett.* 12, 117. doi:10.1007/s40820-020-00459-5

Priye, A., Ball, C. S., and Meagher, R. J. (2018). Colorimetric-Luminance Readout for Quantitative Analysis of Fluorescence Signals with a Smartphone CMOS Sensor. *Anal. Chem.* 90, 12385–12389. doi:10.1021/acs.analchem.8b03521

Sachdeva, S., Davis, R. W., and Saha, A. K. (2020). Microfluidic Point-of-Care Testing: Commercial Landscape and Future Directions. *Front. Bioeng. Biotechnol.* 8, 602659. doi:10.3389/fbioe.2020.602659

Scordo, G., Moscone, D., Palleschi, G., and Arduini, F. (2018). A Reagent-Free Paper-Based Sensor Embedded in a 3D Printing Device for Cholinesterase Activity Measurement in Serum. *Sensors Actuators B: Chem.* 258, 1015–1021. doi:10.1016/j.snb.2017.11.134

Sekine, Y., Kim, S. B., Zhang, Y., Bandodkar, A. J., Xu, S., Choi, J., et al. (2018). A Fluorometric Skin-Interfaced Microfluidic Device and Smartphone Imaging Module for *In Situ* Quantitative Analysis of Sweat Chemistry. *Lab. Chip* 18, 2178–2186. doi:10.1039/c8lc00530c

Seshadri, D. R., Li, R. T., Voos, J. E., Rowbottom, J. R., Alfes, C. M., Zorman, C. A., et al. (2019). Wearable Sensors for Monitoring the Physiological and Biochemical Profile of the Athlete. *NPJ Digit. Med.* 2, 72. doi:10.1038/s41746-019-0150-9

Shaikh, M. O., Srikanth, B., Zhu, P.-Y., and Chuang, C.-H. (2019). Impedimetric Immunosensor Utilizing Polyaniline/gold Nanocomposite-Modified Screen-Printed Electrodes for Early Detection of Chronic Kidney Disease. *Sensors* 19, 3990. doi:10.3390/s19183990

Son, S. U., Seo, S. B., Jang, S., Choi, J., Lim, J.-W., Lee, D. K., et al. (2019). Naked-eye Detection of Pandemic Influenza a (pH1N1) Virus by Polydiacetylene (PDA)-based Paper Sensor as a Point-of-Care Diagnostic Platform. *Sensors Actuators B: Chem.* 291, 257–265. doi:10.1016/j.snb.2019.04.081

Song, Y., Xu, T., Zhu, Q., and Zhang, X. (2020). Integrated Individually Electrochemical Array for Simultaneously Detecting Multiple Alzheimer's Biomarkers. *Biosens. Bioelectron.* 162, 112253. doi:10.1016/j.bios.2020.112253

Spychalska, K., Zając, D., Baluta, S., Halicka, K., and Cabaj, J. (2020). Functional Polymers Structures for (Bio)sensing Application-A Review. *Polymers* 12, 1154. doi:10.3390/polym12051154

Srisomwat, C., Yakoh, A., Chuaypen, N., Tangkijvanich, P., Vilaivan, T., and Chailapakul, O. (2021). Amplification-free DNA Sensor for the One-step Detection of the Hepatitis B Virus Using an Automated Paper-Based Lateral Flow Electrochemical Device. *Anal. Chem.* 93, 2879–2887. doi:10.1021/acs.analchem.0c04283

Sun, Y., Luo, Y., Xu, T., Cheng, G., Cai, H., and Zhang, X. (2021). Acoustic Aggregation-Induced Separation for Enhanced Fluorescence Detection of Alzheimer's Biomarker. *Talanta* 233, 122517. doi:10.1016/j.talanta.2021.122517

Tan, W., Zhang, L., Doery, J. C. G., and Shen, W. (2020). Three-Dimensional Microfluidic Tape-Paper-Based Sensing Device for Blood Total Bilirubin Measurement in Jaundiced Neonates. *Lab. Chip* 20, 394–404. doi:10.1039/c9lc00939f

Tenda, K., van Gerven, B., Arts, R., Hiruta, Y., Merkx, M., and Citterio, D. (2018). Paper-Based Antibody Detection Devices Using Bioluminescent BRET-Switching Sensor Proteins. *Angew. Chem. Int. Ed.* 57, 15369–15373. doi:10.1002/anie.201808070

Tomimuro, K., Tenda, K., Ni, Y., Hiruta, Y., Merkx, M., and Citterio, D. (2020). Thread-Based Bioluminescent Sensor for Detecting Multiple Antibodies in a Single Drop of Whole Blood. *ACS Sens.* 5, 1786–1794. doi:10.1021/acssensors.0c00564

Tricoli, A., and Neri, G. (2018). Miniaturized Bio- and Chemical-Sensors for Point-of-Care Monitoring of Chronic Kidney Diseases. *Sensors* 18, 942. doi:10.3390/s18040942

Udugama, B., Kadhiresan, P., Kozlowski, H. N., Malekjahani, A., Osborne, M., Li, V. Y. C., et al. (2020). Diagnosing COVID-19: The Disease and Tools for Detection. *ACS Nano* 14, 3822–3835. doi:10.1021/acsnano.0c02624

Wang, H., Yang, L., Chu, S., Liu, B., Zhang, Q., Zou, L., et al. (2019a). Semiquantitative Visual Detection of Lead Ions with a Smartphone via a Colorimetric Paper-Based Analytical Device. *Anal. Chem.* 91, 9292–9299. doi:10.1021/acs.analchem.9b02297

Wang, L., Xu, T., and Zhang, X. (2021). Multifunctional Conductive Hydrogel-Based Flexible Wearable Sensors. *Trac Trends Anal. Chem.* 134, 116130. doi:10.1016/j.trac.2020.116130

Wang, X., Li, F., Cai, Z., Liu, K., Li, J., Zhang, B., et al. (2018). Sensitive Colorimetric Assay for Uric Acid and Glucose Detection Based on Multilayer-Modified Paper with Smartphone as Signal Readout. *Anal. Bioanal. Chem.* 410, 2647–2655. doi:10.1007/s00216-018-0939-4

Wang, X., Li, F., and Guo, Y. (2020). Recent Trends in Nanomaterial-Based Biosensors for Point-of-Care Testing. *Front. Chem.* 8, 586702. doi:10.3389/fchem.2020.586702

Wang, Y., Wang, X., Lu, W., Yuan, Q., Zheng, Y., and Yao, B. (2019b). A Thin Film Polyethylene Terephthalate (PET) Electrochemical Sensor for Detection of Glucose in Sweat. *Talanta* 198, 86–92. doi:10.1016/j.talanta.2019.01.104

Wei, X., Guo, J., Lian, H., Sun, X., and Liu, B. (2021). Cobalt Metal-Organic Framework Modified Carbon Cloth/Paper Hybrid Electrochemical Button-Sensor for Nonenzymatic Glucose Diagnostics. *Sensors Actuators B: Chem.* 329, 129205. doi:10.1016/j.snb.2020.129205

White, D., Keramane, M., Capretta, A., and Brennan, J. D. (2020). A Paper-Based Biosensor for Visual Detection of Glucose-6-Phosphate Dehydrogenase from Whole Blood. *Analyst* 145, 1817–1824. doi:10.1039/c9an02219h

Xiao, J., Liu, Y., Su, L., Zhao, D., Zhao, L., and Zhang, X. (2019). Microfluidic Chip-Based Wearable Colorimetric Sensor for Simple and Facile Detection of Sweat Glucose. *Anal. Chem.* 91, 14803–14807. doi:10.1021/acs.analchem.9b03110

Xu, D., Huang, X., Guo, J., and Ma, X. (2018). Automatic Smartphone-Based Microfluidic Biosensor System at the Point of Care. *Biosens. Bioelectron.* 110, 78–88. doi:10.1016/j.bios.2018.03.018

Xu, G., Cheng, C., Yuan, W., Liu, Z., Zhu, L., Li, X., et al. (2019). Smartphone-Based Battery-Free and Flexible Electrochemical Patch for Calcium and Chloride Ions Detections in Biofluids. *Sensors Actuators B: Chem.* 297, 126743. doi:10.1016/j.snb.2019.126743

Xu, Y., Zhao, G., Zhu, L., Fei, Q., Zhang, Z., Chen, Z., et al. (2020). Pencil-Paper On-Skin Electronics. *Proc. Natl. Acad. Sci. U.S.A.* 117, 18292–18301. doi:10.1073/pnas.2008422117

Yang, X., Yao, H., Zhao, G., Ameer, G. A., Sun, W., Yang, J., et al. (2020). Flexible, Wearable Microfluidic Contact Lens with Capillary Networks for Tear Diagnostics. *J. Mater. Sci.* 55, 9551–9561. doi:10.1007/s10853-020-04688-2

Yang, Y., and Gao, W. (2019). Wearable and Flexible Electronics for Continuous Molecular Monitoring. *Chem. Soc. Rev.* 48, 1465–1491. doi:10.1039/c7cs00730b

Yu, Q., Xue, L., Hiblot, J., Griss, R., Fabritz, S., Roux, C., et al. (2018). Semisynthetic Sensor Proteins Enable Metabolic Assays at the Point of Care. *Science* 361, 1122–1126. doi:10.1126/science.aat7992

Zhao, C., Li, X., Wu, Q., and Liu, X. (2021c). A Thread-Based Wearable Sweat Nanobiosensor. *Biosens. Bioelectron.* 188, 113270. doi:10.1016/j.bios.2021.113270

Zhao, H., Liu, F., Xie, W., Zhou, T.-C., Ouyang, J., Jin, L., et al. (2021a). Ultrasensitive Supersandwich-Type Electrochemical Sensor for SARS-CoV-2 from the Infected COVID-19 Patients Using a Smartphone. *Sensors Actuators B: Chem.* 327, 128899. doi:10.1016/j.snb.2020.128899

Zhao, Z., Li, Q., Chen, L., Zhao, Y., Gong, J., Li, Z., et al. (2021b). A Thread/Fabric-Based Band as a Flexible and Wearable Microfluidic Device for Sweat Sensing and Monitoring. *Lab. Chip* 21, 916–932. doi:10.1039/d0lc01075h

Conflict of Interest: The authors declare that the research was conducted in the absence of any commercial or financial relationships that could be construed as a potential conflict of interest.

Publisher's Note: All claims expressed in this article are solely those of the authors and do not necessarily represent those of their affiliated organizations, or those of the publisher, the editors and the reviewers. Any product that may be evaluated in this article, or claim that may be made by its manufacturer, is not guaranteed or endorsed by the publisher.

frontiers in Bioengineering and Biotechnology

ORIGINAL RESEARCH
published: 07 October 2021
doi: 10.3389/fbioe.2021.743322

A CRISPR-Cas12b–Based Platform for Ultrasensitive, Rapid, and Highly Specific Detection of Hepatitis B Virus Genotypes B and C in Clinical Application

Xu Chen[1†], Yan Tan[2†], Shuoshi Wang[1], Xueli Wu[1], Rui Liu[1], Xinggui Yang[3], Yi Wang[4], Jun Tai[5]* and Shijun Li[6]**

[1]Central Laboratory of the Second Affiliated Hospital, Guizhou University of Traditional Chinese Medicine, Guiyang, China, [2]Guizhou Provincial Center for Clinical Laboratory, Guiyang, China, [3]Public Health School, Guizhou Medical University, Guiyang, China, [4]Experimental Research Center, Capital Institute of Pediatrics, Beijing, China, [5]Department of Otolaryngology, Head and Neck Surgery, Children's Hospital Capital Institute of Pediatrics, Beijing, China, [6]Guizhou Provincial Centre for Disease Control and Prevention, Guiyang, China

OPEN ACCESS

Edited by:
Yunlu Pan,
Harbin Institute of Technology, China

Reviewed by:
Hung-Chih Yang,
National Taiwan University, Taiwan
Ming Zhou,
Northeast Normal University, China

***Correspondence:**
Yi Wang
wildwolf0101@163.com
Jun Tai
trenttj@163.com
Shijun Li
zjumedjun@163.com

[†]These authors have contributed equally to this work

Specialty section:
This article was submitted to Biosensors and Biomolecular Electronics, a section of the journal Frontiers in Bioengineering and Biotechnology

Received: 18 July 2021
Accepted: 31 August 2021
Published: 07 October 2021

Citation:
Chen X, Tan Y, Wang S, Wu X, Liu R, Yang X, Wang Y, Tai J and Li S (2021) A CRISPR-Cas12b–Based Platform for Ultrasensitive, Rapid, and Highly Specific Detection of Hepatitis B Virus Genotypes B and C in Clinical Application. Front. Bioeng. Biotechnol. 9:743322. doi: 10.3389/fbioe.2021.743322

Hepatitis B virus (HBV) is one of the most dangerous and prevalent agents that causes acute and chronic liver diseases in humans. Genotyping plays an important role in determining clinical outcomes and response to antiviral treatment in HBV–infected patients. Here, we first devised a CRISPR–based testing platform, termed "CRISPR-HBV," for ultrasensitive, highly specific, and rapid detection of two major HBV genotypes (HBV-B and HBV-C) in clinical application. The CRISPR-HBV employed multiple cross displacement amplification (MCDA) for rapid preamplification and then Cas12b–based detection for decoding the targets. Finally, the detection result was read out with real-time fluorescence and a lateral flow biosensor. The sensitivity of CRISPR-HBV was 10 copies per test. The specificity was one hundred percent, and no cross reactions were observed in other HBV genotypes and pathogens. The whole detection process, including DNA template extraction (15 min), preamplification reaction of MCDA (30 min at 65°C), CRISPR-Cas12b–based detection (5 min at 37°C), and results readout (~2 min), could be completed within 1 h. The feasibility of the CRISPR-HBV assay for genotyping HBV-B and -C as successfully validated with clinical samples. Hence, the CRISPR-HBV assay has remarkable potential to develop a point-of-care testing for identifying and distinguishing HBV genotypes B and C in clinical settings, especially in resource-scarcity countries.

Keywords: hepatitis B virus, CRISPR, Cas12b, multiple cross displacement amplification, lateral flow biosensor

INTRODUCTION

Hepatitis B virus (HBV) is one of the main pathogens that can cause severe liver diseases, such as liver failure, liver cirrhosis, and hepatocellular carcinoma, which could be transmitted through exposure to infected blood and body fluids (Nelson et al., 2016; Nguyen et al., 2020; Bertoletti and Bert, 2018). Approximately 257 million people are living with chronic HBV infection, and it causes 700,000 deaths annually worldwide according to the World Health Organization (WHO) reports (World Health organization, 2017). Therefore, it is still a major public health concern in the world. It has

been reported that there are at least eight genotypes (A–H) that are divergent by >8% across the entire genome (Zhao et al., 2010). In clinical practice, the genotype characteristic is essential for finding the severity of HBV infection and response to antiviral therapy in hepatitis B patients (Wang et al., 2015; Zhao et al., 2010). China has a high incidence of HBV, and genotypes B and C were identified as the most common agents (more than 95%) (Lin and Kao, 2011; Wang et al., 2019; Su et al., 2020). HBV genotype C causes more severe liver fibrosis, which more easily progresses to hepatocellular carcinoma, than genotype B infection (Zhao et al., 2010). Moreover, genotype C is also related to a less response to antiviral treatment than genotype B (Zeng et al., 2008). Hence, identification and discrimination of HBV genotypes B and C is essential for the follow-up clinical therapy and management of HBV–infected patients in the Asia–Pacific region.

Real-time polymerase chain reaction (PCR), restriction fragment length polymorphism (RFLP) analysis, and DNA direct sequencing have been widely used for genotyping in clinical practice (Irshad et al., 2016; Inoue and Tanaka, 2020; Wang et al., 2015). However, these diagnostic services require expensive apparatus, skilled personnel, and specialized labs, which may not be available in many resource-limited countries. Besides, it is also time-consuming. Hence, devising a rapid, specific, sensitive, and easy-to-use assay for genotyping HBV is essential for the follow-up therapy in HBV–infected patients.

A CRISPR/Cas (Clustered Regularly Interspaced Short Palindromic Repeat and CRISPR-Associated Protein) system was discovered first in the adaptive immunity of archaea and bacteria for eliminating invading nucleic acids (Yao et al., 2018). The Cas effector proteins navigated with guide RNA (gRNA) to target and cleave an invading nucleic acid. Over the last few years, CRISPR/Cas systems, such as CRISPR/Cas9, CRISPR/Cas13, and CRISPR/Cas12, have become prominent tools for genome editing. Recently, the CRISPR/Cas system has displayed potential for the development of next-generation nucleic acid–diagnostics methodology owing to its high sensitivity, specificity, and reliability (Gootenberg et al., 2017). The principle of detection with a CRISPR/Cas platform is based on the *trans*-cleavage activities of Cas nucleases, such as Cas13, Cas12a, and Cas12b, which have the ability to nonspecifically and indiscriminately cleave surrounding nontarget ssRNA and ssDNA when Cas nucleases bound to the target sequence under the guidance of CRISPR RNA (gRNA) (Gootenberg et al., 2018). Combined with isothermal amplification, Cas13, Cas12a, and Cas12b have been used to devise rapid target nucleic acid–detection platforms, such as SHERLOCK (specific high-sensitivity enzymatic reporter unlocking), DETECTR (DNA endonuclease-targeted CRISPR *trans*-reporter), and HOLMESv2 (one-hour low-cost multipurpose highly efficient system v2) (Chen et al., 2018; Kellner et al., 2019; Li et al., 2019), respectively. These assays can accurately, sensitively, and rapidly detect various targets, including RNA and DNA viruses, bacteria, DNA genotypes, drug-resistant genes, and cancer mutations (Liang et al., 2019).

Currently, most of the CRISPR/Cas detection platforms rely on expensive fluorescence-based instruments (Liang et al., 2019), which can cause practical inconvenience and make the platform less robust in resource-limited settings. To overcome previous limitations, the nanoparticle-based lateral flow biosensor (LFB) was successfully devised and used to identify CRISPR/Cas detection results due to its visual readout, low-cost, stability, simplicity, and easy-to-use characteristics (Mukama et al., 2020). To increase the sensitivity of CRISPR/Cas diagnostics, the target gene will be preamplified by PCR or isothermal amplification (Pickar-Oliver and Gersbach, 2019). Multiple cross displacement amplification (MCDA), an innovative nucleic acid isothermal amplification technique, has been applied as an attractive alternative to the traditional PCR–related technique and has potential to develop a point-of-care (POC) testing owing to its rapidity, simplicity, and easy operation (Wang et al., 2017; Li et al., 2020). In the current study, we integrated the preamplification step of MCDA with CRISPR-Cas12b–LFB readout to develop a novel assay termed "CRISPR-HBV" for ultrasensitive, highly specific, and rapid detection of HBV genotypes B and C. In addition, a protospacer adjacent motif (PAM) site (TTC) for the CRISPR-Cas12b–based assay was added into the MCDA primers for detecting any sequences that meet the demand of the primer design (even if the target sequences do not contain any PAM sites). We illustrated the principle of the CRISPR-HBV assay in **Figures 1** and **2** and validated its feasibility in genotyping of HBV genotypes B and C with clinical specimens.

MATERIALS AND METHODS

Reagents and Instruments

The universal isothermal amplification kits, colorimetric indicator (malachite green), gold nanoparticle–based LFB, and CRISPR-Cas12b protein (C2c1) were obtained from HuiDeXin Biotechnology (Tianjin, China). Anti-FAM (rabbit anti-fluorescein antibody) and biotin-BSA (biotinylated bovine serum albumin) were obtained from Abcam Co., Ltd. (Shanghai, China). The LFB materials, including a sample pad, an absorbent pad, a conjugate pad, a nitrocellulose membrane (NC), and a backing card, were purchased from the Jie-Yi Biotechnology. Co., Ltd. (Shanghai, China). A dye (crimson red) and streptavidin-coated gold nanoparticles (size, 34.46 ± 4.34 nm; extinction coefficient, 6.0×10^9 M^{-1} cm^{-1} at 506 nm) were purchased from Bangs Laboratories, Inc. (Indiana, United States). A real-time turbidimeter (LA-500) was purchased from Eiken Chemical Co., Ltd. (Japan).

Preparation of Target DNA and Clinical Samples

In this study, the full-length DNA sequences of the *S* gene of HBV genotypes B and C (accession numbers AF100309 and AB014381, respectively) (Zhao et al., 2010) were synthesized and cloned in a pUC57 vector. The two plasmids (genotype B plasmid and genotype C plasmid) were constructed commercially by General Biol (Anhui, China), according to the manufacturer's instruction. The initial concentration of HBV genotype B and C plasmids was 1×10^8 copies per microliter. The two constructed

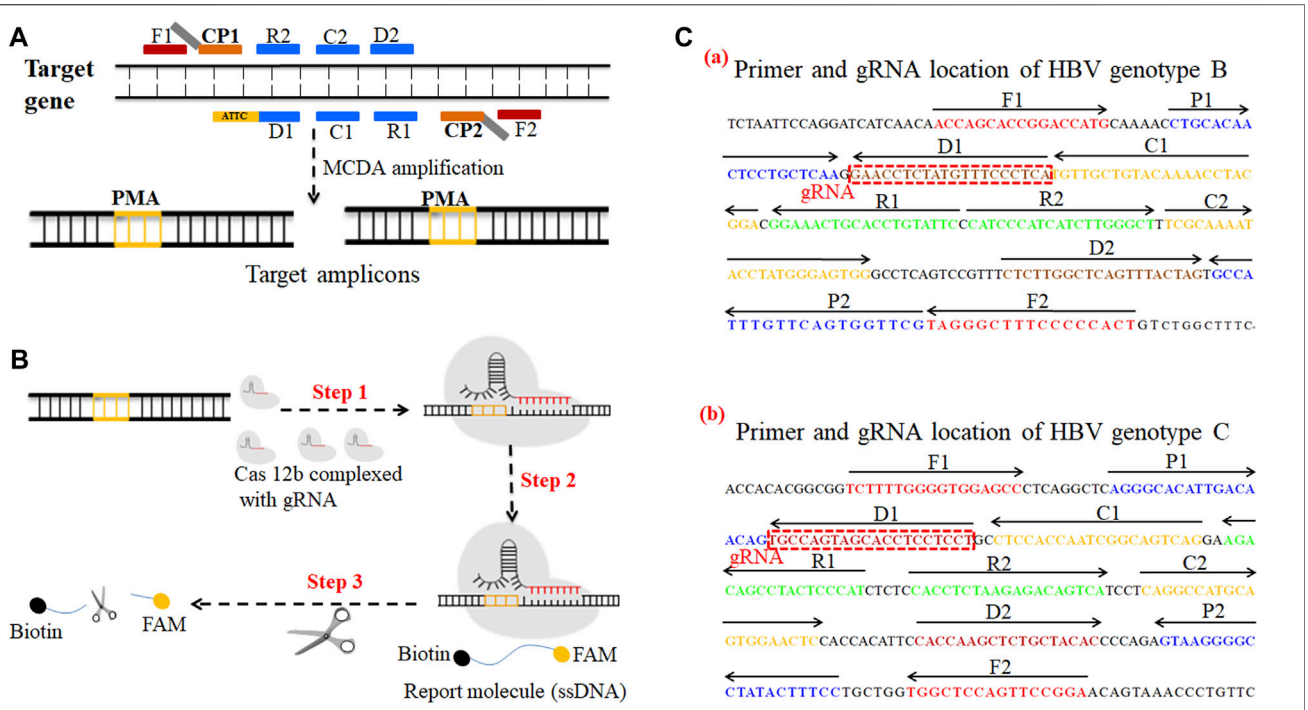

FIGURE 1 | A schematic illustration of the principle of the CRISPR-HBV system. **(A)** Schematic illustration of the principle of MCDA with the modified primer. The amplification primer D1 was modified with a PAM site (TTC). After amplification, a CRISPR-Cas12b recognition site was constructed in the target amplicons. **(B)** Schematic illustration of the CRISPR-Cas12b detection system. Upon recognition of the matching target sequence, the CRISPR-Cas12b complex cleaves a single-stranded DNA reporter molecule. © Sequences and location of the *S* gene of HBV genotypes B and C used to devise the MCDA primers and gRNAs. The sites of MCDA primers are underlined, and the gRNAs are in boxes. Right arrows and left arrows indicate the sense and complementary sequences which were used in this study, respectively.

plasmids acted as the positive control. In addition, the full-length DNA sequences of the *S* gene for HBV genotypes A, D, E, F, G, and H (accession numbers AF090842, X65259, AB032431, AB036910, AF160501, and AY090454) were synthesized and cloned in a pUC57 vector. The 114 suspected HBV–infected serum samples were collected from the Second Affiliated Hospital of Guizhou University of Traditional Chinese Medicine (Guiyang, China) during April 2020 to December 2020. DNA sequencing was used as the gold standard for determining the HBV genotypes. In brief, a portion of the *S* gene was amplified with the primers F 5′-TCTAGACTCGTGGTGGA-3′ and R 5′-GATGATGGGATGGGAATACA-3’ (Zhao et al., 2011), and then, the PCR products were sequenced by Dian Medical Laboratory Center Co., Ltd. (Hangzhou, China) and finally analyzed using NCBI genotyping tools (https://www.ncbi.nlm.nih.gov/projects/genotyping/formpage.cgi). Other various pathogens used in the current study are shown in **Supplementary Table S2**.

Multiple Cross Displacement Amplification Primers and gRNA Design

The HBV genotype B– and C–MCDA primers were designed using PRIMER PREMIER 5.0 software in accordance with the principle of MCDA reaction based on the genotype B *S* gene (GenBank no. AF100309; 157–837) and the genotype C *S* gene (GenBank no. AB014381; 2,848–3,215, 1–835), respectively. The specificity of each MCDA primer was confirmed with the BLAST analysis tool. In addition, two gRNAs for HBV genotypes B and C based on the *S* gene were designed according to the CRISPR-Cas12b detection mechanism. The locations of each MCDA primer and gRNA are shown in **Figure 1C**. Moreover, we added the PAM site (TTC) in each MCDA primer for the CRISPR/12b–based assay; the principle of MCDA and the CRISPR-Cas12b–based assay are shown in **Figures 1A,B**. The MCDA primers and gRNA sequences are shown in **Supplementary Table S1**. All of the oligonucleotides were synthesized and purified by Genscript Biotech Co., Ltd. (Nanjing, China) with HPLC purification grade.

Multiple Cross Displacement Amplification

The preamplification step of MCDA was performed with an isothermal amplification kit, according to the manufacturer's instructions (HuiDeXing Biotech. Co., Ltd. Tianjing, China). In brief, the MCDA reaction system comprise 12.5 μl of 2 × reaction buffer, 0.4 μM each of F1 and F2, 1.6 μM each of CP1 and CP2, 0.8 μM each of C1, C2, D1, D2, R1, and R2, 12.5 μl of 2 × reaction buffer, 1 μl of *Bst* 2.0 DNA polymerase (8 U), 1 μl of AMV reverse transcriptase (10 U) (only used for the RNA template), and a nucleic acid template (1 μl of the standard plasmid and 5 μl of the clinical samples). Finally, 25 μl of double-distilled water was added. The reaction process was

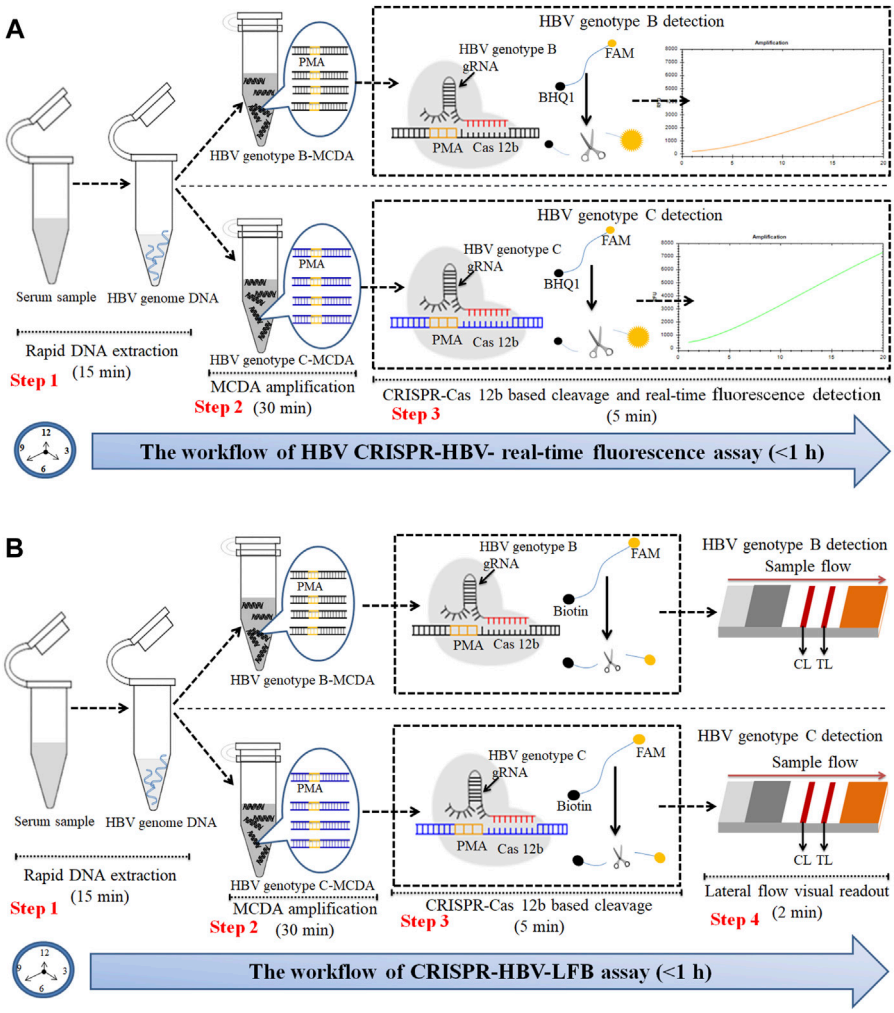

FIGURE 2 | An outline of the CRISPR-HBV workflow. **(A)** The CRISPR-HBV RTF assay employs three closely linked steps: DNA extraction (step 1), MCDA (step 2), and CRISPR-Cas12b cleavage and RTF readout (step 3). The whole detection process could be completed within 1 h. **(B)** CRISPR-HBV–LFB assay employs four closely linked steps: DNA extraction (step 1), MCDA (step 2), CRISPR-Cas12b cleavage (step 3), and LFB readout (step 4). The whole detection process could be completed within 60 min.

carried out with a heat blocker. The amplification results were monitored with real-time turbidity (LA-500) for optimizing the amplification temperature.

CRISPR-Cas12b–Based Assay

In the current study, Cas12b (C2c1) was used for CRISPR-Cas–based *trans*-cleavage detection. In brief, the CRISPR-Cas12b–gRNA complexes were preassembled as follows: 300 nM CRISPR-Cas12b (C2c1) (Cat no. HT100006) and 100 nM gRNA were preincubated in 1 × HDX buffer at 37°C for 10 min; the complexes should be used immediately or stored at low temperatures (0–4°C) no more than 12 h before use.

The CRISPR-Cas12b–based *trans*-cleavage detection system comprised 2 μl of MCDA products, 1.0 μl of the single-strand DNA reporter molecule (50 μM), 4 μl of the CRISPR-Cas12b–gRNA complex, 25 μl of the 2 × HDX buffer, and distilled water up to 50 μl; then, the detection process was performed at 37°C for 5 min, and the results were analyzed using the real-time fluorescence (RTF) and LFB, respectively. For RTF analysis of the CRISPR-Cas12b *trans*-cleavage detection, the Flu-probe (5′-FAM-TTTTTT-BHQ1-3′, 100 μM) was used. For the LFB assay, the reporter should be replaced with a single-strand DNA reporter molecule (5′-FAM-TTTTTT-Biotin-3′, 50 μM).

Gold Nanoparticle–Based Lateral Flow Biosensor Design and Assay

The LFB (size: 60 mm × 4 mm) used in this study is designed and illustrated in **Figure 3**. In brief, the biosensor was composed of four sections, including a sample pad, a conjugate pad, a reaction region (nitrocellulose membrane), and an absorbent pad. All of them were assembled on a plastic adhesive backing card. The streptavidin–gold nanoparticles (SA-GNPs) were deposited on

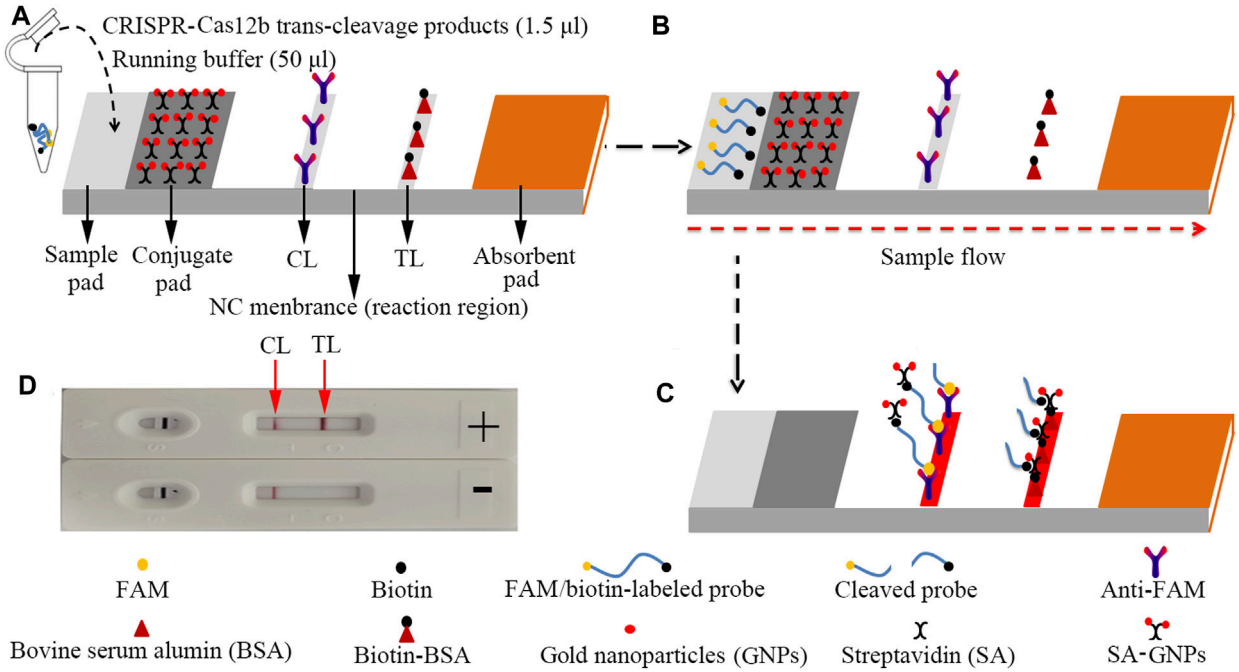

FIGURE 3 | The schematic of the LFB for visualization of HBV genotype B and C products. **(A)** The reaction mixtures (1.5 μl) and the running buffer (50 μl) were deposited on the sample pad. **(B)** The running buffer containing mixtures moved along the LFB owing to capillary action; meanwhile, the dye and streptavidin-coated gold nanoparticles (GNPs) rehydrated in the conjugate region. **(C)** In the positive sample, the ssDNA reporter molecule (5′-FAM-TTTTTT-Biotin-3′) was *trans*-cleaved by the activated CRISPR-Cas12b nuclease and the FAM and biotin were separated. Hence, the biotin–streptavidin–GNPs complex was captured by biotin-BSA at the TL; however, in negative outcomes, the ssDNA reporter molecule was not cleaved and was specifically captured by the anti-FAM at the CL. The biotins of the ssDNA reporter molecule bind streptavidin–GNPs for visualization at the CL. **(D)** Interpretation of the CRISPR-HBV assay results. For positive results, the CL and TL appear on the LFB. When only the CL is observed on the LFB, it indicates negative outcomes. CL: control line; TL: test line.

the conjugate pad. Anti-FAM and biotin-BSA were fixed on the reaction region for a control line (CL) and a test line (TL), respectively, each line separated by 5 mm. The biosensor used in the current study was manufactured by HuiDeXing Biotech. Co., Ltd. (Tianjing, China) in accordance with our experiment. The LFB can be dry-stored at 4°C for 2 years before use.

For the LFB analysis, 1.5 μl of CRISPR-Cas12b *trans*-cleavage products was added on the sample pad; meanwhile, 50 μl of running buffer (100 mM PBS) was dropped on the sample pad. The running buffer containing CRISPR-Cas12b *trans*-cleavage products was absorbed, and the detection results were read out visually on a NC membrane (red line) within 2 min (**Figure 3**).

Sensitivity and Specificity of the CRISPR-HBV Assay

For testing the sensitivity of the CRISPR-HBV assay, two standard plasmids, including HBV genotype B and C plasmids, were 10-fold serially diluted from 1.0×10^5 to 1.0×10^{-1} copies. The CRISPR-HBV assay was performed as previously described, and then, the results were detected with the RTF and LFB. Three replicates of each dilution were tested.

The *S* gene of HBV genotypes A–H (synthesized sequences) and other non-HBV pathogens (**Supplementary Table S2**) were used for verifying the specificity of the CRISPR-HBV assay; distilled water (DW) was applied as the blank control (BC). The CRISPR-HBV assay was performed as previously described and then detected with the RTF and LFB. Each test was confirmed at least three times.

Verification of the Feasibility of the CRISPR-HBV Assay Using Clinical Samples

For further confirming the feasibility of the CRISPR-HBV assay devised in this study, the optimized CRISPR-HBV assay system was assessed with clinical samples. 114 suspected HBV–infected serum samples were collected from the Second Affiliated Hospital of Guizhou University of Traditional Chinese Medicine (Guiyang, China). The CRISPR-HBV operation was performed as described above. Meanwhile, the clinical samples were tested with direct DNA sequencing (Dian Medical Laboratory Center Co., Ltd. Hangzhou, China). Finally, the outcomes of the CRISPR-HBV assay were compared with those of direct DNA sequencing.

RESULTS

Overview of the CRISPR-HBV Detection System

The principle of CRISPR-HBV detection system is illustrated in **Figures 1** and **2**. In brief, the extracted HBV DNA templates were preamplified by the MCDA method. In this detection system, we

modified the MCDA primer D1 at the 5′ end with a PAM site (TTC) (**Figure 1A**) and the HBV-MCDA amplicons contain a newly acquired Cas12b PAM site for the CRISPR-Cas12b–based assay stage (**Figure 1B**); the PAM site can be applied for location by the corresponding CRISPR-Cas12b/gRNA system (**Figure 1B**, Step 1). Then, the CRISPR-Cas12b effector was activated for *trans*-cleavage activity, and the single-strand DNA reporter molecules (5′-FAM-TTTTTT-Biotin-3′) were ultrafast digested (**Figure 1B**, Step 2 and Step 3). After CRISPR-Cas12b cleavage, the reaction mixtures (1.5 μl) and the running buffer (50 μl) were deposited on the sample region of the LFB (**Figure 3A**); the running buffer containing reaction mixtures moved along the LFB owing to capillary action, and the streptavidin–GNPs were rehydrated in the conjugate region (**Figure 3B**). In negative outcomes, the ssDNA reporter molecule was not cleaved and specifically seized by the anti-FAM at the CL. Hence, the biotins of the ssDNA probe (5′-FAM-TTTTTT-Biotin-3′) bind streptavidin–GNPs for visualization readout at the CL (**Figure 3C**). However, in the positive sample, the ssDNA reporter molecule was *trans*-cleaved by the activated CRISPR-Cas12b nuclease, and the biotin and FAM were separated. Finally, the biotin–streptavidin–GNPs complex was seized by biotin-BSA at the TL (**Figure 3C**). The interpretation of the CRISPR-HBV assay using the LFB analysis is displayed in **Figure 2B** and **Supplementary Figure S1**. The detection results were reported simultaneously using RTF with the Flu-probe (5′-FAM-TTTTTT-BHQ1-3′); the principle is illustrated in **Figure 2A**.

Optimal Reaction Conditions for the CRISPR-HBV Assay

Temperature is critical for isothermal amplification. The reaction temperature of the preamplification stage of MCDA was optimized from 60 to 67°C using HBV genotype B and C plasmids (1.0×10^3 copies per reaction), respectively. The results indicated that 65°C was deemed an optimal reaction temperature for the preamplification step of HBV MCDA (**Supplementary Figures S2 and S3**). Then, the reaction time (1, 2, 5, 10, and 20 min) of CRISPR-Cas12b detection was optimized. The results were read out simultaneously with the LFB and RTF. As shown in **Supplementary Figure S4**, the stable visual signal was observed by the LFB within 5 min (**Supplementary Figures S4A and B**) and the fluorescent signal was monitored within 1 min (**Supplementary Figures S4C and D**).

Sensitivity and Specificity of the CRISPR-HBV Assay

The sensitivity of CRISPR-HBV detection was evaluated using HBV genotype B and C plasmids with serial dilutions (ranging from 1.0×10^5 to 1.0×10^{-1} copies per reaction). The CRISPR-HBV assay was performed as described above, and the outcomes were read out through the RTF and LFB. For RTF detection, the results indicated that the limit of detection (LoD) of the CRISPR-HBV assay was 10 copies per test (**Figures 4B,D**), which was completely consistent with the LFB assay (**Figures 4A,C**).

The specificity evaluation of the CRISPR-HBV assay was confirmed using synthesized templates, HBV genotype B– and C–positive clinical samples, and various non-HBV pathogens (**Supplementary Table S2**). The CRISPR-HBV assay was manipulated by the optimal reaction conditions verified above, and the outcomes were analyzed using the LFB and RTF. The positive outcomes appeared only when the templates were extracted from HBV genotype B or C agents, while other HBV genotypes, non-HBV pathogens, and the blank control presented negative outcomes (**Figure 5**, **Supplementary Figures S5, and S6**). No cross reactions were observed in the CRISPR-HBV assay. Therefore, the CRISPR-HBV assay designed in the current study was highly selective to the target sequences.

Confirming the Feasibility of the CRISPR-HBV Assay in Clinical Samples

To further validate whether the CRISPR-HBV assay could be used for distinguishing between HBV genotypes B and C in clinical application, 114 suspected HBV–infected serum specimens were assayed simultaneously using CRISPR-HBV and direct sequencing. According to the sequencing results, 36 samples were confirmed as genotype B, 28 samples were recognized as genotype C, five samples were identified as genotype B/C, three samples were recognized as genotype D, and 42 samples were tested as non-HBV infection. The results were in accordance with the CRISPR-HBV assay outcomes (**Supplementary Table S3**). These results indicated that the CRISPR-HBV assay developed in this study could be considered as an advanced technique to distinguish between HBV genotypes B and C in clinical application.

DISCUSSION

HBV is one of the most dangerous and prevalent agents that causes acute and chronic liver diseases in humans (Pisaturo et al., 2019; Meng et al., 2020). Several investigations have indicated that different HBV genotypes could affect the clinical outcomes and response to antiviral treatment in hepatitis B patients. Genotypes B and C are the two most common agents (accounting for approximately 95%) in China (Lin and Kao, 2011; Wang et al., 2019; Su et al., 2020). Previous studies demonstrated that HBV genotype C was associated with a higher risk of reactivation of hepatitis B, with more severe liver fibrosis, and can more easily progress to hepatocellular carcinoma than genotype B infection (Lin and Kao, 2011). Moreover, HBV genotype C is also associated with a lower response rate to antiviral therapy (Zeng et al., 2008). A previous study demonstrated that genotype B had a better virological response to adefovir dipivoxil therapy than genotype C (Zhao et al., 2010). Hence, detection and discrimination of HBV genotypes B and C are essential for the follow-up clinical treatment and management of HBV–infected patients in the Asia–Pacific region. In the current study, a novel CRISPR-HBV assay, which integrated CRISPR-Cas12b detection with MCDA, was established for identifying and distinguishing HBV genotypes B and C in clinical samples.

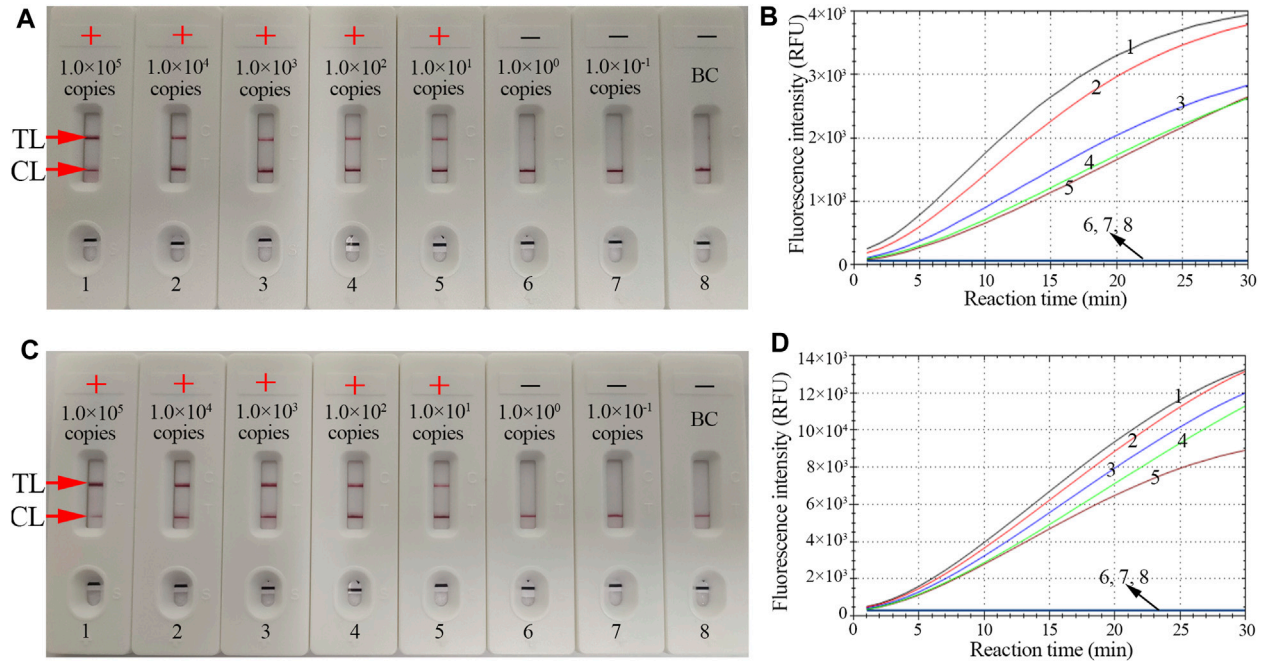

FIGURE 4 | The sensitivity of the CRISPR-HBV assay. LFB and RTF techniques were simultaneously applied for reporting the CRISPR-HBV assay results. LFB **(A)** and RTF **(B)** 1–8 represent the HBV genotype B-*S* plasmid concentrations of 1×10^5, 1×10^4, 1×10^3, 1×10^2, 1×10^1, 1×10^0, and 1×10^{-1} copies per reaction and the blank control (DW), respectively. LFB **(B)** and RTF **(D)** 1–8 represent the HBV genotype C-*S* plasmid concentrations of 1×10^5, 1×10^4, 1×10^3, 1×10^2, 1×10^1, 1×10^0, and 1×10^{-1} copies per reaction and the blank control (DW), respectively. The LoD of the CRISPR-HBV assay was 10 copies per reaction. CL: control line; TL: test line; "+": positive; "–": negative.

An ideal laboratory diagnostic technique for confirmation and distinction of HBV genotypes B and C should be rapid, specific, sensitive, and easy to use. Currently, real-time PCR, RFLP analysis, and direct DNA sequencing have been widely applied for genotyping in clinical practice (Zhao et al., 2011; Wang et al., 2015; Lin and Kao, 2011). However, their use in low- and middle-income regions is significantly limited due to the requirement of expensive instruments and trained experts. A CRISPR/Cas system was discovered first in the adaptive immunity of archaea and bacteria for eliminating invading nucleic acids (Yao et al., 2018; Shiriaeva et al., 2020). The Cas effector proteins were navigated with gRNA to target and cleave an invading nucleic acid (Zhou et al., 2018). Over the last few years, CRISPR/Cas systems, such as CRISPR/Cas9, CRISPR/Cas12, and CRISPR/Cas13, have become a prominent tool for genome editing (Myhrvold et al., 2018; Zhu et al., 2021). Recently, Cas12 and Cas13 effectors were demonstrated to have remarkable potential in developing novel nucleic acid–detection technologies based on their unique characteristic of collateral cleavage of target genes and nonspecific single-stranded nucleic acids (Pickar-Oliver and Gersbach, 2019; Broughton et al., 2020). In this study, we designed successfully the specific gRNAs for HBV genotypes B and C, and the gRNAs navigated Cas12b effector proteins to each of the target sequences. The specificity of the CRISPR-HBV system was strongly confirmed with HBV agents and other pathogens. The results have shown that the CRISPR-HBV assay could clearly distinguish HBV genotypes B and C and have no cross reactions with other pathogens (**Supplementary Figures 5S5S6**). Hence, the CRISPR-HBV assay displayed a high level of specificity for distinguishing HBV genotypes B and C. Apart from its remarkable specificity, the novel CRISPR-HBV assay could detect as low as 10 copies of genomic DNA per test (**Figure 4**). Owing to the lack of reference strains for HBV genotypes B and C in our laboratory, the full-length DNA sequences of the *S* gene for HBV genotypes B and C (accession number AF100309 and AB014381, respectively) were synthesized and cloned in the pUC57 vector, respectively. The synthesized plasmids were considered as HBV genotype B and C reference strains. In order to further confirm the sensitivity of the CRISPR-HBV assay in the human serum, the HBV genotype B-*S* or C-*S* plasmids were added into 100 µl serum of a healthy volunteer and the final concentrations of HBV genotype B-*S* or C-*S* genes were made ranging from 1.0×10^5 to 1.0×10^{-1} copies/µl, respectively. The nucleic acid was extracted using a Rapid Nucleic Acid Extraction kit (Jiangsu Bioperfectus Technologies Co., Ltd., China) and dissolved into 100 µl distilled water, and then, 1 µl nucleic acid was used for the CRISPR-HBV assay. The results showed that the sensitivity of this assay was also 10 copies (data not shown). More importantly, we also successfully applied the CRISPR-HBV assay to clinical samples. The suspected HBV–infected serum samples were simultaneously detected with the CRISPR-HBV assay and direct DNA sequencing, and the concordance results of the former and latter detections were given (**Supplementary Table S3**). It is indicated that the CRISPR-HBV assay could be used as a reliable tool for detecting and distinguishing HBV genotypes B

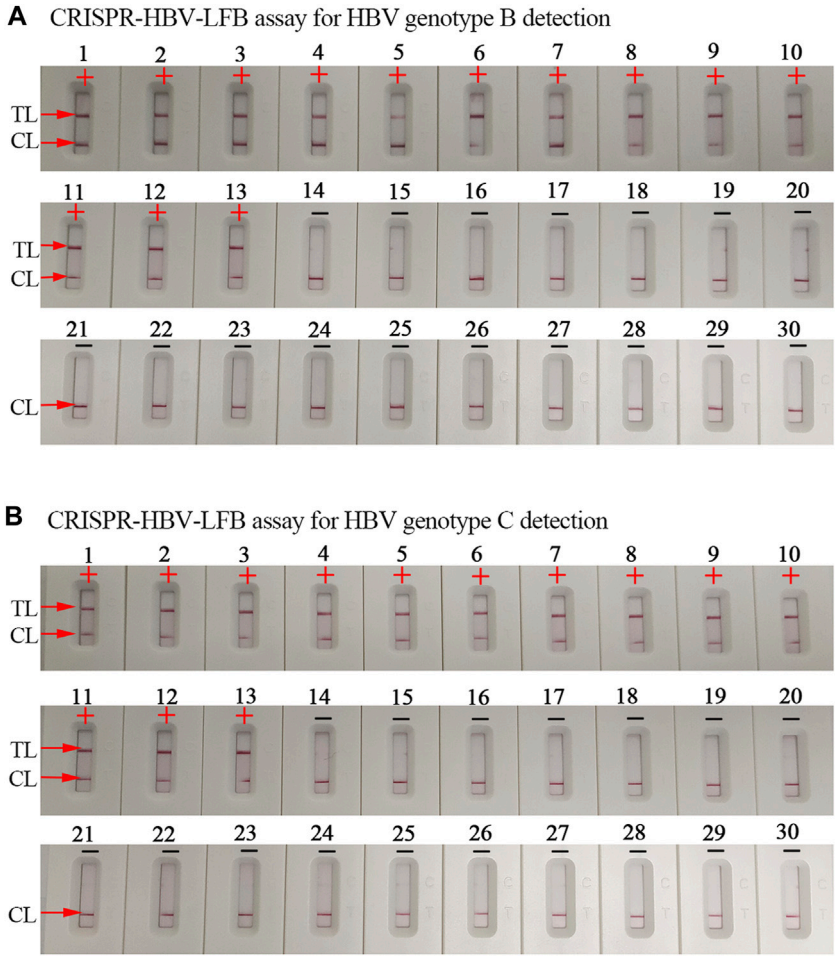

FIGURE 5 | The specificity of the CRISPR-HBV assay. **(A)** The specificity of the CRISPR-HBV–LFB assay for HBV genotype B detection. Biosensor 1, HBV genotype B-*S* plasmid; biosensors 2–9, HBV genotype B agents (clinical samples); biosensors 10–13, HBV genotype B/C agents (clinical samples); biosensor 14, HBV genotype A-*S* plasmid; biosensor 15, HBV genotype C-*S* plasmid; biosensor 16, HBV genotype D-*S* plasmid; biosensor 17, HBV genotype E-*S* plasmid; biosensor 18, HBV genotype F-*S* plasmid; biosensor 19, HBV genotype G-*S* plasmid; biosensor 20, HBV genotype H-*S* plasmid; biosensor 21, hepatitis C virus (standard substance); biosensor 22, human immunodeficiency virus (standard substance); biosensor 23, human rhinovirus; biosensor 24, adenovirus; biosensor 25, *Mycobacterium tuberculosis*; biosensor 26, *Bordetella pertussis*; biosensor 27, *Bacillus cereus*; biosensor 28, *Haemophilus influenzae*; biosensor 29, *Staphylococcus aureus*; and biosensor 30, blank control. CL: control line; TL: test line; "+": positive; "–": negative. **(B)** The specificity of the CRISPR-HBV–LFB assay for HBV genotype C detection. Biosensor 1, HBV genotype C-*S* plasmid; biosensors 2–9, HBV genotype C agents (clinical samples); biosensors 10–13, HBV genotype B/C agents (clinical samples); biosensor 14, HBV genotype A-*S* plasmid; biosensor 15, HBV genotype B-*S* plasmid; biosensor 16, HBV genotype D-*S* plasmid; biosensor 17, HBV genotype E-*S* plasmid; biosensor 18, HBV genotype F-*S* plasmid; biosensor 19, HBV genotype G-*S* plasmid; biosensor 20, HBV genotype H-*S* plasmid; biosensor 21, hepatitis C virus (standard substance); biosensor 22, human immunodeficiency virus (standard substance); biosensor 23, human rhinovirus; biosensor 24, adenovirus; biosensor 25, *Mycobacterium tuberculosis*; biosensor 26, *Bordetella pertussis*; biosensor 27, *Bacillus cereus*; biosensor 28, *Haemophilus* influenzae; biosensor 29, *Staphylococcus aureus*; and biosensor 30, blank control. CL: control line; TL: test line; "+": positive; "–": negative.

and C in clinical application. The CRISPR-HBV assay developed in the current study only has the ability to detect and distinguish HBV genotypes B and C, but not HBV subgenotypes. For conservation across the sequences of entire HBV genotypes B and C, the HBV genotype B and C MCDA primers and gRNA sequences were designed based on the *S* gene that come from the NCBI's recommended reference sequence strains for genotype B (accession number: AF100309) and genotype C (accession number: AB014381) (Zhao et al., 2010).

In order to improve the sensitivity of the CRISPR-HBV assay, the MCDA method was used for preamplifying the target genes (HBV genotype B-*S* and genotype C-*S*). MCDA was considered as a novel isothermal amplification technique, which is more sensitive than PCR and LAMP assays (Wang et al., 2015; Jiao et al., 2019; Wang et al., 2017). The isothermal amplification of the target sequence through a set of 10 primers spanning 10 different regions of the target gene was conducted (Wang and Wang et al., 2015), which comprised a pair of displacement primers (F1 and F2), a pair of cross primers (CP1 and CP2), and three pairs of amplification primers (C1, C2, D1, D2, R1, and R2) (**Figure 1A**). More importantly, in the current study, the

MCDA-D1 primers were modified with a Cas12b PAM site (TTC); after MCDA, the PAM site was applied for location by the corresponding CRISPR-Cas12b/gRNA complex to target sequences, then the Cas12b nuclease was activated, and the single-strand DNA reporter molecules were ultrafast *trans*-cleaved.

In this report, the gold nanoparticle–based LFB was used for reading out CRISPR-HBV outcomes. Currently, gold nanoparticles have become the most appropriate nanomaterials used as a biosensor owing to high adsorption, the high surface-to-volume ratio, well biocompatibility, and easy synthesis and manipulation (Quesada-González and Merkoçi, 2015; Aldewachi et al., 2017; Huang et al., 2019). The LFB could visually respond to the CRISPR-HBV assay for labeling with biotin-BSA and anti-FAM on the biosensor. In positive results, the ssDNA reporter molecule (5′-FAM-TTTTTT-Biotin-3′) was *trans*-cleaved by the activated CRISPR-Cas12b nuclease, the FAM and biotin probes were separated, and the biotin–streptavidin–GNPs complex was arrested by biotin-BSA and visually observed at the TL. However, in negative results, the ssDNA probe was not cleaved, was specifically captured by the anti-FAM, and was visualized at the CL (**Figure 3**). Although the RTF technique and the LFB method could be used for identifying the CRISPR-HBV assay, the former requires special instruments and complex operation, whereas the LFB is simple and easy to operate. Hence, LFB was considered as an optimal mean for the CRISPR-HBV assay. The whole detection process, including genomic DNA template preparation (~15 min), MCDA (30 min), CRISPR-Cas12b/gRNA detection (5 min), and results readout (~2 min), could be completed within 60 min. Therefore, the CRISPR-HBV assay has potential to develop a POC testing for identifying and distinguishing HBV genotypes B and C in clinical settings, especially in economically impoverished regions of the world. The shortcoming of this study is that we just use CRISPR-Cas12b–based platform for detection of two major HBV genotypes (B and C) in China. Next, we will further utilize the CRISPR-Cas12b–based platform to devise more assays for identifying various kinds of HBV genotypes.

CONCLUSION

We combined the preamplification reaction of MCDA with CRISPR-Cas12b and LFB readout to devise a novel assay, termed "CRISPR-HBV," for ultrasensitive, highly specific, and rapid detection of HBV genotypes B and C in clinical practice. The CRISPR-HBV assay was able to detect 10 copies of genomic DNA per test and has no cross reactions with other agents. The whole assay process could be completed within 60 min and does not require costly facilities. Hence, these traits of our CRISPR-HBV assay have potential to be an important POC testing for identifying and distinguishing HBV genotypes B and C in clinical application, especially in resource-constrained areas.

DATA AVAILABILITY STATEMENT

The original contributions presented in the study are included in the article/**Supplementary Material**; further inquiries can be directed to the corresponding authors.

ETHICS STATEMENT

This study was approved by the Human Ethics Committee of the Second Affiliated Hospital of Guizhou University of Traditional Chinese Medicine and complied with the Declaration of Helsinki. Before our team obtained the clinical samples and conducted the study, any personal identifiers of the suspected HBV–infected patients had been removed by the monitoring stations. Hence, the patient informed consent was waived by the Second Affiliated Hospital of Guizhou University of Traditional Chinese Medicine.

AUTHOR CONTRIBUTIONS

XC was involved in conceptualization, data curation, project administration, investigation, validation, supervision, original draft preparation, and funding acquisition. YT carried out project administration, data curation, supervision, validation, and original draft preparation. SW was responsible for data curation, project administration, investigation, and validation. XW and RL performed data curation, project administration, investigation, and validation. XY conducted data curation. YW performed conceptualization, project administration, supervision, funding acquisition, and reviewing and editing. JT was involved in project administration, supervision, validation, and reviewing and editing. SL was responsible for conceptualization, project administration, supervision, validation, and reviewing and editing.

FUNDING

This work was supported by the Program of Scientific and Technological Project in Guizhou Province (Grant No. Qian Ke He (2020)4Y184), the Scientific and Technological in Guiyang City (Grant No. Zhu Ke He (2020)-10-5), and the Public Welfare Technology Research Program in Zhejiang Province (Grant No. LGF21H190001).

ACKNOWLEDGMENTS

The authors would like to express their sincere appreciation to the medical workers in the 2nd GZUTCM and GZCDC for their contribution in the current study.

SUPPLEMENTARY MATERIAL

The Supplementary Material for this article can be found online at: https://www.frontiersin.org/articles/10.3389/fbioe.2021.743322/full#supplementary-material

REFERENCES

Aldewachi, H., Chalati, T., Woodroofe, M. N., Bricklebank, N., Sharrack, B., and Gardiner, P. (2017). Gold Nanoparticle-Based Colorimetric Biosensors. *Nanoscale* 10 (1), 18–33. doi:10.1039/c7nr06367a

Bertoletti, A., and Bert, N. L. (2018). Immunotherapy for Chronic Hepatitis B Virus Infection. *Gut. Liver.* 12 (5), 497–507. doi:10.5009/gnl17233

Broughton, J. P., Deng, X., Yu, G., Fasching, C. L., Servellita, V., Singh, J., et al. (2020). CRISPR-Cas12-based Detection of SARS-CoV-2. *Nat. Biotechnol.* 38 (7), 870–874. doi:10.1038/s41587-020-0513-4

Chen, J. S., Ma, E., Harrington, L. B., Da Costa, M., Tian, X., Palefsky, J. M., et al. (2018). CRISPR-Cas12a Target Binding Unleashes Indiscriminate Single-Stranded DNase Activity. *Science* 360 (6387), 436–439. doi:10.1126/science.aar6245

Gootenberg, J. S., Abudayyeh, O. O., Kellner, M. J., Joung, J., Collins, J. J., and Zhang, F. (2018). Multiplexed and Portable Nucleic Acid Detection Platform with Cas13, Cas12a, and Csm6. *Science* 360 (6387), 439–444. doi:10.1126/science.aaq0179

Gootenberg, J. S., Abudayyeh, O. O., Lee, J. W., Essletzbichler, P., Dy, A. J., Joung, J., et al. (2017). Nucleic Acid Detection with CRISPR-Cas13a/C2c2. *Science* 356 (6336), 438–442. doi:10.1126/science.aam9321

Huang, Y., Xu, T., Wang, W., Wen, Y., Li, K., Qian, L., et al. (2019). Lateral Flow Biosensors Based on the Use of Micro- and Nanomaterials: A Review on Recent Developments. *Microchim Acta.* 187 (1), 70. doi:10.1007/s00604-019-3822-x

Inoue, T., and Tanaka, Y. (2020). Cross-Protection of Hepatitis B Vaccination Among Different Genotypes. *Vaccines* 8 (3), 456. doi:10.3390/vaccines8030456

Irshad, M., Gupta, P., Mankotia, D. S., and Ansari, M. A. (2016). Multiplex qPCR for Serodetection and Serotyping of Hepatitis Viruses: A Brief Review. *Wjg* 22 (20), 4824. doi:10.3748/wjg.v22.i20.4824

Jiao, W.-W., Wang, Y., Wang, G.-R., Wang, Y.-C., Xiao, J., Sun, L., et al. (2019). Development and Clinical Validation of Multiple Cross Displacement Amplification Combined with Nanoparticles-Based Biosensor for Detection of mycobacterium Tuberculosis: Preliminary Results. *Front. Microbiol.* 10, 2135. doi:10.3389/fmicb.2019.02135

Kellner, M. J., Koob, J. G., Gootenberg, J. S., Abudayyeh, O. O., and Zhang, F. (2019). SHERLOCK: Nucleic Acid Detection with CRISPR Nucleases. *Nat. Protoc.* 14 (10), 2986–3012. doi:10.1038/s41596-019-0210-2

Li, L., Li, S., Wu, N., Wu, J., Wang, G., Zhao, G., et al. (2019). HOLMESv2: A CRISPR-Cas12b-Assisted Platform for Nucleic Acid Detection and DNA Methylation Quantitation. *ACS Synth. Biol.* 8 (10), 2228–2237. doi:10.1021/acssynbio.9b00209

Li, S., Jiang, W., Huang, J., Liu, Y., Ren, L., Zhuang, L., et al. (2020). Highly Sensitive and Specific Diagnosis of COVID-19 by Reverse Transcription Multiple Cross-Displacement Amplification-Labelled Nanoparticles Biosensor. *Eur. Respir. J.* 56 (6), 2002060. doi:10.1183/13993003.02060-2020

Liang, M., Li, Z., Wang, W., Liu, J., Liu, L., Zhu, G., et al. (2019). A CRISPR-Cas12a-Derived Biosensing Platform for the Highly Sensitive Detection of Diverse Small Molecules. *Nat. Commun.* 10 (1), 3672. doi:10.1038/s41467-019-11648-1

Lin, C.-L., and Kao, J.-H. (2011). The Clinical Implications of Hepatitis B Virus Genotype: Recent Advances. *J. Gastroen. Hepatol.* 26, 123–130. doi:10.1111/j.1440-1746.2010.06541.x

Meng, Z., Chen, Y., and Lu, M. (2020). Advances in Targeting the Innate and Adaptive Immune Systems to Cure Chronic Hepatitis B Virus Infection. *Front. Immunol.* 10, 3127. doi:10.3389/fimmu.2019.03127

Mukama, O., Wu, J., Li, Z., Liang, Q., Yi, Z., Lu, X., et al. (2020). An Ultrasensitive and Specific point-of-care CRISPR/Cas12 Based Lateral Flow Biosensor for the Rapid Detection of Nucleic Acids. *Biosens. Bioelectron.* 159, 112143. doi:10.1016/j.bios.2020.112143

Myhrvold, C., Freije, C. A., Gootenberg, J. S., Abudayyeh, O. O., Metsky, H. C., Durbin, A. F., et al. (2018). Field-deployable Viral Diagnostics Using CRISPR-Cas13. *Science* 360 (6387), 444–448. doi:10.1126/science.aas8836

Nelson, N. P., Easterbrook, P. J., and McMahon, B. J. (2016). Epidemiology of Hepatitis B Virus Infection and Impact of Vaccination on Disease. *Clin. Liver Dis.* 20 (4), 607–628. doi:10.1016/j.cld.2016.06.006

Nguyen, M. H., Wong, G., Gane, E., Kao, J.-H., and Dusheiko, G. (2020). Hepatitis B Virus: Advances in Prevention, Diagnosis, and Therapy. *Clin. Microbiol. Rev.* 33 (2), e00046-19. doi:10.1128/CMR.00046-19

Pickar-Oliver, A., and Gersbach, C. A. (2019). The Next Generation of CRISPR-Cas Technologies and Applications. *Nat. Rev. Mol. Cell Biol.* 20 (8), 490–507. doi:10.1038/s41580-019-0131-5

Pisaturo, M., Macera, M., Alessio, L., Calò, F., and Coppola, N. (2019). Hepatitis B Virus (HBV) Reactivation Following Pharmacological Eradication of Hepatitis C Virus (HCV). *Viruses* 11 (9), 850. doi:10.3390/v11090850

Quesada-González, D., and Merkoçi, A. (2015). Nanoparticle-based Lateral Flow Biosensors. *Biosens. Bioelectron.* 73, 47–63. doi:10.1016/j.bios.2015.05.050

Shiriaeva, A., Fedorov, I., Vyhovskyi, D., and Severinov, K. (2020). Detection of CRISPR Adaptation. *Biochem. Soc. T.* 48 (1), 257–269. doi:10.1042/BST20190662

Su, Q.-d., Zhang, S., Wang, F., Liu, H., Zhang, G.-m., Zheng, H., et al. (2020). Epidemiological Distribution of Hepatitis B Virus Genotypes in 1-29-Year-Olds in the mainland of China. *Vaccine* 38 (51), 8238–8246. doi:10.1016/j.vaccine.2020.09.083

Wang, W., Shu, Y., Bao, H., Zhao, W., Wang, W., Wang, Q., et al. (2019). Genotypes and Hot Spot Mutations of Hepatitis B Virus in Northwest Chinese Population and its Correlation with Diseases Progression. *Biomed. Res. Int.* 2019, 1–9. doi:10.1155/2019/3890962

Wang, Y., Li, H., Wang, Y., Li, H., Luo, L., Xu, J., et al. (2017). Development of Multiple Cross Displacement Amplification Label-Based Gold Nanoparticles Lateral Flow Biosensor for Detection of *Listeria Monocytogenes*. *Ijn* 12, 473–486. doi:10.2147/IJN.S123625

Wang, Y., Shan, X., Liang, Z., Shan, Y., Huang, W., Zhang, D., et al. (2015a). Deep Sequencing Analysis of HBV Genotype Shift and Correlation with Antiviral Efficiency during Adefovir Dipivoxil Therapy. *PLoS One* 10 (6), e0131337. doi:10.1371/journal.pone.0131337

Wang, Y., Wang, Y., Ma, A.-J., Li, D.-X., Luo, L.-J., Liu, D.-X., et al. (2015b). Rapid and Sensitive Isothermal Detection of Nucleic-Acid Sequence by Multiple Cross Displacement Amplification. *Sci. Rep.* 5, 11902. doi:10.1038/srep11902

World Health Organization (2017). Global Hepatitis Report 2017. (Geneva, Switzerland: World Health Organization). Available at: http://apps.who.int/iris/bitstream/handle/10665/255016/9789241565455-eng.pdf?sequence=1.

Yao, R., Liu, D., Jia, X., Zheng, Y., Liu, W., and Xiao, Y. (2018). CRISPR-Cas9/Cas12a Biotechnology and Application in Bacteria. *Synth. Syst. Biotechnol.* 3 (3), 135–149. doi:10.1016/j.synbio.2018.09.004

Zeng, A.-Z., Deng, H., Yang, C., Xin, X.-J., Li, Q.-L., Guo, J.-J., et al. (2008). Hepatitis B Virus Genotype-Associated Variability in Antiviral Response to Adefovir Dipivoxil Therapy in Chinese Han Population. *Tohoku J. Exp. Med.* 216 (3), 205–211. doi:10.1620/tjem.216.205

Zhao, Y., Zhang, X.-Y., Guo, J.-J., Zeng, A.-Z., Hu, J.-L., Huang, W.-X., et al. (2010). Simultaneous Genotyping and Quantification of Hepatitis B Virus for Genotypes B and C by Real-Time PCR Assay. *J. Clin. Microbiol.* 48 (10), 3690–3697. doi:10.1128/JCM.00741-10

Zhao, Y., Zhang, X.-Y., Hu, Y., Zhang, W.-L., Hu, J.-L., Zeng, A.-Z., et al. (2011). Comparison of a Novel Real-Time PCR Assay with Sequence Analysis, Reverse Hybridization, and Multiplex PCR for Hepatitis B Virus Type B and C Genotyping. *J. Clin. Microbiol.* 49 (9), 3392–3394. doi:10.1128/JCM.00543-11

Zhou, L., Peng, R., Zhang, R., and Li, J. (2018). The Applications of CRISPR/Cas System in Molecular Detection. *J. Cell. Mol. Med.* 22 (12), 5807–5815. doi:10.1111/jcmm.13925

Zhu, X., Wang, X., Li, S., Luo, W., Zhang, X., Wang, C., et al. (2021). Rapid, Ultrasensitive, and Highly Specific Diagnosis of COVID-19 by CRISPR-Based Detection. *ACS Sens.* 6 (3), 881–888. doi:10.1021/acssensors.0c01984

Conflict of Interest: The authors declare that the research was conducted in the absence of any commercial or financial relationships that could be construed as a potential conflict of interest.

Publisher's Note: All claims expressed in this article are solely those of the authors and do not necessarily represent those of their affiliated organizations, or those of the publisher, the editors, and the reviewers. Any product that may be evaluated in this article, or claim that may be made by its manufacturer, is not guaranteed or endorsed by the publisher.

frontiers in Bioengineering and Biotechnology

METHODS
published: 22 October 2021
doi: 10.3389/fbioe.2021.748746

A Novel Real-Time Reverse Transcription Loop-Mediated Isothermal Amplification Detection Platform: Application to Diagnosis of COVID-19

Yi Wang[1]†, Xiaoxia Wang[2†], Hai Chen[2], Limei Han[2], Licheng Wang[2], Ting Chen[2], Sha Li[2], Huan Li[2], Yuanli Li[2], Zhengkun Li[2], Xiaoying Fu[2], Shaojin Chen[2], Mei Xing[3], Jun Tai[4]* and Xiong Zhu[2]**

[1]Experimental Research Center, Capital Institute of Pediatrics, Beijing, China, [2]Central and Clinical Laboratory of Sanya People's Hospital, Sanya, China, [3]Wenchang People's Hospital, Wenchang, China, [4]Department of Otolaryngology, Head and Neck Surgery, Children's Hospital Capital Institute of Pediatrics, Beijing, China

The ongoing Corona virus disease (COVID-19) outbreak has become a huge global health concern. Here, we reported a novel detection platform based on the loop-mediated isothermal amplification (LAMP), termed real-time reverse transcription LAMP (rRT-LAMP) and applied it for the diagnosis of COVID-19 (COVID-19 rRT-LAMP). rRT-LAMP integrates reverse transcription, LAMP amplification, restriction endonuclease cleavage and real-time fluorescence detection into one-pot reaction, and facilitates the diagnosis of COVID-19 at 64°C for only 35 min. The ORF1ab (opening reading frame 1a/b) and NP (nucleoprotein) genes of SARS-CoV-2 were detected for diagnosing COVID-19. The limit of detection (LoD) of COVID-19 rRT-LAMP assay was 14 copies (for each marker) per vessel, and no positive results were obtained from non-SARS-CoV-2 templates. To demonstrate its feasibility, a total of 33 oropharynx swab samples collected from COVID-19 patients also were diagnosed as SARS-CoV-2 infection using COVID-19 rRT-LAMP protocol. No cross-reactivity was yielded from 41 oropharynx swab samples collected from non-COVID-19 patients. These data suggesting that the COVID-19 rRT-LAMP assay is a potential detection tool for the diagnosis of SARS-CoV-2 infection in clinical, field and disease control laboratories, and will be valuable for controlling the COVID-19 epidemic.

Keywords: COVID-19, SARS-CoV-2, rRT-LAMP, reverse transcription, loop-mediated isothermal amplification

OPEN ACCESS

Edited by:
Tailin Xu,
Shenzhen University, China

Reviewed by:
Mengyun Zhou,
Shenzhen University, China
Yang Liu,
Beijing Genomics Institute (BGI), China

***Correspondence:**
Yi Wang
wildwolf0101@163.com
Jun Tai
trenttj@163.com
Xiong Zhu
zhuxiong6@163.com

†These authors have contributed equally to this work

Specialty section:
This article was submitted to Biosensors and Biomolecular Electronics, a section of the journal Frontiers in Bioengineering and Biotechnology

Received: *28 July 2021*
Accepted: *11 October 2021*
Published: *22 October 2021*

Citation:
Wang Y, Wang X, Chen H, Han L, Wang L, Chen T, Li S, Li H, Li Y, Li Z, Fu X, Chen S, Xing M, Tai J and Zhu X (2021) A Novel Real-Time Reverse Transcription Loop-Mediated Isothermal Amplification Detection Platform: Application to Diagnosis of COVID-19. Front. Bioeng. Biotechnol. 9:748746. doi: 10.3389/fbioe.2021.748746

INTRODUCTION

The ongoing COVID-19 (Corona virus disease) epidemic caused by SARS-CoV-2 (severe acute respiratory syndrome coronavirus 2) that had previously not been documented in animals or humans, has become a major global public health concern (Huang et al., 2020). SARS-CoV-2 infection has spread rapidly to more than 200 countries/regions overseas (World Health Organization, COVID-19 Situation Report). Given the rapid spread speed (R_0 3.28) and mortality rate (2.3%) of SARS-CoV-2 infection, the valuable diagnostic tools are urgently required for rapidly screening suspected cases, accurately diagnosing COVID-19 and performing epidemiological surveillance.

The detection of SARS-CoV-2 RNA has been approved to be useful for the diagnosis of COVID-19, which was beneficial to preventing the spreading, controlling the sources of infection and helping patients to prevent the disease progression (Li et al., 2020; Shen et al., 2020). The spectrum of the available molecular methods for diagnosis of COVID-19 is very tight because SARS-CoV-2 is a newly emerged human coronavirus (Wu et al., 2020a). At the early stage of COVID-19 epidemic, the next-generation sequencing was employed for detecting SARS-CoV-2 RNA in various clinical specimens, while it was not available in field and clinic settings due to its longer sequencing time and high needs for equipment (Wu et al., 2020b; Zhu et al., 2021). Polymerase chain reaction (PCR)-based methodologies, including real-time PCR (RT-PCR) and real-time reverse transcription PCR (rRT-PCR) are characterized by rapid detection, high specificity and sensitivity, which have been employed for diagnosis of COVID-19 (Carter et al., 2020). However, PCR-based assays strongly rely on expensive laboratory apparatus and experienced laboratory workers, and also are time-consuming (Li et al., 2020). Unfortunately, a relatively high proportion (approximately 30%) of COVID-19 patients that were further diagnosed by chest CT were diagnosed as false negative results using the commercial COVID-19 rRT-PCR kits (To et al., 2020; Wu and McGoogan, 2020). Herein, further development of simpler, more rapid and sensitive detection tools to diagnose COVID-19 are still needed.

LAMP (Loop-mediated isothermal amplification) is the most commonly applied isothermal amplification method, and has been regarded as an attractive alternative to PCR-based methodologies due to its speed, simplicity, specificity, sensitivity and cost-effectiveness (Obande and Banga Singh, 2020). As LAMP amplification is conducted at a fixed temperature (usually between 60°C to 67°C), thus an extremely simple instrument (e.g., a water bath) is sufficient for LAMP-based assays, eliminating the use of an expensive thermal cycler. By the use of reverse transcriptase together with *Bst* 2.0 polymerase, LAMP method has been proved for amplifying and detecting RNA sequences at an isothermal step, and the reverse transcription LAMP (RT-LAMP) assay has been applied for detecting a variety of RNA viruses (Obande and Banga Singh, 2020; Shen et al., 2020). Thus, RT-LAMP assay has the potential to be a simple, rapid and reliable method for the laboratory detection of the emergence of SARS-CoV-2.

Up to now, several RT-LAMP-based methods have been developed for the diagnosis of COVID-19 (Yu et al., 2020; Zhu et al., 2020; El-Tholoth et al., 2021). However, traditional monitoring techniques (such as PH reagents, SYBR Green dyes and agarose gel electrophoresis) were employed for reporting the COVID-19 RT-LAMP results. Reporting the COVID-19 RT-LAMP results using PH reagents or SYBR Green dyes may be ambiguous when the concentration of SARS-CoV-2 RNA is lower in a clinical sample, because it is difficult to indicate weakly positive results by color change. Electrophoresis is a tedious, time-consuming procedure, and carries the huge risk of carryover contamination. Particularly, only a genetic molecule (e.g., ORF1ab) of SARS-CoV-2 was employed for establishing the COVID-19 RT-LAMP assays, and the analytical sensitivity, especially for clinical samples, may not be outstanding when compared with these LAMP-based assays using at least two genetic molecules. Herein, the novel RT-LAMP-based methods, which can overcome these shortcomings posed by the developed COVID-19 RT-LAMP assays, are in pressing demand.

Here, we reported a novel mode of RT-LAMP, termed real-time reverse transcription LAMP (rRT-LAMP), which was employed for diagnosing COVID-19 (COVID-19 rRT-LAMP). COVID-19 rRT-LAMP facilitated rapid detection of ORF1ab (opening reading frame 1a/b) and NP (nucleoprotein) genes of SARS-CoV-2 at a one-step, single-tube reaction within 35 min. This report expounds the basic rRT-LAMP principle, and validates its application for the diagnosis of COVID-19.

MATERIALS AND METHODS

Primer Design

According to the rRT-LAMP principle, two LAMP primer sets (**Figure 1**), which targeted the ORF1ab and NP genes of SARS-CoV-2 (GenBank MN908947, Wuhan-Hu-1), were designed using PrimerExplorer V5 software (http://primerexplorer.jp/e). Each LAMP primer set, which recognizes eight different regions to amplify each gene marker, consisted of forward outer primer (F3), backward outer primer (B3), forward inner primer (FIP), back inner primer (BIP), forward loop primer (LF), and backward loop primer (LB). The specificity of the two LAMP primer sets was examined by NCBI (National Center for Biotechnology Information) BLAST, and OligoAnalyzer online software (Version 3.1, Integrated DNA Technologies, Coralville, IA) was employed for secondary structure and primer dimer analysis. Details of ORF1ab- and NP-LAMP primer sets, including sequences, locations and modifications, were listed in **Supplementary Table S1**; **Figure 1**. All of the oligomers were synthesized by Tianyi-Huiyuan Biotech. Co., Ltd. (Beijing, China), and purified at HPLC grade.

rRT-LAMP Reaction

The rRT-LAMP (ORF1ab- and NP-rRT-LAMP) was carried out in a one-step 25 μL reaction mixture containing 12.5 μL 2 × isothermal reaction buffer (Huidexin Biotechnology. Co., Ltd. Tianjin, China) [40 mM Tris-HCl (pH 8.8), 40 mM KCl, 16 mM $MgSO_4$, 20 mM $(NH_4)_2SO_4$, 2 M betaine and 0.2 % Tween-20], 8 U of Bst 2.0 DNA polymerase, 5 U of avian myeloblastosis virus reverse transcriptase V3.0 (AMV, Takara), 1 U Nb. BsrDI (New England Biolabs), 1.4 mM dATP, 1.4 mM dCTP, 1.4 mM dGTP, 1.4 mM dTTP, 0.4 μM each of F3 and B3, 0.8 μM each of LF* and LB, 1.6 μM each of FIP and BIP, and template (1 μL for the standard plasmid/5 μL for clinical samples). Real-time fluorescence, real-time turbidity (LA-320C) and agarose gel electrophoresis were employed for reporting the rRT-LAMP reactions and for optimizing the amplification parameters (e.g. assay's temperature and time).

Sensitivity of the rRT-LAMP Assay

Two standard plasmids (named as ORF1ab-plasmid and NP-plasmid) were commercially constructed by Tianyi-Huiyuan

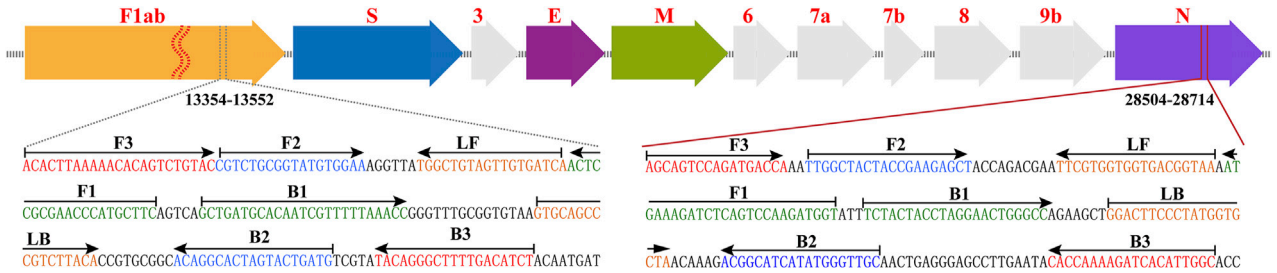

FIGURE 1 | Primer design of COVID-19 rRT-LAMP method. Up row, SARS-CoV-2 genome organization (GenBank: MN908947, Wuhan-Hu-1). Bottom row, nucleotide sequence and location of ORF1ab and np gene used to design COVID-19 rRT-LAMP primers. Only part of the nucleotide sequences of ORF1ab (Left) and NP (Right) are showed. Left arrows and Right arrows show the complementary and sense sequences that are designed. The sites of primer sequence are underlined. * Note [1]: The length of all genes is not displayed in scale (Up row). * Note [2]: ORF1ab (Open reading frame 1a/b); S (Spike protein); E (Envelope protein); M (Membrane protein); NP (Nucleoprotein); Accessory proteins (3, 6, 7a, 7b, and 9b).

TABLE 1 | Detection results of COVID-19 rRT-LAMP for pharyngeal swab samples.

Sample number	Gender	Age	Judgment result of RT-PCR I	Result of RT-PCR I		Judgment result of RT-PCR II	Result of RT-PCR II		Judgment result of rRT-LAMP	Result of rRT-LAMP		Clinical diagnosis[a]
				ORF1ab	NP		ORF1ab	NP		ORF1ab	NP	
S1	F	36	Positive	+	+	Positive	+	+	Positive	+	+	+
S2	F	56	Positive	+	+	Positive	+	+	Positive	+	+	+
S3	M	26	Positive	+	+	Positive	+	+	Positive	+	+	+
S4	M	25	Positive	+	+	Positive	+	+	Positive	+	+	+
S5	M	62	Positive	+	—	Positive	+	—	Positive	+	—	+
S6	F	65	Positive	—	+	Positive	—	+	Positive	—	+	+
S7	F	65	Positive	+	+	Positive	+	+	Positive	+	+	+
S8	M	73	Positive	+	+	Positive	+	+	Positive	+	+	+
S9	M	71	Positive	+	+	Positive	+	+	Positive	+	+	+
S10	F	31	Positive	+	+	Positive	+	+	Positive	+	+	+
S11	M	71	Positive	+	+	Positive	+	+	Positive	+	+	+
S12	M	62	Positive	+	+	Positive	+	+	Positive	+	+	+
S13	F	76	Positive	+	+	Positive	+	+	Positive	+	+	+
S14	M	39	Positive	+	+	Positive	+	+	Positive	+	+	+
S15	M	41	Positive	+	—	Positive	+	—	Positive	+	—	+
S16	F	65	Positive	+	+	Positive	+	+	Positive	+	+	+
S17	M	62	Positive	+	+	Positive	+	+	Positive	+	+	+
S18	F	38	Positive	+	+	Positive	+	+	Positive	+	+	+
S19	M	39	Positive	+	+	Positive	+	+	Positive	+	+	+
S20	M	73	Positive	+	+	Positive	+	+	Positive	+	—	+
S21	F	56	Positive	+	+	Positive	+	+	Positive	+	+	+
S22	M	71	Positive	+	+	Positive	+	+	Positive	+	+	+
S23	F	38	Negative	—	+	Positive	—	+	Positive	—	+	+
S24	F	46	Negative	—	+	Positive	+	+	Positive	—	+	+
S25	F	37	Positive	+	+	Positive	+	+	Positive	+	+	+
S26	M	73	Positive	+	+	Positive	+	+	Positive	+	+	+
S27	M	31	Negative	—	—	Positive	—	+	Positive	—	+	+
S28	F	42	Positive	+	+	Positive	+	+	Positive	+	+	+
S29	M	65	Positive	—	+	Positive	—	+	Positive	+	+	+
S30	F	36	Positive	+	+	Positive	+	+	Positive	+	+	+
S31	M	68	Positive	—	—	Positive	—	+	Positive	—	+	+
S32	M	37	Positive	—	+	Positive	—	+	Positive	—	+	+
S33	F	56	Positive	+	—	Positive	+	+	Positive	+	—	+

[a]*The "+" represent the patient of COVID-19.*

Biotech. Co., Ltd. (Beijing, China), which contain the ORF1ab and NP sequences, respectively. The initial concentrations of ORF1ab- and NP-plasmids were 1.4×10^8 copies/μl, then ten-fold serial dilutions (1.4×10^5 to 1.4×10^{-1} copies) of ORF1ab-plasmid and NP-plasmid were prepared. The serial dilutions of ORF1ab-plasmid and NP-plasmid were used for defining the limit of detection (LoD) of COVID-19 rRT-LAMP, and a volume of 1 μL of these templates were used for COVID-19 rRT-LAMP reactions.

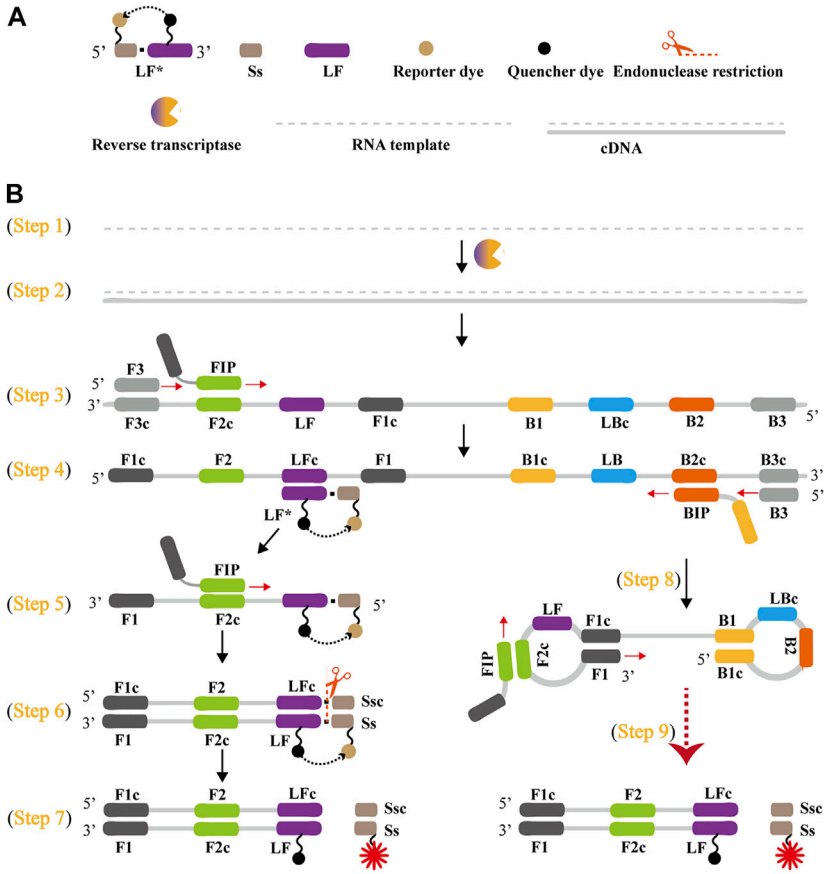

FIGURE 2 | Outline of rRT-LAMP assay. **(A)** Schematic depiction of a new forward loop primer (LF*)/backward loop primer (LB*). LF*/LB* is an extension of the conventional LF/LB with an endonuclease recognition site (Ss, its complementary sequence named Ssc) at the 5′ end. LF*/LB* is modified with a reporter at the 5′-end, and is labeled with quencher dye in the middle. **(B)**, Outline of rRT-LAMP technology. Six primers, including forward displacement primer (F3), backward displacement primer (B3), forward inner primer (FIP), backward inner primer (BIP), LB and new LF*, are displayed for illustrating the rRT-LAMP principle. .

Specificity of the COVID-19 rRT-LAMP Assay

The specificity of the COVID-19 rRT-LAMP assay was evaluated using various templates, including synthetic nucleic acid sequences, viruses, bacteria and fungi (**Supplementary Table S2**).

Feasibility of COVID-19 rRT-LAMP Using Clinical Samples

A total of 33 respiratory samples (pharyngeal/nasal swabs), which were collected from 33 COVID-19 patients (Sanya People's Hospital, Hainan) (**Table 1**), were defined according to standard diagnostic and treatment criteria of COVID-19 (Trial Version 6). The pharyngeal and nasal swab samples were collected using a Flocked sterile plastic swab applicator, which was placed in a Universal Viral Transport Medium (UVIM) for viruses (HiDNA biotech. Co., Ltd.). Particularly, aliquots (200 μL) of UVIM (pharyngeal and nasal swab samples) were subjected to extract the RNA templates, and the process only required 15 min using a rapid RNA Extraction Kit (Daan Nucleic Acid Isolation Kit, Daanene Co. LtD.) with an automatic instrument (Smart 32, Daanene Co. LtD.). These templates were firstly used for clinical and laboratory diagnosis, which was performed using two RT-qPCR kits (Daangene Co. LtD. and BGI Co. LtD.) as recommended by the China CDC and Hainan CDC. Then, a volume of 5 μL of templates was used as the input template for COVID-19 rRT-LAMP test.

Collection and analysis of these RNA templates were approved by Sanya People's Hospital (Ethical approval: SYPH-2019[41]-2020-03-06).

RESULTS

Rational Design of rRT-LAMP Design

The schematic reaction mechanism of rRT-LAMP is exhibited in **Figure 2**. The rRT-LAMP system integrates reverse transcription, isothermal amplification, restriction endonuclease digestion and real-time fluorescence detection into a one-pot reaction mixture. In particular, a loop primer (LF or LB) is modified with short sequence (named as Ss) at the 5′ end, and the new LF or LB is named as LF* or LB*. The Ss can be recognized by NB. *bsrDI*

enzyme. Then, LF* or LB* is labeled at 5′ end with a reporter dye and in the middle with a corresponding dark quencher (**Figure 2A**). The reporter molecule and quenching dye are very close to each other, thus this successfully prevents the emitted fluorescence of the reporter dye.

A Nb. *BsrDI* enzyme is employed for achieving the rRT-LAMP reaction, because it is able to specially recognize the short sequence (Ss) 5′-GCAATGNN-3' (N = A, G, C and T) and cleavages Ss 5′-GCAATG-3′ at a constant temperature (60°C-65 °C). Thus, Ss (5′-GCAATG-3′) is added to the 5′ end to construct LF* or LB*, and an additional base (T) also is added to the 5′ end of Ss to protect the recognition site. As a result, the LF* or LB* primer maintains its function as a loop primer with the added advantage of simultaneous detection of the rRT-LAMP reactions by release of quenching (**Figure 2B**).

The outline of rRT-LAMP assay with LF* or LB* is depicted in **Figure 2B**. For clarity, the LB* primer is not displayed. In the rRT-LAMP system, a total of six primers, including F3, B3, FIP, BIP, LF* and LB, was used. The RNA templates were firstly converted to cDNA with the assistance of reverse transcriptase (e.g., avian myeloblastosis virus reverse transcriptase, AMV), and then the cDNA serves as the initial template for subsequent LAMP reaction (**Figure 2B,** step 1 and 2). During the LAMP amplification stage, FIP hybridized to F2c in the target sequence and initiated complementary strand synthesis (**Figure 2B**, step 3). The primer F3 then hybridizes to F3c in the target sequence, which initiates strand displacement synthesis (**Figure 2B**, step 3). Thus, the newly synthesized strand derived from FIP primer is displaced by the F3 primer synthesis, producing a single strand (**Figure 2B**, Step 3). This single-stranded DNA serves as templates for subsequent LF*-primed strand displacement DNA synthesis, BIP-initiated DNA synthesis and B3-primed strand displacement synthesis (**Figure 2B**, Step 4). As a result, the strand displacement polymerase (*Bst 2.0*) extends in tandem generating two different products. In particular, the LF* strand acts as the template for subsequent extension by FIP (**Figure 2B**, Step 5), and the new double-stranded terminal sequence (Ss and its complementary Ssc sequences) are cleaved by NB. *bsrDI* enzyme (**Figure 2B**, Step 6), resulting a gain of fluorescence signal (**Figure 2B**, Step 7). Furthermore, the BIP strand (from Step 4) forms a dumbbell-shaped product, which is rapidly converted to a stem-loop form by self-primed synthesis. This stem-loop form then serves as the starting templates for subsequent amplification cycling, the second stage of the LAMP amplification (elongation and cycling steps) (**Figure 2**, step 8). The subsequent exponential amplification also releases the quenching, which gives rise to additional release of fluorophores, resulting in exponential signal detection.

Rational Design of COVID-19 rRT-LAMP Design

The COVID-19 rRT-LAMP design scheme is depicted in **Figure 3**. In the COVID-19 rRT-LAMP system, one reported dye, FAM (6-carboxy-fluorescein) is modified at the 5′ end of ORF1ab-LF* primer (**Figure 3A**), another, HEX (Hexachloro-fluorescein) is labeled to the 5′ end of NP-LF* primer (**Figure 3B**). To emit fluorescence of the reporter molecule, the quenching dye (Black Hole Quencher-1, BHQ1) is modified in the middle of the ORF1ab-LF* and NP-LF* primers. Thus, the ORF1ab-LF* is labeled simultaneously with FAM and BHQ1, NP-LF* for HEX and BHQ1 (**Figure 3**, Step 1). The SARS-CoV-2 RNA firstly is converted to cDNA with the assistance of reverse transcriptase AMV, and then serves as the initial template for subsequent LAMP amplification (**Figure 3**, Step 2). During the LAMP amplification stage, the terminals of double-stranded products derived from ORF1ab-LF* and NP-LF* primers can be digested by the NB. *bsrDI* enzyme, thus the reporter dyes (FAM and HEX) are separated from the quenching dye (BHQ1) leading to the gain of fluorescent signals (Green and Yellow signals) (**Figure 3**, Step 3). The fluorescent signals released from COVID-19 rRT-LAMP reactions can be detected by a real-time system (e.g., Genie III).

Validation of ORF1ab- and NP-RT-LAMP Amplifications

To confirm the correct amplification of rRT-LAMP assay, we performed the ORF1ab- and NP-rRT-LAMP reactions in the presence or absence of plasmid templates. Using real-time detection, the release of quenching was obtained as a robust increase of FAM (Green channel) and HEX (Yellow channel) signals in the positive results, but not in negative and blank controls (**Supplementary Figures S1A,C**, Left row). Then, the rRT-LAMP products were electrophoresed to verify the presence of the expected ladder bands (**Supplementary Figures S1B,D**, Right row). Hence, each set of rRT-LAMP primers designed in this study could amplify the predicted product specifically from the templates of the corresponding plasmids. These results suggested that the rRT-LAMP method using ORF1ab- and NP-LAMP primer sets could be applied for the detection of SARS-CoV-2. Furthermore, the optimal reaction temperature for COVID-19 rRT-LAMP was also confirmed with 64 °C shown to be the best for COVID-19 rRT-LAMP reaction (**Supplementary Figures S2, S3**).

Analytical Sensitivity of COVID-19 rRT-LAMP Assay

Then, we tested the rRT-LAMP's sensitivity. rRT-LAMP amplified ORF1ab and NP genes with pure templates from ORF1ab-plasmid and NP-plasmid, respectively. The fluorescent intensity-reaction time curves synchronized well among two replicates containing same dilution of target plasmids. The release of quenching was generated from 1.4×10^5 copies to 1.4×10^1 copies of plasmid templates, and the FAM and HEX signals corresponded to ORF1ab and NP detection, respectively (**Figures 4A,B**). Thus, the analytical sensitivity of rRT-LAMP for ORF1ab and NP detection was 1.4×10^1 copies per reaction.

Particularly, the positive results can be observer in as short as 10 min (**Figure 4**), and only 35 min are required for COVID-19 rRT-LAMP test. Thus, the whole diagnostic test, including sample collection (3 min), rapid SARS-CoV-2 RNA extraction

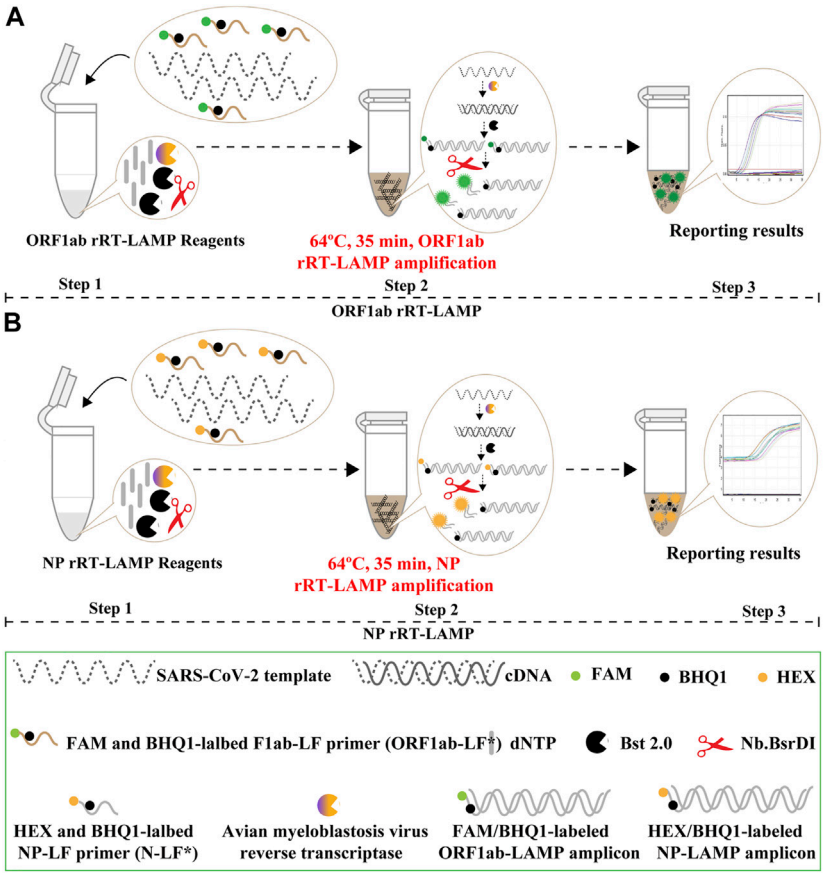

FIGURE 3 | Mechanistic description of the COVID-19 rRT-LAMP assay. **(A)**. rRT-LAMP for ORF1ab detection. **(B)**. rRT-LAMP assay for NP detection. Step 1, Preparing the COVID-19 rRT-LAMP amplification mixtures. Step 2, COVID-19 rRT-LAMP reaction. Step 3, The result interpretation of the COVID-19 rRT-LAMP reaction.

(15 min), rRT-LAMP reaction and results reporting (35 min), can be finished within 55 min (**Figure 5**).

Specificity of the COVID-19 rRT-LAMP Technology

The specificity of COVID-19 rRT-LAMP assay was tested in relation to data with nucleic acids from synthetic nucleic acid sequences, viruses, bacteria and fungi templates (**Supplementary Table S2**). The positive fluorescence signals were obtained only when nucleic acids of ORF1ab-plasmid and NP-plasmid were applied as the templates for COVID-19 rRT-LAMP analysis, and the target sequences could be by correctly identified (**Figure 6**). As expected, no positive signals were observed with any of the nucleic acids from non-ORF1ab-plasmid and non-NP-plasmid templates. These results indicated that the specificity of COVID-19 rRT-LAMP methodology was 100% in this study.

Evaluation of the COVID-19 rRT-LAMP Methodology in

A total of 74 clinical samples, which were initially diagnosed using rRT-RCR assays, were collected in Sanya People's Hospital in 2020. Particularly, 33 were COVID-19 positive samples, and 41 samples were diagnosed with pneumonia and confirmed to be caused by non-SARS-CoV-2 pathogens (e.g., *Mycoplasma pneumoniae*, *Pseudomonas aerugiosa*, *Klebsiella pneumoniae*, infuenza virus A and B etc.). The templates were leftover RNA extracted from 74 clinical samples after rRT-PCR analysis. Using COVID-19 rRT-LAMP assay, 33 COVID-19 samples also were diagnosed as SARS-CoV-2 infection (**Table 1**), and no positive results were obtained from 41 COVID-19 negative samples. These data preliminarily demonstrated that the COVID-19 rRT-LAMP methodology had a highly analytical sensitivity and specificity for the diagnosis of COVID-19.

DISCUSSION

The ongoing outbreak of COVID-19 poses a huge global public health concern (Heymann and Shindo, 2020; Hui et al., 2020). Due to the lack of effective antiviral drugs or vaccines for COVID-19, rapid, reliable and early diagnostic technologies for SARS-CoV-2 is of top priority for achieving public health interventions that can decrease or prevent further spread of COVID-19 (Wu et al., 2020c). Importantly, such diagnostic

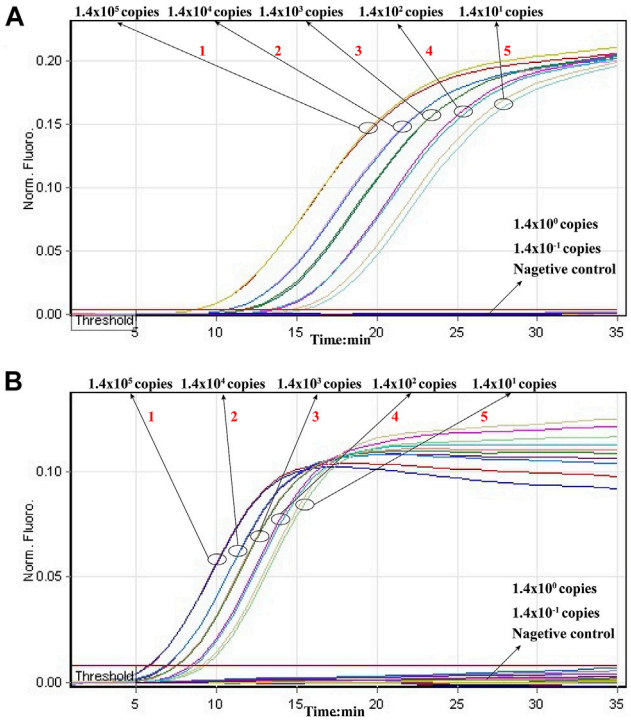

FIGURE 4 | Sensitivity of rRT-LAMP assay. Two sets of rRT-LAMP primer targeting ORF1ab and NP genes were in different reactions: ORF1ab [**(A)**, FAM channel] and NP [**(B)**, Hex channel]. The template levels from 1.4×10^5 copies to 1.4×10^1 copies per tube generated the positive signals, 1.4×10^0 copies and 1.4×10^{-1} copies per reaction and negative control generated negative signal.

tests are needed not only in regions/countries where COVD-19 is already spreading but also in regions/countries where COVID-19 has not yet occurred.

To achieve more such effective diagnostic technologies, we successfully devised a novel LAMP-based assay that offers simple, rapid and reliable diagnosis for SARS-CoV-2 infection. COVID-19 rRT-LAMP simultaneously integrates reverse transcription, LAMP amplification, restriction endonuclease cleavage and real-time fluorescence detection into one-pot reaction, and achieves the detection of SARS-CoV-2 RNA at a constant temperature. Our diagnostic test only requires a relatively simple fluorescent instrument (e.g., Genie III) to maintain a fixed temperature (64°C) for 35 min. Comparing with these COVID-19 RT-LAMP techniques developed by previous reports, the rRT-LAMP results were detected by real-time fluorescence analysis, which eliminates the requirements of special reagents (e.g., pH indicators), complex processes (e.g., electrophoresis) and expensive instruments (e.g., real-time turbidity) (Lamb et al., 2020; Yu et al., 2020). The whole detection procedure can be finished within 55 min including sample collection (3 min), rapid SARS-CoV-2 RNA preparation (15 min), rRT-LAMP amplification and result interpretation (35 min). Regarding these traits, the COVID-19 rRT-LAMP methodology is a technically simple, rapid and economical technique, which provides practical solutions for clinical, field and disease control laboratories, especially in low-resource settings.

Two sets of rRT-LAMP primer, including ORF1ab-rRT-LAMP and NP-rRT-LAMP primer sets, were specifically designed according to the rRT-LAMP principle. The primer sets of ORF1ab- and NP-rRT-LAMP contain six primers (ORF1ab/NP-F3, ORF1ab/NP-B3, ORF1ab/NP-FIP and ORF1ab/NP-BIP), which recognize eight regions within the ORF1ab and NP genes, respectively (**Figure 1**). Thus, rRT-LAMP primer sets ensure that our COVID-19 rRT-LAMP has high selectivity for target sequence detection. The data produced from specificity tests suggested that all positive results were obtained from positive control and SARS-CoV-2 RNA templates (**Figure 6**; **Table 1**), and all negative results were yielded from non-SARS-CoV-2 templates. Hence, our technology could effectively prevent any false-positive or false-negative results from current SARS-CoV-2 RT-LAMP methods that only amplify a single genetic target (e.g., ORF1ab gene) (Lamb et al., 2020; Yu et al., 2020).

The analytical sensitivity of COVID-19 rRT-LAMP methodology also is sufficient for the detection of SARS-CoV-2. Our data revealed that COVID-19 rRT-LAMP assay was able to detect down to 14 copies each of the targets (ORF1ab- and np-plasmids) (**Figure 4**). Particularly, we did not compare the sensitivity result yielded from commercial rRT-PCR kits with COVID-19 rRT-LAMP

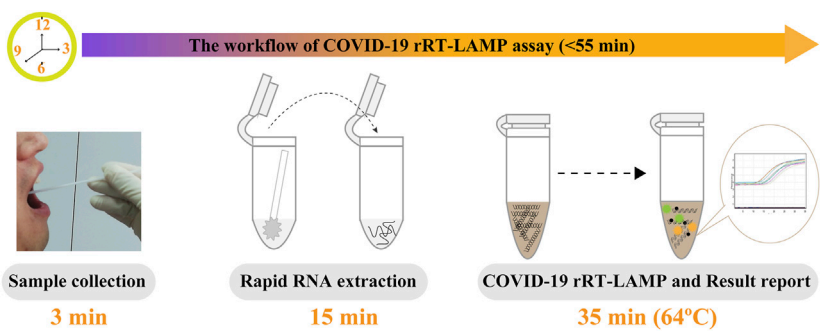

FIGURE 5 | The workflow of COVID-19 rRT-LAMP assay. Three steps, including sample collection (3 min), rapid RNA preparation (15 min), rRT-LAMP reaction and result reporting (35 min), were need for performing the COVID-19 rRT-LAMP diagnosis test, and the whole procedure could be finished within 55 min.

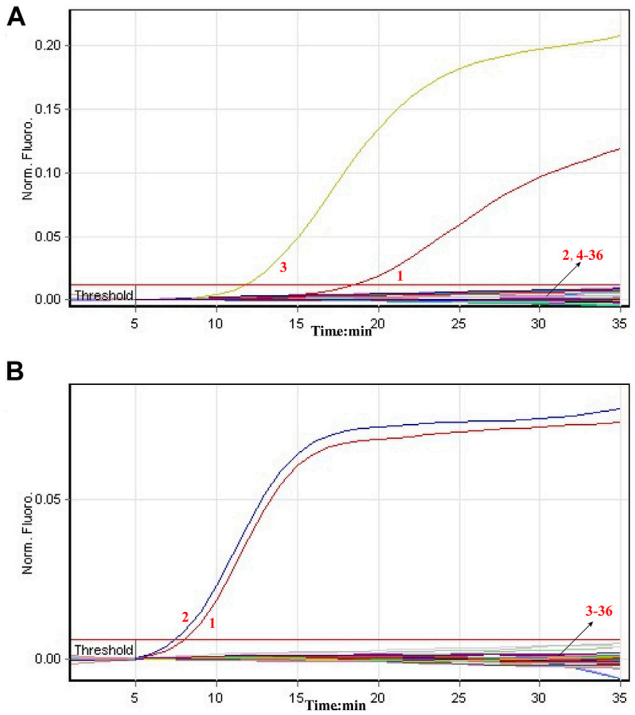

FIGURE 6 | Specificity of COVID-19 rRT-LAMP assay. The COVID-19 rRT-LAMP reactions were carried out using different genomic templates and the results were monitored by means of real-time analysis. **(A)** and **(B)** were produced from FAM (Green) and HEX (Yellow) channels, respectively. Signal 1, positive control (1.4×10^2 copies of ORF1ab- and NP-plasmids); Signal 2, positive control (1.4×10^2 copies of NP-plasmids); Signal 3, positive control (1.4×10^2 copies of ORF1ab-plasmids); Signals 4-36, coronavirus HKU1 (ORF1ab), coronavirus HKU1 (NP), coronavirus 229E (ORF1ab), coronavirus 229E (NP), coronavirus NL63 (ORF1ab), coronavirus NL63 (NP), coronavirus OC43 (ORF1ab), coronavirus OC43 (NP), coronavirus SARS (ORF1ab), coronavirus SARS (NP), coronavirus MERS (ORF1ab), coronavirus MERS (NP), *Infuenza virus A* (H1N1), *Infuenza virus A* (unidentified subtype), *Infuenza virus B* (unidentified subtype), *Parainfluenza Virus*, *Human Adenovirus*, *Syncytial Virus*, *Human enterovirus* (EV71), Coxsackievirus (CAV16), *Mycoplasma*, *Chlamydia*, *Lpneumophila*, *Pseudomonas aeruginosa*, *Klebsiella pneumoniae*, *Neisseria meningitidis*, *Acinetobacter baumannii*, *Staphylococcus aureus*, *Staphylococcus saprophytics*, *Candida tropicalis*, *Cryptoccus neo formas*, *Streptococcus pneumona*, *Candida albicans*.

assay, because the quality of commercial COVID-19 rRT-PCR kits used in Sayan People's Hospital remains uneven. These rRT-PCR kits generated inconsistent sensitivity results when they were used for detecting the 10-fold serially diluted ORF1ab-plasmid NP-plasmid templates.

For the analysis of clinical samples, the COVID-19 rRT-LAMP assay showed high sensitivity and specificity, and able to correctly diagnose 100% (33/33) of COVID-19 samples determined by rRT-PCR (**Table 1**) and 100% (41/41) of samples from non-COVID-19 patients. The concordance of high reliability between our assay and commercial rRT-PCR kits for the diagnosis of COVID-19 was preliminarily demonstrated using 74 clinical samples. Some factors may contribute to this. The COVID-19 rRT-LAMP technology, as a novel LAMP-based methodology, was less affected by the presence of various inhibitors and salts, or able to tolerate the inhibitory effect of various nucleic acids in the reaction mixtures (Kaneko et al., 2007). Simultaneously, some factors may affect COVID-19 rRT-LAMP performance. The genomic templates of SARS-CoV-2 are the RNA, which is extremely sensitive to degradation by postmortem procedures, inadequate sample handing or storage. Hence, the quality of target templates (such as integrity and purity) is a key factor for the success of COVID-19 rRT-LAMP diagnosis. In addition, other elements may affect COVID-19 rRT-LAMP diagnostic results including sampling timing (different periods of the disease development) or specimen's source (lower or upper respiratory tract).

CONCLUSION

A novel diagnostic test, termed rRT-LAMP, was successfully devised and applied to diagnosis of COVID-19 (COVID-19 rRT-LAMP). COVID-19 rRT-LAMP was preliminarily validated using pure nucleic acid templates and clinical samples. The whole test procedure from sample collection to result interpretation could be completed within 55 min. The relatively simple instrument was required, which makes it feasible to conduct COVID-19 diagnosis in various laboratories. The rapidity, feasibility, sensitivity, high specificity, its low cost and ease of use make the COVID-19 rRT-LAMP assay a promising test tool for application in public health, disease control and clinic laboratories.

DATA AVAILABILITY STATEMENT

The original contributions presented in the study are included in the article/**Supplementary Material**, further inquiries can be directed to the corresponding authors.

ETHICS STATEMENT

This study was approved by the Ethics Committee of the Sanya People's Hospital [SYPH-2019(41)-2020-03-06].

AUTHOR CONTRIBUTIONS

YW conceived and designed this study. JT and YW supervised this study. XZ, XW, HC, LH, LW, TC, SL, HL, YL, ZL, XF, SC, MX, and YW performed the experiments. XZ, XW, HC, LH, LW, TC, SL, HL, YL, ZL, XF, and SC conducted the clinical evaluation. XW, XZ, and YW analyze the data. XZ, XW, and YW contributed the reagents and analysis tools. XZ, XW, HC, LH, LW, TC, SL, HL, YL, ZL, XF, and SC contributed the materials. YW conducted the software. XZ and XW drafted the manuscript. XZ and YW revised the manuscript.

FUNDING

This work was supported by the grants from the Key Research and Development Program of Hainan Province (ZDYF2019149), State Key Laboratory of Infectious Disease Prevention and Control (2020SKLID303), Public service development and reform pilot project of Beijing Medical Research Institute (BMR 2019-11), National natural science foundation of China (81970900) and Beijing Social Science Foundation Project (19GLB033). The research also was supported by Hainan Province Clinical Medical Center.

SUPPLEMENTARY MATERIAL

The Supplementary Material for this article can be found online at: https://www.frontiersin.org/articles/10.3389/fbioe.2021.748746/full#supplementary-material

REFERENCES

Carter, L. J., Garner, L. V., Smoot, J. W., Li, Y., Zhou, Q., Saveson, C. J., et al. (2020). Assay Techniques and Test Development for COVID-19 Diagnosis. *ACS Cent. Sci.* 6, 591–605. doi:10.1021/acscentsci.0c00501

El-Tholoth, M., Bau, H. H., and Song, J. (2021). A Single and Two-Stage, Closed-Tube, Molecular Test for the 2019 Novel Coronavirus (COVID-19) at Home, Clinic, and Points of Entry. *Anal. Chem.* 93 (38), 13063–13071. doi:10.26434/chemrxiv.11860137

Heymann, D. L., and Shindo, N. (2020). COVID-19: What Is Next for Public Health? *Lancet* 395 (10224), 542–545. doi:10.1016/S0140-6736(20)30374-3

Huang, C., Wang, Y., Li, X., Ren, L., Zhao, J., Hu, Y., et al. (2020). Clinical Features of Patients Infected with 2019 Novel Coronavirus in Wuhan, China. *The Lancet* 395, 497–506. doi:10.1016/s0140-6736(20)30183-5

Hui, D. S., I Azhar, E., Madani, T. A., Ntoumi, F., Kock, R., Dar, O., et al. (2020). The Continuing 2019-nCoV Epidemic Threat of Novel Coronaviruses to Global Health - The Latest 2019 Novel Coronavirus Outbreak in Wuhan, China. *Int. J. Infect. Dis.* 91, 264–266. doi:10.1016/j.ijid.2020.01.009

Kaneko, H., Kawana, T., Fukushima, E., and Suzutani, T. (2007). Tolerance of Loop-Mediated Isothermal Amplification to a Culture Medium and Biological Substances. *J. Biochem. Biophysical Methods* 70, 499–501. doi:10.1016/j.jbbm.2006.08.008

Lamb, L. E., Bartolone, S. N., Ward, E., and Chancellor, M. B. (2020). Rapid Detection of Novel coronavirus/Severe Acute Respiratory Syndrome Coronavirus 2 (SARS-CoV-2) by Reverse Transcription-Loop-Mediated Isothermal Amplification. *PLoS ONE* 15 (6), e0234682, 2020 . Available at SSRN 3539654. doi:10.1371/journal.pone.0234682

Li, S., Jiang, W., Huang, J., Liu, Y., Ren, L., Zhuang, L., et al. (2020). Highly Sensitive and Specific Diagnosis of COVID-19 by Reverse Transcription Multiple Cross-Displacement Amplification-Labelled Nanoparticles Biosensor. *Eur. Respir. J* 56 (6), 2002060. doi:10.1183/13993003.02060-2020

Obande, G. A., and Banga Singh, K. K. (2020). Current and Future Perspectives on Isothermal Nucleic Acid Amplification Technologies for Diagnosing Infections. *Infect. Drug Resist.* 13, 455–483. doi:10.2147/idr.s217571

Shen, M., Zhou, Y., Ye, J., Al-maskri, A. A. A., Kang, Y., Zeng, S., et al. (2020). Recent Advances and Perspectives of Nucleic Acid Detection for Coronavirus. *J. Pharm. Anal.* 10 (2), 97–101. doi:10.1016/j.jpha.2020.02.010

To, K. K.-W., Tsang, O. T. Y., Chik-Yan Yip, C., Chan, K.-H., Wu, T.-C., Chan, J., et al. (2020). Consistent Detection of 2019 Novel Coronavirus in Saliva. *Clin. Infect. Dis.* 71, 841–843. doi:10.1093/cid/ciaa149

Wu, A., Peng, Y., Huang, B., Ding, X., Wang, X., Niu, P., et al. (2020). Genome Composition and Divergence of the Novel Coronavirus (2019-nCoV) Originating in China. *Cell Host & Microbe* 27 (3), 325–328. doi:10.1016/j.chom.2020.02.001

Wu, F., Zhao, S., Yu, B., Chen, Y.-M., Wang, W., Song, Z.-G., et al. (2020). A New Coronavirus Associated with Human Respiratory Disease in China. *Nature* 579 (7798), 265–269. doi:10.1038/s41586-020-2008-3

Wu, J. T., Leung, K., and Leung, G. M. (2020). Nowcasting and Forecasting the Potential Domestic and International Spread of the 2019-nCoV Outbreak Originating in Wuhan, China: A Modelling Study. *The Lancet* 395, 689–697. doi:10.1016/s0140-6736(20)30260-9

Wu, Z., and McGoogan, J. M. (2020). Characteristics of and Important Lessons from the Coronavirus Disease 2019 (COVID-19) Outbreak in China: Summary of a Report of 72 314 Cases from the Chinese Center for Disease Control and Prevention. *JAMA* 323 (13), 1239–1242. doi:10.1001/jama.2020.2648

Yu, L., Wu, S., Hao, X., Li, X., Liu, X., Ye, S., et al. (2020). Rapid Colorimetric Detection of COVID-19 Coronavirus Using a Reverse Transcriptional Loop-Mediated Isothermal Amplification (RT-LAMP) Diagnostic Platform: iLACO. *medRxiv*. doi:10.1101/2020.02.20.20025874

Zhu, X., Wang, X., Han, L., Chen, T., Wang, L., Li, H., et al. (2020). Multiplex Reverse Transcription Loop-Mediated Isothermal Amplification Combined with Nanoparticle-Based Lateral Flow Biosensor for the Diagnosis of COVID-19. *Biosens. Bioelectron.* 166, 112437. doi:10.1016/j.bios.2020.112437

Zhu, X., Wang, X., Li, S., Luo, W., Zhang, X., Wang, C., et al. (2021). Rapid, Ultrasensitive, and Highly Specific Diagnosis of COVID-19 by CRISPR-Based Detection. *ACS Sens.* 6, 881–888. doi:10.1021/acssensors.0c01984

Conflict of Interest: The authors declare that the research was conducted in the absence of any commercial or financial relationships that could be construed as a potential conflict of interest.

Publisher's Note: All claims expressed in this article are solely those of the authors and do not necessarily represent those of their affiliated organizations, or those of the publisher, the editors and the reviewers. Any product that may be evaluated in this article, or claim that may be made by its manufacturer, is not guaranteed or endorsed by the publisher.

frontiers in Bioengineering and Biotechnology

REVIEW
published: 01 November 2021
doi: 10.3389/fbioe.2021.765987

Recent Progress in Intelligent Wearable Sensors for Health Monitoring and Wound Healing Based on Biofluids

Siyang Cheng[1†], Zhen Gu[1†], Liping Zhou[1†], Mingda Hao[1], Heng An[1], Kaiyu Song[1], Xiaochao Wu[2], Kexin Zhang[1], Zeya Zhao[1], Yaozhong Dong[3*] and Yongqiang Wen[1]*

[1]Beijing Key Laboratory for Bioengineering and Sensing Technology, Daxing Research Institute, School of Chemistry and Biological Engineering, University of Science and Technology Beijing, Beijing, China, [2]School of Material Science and Engineering, Zhengzhou University, Zhengzhou, China, [3]Yantai Yuhuangding Hospital, Yantai, China

OPEN ACCESS

Edited by:
Tailin Xu,
Shenzhen University, China

Reviewed by:
Yunlu Pan,
Harbin Institute of Technology, China
Ming Zhou,
Northeast Normal University, China
Zhaohui Li,
Zhengzhou University, China

***Correspondence:**
Zhen Gu
guzhen@ustb.edu.cn
Yaozhong Dong
cathleen0806@sina.com

[†]These authors have contributed equally to this work and share first authorship

Specialty section:
This article was submitted to Biosensors and Biomolecular Electronics, a section of the journal Frontiers in Bioengineering and Biotechnology

Received: *28 August 2021*
Accepted: *12 October 2021*
Published: *01 November 2021*

Citation:
Cheng S, Gu Z, Zhou L, Hao M, An H, Song K, Wu X, Zhang K, Zhao Z, Dong Y and Wen Y (2021) Recent Progress in Intelligent Wearable Sensors for Health Monitoring and Wound Healing Based on Biofluids. Front. Bioeng. Biotechnol. 9:765987. doi: 10.3389/fbioe.2021.765987

The intelligent wearable sensors promote the transformation of the health care from a traditional hospital-centered model to a personal portable device-centered model. There is an urgent need of real-time, multi-functional, and personalized monitoring of various biochemical target substances and signals based on the intelligent wearable sensors for health monitoring, especially wound healing. Under this background, this review article first reviews the outstanding progress in the development of intelligent, wearable sensors designed for continuous, real-time analysis, and monitoring of sweat, blood, interstitial fluid, tears, wound fluid, etc. Second, this paper reports the advanced status of intelligent wound monitoring sensors designed for wound diagnosis and treatment. The paper highlights some smart sensors to monitor target analytes in various wounds. Finally, this paper makes conservative recommendations regarding future development of intelligent wearable sensors.

Keywords: intelligent, wearable, health monitoring, biofluids, targeted analytes, wound healing

INTRODUCTION

The development and design of wearable intelligent sensors have led to excellent potential applications in the fields of public health monitoring and health care. Although this field is in its infancy, the foundational research in the interdisciplinary area of wearable sensing is well established. The preparation of novel devices tends to be tightly integrated with the development of various emerging technologies, including biocompatible materials (He S. et al., 2020); flexible electronics (Zhang et al., 2019); optical and electrochemical sensors (Gao et al., 2016a; Gao et al., 2016b; Nyein et al., 2016); microfluidics (Kim et al., 2020); near-field communication (NFC) (Kim et al., 2015); painless microneedles (Guo et al., 2019; Li et al., 2019); big data; and cloud computing (Yang et al., 2016). In addition, intelligent, wearable sensors are often associated with the human body in the form of tattoos; patches; and gloves or dressings. Live sensing, data recording, and computing have been performed using external devices and portable systems (Wang C. et al., 2018; Ershad et al., 2020; Hanna et al., 2020). Compared with the traditional medical health monitoring that relies on a typical medical infirmary, the intelligent biochemical sensors have attracted ever-increasing attentions for their flexibility, rapidity, biocompatibility, high specificity, and low cost (Kim et al., 2019; Bocchetta et al., 2020; Koralli and Mouzakis, 2021). More importantly, this technology creates two-way feedback between doctors and patients to develop more personalized

TABLE 1 | The four stages of wound healing and their characteristics.

Hemostatic stage	Interconnection between blood vessels slows blood flow to the injured tissue and minimizes bleeding caused by the wound (Furie and Furie, 2008; Rodrigues et al., 2019). Platelets can activate and release transforming growth factor (TGF- α, TGF-β), platelet derived growth factor, and other important active factors, which aid subsequent healing stages (Pool, 1977)
Inflammatory stage	Neutrophils are the first cells to arrive at the wound. Their phagocytic ability can effectively remove damaged matrix material, dead cells, and other foreign bodies. Monocytes are recruited subsequently. They differentiate into macrophages and dendritic cells in various tissues. The differentiated cells induce the release of signal factors, which can initiate apoptosis or infection protection, and then effectively remove tissue debris and coagulum (FrykbergRobert and Banks, 2015; Kratofil et al., 2017)
Proliferation stage	The release of Interleukin-1 (IL-1) and tumor necrosis factor-α (TNF-α) can stimulate fibroblast secretion (Kiwanuka et al., 2012). Keratinocytes migrate to the wound surface after replacing dead cells. Granulation tissue formation not only can promote the maturation of keratinocytes, but also can stimulate the release of signal transforming factors, transform fibroblasts into muscle fibroblasts, and complete cell epithelialization (Gonzalez et al., 2016)
Remodeling stage	Type III collagen can be transformed into more stable type-I collagen gradually under the action of matrix metalloproteinases (MMPs). Fibroblasts also migrate to the wound site, deposit new type-I collagen, and eventually complete epidermal tissue replacement or scar tissue repair (Gurtner et al., 2008; Guo and Dipietro, 2010)

and scientific health care programs (Hughes, 2008). It can monitor specific information-carrying molecules and signals that are related to human physiology and disease pathology and output data about target analytes to external terminal equipment continuously and in real time, thus aiding in prediction and diagnosis (Dervisevic et al., 2020). Efficient acquisition of target analytes is achieved by collecting biofluids that are naturally secreted by or are part of the human body, including sweat, tears, skin interstitial fluid (IFS), blood, and wound fluids (Kassal et al., 2017; Li and Wen, 2020). Below, we discuss some biofluids for providing physiological and pathological information.

Sweat is the fluid secreted by sweat glands and contains a number of biomolecular and biochemical signaling analytes. Sweat is also a representative source of analytes in the field of intelligent wearable sensors. The analytes include ionic electrolytes (Na^+, K^+) (Gao et al., 2016a), metabolites (glucose, lactate) (Valdes-Ramirez et al., 2014; Koh et al., 2016), and heavy metal species (copper, iron, zinc) (Sekine et al., 2018).

Blood distributes throughout the body and typically requires being invasively collected prior to analysis and monitoring in wearable sensor devices. Some advanced blood sensing devices have been developed recently for continuous detection of health care (He S. et al., 2020; Hanna et al., 2020).

Interstitial Fluid (ISF) is another source of biomarkers such as protein and glucose in serum and plasma (Koschinsky et al., 2003; Tran et al., 2018). ISF is often collected and analyzed using microneedle patch (Ventrelli et al., 2015).

Tears' composition is not as complex as that of blood, due to the presence of the blood-tear barrier. Tears often contain analytes similar to other biofluids, including glucose, Na^+, and K^+ (Tseng et al., 2018). Contact lens-based portable sensors enable tear collection efforts, but sophisticated sensor design concepts are often required (Kim et al., 2017c; Liu et al., 2021).

Wound fluid is derived from various types of skin, mucosal surface or organ tissue injuries and consists of a highly inhomogeneous mixture whose physicochemical markers are assumed to reflect the clinical status of the wound healing (Löffler et al., 2013). The wound biomarkers include biochemical molecules [C-reactive protein, potential hydrogen (pH), glucose, uric acid, etc.] (Pasche et al., 2008; Kassal et al., 2015; Jankowska et al., 2017; Pan et al., 2019), biochemical signals (such as wound temperature, pressure, and redox state) (Farooqui and Shamim, 2016; Sun et al., 2018), and pathogens (such as *Pseudomonas aeruginosa*) (Brunauer et al., 2021). Wound monitoring is a key challenge for the next generation of smart dressing development.

Wounds are inevitably caused by internal factors (such as chronic diseases) (Siddiqui and Bernstein, 2010) or external factors (such as mechanical and thermal) (Demidova-Rice et al., 2012; Zahedi et al., 2010). It is usually painful for patients to face wounds with stress. It is urgent to develop effective wound management systems and strategies to promote complex wounds healing. The wound healing stages include hemostasis, inflammation, proliferation, and remodeling (Aderibigbe and Buyana, 2018; Gonzalez et al., 2016). **Table 1** shows the repair characteristics of the various wound healing stages. Any abnormal or incomplete recovery stage can lead to wound healing delays (Nunan et al., 2014). In clinics, wound-related information indicators are often monitored using visual examination and laboratory analysis of exudate swabs, but the efficiency of this type of wound care is typically low and advanced preventative nursing methods are needed.

The intelligent wearable sensors provide unprecedented data and convenience to support the rational management of patient wounds. These intelligent dressing sensors provide real-time information about wound characteristics for doctors and users. In addition, the collected wound biomarkers data can be transferred to external devices by wireless real-time communication to perform *in-situ*, multi-parameter, and real-time monitoring and healing of a wound (Foster and Sethares, 2014). Therefore, patients no longer need to bear medical expenses related to wound prevention, care, surgery, and long-term hospitalization.

In this review, we first introduce the latest progress in the application of intelligent wearable senors in the fields of health monitoring *via* analysis of various biofluids (sweat, blood, interstitial fluid, tears, wound fluid, etc.). Second, for various types of wound models (infected wounds, chronic wounds, and acute wounds), we review the monitoring of various biomarkers (biochemical molecules, biochemical signals, etc.) in wound fluids. Finally, we make concluding comments and conservatively analyze prospects for the future and the limitations of ideal modern wearable devices.

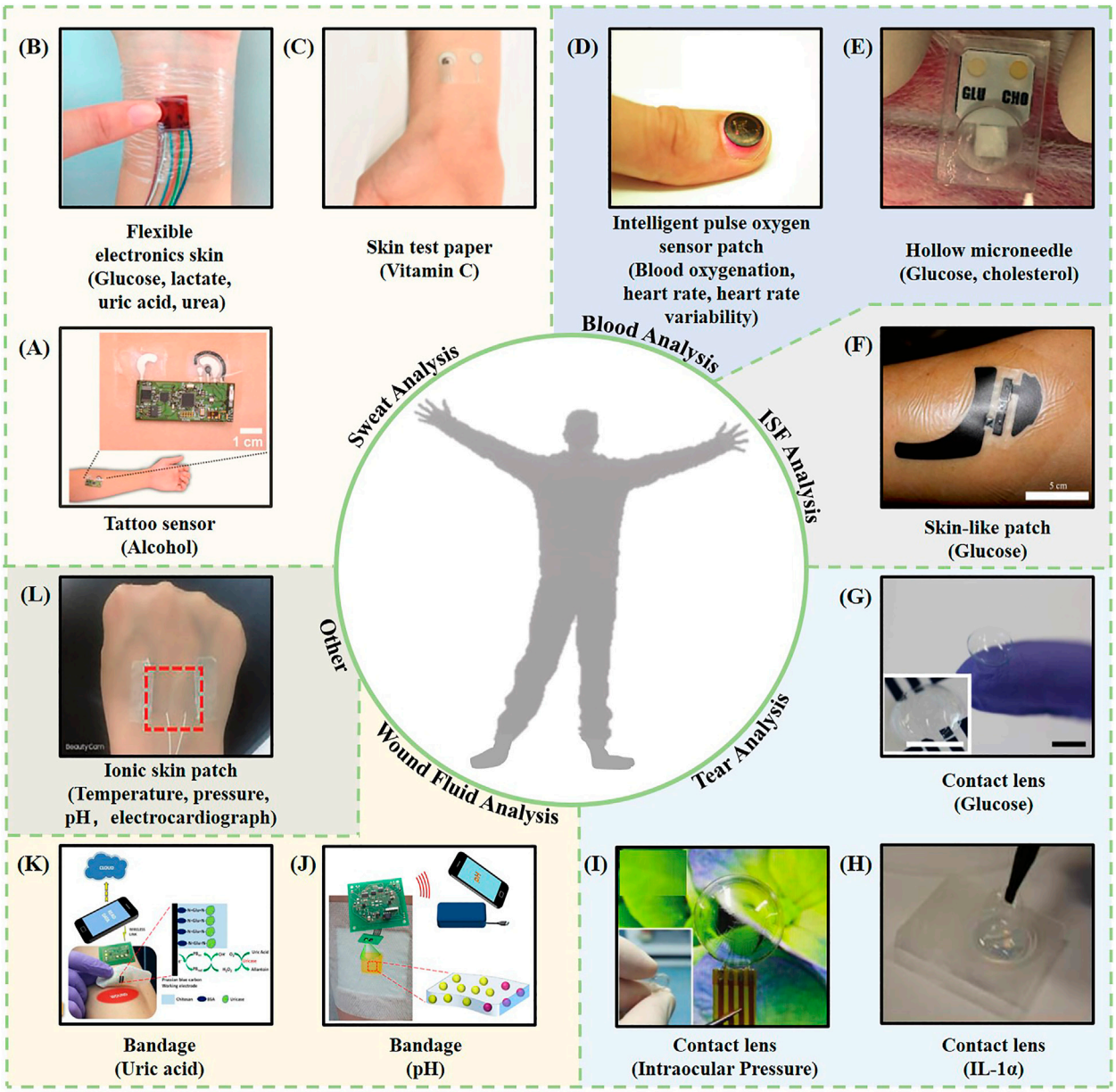

FIGURE 1 | Representative examples of intelligent wearable sensors based on biofluids. **(A)** A wearable tattoo sensor for alcohol detection in sweat (Kim et al., 2016). **(B)** A flexible electronic skin based on a piezoelectric biosensor matrix for monitoring of lactic acid, glucose, uric acid, and urea (Han et al., 2017). **(C)** A skin test paper used for vitamin C monitoring (Sempionatto et al., 2020). **(D)** An intelligent pulse oxygen sensor patch that outputs information such as the blood oxygen, heart rate, and heart rate variability (Kim et al., 2017b). **(E)** A one-touch-activated blood multidiagnostic system (OBMS) for monitoring blood glucose and cholesterol (Li et al., 2015). **(F)** A skin-like patch for noninvasive blood glucose monitoring (Chen et al., 2017). **(G)** A contact lens sensing device for monitoring blood sugar (Kim et al., 2017c). **(H)** A thermotherapy recessive lens for monitoring IL-1α (Mak et al., 2015). **(I)** A contact lens sensor capable of continuous intraocular pressure monitoring (Liu et al., 2021). **(J)** A smart bandage for optical monitoring of pH (Kassal et al., 2017). **(K)** An intelligent bandage for monitoring the uric acid index in a wound (Kassal et al., 2015). **(L)** An ionic bioelectronic skin patch for monitoring of temperature, pressure, pH, and electrocardiogram data (Shi and Wu, 2021).

INTELLIGENT WEARABLE SENSORS

In modern medical nursing, the medical characteristics of preventive, predictive, personalized, and participatory medicine (the 4P medical model) are the focus of advanced wearable devices (Lin, 2019). Intelligent wearable medical sensors can accurately sense patient pathophysiological information and monitor patient physiological statuses in real time. Specifically, wearable sensors detect target analytes in various biological body fluids (sweat, interstitial fluid, blood, tears, wound fluid, etc.) *in vitro* and *in vivo* for health monitoring (Sturgeon et al., 2008; Jia et al., 2012; Gromov et al., 2013; Broza et al., 2015; Heikenfeld et al., 2019; Shrivastava et al., 2020). These biomarkers include physiological metabolites (Han et al., 2017; Tur-Garcia et al.,

TABLE 2 | Representative new intelligent wearable sensor platforms based on biofluids.

Biological fluid sampled		Material or platform	Targeted analyte	Detection limit	Biosensing format	Ref
Biofluid	Sweat	Sweatband	Zn, Cd, Pb, Cu, Hg	NR	Electrochemical-stripping voltammetry	Gao et al. (2016a)
		Microfluidic patch	Lactate, glucose	50 μM (Glucose)	Electrochemical-amperometry	Martin et al. (2017)
		Polyamide film	Glucose, cortisol	0.1 mg/dl (Glucose)	Electrochemical-amperometry and impedance	Munje et al. (2017)
		Polycarbonate membrane	Lactate	0.2 mM	Electrochemical-amperometry	Tur-Garcia et al. (2017)
		Flexible electronics skin	Glucose, lactate, uric acid, urea	NR	Piezoelectric system	Han et al. (2017)
		Microfluidic patch	Lactate, pH, glucose, and chloride	NR	Colorimetry	Koh et al. (2016)
		Temporary tattoo	Alcohol	NR	Amperometry	Kim et al. (2016)
		Stretchable patch	Glucose, pH	1.3 μM (Glucose)	Amperometry	Oh et al. (2018)
		Microfluidic patch	Na+	NR	Potentiometry	Nyein et al. (2018)
		PANi-Nafion-OPH/PVA hydrogel	Diisopropyl fluorophosphates	NR	Potentiometry	Mishra et al. (2018)
		Glucose colorimetric assay kit	Glucose	NR	Colorimetry	Choi et al. (2019)
		In_2O_3- Au/chitosan-SWCNT/GOx	Glucose	10 nM	Field-effect transistor	Liu et al. (2018)
		3D-printed e-ring bridges	Glucose	1.2 μM	Electrochemical-amperometry	Katseli et al. (2021)
		Skin test paper	Vitamin C	NR	Amperometry	Sempionatto et al. (2020)
	Blood	Intelligent pulse oxygen sensing ring	Blood oxygenation, pulse rate	NR	Optoelectronic system	Lochner et al. (2014)
		PEGDA	Lactate	1 μM	Cyclic voltammetry	Caliò et al. (2016)
		Intelligent pulse oxygen sensing patch	Blood oxygenation heart rate, heart rate variability	NR	Electrochemical-amperometry	Kim et al. (2017b)
		Hollow microneedle	Glucose and cholesterol	NR	Colorimetry	Li et al. (2015)
		Embroidered bandage	Glucose, lactate	NR	Electrochemical-amperometry	Liu and Lillehoj (2016)
		Epidermis sensing gloves	Glucose	NR	Electromagnetic system	Hanna et al. (2020)
	Interstitial fluid	PtNps/PANi/MEA/GOx	Glucose	260 μM	Cyclic voltammetry	Gao et al. (2019a)
		PtNps/PANi/MEA/UOx	Uric acid	4 μM		
		PtNps/PANi/MEA/ChOx	Cholesterol	440 μM		
		Skin-like patch	Glucose	NR	Amperometry	Chen et al. (2017)
		Microneedle patch	Methyl paraoxon	4 μM	Amperometry	Mishra et al. (2017)
		Microneedle patch	Glucose	NR	Amperometry	Li et al. (2021)
		Microneedle patch	Glucose	0.66 mM	Electrochemical-amperometry	Dervisevic et al. (2021)
	Tears	AuMNA- P(GMA-co-VFc)	Urea	2.8 μM	Cyclic voltammetry	Senel et al. (2019)
		Contact lens	Glucose	0.4 mM	Field-effect transistor	Kim et al. (2017c)
		Contact lens	Glucose	12.57 mM	Field-effect transistor	Park et al. (2018a)
		Contact lens	Interleukin-1α (IL-1α)	1.43 pg/ml	Amperometry	Mak et al. (2015)
		Contact lens	Intraocular Pressure	3.166 mV mm Hg^{-1} (on the porcine eye)	Amperometry	Liu et al. (2021)
	Wound fluid	Bandage	Uric acid	NR	Amperometry	Kassal et al. (2015)
		Bandage	pH	6.5–8.5	Optical	Kassal et al. (2017)
		Bandage	Tyrosinase	NR	Amperometry	Ciui et al. (2018)
		Wound dressing	pH	6.0–9.0	Colorimetry	Pan et al. (2019)
		Wound dressing	Reduction state	NR	Colorimetry	He et al. (2020a)
		Epidermal electronics system	Temperature, thermal conductivity	NR	Amperometry	Hattori et al. (2014)
		Intelligent conductive hydrogel	Large deformation movement of human body	NR	Amperometry	Zhao et al. (2019)
Other					Amperometry	Ershad et al. (2020)
	Epidermis	Temporary tattoo	Moisture, heart rate	NR	Electrochemical-amperometry and impedance	Shi and Wu (2021)
		Ionic skin patch	Temperature, pressure, pH,electrocardiograph	NR	Ultrasound wall-tracking technique,	
		Flexible monitoring patch	Blood pressure	NR	Electrochemical-amperometry	Wang et al. (2018a)

2017; Mishra et al., 2018; Choi et al., 2019), small molecules (Munje et al., 2017; Parlak et al., 2018; Li et al., 2021), biochemical factors (Mak et al., 2015), and environmental signals (Pal et al., 2020; Liu et al., 2021; Shi and Wu, 2021). This section systematically summarizes the latest applications of intelligent wearable sensors for monitoring biomarkers in various biofluids (**Figure 1**) as summarized in **Table 2**.

Basic Composition and Design Principles for Intelligent Wearable Sensors

Intelligent wearable sensors often exist in biological and chemical-based sensing modes. A typical biochemical sensor includes three essential functional elements: 1) Substrate for integrating complete sensors; 2) A "receptor probe" element that can selectively identify target analytes; 3) A signal output element that converts an event recognized by the receptor into a readable signal (electrochemical mode, optical mode et al.) (Bandodkar and Wang, 2014; Kim et al., 2019). Suitable substrate materials in intelligent wearable sensors often utilized polyethylene terephthalate (PET), polyethylene (PE), and inkjet temporary tattoo paper (Bandodkar et al., 2015; Gao et al., 2016a; Wang J. et al., 2018). However, their poor air permeability and tensile properties limit the miniaturization of the sensors. Biodegradable flexible materials such as cellulose, wool, polyacrylonitrile (PAN) and poly (styrene-butadiene-styrene) (PSBS) fiber are usually more attractive as substrates (Bandodkar et al., 2015; Kim D. et al., 2017; Wu et al., 2017; Marriam et al., 2018).

Selecting and fixing an appropriate receptor probe on the substrate are the most critical step for intelligent wearable sensors, and the design principles are as follows: 1) The substrate used for fixing receptor probe cannot interact with the target analyte; 2) To stabilize the receptor probe on the substrate, it is usually necessary to modify the substrate and probe with appropriate functional groups or introduce intermediate connecting media; 3) The fixation must be reliable, repeatable, and capable of ensuring the biochemical activity of the receptor probe to achieve efficient detection of the target analyte.

Signal output elements can quantify target analytes and provide convertible or intuitive signals, including electrochemical and optical sensing. For example, the target analyte will undergo an oxidation-reduction reaction with the electrode when the electrochemical sensor is working, thereby generating a small current (Curto et al., 2012). Specific enzyme amperometric sensors (lactate oxidase, urate oxidase, and urate oxidase) are often used to monitor lactic acid, uric acid, and lactic acid. The sensor can measure the potential between the working electrode and the reference electrode in the electrochemical cell. The method of conductance measurement usually adopts the mode of field-effect transistor (FET) (Bandodkar et al., 2019). Its sensing principle can be summarized as follows: the channel current between the source and drain of the sensor varies with the charge density which is sensitive to the target material on the surface of the transistor (Sang et al., 2016). If the material used in the channel is graphene, it is called a graphene field-effect transistor (GFET) (Prattis et al., 2021). For example, a peptide nucleic acid (PNA) based GFET quantitatively detected RNA target with the graphene (Tian et al., 2020). The PNA probe with an amine bond frame provided specific binding efficiency to DNA and RNA targets, thus reducing the detection time (Mat Zaid et al., 2017; Movilli et al., 2018). Under the global COVID-19 epidemic background, a team has developed a GFET sensor with an anti-virus spike protein antibody for rapid detection of severe acute respiratory syndrome coronavirus (SARS-CoV-2). The lowest detection limit is 1 fg/ml (Seo et al., 2020).

Electronic sensing devices often require continuous power supply. Optical sensors based colorimetric or fluorescence analysis modes consume almost no energy. Compared with amperometric sensing devices, colorimetric and fluorescent sensors also have the advantages of simple structure, low cost, and portable design without power supply operation (Zhu et al., 2021). For example, fluorescence biosensors consist of excitation light sources (lasers), fluorophore molecules, and photodetectors for fluorescence intensity and spectrum recording (Chen et al., 2017). Among them, fluorophore molecules include small molecules, proteins, nucleic acids, etc., (Jensen, 2012). In addition to the above-mentioned sensing technology, microfluidics technology become prominent in wearable intelligent sensor platforms for reducing samples and solvents (Li et al., 2020; Mejía-Salazar et al., 2020).

Sweat

Sweat is relatively easy to obtain and rich in biochemical information (Such as biomolecules, inorganic salts, metal elements, etc.) for non-invasive monitoring of the wearer's physiological status. Sempionatto's team developed a flexible vitamin C tattoo patch sensor to monitor the time distribution of vitamin C levels in sweat by attaching ascorbate oxidase (AAOx) to a flexible, printable tattoo electrode patch (Sempionatto et al., 2020). Excessive cortisol molecules can lead to the development of diabetes, so it is necessary to measure cortisol indicators in the body through a portable method (Jones and Gwenin, 2021). Parlak et al. (2018) reported a wearable senor with a molecularly selective organic electrochemical transistor layer can collect 10–50 μl of sweat at a time and evaluate cortisol levels accurately. Electrolyte imbalance can cause abnormal health conditions of the human body and change the composition of sweat. Nyein et al. (2018) proposed a flexible microfluidic sweat sensor patch (**Figure 2A**), in which a commercially printed circuit board (PCB) and a sweat rate sensor based on electrochemical and electrical impedance were integrated into the microfluidic channel. The device can be used to monitor Na+ concentration and sweat rate signals simultaneously.

Continuous operation of intelligent sensors usually requires strict energy supply quality (Park S. et al., 2018). Recently, investigators demonstrated that a wearable flexible microarray sensor provided multi-channel real-time detection of trace heavy metals (Zn, Cd, Pb, Cu, and Hg) in sweat (Gao et al., 2016b). Ordinary batteries often suffer from insufficient availability and battery life (Zamarayeva et al., 2017; Zeng et al., 2014). Obtaining energy directly from bioenergy including human body heat and

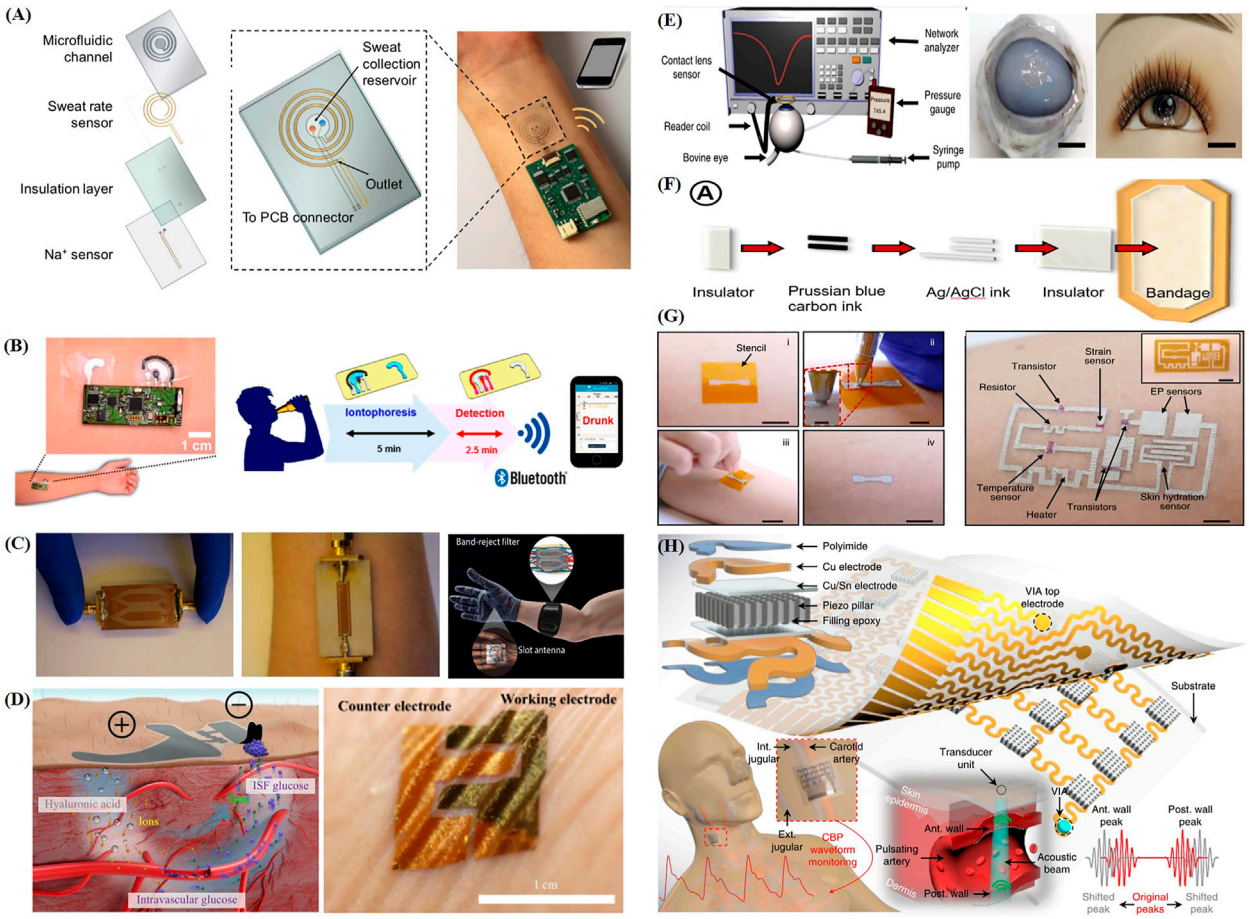

FIGURE 2 | Recent progress of representative intelligent wearable sensors designed for health monitoring. **(A)** Schematic diagram of the structure and principle of a wearable sweat patch (Nyein et al., 2018). **(B)** Schematic illustration of the application of a skin tattoo-based wearable alcohol sensor patch to the skin and its wireless sensing principle (Kim et al., 2016). **(C)** Optical image of a wrist and back of hand based on an electromagnetic wave-sensing wearable device that imitates the vascular anatomy (Hanna et al., 2020). **(D)** Schematic diagram of a wearable skin biosensor system for non-invasive electrochemical monitoring of glucose in ISF (Chen et al., 2017). **(E)** Schematic of a contact lens sensing device used to monitor blood glucose and intraocular pressure and its appearance when fitted (Kim et al., 2017c). **(F)** Schematic diagram of screen printing bandage sensor preparation (Kassal et al., 2015). **(G)** Schematic illustration of the DoS circuit preparation process and structure (Ershad et al., 2020). **(H)** Schematic diagram of the structure and operation principle of a wearable flexible monitoring patch that uses ultrasound (Wang C. et al., 2018).

biomoleculars are potential sources of power for the sustainable development of intellegent sensors in the future (Barros, 2013; Dienel and Hertz, 2001). Yu et al. (2020) proposed a biofuel-driven sensing electronic skin that consisted of a multimode sensor and a high-efficiency lactic acid biofuel cell. The lactic acid present in the sweat was catalyzed by the lactate oxidase in the anode of the electronic skin to generate pyruvate, and the cathode reduces the oxygen in the environment to water. The stable current generated in the process could realize the self-powering of the sensor. The electronic skin could also selectively monitor physiological information such as urea, pH, and glucose, as well as body temperature and sweat characteristics in real-time. Unlike using human endogenous biofuels (glucose or lactate secreted by the human body) for power generation, another work reports a flexible portable epidermal biofuel cell based on human exogenous substances (Sun et al., 2021a). The device consists of two parts, one is a sweat transport microfluidic module for sampling, storage and excretion, the other part is a non-invasive real-time biological organism *in situ* generations of flexible ethanol/oxygen biofuel cell module. The epidermal biofuel cell uses exogenous substances (such as ethanol) instead of endogenous substances as a new generation of promising energy-saving products, which can be used for sweat collection and sweat power generation on the skin of drinkers at the same time. To prevent and monitor unsafe drinking behavior, Kim et al. (2016) developed a wearable alcohol sensor patch based on a skin tattoo (**Figure 2B**). The patch consisted of an iontophoretic-biosensing temporary tattoo system and flexible electronics. It was coated with the drug pilocarpine. Drugs can be released through the skin in *via* iontophoresis, which induced the epidermis to produce sweat. Alcohol oxidase and Prussian blue electrode transducer can be used to monitor alcohol molecules in sweat.

Glucose in sweat is reported to be associated with blood glucose metabolism (Talary et al., 2007). Studies have reported an attachable, expandable electrochemical sensor that could continuously monitor blood glucose concentrations and pH changes caused by eating, exercise, or disease for long periods (Oh et al., 2018). Katseli et al. (2021) developed a wearable electrochemical ring (e-ring) to self-test the blood glucose level in human sweat upon connecting the smartphone to a micro-potentiostat by 3D printing technology. Xiao et al. (2019) developed a wearable colorimetric sensor based on a microfluidic chip, in which five microfluidic channels guided sweat into a detection microcavity. Each channel had a check valve to ensure that the reagent could not flow back from the microcavity (Xiao et al., 2019). The colorimetric response of the enzymatic oxidation of o-dianisidine supplied the detection of 0.10–0.50 mM glucose with a detection limit of 0.03 mM in sweat. The field-effect transistor (FET), a new type of sensing device, has attracted substantial attention in the field of sensing because of its low manufacturing cost, industrial production, and high sensitivity (Syu et al., 2018). The principle of a FET biosensor can be summarized as follows: the channel current between the source and drain of the sensor varies with the charge density which is sensitive to the targeted substances on the specific surface of the transistor (Sang et al., 2016). Liu et al. (2018) developed a highly sensitive In_2O_3 nanobelt based on FET biosensing. It integrated FET biosensors with an on-chip gold side gate and offered good electrical properties on highly flexible substrates (Liu et al., 2018). Further research has shown that the device can detect glucose concentrations in the range of 10 nM–1 mM, and its sensitivity is sufficient to cover the range of abnormal glucose content in human biological fluids caused by diabetes. Although sweat monitoring has many advantages in the field of sensing, problems such as the inability to obtain sweat immediately in winter and easy contamination of sweat are still constraints and challenges for the development of clinical diagnosis.

Although great progress has been made in sweat analysis with intelligent wearable sweat sensors, there are also some key challenges. 1) The perspiration rate is related to the season, so the actual efficacy of the sensor is unstable throughout the year; 2) Sweat is exposed to the outside world when it is secreted, and it is easy to be contaminated, thus affecting the results of sweat analysis. 3) Somatic species lack volume control over sweat evaporation and collection. Solving these problems requires breakthroughs in sweat collection and transportation, such as the development of new materials as well as novel overall encapsulation strategies (Heikenfeld, 2016).

Blood

Blood is the liquid in the circulatory systems of humans and higher animals. It transports oxygen and nutrients (glucose, amino acids, and acids), removes wastes (carbon dioxide, uric acid, lactic acid), and provides immune and information functions. Blood tests contribute to detecting internal health at the level of cytology, and providing reasonable health care suggestions (Hallek et al., 2008; Peters et al., 2004). A variety of devices have been developed to monitor target analytes in blood (Lee et al., 2009; Lee et al., 2011; Zheng et al., 2015). Lochner et al. reported a flexible substrate-compatible sensor composed entirely of organic optoelectronic devices for measuring the human pulse and arterial oxygen partial pressure with errors of 1 and 2%, respectively (Lochner et al., 2014). Li et al. (2015) reported an intelligent one-touch-activated blood multidiagnostic system (OBMS) for detecting the glucose and cholesterol. Within 3 min, one press of the finger started the diagnostic, including human blood collection, red blood cell separation, serum transportation and detection. Liu and Lillehoj (2016) reported a dual electrochemical sensor prepared by embroidery technology with simultaneous detection of glucose and lactate at high-sensitivity. In recent years, wearable devices tend to be miniaturized, battery-free, lightweight, and noninvasive. Kim et al. (2017b) reported a millimeter-scale and battery-free pulse oximeter mounted on the fingernail for capturing quantitative information such as the blood oxygen level, heart rate, and heart rate variability. Another study proposed a blood glucose measurement sensor system based on electromagnetic waves (EM) and integrated it with gloves for noninvasive detection of glucose in the blood (**Figure 2C**) (Hanna et al., 2020). The working microwave frequency band of the sensor is designed between 500 MHz and 3 GHz. The microwave energy in this frequency range reaches the vessel across the epidermis and muscle tissue layer with high sensitivity, ensuring that the sensor monitors glucose in a wide frequency range. The results of a controlled experiment in diabetic mice and healthy humans showed that the physical characteristic information fed back by the sensor system has a highly linear relationship with the measured blood glucose level (>0.9). The intelligent non-invasive blood glucose monitoring system can avoid the discomfort caused by acupuncture, optimize the patient's medical experience, and also bring great chances to medical diagnosis and health management. Besides sensor devices driven by biofuel cells used in sweat, Sun et al. (2021b) reported a biofuel cell-driven medical nanodevice used in serum, which includes two parts: a vitamin C sensor chip (iezCard) for self-powered energy and an output chip for signal processing. The iezCard in the device integrates a special Kimwipes (A common laboratory paper) microfluidic channel, which can achieve efficient transmission of the serum to be tested. In addition, the Kimwipes microchannel has a filtering effect on proteins, and the device can directly detect vitamin C from the serum. The device uses a drop of serum to realize the immediate detection of scurvy caused by the lack of vitamin C. In another study, to improve human immunodeficiency virus (HIV) testing, a side-flow detection platform based on microfluidic fuel cells was developed, which includes a biological anode that can be used to oxidize glucose in the blood and a biological cathode that can be used to reduce the transport of oxygen in the air (Dector et al., 2017). The biological anode is composed of methylene blue electropolymerization paper deposited with tetrabutylammonium bromide deionized water, glutaraldehyde, Nafion, and glucose oxidase. The biological cathode is composed of Pt/C on methylene blue electropolymerized paper. This work proves that the fuel cell integrated in HIV side flow detection has considerable real-time testing potential in the energy field. Blood

is still the most critical biological fluid in personal health monitoring. To sum up, blood is still an essential biological fluid in personal health monitoring. Its screening can not only provide a basis for disease diagnosis, curative effect diagnosis, and post-medical prediction of the blood system but also provide an essential reference for the diagnosis and treatment of diseases that cause secondary changes in blood composition. It seems excessive to rely on intrusive sensing methods to monitor glucose and vitamin C, as sensors for sweat analysis are also reported to be used for related molecular monitoring. Therefore, blood sensor detection should monitor target analytes not found in other biological fluids—for example, CA125 markers of ovarian cancer and cardiac troponin markers suspected of an acute coronary syndrome (Saorin et al., 2020). Advanced blood sensors will rely on more serious power supply technical problems. Commercial coin batteries are the most widely used but have disadvantages in weight, volume, and rigid mechanical properties. To overcome this problem, the biofuel cell outlined above is considered an effective way to generate electricity *in situ*.

ISF

ISF is a combination of serum and cellular material, produced *via* transcapillary filtration of blood and cleared by lymphatic vessels (Wiig and Swartz, 2012). ISF includes small molecular metabolites such as salt, protein, glucose, and ethanol, much like blood (Fogh-Andersen et al., 1995; Tran et al., 2018). Therefore, ISF is an ideal blood substitute for medical health monitoring, as it offers convenient collection, sustainable monitoring, non-coagulation, and good applicability to the field of sensing (Kastellorizios and Burgess, 2015).

Chen et al. (2017) developed a skin-like biosensor system for non-invasive blood glucose monitoring. The system consisted of an ultra-thin, skin-like biosensor and electrochemical twin channels (ETCs) that functioned as a paper battery. ETCs increased the ISF osmotic pressure *via* iontophoresis and drove glucose in blood vessels to be transported to the skin surface, thus achieving sensitive and accurate glucose monitoring (**Figure 2D**). In agricultural environments, farmers are often exposed to organophosphorus (OP). Because organophosphorus pesticides are easily absorbed by the skin and highly toxic, there is an urgent need for fast, sensitive, and reliable OP sensing tools. Mishra et al. developed an invisible microneedle sensing system based on organophosphorus hydrolase (OPH) (Mishra et al., 2017). A carbon paste electrode transducer was used to wrap the hollow microneedles and couple the biocatalytic OPH with the sensor. The enzyme reaction products on epidermal sample were sensitized and detected using fast square-wave voltammetry in the presence of OP. Studies have shown that the OPH microneedle sensing system can directly, quickly, and selectively detect methyl paraoxon products in the 20–180 μM range in ISF. Dervisevic et al. reported a type of high-density silicon microneedle array patch for *in-situ* monitoring of blood in ISF (Dervisevic et al., 2021). Another study proposed an integrated wearable closed-loop system based on mesoporous microneedle iontophoresis with a diabetes treatment system (Li et al., 2021). In addition to the minimally invasive extraction of ISF in the form of microneedles mentioned above, ISF can also be extracted to the skin's surface by reverse iontophoresis or ultrasonic introduction (Leboulanger et al., 2004; Yu et al., 2012). However, similar to sweat sensing, contamination in the process of collecting ISF will affect the accuracy of sensing, so it is necessary to develop more innovative and refined extraction methods.

Tears

Tears are transparent water forms secreted by lacrimal glands and conjunctival goblet cells. They contain a variety of chemical components, such as water, proteins, electrolytes, sugars, and organic acids (Butovich, 2008; Pankratov et al., 2016). The dynamic balance of the various components within tears ensures the health of individuals. Changes in tear composition can also be used to predict some disease information (Sempionatto et al., 2019). For example, breast cancer patients express a complement protein which is different from non-patients (Evans et al., 2001). Continuous monitoring of tear glucose concentrations can be used in the adjuvant treatment of diabetes (Sen and Sarin, 1980; von Thun und Hohenstein-Blaul et al., 2013). Elevated intraocular pressure is the risk factor for glaucoma and lead to blindness in severe cases (Leonardi et al., 2004; Mansouri et al., 2012; Chen et al., 2013). These indicate analysis of the eye microenvironment including specific analytes in tears is crucial means for long-term, non-invasive monitoring of human health.

Herpes simplex virus serotype-1 (HSV-1) is a major infectious disease that causes blindness in people all over the world (Carr et al., 2001; Streilein et al., 1997). From infection to virus activation and then to disease, patients exhibit signs of corneal scar formation, thinning, neovascularization, etc., accompanied by inflammatory reactions (Hamrah et al., 2010; Liesegang, 2001). Therefore, it is vital to identify and monitor enough biomarkers to predict the pathological state before the virus is activated in the patient. Mak et al. (2015) adopted a facile layer-by-layer (LBL) surface engineering technique to develop a hyperthermic recessive lens with a bifunctional hybrid surface that could be used to interfere with the activity of HSV-1. The contact lenses offered excellent surface wettability and optical transparency, and were non-toxic to human corneal epithelial cells (HCECs). Furthermore, the device promoted high analytical sensitivity to interleukin-1α, and the detection limit was 1.43 pg ml^{-1}. Kim et al. developed a contact lens with a built-in wireless smart sensor (**Figure 2E**) (Kim et al., 2017c). The contact lenses include highly stretchable, transparent graphene sheets, and metal nanowires, which endowed the glasses with high transparency (>91%) and elongation (~25%), thus ensuring good eye comfort and visual patency. The intraocular pressure (IOP) was measured by a non-conductive dielectric layer. As the intraocular pressure increasesd the radius of corneal curvature became larger. IOP sensors embedded in contact lenses can detect this and send information to a wireless antenna. In addition, tear glucose monitoring was performed using a highly sensitive FET biosensor. Liu et al. (2021) designed and fabricated an ultra-sensitive contact lens sensor to continuously monitor IOP. The contact lens was formed by compounding a uniform graphene

film on a flexible polyimide substrate *via* face-to-face water transfer technology. Its average sensitivities on silicone eyes and pig eyes were 1.0164 mV $mmHg^{-1}$ and 3.166 mV $mmHg^{-1}$, respectively. Another study developed an intelligent flexible contact lens by integrating glucose sensor, wireless energy transmission circuit and wireless sensor signal display (Park J. et al., 2018). The sensor contained graphene channels on which glucose oxidase (GOD) was immobilized. When the channels were soaked with tears, glucose molecules and their reduction products could be oxidized by GOD and oxygen molecules in turn to generate main carriers such as protons and electrons. The density of main carrier was positively correlated with glucose concentration which can be detected by establishing the function of relative change of sensor resistance and glucose concentration. The sensing contact lens can detect tears with glucose concentration greater than 0.9 mM, and the minimum detection concentration is 12.57 μM. Contact lens sensor is a suitable tear monitoring platform. It does not cause any irritation to the eyes but can continuously contact with tears and does not need to provide a liquid collection device based on an ISF analysis sensor (Pankratov et al., 2016). Besides glucose monitoring, non-invasive monitoring with MMP-9 in tears as a nonspecific inflammation analyte may improve the diagnosis of eye inflammation (Chotikavanich et al., 2009; Wei et al., 2013). The levels of tear cytokines Th1 and Th17 are usually associated with dry eye disease (Fujishima et al., 2016). The changes in the content of these potential tear target analytes are consistent with those in the blood, it needs to be further verified whether they follow the tear-blood concentration correlation.

Wound Fluid

Wound management requires optimization by monitoring wound indicators and information-containing molecules in wound fluids. Wearable wound dressings and bandages for real-time monitoring contribute to detecting the wound healing state and evaluating potential follow-up treatments. Changes in uric acid levels are related to the degree of damage to the leg venous ulcer wound and oxidative stress (Fernandez et al., 2012). Kassal's team prepared uric acid sensor with Prussian blue-carbon electrode on soft dressings by screen printing process, and then combined with a customized wearable potentiostat to develop a smart bandage with wireless capability (Kassal et al., 2015) (**Figure 2F**). The team also developed an intelligent bandage could optically monitor pH changes at the wound with high precision (Kassal et al., 2017). Pan et al. (2019) developed a simple color-changing fiber sensing material by adding curcumin, a functional biocompatibility indicator, to monitor the pH of a wound in real time. Another study used polyvinyl alcohol (PVA) foams and sodium carboxymethyl cellulose (CMC) nanofibrous membranes as composite substrates filled with stearyl trimethyl ammonium chloride and methylene ammonium bromide to prepare a multilayer net wound dressing (He M. et al., 2020). CMC had certain hemostatic properties because of its irregular reticular structure, while PVA foam had excellent adsorption properties and can repair the wound exudate. Under 650 nm laser irradiation, the killing of bacteria could be achieved by activating the photodynamic reaction of MB and thus generating bactericidal reactive oxygen species. The detailed discussions are in the next section "*Detection and Treatment During Wound Healing*".

Intelligent wearable sensor devices can provide real-time information about the state of wound lesions. The wound healing cycle is often long, and the sensors based on wound fluids usually cannot work until the wounds are healed and are easily contaminated. Therefore, it requires a high degree of consistency in the sensor's detecting performance during the healing process. In addition, the development of the sensor with self-cleaning performance is an exciting research direction, which can reduce the number of sensor replacements, production costs and patient compliance.

Other

In addition to the intelligent bandages and dressings introduced above, wearable sensing devices embedded directly to the surface of the epidermis are another potential future epidermal and wound sensing solution.

In 2014, Hattori et al. (2014) proposed a skin-like epidermal electronic system that could be laminated gently onto the wound and provided accurate real-time monitoring of wound healing in a clinical environment. Several groups of miniature metal resistors in this system could measure the wound surface temperature with multi-mode and high precision. A soft film was covered with miniature metal wires and precision skin temperature measurement and curve determination were achieved using high-end infrared cameras. In addition, the system could record the thermal conductivity of the focus tissue after disinfection. Inspired by the natural structure and function of the skin, Zhao et al. (2019) developed a novel antibacterial conductive hydrogel (PDA@AgNPs/CPHs) made *via* supramolecular assembly of polydopamine-modified silver nanoparticles (PDA@AgNPs), polyaniline, and polyvinyl alcohol. PDA@AgNPs/CPHs not only offer adjustable mechanical and electrochemical properties, good self-healing ability, and repeatable adhesion, but also can monitor large-scale human movements in real time. Further research revealed that the hydrogel could promote wound healing of a diabetic foot *via* promotion of angiogenesis when attached to the mouse model of an ulcerated wound. It accelerated collagen deposition, inhibited bacterial growth, and controlled wound infection. In another study, Ershadetal et al. (2020) proposed a new type of biomedical circuit: a super-conformal drawn-on-skin (DoS) electronic device. It could be used to treat skin wounds of arbitrary shape and to track and monitor physiological signals such as muscle signals, the heart rate, and the skin moisture content (**Figure 2G**). DoS electronic products are directly "written" on human skin using liquid functional ink to form wearable electronic devices that are super-conformal, expandable, and unaffected by movement. In addition, DoS devices offer stable performance during perspiration, capture electrophysiological signals reliably for long periods, adhere well to skin, and are immune to motion artifacts during sensing. After using the DoS electrode to draw circuits on the backs of depilated mice and

perform electrical stimulation, it was found that the degree of wound healing was higher in electrically treated mice than that in untreated mice, thus confirming that skin pulse electrical stimulation driven by skin electronics can promote wound healing. Hydrogel-based multi-functional products have gradually become materials of interest for simulation of human skin perception and provision of protection functions. However, there are few cases of hydrogels with conductive sensing functions that work with interfacial interactions between the environment and hydrogel materials (Ge et al., 2020). For this reason, Lei et al. (2021) proposed a new generation of hydrogel ion skin materials with biomimetic ion channels. These materials could achieve signal transmission between biological and abiotic interfaces and are expected to extend simple skin sensory diagnosis to effective treatment in clinical applications (Lei et al., 2021). A more advanced "intelligently adhered" polyelectrolyte hydrogel (QAAH)-ionized skin based on quaternized chitosan (QCS) was reported in another study. It could be used for medical monitoring of multiple physiological signals (temperature, pressure, pH, and ECG) (Shi and Wu, 2021). The thermal response behavior of QAAH was enabled *via in-situ* polymerization of acrylic acid (AA) monomer in QCS aqueous solution. The pH response behavior is related to the protonation effect of the amino group in QCS. The excellent conductivity, adhesion, and formability are the result of reversible ion association and hydrogen bond physical crosslinking of QAAH. This type of green material, which offers multi-signal resolution and adjustable mechanical and visual effects, has substantial value in clinical medical auxiliary device and intelligent wound management applications. Wang C. et al. (2018) introduced a type of ultrasonic-based wearable flexible monitoring patch that can be in close contact with the skin. It is used for non-invasive, continuous, accurate monitoring of vascular signals in many parts of the human body (**Figure 2H**). The entire device is assembled layer-by-layer using polyimide, copper electrode, copper/tin electrode, piezoelectric column, and epoxy resin layers. When installed in the human neck, the device can monitor the central blood pressure by capturing the vascular diameters of the carotid artery, internal jugular (int. jugular) vein, and external jugular (ext. jugular) vein. In addition, the device can use a highly directional ultrasound beam to locate the dynamic anterior (ant.) and posterior (post.) walls of blood vessels, and display the corresponding shifting echo radiofrequency signals reflected. This is an example of a new type of conformal telescopic ultrasound equipment that can be used to record a series of key central blood vessel features and is safe and reliable.

There are considerable innovative achievements related to new, intelligent wearable sensors in the field of public health monitoring and medical care. In the future, researchers should focus on the development of multi-functional sensors for all aspects of human physiological information detection and human motion signal tracking. These will help to improve the current medical service and health care system.

DETECTION AND TREATMENT DURING WOUND HEALING

The rate of chronic complex trauma diagnoses increases every year worldwide. Health care institutions and hospitals must invest large amounts of resources in the diagnosis and management of wounds. At the same time, wound refractory symptoms caused by traumatic infection, spontaneous ulcers, and other chronic diseases are becoming increasingly common. Patients must bear costly medical expenses related to wound prevention, care, surgery, and long-term hospitalization (FrykbergRobert and Banks, 2015; Sen et al., 2009). The skin is the human organ with the largest surface area. It serves to regulate the body temperature and repairs itself automatically (Vig et al., 2017). Exudate flows out when the skin is injured. During different stages of wound healing, the exudate may contain various biomolecules (such as potential hydrogen, glucose, uric acid, and glutathione), biochemical factors (such as tumor necrosis factor-α and interleukin-6), and pathogens (such as *Pseudomonas aeruginosa*). Their concentrations and properties provide key information about the state of the wound. In addition, wound healing is accompanied by changes in several biological signals (redox state, pressure, temperature), which can be used to predict wound development and trauma-related changes. A typical wound monitoring sensor is composed of target analyte identification, signal processing, and signal acquisition elements (**Figure 3**). Wearable devices based on various sensing modes are widely used to monitor the wound environment and exudate markers (McLister et al., 2014; Steinberg et al., 2016), including screen-printed electrode potential sensing, cyclic voltammetry sensing, linear fast voltammetry sensing, amperometric sensing, and colorimetric sensing (Guinovart et al., 2014; Steinberg et al., 2015; Kafi et al., 2019) (**Table 3**).

Biochemical Molecules

The levels of various biochemical molecules [C-reactive protein, potential hydrogen (pH), glucose, uric acid, etc.] are dynamic balances in the normal skin. However, the wounds break the healthy balance of various biochemical molecules in skin environment. Specific wound types induce responding changes in the levels of biochemical molecules, and these parameters can provide reliable information for evaluating wound healing. The proteins in the wound exudate are closely related with the symptoms. For example, acute-phase proteins such as C-reactive protein (CRP) indicate the presence of infection when the local concentration increases (James et al., 2000). To facilitate the monitoring of biochemical molecules in wounds, Voirin and colleagues developed responsive hydrogels with functional surfaces to monitor pH changes and CRP concentrations, respectively (Pasche et al., 2008). The pH-responsive hydrogel systerm can continuously monitor the pH of serum with the adjustable pH measurement range. In addition, the hydrogel was marked with the optically sensitive CRP receptor. Specific adsorption of CRP leaded to changes in the interfacial refractive index detected by a spectrometer in real-time wound state. An increase in CRP indicated a serious infection and

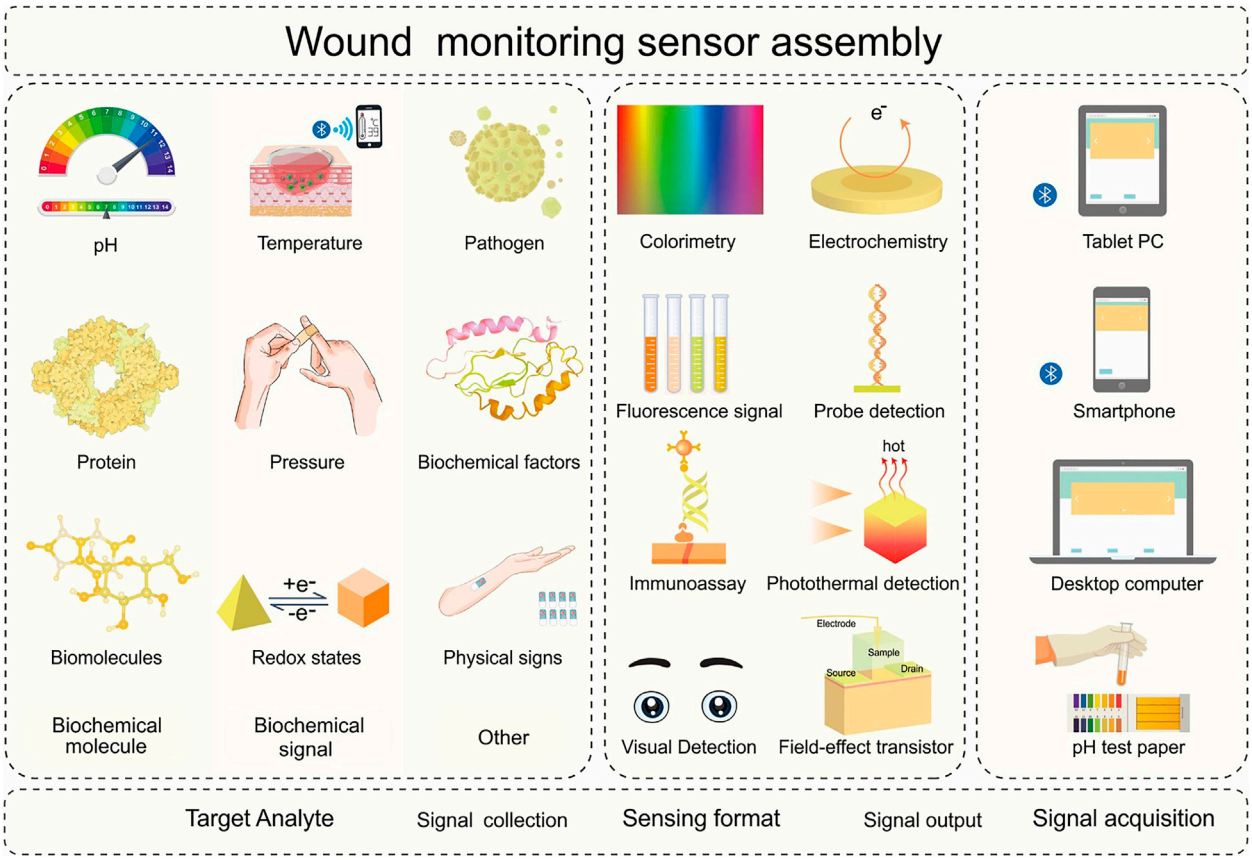

FIGURE 3 | Schematic diagram of the sensing process and integration of the wound monitoring sensor. The target analyte identification element in the wound monitoring sensor can selectively collect various target analytes in different biofluids. The signal processing elements can collect signals using various biochemical sensing formats. The signal acquisition element can process and output analytical results intelligently. The target analytes may include biochemical molecules (potential hydrogen, protein, biomolecules), biochemical signals (temperature, pressure, redox status), and other parameters (pathogens, biochemical factors, physical signs). Sensing formats include colorimetry, fluorescence signal, immunoassay, visual detection, electrochemistry, probe detection, photothermal detection, and Field-effect transistor. Signal acquisition components include pH test strips, computers, tablets, and mobile phones.

a decrease indicated the end of infection. Jankowska et al. (2017) developed a fluorescent sensor for simultaneous detection of pH and glucose concentrations. It can be used to distinguish the common and chronic wounds during their early stages (**Figure 4A**). The sensitivity of pH dye for a chronic wound environment reached the range of 6–8. The metabolic enzyme system sensing can identify low glucose concentrations in the exudate of an artificial wound. To optimize the treatment of wound sensors in chronic and complex wounds, Mirani et al. (2017) proposed a smart hydrogel dressing (GelDerm) with a colorimetric pH sensor and drug-eluting stent. It can perform continuous local release of antibiotics without imposing adverse side effects on other organs based on highly accurate inspection of bacterial infection and visual pH detection (**Figure 4B**). Cui et al. (2020) developed an intelligent wound dressing of alginate fibers with enhanced antibacterial properties and a visual monitoring of wound healing by continuous pH range detection from 2 to 11. Pal et al. (2018) suggested a simple, low-cost, non-invasive wound detection strategy, and prepared omniphobic paper-based smart bandages (OPSBs) by fixing a reusable wearable potentiostat between the adhesive layer and the absorption pad of a commercial bandage to detect pH and uric acid levels simultaneously and communicate the wound status to users or medical staff *via* wireless reports. Liu and Lillehoj (2017) utilized embroidery technology to integrate an electrochemical sensor into a flexible cotton gauze for excellent wound evaluation by continuously detecting uric acid (**Figure 4C**). Roychoudhury et al. (2018) compounded an enzyme potentiometric biosensor onto the soft cloth of a medical bandage *via* screen printing for sensitive real-time detection of uric acid in wounds as small as 0.5 μl. In addition, the sensing bandage contained a data processing microcontroller for information transmission.

Biochemical Signals

In addition to biochemical molecules for wounds monitoring, biochemical signals (wound temperature, pressure, and redox state) are also significant for wounds detection and treatment. Sun et al. (2018) prepared a sensor dressing to detect redox state changes during wound healing. First, they successfully constructed a redox-sensitive surface-enhanced Raman

TABLE 3 | Representative new intelligent sensor platforms for wound healing.

		Target analyte	Material or platform	Wound type	Detection limit	Biosensing format	References
Wound monitoring sensor	Biochemical molecule	pH, C-reactive protein (CRP)	Integrated portable system	Acute wound	6–8 (pH) 1 μg/ml (CRP)	Optical signal	Pasche et al. (2008)
		pH, Glucose	Fluorescence sensing system	Chronic wound	6.0–7.7 (pH) 2.5 Mm (Glucose)	Fluorescence signal	Jankowska et al. (2017)
		pH	Wound dressing	Acute or chronic wound	NR	Colorimetry	Mirani et al. (2017)
		pH	Wound dressing	Acute or chronic wound	2–11	Colorimetry	Cui et al. (2020)
		Uric acid	Wound dressing	Simulated wound fluid	NR	Amperometry	Liu and Lillehoj (2017)
		Uric acid, Ph	Bandage	Pressure ulcers	0.2 mM (Uric acid) 5.5–8.5 (pH)	Amperometry	Pal et al. (2018)
		Uric acid	Bandage	Chronic wound	NR	Amperometry	RoyChoudhury et al. (2018)
		Glucose, cell proliferation rate	Thin flexible patch Spatially sensitive	Diabetic wound	10 mM (Glucose)	Cyclic voltammetry, linear swift voltammetry	Kafi et al. (2019)
		Glutathione	Hydrogel system	Chronic wound	NR	Visual detection	Gao et al. (2019b)
		Redox states	Wound dressing	Acute wound	NR	Probe detection	Sun et al. (2018)
		Pressure	Bandage	Chronic wound	0.1 kPa	Fluorescence signal	Leal-Junior et al. (2021)
		Pressure	Bandage	Pressure ulcers	5 mmHg	Amperometry	Farooqui and Shamim, (2016)
	Biochemical signal	Temperature	Electronic skins	Infected wound	30–70°C	Amperometry	Gong et al. (2019)
		Temperature	Flexible wound healing system	Infected wound	39–39.5°C	Amperometry	Lou et al. (2020)
		Temperature	Wound Dressing	Infected wound	25–45°C	Amperometry	Pang et al. (2020)
		Temperature	Wound Dressing	Infected wound	25–45°C	Amperometry	Xu et al. (2021)
		Temperature	Flexible integrated sensing platform	Infected wound	33–41°C	Amperometry	Zhang et al. (2021)
	Other	P. aeruginosa	Microfluidic patch	Infected wound	2.1×10^5 CFU/ml	Flow immunoassay	Brunauer et al. (2021)
		Tumor necrosis factor–α, interleukin-6 (IL-6), IL-8, transforming growth factor–β1	Flexible multi- Venous channel immune ulcer patch	Leg	NR	Electrochemical-amperometry	Gao et al. (2021)
		S. aureus	Paper-based biosensor		7 CFU/ml	Colorimetric	Suaifan et al. (2017)

scattering (SERS) probe by modifying redox-sensitive anthraquinone molecules on gold nano-shells (GNSSs). Then, the SERS probe was attached to the surface of a chitosan film. Finally, the temporal and spatial evolutions of the wound healing redox state were measured *via in-situ* and non-invasive collection of SERS spectroscopy. The study found that it may be necessary for the redox potential to be minimized during wound healing. Normal wound healing is affected by both the internal pressure of the wound environment and the external pressure exerted by the bandage. The Leal-Junior team proposed a smart bandage based on a highly flexible polymer fiber to evaluate the pressure and pH of the wound area simultaneously (Leal-Junior et al., 2021). The intelligent bandage includes a pH sensitive fiber made from rhodamine B dye-doped polydimethylsiloxane (PDMS) and traditional medical gauze. The low Young's modulus of the PDMS fiber ensures the high sensitivity of the pressure sensor. The bandage can measure pressures as low as 0.1 kPa and exhibits a highly linear correlation over the 0–0.3 kPa range. Farooqui et al. developed an intelligent bandage using inkjet printing technology to continuously monitor irregular bleeding, pH, and external pressure of the wound (Farooqui and Shamim, 2016). The intelligent bandage assembly includes a disposable tape on which the reusable sensors were printed. The capacitive

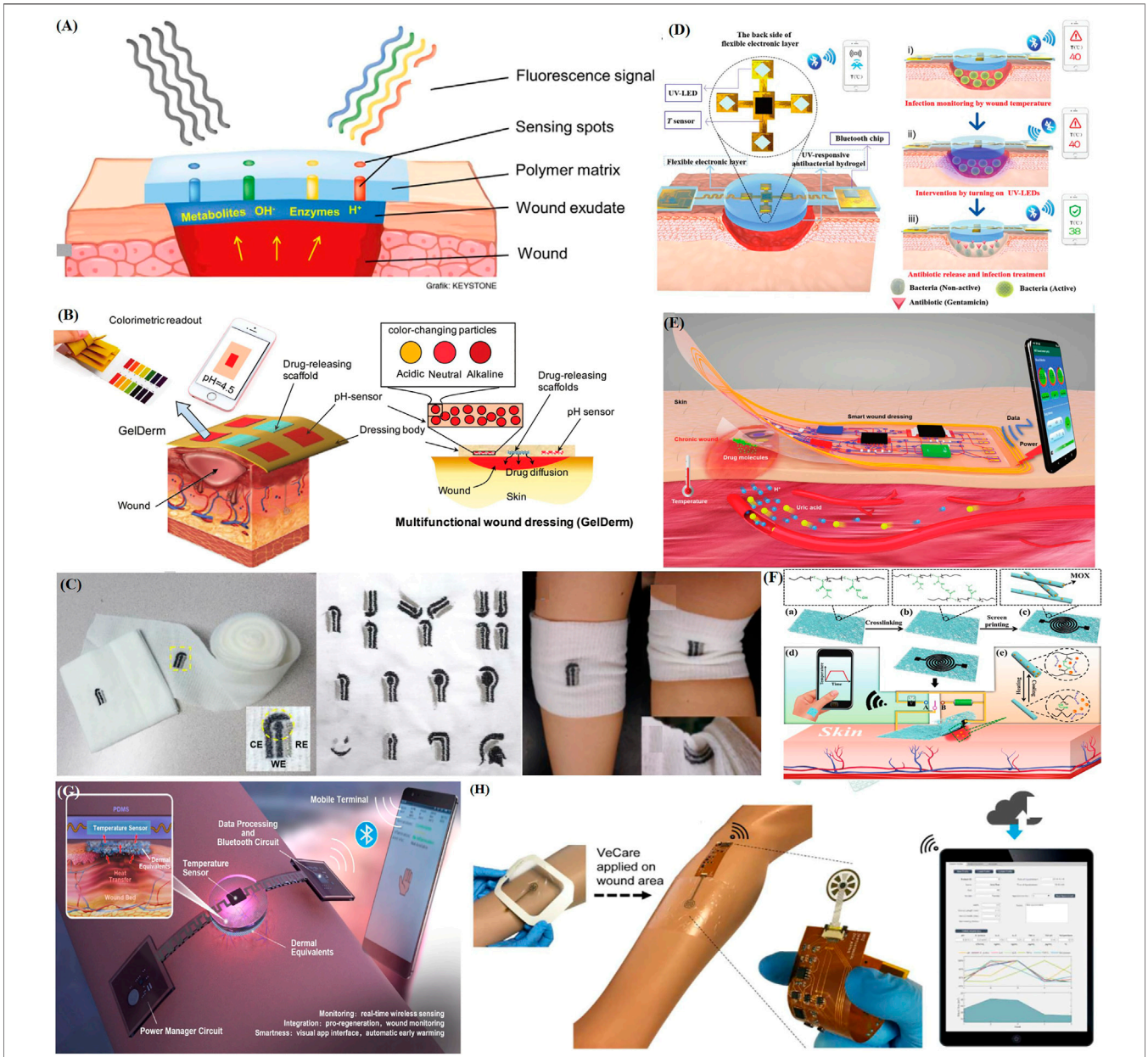

FIGURE 4 | Recent applications of representative intelligent wearable sensors for wound healing. **(A)** Schematic diagram of a fluorescence sensing system with glucose concentration and pH detection (Jankowska et al., 2017). **(B)** Schematic diagram of an intelligent hydrogel dressing (GelDerm) with pH sensitive and drug eluting components for treatment of epidermal wounds (Mirani et al., 2017). **(C)** An electrochemical sensor fabricated on gauze, a wound dressing produced *via* embroidery, and examples of their application to an elbow (Liu and Lillehoj, 2017). **(D)** Intelligent electronic temperature sensing dressing composition and principle schematic diagram (Pang et al., 2020). **(E)** Schematic diagram of a battery-free wireless wound dressing for wound infection monitoring and electronically controlled on-demand wound-site drug delivery (Xu et al., 2021). **(F)** Flow chart showing the preparation of a flexible, breathable skin-based electronic device with temperature sensing capabilities and temperature-based on-demand drug release (Gong et al., 2019). **(G)** Schematic diagram of the structure and sensing principle of a flexible wound healing system (FWHS) (Lou et al., 2020). **(H)** Schematic diagram of a flexible microfluidic multi-immunosensor platform for chronic wound monitoring; a built-in flexible printed circuit board (FPCB) is connected to a wireless portable analyzer and external mobile applications that can be used for patient files, medical records, data records, and data analysis (Gao et al., 2021).

sensor can detect irregular bleeding-driven changes in the dielectric constant between the electrodes on the two sides of the bandage. Changes in the wound pressure lead to changes in the distance between the electrodes. In addition, the conductivity of the resistive sensor carbon electrode varied with the pH.

Bacterial infection of wounds is an increasingly serious public health problem and imposes large medical and economic burdens. If bacterial reproduction and transfer can be detected and stopped at the early stage, further deterioration of the lesion can be prevented (Ivnitski et al., 1999). Hao et al. (2021) proposed

a vancomycin-doped Prussian blue nanoparticle (PB-VANNP) platform that could perform high-sensitivity bacterial detection and avoid secondary pollution by killing bacteria efficiently. The multi-functional nano-platform has the advantages of high sensitivity, low cost, and simple detection. Mostafalu et al. (2018) prepared a smart dressing consisted of two parts: a disposable patch and a reusable pH and temperature sensors with a thermally responsive drug-release bead and a microcontroller. The dressing could indicate the wound state in real time, process sensor data and manage individualized drug release. A recent innovative study demonstrated a drug release dressing controlled by a single exogenous stimulus. The dressing had a double-layer structure in which the upper layer was a flexible electronic device with a temperature sensor and an ultraviolet light-emitting diode encapsulated in polydimethylsiloxane. The lower layer was an ultraviolet (UV)-responsive antibacterial hydrogel (Pang et al., 2020). The wound temperature was monitored continuously using a temperature sensor and transmitted to a foreign terminal device (for example, a smartphone) *via* Bluetooth. When the wound temperature remained above a preset threshold (for example, 40°C) for a period of time, the infected wound was diagnosed and the integrated UV-LED activated to achieve *in-situ* antibiotic release in order to inhibit wound infection. This eventually lowered the wound temperature (**Figure 4D**). This study combined advanced biomaterials with flexible sensors to provide a new dynamic intervention-based therapy strategy. Xu et al. (2021) used flexible electronic processing technology to construct a wireless intelligent dressing to perform *in-situ*, multi-parameter, and real-time monitoring of a wound and control antibiotic release electronically (**Figure 4E**). The intelligent dressing can detect changes in physiological parameters such as the pH, uric acid content and temperature of the wound to determine the degree of infection and provide sufficient information for doctors to adjust the treatment plan accurately. The dressing included NFC technology to achieve information transmission and signal processing using external equipment. It can also treat the wound by releasing the antibacterial drug cefazolin on the wound surface by controlling the voltage of the drug delivery module. This wound care management technology can be used widely in the fields of multi-functional and personalized medicine and health care.

A flexible, breathable electronic device with real-time temperature sensing functions was proposed to monitor the infection or inflammation at the wound site and eliminate bacterial infection on demond by a thermally responsive fiber (Gong et al., 2019). The device was assembled from cross-linked electrospun moxifloxacin hydrochloride (MOX) loaded with a thermally responsive poly(N-isopropyl acrylamide-co-N-methylol acrylamide) (C-PNHM) nano-mesh film. The nano-mesh film contained a screen-printed conductive pattern (SC-PNHM) (**Figure 4F**). Lou et al. (2020) developed a flexible wound healing system (FWHS) to monitor the significant physiological process of wound healing and provide early warning and diagnosis of infection and wound invasion (**Figure 4G**). The system consisted of a double-layer: the upper layer included a flexible temperature sensor, a power-management circuit and a data processing circuit; the lower layer was composed of a collagen-chitosan dermal substitute. The system displayed good reliability and *in vitro* biocompatibility, as well as good accuracy, stability, and scalability. Zhang et al. (2021) proposed a flexible, integrated sensing platform (FISP) for monitoring local wound temperature as a reference for early prediction of pathological wound infection. The real-time wound temperature during each infected period was analyzed *via* multiple logarithmic regression. The higher the local temperature of the wound, the greater the risk of infection with gram-positive bacteria. In addition, the resulting data could be transmitted to the external device *via* Bluetooth. This work is expected to play an important role in wound diagnosis, remote treatment and artificial intelligence diagnosis.

Other

Although there are researches for monitoring pathogens in wounds and treating infected wounds, the infection detection, and wound treatment are designed for broad-spectrum pathogen detection and inhibition (Lister et al., 2009; Bui et al., 2019; Edwards and Harding, 2004). Blind, untargeted administration will lead to additional side effects. To accurately and quantitatively obtain reliable POCT data such as *Pseudomonas aeruginosa* (*P. aeruginosa*), Brunauer et al. (2021) proposed a nucleic-acid lateral flow immunoassay approach to achieve rapid detection of specific infected wound pathogens. First, the gene DNA (gDNA) from the rough cleavage fluid was amplified by beading the pathogen. Then, the amplified product was detected using a nucleic acid lateral flow immunoassay. Rapid process chain analysis of pathogens could be completed *via* a simple diagnostic process. The time required for *P. aeruginosa* was less than 30 min and the lowest wound exudate detection limit was 2.1×10^5 CFU/ml. Complex wounds are the result of slow healing due to a variety of environmental and physiological factors. These factors are reflected in the composition of the wound exudate, which includes a dynamic mixture of biochemical factors (cytokines, growth factors) and microorganisms during wound healing (Drinkwater et al., 2002). In order to better monitor potential multivariable pathological factors in chronic wounds and implement more personalized treatment strategies, Gao et al. (2021) proposed a flexible microfluidic multiple immunosensor platform for multivariate analysis of the wound microenvironment at care points (**Figure 4H**). The sensor system integrated a sensor array, a microflow wound exudate collector, and flexible electronic devices for real-time detection of inflammatory mediators (tumor necrosis factor-α, IL-6, IL-8 and transforming growth factor-β 1), the microbial load (*S. aureus*) and various physicochemical parameters (temperature and pH). The detection results can be read wirelessly. Thus, the data can be collected, analyzed, and visually referenced using external devices. This approach is expected to produce intelligent auxiliary dressings for clinical treatment and provide more personalized clinical diagnostic information.

As we all know, judging the condition of a wound based on single or partial biochemical information cannot replace standard pathological diagnosis. One cannot infer the wound infection

stage and pathogen type using only a single reading of the wound pH, temperature, and pressure. However, the above-mentioned sensing technology designed for wound monitoring and healing can provide preliminary analysis of wound lesions during the window period before pathological diagnosis. This can reduce patient psychological burdens and mental stress. Although a variety of wearable sensor devices were designed for wound window diagnosis, research and development of multi-marker analysis sensor devices are required to provide more comprehensive real-time wound infection and healing information. In the future, an advanced generation of wearable devices will provide users or patients with more comprehensive and accurate real-time physiological information based on molecular or environmental signals and transmit the relevant information to a variety of applications for medical wound and health care management. Before these multi-functional and wearable sensors are used widely in clinics, they must pass a series of scientific and human application tests. There must also be a good understanding of the correlation between sensor information and a medical diagnosis. Therefore, substantial further research on intelligent, wearable sensor devices is required. Future studies may focus on material innovation and the development of a variety of analysis systems. We look forward to exciting new developments in this field shortly, as well as to continuous improvements in patient quality of life and the medical environment.

DISCUSSION, CONCLUSIONS, AND FUTURE RESEARCH

The purpose of this review is to summarize the opportunities provided by the development of intelligent, wearable sensors for healthcare and wound heal. We illustrate how researchers have designed intelligent, wearable sensors to collect and analyze target analytes from various biofluids. In addition to providing a tabulated summary of new biochemical sensing modalities and novel sensing platforms, we highlight the extension of the utility of these new monitoring platforms for assessing human health status and healthcare applications. These include achieving simultaneous monitoring of multiple informative metrics to detect specific diseases and expanding intelligent wearable sensors from the laboratory scale to a more natural clinical setting wherever possible. Since the advent of lab-scale intelligent sensing devices, health monitoring and wearable biochemical sensors have often been linked to the human skin and tissue interface. With the deeper implementation of related studies, other advanced sensing technologies, including microneedle sensing technology, will become an important part of future medical services. The microneedle sensing device can obtain and analyze biofluids painlessly and minimally invasively, which can avoid tissue damage and foreign body reactions to the greatest extent and is quite important for early human health monitoring and disease prevention. In addition, the future design of microneedle sensor needs to pay attention to the following points: After the device is implanted in the epidermis, in addition to monitoring the target analyte, it can also analyze and monitor the inflammatory response that may occur in the body due to the foreign body reaction, which may provide a reference for the development of minimally invasive microneedle devices with more precise and independent monitoring performance. Moreover, larger and more circumscribed improvements, such as the development of rapid, durable, reliable, and miniaturized sensor strategies, will be necessary for clinical analysis and the application of continuous health monitoring to chronic diseases and human health data. Meantime, the integrated analysis-diagnosis-treatment sensor device can provide great convenience for patients with self-care ability.

Although some progress has been made in developing advanced intelligent wearable sensors, there are still a series of challenges as follows: 1) Although most of the sensors with high sensitivity and high precision have good clinical application prospects, the performance of the sensor will degrade with the continuous operation, and the quality of the sensor still needs to be improved. At the same time, when the sensor continues to collect, transport, and analyze biological fluids, it is necessary to improve the reliability of the sensor and the consistency with the relevant target analyte concentration changes, to avoid frequent sensor replacement. 2) The accuracy and sensitivity of the sensor are also related to its surface fouling. If the sensor collects biological fluid with relatively complex components or turbid adhesion (such as pus exudated from infectious wounds), it may affect the regular operation of the sensor. Therefore, developing advanced sensing devices with surface antifouling properties and self-sensing calibration modes (multi-detection modes or multi-analyte sensors) is necessary. 3) Most intelligent wearable sensors can only detect target analytes in common biological fluids. People also need to develop the sensor systems for analysis of more other body fluids. For example, nipple secretion can be obtained directly in a non-invasive way, and the level of hormones and protein contained may strongly correlate with certain diseases. Nipple aspiratefluid steroid hormone levels and plasminogen activator inhibitors can be used as target analytes to detect breast cancer (Shidfar et al., 2016; Shaheed et al., 2017). 4) Some self-powered sensor devices can only meet the operational needs of the sensor itself. However, the sensor needs more energy supplement in data analysis, acquisition, and wireless communication. Therefore, it is urgent to integrate more efficient power supply methods. At present, energy storage devices (supercapacitors) (Wang et al., 2016), organic solar cells (O'Connor et al., 2016), biofuel cells (Jia et al., 2013), thermoelectric generators (Oh et al., 2016), and their composition are integrated to solve this challenge.

In the first half of this article, we chronicled recent advances in wearable intelligent sensing devices for personal healthcare and emphasized their advantages concerning achieving high precision, high sensitivity, and high stability health diagnoses. We gave an overview of various intelligent sensors (patches, dressings, microneedles, tattoos) and the related detection principles (colorimetry, security, probe assay, fluorescent signaling method). Judging from current areas of research interest, advances in microfluidic biosensors and electrochemically integrated sensors are focused on

miniaturization design. This greatly enhances biosensor sensitivity, stability, and portability. Colorimetric biosensors are widely used for their visual readout features; wearable chemical and biosensors increasingly tend to energy autonomy. Cheap, simple, efficient wearable sensors can be made *via* inkjet, screen, and 3D printing technologies. Intelligent, wearable sensors can be used to monitor specially targeted analytes in raw fluids for early detection of human health changes. Blood remains the most authoritative biological fluid for human physical examination and screening. However, additional attention has been paid to more easily available, naturally secreted biofluids (sweat, interstitial fluid, tears, and wound fluid). Sample liquids are collected by an advanced sensor system and analyte information is collected. The results are transmitted to the user's or patient's interface either directly or *via* Bluetooth, NFC, or high-frequency passive RFID to provide appropriate information to patients, users, and doctors. However, the current challenge is that the associated communication often suffers from defects such as a low transmission rate or incompatible equipment. Therefore, other next-generation technologies, such as optical wireless technology, are needed urgently to develop information transmission algorithms and apply them to wearable devices.

The difficulty of nursing complex wounds should not be underestimated. Intelligent wound dressings are needed for diagnosis, treatment, monitoring, practical application, and sensor function. The second half of this paper summarized the application of emerging "smart + connected" wound sensing devices to monitor various target analytes from different types of wound models (i.e., infected, chronic, and acute wounds). It provided a new strategy for scientific wound care and reliable prediction. We believe that there will be more advanced and innovative scientific experiments and methods that can extend the concepts of wearable sensing devices to clinical medicine and health care. By reasonably weighing the public treatment strategies, this type of equipment can help a transition from a profit-based product model to a shared health care model based on the nature of public services. If this trend succeeds, it will be a vital achievement for the health care industry and will help users to have healthy lives.

AUTHOR CONTRIBUTIONS

SC wrote the manuscript. SC, LZ, MH, HA, KS, XW, ZZ, YD, and KZ revised the manuscript. ZG, YD, and YW designed the work of review and revised the manuscript. All authors contributed to the article and approved the submitted version.

FUNDING

National Natural Science Foundation of China (21975019), Beijing Science Technology New Star Cross Subject (2018019), Fundamental Research Funds for the Central Universities (FRF-TP-20-019A2, FRF-BR-20-03B), Beijing National Science Foundation (2172039), and the Fundamental Research Funds for the Central Universities and University of Science and Technology Beijing (USTB).

REFERENCES

Aderibigbe, B., and Buyana, B. (2018). Alginate in Wound Dressings. *Pharmaceutics* 10, 42. doi:10.3390/pharmaceutics10020042

Bandodkar, A. J., Jeang, W. J., Ghaffari, R., and Rogers, J. A. (2019). Wearable Sensors for Biochemical Sweat Analysis. *Annu. Rev. Anal. Chem.* 12, 1–22. doi:10.1146/annurev-anchem-061318-114910

Bandodkar, A. J., Jia, W., Yardımcı, C., Wang, X., Ramirez, J., and Wang, J. (2015). Tattoo-based Noninvasive Glucose Monitoring: A Proof-Of-Concept Study. *Anal. Chem.* 87, 394–398. doi:10.1021/ac504300n

Bandodkar, A. J., and Wang, J. (2014). Non-invasive Wearable Electrochemical Sensors: A Review. *Trends Biotechnol.* 32, 363–371. doi:10.1016/j.tibtech.2014.04.005

Barros, L. F. (2013). Metabolic Signaling by Lactate in the Brain. *Trends Neurosciences* 36, 396–404. doi:10.1016/j.tins.2013.04.002

Bocchetta, P., Frattini, D., Ghosh, S., Mohan, A. M. V., Kumar, Y., and Kwon, Y. (2020). Soft Materials for Wearable/flexible Electrochemical Energy Conversion, Storage, and Biosensor Devices. *Materials* 13, 2733. doi:10.3390/ma13122733

Broza, Y. Y., Mochalski, P., Ruzsanyi, V., Amann, A., and Haick, H. (2015). Hybrid Volatolomics and Disease Detection. *Angew. Chem. Int. Ed.* 54, 11036–11048. doi:10.1002/anie.201500153

Brunauer, A., Verboket, R. D., Kainz, D. M., von Stetten, F., and Früh, S. M. (2021). Rapid Detection of Pathogens in Wound Exudate via Nucleic Acid Lateral Flow Immunoassay. *Biosensors* 11, 74. doi:10.3390/bios11030074

Bui, U. T., Finlayson, K., and Edwards, H. (2019). The Diagnosis of Infection in Chronic Leg Ulcers: A Narrative Review on Clinical Practice. *Int. Wound J.* 16, 601–620. doi:10.1111/iwj.13069

Butovich, I. A. (2008). On the Lipid Composition of Human Meibum and Tears: Comparative Analysis of Nonpolar Lipids. *Invest. Ophthalmol. Vis. Sci.* 49, 3779–3789. doi:10.1167/iovs.08-1889

Caliò, A., Dardano, P., Di Palma, V., Bevilacqua, M. F., Di Matteo, A., Iuele, H., et al. (2016). Polymeric Microneedles Based Enzymatic Electrodes for Electrochemical Biosensing of Glucose and Lactic Acid. *Sensors Actuators B: Chem.* 236, 343–349. doi:10.1016/j.snb.2016.05.156

Carr, D. J. J., Härle, P., and Gebhardt, B. M. (2001). The Immune Response to Ocular Herpes Simplex Virus Type 1 Infection. *Exp. Biol. Med. (Maywood)* 226, 353–366. doi:10.1177/153537020122600501

Chen, G.-Z., Chan, I.-S., and Lam, D. C. C. (2013). Capacitive Contact Lens Sensor for Continuous Non-invasive Intraocular Pressure Monitoring. *Sensors Actuators A: Phys.* 203, 112–118. doi:10.1016/j.sna.2013.08.029

Chen, Y., Lu, S., Zhang, S., Li, Y., Qu, Z., Chen, Y., et al. (2017). Skin-like Biosensor System via Electrochemical Channels for Noninvasive Blood Glucose Monitoring. *Sci. Adv.* 3, e1701629. doi:10.1126/sciadv.1701629

Choi, J., Bandodkar, A. J., Reeder, J. T., Ray, T. R., Turnquist, A., Kim, S. B., et al. (2019). Soft, Skin-Integrated Multifunctional Microfluidic Systems for Accurate Colorimetric Analysis of Sweat Biomarkers and Temperature. *ACS Sens.* 4, 379–388. doi:10.1021/acssensors.8b01218

Chotikavanich, S., de Paiva, C. S., Li, D. Q., Chen, J. J., Bian, F., Farley, W. J., et al. (2009). Production and Activity of Matrix Metalloproteinase-9 on the Ocular Surface Increase in Dysfunctional Tear Syndrome. *Invest. Ophthalmol. Vis. Sci.* 50, 3203–3209. doi:10.1167/iovs.08-2476

Ciui, B., Martin, A., Mishra, R. K., Brunetti, B., Nakagawa, T., Dawkins, T. J., et al. (2018). Wearable Wireless Tyrosinase Bandage and Microneedle Sensors: Toward Melanoma Screening. *Adv. Healthc. Mater.* 7, 1701264. doi:10.1002/adhm.201701264

Cui, L., Hu, J.-j., Wang, W., Yan, C., Guo, Y., and Tu, C. (2020). Smart Ph Response Flexible Sensor Based on Calcium Alginate Fibers Incorporated with Natural Dye for Wound Healing Monitoring. *Cellulose* 27, 6367–6381. doi:10.1007/s10570-020-03219-1

Curto, V. F., Fay, C., Coyle, S., Byrne, R., O'Toole, C., Barry, C., et al. (2012). Real-time Sweat Ph Monitoring Based on a Wearable Chemical Barcode Micro-

fluidic Platform Incorporating Ionic Liquids. *Sensors Actuators B: Chem.* 171-172, 1327–1334. doi:10.1016/j.snb.2012.06.048

Dector, A., Galindo-de-la-Rosa, J., Amaya-Cruz, D. M., Ortíz-Verdín, A., Guerra-Balcázar, M., Olivares-Ramírez, J. M., et al. (2017). Towards Autonomous Lateral Flow Assays: Paper-Based Microfluidic Fuel Cell inside an Hiv-Test Using a Blood Sample as Fuel. *Int. J. Hydrogen Energ.* 42, 27979–27986. doi:10.1016/j.ijhydene.2017.07.079

Demidova-Rice, T. N., Hamblin, M. R., and Herman, I. M. (2012). Acute and Impaired Wound Healing. *Adv. Skin Wound Care* 25, 304–314. doi:10.1097/01.ASW.0000416006.55218.d0

Dervisevic, M., Alba, M., Prieto-Simon, B., and Voelcker, N. H. (2020). Skin in the Diagnostics Game: Wearable Biosensor Nano- and Microsystems for Medical Diagnostics. *Nano Today* 30, 100828. doi:10.1016/j.nantod.2019.100828

Dervisevic, M., Alba, M., Yan, L., Senel, M., Gengenbach, T. R., Prieto-Simon, B., et al. (2021). Transdermal Electrochemical Monitoring of Glucose via High-Density Silicon Microneedle Array Patch. *Adv. Funct. Mater.*, 2009850. doi:10.1002/adfm.202009850

Dienel, G. A., and Hertz, L. (2001). Glucose and Lactate Metabolism during Brain Activation. *J. Neurosci. Res.* 66, 824–838. doi:10.1002/jnr.10079

Drinkwater, S. L., Smith, A., and Burnand, K. G. (2002). What Can Wound Fluids Tell Us about the Venous Ulcer Microenvironment? *Int. J. Low Extrem Wounds* 1, 184–190. doi:10.1177/153473460200100307

Edwards, R., and Harding, K. G. (2004). Bacteria and Wound Healing. *Curr. Opin. Infect. Dis.* 17, 91–96. doi:10.1097/00001432-200404000-00004

Ershad, F., Thukral, A., Yue, J., Comeaux, P., Lu, Y., Shim, H., et al. (2020). Ultra-conformal Drawn-On-Skin Electronics for Multifunctional Motion Artifact-free Sensing and point-of-care Treatment. *Nat. Commun.* 11, 3823. doi:10.1038/s41467-020-17619-1

Evans, V., Vockler, C., Friedlander, M., Walsh, B., and Willcox, M. D. (2001). Lacryglobin in Human Tears, a Potential Marker for Cancer. *Clin. Exp. Ophthalmol.* 29, 161–163. doi:10.1046/j.1442-9071.2001.00408.x

Farooqui, M. F., and Shamim, A. (2016). Low Cost Inkjet Printed Smart Bandage for Wireless Monitoring of Chronic Wounds. *Sci. Rep.* 6, 28949. doi:10.1038/srep28949

Fernandez, M. L., Upton, Z., Edwards, H., Finlayson, K., and Shooter, G. K. (2012). Elevated Uric Acid Correlates with Wound Severity. 9, 139–149. doi:10.1111/j.1742-481X.2011.00870.x

Fogh-Andersen, N., Altura, B. M., Altura, B. T., and Siggaard-Andersen, O. (1995). Composition of Interstitial Fluid. *Clin. Chem.* 41, 1522–1525. doi:10.1093/clinchem/41.10.1522

Foster, M. V., and Sethares, K. A. (2014). Facilitators and Barriers to the Adoption of Telehealth in Older Adults. *Comput. Inform. Nurs.* 32, 523–533. doi:10.1097/CIN.0000000000000105

Frykberg, R. G., and Banks, J. (2015). Challenges in the Treatment of Chronic Wounds. *Adv. Wound Care* 4, 560–582. doi:10.1089/wound.2015.0635

Fujishima, H., Okada, N., Matsumoto, K., Fukagawa, K., Igarashi, A., Matsuda, A., et al. (2016). The Usefulness of Measuring Tear Periostin for the Diagnosis and Management of Ocular Allergic Diseases. *J. Allergy Clin. Immunol.* 138, 459–467. doi:10.1016/j.jaci.2015.11.039

Furie, B., and Furie, B. C. (2008). Mechanisms of Thrombus Formation. *N. Engl. J. Med.* 359, 938–949. doi:10.1056/NEJMra0801082

Gao, J., Huang, W., Chen, Z., Yi, C., and Jiang, L. (2019a). Simultaneous Detection of Glucose, Uric Acid and Cholesterol Using Flexible Microneedle Electrode Array-Based Biosensor and Multi-Channel Portable Electrochemical Analyzer. *Sensors Actuators B: Chem.* 287, 102–110. doi:10.1016/j.snb.2019.02.020

Gao, W., Emaminejad, S., Nyein, H. Y. Y., Challa, S., Chen, K., Peck, A., et al. (2016a). Fully Integrated Wearable Sensor Arrays for Multiplexed *In Situ* Perspiration Analysis. *Nature* 529, 509–514. doi:10.1038/nature16521

Gao, W., Nyein, H. Y. Y., Shahpar, Z., Fahad, H. M., Chen, K., Emaminejad, S., et al. (2016b). Wearable Microsensor Array for Multiplexed Heavy Metal Monitoring of Body Fluids. *ACS Sens.* 1, 866–874. doi:10.1021/acssensors.6b00287

Gao, Y., Nguyen, D. T., Yeo, T., Lim, S. B., Tan, W. X., Madden, L. E., et al. (2021). A Flexible Multiplexed Immunosensor for point-of-care *In Situ* Wound Monitoring. *Sci. Adv.* 7, eabg9614. doi:10.1126/sciadv.abg9614

Gao, Z., Golland, B., Tronci, G., and Thornton, P. D. (2019b). A Redox-Responsive Hyaluronic Acid-Based Hydrogel for Chronic Wound Management. *J. Mater. Chem. B* 7, 7494–7501. doi:10.1039/c9tb01683j

Ge, G., Lu, Y., Qu, X., Zhao, W., Ren, Y., Wang, W., et al. (2020). Muscle-inspired Self-Healing Hydrogels for Strain and Temperature Sensor. *ACS Nano* 14, 218–228. doi:10.1021/acsnano.9b07874

Gong, M., Wan, P., Ma, D., Zhong, M., Liao, M., Ye, J., et al. (2019). Flexible Breathable Nanomesh Electronic Devices for On-Demand Therapy. *Adv. Funct. Mater.* 29, 1902127. doi:10.1002/adfm.201902127

Gonzalez, A. C. d. O., Costa, T. F., Andrade, Z. d. A., and Medrado, A. R. A. P. (2016). Wound Healing - a Literature Review. *Bras. Dermatol.* 91, 614–620. doi:10.1590/abd1806-4841.20164741

Gromov, P., Gromova, I., Olsen, C. J., Timmermans-Wielenga, V., Talman, M.-L., Serizawa, R. R., et al. (2013). Tumor Interstitial Fluid - A Treasure Trove of Cancer Biomarkers. *Biochim. Biophys. Acta (Bba) - Proteins Proteomics* 1834, 2259–2270. doi:10.1016/j.bbapap.2013.01.013

Guinovart, T., Valdés-Ramírez, G., Windmiller, J. R., Andrade, F. J., and Wang, J. (2014). Bandage-based Wearable Potentiometric Sensor for Monitoring Wound pH. *Electroanalysis* 26, 1345–1353. doi:10.1002/elan.201300558

Guo, S., and Dipietro, L. A. (2010). Factors Affecting Wound Healing. *J. Dent Res.* 89, 219–229. doi:10.1177/0022034509359125

Guo, S., Lin, R., Wang, L., Lau, S., Wang, Q., and Liu, R. (2019). Low Melting point Metal-Based Flexible 3d Biomedical Microelectrode Array by Phase Transition Method. *Mater. Sci. Eng. C* 99, 735–739. doi:10.1016/j.msec.2019.02.015

Gurtner, G. C., Werner, S., Barrandon, Y., and Longaker, M. T. (2008). Wound Repair and Regeneration. *Nature* 453, 314–321. doi:10.1038/nature07039

Hallek, M., Cheson, B. D., Catovsky, D., Caligaris-Cappio, F., Dighiero, G., Döhner, H., et al. (2008). Guidelines for the Diagnosis and Treatment of Chronic Lymphocytic Leukemia: a Report from the International Workshop on Chronic Lymphocytic Leukemia Updating the National Cancer Institute-Working Group 1996 Guidelines. *Blood* 111, 5446–5456. doi:10.1182/blood-2007-06-093906

Hamrah, P., Cruzat, A., Dastjerdi, M. H., Zheng, L., Shahatit, B. M., Bayhan, H. A., et al. (2010). Corneal Sensation and Subbasal Nerve Alterations in Patients with Herpes Simplex Keratitis. *Ophthalmology* 117, 1930–1936. doi:10.1016/j.ophtha.2010.07.010

Han, W., He, H., Zhang, L., Dong, C., Zeng, H., Dai, Y., et al. (2017). A Self-Powered Wearable Noninvasive Electronic-Skin for Perspiration Analysis Based on Piezo-Biosensing Unit Matrix of Enzyme/zno Nanoarrays. *ACS Appl. Mater. Inter.* 9, 29526–29537. doi:10.1021/acsami.7b07990

Hanna, J., Bteich, M., Tawk, Y., Ramadan, A. H., Dia, B., Asadallah, F. A., et al. (2020). Noninvasive, Wearable, and Tunable Electromagnetic Multisensing System for Continuous Glucose Monitoring, Mimicking Vasculature Anatomy. *Sci. Adv.* 6, eaba5320. doi:10.1126/sciadv.aba5320

Hao, Z., Lin, X., Li, J., Yin, Y., Gao, X., Wang, S., et al. (2021). Multifunctional Nanoplatform for Dual-Mode Sensitive Detection of Pathogenic Bacteria and the Real-Time Bacteria Inactivation. *Biosens. Bioelectron.* 173, 112789. doi:10.1016/j.bios.2020.112789

Hattori, Y., Falgout, L., Lee, W., Jung, S.-Y., Poon, E., Lee, J. W., et al. (2014). Multifunctional Skin-like Electronics for Quantitative, Clinical Monitoring of Cutaneous Wound Healing. *Adv. Healthc. Mater.* 3, 1597–1607. doi:10.1002/adhm.201400073

He, M., Ou, F., Wu, Y., Sun, X., Chen, X., Li, H., et al. (2020a). Smart Multi-Layer Pva Foam/Cmc Mesh Dressing with Integrated Multi-Functions for Wound Management and Infection Monitoring. *Mater. Des.* 194, 108913. doi:10.1016/j.matdes.2020.108913

He, S., Feng, S., Nag, A., Afsarimanesh, N., Han, T., and Mukhopadhyay, S. C. (2020b). Recent Progress in 3d Printed Mold-Based Sensors. *Sensors* 20, 703. doi:10.3390/s20030703

Heikenfeld, J., Jajack, A., Feldman, B., Granger, S. W., Gaitonde, S., Begtrup, G., et al. (2019). Accessing Analytes in Biofluids for Peripheral Biochemical Monitoring. *Nat. Biotechnol.* 37, 407–419. doi:10.1038/s41587-019-0040-3

Heikenfeld, J. (20162016). Non-invasive Analyte Access and Sensing through Eccrine Sweat: Challenges and Outlook Circa 2016. *Electroanalysis* 28, 1242–1249. doi:10.1002/elan.201600018

Hughes, R. (2008). *Patient Safety and Quality: An Evidence-Based Handbook for Nurses*. Rockville, MD: Agency for Healthcare Research and Quality.

Ivnitski, D., Abdel-Hamid, I., Atanasov, P., and Wilkins, E. (1999). Biosensors for Detection of Pathogenic Bacteria. *Biosens. Bioelectron.* 14, 599–624. doi:10.1016/S0956-5663(99)00039-1

James, T. J., Hughes, M. A., Cherry, G. W., and Taylor, R. P. (2000). Simple Biochemical Markers to Assess Chronic Wounds. *Wound Repair Regen.* 8, 264–269. doi:10.1046/j.1524-475x.2000.00264.x

Jankowska, D. A., Bannwarth, M. B., Schulenburg, C., Faccio, G., Maniura-Weber, K., Rossi, R. M., et al. (2017). Simultaneous Detection of Ph Value and Glucose Concentrations for Wound Monitoring Applications. *Biosens. Bioelectron.* 87, 312–319. doi:10.1016/j.bios.2016.08.072

Jensen, E. C. (2012). Use of Fluorescent Probes: Their Effect on Cell Biology and Limitations. *Anat. Rec.* 295, 2031–2036. doi:10.1002/ar.22602

Jia, M., Belyavskaya, E., Deuster, P., and Sternberg, E. M. (2012). Development of a Sensitive Microarray Immunoassay for the Quantitative Analysis of Neuropeptide Y. *Anal. Chem.* 84, 6508–6514. doi:10.1021/ac3014548

Jia, W., Valdés-Ramírez, G., Bandodkar, A. J., Windmiller, J. R., and Wang, J. (2013). Epidermal Biofuel Cells: Energy Harvesting from Human Perspiration. *Angew. Chem. Int. Ed.* 52, 7233–7236. doi:10.1002/anie.201302922

Jones, C., and Gwenin, C. (2021). Cortisol Level Dysregulation and its Prevalence-Is it Nature's Alarm Clock? *Physiol. Rep.* 8, e14644. doi:10.14814/phy2.14644

Kafi, M. A., Paul, A., Vilouras, A., Hosseini, E. S., and Dahiya, R. S. (2020). Chitosan-graphene Oxide-Based Ultra-thin and Flexible Sensor for Diabetic Wound Monitoring. *IEEE Sensors J.* 20, 6794–6801. doi:10.1109/JSEN.2019.2928807

Kassal, P., Kim, J., Kumar, R., de Araujo, W. R., Steinberg, I. M., Steinberg, M. D., et al. (2015). Smart Bandage with Wireless Connectivity for Uric Acid Biosensing as an Indicator of Wound Status. *Electrochemistry Commun.* 56, 6–10. doi:10.1016/j.elecom.2015.03.018

Kassal, P., Zubak, M., Scheipl, G., Mohr, G. J., Steinberg, M. D., and Murković Steinberg, I. (2017). Smart Bandage with Wireless Connectivity for Optical Monitoring of Ph. *Sensors Actuators B: Chem.* 246, 455–460. doi:10.1016/j.snb.2017.02.095

Kastellorizios, M., and Burgess, D. J. (2015). Continuous Metabolic Monitoring Based on Multi-Analyte Biomarkers to Predict Exhaustion. *Sci. Rep.* 5, 10603. doi:10.1038/srep10603

Katseli, V., Economou, A., and Kokkinos, C. (2021). Smartphone-addressable 3d-Printed Electrochemical Ring for Nonenzymatic Self-Monitoring of Glucose in Human Sweat. *Anal. Chem.* 93, 3331–3336. doi:10.1021/acs.analchem.0c05057

Kim, D., Keum, K., Lee, G., Kim, D., Lee, S.-S., and Ha, J. S. (2017a). Flexible, Water-Proof, Wire-type Supercapacitors Integrated with Wire-type Uv/no2 Sensors on Textiles. *Nano Energy* 35, 199–206. doi:10.1016/j.nanoen.2017.03.044

Kim, J., Banks, A., Xie, Z., Heo, S. Y., Gutruf, P., Lee, J. W., et al. (2015). Miniaturized Flexible Electronic Systems with Wireless Power and Near-Field Communication Capabilities. *Adv. Funct. Mater.* 25, 4761–4767. doi:10.1002/adfm.201501590

Kim, J., Campbell, A. S., de Ávila, B. E.-F., and Wang, J. (2019). Wearable Biosensors for Healthcare Monitoring. *Nat. Biotechnol.* 37, 389–406. doi:10.1038/s41587-019-0045-y

Kim, J., Gutruf, P., Chiarelli, A. M., Heo, S. Y., Cho, K., Xie, Z., et al. (2017b). Miniaturized Battery-Free Wireless Systems for Wearable Pulse Oximetry. *Adv. Funct. Mater.* 27, 1604373. doi:10.1002/adfm.201604373

Kim, J., Jeerapan, I., Imani, S., Cho, T. N., Bandodkar, A., Cinti, S., et al. (2016). Noninvasive Alcohol Monitoring Using a Wearable Tattoo-Based Iontophoretic-Biosensing System. *ACS Sens.* 1, 1011–1019. doi:10.1021/acssensors.6b00356

Kim, J., Kim, M., Lee, M.-S., Kim, K., Ji, S., Kim, Y.-T., et al. (2017c). Wearable Smart Sensor Systems Integrated on Soft Contact Lenses for Wireless Ocular Diagnostics. *Nat. Commun.* 8, 14997. doi:10.1038/ncomms14997

Kim, S. B., Koo, J., Yoon, J., Hourlier-Fargette, A., Lee, B., Chen, S., et al. (2020). Soft, Skin-Interfaced Microfluidic Systems with Integrated Enzymatic Assays for Measuring the Concentration of Ammonia and Ethanol in Sweat. *Lab. Chip* 20, 84–92. doi:10.1039/c9lc01045a

Kiwanuka, E., Junker, J., and Eriksson, E. (2012). Harnessing Growth Factors to Influence Wound Healing. *Clin. Plast. Surg.* 39, 239–248. doi:10.1016/j.cps.2012.04.003

Koh, A., Kang, D., Xue, Y., Lee, S., Pielak, R. M., Kim, J., et al. (2016). A Soft, Wearable Microfluidic Device for the Capture, Storage, and Colorimetric Sensing of Sweat. *Sci. Translational Med.* 8, 366ra165. doi:10.1126/scitranslmed.aaf2593

Koralli, P., and Mouzakis, D. E. (2021). Advances in Wearable Chemosensors. *Chemosensors* 9, 99. doi:10.3390/chemosensors9050099

Koschinsky, T., Jungheim, K., and Heinemann, L. (2003). Glucose Sensors and the Alternate Site Testing-like Phenomenon: Relationship between Rapid Blood Glucose Changes and Glucose Sensor Signals. *Diabetes Technology Ther.* 5, 829–842. doi:10.1089/152091503322527030

Kratofil, R. M., Kubes, P., and Deniset, J. F. (2017). Monocyte Conversion during Inflammation and Injury. *Atvb* 37, 35–42. doi:10.1161/ATVBAHA.116.308198

Leal-Junior, A., Guo, J., Min, R., Fernandes, A. J., Frizera, A., and Marques, C. (2021). Photonic Smart Bandage for Wound Healing Assessment. *Photon. Res.* 9, 272–280. doi:10.1364/prj.410168

Leboulanger, B., Guy, R. H., and Delgado-Charro, M. B. (2004). Reverse Iontophoresis for Non-invasive Transdermal Monitoring. *Physiol. Meas.* 25, R35–R50. doi:10.1088/0967-3334/25/3/r01

Lee, B. S., Lee, J.-N., Park, J.-M., Lee, J.-G., Kim, S., Cho, Y.-K., et al. (2009). A Fully Automated Immunoassay from Whole Blood on a Disc. *Lab. Chip* 9, 1548–1555. doi:10.1039/b820321k

Lee, B. S., Lee, Y. U., Kim, H.-S., Kim, T.-H., Park, J., Lee, J.-G., et al. (2011). Fully Integrated Lab-On-A-Disc for Simultaneous Analysis of Biochemistry and Immunoassay from Whole Blood. *Lab. Chip* 11, 70–78. doi:10.1039/c0lc00205d

Lei, Z., Zhu, W., Zhang, X., Wang, X., and Wu, P. (2021). Bio-Inspired Ionic Skin for Theranostics. *Adv. Funct. Mater.* 31, 2008020. doi:10.1002/adfm.202008020

Leonardi, M., Leuenberger, P., Bertrand, D., Bertsch, A., and Renaud, P. (2004). First Steps toward Noninvasive Intraocular Pressure Monitoring with a Sensing Contact Lens. *Invest. Ophthalmol. Vis. Sci.* 45, 3113–3117. doi:10.1167/iovs.04-0015

Li, C. G., Joung, H.-A., Noh, H., Song, M.-B., Kim, M.-G., and Jung, H. (2015). One-touch-activated Blood Multidiagnostic System Using a Minimally Invasive Hollow Microneedle Integrated with a Paper-Based Sensor. *Lab. Chip* 15, 3286–3292. doi:10.1039/c5lc00669d

Li, G., and Wen, D. (2020). Wearable Biochemical Sensors for Human Health Monitoring: Sensing Materials and Manufacturing Technologies. *J. Mater. Chem. B* 8, 3423–3436. doi:10.1039/c9tb02474c

Li, S., Ma, Z., Cao, Z., Pan, L., and Shi, Y. (2020). Advanced Wearable Microfluidic Sensors for Healthcare Monitoring. *Small* 16, 1903822. doi:10.1002/smll.201903822

Li, W., Tang, J., Terry, R. N., Li, S., Brunie, A., Callahan, R. L., et al. (2019). Long-acting Reversible Contraception by Effervescent Microneedle Patch. *Sci. Adv.* 5, eaaw8145. doi:10.1126/sciadv.aaw8145

Li, X., Huang, X., Mo, J., Wang, H., Huang, Q., Yang, C., et al. (2021). A Fully Integrated Closed-Loop System Based on Mesoporous Microneedles-Iontophoresis for Diabetes Treatment. *Adv. Sci.* 8, 2100827. doi:10.1002/advs.202100827

Liesegang, T. J. (2001). Herpes Simplex Virus Epidemiology and Ocular Importance. *Cornea* 20, 1–13. doi:10.1097/00003226-200101000-00001

Lin, B. (2019). Wearable Smart Devices for P4 Medicine in Heart Disease: Ready for Medical Cyber-Physical Systems? *OMICS: A J. Integr. Biol.* 23, 291–292. doi:10.1089/omi.2019.0059

Lister, P. D., Wolter, D. J., and Hanson, N. D. (2009). Antibacterial-Resistant *Pseudomonas aeruginosa* : Clinical Impact and Complex Regulation of Chromosomally Encoded Resistance Mechanisms. *Clin. Microbiol. Rev.* 22, 582–610. doi:10.1128/CMR.00040-09

Liu, Q., Liu, Y., Wu, F., Cao, X., Li, Z., Alharbi, M., et al. (2018). Highly Sensitive and Wearable In2o3 Nanoribbon Transistor Biosensors with Integrated On-Chip Gate for Glucose Monitoring in Body Fluids. *ACS Nano* 12, 1170–1178. doi:10.1021/acsnano.7b06823

Liu, X., and Lillehoj, P. B. (2016). Embroidered Electrochemical Sensors for Biomolecular Detection. *Lab. Chip* 16, 2093–2098. doi:10.1039/c6lc00307a

Liu, X., and Lillehoj, P. B. (2017). Embroidered Electrochemical Sensors on Gauze for Rapid Quantification of Wound Biomarkers. *Biosens. Bioelectron.* 98, 189–194. doi:10.1016/j.bios.2017.06.053

Liu, Z., Wang, G., Ye, C., Sun, H., Pei, W., Wei, C., et al. (2021). An Ultrasensitive Contact Lens Sensor Based on Self-Assembly Graphene for Continuous Intraocular Pressure Monitoring. *Adv. Funct. Mater.* 31, 2010991. doi:10.1002/adfm.202010991

Lochner, C. M., Khan, Y., Pierre, A., and Arias, A. C. (2014). All-organic Optoelectronic Sensor for Pulse Oximetry. *Nat. Commun.* 5, 5745. doi:10.1038/ncomms6745

Löffler, M. W., Schuster, H., Bühler, S., and Beckert, S. (2013). Wound Fluid in Diabetic Foot Ulceration. *The Int. J. Lower Extremity Wounds* 12, 113–129. doi:10.1177/1534734613489989

Lou, D., Pang, Q., Pei, X., Dong, S., Li, S., Tan, W.-q., et al. (2020). Flexible Wound Healing System for Pro-regeneration, Temperature Monitoring and Infection Early Warning. *Biosens. Bioelectron.* 162, 112275. doi:10.1016/j.bios.2020.112275

Mak, W. C., Cheung, K. Y., Orban, J., Lee, C.-J., Turner, A. P. F., and Griffith, M. (2015). Surface-engineered Contact Lens as an Advanced Theranostic Platform for Modulation and Detection of Viral Infection. *ACS Appl. Mater. Inter.* 7, 25487–25494. doi:10.1021/acsami.5b08644

Mansouri, K., Medeiros, F. A., Tafreshi, A., and Weinreb, R. N. (2012). Continuous 24-Hour Monitoring of Intraocular Pressure Patterns with a Contact Lens Sensor. *Arch. Ophthalmol.* 130, 1534–1539. doi:10.1001/archophthalmol.2012.2280

Marriam, I., Wang, X., Tebyetekerwa, M., Chen, G., Zabihi, F., Pionteck, J., et al. (2018). A Bottom-Up Approach to Design Wearable and Stretchable Smart Fibers with Organic Vapor Sensing Behaviors and Energy Storage Properties. *J. Mater. Chem. A.* 6, 13633–13643. doi:10.1039/c8ta03262a

Martín, A., Kim, J., Kurniawan, J. F., Sempionatto, J. R., Moreto, J. R., Tang, G., et al. (2017). Epidermal Microfluidic Electrochemical Detection System: Enhanced Sweat Sampling and Metabolite Detection. *ACS Sens.* 2, 1860–1868. doi:10.1021/acssensors.7b00729

Mat Zaid, M. H., Abdullah, J., Yusof, N. A., Sulaiman, Y., Wasoh, H., Md Noh, M. F., et al. (2017). Pna Biosensor Based on Reduced Graphene Oxide/water Soluble Quantum Dots for the Detection of mycobacterium Tuberculosis. *Sensors Actuators B: Chem.* 241, 1024–1034. doi:10.1016/j.snb.2016.10.045

McLister, A., Phair, J., Cundell, J., and Davis, J. (2014). Electrochemical Approaches to the Development of Smart Bandages: A Mini-Review. *Electrochemistry Commun.* 40, 96–99. doi:10.1016/j.elecom.2014.01.003

Mejía-Salazar, J. R., Rodrigues Cruz, K., Materón Vásques, E. M., and Novais de Oliveira Jr., O., Jr. (2020). Microfluidic point-of-care Devices: New Trends and Future Prospects for Ehealth Diagnostics. *Sensors* 20, 1951. doi:10.3390/s20071951

Mirani, B., Pagan, E., Currie, B., Siddiqui, M. A., Hosseinzadeh, R., Mostafalu, P., et al. (2017). An Advanced Multifunctional Hydrogel-Based Dressing for Wound Monitoring and Drug Delivery. *Adv. Healthc. Mater.* 6, 1700718. doi:10.1002/adhm.201700718

Mishra, R. K., Barfidokht, A., Karajic, A., Sempionatto, J. R., Wang, J., and Wang, J. (2018). Wearable Potentiometric Tattoo Biosensor for On-Body Detection of G-type Nerve Agents Simulants. *Sensors Actuators B: Chem.* 273, 966–972. doi:10.1016/j.snb.2018.07.001

Mishra, R. K., Vinu Mohan, A. M., Soto, F., Chrostowski, R., and Wang, J. (2017). A Microneedle Biosensor for Minimally-Invasive Transdermal Detection of Nerve Agents. *Analyst* 142, 918–924. doi:10.1039/c6an02625g

Mostafalu, P., Tamayol, A., Rahimi, R., Ochoa, M., Khalilpour, A., Kiaee, G., et al. (2018). Smart Bandage for Monitoring and Treatment of Chronic Wounds. *Small* 14, 1703509. doi:10.1002/smll.201703509

Movilli, J., Rozzi, A., Ricciardi, R., Corradini, R., and Huskens, J. (2018). Control of Probe Density at DNA Biosensor Surfaces Using Poly(l-Lysine) with Appended Reactive Groups. *Bioconjug. Chem.* 29, 4110–4118. doi:10.1021/acs.bioconjchem.8b00733

Munje, R. D., Muthukumar, S., and Prasad, S. (2017). Lancet-free and Label-free Diagnostics of Glucose in Sweat Using Zinc Oxide Based Flexible Bioelectronics. *Sensors Actuators B: Chem.* 238, 482–490. doi:10.1016/j.snb.2016.07.088

Nunan, R., Harding, K. G., and Martin, P. (2014). Clinical Challenges of Chronic Wounds: Searching for an Optimal Animal Model to Recapitulate Their Complexity. *Dis. Model. Mech.* 7, 1205–1213. doi:10.1242/dmm.016782

Nyein, H. Y. Y., Gao, W., Shahpar, Z., Emaminejad, S., Challa, S., Chen, K., et al. (2016). A Wearable Electrochemical Platform for Noninvasive Simultaneous Monitoring of Ca2+ and pH. *ACS Nano* 10, 7216–7224. doi:10.1021/acsnano.6b04005

Nyein, H. Y. Y., Tai, L.-C., Ngo, Q. P., Chao, M., Zhang, G. B., Gao, W., et al. (2018). A Wearable Microfluidic Sensing Patch for Dynamic Sweat Secretion Analysis. *ACS Sens.* 3, 944–952. doi:10.1021/acssensors.7b00961

O'Connor, T. F., Zaretski, A. V., Savagatrup, S., Printz, A. D., Wilkes, C. D., Diaz, M. I., et al. (2016). Wearable Organic Solar Cells with High Cyclic Bending Stability: Materials Selection Criteria. *Solar Energ. Mater. Solar Cell* 144, 438–444. doi:10.1016/j.solmat.2015.09.049

Oh, J. Y., Lee, J. H., Han, S. W., Chae, S. S., Bae, E. J., Kang, Y. H., et al. (2016). Chemically Exfoliated Transition Metal Dichalcogenide Nanosheet-Based Wearable Thermoelectric Generators. *Energy Environ. Sci.* 9, 1696–1705. doi:10.1039/C5EE03813H

Oh, S. Y., Hong, S. Y., Jeong, Y. R., Yun, J., Park, H., Jin, S. W., et al. (2018). Skin-attachable, Stretchable Electrochemical Sweat Sensor for Glucose and Ph Detection. *ACS Appl. Mater. Inter.* 10, 13729–13740. doi:10.1021/acsami.8b03342

Pal, A., Goswami, D., Cuellar, H. E., Castro, B., Kuang, S., and Martinez, R. V. (2018). Early Detection and Monitoring of Chronic Wounds Using Low-Cost, Omniphobic Paper-Based Smart Bandages. *Biosens. Bioelectron.* 117, 696–705. doi:10.1016/j.bios.2018.06.060

Pal, A., Nadiger, V. G., Goswami, D., and Martinez, R. V. (2020). Conformal, waterproof Electronic Decals for Wireless Monitoring of Sweat and Vaginal Ph at the point-of-care. *Biosens. Bioelectron.* 160, 112206. doi:10.1016/j.bios.2020.112206

Pan, N., Qin, J., Feng, P., Li, Z., and Song, B. (2019). Color-changing Smart Fibrous Materials for Naked Eye Real-Time Monitoring of Wound Ph. *J. Mater. Chem. B* 7, 2626–2633. doi:10.1039/c9tb00195f

Pang, Q., Lou, D., Li, S., Wang, G., Qiao, B., Dong, S., et al. (2020). Smart Flexible Electronics-Integrated Wound Dressing for Real-Time Monitoring and On-Demand Treatment of Infected Wounds. *Adv. Sci.* 7, 1902673. doi:10.1002/advs.201902673

Pankratov, D., González-Arribas, E., Blum, Z., and Shleev, S. (2016). Tear Based Bioelectronics. *Electroanalysis* 28, 1250–1266. doi:10.1002/elan.201501116

Park, J., Kim, J., Kim, S.-Y., Cheong, W. H., Jang, J., Park, Y.-G., et al. (2018a). Soft, Smart Contact Lenses with Integrations of Wireless Circuits, Glucose Sensors, and Displays. *Sci. Adv.* 4, eaap9841. doi:10.1126/sciadv.aap9841

Park, S., Heo, S. W., Lee, W., Inoue, D., Jiang, Z., Yu, K., et al. (2018b). Self-powered Ultra-flexible Electronics via Nano-Grating-Patterned Organic Photovoltaics. *Nature* 561, 516–521. doi:10.1038/s41586-018-0536-x

Parlak, O., Keene, S. T., Marais, A., Curto, V. F., and Salleo, A. (2018). Molecularly Selective Nanoporous Membrane-Based Wearable Organic Electrochemical Device for Noninvasive Cortisol Sensing. *Sci. Adv.* 4, eaar2904. doi:10.1126/sciadv.aar2904

Pasche, S., Angeloni, S., Ischer, R., Liley, M., Luprano, J., and Voirin, G. (2008). Wearable Biosensors for Monitoring Wound Healing. *Ast* 57, 80–87. doi:10.4028/www.scientific.net/ast.57.80

Peters, R. P., van Agtmael, M. A., Danner, S. A., Savelkoul, P. H., and Vandenbroucke-Grauls, C. M. (2004). New Developments in the Diagnosis of Bloodstream Infections. *Lancet Infect. Dis.* 4, 751–760. doi:10.1016/S1473-3099(04)01205-8

Pool, J. G. (1977). Normal Hemostatic Mechanisms: A Review. *Am. J. Med. Technol.* 43, 776–780.

Prattis, I., Hui, E., Gubeljak, P., Kaminski Schierle, G. S., Lombardo, A., and Occhipinti, L. G. (2021). Graphene for Biosensing Applications in point-of-care Testing. *Trends Biotechnol.* 39, 1065–1077. doi:10.1016/j.tibtech.2021.01.005

Rodrigues, M., Kosaric, N., Bonham, C. A., and Gurtner, G. C. (2019). Wound Healing: A Cellular Perspective. *Physiol. Rev.* 99, 665–706. doi:10.1152/physrev.00067.2017

RoyChoudhury, S., Umasankar, Y., Jaller, J., Herskovitz, I., Mervis, J., Darwin, E., et al. (2018). Continuous Monitoring of Wound Healing Using a Wearable Enzymatic Uric Acid Biosensor. *J. Electrochem. Soc.* 165, B3168–B3175. doi:10.1149/2.0231808jes

Sang, S., Wang, Y., Feng, Q., Wei, Y., Ji, J., and Zhang, W. (2016). Progress of New Label-free Techniques for Biosensors: A Review. *Crit. Rev. Biotechnol.* 36, 1–17. doi:10.3109/07388551.2014.991270

Saorin, A., Di Gregorio, E., Miolo, G., Steffan, A., and Corona, G. (2020). Emerging Role of Metabolomics in Ovarian Cancer Diagnosis. *Metabolites* 10, 419. doi:10.3390/metabo10100419

Sekine, Y., Kim, S. B., Zhang, Y., Bandodkar, A. J., Xu, S., Choi, J., et al. (2018). A Fluorometric Skin-Interfaced Microfluidic Device and Smartphone Imaging Module for *In Situ* Quantitative Analysis of Sweat Chemistry. *Lab. Chip* 18, 2178–2186. doi:10.1039/c8lc00530c

Sempionatto, J. R., Brazaca, L. C., García-Carmona, L., Bolat, G., Campbell, A. S., Martin, A., et al. (2019). Eyeglasses-based Tear Biosensing System:

Non-invasive Detection of Alcohol, Vitamins and Glucose. *Biosens. Bioelectron.* 137, 161–170. doi:10.1016/j.bios.2019.04.058

Sempionatto, J. R., Khorshed, A. A., Ahmed, A., De Loyola e Silva, A. N., Barfidokht, A., Yin, L., et al. (2020). Epidermal Enzymatic Biosensors for Sweat Vitamin C: Toward Personalized Nutrition. *ACS Sens.* 5, 1804–1813. doi:10.1021/acssensors.0c00604

Sen, C. K., Gordillo, G. M., Roy, S., Kirsner, R., Lambert, L., Hunt, T. K., et al. (2009). Human Skin Wounds: A Major and Snowballing Threat to Public Health and the Economy. *Wound Repair Regen.* 17, 763–771. doi:10.1111/j.1524-475X.2009.00543.x

Sen, D. K., and Sarin, G. S. (1980). Tear Glucose Levels in normal People and in Diabetic Patients. *Br. J. Ophthalmol.* 64, 693–695. doi:10.1136/bjo.64.9.693

Senel, M., Dervisevic, M., and Voelcker, N. H. (2019). Gold Microneedles Fabricated by Casting of Gold Ink Used for Urea Sensing. *Mater. Lett.* 243, 50–53. doi:10.1016/j.matlet.2019.02.014

Seo, G., Lee, G., Kim, M. J., Baek, S.-H., Choi, M., Ku, K. B., et al. (2020). Rapid Detection of Covid-19 Causative Virus (Sars-cov-2) in Human Nasopharyngeal Swab Specimens Using Field-Effect Transistor-Based Biosensor. *ACS Nano* 14, 5135–5142. doi:10.1021/acsnano.0c02823

Shaheed, S.-u., Tait, C., Kyriacou, K., Mullarkey, J., Burrill, W., Patterson, L. H., et al. (2017). Nipple Aspirate Fluid-A Liquid Biopsy for Diagnosing Breast Health. *Prot. Clin. Appl.* 11, 1700015. doi:10.1002/prca.201700015

Shi, X., and Wu, P. (2021). A Smart Patch with On-Demand Detachable Adhesion for Bioelectronics. *Small* 17, 2101220. doi:10.1002/smll.202101220

Shidfar, A., Fatokun, T., Ivancic, D., Chatterton, R. T., Khan, S. A., and Wang, J. (2016). Protein Biomarkers for Breast Cancer Risk Are Specifically Correlated with Local Steroid Hormones in Nipple Aspirate Fluid. *Horm. Canc* 7, 252–259. doi:10.1007/s12672-016-0264-3

Shrivastava, S., Trung, T. Q., and Lee, N.-E. (2020). Recent Progress, Challenges, and Prospects of Fully Integrated mobile and Wearable point-of-care Testing Systems for Self-Testing. *Chem. Soc. Rev.* 49, 1812–1866. doi:10.1039/c9cs00319c

Siddiqui, A. R., and Bernstein, J. M. (2010). Chronic Wound Infection: Facts and Controversies. *Clin. Dermatol.* 28, 519–526. doi:10.1016/j.clindermatol.2010.03.009

Steinberg, M. D., Kassal, P., Kereković, I., and Steinberg, I. M. (2015). A Wireless Potentiostat for mobile Chemical Sensing and Biosensing. *Talanta* 143, 178–183. doi:10.1016/j.talanta.2015.05.028

Steinberg, M. D., Kassal, P., and Steinberg, I. M. (2016). System Architectures in Wearable Electrochemical Sensors. *Electroanalysis* 28, 1149–1169. doi:10.1002/elan.201600094

Streilein, J. W., Dana, M. R., and Ksander, B. R. (1997). Immunity Causing Blindness: Five Different Paths to Herpes Stromal Keratitis. *Immunol. Today* 18, 443–449. doi:10.1016/s0167-5699(97)01114-6

Sturgeon, C. M., Duffy, M. J., Stenman, U.-H., Lilja, H., Brünner, N., Chan, D. W., et al. (2008). National Academy of Clinical Biochemistry Laboratory Medicine Practice Guidelines for Use of Tumor Markers in Testicular, Prostate, Colorectal, Breast, and Ovarian Cancers. *Clin. Chem.* 54, e11–e79. doi:10.1373/clinchem.2008.105601

Suaifan, G. A. R. Y., Alhogail, S., and Zourob, M. (2017). Rapid and Low-Cost Biosensor for the Detection of staphylococcus Aureus. *Biosens. Bioelectron.* 90, 230–237. doi:10.1016/j.bios.2016.11.047

Sun, J., Han, S., Wang, Y., Zhao, G., Qian, W., and Dong, J. (2018). Detection of Redox State Evolution during Wound Healing Process Based on a Redox-Sensitive Wound Dressing. *Anal. Chem.* 90, 6660–6665. doi:10.1021/acs.analchem.8b00471

Sun, M., Gu, Y., Pei, X., Wang, J., Liu, J., Ma, C., et al. (2021a). A Flexible and Wearable Epidermal Ethanol Biofuel Cell for On-Body and Real-Time Bioenergy Harvesting from Human Sweat. *Nano Energy* 86, 106061. doi:10.1016/j.nanoen.2021.106061

Sun, M., Xin, T., Ran, Z., Pei, X., Ma, C., Liu, J., et al. (2021b). A Bendable Biofuel Cell-Based Fully Integrated Biomedical Nanodevice for point-of-care Diagnosis of Scurvy. *ACS Sens.* 6, 275–284. doi:10.1021/acssensors.0c02335

Syu, Y.-C., Hsu, W.-E., and Lin, C.-T. (2018). Review-field-effect Transistor Biosensing: Devices and Clinical Applications. *ECS J. Solid State. Sci. Technol.* 7, Q3196–Q3207. doi:10.1149/2.0291807jss

Talary, M. S., Dewarrat, F., Huber, D., and Caduff, A. (2007). *In Vivo* life Sign Application of Dielectric Spectroscopy and Non-invasive Glucose Monitoring. *J. Non-Crystalline Sol.* 353, 4515–4517. doi:10.1016/j.jnoncrysol.2007.03.038

Tian, M., Qiao, M., Shen, C., Meng, F., Frank, L. A., Krasitskaya, V. V., et al. (2020). Highly-sensitive Graphene Field Effect Transistor Biosensor Using Pna and DNA Probes for Rna Detection. *Appl. Surf. Sci.* 527, 146839. doi:10.1016/j.apsusc.2020.146839

Tran, B. Q., Miller, P. R., Taylor, R. M., Boyd, G., Mach, P. M., Rosenzweig, C. N., et al. (2018). Proteomic Characterization of Dermal Interstitial Fluid Extracted Using a Novel Microneedle-Assisted Technique. *J. Proteome Res.* 17, 479–485. doi:10.1021/acs.jproteome.7b00642

Tseng, R., Chen, C.-C., Hsu, S.-M., and Chuang, H.-S. (2018). Contact-lens Biosensors. *Sensors* 18, 2651. doi:10.3390/s18082651

Tur-García, E. L., Davis, F., Collyer, S. D., Holmes, J. L., Barr, H., and Higson, S. P. J. (2017). Novel Flexible Enzyme Laminate-Based Sensor for Analysis of Lactate in Sweat. *Sensors Actuators B: Chem.* 242, 502–510. doi:10.1016/j.snb.2016.11.040

Valdés-Ramírez, G., Li, Y.-C., Kim, J., Jia, W., Bandodkar, A. J., Nuñez-Flores, R., et al. (2014). Microneedle-based Self-Powered Glucose Sensor. *Electrochemistry Commun.* 47, 58–62. doi:10.1016/j.elecom.2014.07.014

Ventrelli, L., Marsilio Strambini, L., and Barillaro, G. (2015). Microneedles for Transdermal Biosensing: Current Picture and Future Direction. *Adv. Healthc. Mater.* 4, 2606–2640. doi:10.1002/adhm.201500450

Vig, K., Chaudhari, A., Tripathi, S., Dixit, S., Sahu, R., Pillai, S., et al. (2017). Advances in Skin Regeneration Using Tissue Engineering. *Ijms* 18, 789. doi:10.3390/ijms18040789

von Thun und Hohenstein-Blaul, N., Funke, S., and Grus, F. H. (2013). Tears as a Source of Biomarkers for Ocular and Systemic Diseases. *Exp. Eye Res.* 117, 126–137. doi:10.1016/j.exer.2013.07.015

Wang, C., Li, X., Hu, H., Zhang, L., Huang, Z., Lin, M., et al. (2018a). Monitoring of the central Blood Pressure Waveform via a Conformal Ultrasonic Device. *Nat. Biomed. Eng.* 2, 687–695. doi:10.1038/s41551-018-0287-x

Wang, J., Jeevarathinam, A. S., Jhunjhunwala, A., Ren, H., Lemaster, J., Luo, Y., et al. (2018b). A Wearable Colorimetric Dosimeter to Monitor Sunlight Exposure. *Adv. Mater. Technol.* 3, 1800037. doi:10.1002/admt.201800037

Wang, Q., Yan, J., and Fan, Z. (2016). Carbon Materials for High Volumetric Performance Supercapacitors: Design, Progress, Challenges and Opportunities. *Energ. Environ. Sci.* 9, 729–762. doi:10.1039/C5EE03109E

Wei, Y., Gadaria-Rathod, N., Epstein, S., and Asbell, P. (2013). Tear Cytokine Profile as a Noninvasive Biomarker of Inflammation for Ocular Surface Diseases: Standard Operating Procedures. *Invest. Ophthalmol. Vis. Sci.* 54, 8327–8336. doi:10.1167/iovs.13-12132

Wiig, H., and Swartz, M. A. (2012). Interstitial Fluid and Lymph Formation and Transport: Physiological Regulation and Roles in Inflammation and Cancer. *Physiol. Rev.* 92, 1005–1060. doi:10.1152/physrev.00037.2011

Wu, S., Liu, P., Zhang, Y., Zhang, H., and Qin, X. (2017). Flexible and Conductive Nanofiber-Structured Single Yarn Sensor for Smart Wearable Devices. *Sensors Actuators B: Chem.* 252, 697–705. doi:10.1016/j.snb.2017.06.062

Xiao, J., Liu, Y., Su, L., Zhao, D., Zhao, L., and Zhang, X. (2019). Microfluidic Chip-Based Wearable Colorimetric Sensor for Simple and Facile Detection of Sweat Glucose. *Anal. Chem.* 91, 14803–14807. doi:10.1021/acs.analchem.9b03110

Xu, G., Lu, Y., Cheng, C., Li, X., Xu, J., Liu, Z., et al. (2021). Battery-Free and Wireless Smart Wound Dressing for Wound Infection Monitoring and Electrically Controlled On-Demand Drug Delivery. *Adv. Funct. Mater.*, 2100852. doi:10.1002/adfm.202100852

Yang, K., Peretz-Soroka, H., Liu, Y., and Lin, F. (2016). Novel Developments in mobile Sensing Based on the Integration of Microfluidic Devices and Smartphones. *Lab. Chip* 16, 943–958. doi:10.1039/c5lc01524c

Yu, H., Li, D., Roberts, R. C., Xu, K., and Tien, N. C. (2012). An Interstitial Fluid Transdermal Extraction System for Continuous Glucose Monitoring. *J. Microelectromech. Syst.* 21, 917–925. doi:10.1109/JMEMS.2012.2192910

Yu, Y., Nassar, J., Xu, C., Min, J., Yang, Y., Dai, A., et al. (2020). Biofuel-powered Soft Electronic Skin with Multiplexed and Wireless Sensing for Human-Machine Interfaces. *Sci. Robot.* 5, eaaz7946. doi:10.1126/scirobotics.aaz7946

Zahedi, P., Rezaeian, I., Ranaei-Siadat, S.-O., Jafari, S.-H., and Supaphol, P. (2010). A Review on Wound Dressings with an Emphasis on Electrospun Nanofibrous Polymeric Bandages. *Polym. Adv. Technol.* 21, 77–95. doi:10.1002/pat.1625

Zamarayeva, A. M., Ostfeld, A. E., Wang, M., Duey, J. K., Deckman, I., Lechêne, B. P., et al. (2017). Flexible and Stretchable Power Sources for Wearable Electronics. *Sci. Adv.* 3, e1602051. doi:10.1126/sciadv.1602051

Zeng, W., Shu, L., Li, Q., Chen, S., Wang, F., and Tao, X.-M. (2014). Fiber-Based Wearable Electronics: A Review of Materials, Fabrication, Devices, and Applications. *Adv. Mater.* 26, 5310–5336. doi:10.1002/adma.201400633

Zhang, Y., Castro, D. C., Han, Y., Wu, Y., Guo, H., Weng, Z., et al. (2019). Battery-free, Lightweight, Injectable Microsystem for *In Vivo* Wireless Pharmacology and Optogenetics. *Proc. Natl. Acad. Sci. USA.* 116, 21427–21437. doi:10.1073/pnas.1909850116

Zhang, Y., Lin, B., Huang, R., Lin, Z., Li, Y., Li, J., et al. (2021). Flexible Integrated Sensing Platform for Monitoring Wound Temperature and Predicting Infection. *Microb. Biotechnol.* 14, 1566–1579. doi:10.1111/1751-7915.13821

Zhao, Y., Li, Z., Song, S., Yang, K., Liu, H., Yang, Z., et al. (2019). Skin-Inspired Antibacterial Conductive Hydrogels for Epidermal Sensors and Diabetic Foot Wound Dressings. *Adv. Funct. Mater.* 29, 1901474. doi:10.1002/adfm.201901474

Zheng, T., Pierre-Pierre, N., Yan, X., Huo, Q., Almodovar, A. J. O., Valerio, F., et al. (2015). Gold Nanoparticle-Enabled Blood Test for Early Stage Cancer Detection and Risk Assessment. *ACS Appl. Mater. Inter.* 7, 6819–6827. doi:10.1021/acsami.5b00371

Zhu, D., Liu, B., and Wei, G. (2021). Two-Dimensional Material-Based Colorimetric Biosensors: A Review. *Biosensors* 11, 259. doi:10.3390/bios11080259

Conflict of Interest: The authors declare that the research was conducted in the absence of any commercial or financial relationships that could be construed as a potential conflict of interest.

The Reviewer A.C declared a shared affiliation with the Author (Z.Z) to the Handling Editor at the time of review.

Publisher's Note: All claims expressed in this article are solely those of the authors and do not necessarily represent those of their affiliated organizations, or those of the publisher, the editors and the reviewers. Any product that may be evaluated in this article, or claim that may be made by its manufacturer, is not guaranteed or endorsed by the publisher.

frontiers in Bioengineering and Biotechnology

ORIGINAL RESEARCH
published: 15 November 2021
doi: 10.3389/fbioe.2021.761548

Artificial Intelligent Multi-Modal Point-of-Care System for Predicting Response of Transarterial Chemoembolization in Hepatocellular Carcinoma

*Zhongqi Sun, Zhongxing Shi, Yanjie Xin, Sheng Zhao, Hao Jiang, Dandan Wang, Linhan Zhang, Ziao Wang, Yanmei Dai and Huijie Jiang**

Department of Radiology, The Second Affiliated Hospital of Harbin Medical University, Harbin, China

OPEN ACCESS

Edited by:
Tailin Xu,
Shenzhen University, China

Reviewed by:
Yingying Wang,
First Affiliated Hospital of Jinan University, China
Zhenwei Peng,
The First Affiliated Hospital of Sun Yat-sen University, China
Hongjia Ren,
Jilin University, China

***Correspondence:**
Huijie Jiang
jianghuijie@hrbmu.edu.cn

Specialty section:
This article was submitted to Biosensors and Biomolecular Electronics, a section of the journal Frontiers in Bioengineering and Biotechnology

Received: *20 August 2021*
Accepted: *22 October 2021*
Published: *15 November 2021*

Citation:
Sun Z, Shi Z, Xin Y, Zhao S, Jiang H, Wang D, Zhang L, Wang Z, Dai Y and Jiang H (2021) Artificial Intelligent Multi-Modal Point-of-Care System for Predicting Response of Transarterial Chemoembolization in Hepatocellular Carcinoma. Front. Bioeng. Biotechnol. 9:761548. doi: 10.3389/fbioe.2021.761548

Hepatocellular carcinoma (HCC) ranks the second most lethal tumor globally and is the fourth leading cause of cancer-related death worldwide. Unfortunately, HCC is commonly at intermediate tumor stage or advanced tumor stage, in which only some palliative treatment can be used to offer a limited overall survival. Due to the high heterogeneity of the genetic, molecular, and histological levels, HCC makes the prediction of preoperative transarterial chemoembolization (TACE) efficacy and the development of personalized regimens challenging. In this study, a new multi-modal point-of-care system is employed to predict the response of TACE in HCC by a concept of integrating multi-modal large-scale data of clinical index and computed tomography (CT) images. This multi-modal point-of-care predicting system opens new possibilities for predicting the response of TACE treatment and can help clinicians select the optimal patients with HCC who can benefit from the interventional therapy.

Keywords: hepatocellular carcinoma, artificial intelligence, computed tomography imaging, inflammation-based index, point-of-care predicting

INTRODUCTION

Liver cancer is the second most lethal tumor after pancreatic cancer and ranks the fourth leading cause of cancer-related death worldwide (Craig et al., 2020; Villanueva et al., 2019; Tao et al., 2020). In China, the 5-year survival rates have been reported to be 12% (Zheng et al., 2018). Hepatocellular carcinoma (HCC), which is the most common form of liver cancer (~90% of liver cancer), remains a health challenge in the world (Llovet et al., 2021; Yu et al., 2020). In order to predict the prognosis of patients with HCC, the Barcelona Clinic Liver Cancer (BCLC) staging classification, which is approved by European Association for the Study of the Liver (EASL) and American Association for the Study of Liver Diseases (AASLD), has emerged as the standard classification in recent years (Llovet et al., 2008; Vitale et al., 2011; Yang et al., 2012). However, HCC is commonly at intermediate tumor stage (BCLC stage B) or advanced tumor stage (BCLC stage C), in which only some palliative treatment can be used to offer a limited overall survival (~11–20 months) (Llovet et al., 2002; Hucke et al., 2011; Sieghart et al., 2015). According to international guidelines, transarterial chemoembolization (TACE) is the recommended treatment for Barcelona stage B patients with localized liver disease and good liver function (Camma et al., 2002; Otto et al., 2006; Takayasu et al.,

2006). However, HCC is highly heterogeneous at the genetic, molecular, and histological levels, which makes the prediction of preoperative TACE efficacy and the development of personalized regimens challenging. Therefore, there are growing demands for exploiting a method to accurately predict response of TACE in HCC. Imaging setting, which included ultrasound, computed tomography (CT), and magnetic resonance imaging (MRI), can be a promising tool for the detection stage and risk assessment of HCC (Banerjee et al. (2015); Woodall et al., 2007). Due to the high sensitivity, worldwide availability, and easy interpretability, CT is still the most commonly used in the field of response of TACE therapy. The best response of TACE cannot always be achieved after one session of CT imaging, especially for patients with large tumors. However, multiple CT examinations can easily damage the liver function of patients. Therefore, other clinical evaluation indexes should be added to build a point-of-care predicting system for improving the predicting accuracy of TACE responses. Crucially, inflammation has been recognized as a major role in the tumorigenic process for HCC. Recent studies confirm that inflammation also plays a prognostic role in the whole clinical process of malignancy (Sanghera et al., 2019; Chan et al., 2020; Wang et al., 2021). A number of inflammation-based indexes (IBIs) are derived from peripheral blood counts for prognostic purposes, with examples including neutrophil-to-lymphocyte ratio (NLR), platelet-to-lymphocyte ratio (PLR), monocyte-to-lymphocyte ratio (MLR), systemic immune-inflammation index (SII), and neutrophil-to-lymphocyte ratio (SIRI) (Pinato et al., 2012; Yang et al., 2020). Therefore, combined CT images with inflammation-based indexes to predict postoperative treatment responses and accurately identify patients who responded after TACE is of important clinical guiding significance. Recently, artificial intelligence (AI), which is capable of maximizing the predictive accuracy from static or dynamic data sources using analytic or probabilistic models, has markedly extended the reach of human beings in biomedical tasks (Esteva et al., 2017; Li et al., 2017; Kermany et al., 2018; Li et al., 2018; Chang et al., 2019; Zhang et al., 2020). Deep learning is especially recognized as demonstrating good performance for assessing radiological and recognizing images. Because of the multifactorial and complex nature of HCC, the convolutional neural network of deep learning algorithms has shown great potential in fully mining image information. This approach does not need to manually screen image features, and it shows good training performance for high-dimensional data processing (Gulshan et al., 2016; Peng et al., 2019; Liu et al., 2020). The texture analysis based on contrast-enhanced pretherapeutic dynamic CT may act as imaging biomarkers to predict response for HCC. Higher gray-level co-occurrence matrix and smaller tumor size are significant signs. However, the highest AUC was only 0.72 (Park et al., 2017; Kermany et al., 2018). It is necessary to find a new method to increase predicting accuracy of TACE responses. Because of the multifactorial and complex nature of HCC, building a deep learning point-of-care predicting system to integrate multiple factors (e.g., CT images and inflammation-based indexes) would appear to be a highly effective technique to autonomously predict the response of TACE therapy. In this paper, we aim to develop a point-of-care system for predicting the response of TACE in HCC by a concept of multi-modal large-scale data by combining clinical indexes with CT images. This multi-modal point-of-care predicting system opens new possibilities for predicting the response of TACE treatment and can help clinicians to select optimum patients with HCC who can benefit from the interventional therapy.

MATERIALS AND METHODS

Patients

This study included patients in the Second Affiliated Hospital of Harbin Medical University. A total of 1,890 patients who underwent TACE were recruited from January 2011 to September 2020. Finally, 399 patients were enrolled. The patients who matched inclusion criteria were as follows: (1) Patients were diagnosed as HCCs *via* biopsy or radiological for the Study. (2) All patients did not have a history of previous TACE of HCC before CT examination. (3) Those who had hepatic-arterial CT imaging within 7 days before and 1 month after treatment. (4) Patients with BCLC stage B. The exclusion criteria were as follows: (1) Those with a history of previous TACE, liver transplantation, targeting therapy, radiotherapy, and palliative care treatment. (2) Patients with major thrombosis in portal vein or abdominal lymph node or distant metastases. (3) Other liver tumors that were confirmed with pathology or imaging. The response of hepatic-arterial CT images was classified into objective response [containing complete response (CR) and partial response (PR)] and non-response [containing progressive disease (PD) and stable disease (SD)] according to the modified Response Evaluation Criteria in Solid Tumors (mRECIST).

CT Scan Protocols and Region-of-Interest Segmentation

Contrast-enhanced computed tomography (CECT) was performed with a 64-detector row scanner CT machine (GE Healthcare, United States). The scanning parameters were as follows: tube current, 250 mA; tube voltage, 120 kV; and slice thickness, 5 mm. Contrast agent (Ultravist, Bayer, Germany) for CECT was injected through a pump injector at a rate of 3.0 ml/s from the antecubital vein. Hepatic-arterial phase CT images were obtained at 35 s. All CT images were input into the Dr. wise AI software (Deepwise Inc., China). The regions of interest (ROIs) were delineated manually by two senior radiologists who had 15 years experience (reader 1, Prof. Huijie Jiang) and 13 years experience (reader 2, Prof. Jinling Zhang). The entire cohort included 399 patients who were randomly divided into a training dataset (319 cases) and validation dataset (80 cases) by a ratio of 8: 2. The validation dataset evaluated the accuracy of the training dataset. The ROIs of CT images from the training cohort and the validation cohorts were manually segmented by the two readers

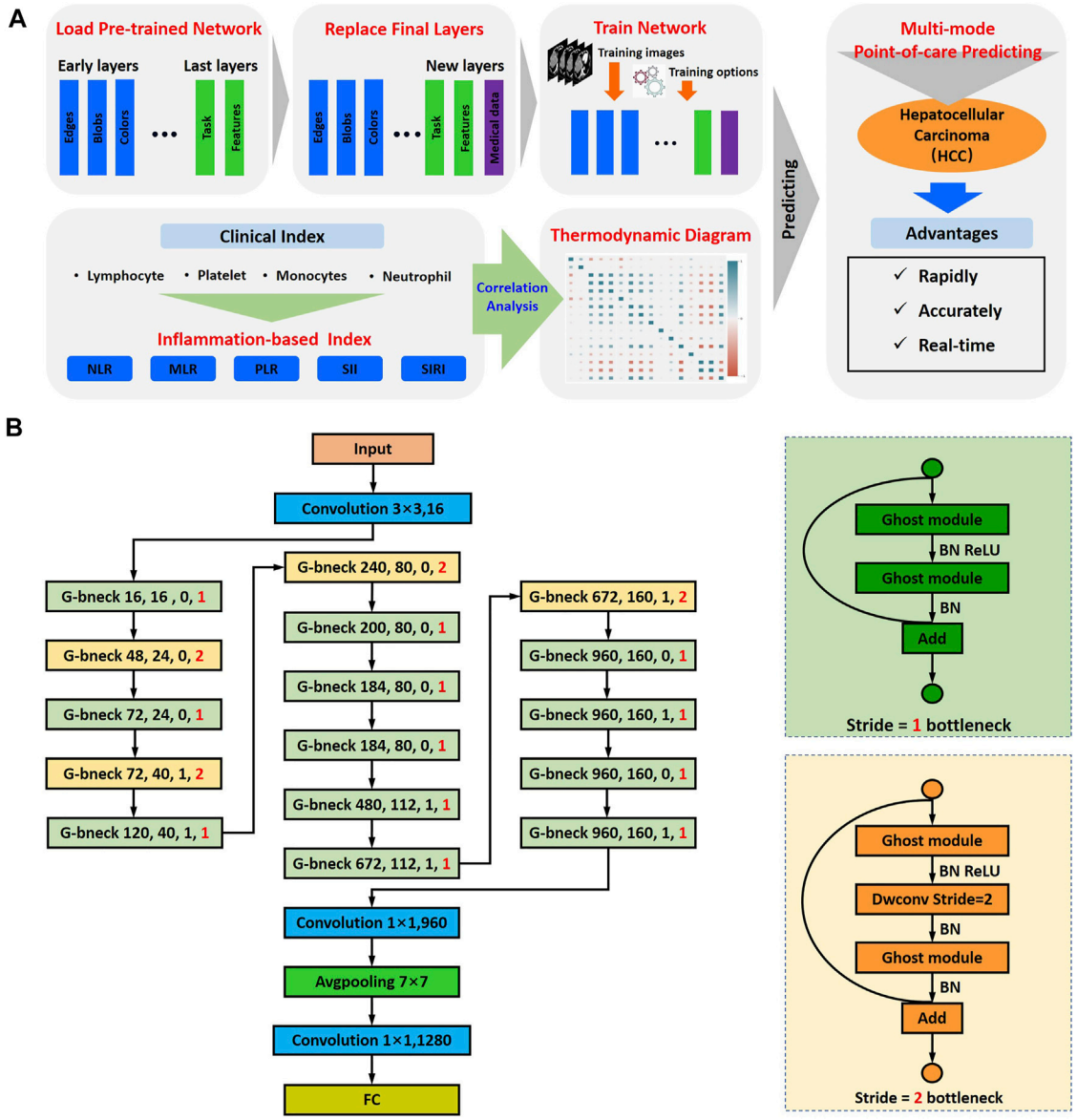

FIGURE 1 | Schematic of multi-modal point-of-care predicting system. **(A)** Schematic of point-of-care system to predicting the response of TACE in HCC by integrating multi-modal large-scale CT imaging and clinical evaluation indexes. **(B)** The architecture of GhostNet and deep learning model flowchart.

who were specifically blinded to the therapy outcome of the patients.

Image Analysis and Preprocessing

All CT original images were reconstructed using a post-processing workstation to achieve uniform slice thickness and input the reconstructed image into Deepwise software to delineate the ROIS. We saved one CT image and the corresponding mask of ROIs for each patient from the largest tumor area in hepatic-arterial phase CT images. ROI was delineated around the largest tumor area selected by transverse and sagittal observations, and the ROI area was outlined close to the edge of the tumor. A total of 319 patients were used as the training set and 80 patients were used as the validation set. Random image cropping and patching (RICAP) were employed for data augmentation for deep convolutional neural network training (Takahashi et al., 2018). The details are as follows: RICAP cropped new training CT images randomly from the original CT images and patched them to compose new training CT images set. Using this method, 5,460 patches

were used to construct the new training set. In order to enhance the generalization ability of the model, the RICAP-based data augmentation was used in real time.

Deep Learning Convolutional Neural Network

GhostNet is an improved deep convolution neural network developed by Huawei Noah Ark Laboratory (Han et al., 2020; Paoletti et al., 2021). A GhostNet is a type of convolutional neural network that is built using Ghost modules, which aim to generate more features by using fewer parameters (allowing for greater efficiency). The architecture of GhostNet and the flowchart of deep learning for CT images are shown in **Figure 1B**. There are two important constituent concepts in the GhostNet. One is the Ghost module that can generate more feature maps from cheap operations. Through a series of linear transformations, ghost module can generate many ghost feature maps that can fully reveal the information behind the intrinsic features at a low computational cost. Another important concept is the Ghost bottleneck, which is designed to stack Ghost modules. The Ghost bottleneck appears to be the basic block in Ghostnet in which several convolutional layers and shortcuts are integrated. In general, the ghost bottleneck consists of two stacked Ghost modules. The first Ghost module expands the number of channels and the second Ghost module reduces the number of channels to match the shortcut path. Then, there is shortcut connected between the inputs and the outputs of these two Ghost modules. After each layer, the ReLU nonlinearity and batch normalization (BN) are applied, except that ReLU is not used after the second Ghost module. GhostNet mainly consists of a stack of Ghost bottlenecks that consist of the Ghost modules as the building block. Here, we clearly explain the meaning of the parameters of "G-bneck a, b, c, d" in the figure. The G-bneck denotes Ghost bottleneck, the first parameter "a" means expansion size, "b" means the number of output channels, "c" denotes whether using SE module, and "d" denotes the stride. The first layer is a standard convolutional layer with 16 filters and then a series of Ghost bottlenecks with gradually increased channels connected in turn. According to the sizes of their input feature maps, these Ghost bottlenecks are grouped into different stages, and all the Ghost bottlenecks in each stage are applied with stride = 1 except that the last one is with stride = 2. At the end of the Ghostnet, the global average pooling (7×7) and the convolutional layer are utilized to transform the feature maps to a 1,280-dimensional feature vector for final classification. In the Ghostnet, some ghost bottlenecks also contain the squeeze and excite (SE) module. However, there is no hard-swish nonlinearity function due to its large latency, which is different from the MobileNetV3.

Implementation Details

Our implementation was based on the package for the Ghostnet Network in python (version 3.7.1). Our training experiments were performed in a Windows 10 environment on a computer server with the following specifications: CPU Intel Xeon Processor Platinum 8124 M at 3.00 GHz, GPU NVIDIA RTX 3060, and 128 GB RAM.

TABLE 1 | Participant characteristics in the training and validation cohorts.

Characteristic	Training cohort (n = 319)	Validation cohort (n = 80)
Age (years)		
≤60	211 (66.3%)	45 (56.5%)
>60	108 (33.7%)	35 (43.5%)
Sex		
Male	232 (72.8%)	55 (69.0%)
Female	87 (27.2%)	25 (31.0%)
HBsAg status		
Positive	289 (90.5%)	77 (95.6%)
Negative	30 (9.5%)	3 (4.4%)
Child–Pugh classification		
A	248 (77.9%)	64 (79.67%)
B	71 (22.1%)	16 (21.33%)
ALT (U/ml)		
≤40	173 (54.2%)	52 (64.7%)
>40	146 (45.8%)	28 (35.3%)
AST (U/ml)		
≤40	105 (32.9%)	24 (30.3%)
>40	214 (67.1%)	56 (69.7%)
AFP (ng/ml)		
≤20	152 (47.5%)	40 (50.3%)
>20	167 (52.5%)	40 (49.7%)
Hepatocirrhosis status		
Present	195 (61.0%)	44 (54.9%)
Absent	124 (39.0%)	36 (45.1%)
Response to therapy		
Objective response	184 (57.7%)	50 (62.5%)
Non-response	135 (42.3%)	30 (37.5%)

Statistical Analysis

Statistical analyses were performed with R statistical software (R Core Team, 2018) and Origin 9.1 (OriginLab Corporation, United States). Categorical variables were described as frequency (percentage), use Ghostnet to perform 50 iterations on the data, and finally calculate the AUC value (95% confidence interval). The performance of the prediction model was evaluated with the area under the receiver operating characteristic (ROC) curve, and the confusion matrices were plotted in validation cohorts to calculate the accuracies of estimating the response of TACE therapy.

RESULTS

Multi-Modal Point-of-Care Predicting System

In order to predict the response of TACE for HCC therapy, we developed a point-of-care system by a concept of integrating multi-modal large-scale data of CT imaging and clinical indexes (**Figure 1A**). This artificial intelligent predicting system could be divided into two parts: the computed tomography image-based predicting response of TACE and the clinical index-based

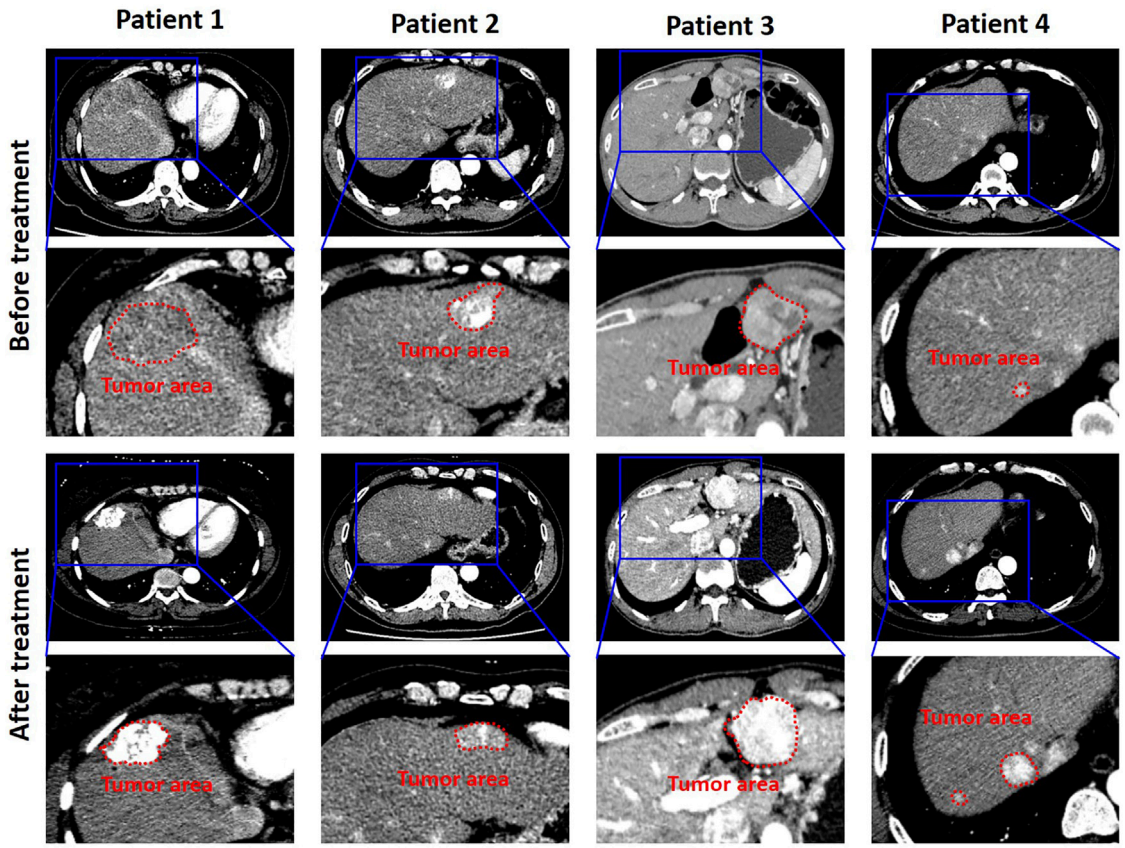

FIGURE 2 | CT images were collected 7 days before treatment and 1 month after treatment, respectively. The measurement range was the longest diameter of the enhanced lesion in the tumor area. The tumor area of validation cohort with HCC of TACE therapy is shown in the red box.

evaluation of HCC therapy. The GhostNet, which was developed by Huawei Noah Ark Laboratory, was employed as a deep learning score for predicting the response of patients with HCC after treatment. The architecture of GhostNet and the flowchart of deep learning for CT images are shown in **Figure 1B**. The GhostNet consisted of two important constituent concepts. Firstly, the Ghost module could generate more feature maps from cheap operations. Secondly, the Ghost bottleneck was designed to stack Ghost modules. More details can be seen in *Materials and Methods*.

Patients Clinical Characteristics

Our retrospective study had been approved by the institutional review board and Ethical Committee (KY 2019-217). Finally, 399 patients with HCC were enrolled in this study: 319 patients and 80 patients were allocated to the training cohort and validation cohort, respectively. **Table 1** listed the detailed clinical characteristics of the two cohorts. In the training cohort, the age of 108 (33.7%) patients was more than 60 years, 87 (27.2%) were female patients, 289 (90.5%) of the patients were diagnosed with hepatitis B virus, patients with AST and ALT over 20 U/ml were 214 (67.1%) and 146 (45.8%), respectively. Patients with abnormal AFP were 167 (52.5%). Similarly, hepatitis B virus positive in the validation cohort was 77 (95.6%); patients with higher than normal AST, ALT, and AFP were 56 (69.7%), 28 (35.3%), and 40 (49.7%), respectively. As can be seen, no significant differences were observed between the training cohorts and validation cohorts in the clinical database.

Classification of the TACE Therapy Response

Four typical CT images with different TACE responses from the validation cohort are shown in **Figure 2**. According to the mRECIST standards, the responses of patients after TACE treatment could be divided into two groups: the objective response and non-response. The objective response was defined as the tumor disappearance or the tumor area and corresponding cross-sectional diameter decreased at least 30%. After the TACE therapy, the cross-sectional diameter gradient of tumor of patients 1 and 2 were 43.9% (from 38.2 to 21.3 mm) and 40.7% (from 31.6 to 12.8 mm), respectively. Therefore, patients 1 and 2 were the typical objective response. The non-response was defined as the tumor area and corresponding cross-sectional diameter decreased less than 30% or the tumor progressed. Patients 3 and 4 belonged to the non-response. As can be seen, the cross-sectional diameter of tumor of patient 3 decreased from 32.5 to 30.7 mm (~5.5%). Especially for patient 4, the cross-sectional diameter showed an increased trend

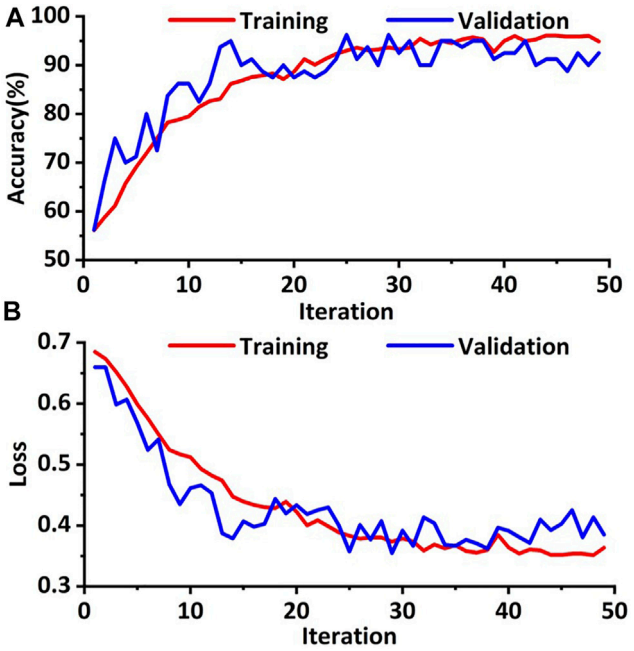

FIGURE 3 | Training and validation processes of the deep learning model based on the CT images. **(A)** The accuracies of training and validation cohort *via* the ghost network model were approximately 98.0%. **(B)** The final training and validation losses were close to 0.4.

(from 11.8 to 20.3 mm). In addition, a new tumor lesion occurred in the bottom of the left lobe of liver.

Training and Validation of the Point-of-Care Predicting System

The training cohort was augmented through the way of RICP to avoid data overfitting. In order to increase the robustness of the model, an improved deep convolution neural network (GhostNet) was used for data training. As shown in **Figures 3A,B**, the accuracy of the improved deep learning model was approximately 98% and the cross-entropy loss was close to 0.4 after training (~50 training epoch). These results indicated that the improved deep learning model showed good performance on distinguishing the response of TACE therapy in these cohorts.

In order to evaluate the training effect of the GhostNet based improved deep learning model, the AUC of the receiver operating characteristic curve was calculated. As shown in **Figure 4A**, the AUC of the deep learning model was about 0.98. The predictive accuracy of the deep learning model in each patch by confusion matrix after 50 epochs training was also investigated. The number of true-positive (TP) patches, false-positive (FP) patches false-negative (FN) patches, and true-negative (TN) patches were 30, 2, 0, and 48, respectively as shown in **Figure 4B**. Hence, the precision, F1 score, and accuracy were 0.94, 0.97, and 0.98, respectively. These results indicated that the improved deep learning model could increase the robust accuracy of predicting the TACE response.

IBI-Based Predicting of TACE Response

The best response of TACE could not always be achieved after one session of CT imaging, especially for patients with large tumors. In addition, the CT image could not be achieved frequently due to damage of ionizing radiation on the patients. Therefore, other evaluation clinical indexes should be added to this model for efficiently predicting the response of TACE therapy. Recent studies confirmed that IBI also plays a prognostic role in the whole clinical process of malignancies. **Figure 5** illustrates the boxplot of the clinical evaluation indexes. As can be seen, the box and median of objective response for NLR was extremely larger than that of non-response. Hence, SIRI had significant association with the response relation of TACE. Other clinical evaluation indexes had a certain correlation with the response relation. All the p values of the factors are less than 0.05. It presented that there are significant differences between the evaluation values of the six factors in response and non-response.

To further investigate the correlation of clinical evaluation indexes with TACE therapy, the thermodynamic diagram was also achieved by statistical analysis. **Figure 6** shows the association between the IBI and the objective response and non-response. Create a dummy variable for the reaction variable, and then the correlation was calculated; 1 represented the objective response. According to the correlation coefficient thermodynamic diagram, among the six

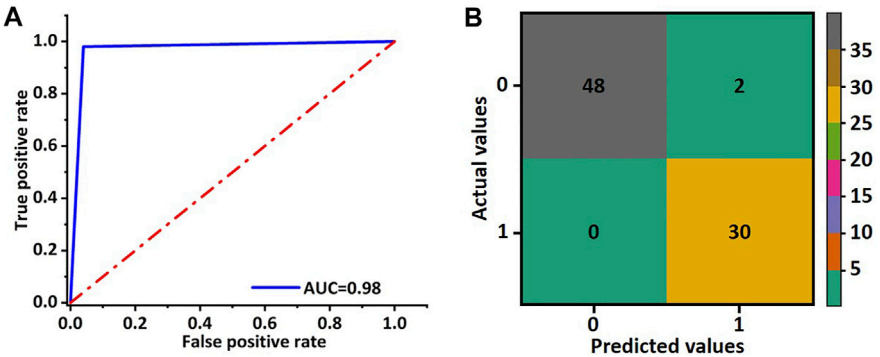

FIGURE 4 | Receiver operating characteristic curve and confusion matrix of validation cohort for the ghost network. **(A)** The AUC value of the ROC was used to evaluate the training effect of the model. **(B)** The accuracy of the ghost model in image classification was evaluated by the obfuscation matrix.

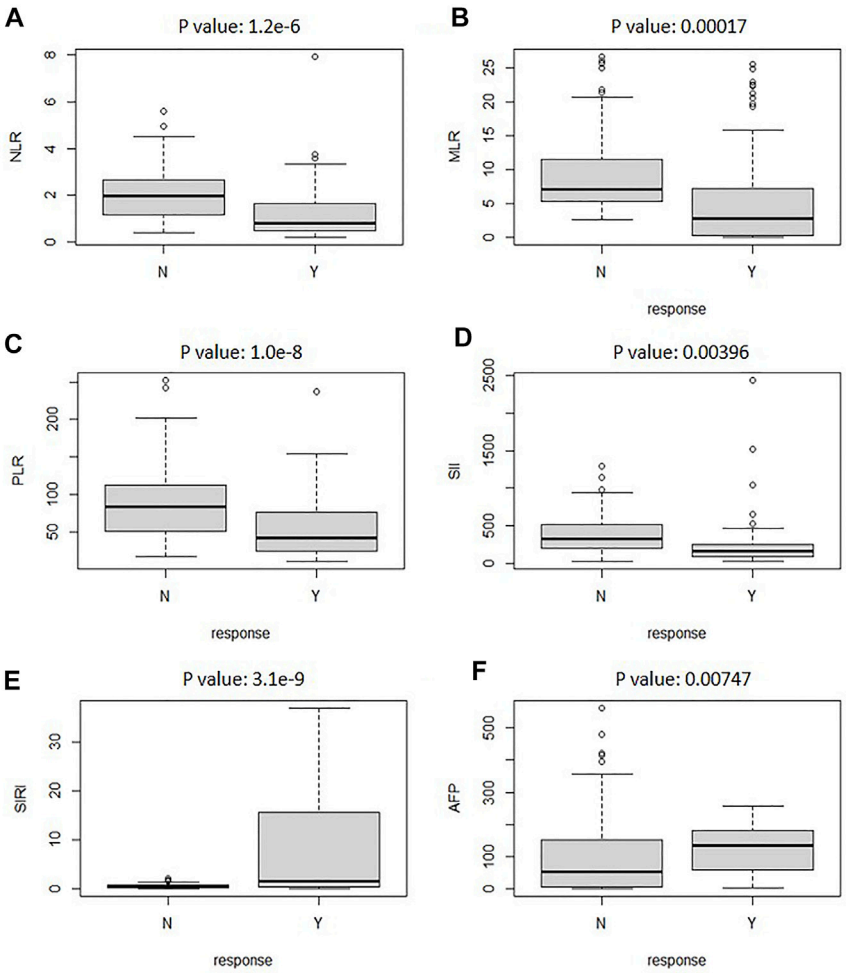

FIGURE 5 | The boxplot analyzed the relationship between reactive and nonreactive values for clinical evaluation indexes of NLR **(A)**, AFP **(B)**, SIRI **(C)**, SII **(D)**, MLR **(E)**, and PLR **(F)**.

factors, all factors had a certain correlation with the response relation, among which SIRI had a significant association with a correlation of 0.53, and AFP had no significant association with the response relation with a correlation of 0.16. Among them, PLR had a significant association. Hence, SIRI and PLR could be used to predict the response of TACE therapy.

DISCUSSION

In this study, we demonstrated a new artificial intelligent point-of-care multi-modal system for predicting the response of TACE therapy on patients with HCC. Based on integrating the multi-modal data of CT images and IBI, an improved deep learning model was employed to formulate precisely the interventional treatment plan for HCC (especially for patients at intermediate tumor stage or advanced tumor stage).

According to international guidelines, the TACE was recommended as the optimal treatment for patients with HCC at the intermediate tumor stage. The response of TACE therapy was crucial for clinicians to accurately identify patients who responded after TACE. Recent studies showed that CT imaging setting could be a promising tool for the detection, stage, and risk assessment of HCC (Woodall et al., 2007; Banerjee et al., 2015). In our study, 399 patients with HCC who underwent TACE had preoperative and postoperative CT enhanced images and clinical information, were enrolled to training a new deep learning model for predicting the response of TACE before operation. Using the random image cropping and patching method, 5,460 patches, which were cropped and patched from the original CT images, were used to construct a new training set. The accuracy of the improved deep learning model was approximately 98.0%, and the cross-entropy loss was close to 0.4. These results indicated that the improved deep learning model showed a good performance on the distinguishing of the response of TACE therapy in these cohorts.

However, CT was inapplicable for suspicious recurrence or atypical image. In addition, the CT images could not be achieved frequently due to damage of ionizing radiation on patients. Hence, it was necessary to find other clinical indexes combined with CT images for TACE response prediction. The included inflammation indexes (such as the NLR, MLR, PLR, SII,

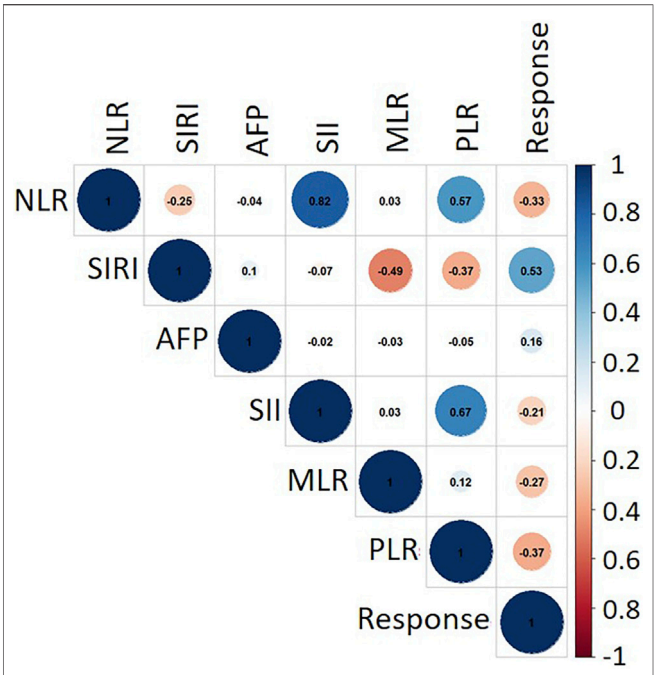

FIGURE 6 | Correlation matrix between clinical evaluation indexes. The closer the absolute value of correlation coefficient was to 1, the stronger the correlation between variables was. The closer the absolute value of correlation coefficient was to 0, the weaker the correlation between variables was. The blue circle denotes a positive correlation, while red indicates a negative correlation.

and SIRI) and AFP, which were derived from peripheral blood counts (e.g., neutrophil, lymphocyte, and platelet) and acute-phase proteins [e.g., C-reactive protein (CRP) and albumin], represented enabling tumor characteristics. Hence, task challenge remained about how to preferably integrate multi-modal data such as clinical index and CT images into an artificial intelligent system that enabled patients' outlook to be predicted accurately. The studies showed that SIRI and PLR are significantly correlated with the response of TACE therapy.

We showed that this artificial intelligent point-of-care system integrating multi-modal data of CT images, SIRI, and PLR could be used for precisely predicting the response of the patients with HCC. However, our study has several limitations. First, this was a retrospective research. Second, multi-center prospective data will be collected for external verification of GhostNet performance in the following study. In the future, we would apply other feature selection techniques and clinical indexes (such as genes and proteins) to further improve the accuracy of diagnosis of HCC.

CONCLUSION

In summary, a new artificial intelligent point-of-care multi-modal system based on CT images and clinical evaluation indexes would potentially serve as a new tool for predicting the response of TACE therapy on patients with HCC. The accuracy of this artificial intelligent system was approximately 98.0%, and the cross-entropy loss was close to 0.4. In addition, SIRI and PLR had a significant association with the responses of TACE therapy. These results indicated that this system showed a good performance on distinguishing the response of TACE therapy. This multi-modal point-of-care predicting system opened new possibilities to help clinicians select optimum patients with HCC who could benefit from the interventional therapy.

DATA AVAILABILITY STATEMENT

The raw data supporting the conclusion of this article will be made available by the authors, without undue reservation.

ETHICS STATEMENT

The studies involving human participants were reviewed and approved by The Second Affiliated Hospital of Harbin Medical University. The patients/participants provided their written informed consent to participate in this study.

AUTHOR CONTRIBUTIONS

ZSu and HJ conceived the project, performed the experiments, collected and analyzed the data, performed the analysis, and wrote the manuscript. ZSh, YX, DW, HJ, and ZW performed experiments and/or collected the data. SZ, HJ, LZ, and YD. revised the manuscript. All authors contributed to the article and approved the submitted version.

FUNDING

The authors gratefully acknowledge funding support by the National Key Research and Development Program of China (2019YFC0118102), the National Natural Science Foundation of China (81873910), and the General Financial Grant from the Heilongjiang Postdoctoral Science Foundation (LBH-Z20078).

ACKNOWLEDGMENTS

The authors are grateful to Dr. Liu from Deepwise Inc. for helpful discussions.

REFERENCES

Banerjee, S., Wang, D. S., Kim, H. J., Sirlin, C. B., Chan, M. G., Korn, R. L., et al. (2015). A Computed Tomography Radiogenomic Biomarker Predicts Microvascular Invasion and Clinical Outcomes in Hepatocellular Carcinoma. *Hepatology* 62, 792–800. doi:10.1002/hep.27877

Cammà, C., Schepis, F., Orlando, A., Albanese, M., Shahied, L., Trevisani, F., et al. (2002). Transarterial Chemoembolization for Unresectable Hepatocellular Carcinoma: Meta-Analysis of Randomized Controlled Trials. *Radiology* 224, 47–54. doi:10.1148/radiol.2241011262

Chan, S. L., Wong, L.-L., Chan, K.-C. A., Chow, C., Tong, J. H.-M., Yip, T. C.-F., et al. (2020). Development of a Novel Inflammation-Based index for Hepatocellular Carcinoma. *Liver Cancer* 9, 167–181. doi:10.1159/000504252

Chang, X., Tang, W., Feng, Y., Yu, H., Wu, Z., Xu, T., et al. (2019). Coexisting Cooperative Cognitive Micro-/Nanorobots. *Chem. Asian J.* 14, 2357–2368. doi:10.1002/asia.201900286

Craig, A. J., von Felden, J., Garcia-Lezana, T., Sarcognato, S., and Villanueva, A. (2020). Tumour Evolution in Hepatocellular Carcinoma. *Nat. Rev. Gastroenterol. Hepatol.* 17, 139–152. doi:10.1038/s41575-019-0229-4

Esteva, A., Kuprel, B., Novoa, R. A., Ko, J., Swetter, S. M., Blau, H. M., et al. (2017). Dermatologist-level Classification of Skin Cancer with Deep Neural Networks. *Nature* 542, 115–118. doi:10.1038/nature21056

Gulshan, V., Peng, L., Coram, M., Stumpe, M. C., Wu, D., Narayanaswamy, A., et al. (2016). Development and Validation of a Deep Learning Algorithm for Detection of Diabetic Retinopathy in Retinal Fundus Photographs. *JAMA* 316, 2402–2410. doi:10.1001/jama.2016.17216

Han, K., Wang, Y., Tian, Q., Guo, J., Xu, C., and Xu, C. (20202020). Ghostnet: More Features from Cheap Operations. *Proc. IEEE/CVF Conf. Comput. Vis. Pattern Recognition (Cvpr)*, 1580–1589. doi:10.1109/cvpr42600.2020.00165

Hucke, F., Sieghart, W., Schöniger-Hekele, M., Peck-Radosavljevic, M., and Müller, C. (2011). Clinical Characteristics of Patients with Hepatocellular Carcinoma in Austria - Is There a Need for a Structured Screening Program? *Wien. Klin. Wochenschr.* 123, 542–551. doi:10.1007/s00508-011-0033-9

Kermany, D. S., Goldbaum, M., Cai, W., Valentim, C. C. S., Liang, H., Baxter, S. L., et al. (2018). Identifying Medical Diagnoses and Treatable Diseases by Image-Based Deep Learning. *Cell* 172, 1122–1131. doi:10.1016/j.cell.2018.02.010

Li, T., Chang, X., Wu, Z., Li, J., Shao, G., Deng, X., et al. (2017). Autonomous Collision-free Navigation of Microvehicles in Complex and Dynamically Changing Environments. *ACS Nano* 11, 9268–9275. doi:10.1021/acsnano.7b04525

Li, T., Zhang, A., Shao, G., Wei, M., Guo, B., Zhang, G., et al. (2018). Janus Microdimer Surface Walkers Propelled by Oscillating Magnetic fields. *Adv. Funct. Mater.* 28, 1706066. doi:10.1002/adfm.201706066

Liu, Q. P., Xu, X., Zhu, F. P., Zhang, Y. D., and Liu, X. S. (2020). Prediction of Prognostic Risk Factors in Hepatocellular Carcinoma with Transarterial Chemoembolization Using Multi-Modal Multi-Task Deep Learning. *EClinicalMedicine* 23, 100379. doi:10.1016/j.eclinm.2020.100379

Llovet, J. M., Di Bisceglie, A. M., Bruix, J., Kramer, B. S., Lencioni, R., Zhu, A. X., et al. (2008). Design and Endpoints of Clinical Trials in Hepatocellular Carcinoma. *J. Natl. Cancer Inst.* 100, 698–711. doi:10.1093/jnci/djn134

Llovet, J. M., Kelley, R. K., Villanueva, A., Singal, A. G., Pikarsky, E., Roayaie, S., et al. (2021). Hepatocellular Carcinoma. *Nat. Rev. Dis. Primers.* 7, 6. doi:10.1038/s41572-020-00240-3

Llovet, J. M., Real, M. I., Montaña, X., Planas, R., Coll, S., Aponte, J., et al. (2002). Arterial Embolisation or Chemoembolisation versus Symptomatic Treatment in Patients with Unresectable Hepatocellular Carcinoma: a Randomised Controlled Trial. *The Lancet* 359, 1734–1739. doi:10.1016/s0140-6736(02)08649-x

Otto, G., Herber, S., Heise, M., Lohse, A. W., Mönch, C., Bittinger, F., et al. (2006). Response to Transarterial Chemoembolization as a Biological Selection Criterion for Liver Transplantation in Hepatocellular Carcinoma. *Liver Transpl.* 12, 1260–1267. doi:10.1002/lt.20837

Paoletti, M. E., Haut, J. M., Pereira, N. S., Plaza, J., and Plaza, A. (2021). Ghostnet for Hyperspectral Image Classification. *IEEE Trans. Geosci. Remote Sensing*, 1–16. doi:10.1109/TGRS.2021.3050257

Park, H. J., Kim, J. H., Choi, S.-y., Lee, E. S., Park, S. J., Byun, J. Y., et al. (2017). Prediction of Therapeutic Response of Hepatocellular Carcinoma to Transcatheter Arterial Chemoembolization Based on Pretherapeutic Dynamic CT and Textural Findings. *Am. J. Roentgenology* 209, W211–W220. doi:10.2214/ajr.16.17398

Peng, J., Kang, S., Ning, Z., Deng, H., Shen, J., Xu, Y., et al. (2019). Residual Convolutional Neural Network for Predicting Response of Transarterial Chemoembolization in Hepatocellular Carcinoma from CT Imaging. *Eur. Radiol.* 30, 413–424. doi:10.1007/s00330-019-06318-1

Pinato, D. J., Stebbing, J., Ishizuka, M., Khan, S. A., Wasan, H. S., North, B. V., et al. (2012). A Novel and Validated Prognostic index in Hepatocellular Carcinoma: The Inflammation Based index (IBI). *J. Hepatol.* 57, 1013–1020. doi:10.1016/j.jhep.2012.06.022

Sanghera, C., Teh, J. J., and Pinato, D. J. (2019). The Systemic Inflammatory Response as a Source of Biomarkers and Therapeutic Targets in Hepatocellular Carcinoma. *Liver Int.* 39, 2008–2023. doi:10.1111/liv.14220

Sieghart, W., Hucke, F., and Peck-Radosavljevic, M. (2015). Transarterial Chemoembolization: Modalities, Indication, and Patient Selection. *J. Hepatol.* 62, 1187–1195. doi:10.1016/j.jhep.2015.02.010

Takahashi, R., Matsubara, T., and Uehara, K. (2018). Data Augmentation Using Random Image Cropping and Patching for Deep CNNs. *IEEE Trans. Circuits Syst. Video Technol.* 30, 2917–2931.

Takayasu, K., Arii, S., Ikai, I., Omata, M., Okita, K., Ichida, T., et al. (2006). Prospective Cohort Study of Transarterial Chemoembolization for Unresectable Hepatocellular Carcinoma in 8510 Patients. *Gastroenterology* 131, 461–469. doi:10.1053/j.gastro.2006.05.021

Tao, Y., Wang, J., and Xu, X. (2020). Emerging and Innovative Theranostic Approaches for Mesoporous Silica Nanoparticles in Hepatocellular Carcinoma: Current Status and Advances. *Front. Bioeng. Biotechnol.* 8, 184. doi:10.3389/fbioe.2020.00184

Villanueva, A. (2019). Hepatocellular Carcinoma. *N. Engl. J. Med.* 380, 1450–1462. doi:10.1056/nejmra1713263

Vitale, A., Ramirez Morales, R., Zanus, G., Farinati, F., Burra, P., Angeli, P., et al. (2011). Barcelona Clinic Liver Cancer Staging and Transplant Survival Benefit for Patients with Hepatocellular Carcinoma: a Multicentre, Cohort Study. *Lancet Oncol.* 12, 654–662. doi:10.1016/s1470-2045(11)70144-9

Wang, Z.-C., Jiang, W., Chen, X., Yang, L., Wang, H., and Liu, Y.-H. (2021). Systemic Immune-Inflammation index Independently Predicts Poor Survival of Older Adults with Hip Fracture: a Prospective Cohort Study. *BMC. Geriatr.* 21, 155. doi:10.1186/s12877-021-02102-3

Woodall, C. E., Scoggins, C. R., Loehle, J., Ravindra, K. V., McMasters, K. M., and Martin, R. C. G. (2007). Hepatic Imaging Characteristics Predict Overall Survival in Hepatocellular Carcinoma. *Ann. Surg. Oncol.* 14, 2824–2830. doi:10.1245/s10434-007-9525-2

Yang, J., Bao, Y., Chen, W., Duan, Y., and Sun, D. (2020). Nomogram Based on Systemic Immune Inflammation Index and Prognostic Nutrition Index Predicts Recurrence of Hepatocellular Carcinoma after Surgery. *Front. Oncol.* 10, 551668. doi:10.3389/fonc.2020.551668

Yang, T., Lin, C., Zhai, J., Shi, S., Zhu, M., Zhu, N., et al. (2012). Surgical Resection for Advanced Hepatocellular Carcinoma According to Barcelona Clinic Liver Cancer (BCLC) Staging. *J. Cancer Res. Clin. Oncol.* 138, 1121–1129. doi:10.1007/s00432-012-1188-0

Yu, L., Xu, F., and Gao, L. (2020). Predict New Therapeutic Drugs for Hepatocellular Carcinoma Based on Gene Mutation and Expression. *Front. Bioeng. Biotechnol.* 8, 8. doi:10.3389/fbioe.2020.00008

Zhang, Z.-M., Tan, J.-X., Wang, F., Dao, F.-Y., Zhang, Z.-Y., and Lin, H. (2020). Early Diagnosis of Hepatocellular Carcinoma Using Machine Learning Method. *Front. Bioeng. Biotechnol.* 8, 254. doi:10.3389/fbioe.2020.00254

Zheng, R., Qu, C., Qu, C., Zhang, S., Zeng, H., Sun, K., et al. (2018). Liver Cancer Incidence and Mortality in China: Temporal Trends and Projections to 2030. *Chin. J. Cancer Res.* 30, 571–579. doi:10.21147/j.issn.1000-9604.2018.06.01

Conflict of Interest: The authors declare that the research was conducted in the absence of any commercial or financial relationships that could be construed as a potential conflict of interest.

frontiers in Bioengineering and Biotechnology

ORIGINAL RESEARCH
published: 16 November 2021
doi: 10.3389/fbioe.2021.777344

Bioinspired Synthesis of ZnO@polydopamine/Au for Label-Free Photoelectrochemical Immunoassay of Amyloid-β Protein

Guangli He[1], Yue Zhou[1], Mifang Li[2], Yanzhen Guo[1], Hang Yin[1], Baocheng Yang[1], Shouren Zhang[1]* and Yibiao Liu[2]**

[1]Henan Key Laboratory of Nanocomposites and Applications, Institute of Nanostructured Functional Materials, Huanghe Science and Technology College, Zhengzhou, China, [2]Shenzhen Longgang Central Hospital (The Second Affiliated Hospital of the Chinese University of Hong Kong, Shenzhen, China

OPEN ACCESS

Edited by:
Tailin Xu,
Shenzhen University, China

Reviewed by:
Shuqi Wang,
Suzhou Institute of Nano-tech and Nano-bionics (CAS), China
Guangyao Zhang,
Qingdao University, China

***Correspondence:**
Baocheng Yang
baochengyang@infm.hhstu.edu.cn
Shouren Zhang
shourenzhang@infm.hhstu.edu.cn
Yibiao Liu
liuyibiao12345@126.com

Specialty section:
This article was submitted to Biosensors and Biomolecular Electronics, a section of the journal Frontiers in Bioengineering and Biotechnology

Received: 15 September 2021
Accepted: 18 October 2021
Published: 16 November 2021

Citation:
He G, Zhou Y, Li M, Guo Y, Yin H, Yang B, Zhang S and Liu Y (2021) Bioinspired Synthesis of ZnO@polydopamine/Au for Label-Free Photoelectrochemical Immunoassay of Amyloid-β Protein. Front. Bioeng. Biotechnol. 9:777344. doi: 10.3389/fbioe.2021.777344

Amyloid-β protein (Aβ) is an important biomarker and plays a key role in the early stage of Alzheimer's disease (AD). Here, an ultrasensitive photoelectrochemical (PEC) sensor based on ZnO@polydopamine/Au nanocomposites was constructed for quantitative detection of Aβ. In this sensing system, the ZnO nanorod array decorated with PDA films and gold nanoparticles (Au NPs) have excellent visible-light activity. The PDA film was used as a sensitizer for charge separation, and it also was used for antibody binding. Moreover, Au NPs were loaded on the surface of PDA film by *in situ* deposition, which further improved the charge transfer efficiency and the PEC activity in visible light due to the localized surface plasmon resonance effect of Au NPs. Therefore, in ZnO@polydopamine/Au nanocomposites, a significantly enhanced photocurrent response was obtained on this photoelectrode, which provides a good and reliable signal for early detection of AD. Under the optimized conditions, the PEC immunosensor displayed a wide linear range from 1 pg/mL to 100 ng/mL and a low detection limit of 0.26 pg/mL. In addition, this PEC immunosensor also presented good selectivity, stability, and reproducibility. This work may provide a promising point-of-care testing method toward advanced PEC immunoassays for AD biomarkers.

Keywords: photoelectrochemical sensor, ZnO, polydopamine, gold nanoparticles, Alzheimer's disease

INTRODUCTION

As a most prevalent type of dementia, Alzheimer's disease (AD) is a fatal and irreversible neurodegenerative disorder, occurring mainly in aged people.(Evans, Funkenstein et al., 1989; Matthews, Arthur et al., 2013) Although massive effort has been made to cure this disease, there is still no efficient treatment for it. AD is marked by a slow degeneration progression and the neurodegeneration process starts several decades before the first clinical symptoms appear.(Jack et al., 2010; Selkoe 2012; Yang et al., 2021) Therefore, early diagnosis of AD allows timely treatment to ameliorate the deterioration symptoms of the patient, which has important directive significance to clinical works.(Butterfield, Drake et al., 2002; Hardy 2002; Jack et al., 2010; Murphy and Rd 2010) One of the important traits of AD is cerebral extracellular amyloid plaques, which are formed through aggregation of amyloid-β (Aβ) protein. Aβ protein is a polypeptide consisting of 39–42 amino acids. There are two primary variants: Aβ40 and Aβ42. PET

and the level of Aβ (Aβ40, Aβ42) in cerebrospinal fluid (CSF) are the gold standard of AD clinical diagnosis.(Grimmer, Riemenschneider et al., 2009; Marcus, Mena et al., 2014; Guilherme, Marina et al., 2020) However, this diagnosis method is unlikely to become popularized in the public because of high-cost PET and unavailable CSF. Therefore, the development of low-cost, noninvasive, and accessible tools to accurately quantify Aβ protein in blood for the early diagnosis of AD is required.(Nakamura, Kaneko et al., 2018; Laís Canniatti, Isabella et al., 2019) In blood, the physiological concentrations of Aβ is several picograms per milliliter. To date, a great deal of sensing techniques has been performed to detect Aβ protein, including ELISA(Linan, Son et al., 2016), ion mobility-mass spectrometry (IM-MS)(Obata, Murakami et al., 2020), colorimetric biosensor(Xi, Shuangling et al., 2021), electrochemical(Carneiro, Loureiro et al., 2017), fluorescence(Lee, Park et al., 2019; Wang, Du et al., 2020; Wen-Kai, Liu et al., 2021), surface-enhanced Raman spectroscopy(Yang, Hwang et al., 2019), and photoelectrochemical (PEC) immunosensors(Wang, Fan et al., 2018). Among them, the PEC biosensor is an innovative and attractive analytical technique for quantitative study in the biological analysis due to its intrinsic merits such as label-free, high signal-to-noise ratio, rapid response, and is more readily miniaturized.(Shu and Tang 2019)

For the construction of the PEC biosensor, various kinds of semiconductor materials have been developed to construct the photoelectrode for PEC sensing. Zinc oxide (ZnO) is one of the most extensively used n-type semiconductor photoactive substrates with the advantages of environmental friendliness, abundant natural resources, low cost, and high stability.(Wei, Ke et al., 2012; Zhang, Wang et al., 2016) However, ZnO has the inherent limitations of inefficient utilization of sunlight and low separation efficiency of electron hole, which cannot meet the demands for higher sensitivity of PEC detection. To improve the light-harvesting efficiency and prolong the life of photo-generated carriers, combining with plasmon metals including Au, Ag, and Cu exhibits great superiority in improving the light absorption range and separation efficiency of charge carriers of ZnO-based systems over the other strategies due to the surface plasmon resonance (SPR) effect.(Zheng, Zheng et al., 2007; Xiao, Liu et al., 2015; Kang, Yan et al., 2016; Yang, Li et al., 2017; Zhang, He et al., 2018) Based on the localized surface plasmon resonance (LSPR) of Au nanoparticles (Au NPs), the strong visible light absorption and the effective photo-generated carrier separation at the metal–semiconductor interface can successfully generate remarkable readout photocurrent signals.(Zhu, Zhang et al., 2016; Zhang; Wang et al., 2018; Dong, Xu et al., 2019) For PEC biosensor, the efficient immobilization of biomolecules on photoactive materials of the photoelectrode is also a crucial factor for achieving excellent performance.(Shu and Tang 2019) For ZnO/Au substrates, the antibody immobilization is mainly through Au-NH_2 bonding(Parviz Norouzi and Ganjali 2011; Gasparotto, Costa et al., 2017), but the amount of the immobilized antibody is limited by the low Au content. Recently, inspired by the mussel-adhesion phenomenon, polydopamine (PDA) has attracted intensive attention as a multifunctional biocompatible material with unique properties.(Lee, Dellatore et al., 2007; Lynge, van der Westen et al., 2011; Liu, Ai et al., 2014) Through self-polymerization of dopamine in alkaline aqueous solutions at room temperature, PDA can coat on the surface of various kinds of substrates with strong affinity. The as-formed adherent PDA thin film has abundant active functional groups (catechol, amine, indole, and quinone), capable to serve as universal platforms including cross-linker reagents for biomolecule immobilization and reductants for *in situ* metal deposition. Besides, PDA possesses broadband light absorption and can work as an electron donor.(Hu, He et al., 2014; Wang, Ma et al., 2017; Yu, Huang et al., 2018; He, Gao et al., 2019) Thus, PDA that is used to build up PEC immunosensor exhibits great advantages as a multifunctional platform.

In this work, a novel plasmonic PEC immunosensor was successfully constructed based on ZnO nanorod array@ polydopamine heterointerface modified with Au NPs (ZnO@PDA/Au) for sensitive detection of Aβ. The stepwise process for the PEC immunosensor fabrication and the charge transfer mechanism are displayed in **Figure 1**. The PDA coating involving in the system is used as a multifunctional platform such as a sensitizer for enhancing the photo-to-electron conversion efficiency, a binder for antibody bonding, and a reductant for *in situ* Au deposition. Both PDA film and Au NPs can enhance the light absorption and loading content of antibody. The as-prepared PEC immunosensor realized label-free detection of Aβ, which exhibits a wide linear range from 1 pg/mL to 100 ng/mL, low detection limit of 0.26 pg/mL, high sensitivity, and good stability. This work provides a promising future for the early diagnosis of AD.

EXPERIMENTAL SECTION

Chemicals and Materials

Aβ40, Aβ42, and Aβ42 antibodies were purchased from Bio-Techne China Co., Ltd (Shanghai, China). Bovine serum albumin (BSA) was obtained from Kuer Chemical Technology (Beijing) Co., Ltd (Beijing, China). Zinc nitrate hexahydrate ($Zn(NO_3)_2{\cdot}6H_2O$), ammonia hydroxide ($NH_3{\cdot}H_2O$), ethylenediamine, and potassium permanganate ($KMnO_4$) were acquired from Sinopharm Chemical Reagent Co., Ltd (Shanghai, China). Dopamine, sodium chloride (NaCl), potassium chloride (KCl), $Na_2HPO_4{\cdot}12H_2O$, KH_2PO_4, and ascorbic acid (AA) were purchased from Aladdin Biochemical Technology Co., Ltd., (Shanghai, China). Indium-doped tin oxide (ITO) conducting glass (sheet resistance 8 Ω) was acquired from Wuhan Jinge Solar Technology Co., Ltd., (China). All the chemical reagents were of analytical grade and used directly as received. All the solutions used in all experiments were prepared with ultrapure water (Milli-Q, 18.2 MΩ).

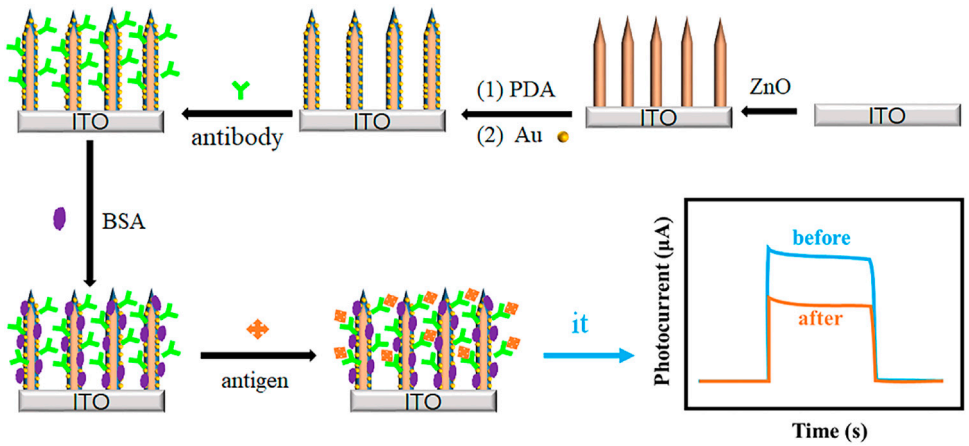

FIGURE 1 | The stepwise fabrication process of the ZnO@PDA/Au PEC immunosensor.

Characterization and Measurement

The morphology was characterized using field emission scanning electron microscopy (FESEM; Quanta 250, FEI, OR, United States). The energy-dispersive X-ray spectroscopy was used to reveal the elemental composition of all composites equipped with FESEM. The X-ray diffraction analyzer (XRD; Bruker D8 diffractometer, Germany) using Cu Kα radiation (40 kV, 40 mA) was employed to determine the crystal phase of the obtained samples. The UV–vis diffuse reflectance spectra (DRS) of the samples were collected using a Thermo U-4100 UV–vis spectrophotometer. The X-ray photoelectron spectroscopy (XPS) data of the composite was obtained on a Thermo Scientific K-Alpha X-ray photoelectron spectrometer with a monochromatized Mg Kα X ray source. All the electrochemical measurements were carried out on a CHI760E Electrochemical Analyzer (Chenhua Instruments, Shanghai, China).

Preparation of ZnO@PDA/Au Modified ITO Electrode

The ZnO nanorod array was grown onto ITO substrate based on the previous literature.(Yang and Hu 2017; He, Gao et al., 2019) In brief, a piece of clean ITO (tailored as size of 2.5 × 1 cm) was first immersed into freshly prepared $KMnO_4$ (5 mM) solution for 30 min at room temperature. After thoroughly rinsing with deionized water, the ITO was then placed with the conductive side facing down in a glass bottle with 10 mL precursor solution containing $Zn(NO_3)_2$ (0.1 M), ammonium hydroxide (3% v/v), and ethylenediamine (4% v/v). The reaction was carried out at 75°C in a water bath for 3 h. The obtained ZnO-ITO was rinsed with water and dried under gentle N_2 flow for later use. Then, the ZnO-ITO electrodes were further coated with PDA *via* a simple dip-coating method. Typically, the as-synthesized ZnO-ITO were dipped into 20 mL of Tris–HCl solution (10 mM, pH 8.5) containing 25 mg dopamine and kept for 4 h at room temperature, followed by gently rinsing with DI water several times. The as-obtained ZnO@PDA electrodes were stored at 4°C for the following use. Au NPs decorated ZnO@PDA-ITO was obtained based on the following *in situ* growth method. Then 0.2 mL of $HAuCl_4$ (1%) aqueous solution was added to 10 mL H_2O solvent to obtain a homogeneous solution. Then the prepared ZnO@PDA-ITO were immersed into the solution and incubated for 60 min. These were then taken out and rinsed gently with DI water and stored at 4°C for next use.

Construction of the Label-free PEC Immunosensors

First, the ZnO@PDA/Au electrode was incubated with 0.02 mL anti-Aβ (10 μg mL^{-1}) PBS solution (pH = 7.4) on the electrode surface for 1 h at room temperature. Second, the electrode was rinsed with PBS solution to remove the physical adsorption of antibodies. Third, the electrode was dipped into bovine serum albumin (BSA, 1 mg/mL) PBS solution for 1 h to block the non-specific binding sites. Finally, 10 μL of Aβ with different concentrations was dropped onto the electrode surface and incubated 1 h at room temperature. After thoroughly washing with PBS buffer, the sensors used for the following PEC detection were obtained.

Photoelectrochemical Detection

All the PEC tests were performed on a CHI 760E electrochemical workstation adopting a standard three-electrode system, in which the as-prepared photo-electrode was used as the working electrode, platinum (Pt) sheet as the counter electrode, and saturated Ag/AgCl electrode as the reference electrode. A 500-W Xe lamp equipped with an AM 1.5 G filter was employed as the irradiation source for the photo-response of the as-obtained photoelectrodes. The power density is 100 mW cm^{-2}. 25 mL of PBS (0.1 M, pH 7.4) solution containing 1 mM AA served as the supporting

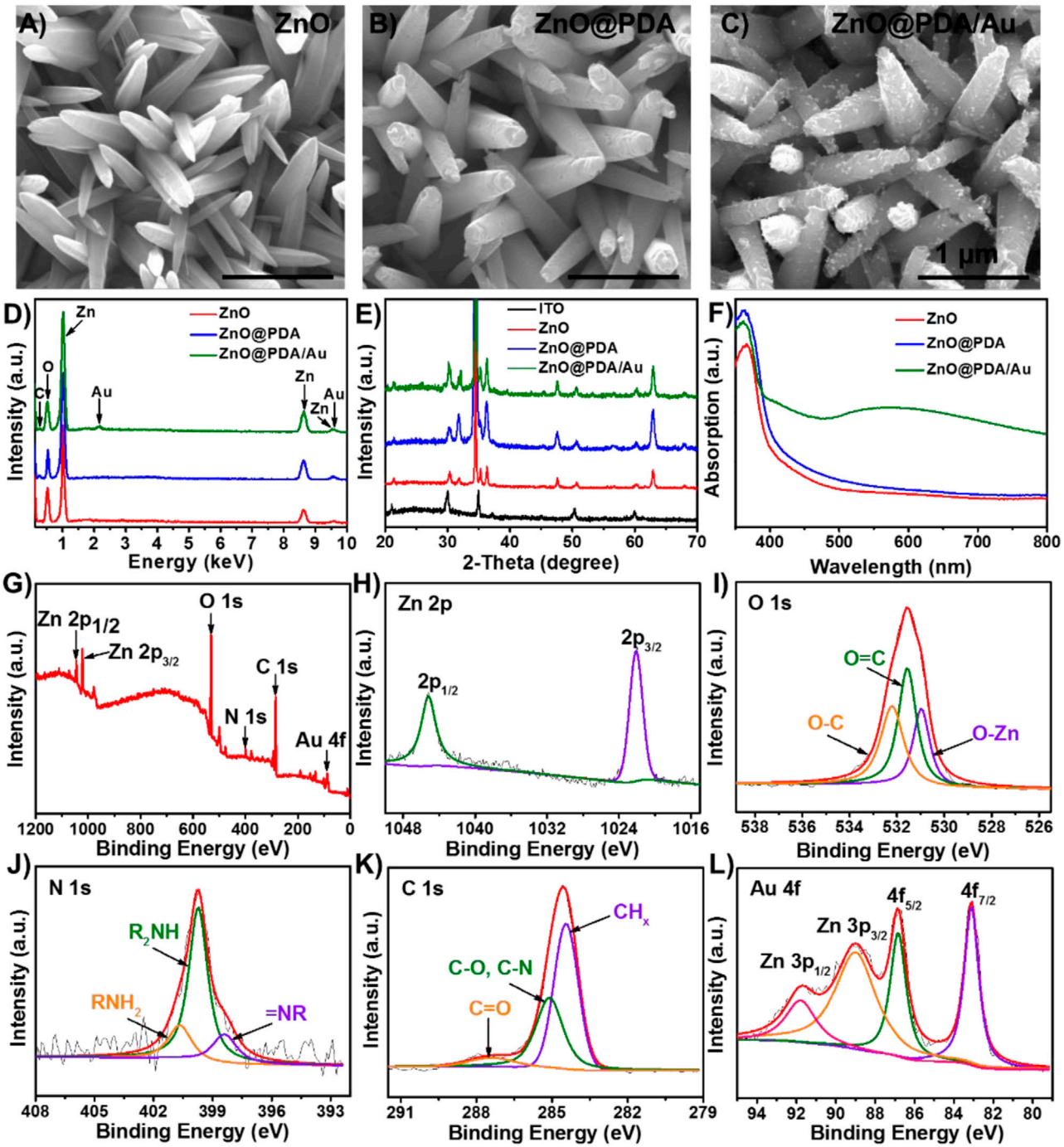

FIGURE 2 | SEM images of **(A)** ZnO NRs, **(B)** ZnO@PDA, **(C)** ZnO@PDA/Au, and **(D)** EDS spectrum of ZnO NRs, ZnO@PDA and ZnO@PDA/Au. **(E)** XRD pattern of ITO, ZnO NRs, ZnO@PDA, and ZnO@PDA/Au. **(F)** UV–vis absorption spectra for ZnO NRs, ZnO@PDA, and ZnO@PDA/Au. XPS spectra of ZnO@PDA/Au. **(G)** Survey; (**H**) Zn 2p; **(I)** O 1s; **(J)** N 1s; **(K)** C 1s; **(L)** Au 4f and Zn 3p.

electrolyte. Linear sweep voltammetry (LSV) curves were recorded from −0.05 to 0.3 V with a scan rate of 50 mV s^{-1}. Electrochemical impedance spectroscopy (EIS) experiment was carried out at open circuit potential in the frequency range of 100 kHz to 0.1 Hz with an amplitude of 5 mV. The photocurrent response measurements of the working electrode were collected under light irradiation switching on and off every 10 s at the applied potential of 0.05 V.

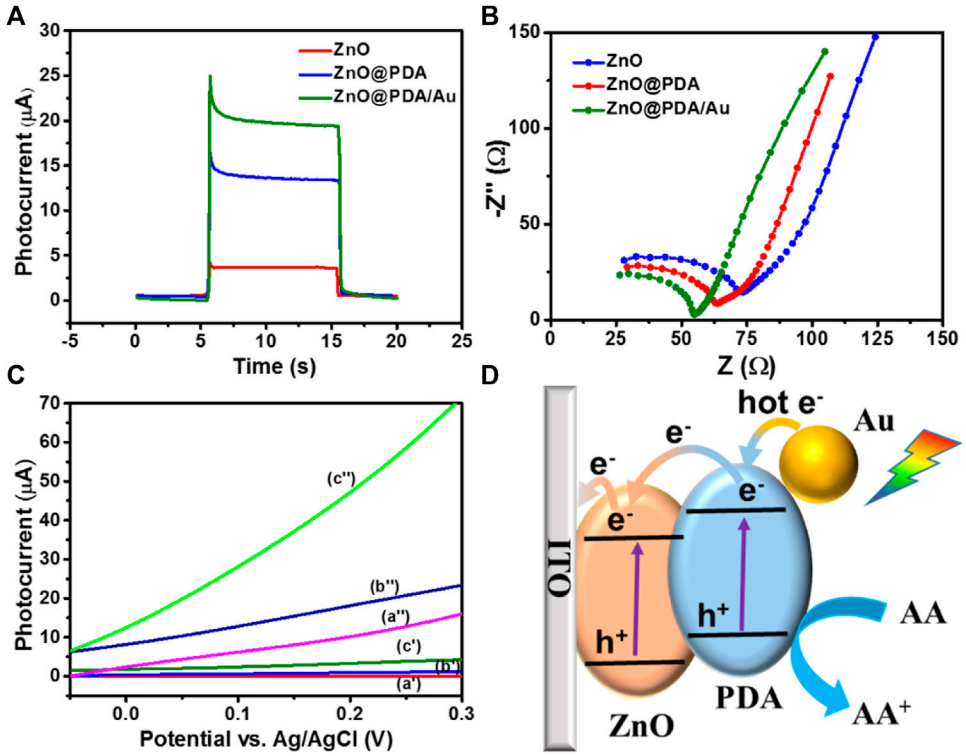

FIGURE 3 | (A) Photocurrent response of ZnO NRs/ITO, ZnO@PDA, and ZnO@PDA/Au toward on/off cycles of simulated sunlight illumination at 0.1 V. Electrolyte solution was 0.1 M PBS containing 1 mM ascorbic acid, potential sweep rate at 50 mV s^{-1}. **(B)** EIS Nyquist plots spectra of different modified electrodes ZnO NRs/ITO, ZnO@PDA, and ZnO@PDA/Au. **(C)** LSV curves of ZnO NRs/ITO (a′, a″), ZnO@PDA/ITO (b′, b″), and ZnO@PDA/Au/ITO (c′, c″) without/with simulated sunlight illumination, respectively. **(D)** The charge transfer mechanism of this PEC immunosensor.

RESULTS AND DISCUSSION

Characterization of the as-prepared Electrodes

The morphology, structure, and composition of ZnO, ZnO@PDA, and ZnO@PDA/Au modified electrodes were recorded. The top and cross-sectional view SEM images in **Figure 2A**; **Supplementary Figure S1** display that a large scale of ZnO nanorods with lengths of around 1.2 μm and diameters of less than 200 nm are grown on the ITO glass. The one-dimensional structure and large gap between the ZnO nanorods can provide a high surface area to facilitate light harvest and further biomaterial assembly. As shown in **Figure 2B**; **Supplementary Figure S2A**, after coating with PDA, the surface of modified nanorods become rougher compared with that of bare ZnO nanorods indicating that the ZnO nanorods have been successfully enwrapped by PDA to form a core/shell. The original structure of the ZnO nanorods still remained. The color of the substrate turns obviously from white to dark yellow during this process, as shown in **Supplementary Figure S3**. The ZnO@PDA were further used for *in situ* deposition of Au NPs basing on the reducing action of PDA coating. In **Figure 2C**; **Supplementary Figure S2B**, various Au NPs are observed homogeneously adhering on the surfaces of ZnO@PDA. At this time, the color of the electrode turned dark red (**Supplementary Figure S3**). EDS spectrum was conducted to further analyze the elemental composition of the electrode with different modifications. The results in **Figure 1D** exhibit that the ZnO nanorods mainly contain Zn and O elements. The content of the C element increases after PDA coating providing another evidence for the existence of PDA. The distinctive Au signal of the ZnO@PDA/Au further confirms that Au has been introduced to the coating substrate successfully. **Figure 2E** shows the XRD patterns for the structural analysis of all the samples. The ZnO exhibits sharp diffraction peaks at 31.7°, 34.5°, 36.3°, 47.6°, and 62.9°, which could be assigned to the hexagonal ZnO phase (JCPDS No. 70–2551). Compared with the original ZnO, PDA-coated ZnO show no peak positions altering and additional peaks, indicating that wrapping PDA does not affect its crystal phase, while a minor increase of the peak intensity can be seen, which might be owing to the low content of PDA in the complex and the positive effect of PDA on the crystallization of ZnO. After loading Au NPs, the emerging characteristic peak of Au at 38.4° proves that Au NPs exist in the ZnO@PDA/Au composite.

Also, the optical properties of these samples were determined by UV–vis diffuse reflectance spectra (DRS). As presented in **Figure 2F**, the light absorbance of bare ZnO is weak in the visible region, which is ascribed to its intrinsic wide bandgap. However,

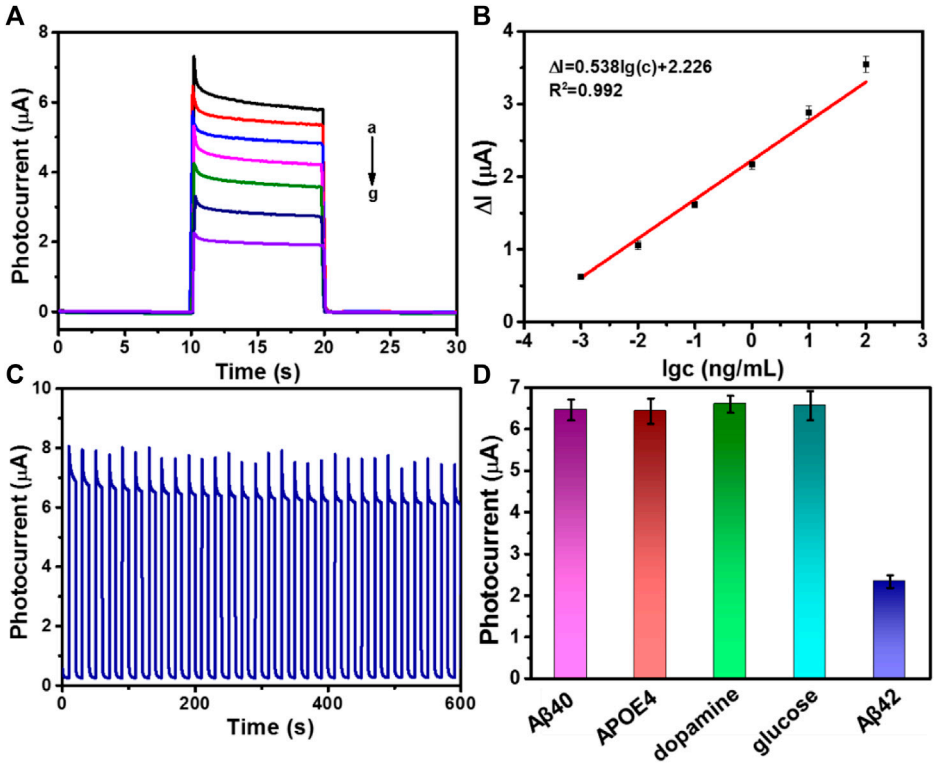

FIGURE 4 | (A) Photocurrent responses of Aβ with different concentration, from (**a**) to (**g**): 0, 0.001, 0.01, 0.1, 1, 10, and 100 ng/mL. **(B)** The linear calibration curve for photocurrent densities versus various concentrations of Aβ ($\Delta I = I_0 - I$, I_0 is the photocurrent response of the PEC sensor without Aβ and I is the photocurrent response containing antigen). Error bars = RSD (n = 3). **(C)** Stable photocurrent response curve of ZnO@PDA/Au electrode incubated with 1 pg/mL Aβ. **(D)** Selectivity of the PEC immunosensor. Photocurrent responses of the PEC immunosensor for different proteins including 1000 pg/mL Aβ40, 1,000 pg/mL APOE4, 1,000 pg/mL dopamine, 1,000 pg/mL glucose, or 10 pg/mL Aβ42.

owing to the homogeneous coating of the PDA shell, ZnO@PDA shows an extended absorption range to the visible light region and increased absorption intensity, indicating that PDA can efficiently absorb visible light and works as a photosensitizer to improve the charge separation. The ZnO@PDA/Au exhibits an obvious absorption peak at about 560 nm, which is assigned to the SPR peak of Au NPs. The aforementioned results prove that by combining the PDA core–shell heterostructure and the LSPR effect of Au NPs, more photoelectric carriers can be generated and separated, which plays a crucial role in enhancing the utilization of sunlight for PEC sensing. In addition, the XPS spectrum is used to analyze the chemical composition and electronic structures of ZnO@PDA/Au. The XPS survey spectrum (**Figure 2G**) shows the existence of Zn, O, N, C, and Au elements in the hybrid composite. As displayed in **Figure 2H**, two peaks of Zn 2p at about 1,022.1 and 1,045.2 eV can be indexed to the binding energy of Zn $2p_{3/2}$ and Zn $2p_{1/2}$, respectively. In **Figure 2I**, the O 1s peak is split into three peaks at 530.8, 531.5, and 532.3 eV, assigning to O–Zn bond binding energy in the structure of ZnO, O=C, and O–C in the PDA film, respectively (*Applied Surface Science* 457 (2018) 1096). As for the N 1s spectrum (**Figure 3J**), the three deconvoluted peaks centered at 398.4, 399.7, and 400.8 eV can be ascribed to primary (R = NH_2), secondary (R–NH–R), and tertiary/aromatic (=N–R) amine functional groups in PDA, respectively. The C 1s spectrum (**Figure 3K**) exhibits three characteristic peaks at 284.4 eV for CH_x species, 285.1 eV for C–O/C–N, and 287.5 eV for C=O in PDA. In **Figure 3L**, the XPS spectrum of Au 4f strongly overlaps with the peaks of Zn 3p; thus, it was fitted into four peaks. The two peaks with the lower binding energy located in 83.1 and 86.8 eV have corresponded to the Au $4f_{7/2}$ and Au $4f_{5/2}$, respectively. Meanwhile, another two peaks can be indexed to Zn $3p_{3/2}$ (89.1 eV) and Zn $3p_{1/2}$ (91.9 eV), respectively. Therefore, the aforementioned findings confirm the successful synthesis of ZnO@PDA/Au.

Photoelectrochemical behaviors and charge transfer mechanism of the PEC immunosensor

Transient photocurrent, electrochemical impedance analysis (EIS), and linear sweep voltammograms (LSVs) were applied to estimate intrinsic electrochemical behavior and photocurrent response in the ZnO@PDA/Au system. The transient photocurrent responses of the as-fabricated electrodes have been measured at 0.05 V (**Figure 3A**). The ZnO@PDA/Au electrode owns the highest photocurrent, which is about fivefold of the pristine ZnO. The excellent PEC performance of ZnO@PDA/Au benefits from the synergistic action of PDA and

Au NPs, which broaden the light absorption range and enhance the separation efficiency of photo-generated electron–hole pairs. Moreover, EIS was used to test the electron transfer resistance change of different modification processes. As shown in **Figure 3B**, compared with ZnO and ZnO@PDA, the ZnO@PDA/Au shows the smallest interfacial electron transfer resistance.

The LSV curves of the ZnO, ZnO@PDA, and ZnO@PDA/Au electrodes were recorded in dark and under illumination with the applied potential ranging between −0.05 and 0.3 V. As shown in **Figure 3C**, all the as-prepared photoelectrodes display negligible current in the dark condition although the current density of ZnO@PDA/Au is slightly higher than the other two electrodes. Under irradiation, the PDA-coated ZnO displays a higher photocurrent than that of the original ZnO. This increase of photocurrent is attributed to the enhanced light harvest capability by using PDA as the photosensitizer. Obviously, after the subsequent decoration of Au NPs on the ZnO@PDA, the photocurrent significantly increases under the same potential because of higher light absorption and the photocarriers' generation ability of Au nanoparticles. As a control, LSV curves of ITO are presented without/with simulated sunlight illumination, respectively, and the result is shown in **Supplementary Figure S4A**. Moreover, photocurrent responses of ITO, ITO/anti-Aβ/BSA, and ITO/anti-Aβ/BSA/Aβ toward on/off cycles of simulated sunlight illumination at 0.1 V were also performed as shown in **Supplementary Figure S4B**. These results demonstrated that ITO has no PEC performance. According to the aforementioned analysis, the decoration of PDA and Au NPs on ZnO can bring excellent PEC performance.

According to the aforementioned results, the possible photo-generated charge transfer mechanism of the ZnO@PDA/Au is illustrated in **Figure 3D**. Under the solar light illumination, each component of the as-prepared photoanode could be excited to generate carriers simultaneously. Light irradiation of the ZnO induces the excited electrons from the valence band (VB) to the conduction band (CB) and further transfer to the surface of ITO. At the interface of PDA and ZnO, the generated electrons on the lowest unoccupied molecular orbital (LUMO) of PDA could transfer to the CB of ZnO to generate a built-in electric field due to the matching energy level, which effectively blocks the photo-generated charge recombination and enhance the charge separation and transfer efficiency. In addition, the plasmonic Au NPs could generate hot electrons with sufficient energy and inject into the LUMO of PDA under visible light excitation. The enriched electrons on the ZnO would transfer to the counter Pt photocathode through an external circuit to obtain the photocurrent signal for the PEC detection. Meanwhile, the remaining holes on the VB of ZnO transfer to the highest occupied molecular orbital of PDA. Both the accumulated holes on PDA and hot holes left on the Au NPs can be rapidly consumed by AA (electron donor) in the electrolyte against the photoinduced carrier recombination. Accordingly, by integrating the photosensitization of PDA and LSPR effect of Au NPs, the ZnO@PDA/Au is considered to be an excellent substrate material for photocurrent response.

Optimization of Detection Conditions

To obtain the best detection performance of photoelectrode, the AA concentration and the pH values, which have a direct effect on PEC response signal through electron transfer, were optimized in detail. AA can be used as the scavenger to consume the photoinduced hole and an efficient antioxidant to reduce the photo-oxidized PDA film. The change of photocurrent with the AA concentration range from 0.01 to 100 mM is shown in **Supplementary Figure S5A**. The photocurrent signal of the ZnO@PDA/Au electrode displays a significant increment along with the increasing AA concentration at first and then reaches a peak at 1 mM. A decrease in photocurrent density can be seen, when the AA concentration in the solution continues to increase. When the photo-generated electrons are injected into ZnO, the PDA and Au NPs could be regenerated through gaining electrons from the electron donor to achieve effective separation of photo-generated charge. At the same time, the excess AA in the electrolyte solution leads to the quenching absorption of the solution, which impacts the irradiation reaching the photoanode and reduces the intensity and efficiency of the excitation electron-hole center. Thus, 1 mM was selected as the optimal concentration of AA in this work.

Furthermore, the effect of pH value on the detection photocurrent was recorded in **Supplementary Figure S5B**. The photocurrent gradually increases with the pH of the buffer solution rising from 6.5 to 7.4. When the pH value further enhances to 8.5, the photocurrent shows an obvious decrement. This result may be ascribed to the bioactivity of the immobilized antigen that could be disrupted in the acidic or alkaline environment. The PBS solution with pH 7.4 is similar to the physiological environment to maintain the good activity of the biomolecules. Thus, to obtain an excellent photocurrent response and immunocomplex layer on the photoanode, pH 7.4 was selected in the following detection. In addition, the concentration of antibody was optimized, and the result shows the optimal concentration is 10 μg/mL (**Supplementary Figure S6**).

Analytical Performance of the Photoelectrochemical Immunosensor

Based on the aforementioned optimal conditions, the photocurrent density was collected to track the succession process for the fabrication of the PEC immunosensor. In **Supplementary Figure S7**, after the immobilization of anti-Aβ (curve b) and subsequent BSA blocking (curve c), the photocurrent intensity reduces significantly. This is ascribed to the binding molecules on the surface of the photoanode that partly hinder the access and reaction of AA with the photoinduced holes. The further decrease of photocurrent can be seen after continued incubation with Aβ, owing to the formation of the antigen–antibody immunocomplexes on the photoelectrode surface. These results confirm the successful construction of the label-free PEC immunosensor.

The photocurrent intensity has a direct relationship with the concentration of Aβ. Thus, the as-fabricated immunosensor based on ZnO@PDA/Au was applied to detect Aβ with different concentrations. **Figure 4A** displays the photocurrent change of the as-fabricated PEC biosensor with different concentrations of Aβ at the optimal condition. It can be seen that along with the

increase of the Aβ concentration, the photocurrent reduces gradually. The linear relationship related to the change of the photocurrent intensity (ΔI) and the logarithm of Aβ concentration in the range from 1 pg mL^{-1} to 100 ng mL^{-1} is presented in **Figure 4B**. The regression equation is displayed as $\Delta I = 0.538 \log c + 2.226$ (R^2 = 0.992). The limit of detection (LOD) is determined to be 0.26 pg mL^{-1} (S/N = 3). The LOD is calculated by three times the SD of the blank according to our previous report.(Yibiao, Qing et al., 2021) As a control, a typical ELISA has been used to validate our method. As shown in **Supplementary Figure S8**, the ELISA calibration curve was constructed by plotting the optical density of Aβ42 at 450 nm (TMB as substrate). And the range of Aβ42 concentration is 1–800 pg/mL. The relationship between the optical density at 450 nm and the Aβ42 concentration follows the regression equation $y = 0.00099x + 0.072$ (R^2 = 0.9991). The detection limit is 18.59 pg/mL, and the linear range is from 10 to 800 pg/mL. Compared with typical ELISA, our prepared PEC sensor based on ZnO@PDA/Au exhibited lower LOD and wider linear range. Compared with several previous reports for the detection of Aβ, the proposed PEC immunosensor in our work exhibits a much wider sensing range and competitive LOD. A comparison is shown in Supplementary Table S1. What is more, the as-fabricated material is environment friendly and possesses good biocompatibility. Therefore, the ZnO@PDA/Au is a very promising material used for the construction of sensitive PEC immunosensors.

Stability, Reproducibility, and Specificity

The stability, reproducibility, and specificity are very crucial factors for the successful construction of immunosensor in biological application. The photocurrent response of as-prepared immunosensor incubated with 1 pg mL^{-1} Aβ was tested by 30 on/off cycles of illumination to access its stability. Observing from **Figure 4C**, the photocurrent response shows no distinct variation. Moreover, the as-fabricated immunosensor was stored at 4°C to investigate the storage stability. After 2 weeks of restoring, the photocurrent density could still retain 90.1% of its initial response (**Supplementary Figure S9**). In addition, the reproducibility of this ZnO@PDA/Au electrode was also measured, and the result is shown in **Supplementary Figure S10**, which demonstrated that the ZnO@PDA/Au electrode had excellent reproducibility. To evaluate the specificity of the fabricated PEC biosensor, several biological interfering species including Aβ40, human apolipoprotein E4 (APOE4), dopamine, and glucose with a 100-fold higher concentration were chosen for the test. As shown in **Figure 4D**, the photocurrent response to the interfering substances appears imperceptible, compared with that of the specific target Aβ42, which implied that the PEC immunosensor possesses excellent anti-interference ability and specificity. The aforementioned results prove that this proposed sensing platform owns superior stability, reproducibility, and specificity.

Aβ Detection in Serum Sample

To further certify the practicability of the prepared PEC immunosensor, the tests were also carried out in real biological samples. The diluted serum samples were spiked with different concentrations of Aβ42(1, 10, 100, 1,000, 10,000 pg/mL), and then the photocurrent changes were recorded in Supplementary Table S2. The detection results are close to that of the added values with satisfactory recoveries ranging from 97.1 to 109.1%, revealing that the proposed PEC immunosensor based on ZnO@PDA/Au has excellent sensitivity and reliability for the detection of Aβ in real serum sample analysis and can be capable for the clinical diagnosis.

CONCLUSION

In summary, a novel PEC immunosensor based on PDA and Au NP co-decorated ZnO was successfully designed for ultrasensitive and label-free detection of Aβ. The ZnO@PDA/Au substrate obtained by self-polymerization and *in situ* self-reduction exhibits superior optoelectronic property by taking the advantage of the photosensitization of PDA and SPR effect of Au NPs together. What is more, the PDA film and Au NPs can also be used as a biocompatible functional layer for the immobilization of biomolecules. The interfacial charge transfer mechanism of the proposed biosensing platform was investigated in detail. The as-fabricated PEC immunosensor displays apparent merits for Aβ detection including broad linear range, low detection limit, and good anti-interference performance and stability. In addition, it can also realize the acceptable quantitative analysis of Aβ in real serum sample. Due to the aforementioned advantages, the PEC electrode provides a versatile sensing platform and has good potential in other bioanalysis applications for early disease diagnosis.

DATA AVAILABILITY STATEMENT

The original contributions presented in the study are included in the article/**Supplementary Material**, further inquiries can be directed to the corresponding authors.

AUTHOR CONTRIBUTIONS

YL elaborated the concept and revised the article. Baochengyang and SZ supervised the paper. GH, YZ, ML, YG, and HY consulted literature, reorganized materials and drew the figures. All the authors participated in scientific discussions and wrote the paper.

FUNDING

This work was supported by the Natural Science Foundation of China (51872110), Guangdong-Hong Kong-Macao Greater Bay Area Center for Brain Science and Brain-Inspired Intelligence Fund (NO.2019027), the Training Program of Youth Backbone Teacher of Henan Province of 2018 (2018GGJS178), the special fund project of Zhengzhou basic and applied basic research (ZZSZX202001 and ZZSZX202002).

SUPPLEMENTARY MATERIAL

The Supplementary Material for this article can be found online at: https://www.frontiersin.org/articles/10.3389/fbioe.2021.777344/full#supplementary-material

REFERENCES

Brazaca, L. C., Sampaio, I., Zucolotto, V., and Janegitz, B. C. (2020). Applications of Biosensors in Alzheimer's Disease Diagnosis. *Talanta* 210, 120644. doi:10.1016/j.talanta.2019.120644

Butterfield, D. A., Drake, J., Pocernich, C., and Castegna, A. (2002). Evidence of Oxidative Damage in Alzheimer's Disease Brain: central Role for Amyloid Beta-Peptide. *Trends Mol. Med.* 7, 548–554. doi:10.1016/S1471-4914(01)02173-6

Carneiro, P., Loureiro, J., Delerue-Matos, C., Morais, S., and do Carmo Pereira, M. (2017). Alzheimer's Disease: Development of a Sensitive Label-free Electrochemical Immunosensor for Detection of Amyloid Beta Peptide. *Sensors Actuators B: Chem.* 239, 157–165. doi:10.1016/j.snb.2016.07.181

Dong, X., Xu, C., Yang, C., Chen, F., Manohari, A. G., Zhu, Z., et al. (2019). Photoelectrochemical Response to Glutathione in Au-Decorated ZnO Nanorod Array. *J. Mater. Chem. C* 7, 5624–5629. doi:10.1039/c9tc00901a

Evans, D. A., Funkenstein, H. H., Albert, M. S., Scherr, P. A., Cook, N. R., and Chown, M. J. (1989). Prevalence of Alzheimer's Disease in a Community Population of Older Persons. *Jama* 262, 2551–2556. doi:10.1001/jama.1989.03430180093036

Fang, W.-K., Liu, L., Zhang, L.-l., Liu, D., Liu, Y., and Tang, H.-W. (2021). Detection of Amyloid β Oligomers by a Fluorescence Ratio Strategy Based on Optically Trapped Highly Doped Upconversion Nanoparticles-SiO2@ Metal-Organic Framework Microspheres. *Anal. Chem.* 93, 12447–12455. doi:10.1021/acs.analchem.1c02679

Folego, G., Weiler, M., Casseb, R. F., Pires, R., and Rocha, A. (2020). Alzheimer's Disease Detection through Whole-Brain 3D-CNN MRI. *Front. Bioeng. Biotechnol.* 8. doi:10.3389/fbioe.2020.534592

Gasparotto, G., Costa, J. P. C., Costa, P. I., Zaghete, M. A., and Mazon, T. (2017). Electrochemical Immunosensor Based on ZnO Nanorods-Au Nanoparticles Nanohybrids for Ovarian Cancer Antigen CA-125 Detection. *Mater. Sci. Eng. C* 76, 1240–1247. doi:10.1016/j.msec.2017.02.031

Grimmer, T., Riemenschneider, M., Förstl, H., Henriksen, G., Klunk, W. E., Mathis, C. A., et al. (2009). Beta Amyloid in Alzheimer's Disease: Increased Deposition in Brain Is Reflected in Reduced Concentration in Cerebrospinal Fluid. *Biol. Psychiatry* 65, 927–934. doi:10.1016/j.biopsych.2009.01.027

Hardy, J., and Selkoe, D. J. (2002). The Amyloid Hypothesis of Alzheimer's Disease: Progress and Problems on the Road to Therapeutics. *Science* 297, 353–356. doi:10.1126/science.1072994

He, G., Gao, F., Li, W., Li, P., Zhang, X., Yin, H., et al. (2019). Electrochemical Sensing of H2O2 Released from Living Cells Based on AuPd alloy-modified PDA Nanotubes. *Anal. Methods* 11, 1651–1656. doi:10.1039/C8AY02743A

Hu, W., He, G., Zhang, H., Wu, X., Li, J., Zhao, Z., et al. (2014). Polydopamine-Functionalization of Graphene Oxide to Enable Dual Signal Amplification for Sensitive Surface Plasmon Resonance Imaging Detection of Biomarker. *Anal. Chem.* 86, 4488–4493. doi:10.1021/ac5003905

Jack, C. R., Knopman, D. S., Jagust, W. J., Shaw, L. M., Aisen, P. S., Weiner, M. W., et al. (2010). Hypothetical Model of Dynamic Biomarkers of the Alzheimer's Pathological cascade. *Lancet Neurol.* 9, 4–5. doi:10.1016/S1474-4422(09)70299-6

Kang, Z., Yan, X., Wang, Y., Zhao, Y., Bai, Z., Liu, Y., et al. (2016). Self-powered Photoelectrochemical Biosensing Platform Based on Au NPs@ZnO Nanorods Array. *Nano Res.* 9, 344–352. doi:10.1007/s12274-015-0913-9

Lee, H., Dellatore, S. M., Miller, W. M., and Messersmith, P. B. (2007). Mussel-Inspired Surface Chemistry for Multifunctional Coatings. *Science* 318, 426–430. doi:10.1126/science.1147241

Lee, S.-C., Park, H.-H., Kim, S.-H., Koh, S.-H., Han, S.-H., and Yoon, M.-Y. (2019). Ultrasensitive Fluorescence Detection of Alzheimer's Disease Based on Polyvalent Directed Peptide Polymer Coupled to a Nanoporous ZnO Nanoplatform. *Anal. Chem.* 91, 5573–5581. doi:10.1021/acs.analchem.8b03735

Liu, Y., Ai, K., and Lu, L. (2014). Polydopamine and its Derivative Materials: Synthesis and Promising Applications in Energy, Environmental, and Biomedical Fields. *Chem. Rev.* 114, 5057–5115. doi:10.1021/cr400407a

Liu, Y., Xu, Q., Zhang, Y., Ren, B., Huang, L., Cai, H., et al. (2021). An Electrochemical Aptasensor Based on AuPt alloy Nanoparticles for Ultrasensitive Detection of Amyloid-β Oligomers. *Talanta* 231, 122360. doi:10.1016/j.talanta.2021.122360

Lynge, M. E., van der Westen, R., Postma, A., and Städler, B. (2011). Polydopamine-a Nature-Inspired Polymer Coating for Biomedical Science. *Nanoscale* 3, 4916–4928. doi:10.1039/C1NR10969C

Marcus, C., Mena, E., and Subramaniam, R. M. (2014). Brain PET in the Diagnosis of Alzheimer's Disease. *Clin. Nucl. Med.* 39, e413–6. doi:10.1097/RLU.0000000000000547

Matthews, F. E., Arthur, A., Barnes, L. E., Bond, J., Jagger, C., Robinson, L., et al. (2013). A Two-Decade Comparison of Prevalence of Dementia in Individuals Aged 65 Years and Older from Three Geographical Areas of England: Results of the Cognitive Function and Ageing Study I and II. *The Lancet* 382, 1405–1412. doi:10.1016/S0140-6736(13)61570-6

Murphy, M. P., and LeVine, H. (2010). Alzheimer's Disease and the Amyloid-β Peptide. *Jad* 19, 311–323. doi:10.3233/jad-2010-1221

Nakamura, A., Kaneko, N., Villemagne, V. L., Kato, T., Doecke, J., Doré, V., et al. (2018). High Performance Plasma Amyloid-β Biomarkers for Alzheimer's Disease. *Nature* 554, 249–254. doi:10.1038/nature25456

Norouzi, P., Gupta, V. K., Faridbod, F., Pirali-Hamedani, M., Larijani, B., and Ganjali, M. R. (2011). Carcinoembryonic Antigen Admittance Biosensor Based on Au and ZnO Nanoparticles Using FFT Admittance Voltammetry. *Anal. Chem.* 83, 1564–1570. doi:10.1021/ac102270w

Obata, Y., Murakami, K., Kawase, T., Hirose, K., Izuo, N., Shimizu, T., et al. (2020). Detection of Amyloid β Oligomers with RNA Aptamers in AppNL-G-F/NL-G-F Mice: A Model of Arctic Alzheimer's Disease. *ACS Omega* 5, 21531–21537. doi:10.1021/acsomega.0c02134

Selkoe, D. J. (2012). Preventing Alzheimer's Disease. *Science* 337, 1488–1492. doi:10.1126/science.1228541

Shu, J., and Tang, D. (2019). Recent Advances in Photoelectrochemical Sensing: From Engineered Photoactive Materials to Sensing Devices and Detection Modes. *Anal. Chem.* 92, 363–377. doi:10.1021/acs.analchem.9b04199

Song, L., Lachno, D. R., Hanlon, D., Shepro, A., Jeromin, A., Gemani, D., et al. (2016). A Digital Enzyme-Linked Immunosorbent Assay for Ultrasensitive Measurement of Amyloid-β 1-42 Peptide in Human Plasma with Utility for Studies of Alzheimer's Disease Therapeutics. *Alz Res. Ther.* 8, 58–64. doi:10.1186/s13195-016-0225-7

Wang, R., Ma, H., Zhang, Y., Wang, Q., Yang, Z., Du, B., et al. (2017). Photoelectrochemical Sensitive Detection of Insulin Based on CdS/polydopamine Co-sensitized WO 3 Nanorod and Signal Amplification of Carbon Nanotubes@polydopamine. *Biosens. Bioelectron.* 96, 345–350. doi:10.1016/j.bios.2017.05.029

Wang, X. Z., Du, J., Xiao, N. N., Zhang, Y., Fei, L., LaCoste, J. D., et al. (2020). Driving Force to Detect Alzheimer's Disease Biomarkers: Application of a Thioflavine T@Er-MOF Ratiometric Fluorescent Sensor for Smart Detection of Presenilin 1, Amyloid β-protein and Acetylcholine. *Analyst* 145, 4646–4663. doi:10.1039/D0AN00440E

Wang, Y., Fan, D., Zhao, G., Feng, J., Wei, D., Zhang, N., et al. (2018). Ultrasensitive Photoelectrochemical Immunosensor for the Detection of Amyloid β-protein Based on SnO2/SnS2/Ag2S Nanocomposites. *Biosens. Bioelectron.* 120, 1–7. doi:10.1016/j.bios.2018.08.026

Wei, Y., Ke, L., Kong, J., Liu, H., Jiao, Z., Lu, X., et al. (2012). Enhanced Photoelectrochemical Water-Splitting Effect with a Bent ZnO Nanorod Photoanode Decorated with Ag Nanoparticles. *Nanotechnology* 23, 235401. doi:10.1088/0957-4484/23/23/235401

Xiao, S., Liu, P., Zhu, W., Li, G., Zhang, D., and Li, H. (2015). Copper Nanowires: A Substitute for Noble Metals to Enhance Photocatalytic H2 Generation. *Nano Lett.* 15, 4853–4858. doi:10.1021/acs.nanolett.5b00082

Yang, J. K., Hwang, I. J., Cha, M. G., Kim, H. I., Yim, D., Jeong, D. H., et al. (2019). Reaction Kinetics-Mediated Control over Silver Nanogap Shells as Surface-Enhanced Raman Scattering Nanoprobes for Detection of Alzheimer's Disease Biomarkers. *Small* 15, 1900613. doi:10.1002/smll.201900613

Yang, X., Li, H., Zhang, W., Sun, M., Li, L., Xu, N., et al. (2017). High Visible Photoelectrochemical Activity of Ag Nanoparticle-Sandwiched CdS/Ag/ZnO Nanorods. *ACS Appl. Mater. Inter.* 9, 658–667. doi:10.1021/acsami.6b12259

Yang, Y., and Hu, W. (2017). Bifunctional Polydopamine Thin Film Coated Zinc Oxide Nanorods for Label-free Photoelectrochemical Immunoassay. *Talanta* 166, 141–147. doi:10.1016/j.talanta.2017.01.024

Yang, Z., Wang, Y., and Zhang, D. (2021). 2021 Alzheimer's Disease Facts and Figures. *Alzheimer's Demen.* 17, 327–406. doi:10.1002/alz.12328

Yu, Y., Huang, Z., Zhou, Y., Zhang, L., Liu, A., Chen, W., et al. (2019). Facile and Highly Sensitive Photoelectrochemical Biosensing Platform Based on Hierarchical Architectured Polydopamine/Tungsten Oxide Nanocomposite Film. *Biosens. Bioelectron.* 126, 1–6. doi:10.1016/j.bios.2018.10.026

Zhang, B., Wang, F., Zhu, C., Li, Q., Song, J., Zheng, M., et al. (2016). A Facile Self-Assembly Synthesis of Hexagonal ZnO Nanosheet Films and Their Photoelectrochemical Properties. *Nano-micro Lett.* 8, 137–142. doi:10.1007/s40820-015-0068-y

Zhang, B., Wang, H., Ye, H., Xu, B., Zhao, F., and Zeng, B. (2018). Reversible Redox Mechanism Based Synthesis of Plasmonic WO3/Au Photocatalyst for Selective and Sensitive Detection of Ultra-micro Hg2+. *Sensors Actuators B: Chem.* 273, 1435–1441. doi:10.1016/j.snb.2018.07.070

Zhang, Y., He, S., Guo, W., Hu, Y., Huang, J., Mulcahy, J. R., et al. (2018). Surface-Plasmon-Driven Hot Electron Photochemistry. *Chem. Rev.* 118, 2927–2954. doi:10.1021/acs.chemrev.7b00430

Zheng, Y., Zheng, L., Zhan, Y., Lin, X., Zheng, Q., and Wei, K. (2007). Ag/ZnO Heterostructure Nanocrystals: Synthesis, Characterization, and Photocatalysis. *Inorg. Chem.* 46, 6980–6986. doi:10.1021/ic700688f

Zhou, X., Wang, S., Zhang, C., Lin, Y., Lv, J., Hu, S., et al. (2021). Colorimetric Determination of Amyloid-β Peptide Using MOF-Derived Nanozyme Based on Porous ZnO-Co3O4 Nanocages. *Microchim Acta* 188, 56. doi:10.1007/s00604-021-04705-4

Zhu, Y.-C., Zhang, N., Ruan, Y.-F., Zhao, W.-W., Xu, J.-J., and Chen, H.-Y. (2016). Alkaline Phosphatase Tagged Antibodies on Gold Nanoparticles/TiO2 Nanotubes Electrode: A Plasmonic Strategy for Label-free and Amplified Photoelectrochemical Immunoassay. *Anal. Chem.* 88, 5626–5630. doi:10.1021/acs.analchem.6b01261

Conflict of Interest: The authors declare that the research was conducted in the absence of any commercial or financial relationships that could be construed as a potential conflict of interest.

Publisher's Note: All claims expressed in this article are solely those of the authors and do not necessarily represent those of their affiliated organizations, or those of the publisher, the editors, and the reviewers. Any product that may be evaluated in this article, or claim that may be made by its manufacturer, is not guaranteed or endorsed by the publisher.

frontiers in Bioengineering and Biotechnology

REVIEW
published: 22 November 2021
doi: 10.3389/fbioe.2021.761020

Progress of Wearable and Flexible Electrochemical Biosensors With the Aid of Conductive Nanomaterials

*Tahir Raza[1], Lijun Qu[1], Waquar Ahmed Khokhar[2], Boakye Andrews[1], Afzal Ali[3] and Mingwei Tian[1]**

[1]Research Center for Intelligent and Wearable Technology, College of Textiles and Clothing, State Key Laboratory of Bio-Fibers and Eco-Textiles, Intelligent Wearable Engineering Research Center of Qingdao, Qingdao University, Qingdao, China, [2]College of Physics, Qingdao University, Qingdao, China, [3]Ocean University, Qingdao, China

Conductive nanomaterials have recently gained a lot of interest due to their excellent physical, chemical, and electrical properties, as well as their numerous nanoscale morphologies, which enable them to be fabricated into a wide range of modern chemical and biological sensors. This study focuses mainly on current applications based on conductive nanostructured materials. They are the key elements in preparing wearable electrochemical Biosensors, including electrochemical immunosensors and DNA biosensors. Conductive nanomaterials such as carbon (Carbon Nanotubes, Graphene), metals and conductive polymers, which provide a large effective surface area, fast electron transfer rate and high electrical conductivity, are summarized in detail. Conductive polymer nanocomposites in combination with carbon and metal nanoparticles have also been addressed to increase sensor performance. In conclusion, a section on current challenges and opportunities in this growing field is forecasted at the end.

Keywords: electrochemical biosensor, conductive nanomaterials, non-invasive detection, flexibility, immunosensors, DNA biosensors

OPEN ACCESS

Edited by:
Tailin Xu,
Shenzhen University, China

Reviewed by:
Zhen Gu,
University of Science and Technology Beijing, China
Ang Lu,
Wuhan University, China

****Correspondence:***
Mingwei Tian
mwtian@qdu.edu.cn

Specialty section:
This article was submitted to Biosensors and Biomolecular Electronics, a section of the journal Frontiers in Bioengineering and Biotechnology

Received: *19 August 2021*
Accepted: *11 October 2021*
Published: *22 November 2021*

Citation:
Raza T, Qu L, Khokhar WA, Andrews B, Ali A and Tian M (2021) Progress of Wearable and Flexible Electrochemical Biosensors With the Aid of Conductive Nanomaterials. Front. Bioeng. Biotechnol. 9:761020. doi: 10.3389/fbioe.2021.761020

INTRODUCTION

Today we live in the new era of the internet of things (IoT), where everything is connected, and smart objects like sensors and actuators can communicate with each others as well as generate and exchange information (Li et al., 2017). Wearable sensors are attached to the human body to assist in the constant measurement of the wearer's health and fitness to help physicians and nurses observe patients, prevent illness, and monitor the health of babies at home (Byrne et al., 2010; Tao et al., 2011; Liu et al., 2012; Brodt et al., 2013; Wen and Eychmüller, 2016; Jang and Han, 2017; Qu et al., 2018). Their potential role in handling the emerging pandemic The COVID-19 outbreak has recently gotten much attention (Adans-Dester et al., 2020). Various studies relate Covid-19 to physiological parameters such as comforting heartbeat, breathing rate, skin temperature, blood oxygen saturation, and compatibility. wearable sensors are also being supported and could assist in identifying an event-related viral infection/spread early, and therefore, allowing timely interference to stop imminent spread (Seshadri et al., 2020). Wearable sensors and fitness controllers that detect vital signs and physical moments such as heart rate and blood pressure are also commercially available (Fitbit, WHOOP strap or Apple Watch). In addition to textile-based sensors (Farajikhah et al., 2020), transdermal alcohol vapour sensors with patch-like sensors were also introduced in 1992 (Swift et al., 1992). Although wearable sensors for physiological data collection have been widely used in medical and consumer goods. Even though there was a 0.5–2 h

delay in detection by using body vapour, which encouraged researchers to switch to other methods of detection such as sweat (Schazmann et al., 2010), saliva, tear (Chu et al., 2011) and interstitial fluid (Rebrin et al., 2010; Schazmann et al., 2010). Wearable chemical (electrochemical and biochemical) sensors can offer extensive molecular data in various sectors, including medical, sports, nutrition, fitness, and defence (Fraser et al., 2011; Yang and Gao, 2019). The development of wearable electrochemical biosensors has accelerated in recent decades (Bandodkar et al., 2015b; Kim et al., 2017). These kinds of wearable electrochemical biosensors can non-invasively measure the dynamic variation of biochemical markers in biological fluids such as sweat, saliva, and interstitial fluid (Alizadeh et al., 2018; Kim et al., 2019). Although the latest developments in wearable electrochemical biosensors are achieved through the significant contributions of many influential researchers worldwide. Among the numerous sensing techniques, electrochemical source offers several benefits, including its simple structure with high sensitivity, fast reaction, and low power consumption (Mamalis et al., 2004; Meyyappan, 2004; Pérez López, 2009; Mpanza, 2016). It is widely acknowledged that conventional sensing electrodes are the basic components and play a dominant role in wearable electrochemical biosensors (Lee et al., 2016; Zhu et al., 2019). Recently, nano-structural materials, such as metal nanoparticles, carbon nanomaterials, and conductive polymers, have drawn much interest due to their unique electrical, physical, and chemical properties, as well as their high biocompatibility. Which are being used as sensing electrode materials in wearable electrochemical biosensors as compared to bulk materials (Imani et al., 2016; Lee et al., 2016; Bandodkar et al., 2017; Jeerapan et al., 2020; Li and Wen, 2020). The inherent properties of multidimensional nanomaterials, such as stretchability, provide excellent stability to sensors, which is essential for wearable applications (Feng and Zhu, 2019). Furthermore, the porous structure of nanomaterials provides excellent immobilization for enzymes, thereby effectively increasing the diffusion of both the target and electrolyte, advancing the catalysis for the analyte (Wen and Eychmüller, 2016). These nanomaterial sensing properties improve the performance and design strategies of wearable electrochemical biosensors. Conductive nanomaterials, particularly polymers, stand out as clear frontrunners, with significant advantages in explicit contact surface area, filler content, and operation electron transfer ratio. (Gangopadhyay and De, 2000). Polymers' versatility allows them to be synthesized in different forms, comprising elastomers, gels, and liquid crystal polymers (Dierking, 2010; Li et al., 2019), enlarging the morphology of wearable sensors to patch-like sensors, even micrometres thick, and tattoo-based electrochemical biosensors (Dierking, 2010; Li et al., 2019; Yoon et al., 2019). Electrochemical biosensors, together with immunosensors and DNA biosensors, are rapidly becoming the norm of the day (Kim et al., 2019). Among the numerous transduction systems used, electrochemical immunosensors have sparked the interest of researchers due to benefits such as a good detection limit, ease of automation, low cost, uniformity, and incorporation with miniaturized readouts, and comprehensive compatibility for onsite testing. Their sensing technologies and detection range are frequently improving because of advancements in the distinctive properties of conductive nanomaterials, particularly conductivity and electrochemical activity (Shaikh et al., 2019). Intercalation of interactional fillers into nanomaterials matrices improves the stability of functional electron transfer sites and identification limits, which has an influence on sensing applications. These efficient fillers aid in reducing layer stiffness in nanomaterials, paving the way for ultrathin electrochemical detector technology (Huang and Kaner, 2004; Zhou et al., 2014; Bandodkar et al., 2015a). In this review we have discussed the most recent research on electrode materials based on conductive nanomaterials and mechanized technologies for various types of wearable electrochemical biosensors.

We start with a brief overview of the basic design principle, and components of electrochemical biosensors. Following that, the next section provides a thorough explanation of the analytical applications of conductive nanoparticles in electrochemical biosensing. We discussed essential parameters for developing low-cost, sensitive, and porous sensing platforms with different technologies. Nanomaterials, polymers, and biological receptors create extremely sensitive and selective electrochemical sensing devices for electrode modification. Using other nanomaterials, MXene and composite materials such as conductive polymers in combination with CNT, Graphene, and metals that offer more sensor sensitivity are also addressed. Furthermore, a range of similar applications, such as the manufacture of biosensors, including immunosensor and DNA biosensors, in which conductive nanomaterials play a vital role in sensing performance, have also been investigated. The final section looks into the prospects and challenges of these wearable sensor systems' durability, robustness, and performance.

BASIC DESIGN PRINCIPLE AND COMPONENT OF ELECTROCHEMICAL BIOSENSOR

Electrochemical biosensors work on the principle that an electrical current passes through a sensing electrode produced by an electrochemical reaction (the reaction between the electrode and analyte) that converts the associated information into qualitative or quantitative signals (Curto et al., 2012). In general, the reaction found between the electrodes is the result of electrical and chemical interaction. To obtain valuable information such as the concentration of a single entity in a sample, a molecular chemical receptor and a physicochemical detector component "transducer" are used. The transducer converts the chemical information into the analytical signals of the sample. Which eventually based upon the potentiometry, conductometry, and amperometric/voltammetric measurements. **Table 1** summarizes a comparison of these various measurements with advantages and disadvantages. So, when a biological component like antibody, DNA, enzyme and ionophores is

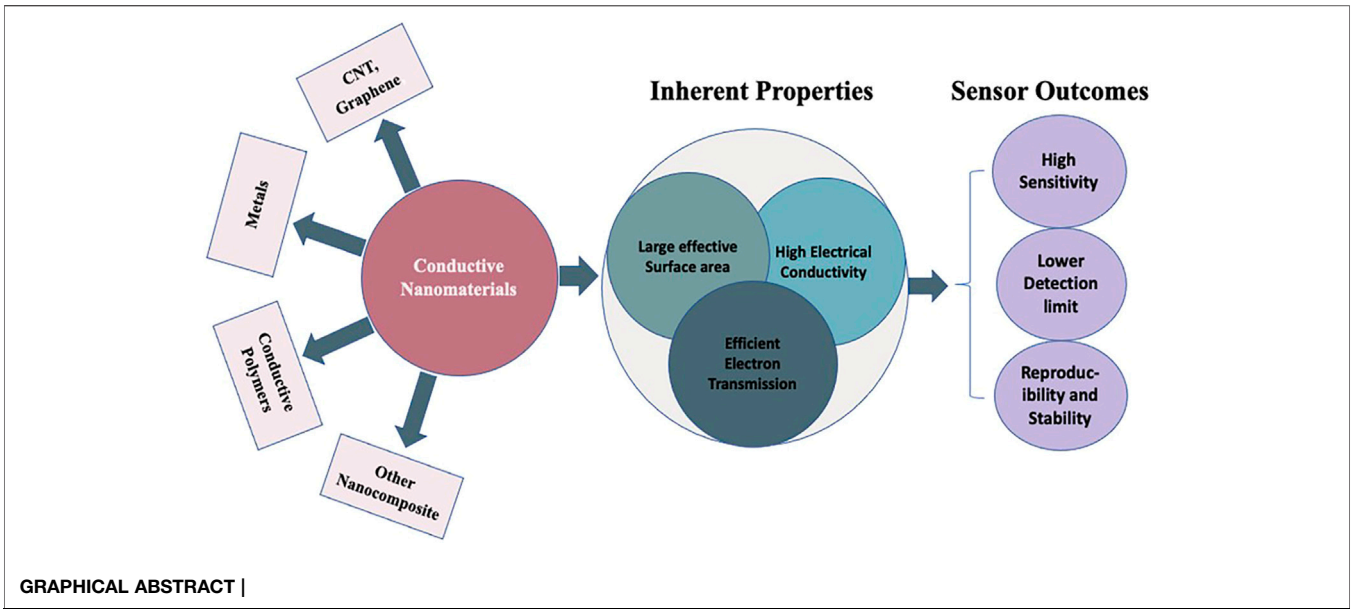

GRAPHICAL ABSTRACT |

TABLE 1 | Comparison of different sensing methods.

Method	Overview	Advantages	Disadvantages	Ref.
Potentiometry	The potential between the active and reference electrodes is measured at a constant current to detect the target analyte, such as the ion concentration.	Signal detection and signal handling are simple and systematic. Superb for charged species with a predetermined charge condition. Excellent for moderately concerted species, particularly in the mM range.	Applicable only to charged species sensing. Since this approach compares action to concentration, a selective membrane layer to target individual ions must be suggested. Contamination from other charges is a big concern for low-concentration ions.	Zdrachek and Bakker (2020)
Amperometry	It measures the current produced at a constant applied potential during the redox reaction that is proportional to the target analyte concentration.	Simple recognition and simple post-processing are needed to change current to concentration. Mediators may be used to reduce the necessary potential and hence power usage.	The Faradaic signal can fall off over time for traces of species below the "μM" scale, resulting in incorrect concentration conversions. An enzyme normally provides selectivity.	Borgmann et al. (2011)
Voltammetry	A voltage scan between the active and reference electrodes is performed, and the current properties are obtained to determine the concentration.	Since various species have different oxidation and reduction potentials, a voltage scan on two identical electrodes will provide information on multiple analytes simultaneously. Therefore, there are several sub-techniques to choose from in order to maximize the signal-to-noise ratios. can be combined with pre-concentration procedures for the identification of trace molecules, resulting in increased limitability.	This method requires more complex postprocessing in order to extract and distinguish the peaks from the necessary analyte. Background reactions may be activated by voltage scans, interfering with the appropriate signals.	Chen and Shah (2013), Dheilly et al. (2008)
Conductometry	Determine the variation in biological element conductance that occurs between a pair of metallic electrodes.	They may not need the use of a reference electrode; they work at low-amplitude alternating voltage, which prevents Faraday processes on electrodes; They are light insensitive;	Despite the fact that electrochemical biosensors are particularly sensitive to hydrogen, their sensitivity decreases with time due to the rapid deterioration of the electrode catalyst, which in process applications is easily polluted by process gases.	Pungor (2016)

used in the recognition/receptor system, the device is referred to as a biosensor. The bioreceptor chosen for the chemical recognition system is analyte dependent and capable of producing analyte concentration in the form of physical or chemical signals with accurate and well-specified sensitivity (Pérez López, 2009) (**Figure 1**). Otherwise, modifying the working electrode with an ion-specific inert allows the sensor to detect specific electrolytes such as sodium, potassium, and

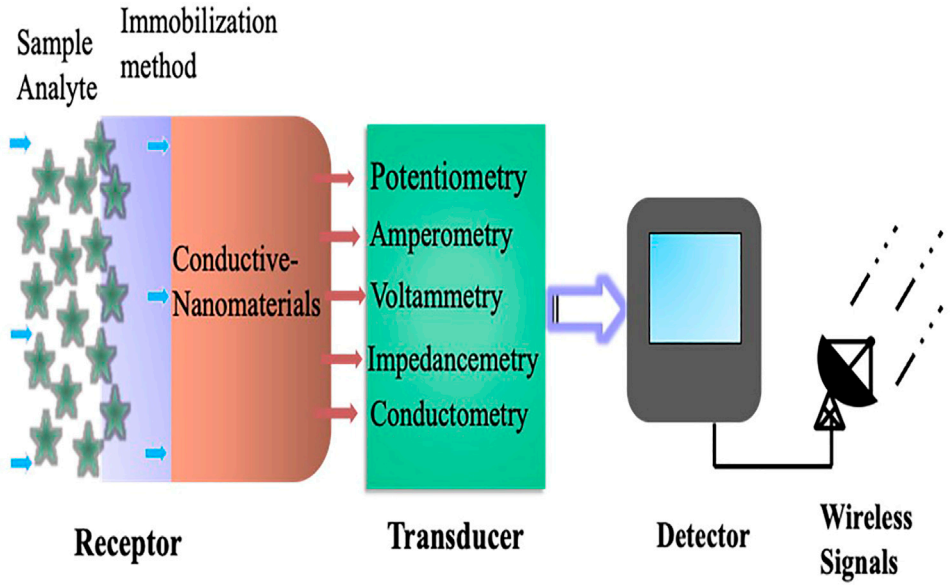

FIGURE 1 | A schematic representation of the basic design principle and key components of an electrochemical biosensor.

calcium, etc. The changes in the flow of current could be seen depending on the concentration of specific metabolites such as glucose, lactate, urea, and other interstitial fluids. The sensor itself can be fabricated with flexible substrates like PDMS, Ecoflex, and textiles (Windmiller and Wang, 2013; Abellán-Llobregat et al., 2017), stretchable elastomers, tattoo papers, or some other plastic based fabric (Bandodkar et al., 2015a; Gao et al., 2016a; Nyein et al., 2016). Polyethylene terephthalate (PET) and polyimide (PI) are also commonly used substrates. Silk fibroin, cellulose, and sponge have recently gained a lot of attention because of their excellent biocompatibility and biodegradability (Bandodkar et al., 2015c; Bandodkar et al., 2016).

ANALYTICAL APPLICATIONS OF CONDUCTIVE NANOMATERIALS IN ELECTROCHEMICAL BIOSENSORS

Carbon Nanomaterials for Wearable Electrochemical Biosensors

Carbon nanomaterials are the main building blocks in nanotechnology, which have attracted much attention because of their large specific surface area, high mechanical strength, inherent structural defects, good electrical conductivity, and excellent chemical and thermal stability (Park et al., 2013). Carbon nanotubes (CNTs), graphene (Grp) and reduced graphene oxide (rGO) are the most commonly used carbon nanomaterials in electrochemical biosensors. It appears to be a fantastic material, with a tensile strength of a hundred times that of steel, more excellent thermal conductivity than diamond, and electrical conductivity equivalent to copper but with the ability to carry a large amoiunt of current. In this section, analytical applications of carbon nanomaterials such as CNT, graphene and reduced graphene oxide have been demonstrated for wearable electrochemical biosensors.

Electrochemical Biosensors Based on "Carbon Nanotube"

Carbon nanotubes (CNTs), as 1-D nanomaterial, have recently gained a lot of attention as a valuable material for developing wearable electrochemical biosensors, particularly amperometry and potentiometric pH sensors, as some of them are listed in **Table 2**. CNTs are fabricated onto electrochemical transducers in different ways, mostly by coating and printing electrode substrates with CNTs or onto the composite electrodes (Park et al., 2013). Analyzing sweat from the human body during exercise may provide valuable information by monitoring the levels of electrolytes, e.g., (pH, Na^+, K^+, and $Ca^{+2)}$ and metabolites (glucose, lactate, urea) as well as skin interstitial fluid (Schazmann et al., 2010;Bandodkar and Wang, 2014). Sam Emaminejad et al. have reported a wearable electrochemical biosensor based on CNT for glucose measurement in human sweat (**Figure 2A**). The fabricated wearable sensor generates current signals proportional to the glucose concentration in a linear range of 0–100 mol/L with a sensitivity of 2.1 nA L m/mol, proving the excellent performances of the proposed glucose sensor, which is fabricated in such a way that CNTs is used as Glucose oxides (GOD's) immobilization matrix as well as H_2O_2 sensing components. The concentration of glucose will be determined indirectly by detecting H_2O_2 (Emaminejad et al., 2017). Wang and his colleagues improved wearable technology combined with electrochemistry, enabling the development of novel new sensing platforms for non-invasive on-body and on-site applications in sports, exercise, and healthcare. His group,

TABLE 2 | Carbon based nanomaterials in electrochemical biosensors.

Sensing material	Bio-fluid	Analyte	Detection range	Method	Ref.
Bare carbon	Sweat	b-nicotinamide adenine dinucleotide	0–3 mM ferrocyanide, 0–25 mM hydrogen peroxide, 0–100 μM NADH	Amperometry	Yang et al. (2010)
Bare carbon	Sweat	Uric acid	-	Voltammetry	Windmiller et al. (2012)
CNTs	Sweat	pH, K^+, NH_4	pH 8.51 to 2.69	Potentiometry	Guinovart et al. (2013)
Prussian blue (PB) onto CNT fibers	Sweat	Glucose	2.15 nA μM^{-1}	Amperometry	Wang et al. (2018)
Graphene doped Au mesh	Sweat	Glucose, pH	10×10^{-6} m (glucose)	Potentiometry	Lee et al. (2016)
CNT	Sweat	Glucose, lactate	0.3×10^{-3} m (lactate)	Amperometry	Jeerapan et al. (2016)
CNT	Sweat	$NH4^+$, Glucose	-	Amperometry	Bandodkar et al. (2016)
CNT	Sweat	Glucose, lactate, Na^+, K^+	-	Amperometry	Gao et al. (2016a)
Carbon/rGO	Sweat	Na^+, K^+, pH,	10–160 mM 2–32 mM 3–8	Potentiometry	Xu et al. (2019)

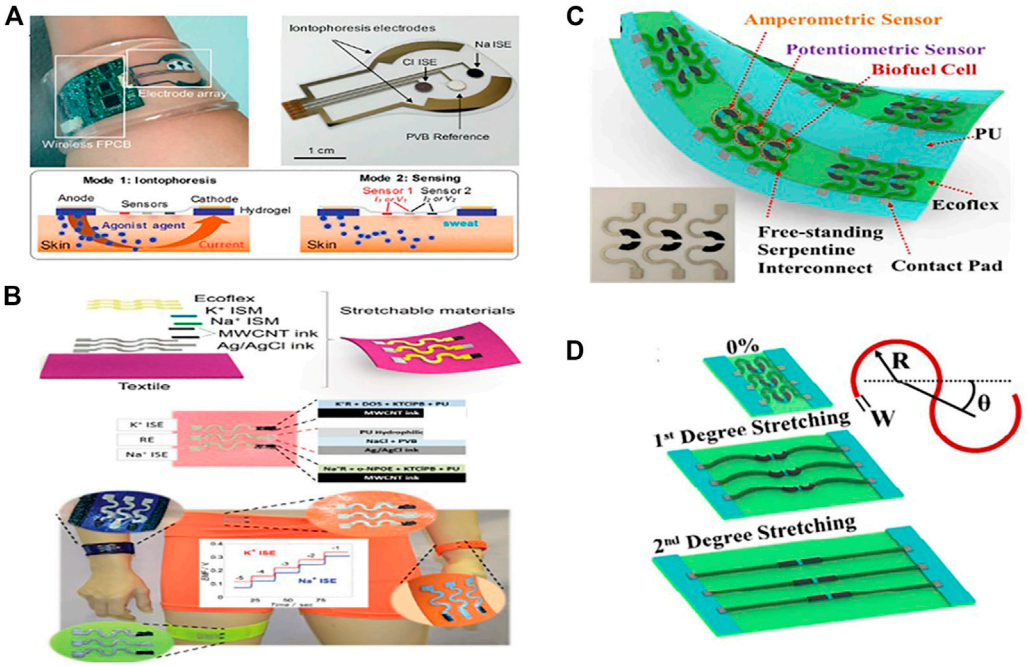

FIGURE 2 | Electrochemical biosensors that can be worn. **(A)** Image of an independent sweat extraction and sensor platform implanted on the skin, with a small layer of agonist agent hydrogel inserted under the iontophoresis electrodes (Copyright 2017; PNAS). **(B)** A wearable and stretchy CNT-based sensor printed on several standard textiles, as well as normal potassium and sodium measurement time trace graphs (Copyright 2016; Advanced Healthcare Materials). **(C)** all-in-one printed electrochemical biosensor and biofuel cell (BFC) arrays (copyright 2015, Nano Letters). **(D)** The two degrees of stretching allow printed arrays to withstand high strain levels (Copyright 2015; Nano Letters).

for example, proposed a CNT-printed textile-based potentiometric pH sensor capable of sensing electrolytes such as sodium and potassium in human sweat (Parrilla et al., 2019). Stretchable components such as (CNT and Ag/AgCl resistive inks) and pu ecoflex were printed in a serpentine pattern array on a textile substrate and then modified with ion-selective membranes (**Figure 2B**) (Parrilla et al., 2016). The sensor is capable of withstanding high tensile stress without cracking. Using open circuit potential readings, the sensor was checked. A calibration curve was recorded between the change in EMF and the time and by adjusting the concentration of NaCl and KCl solutions. The electrocatalytic response for the sodium [Na+] selective electrode was 59.4 mV $\log^{-1}$ for a linear range of 10^{-4} to 10^{-1} m with a detection limit of 104.9 M and the potassium [K^+] selective electrode had an electrocatalytic response of 56.5 mV $\log^{-1}$ over a linear range of 10^{-4} to 10^{-1} m with a detection limit of 104.9 M. While various types of electrochemical biosensors with various

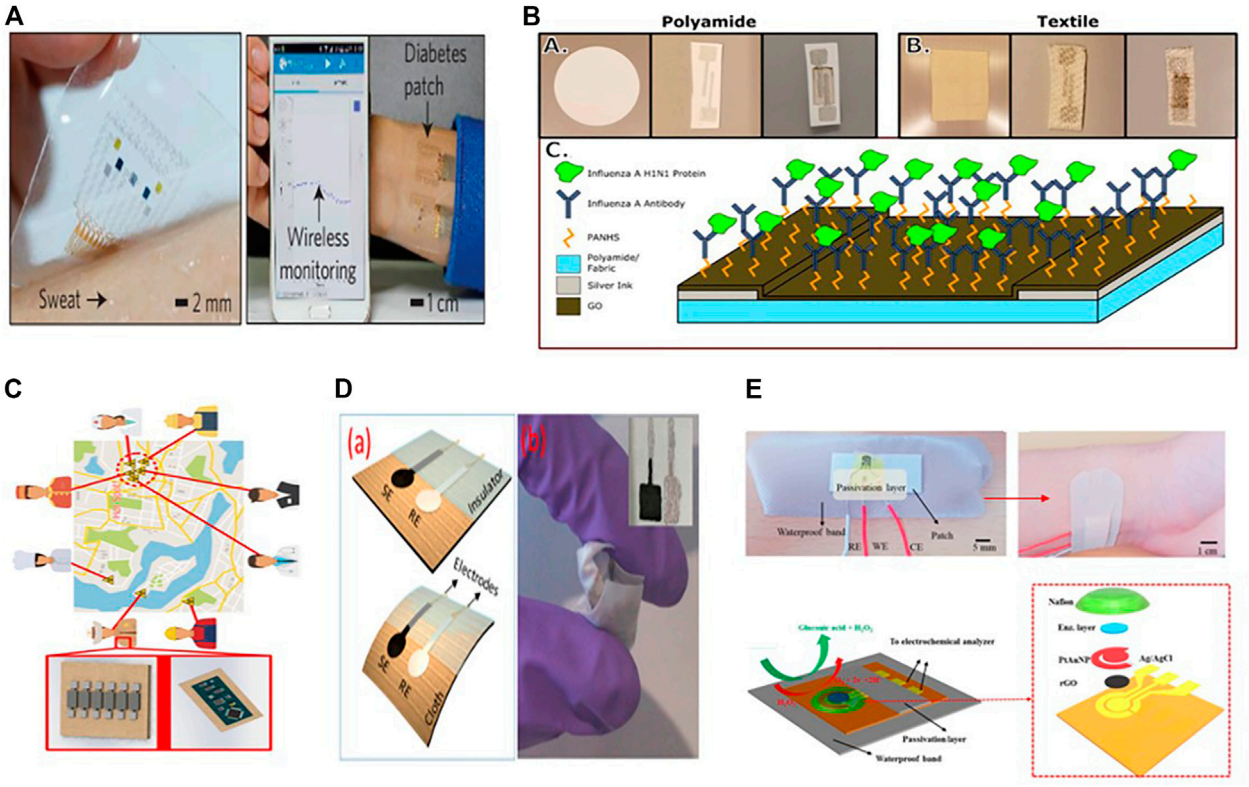

FIGURE 3 | (A) An optical image of a graphene-based hybrid electrochemical device mounted on human skin for automatic diabetes monitoring (Copyright 2016; Nature Technology). **(B)** A screen-printed graphene oxide-based biosensor using graphene oxide transduction film on both nanoporous polyamide and textiles substrates for tracking environmental exposure to influenza a virus (Copyright 2018; Electrochemical Society). **(C)** Schematic diagram of environmental exposure to influenza a virus (Copyright 2018; Electrochemical Society). **(D)** A lightweight potentiometric pH sensor, SE-sensitive electrode, and reference electrode are schematically represented on cloth (Copyright 2019; Biosensor). **(E)** Photographs and schematic representation of the completed sweat-based glucose biosensor mounted on human skin (Copyright 2018; Biosensors and Bioelectronics).

functionalities, such as multifunctional and wireless, have been established, there is still a big challenge in achieving self-powered electronics and energy harvesting techniques in electrochemical sensing.

Wang and his colleagues developed for the first time an all-in-one printed CNT-based electrochemical biosensor and biofuel cell (BFC) array (**Figure 2C**). A framework based on CNT functionalized with selective ionophores and enzymes was designed to understand various applications. Such as amperometric enzyme-based glucose sensors, potentiometric ammonium sensors, self-powered biosensors, and enzymatic glucose biofuel cells (BFCs). It can endure up to 500% strains without losing structural stability or sensor performance (Bandodkar et al., 2016). The electrochemical characterization of the system revealed that repeated strains ranging from 0 to 500%, torsional twisting of 180° for 50 cycles, and indenting stress (5 mm depth for 50 repetitions) has no impact on its device properties (**Figure 2D**). Another CNT-silver nanoink-based BFC with a textile substrate has been used as a self-powered sensor ability to extract perspiration energy and inspect sweat metabolites such as glucose and lactate (Jeerapan et al., 2016). Further, CNTs can be classified into two types: single-wall carbon nanotubes (SWCNTs) and multi-wall carbon nanotubes (MWCNTs) (Willner et al., 1996). Marc Parrilla et al. recently formed MWCNTs-based wearable potentiometric ion sensors (WPISs) to measure pH and ions (Na+, K+, and Cl–) in human sweat during exercise or exercise some other kind of sports. The sensors have Nernstian slopes within the approximate physiological range of each ion analyte, such as (for Na^+: 10–100 mM, K^+: 10–10 mM, Cl^- : 10–100 mM, and pH range: 4.5–7.5) (Parrilla et al., 2019).

Electrochemical Biosensors Based on Graphene

Graphene has become a leading material due to its outstanding properties, such as high charge carrier immovability, chemical stability in aqueous conditions, large effective surface area, and the ability to have a porous 3-dimensional structure. Graphene, on the other hand, can effectively increase the toughness and stretchability of electrodes. Because of its superior mechanical properties and high flexibility, making it more appropriate for use in wearable electrochemical biosensors (Shan et al., 2009; Lin et al., 2020; Zhang et al., 2021), as some of them are listed in **Table 2**. Lee et al. proposed a wearable sweat based glucose sensor using 2-D graphene nanomaterial modified with glucose oxides (Lee et al., 2016). Sweat concentration in glucose was accurately measured to assess the glucose levels (**Figure 3A**). Due to the high flexibility and good mechanical strength of graphene, the

sensitivity of the proposed glucose sensor was maintained well under large stress. In addition, a gold doped graphene and gold mesh render compatible wearable patch with 30% stretchability was also presented for the measurement of metabolite (glucose, lactate) in (10×10^{-6} to 0.7×10^{-3} m) range (Lee et al., 2016). Wang et al. introduce a different sensing electrode made of graphene oxide paper and modified with $Cu_3(btc)_2$ nanotubes and stable amino designed to detect glucose in sweat. This sensing electrode was used for a non-enzymatic electrochemical platform. The built wearable sensor has incredible sensitivity because of the large specific surface area caused by the graphene porous structure.

After all, David et al. developed a textile screen-printed graphene oxide-based biosensor. They used conductive silver ink electrode and graphene oxide transduction film on both nanoporous polyamide and textiles for everyday use to track environmental exposure to the influenza A virus (**Figure 3B**) (Kinnamon et al., 2018). An influenza-specific affinity assay was developed using electrochemical impedance spectroscopy (EIS) to identify the virus in solution on this graphene oxide layer because it is more secure and repeatable on the textile substrate than polyamide. Since the textiles sensor has high detection capabilities, it has a linear dynamic range of 10 ng/ml to 10 g/ml and a maximum 10 ng/ml detection in the biological fluid equivalent (buffer). The sensor demonstrates the ability to be integrated with the internet of things (IoT) devices so that it can wirelessly detect flu detection, helping to build a space-specific heat map of virus contacts (**Figure 3C**), which could be helpful for medical personnel identification and to stop the virus outbreak before it spreads out.

For additional biological applications (Zamora et al., 2018), P. Salvo et al. also demonstrated a potentiometric pH sensor based on a graphene sensitive layer with 40 mV/pH sensitivity in the pH range of 4–10 (**Figure 3D**) (Salvo et al., 2018). Within a week, they tested five sensor prototypes in human serum samples. The average deviation of the average response from the reference value collected by the glass electrode was 0.2 pH units. Recently Manjakkal Libu et al. also reported a graphene-based potentiometric pH sensor for wearable health tracking applications on a textile substrate. A thick G-PU film as a sensitive electrode (SE) was printed on cellulose-polyester blend fabric. The sensor shows a sensitivity of 4 mV/pH and a reaction time of 5 s in the pH range of 6–9. After washing in tap water, the sensor's performance is almost a potential 47 ± 2 mV for a long time (2000 s) (Manjakkal et al., 2019). For wireless monitoring of respiration and bacteria, a graphene printed silk sensor was fabricated and applied to tooth enamel and then functionalized with anti-microbial peptides to actively recognize "Helicobacter pylori" cells in saliva (Mannoor et al., 2012). Notably, in wireless operating mode, the sensor achieved a measurement standard of one bacterium μl^{-1} for a range of 103–108 CFU ml^{-1}.

Reduced Graphene Oxide Based Electrochemical Biosensor

Reduced graphene oxide is an excellent application material for electrochemical biosensor data processing. By easily incorporating functional groups and easy synthesis to parental chain, it has emerged as a viable alternative to other composites. Compared to other sensors on the market, rGO-based electrochemical biosensors provide high stability at lower temperatures without considering humidity. This element of low graphene oxide is likely to be investigated further in low-temperature sensors.

Xuan et al. developed a reduced graphene oxide (rGO) nanocomposite based electrochemical sensor to monitor body sweat measurement. The sensor was successfully fabricated on a flexible polyimide substrate using a simple and low-cost fabrication method. Gold Platinum nanoparticle alloy was deposited onto the (rGO) modified working electrode (**Figure 3E**), the sensor worked well in analytical operation (Xuan et al., 2018).

Metal-Based Nanomaterials for Wearable Electrochemical Biosensors

As electrochemical sensing materials, metal and metal-oxide based nanoparticles have attracted a lot of attention because of their small size, outstanding mechanical, electrical, chemical properties and high catalytic efficiency, as well as their versatility in creating new and better sensing systems (Bhide et al., 2019; Shaikh et al., 2019; Li et al., 2020). they can be categorized into noble and non-noble metal-based nanomaterials. Rh, Ir, Pt, Ru, Au, Os, and Ag are good examples of noble metal nanoparticles (Imamura et al., 2020). As it has been described earlier, metal-based nanomaterials have excellent and promising electro-catalytic properties, especially in wearable glucose non-enzymatic sensors. Like platinum Pt, palladium Pd, gold Au, metallic and oxides such as CuO, NiO, which can directly catalyse glucose (Abellán-Llobregat et al., 2017; Toi et al., 2019; Li and Wen, 2020), some metals based electrochemical biosensors are highlighted in **Table 3**.

Typically, glucose's sensing mechanism consists of non-noble metal-based nanomaterials by the redox reaction of the hydroxyl (−OH) group (Archana et al., 2019). However, metal-based nanomaterials can be used as nanowires or nanosheets to achieve maximum sensitivity; that's why some researchers use metal nanosheets and nanowires to achieve the maximum sensitivity instead of making film electrodes as shown in (**Figures 4A,B**) (Wen et al., 2014;Oh et al., 2018;Bae et al., 2019). In the last few years, gold has become a common active sensing material because of its excellent biocompatibility, and electrochemical property. Amanda et al. made a thin-film gold electrode-based glucose sensor (Imamura et al., 2020). The stretchable electrodes stretchability is almost 210% of its original length and accurately detect the glucose level without enzymes, which is one of the lowest documented for flexible, enzyme-free sensor (**Figure 4C**). Nowadays, metallic aerogels, a new category of 3-D metal-based nanomaterials anticipated by researchers, have recently become a new field of concern, offering enormous glucose bio-electrocatalysis and promise in wearable glucose sensors (Wen et al., 2016). Its porous form and gel state are ideal for immobilization of enzymes and maintaining their activity, which is highly beneficial in extending the life span of

TABLE 3 | Metal based nanomaterials in electrochemical biosensors.

Sensing material	Bio-fluid	Analyte	Detection range	Method	Ref.
ZnO	Body fluid	Pesticide	-	Potentiometric	Hatamie et al. (2015)
(Ag/AgCl)	Sweat	Glycemic	-	Amperometry	Bandodkar et al. (2015b)
Platinum	Sweat	Oxygen	(11 s–90% of a steady-state current)	Amperometry	Mitsubayashi et al. (2003)
Au, Bi	Sweat	Zn	10.4 nAL μg^{-1}	Voltammetry	Gao et al. (2016b)
$NiCo_2O_4$/chitosan	Sweat	Glucose	0.5 μA/μM	Amperometry	Lu et al. (2019)
Bi	Sweat and urine	Cd^{2+}	<100 μg L^{-1}	Voltammetry	Gao et al. (2016b)
Bi, Au	Sweat and urine	Pb^{2+}	<100 μg L^{-1}	Voltammetry	Gao et al. (2016a)
Au	Sweat and urine	Cu^{2+}	100–1,000 μg l–1	Voltammetry	Gao et al. (2016a)
Au	Sweat and urine	Hg^{+}	<100 μg L^{-1}	Voltammetry	Gao et al. (2016a)
Au	Sweat	Glucose Lactate	0–200 μM 0–30 mM	Amperometry	Gao et al. (2016a)
Ag/AgCl	Sweat	Chloride	-	Potentiometric	Gonzalo-Ruiz et al. (2009)
Bare gold	Tears	Electrolytes	-	Conductometry	Ogasawara et al. (1996)
Ag/GOx	On body	Bio fluid influenza A virus	LDR: 10 ng ml^{-1} to 10 μg/ml LOD: 10 ng ml^{-1}	Potentiometry	Kinnamon et al. (2018)
Graphite/Ag/AgCl	Sweat	pH	pH range 6–9	Potentiometry	Manjakkal et al. (2019)
Vertically aligned gold nanowires	Sweat	Na^{+}, K^{+}	(56.1 mV/pH for pH, 58.2 mV/decade for Na^{+} and 41.5 mV/decade for K^{+})	Potentiometry	Wang et al. (2020)
Platinum-decorated graphite	Sweat	Glucose	33 μM and 0.9 mM	Amperometry	Abellán-Llobregat et al. (2017)

wearable glucose sensors (Zhang et al., 2012). Wen et al. developed a glucose sensor by assembling three-dimensional gold aerogels nanostructure modified glucose oxides. The sensor can detect glucose qualitatively and quantitatively in 0.1 mol/L phosphate buffer solution (pH 7.4) (Wen et al., 2016). In addition, compared with a single metal system, a reasonably designed multi-metal nanomaterial can make extensive use of the properties of two or more metal elements. thus enhancing the efficiency of the wearable glucose sensor, which will also become the metal sensor's production path. Wang et al. and his colleagues recently created elastomer-bonded gold nanowire coating technology. Using the same technology, they create lactate-sensing working electrodes, reference electrodes, and counter electrodes for lactate monitoring in human sweat (**Figure 4D**).

In artificial sweat, the sensor has a high sensitivity of 14.6 μA/mM.cm^2. This sensor's sensitivity is maintained even when subjected to high tensile strains of up to 100% without the use of any external structural layout (Wang et al., 2020). Their group has also suggested a gold fibre-based wearable electrochemical biosensor for sweat PH tracking. The manufactured fibre-based pH sensor shows superior sensitivity (60 mV/pH), high selectivity against cationic interference, and high stretchability (up to 100% strain). One benefit of fibre-based sensors is their ability to be incorporated in textiles, which can be integrate into daily garments to detect "unrecognizable" personal health (Wang et al., 2020). Recently, Francesca et al. designed a wearable multifunctional sweat sensing system based on platinum. The device is highly flexible and comprises four electrodes for continuous measurement of analytes such as Li^{+}, Pb^{+2}, K^{+} and Na^{+} in different health applications and sports activities (**Figure 4E**). The sensors show linear responses in artificial sweat. Because of the good biocompatibility, flexibility and accurate sample handling this wearable framework is a significant step forward in the advancement of non-invasive tracking technologies for health, opening the way for better understanding of physiological parameters and clinical needs of individuals (Criscuolo et al., 2021). Metals containing oxides, such as indium oxide and lead oxide, are more sensitive and can be used to make sensing electrodes for wearable electrochemical biosensors. Huajun et al. suggested a pH sensor based on quasi-two-dimensional metal oxide semiconductors for detecting glucose and ph in sweat. The sensor is made of In_2O_3 thin films and has a detection limit of 0.0005 for pH and high accuracy in detecting glucose content (**Figure 4F**) (Chen et al., 2017).

Conductive Polymer Nanomaterials Based Electrochemical Biosensors

Polymer-based novel sensing capabilities represent a significant advancement in electrochemical sensing. Since the electrochemical sensors are integrated into textile structures through weaving, knitting, and embroidery, or need to be directly embedded into garments and coupled at the human skin's surface to detect the target analyte (Allison et al., 2017). It is highly desirable that the sensors should be reliable and flexible enough to reduce motion-induced signal interference. While carbon and metal-based nanomaterials are highly sensitive but they are not flexible enough as the conductive polymer-based nanomaterials. It is well recognized that CPs have advantages such as chemical diversity, low density, durability, corrosion resistance, easy-to-handle shape, terminology and adaptable conductivity. Moreover, the outstanding properties of flexible

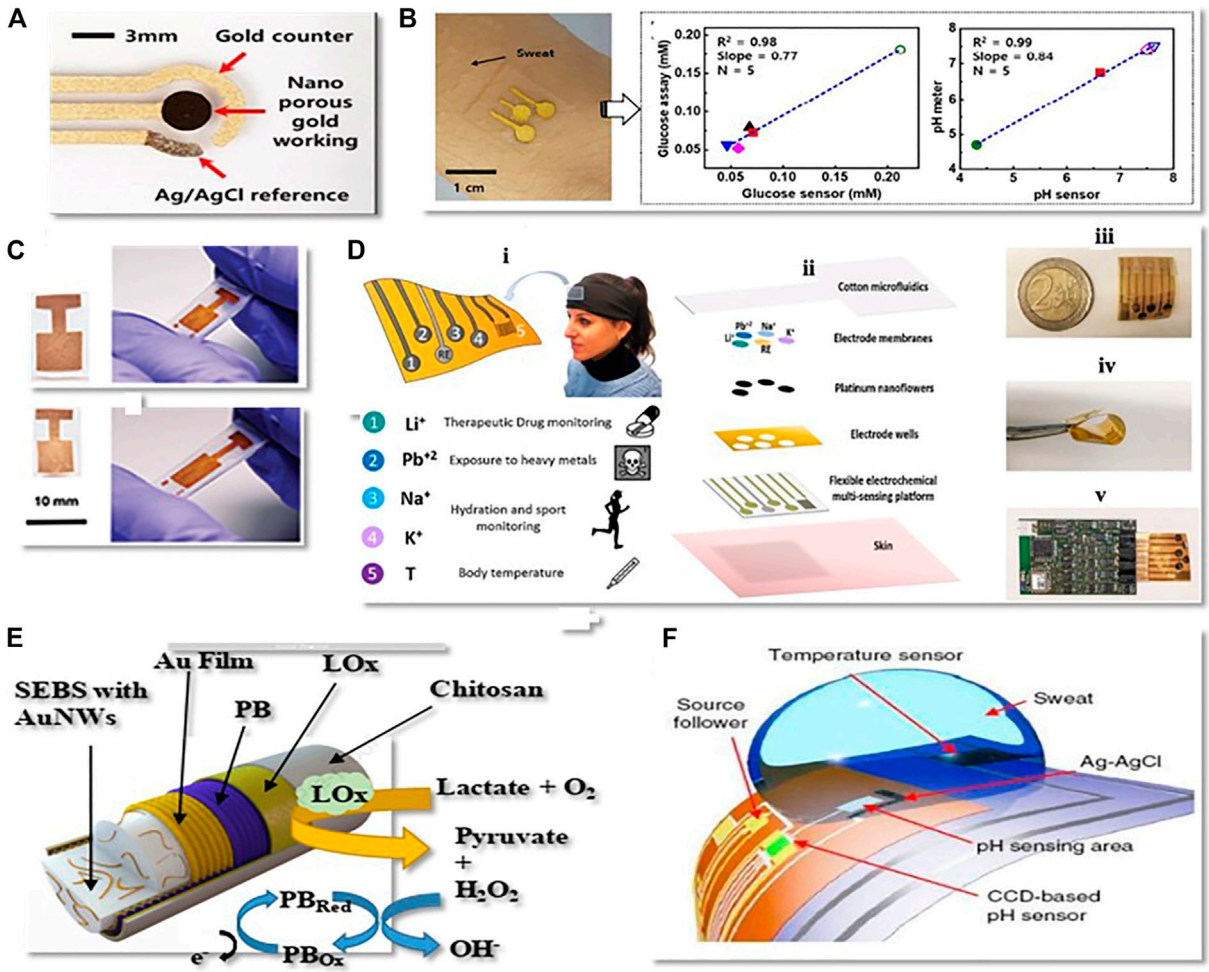

FIGURE 4 | (A) Gold nanoporous based non-enzymatic wearable biochemical sensor (Copyright 2019; American Chemical Society). **(B)** Gold nanosheet-based non-enzymatic wearable biochemical sensor (Copyright 2018; American Chemical Society). **(C)** Unshrunk gold electrode on polyolefin (PO) and shrunk electrode on elastomer substrate (Copyright 2020; Advance Material and Technology). **(D)** Overview of the wearable multi-electrode device for sweat-based healthcare surveillance (Copyright 2020; Sensors and Actuators): (I) testation of health care applications; (II) flexible electrochemical multi-sensing system; II) flexible multi-electrode sensing platform; (IV) bending test; (V) example of interfacing with read-out electronics. **(E)** Lactate tracking electrochemical biosensor based on gold nanofibers. (Copyright 2021; Journal of Materials Chemistry). **(F)** Ultrasensitive potentiometric biosensors based on Quasi-two-dimensional metal oxide semiconductors (Copyright 2018; Springer Nature).

conductive polymer nanomaterials are as follows: 1) they aided in increasing the selectivity and stability of electrochemical biosensors' sensing properties. 2) They usually have a 3-D structure. They can be manufacture in various sizes, including nanometre size and high conductivity, such as 120–130 S cm^{-1} at room temperature, which offers a more precise surface area. 3) The modification of conductive polymers at the sensing electrodes is relatively very easy and simple because it has no special requirements for the evenness of electrodes (Matsumura et al., 2018) (Gerard et al., 2002;Gerard and Malhotra, 2005;Zeng et al., 2014). Researchers discovered and produced conductive polymer nanomaterials such as (PEDOT- PSS) (Abouraddy et al., 2007;Zhao et al., 2018), polypyrrole (ppy) (Gregory et al., 1989; Tzou and Gregory, 1992)), polythiophene (PTh) and polyaniline (PANI) (Huang and Kaner, 2004;Teli et al., 2014), to fabricate the sensing electrodes. Usually, conductive polymers are deposite at working electrodes as a compact film. Some conductive polymer nanomaterial-based wearable electrochemical biosensors are summarized in **Table 4**. Xuesong et al. developed PANI nanoparticle-based sensitive pH sensor. The sensor was fabricated by coaxial electrospinning of PANI nanoparticles and polyurethane (PU) into the core-shell fibres (**Figure 5A**). A Screen-printing method was used to create a sensing electrode assembly on a polyethylene terephthalate (PET) substrate, which consisting of gold as a counter electrode, (Ag/AgCl) reference electrode, and (PANI-PU) working electrode. Here, PU provides mechanical stability to the sensor. The feasibility of detecting sweat pH on the skin was demonstrated by attaching the chip to the arm and electrochemical workstation was used to measure the reaction. The sensor operated linearly in the pH range of 2–7 with a sensitivity of 60 mV/pH and can detect pH changes of less than 0.2 (Hou et al., 2020). Salzitsa et al. developed a fully wearable and

TABLE 4 | Conductive polymer nanomaterials in electrochemical biosensors.

Sensing material	Bio-fluid	Analyte	Detection Range	Method	Ref.
PANi conducting polymer	wounds	pH	pH range (5.5–8)	Potentiometric	Guinovart et al. (2014)
(PEDOT:PSS)	Sweat	Na^+	45.8 mV dec^{-1}	Potentiometry	Wang et al. (2018)
(PEDOT:PSS)	Sweat	K^+	35.9 mV dec^{-1}	Potentiometry	Wang et al. (2018)
(PEDOT:PSS)	Sweat	Ca^{2+}	52.3 mV dec^{-1}	Potentiometry	Wang et al. (2018)
Polyaniline (PANI) onto the CNT fibers	Sweat	pH	-	Potentiometry	Wang et al. (2018)
PEDOT:PSS/Ag/AgCl	Sweat	Cortisol	59.63 mV pH^{-1}	Amperometry	Parlak et al. (2018)
PEDOT/RGO/GC	Rat brain	Dopamine	0.1–175 μM	Amperometry	Xu et al. (2014b)
Polyaniline	Sweat	pH	3–8	Potentiometry	Nyein et al. (2016)
PEDOT	Sweat	Na^+ K^+	-	Potentiometry	Lee et al. (2016)

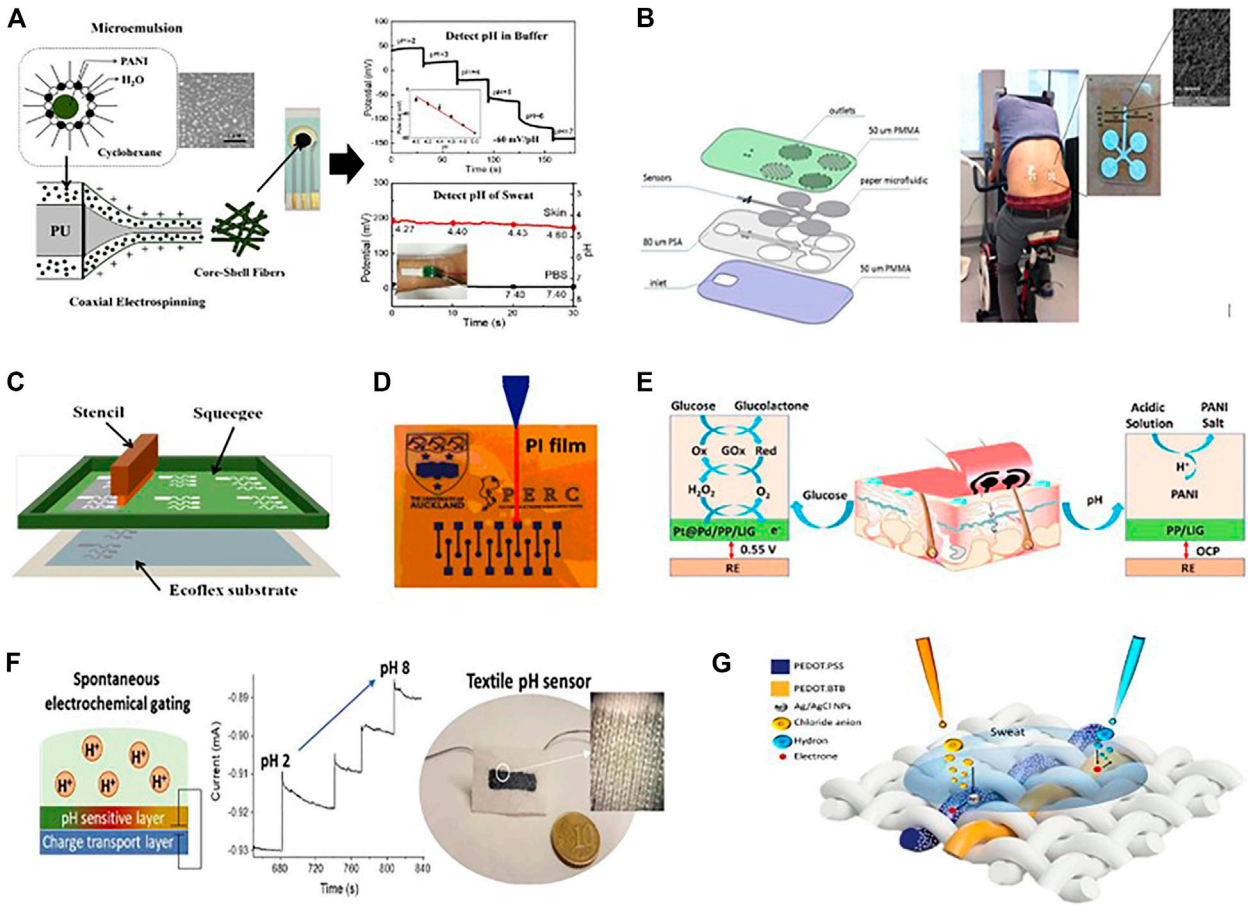

FIGURE 5 | (A) Fiber coaxial electrospinning with graph monitor, pH determination in buffer, and sweat (Copyright 2020; Polymers & Biopolymers). **(B)** A schematic representation of the microfluidic chip fabrication steps is seen, as well as a photograph of the platform attached to the body and an image from scanning electron microscopy (SEM) (Copyright 2017; Biosensors and Bioelectronics). **(C)** Screen-printed stretchable device with custom stretch-resistant (Copyright 2015; Wiley). **(D)** Laser writing using a CO_2 laser. (Copyright 2018; Biosensors and Bioelectronics). **(E)** A wearable glucose sensor based on poly (3, 4-ethylene dioxythiophene)-poly (styrene sulfonate) (Copyright 2020; Elsevier). **(F)** PH sensor with two terminals wearable sensor and magnification of cloth knotwork Current vs time reaction to pH changes (Copyright 2017; Biosensors and Bioelectronics). **(G)** Conductive Polymers based textile chemical sensor for Sweat analysis (Copyright 2020; Scientific Reports).

flexible patch with completely integrated sensing system for on body human sweat testing (**Figure 5B**).

The sensing device is designed so that a steady stream of sweat can flow through an array of compact microneedles with a diameter of 50 μm. The sensors are embedded in a microfluidic channel, which can simultaneously track metabolites (lactate) and electrolytes, for example, pH and sodium ions. The promise of the multi-sensing platform for monitoring the metabolite and electrolyte (sodium, lactate, and cortisol) from saliva is demonstrated in detail. For that, a

potentiometric sodium ion sensor made of poly (3, 4-ethylenedioxythiophene) (PEDOT) and an amperometry lactate sensor were proposed. This sensing device can transmit data wirelessly for easy processing and storage, with the potential for real-time data analytics (Anastasova et al., 2017). As it has been seen, various groups have achieved device dimensional stability through lithographic or coating processes that are either costly or complicated on a large scale. So, for the first time, AJ Bandodkar et al. filled this technological gap by using the screen-printing method to create a low-cost and highly stretchable (PEDOT: PSS) based wearable electrochemical biosensor (**Figure 5C**). The stretchable device exhibits 2-D serpentine interconnects with 180° turns between electrode areas and touchpads (Bandodkar et al., 2015c). This electrochemical device has high sensitivity, can undergo high tensile stress, and meets the stretchability criteria of many applications; it was a good sign for potential and next-generation wearable systems. Tomas Guinevere et al. also developed a screen printed Potentiometric pH sensor based on conductive polymer (PANI) to measure the pH level of wounds in the body (Guinovart et al., 2014). The device works by carefully incorporating a pH sensor into bandages (pH range 5.5–8). These new pH-sensitive bandages opened a new possibility for the realization of telemedicine. In 2018, Xu et al. introduced a new and innovative technique to develop a highly sensitive PEDOT-based electrochemical biosensor for the detection of dopamine (DA) (**Figure 5D**) (Xu et al., 2018). The sensor was fabricated using a PEDOT-modified laser scribed graphene (LSG) method, which shows higher sensitivity and selectivity for detecting dopamine in a complex mixture. These PEDOT-LSG electrodes have a lot of potential for infield or point-of-care biosensing and some other incorporated bioelectronics products. Recently, Zehad et al. used the same technique to develop a PEDOT-PSS modified 3-D stable porous, porous, laser-induced graphene (LIG) to detect glucose and pH in human sweat (Zahed et al., 2020). Where, PEDOT-PSS is used to increase the tensile stability and uniform conductivity of the electrode. The fabricated electrochemical biosensors display a good current response to glucose in a wide linear range of 10 mmol/L to 9.2 mmol/L, with high sensitivity of 247.3 mA L mmol cm^{-2} and a low detection limit of 3 mmol/L. As a new kind of multifunctional sensor, this versatile substrate was further improved with Pt/Pd nanoparticles for glucose detection (**Figure 5E**). Recently Mariani et al. proposed a PEDOT: PSS film based electrochemical potentiometric sensor through a new and different approach. A pH-dependent modification of the current flowing through the PEDOT: PSS film was obtained through the random electrochemical gating caused by the potentiometric transducer (PEDOT: BTB), PEDOT: Bromothymol Blue [27]. The feasibility of this technique was demonstrated by creating a screen-printed pH sensor on a bio-ceramic fabric (**Figure 5F**). Compared to the rigid analogous fabricated on a glass substrate, this textile pH sensor demonstrated a standardized sensitivity of (7.5) $x10^{-3}$ pH^{-1} in the range of 2–7, with no penalty of sensing efficiency. By using the same content PEDOT:PSS and PEDOT:BTB (Mariani et al., 2020). The same technique was used to develop a thread-based pH sensor, as shown in (**Figure 5G**). In conjunction with another thread-based sensor for multi-sensing network and chloride ion (Cl^-) detection, the textile sensor could detect pH selectively during continuous recordings (Possanzini et al., 2020).

Other Sensing Nanomaterials

In accordance with the sensing nanomaterials described above, various novel nanomaterials with good electrical conductivity, large specific surface area, and good biocompatibility are developing in the field of wearable electrochemical biosensors. For example, Polymer nanomaterials flexibility, conductivity, durability and long-term stability would be enhanced further after compound with Carbon and metal-based nanomaterials (Zhou and Shi, 2016; Jia et al., 2019) as some of them have been listed in **Table 5**.

Conductive Polymer Combines With Metallic Nanomaterials

Conductive polymer compound with metallic nanomaterials shows enhanced selectivity and stability for measuring metabolites like glucose and lactate. Xu et al. developed a non-enzymatic glucose sensor by using gold nanoparticles, polyaniline arrays, and a carbon cloth electrode (Xu et al., 2017). PANI was first grown vertically on a flexible carbon cloth (CC) electrode surface to form PANI arrays with a 200 nm height and a 100 nm diameter (**Figure 6A**). And the integrated electrode (AuNPs/PANI/CC) can electrochemically catalyze the oxidation of glucose. The linear range of the flexible non-enzymatic glucose sensor is 10.26 μM to 10.0 mM, with a sensitivity of 150 μA cm^{-2} mM^{-1} with a detection limit of 3.08 μM (S/N = 3) (Xu et al., 2017).

Conductive Polymer Combines With Carbon Nanomaterials

Conductive polymer nanocomposites combine with carbon nano-species such as carbon nanotubes, graphene, and carbon nanofibers have been evolved. These carbon compounds enhance the structural configuration of conductive polymer chains and allow charge carrier passage, which as a result, increases the conductivity. CNT with conductive polymer shows improved sensing properties in electrochemical biosensors with high stability and good selectivity (Rahimi et al., 2017;Zhou et al., 2017). The most Common CNT-based polymer nanocomposite are PEDOT-CNT-CPE, PEDOT-MWCNT, PPy-MWCNT-ITO (Shrivastava et al., 2016). Xu et al. fabricated a nitrobenzene electrochemical biosensor based on a carbon paste electrode, modified with a PEDOT-CNT nanocomposite. This electrode was used to analyze hydroquinone, dopamine, and nitrobenzene (Xu G. et al., 2014). Similarly, K. Sing et al. developed a multi-walled carbon nanotube (MWCNT), polypyrrole (PPY)-*p*-toluene sulfonic acid (PTS) based electrochemical biosensor for cholesterol detection. At 9s, the sensor demonstrates high sensitivity and rapid response (Singh et al., 2012). Recently, Smith et al. created a wearable pH sensor cotton yarn by dipping and drying it in PEDOT: PSS and multi-walled carbon nanotubes (MWCNT), followed by PANI deposition. The graph shows the standard deviation on three different replicant fibres (**Figure 6B**). This resulted in electrodes with substantial biocompatibility and

TABLE 5 | Other conducting nanomaterials in electrochemical biosensors.

Sensing material	Bio-fluid	Analyte	Detection range	Method	Ref.
CNTs/Ag/AgCl/PANI	Interstitial fluid	pH	59.63 mV pH^{-1}	Potentiometry	Mpanza (2016)
CNTs/Ag/AgCl/PANI	Interstitial fluid	Glucose	-	Amperometry	Mpanza (2016)
polymers/SWNT-COOH	On body	Body order Volatile amine	Linear dynamic range LDR:50–1000 ppm	Conductometry	Seesaard et al. (2015)
PEDOT:PSS/Au	Sweat	Na^+ K^+	10–160 mM 1–32 mM	Potentiometry	Gao et al. (2016a)
PEDOT:PSS/Carbon fiber thread	Sweat	Na^+ K^+	0.1–100 mM 0.1–100 mM	Potentiometry	Yoon et al. (2019)
MXene	Sweat	Glucose and lactate	35.3 μA mm^{-1} cm^{-2} for glucose, and 11.4 μA mm^{-1} cm^{-2} for lactate	Amperometry	Lei et al. (2019)
rGO-PANI	Sweat/fluid	PH	75.09 nm/pH at pH 11.35	Potentiometry	Semwal and Gupta (2019)

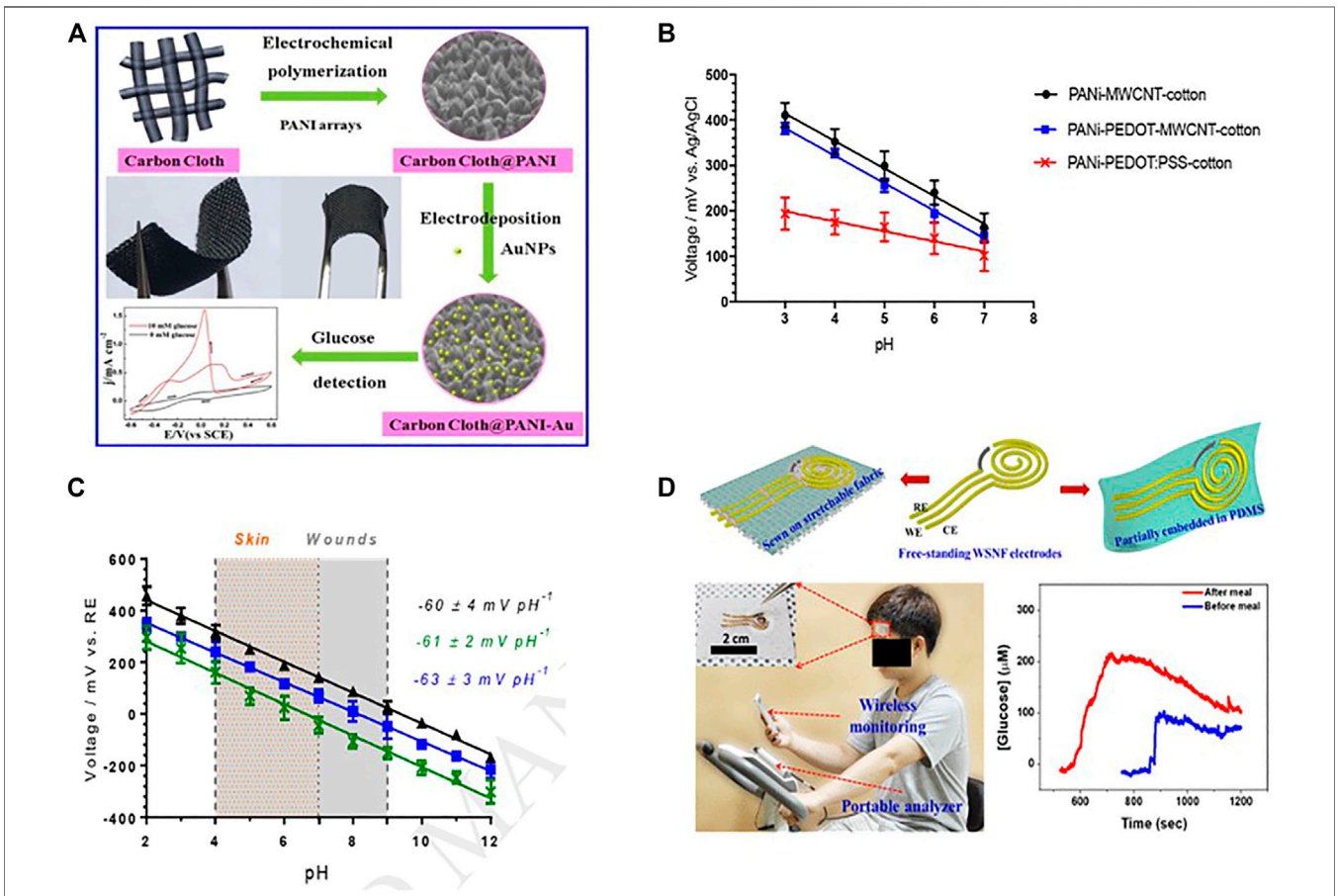

FIGURE 6 | (A) AuNPs/PANI/CC based non-enzymatic glucose sensor (Copyright 2017; Sensors and Actuators). **(B)** PANi-coated conductive cotton yarns' pH sensitivity, the error bars show the standard deviation of measurement on $n = 3$ replication fibers (Copyright 2019; Sensors and Actuators). **(C)** An open circuit PH study potentiometric response of PANi-PEDOT-MWCNT-cotton electrodes. (Copyright 2019; Sensors and Actuators). **(D)** Schematic illustration of rGO/PU-Au nanocomposite fiber used in manufacturing sweat-based wearable electrochemical glucose (Copyright 2019; American Chemical Society).

antibacterial properties, Which could be used in the future to create wearable solid-state pH sensors (along with quasi-reference electrodes) and for real-time wound and skin pH measurement over a broad pH range (2.0–12.0) and achieve a rapid, selective, and Nernstian response (−61 2 mV pH^{-1}) (**Figure 6C**) (Smith et al., 2019).

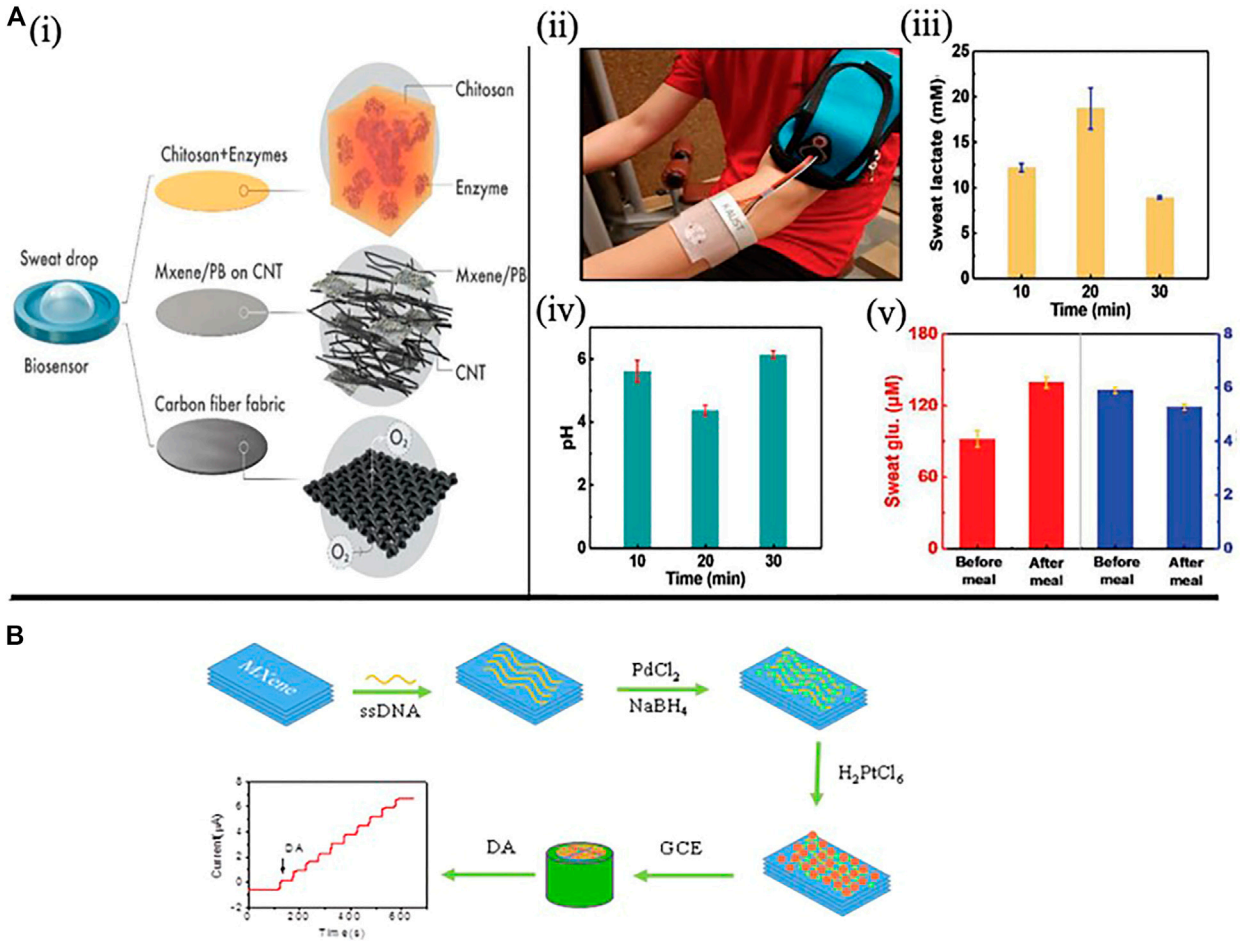

FIGURE 7 | (A) a wearable MXene based electrochemical biosensor. i) the oxygen-rich enzyme electrode is depicted schematically. ii) On the skin, sweat-monitoring wearable patch. iii) Comparison of lactate levels at various points during exercise using three separate lactate sensors. iv) Comparison of pH levels at various points in the exercise using three different pH sensors. v) Glucose levels before and after meals were compared using three different glucose and pH sensors. (Copyright 2019; John Wiley and Sons). **(B)** The Ti_3C_2/DNA/Pd/Pt nanocomposite fabrication process. (Copyright 2018; Journal of Electroanalytical Chemistry).

Polymers combined with graphene (nanocomposites) demonstrate great potential in wearable electrochemical biosensors. This composite modified electrode has combined graphene's excellent conductivity and the advantages of polymer nanomaterials, which can increase the durability, biocompatibility and sensitivity of sensors (Xu G. et al., 2014; Hou et al., 2017; Toi et al., 2019). A highly sensitive fiber optic pH sensor based on reduced graphene oxide-polyaniline (rGO-Pani) nanocomposite is fabricated and characterized using the SPR technique. The *in-situ* approach was used to successfully synthesize the rGO-Pani nanocomposite. The sensor's output is outstanding at low and high pH levels, with a maximum sensitivity of 75.09 nm/pH at pH 11.35 (Semwal and Gupta, 2019).

Phan et al. demonstrated a nonenzymatic wearable patch for on body glucose sensing based on polyurethane (PU) and reduced graphene (rGO) composite fiber, which was further modified with oxygen-containing functional groups. The wearable glucose sensor is highly sensitive (140 mA L $mmol^{-1}cm^{-2}$), with a low detection limit of 500 $nmolL^{-1}$. Furthermore, due to the high rGO-PU fabric stretchability, the proposed wearable glucose sensor could be stretched up to 30% and had a high mechanical resilience under repeated cycles of deformation (**Figure 6D**) (Toi et al., 2019).

MXene Based Electrochemical Biosensors

In addition to the above-mentioned sensing nanomaterials, a new class of 2-D material known as MXene has recently arisen as an inorganic compound, consisting of nitrides, transition metal carbides, or carbonitrides ($Ti_3C_2T_x$) (Guo et al., 2019). It has a thickness of several atomic layers, excellent conductivity, a wide surface area, and excellent biocompatibility, which endows a great prospect in the field of electrochemical biosensors (Yoon et al., 2020). (Tan et al., 2017; Nayak et al., 2018; Wu et al., 2018; He et al., 2020).

The hydrophilic nature of MXene can selectively absorb biomolecules. For instance, Lei et al. proposed a portable multifunctional sweat-based biosensor with 2D MXene for the

long-term and subtle identification of biomarkers (such as pH, glucose and lactate) in sweat (**Figure 7A**). Using artificial sweat, average pH level and electrochemical sensitivity values for lactate 11.4 μA mm^{-1} cm^{-2} and glucose 35.3 μA mm^{-1} cm^{-2} were recorded in three different graphs (Lei et al., 2019). Zheng created sensitive dopamine (DA) sensor using a separate nanomaterial (MXenes/DNA/Pd/Pt), with MXene nanoparticles serving as a conductive matrix for Pd/Pt nanoparticles. The hydrophobic aromatic group adsorbed on the surface of MXenes induces the *in-situ* growth of PdNPs and Pd/Pt nanoparticles (**Figure 7B**). The sensor shows excellent linearity in the DA concentration range of 0.2–1,000 μM, as well as high selectivity against ascorbic acid, glucose and uric acid (Zheng et al., 2018). MXenes nanosheets also have the ability to strip heavy metals as well as to detect heavy metal ions (e.g., Cu, Li, Na, K atoms) (Guo et al., 2015; Shahzad et al., 2017). Aside from small molecules, metal ions and MXenes combine to have a similar doping effect. Zhu et al. studied the electrochemical reaction of MXene to recognise the coexistence of $Cu^{2+,}$ $Pb^{2+,}$ $Hg^{2+,}$ and Cd^{2+} and suggested a new platform for the detection of high sensitivity metal ions. (Zhu et al., 2017).

NANOMATERIAL APPLICATIONS IN ELECTROCHEMICAL IMMUNOSENSORS AND DNA BIOSENSORS

Electrochemical Immunosensors

Electrochemical immunosensors have been extensively used in medical diagnostic and therapeutic applications, doping or impurities, and the food industry to track biological components and biological molecules of environmental origin and influence. where antibodies are probes that form ion complexes with the same antigen pairs with specific targets. Nanomaterials are the best candidates for developing electrochemical immunosensors with good sensitivity and signal transduction capability. A significant number of electrochemical label-free immune strategies have recently been developed and used to identify multiple target biomarkers associated with many kinds of diseases (Tuteja et al., 2018), including viruses (Kaushik et al., 2018), cardiac markers, and other proteins (Dutta and Lillehoj, 2018; Haji-Hashemi et al., 2019). Focused on this label-free method, a non-faradaic impedimetric portable/wearable cortisol sensor was designed using semiconductive MoS2 nanosheets and vertically aligned metal electrodes to calculate cortisol concentration in artificial sweat samples (Kinnamon et al., 2017). As a new immunosensing platform, Stretchable and disposable electrochemical biosensors are eager to identify biomarkers from body fluids such as saliva, interstitial fluids, sweat, or wound fluids, as well as various biomechanical organisms (Kim et al., 2011; Cao et al., 2014; Gao et al., 2016c; Liu et al., 2016; Liu et al., 2017). However, the realization of such stretchable electrochemical biosensors has been narrowed by the challenges of obtaining electrochemical electrodes with high sensitivity, stretchability, and stability during deformation. With that in mind, Bo-Yeong et al. proposed a simple, durable and stretchable disposable point of care electrochemical immunosensor based on metallic nanomaterials. A three-dimensional, micro-patterned stretchable substrate was used to form thermally evaporated gold as working and counter electrodes (**Figure 8A**). The sensor shows high sensitivity and stability when stretching up to 30%. The sensor can detect low concentrations of target molecules, down to 100 fM of TNF- α protein, an inflammation biomarker**.** After all, it was still challenging to develop a soft, skin-interfaced biosensor patch entirely operative lab-on-patch technology, with particular significance for non-invasive detection and differentiation of biomarkers from body fluids (Heikenfeld et al., 2018, 80; Zhao et al., 2019; Lee et al., 2020). It will also be more user-friendly than lab-based immunoassays or in-hospital (POCT) point-of-care testing, which involves numerous *in vitro* sample processing steps and user expertise in sample analysis (Daniels and Pourmand, 2007). Many current immunoassay procedures use labelling to produce a detection signal, in which an antibody, fluorescent markers, or redox pair is added to the detection probe. These methods are time-consuming, need several steps, and cause discomfort to the wearer (Joung et al., 2019). To meet these challenges, Lee et al. developed a stretchable, wearable lab-on-a-patch (LOP) device made up of a label-free impedimetric biosensor and a stretchable microfluidic system for on-body measurement of the hormone, biomarker, and cortisol. A three-dimensional nanostructured gold was used as a sensing electrode to achieve the high sensitivity required to measure the pM-levels of cortisol in sweat (**Figure 8B**). Using an antibody as a probe biomolecule, this biosensor measured sweating cortisol accurately during exercise, ranging from 1 pg/ml to 1 μg/ml, under a 30% strain (Lee et al., 2020). This LOP platform may be enhanced to track other biomarkers in sweat such as cytokines, neuropeptides, therapeutic drugs in sweat and a broader range of biomarkers in other biofluids such as interstitial fluids or wound exudate. Further, we see a great roll of nanomaterials in molecular imprinted polymer-based sensors (MIP's). Huang et al. recently proposed a flexible electrochemical urea sensor (**Figure 8C**). In their first work, they developed the MIP by imprinting urea with electropolymerized (PEDOT) on a network of carbon nanotubes and gold nanotubes (AuNTs) (Liu et al., 2018). The developed flexible sensor demonstrated a strong linear response to physiologically significant urea levels while showing negligible cross reactivity. Their second work fabricated an ECL sensor by coating a specific MIP layer on highly luminescent nanospheres immobilized AuNTs networks (Parlak et al., 2018). The sensor can detect lactate and urea from sweat accurately with high stability. Parlak and his colleagues created a wearable organic electrochemical system focused on a molecularly selective nanoporous membrane for non-invasive cortisol sensing (**Figure 8D**) (Parlak et al., 2018). The cortisol biorecognition is based on a MIP membrane with a laser-patterned microcapillary channel array for sample acquisition and organic electrochemical transistors (OECTs) based on PEDOT:PSS. The wearable sensor's stability and stretchability are offered by the styrene-ethylene-butylene-styrene (SEBS) elastomer substrate. Lately, laser-burned graphene (LBG) has

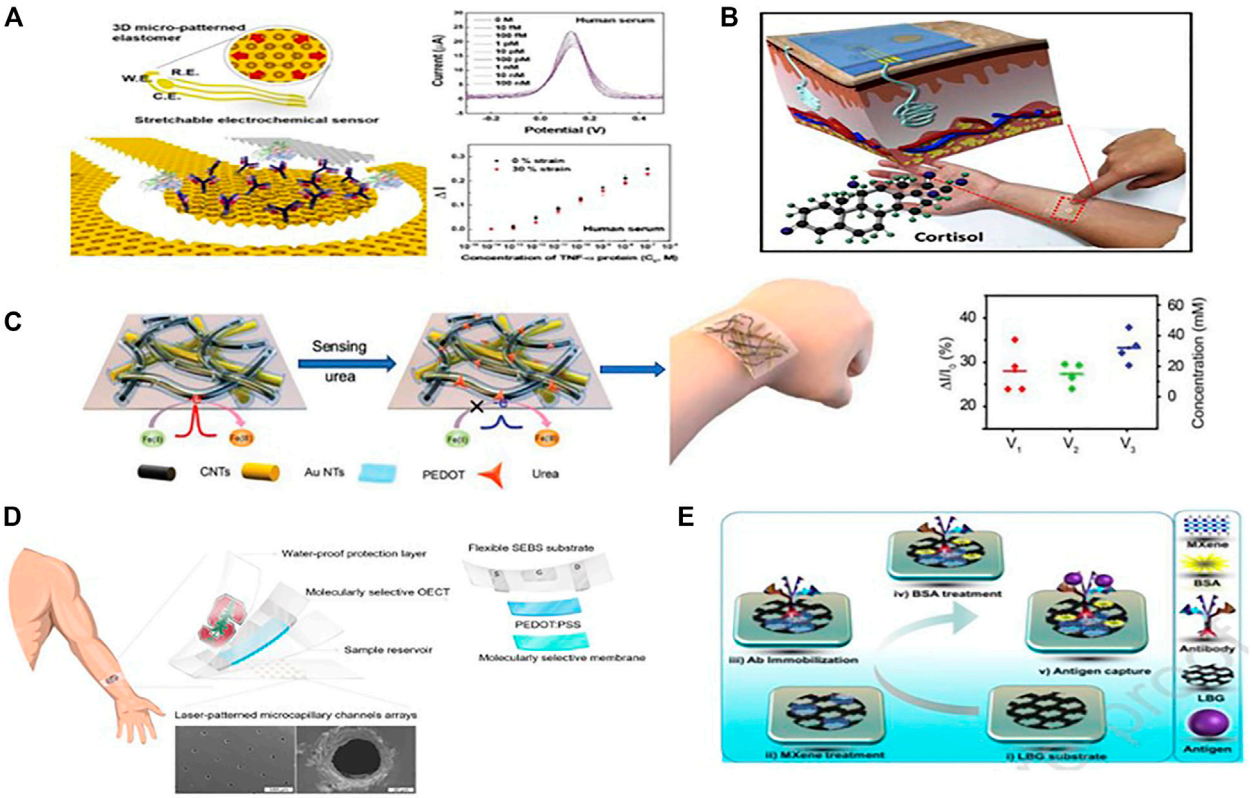

FIGURE 8 | Schematic diagrams of electrochemical immunosensors. **(A)** 3-D micro-patterned elastomeric substrate-based Stretchable electrochemical immunosensor. (Copyright 2019; Sensors and Actuators). **(B)** LOP with microfluidic and electrochemical sensing components for wearable POCT, as well as a schematic diagram of the LOP platform for wearable biomarker detection, fabricated on a mogul-patterned substrate with 3-D nanostructured Au as a working electrode (Copyright 2020; Biosensors and Bioelectronics). **(C)** the development of a flexible sensor for the electrochemical detection of urea (Copyright 2018; American Chemical Society). **(D)** A patch-type wearable cortisol sensor based on carbon nanotubes and a lightweight SEBS elastomer substrate with a PEDOT:PSS semiconductor layer and an MSM. (Copyright 2018; Science Progresses.). **(E)** a $Ti_3C_2T_x$ MXene-loaded laser-induced graphene cortisol immunosensor (Copyright 2021; Sensors and Actuators).

been developed as an excellent electrode matrix for wearable electrochemical sensing applications because of its one-shot fabrication and excellent electrochemical performance (Ugur et al., 2014;Hamblin, 2016). Jong et al. recently proposed a $Ti_3C_2T_x$ (MXene/LBG) based wearable electrochemical impedimetric immunosensor with a 3-D electrode network for noninvasive cortisol biomarker identification in human sweat at the point of treatment (POC). Laser-induced graphene (LBG) is the basic material used in electrode construction since it is stable and has strong electrical properties. $Ti_3C_2T_x$ MXene, which has excellent electrochemical properties and outstanding enzyme loading capabilities, was deposited on the electrode (**Figure 8E**). The cortisol sensor had a very low concentration limit of 3.88 pM and excellent selectivity. This MXene LBG-based flexible noninvasive patch can be used to identify other biomarkers or pathogens. The developed path can be coupled with a wearable electrochemical front-end for impedance signal monitoring and wireless data transmission for smartphone-based biomarkers or pathogen diagnosis properties (San Nah et al., 2021).

DNA Biosensors

Conductive nanomaterials and nanocomposites have lately gained popularity as potential materials for DNA biosensors. Electrochemical biosensors for DNA detection are being developed and used in many human applications such as food, healthcare, environment, etc. (Ramanavičius et al., 2006; Booth et al., 2011). A DNA biosensor is designed by immobilizing a DNA probe on an electrode surface and then using hybridization to label the target DNA sequence. This hybridization, known as transduction in the technological era, can be observed optically and electrochemically. A DNA biosensor for detecting the H5N1 gene sequence of the influenza virus was created using a DNA aptamer immobilized hybrid nanomaterial-modified (MWCNT/PPy) electrode. The modified electrode nanoparticles provide a porous structure with a wide effective surface area. The latest (PANI-AuNPs) nanocomposite based DNA biosensor detected micro RNA-16 using a streptavidin-AP conjugate to biotinylated recognition sites via transduction with a 0.1 nM detection limit (Saberi et al., 2013). Very recently, for the first time, Jiang and his team proposed a cloth-based DNA biosensor by using

nanocomposite (CdTe-MWCNTs) to get a stronger electrochemical signal. Under ideal conditions, target DNA samples (75-bp DNA fragments produced by PCR amplification) were determined in a range of 20 fM to 5 nM, with a detection limit of 8.74 fM and relative standard deviations of 2.04 and 4.75 percent for intra- and inter-assays at 50 pM TD, respectively (Jiang et al., 2020).

PRESENT CHALLENGES AND FUTURE PROSPECTS

Wearable electrochemical biosensors are essential for continuous health and fitness tracking and some other sports applications. The conductive nanomaterials, which are the key components, determine the performance and practical use of such sensors considerably. However, in recent years, emerging conductive nanomaterials have been studied and used to develop wearable electrochemical biosensors due to characteristics like large specific surface area, high porosity, high sensitivity, and selectivity. In this study, different kinds of conductive nanomaterials for sensing electrodes of wearable electrochemical biosensors are summarized.

PRESENT CHALLENGES

Over all, carbon-based nanomaterials (CNTs, graphene, etc.) have been widely used in the fabrication of sensing electrodes for wearable electrochemical biosensors because of their advantages of good electrical conductivity, high biocompatibility, and low cost. However, for metabolite (glucose) detection, glucose oxides (GOD) normally need to be modified on the working electrode as the carbon-based nanomaterials can not catalyze glucose directly. Consequently, the decrease in the life span of the wearable electrochemical biosensor for detecting glucose caused by enzyme inactivation is the main issue limiting its broad applications and commercialization. Metal-based nanomaterials, particularly noble-based metals, having great and promising electrocatalytic properties, particularly in wearable glucose non-enzymatic sensors. They can detect glucose directly without GOD, demonstrating good stability. But the main issue is cost, which is high. Cu nanowires have been studied as a potentially promising material because of their low cost and high conductivity. Still, the weak stability against oxidation and chemical corrosion, as well as the final decrease in conductivity over time, may limit its practical applications for wearable electrochemical biosensors. The use of conductive polymer nanoparticles in wearable electrochemical biosensors aims to improve sensor flexibility in order to ensure optimal sensor performance after mounting on the human body. The output properties of wearable electrochemical biosensors will not vary because of diverse human body motions. As a result, the catalytic property was not as good as that of metal-based nanomaterials.

Future Prospects

Wearable electrochemical biosensors can be manufactured from a variety of nanomaterials depending on the needs of real-time applications. Nowadays, more conductive nanomaterials will be developed and used to generate new sensing electrodes for wearable electrochemical biosensors. The new development trends of sensing nanomaterials in the future will be as follows.'

Firstly, sensing nanomaterials with porous structures, high electrical conductivity, and catalytic activity will be often used in both enzymatic and non-enzymatic sensors to enhance the sensor sensitivity. Second, sensing nanomaterials should have superior mechanical properties in order to improve the sensor's durability and flexibility throughout everyday activities. Third, because there are different interferences (such as glucose, lactate, Na+, K+) in body fluids, nanomaterials with specific identification of analytes like glucose or lactate may attract more attention to increase the selection of sensors. Finally, to produce low-cost, high-performance, and reliable wearable electrochemical biosensors and biosensors, more knowledge of nanomaterial characteristics, as well as advancements in manufacturing and processing procedures, is required. For example, replacing Ag with Cu or carbon-based components and using low-cost CNT synthesis and processing methods. Only preliminary studies on the biocompatibility of nanomaterials for wearable applications have been conducted. More methodical reports on nanomaterials' long-term biocompatibility are urgently needed to support the practical applications of nanomaterials. Graphene has been used to create a variety of wearable electrochemical biosensors, especially for healthcare applications. To ensure high efficiency, additional efforts should be made to improve large-scale advancement with reasonable uniformity and defect-free deposition onto different substrates with high-pitched consistency and yield. However, nanotechnology applications are beginning to emerge, and more research is needed to obtain novel results and uses.

AUTHOR CONTRIBUTIONS

The authors confirm contribution to the paper as follows: paper writing, data collection, and figures analysis: TR Author; proof reading of final manuscript: LQ Author; study conception and assisted in making figures: WK Author, BA Author; analysis and interpretation of results: AA Author; supervise the entire work: MT Author. All authors reviewed the results and approved the final version of the manuscript.

FUNDING

This work was supported by the National Natural Science Foundation of China (51672141), the Natural Science Foundation of Shandong Province of China (ZR2018QEM004), the Shandong Province Key Research and Development Plan (2019JZZY010335, 2019JZZY010340, and 2019GGXI02022), the Anhui Province Special Science and Technology Project (201903a05020028), the Shandong Provincial Universities Youth Innovation Technology Plan Innovation Team (2020KJA013), and the State Key Laboratory of Bio-Fibers and Eco-Textiles (Qingdao University, No. ZKT02).

REFERENCES

Abellán-Llobregat, A., Jeerapan, I., Bandodkar, A., Vidal, L., Canals, A., Wang, J., et al. (2017). A Stretchable and Screen-Printed Electrochemical Sensor for Glucose Determination in Human Perspiration. *Biosens. Bioelectron.* 91, 885–891. doi:10.1016/j.bios.2017.01.058

Abouraddy, A. F., Bayindir, M., Benoit, G., Hart, S. D., Kuriki, K., Orf, N., et al. (2007). Towards Multimaterial Multifunctional Fibres that See, Hear, Sense and Communicate. *Nat. Mater* 6, 336–347. doi:10.1038/nmat1889

Adans-Dester, C. P., Bamberg, S., Bertacchi, F. P., Caulfield, B., Chappie, K., Demarchi, D., et al. (2020). Can mHealth Technology Help Mitigate the Effects of the COVID-19 Pandemic? *IEEE Open J. Eng. Med. Biol.* 1, 243–248. doi:10.1109/ojemb.2020.3015141

Alizadeh, A., Burns, A., Lenigk, R., Gettings, R., Ashe, J., Porter, A., et al. (2018). A Wearable Patch for Continuous Monitoring of Sweat Electrolytes during Exertion. *Lab. Chip* 18, 2632–2641. doi:10.1039/c8lc00510a

Allison, L., Hoxie, S., and Andrew, T. L. (2017). Towards Seamlessly-Integrated Textile Electronics: Methods to Coat Fabrics and Fibers with Conducting Polymers for Electronic Applications. *Chem. Commun.* 53, 7182–7193. doi:10.1039/c7cc02592k

Anastasova, S., Crewther, B., Bembnowicz, P., Curto, V., Ip, H. M., Rosa, B., et al. (2017). A Wearable Multisensing Patch for Continuous Sweat Monitoring. *Biosens. Bioelectron.* 93, 139–145. doi:10.1016/j.bios.2016.09.038

Archana, V., Xia, Y., Fang, R., and Gnana Kumar, G. (2019). Hierarchical CuO/NiO-Carbon Nanocomposite Derived from Metal Organic Framework on Cello Tape for the Flexible and High Performance Nonenzymatic Electrochemical Glucose Sensors. *ACS Sustainable Chem. Eng.* 7, 6707–6719. doi:10.1021/acssuschemeng.8b05980

Bae, C. W., Toi, P. T., Kim, B. Y., Lee, W. I., Lee, H. B., Hanif, A., et al. (2019). Fully Stretchable Capillary Microfluidics-Integrated Nanoporous Gold Electrochemical Sensor for Wearable Continuous Glucose Monitoring. *ACS Appl. Mater. Inter.* 11, 14567–14575. doi:10.1021/acsami.9b00848

Bandodkar, A. J., Jeerapan, I., You, J.-M., Nuñez-Flores, R., and Wang, J. (2016). Highly Stretchable Fully-Printed CNT-Based Electrochemical Sensors and Biofuel Cells: Combining Intrinsic and Design-Induced Stretchability. *Nano Lett.* 16, 721–727. doi:10.1021/acs.nanolett.5b04549

Bandodkar, A. J., Jia, W., and Wang, J. (2015a). Tattoo-Based Wearable Electrochemical Devices: A Review. *Electroanalysis* 27, 562–572. doi:10.1002/elan.201400537

Bandodkar, A. J., Jia, W., Yardımcı, C., Wang, X., Ramirez, J., and Wang, J. (2015b). Tattoo-based Noninvasive Glucose Monitoring: a Proof-Of-Concept Study. *Anal. Chem.* 87, 394–398. doi:10.1021/ac504300n

Bandodkar, A. J., Nuñez-Flores, R., Jia, W., and Wang, J. (2015c). All-Printed Stretchable Electrochemical Devices. *Adv. Mater.* 27, 3060–3065. doi:10.1002/adma.201500768

Bandodkar, A. J., and Wang, J. (2014). Non-invasive Wearable Electrochemical Sensors: a Review. *Trends Biotechnology* 32, 363–371. doi:10.1016/j.tibtech.2014.04.005

Bandodkar, A. J., You, J.-M., Kim, N.-H., Gu, Y., Kumar, R., Mohan, A. M. V., et al. (2017). Soft, Stretchable, High Power Density Electronic Skin-Based Biofuel Cells for Scavenging Energy from Human Sweat. *Energy Environ. Sci.* 10, 1581–1589. doi:10.1039/c7ee00865a

Bhide, A., Cheeran, S., Muthukumar, S., and Prasad, S. (2019). Enzymatic Low Volume Passive Sweat Based Assays for Multi-Biomarker Detection. *Biosensors* 9, 13. doi:10.3390/bios9010013

Booth, M. A., Harbison, S., and Travas-Sejdic, J. (2011). Development of an Electrochemical Polypyrrole-Based DNA Sensor and Subsequent Studies on the Effects of Probe and Target Length on Performance. *Biosens. Bioelectron.* 28, 362–367. doi:10.1016/j.bios.2011.07.051

Borgmann, S., Schulte, A., Neugebauer, S., and Schuhmann, W. (2011). Amperometric Biosensors. *Adv. Electrochem. Sci. Eng.* 2.

Brodt, M., Wycisk, R., and Pintauro, P. N. (2013). Nanofiber Electrodes with Low Platinum Loading for High Power Hydrogen/air PEM Fuel Cells. *J. Electrochem. Soc.* 160, F744–F749. doi:10.1149/2.008308jes

Byrne, R., Benito-Lopez, F., and Diamond, D. (2010). Materials Science and the Sensor Revolution. *Mater. Today* 13, 16–23. doi:10.1016/s1369-7021(10)70124-3

Cao, H., Yu, F., Zhao, Y., Scianmarello, N., Lee, J., Dai, W., et al. (2014). Stretchable Electrochemical Impedance Sensors for Intravascular Detection of Lipid-Rich Lesions in New Zealand White Rabbits. *Biosens. Bioelectron.* 54, 610–616. doi:10.1016/j.bios.2013.11.059

Chen, A., and Shah, B. (2013). Electrochemical Sensing and Biosensing Based on Square Wave Voltammetry. *Anal. Methods* 5, 2158–2173. doi:10.1039/c3ay40155c

Chen, H., Rim, Y. S., Wang, I. C., Li, C., Zhu, B., Sun, M., et al. (2017). Quasi-two-dimensional Metal Oxide Semiconductors Based Ultrasensitive Potentiometric Biosensors. *ACS nano* 11, 4710–4718. doi:10.1021/acsnano.7b00628

Chu, M., Shirai, T., Takahashi, D., Arakawa, T., Kudo, H., Sano, K., et al. (2011). Biomedical Soft Contact-Lens Sensor for *In Situ* Ocular Biomonitoring of Tear Contents. *Biomed. Microdevices* 13, 603–611. doi:10.1007/s10544-011-9530-x

Criscuolo, F., Ny Hanitra, I., Aiassa, S., Taurino, I., Oliva, N., Carrara, S., et al. (2021). Wearable Multifunctional Sweat-Sensing System for Efficient Healthcare Monitoring. *Sensors Actuators B: Chem.* 328, 129017. doi:10.1016/j.snb.2020.129017

Curto, V. F., Fay, C., Coyle, S., Byrne, R., O'Toole, C., Barry, C., et al. (2012). Real-time Sweat pH Monitoring Based on a Wearable Chemical Barcode Micro-fluidic Platform Incorporating Ionic Liquids. *Sensors Actuators B: Chem.* 171-172, 1327–1334. doi:10.1016/j.snb.2012.06.048

Daniels, J. S., and Pourmand, N. (2007). Label-Free Impedance Biosensors: Opportunities and Challenges. *Electroanalysis* 19, 1239–1257. doi:10.1002/elan.200603855

Dheilly, A., Linossier, I., Darchen, A., Hadjiev, D., Corbel, C., and Alonso, V. (2008). Monitoring of Microbial Adhesion and Biofilm Growth Using Electrochemical Impedancemetry. *Appl. Microbiol. Biotechnol.* 79, 157–164. doi:10.1007/s00253-008-1404-7

Dierking, I. (2010). Recent Developments in Polymer Stabilised Liquid Crystals. *Polym. Chem.* 1, 1153–1159. doi:10.1039/c0py00087f

Dutta, G., and Lillehoj, P. B. (2018). Wash-free, Label-free Immunoassay for Rapid Electrochemical Detection of PfHRP2 in Whole Blood Samples. *Sci. Rep.* 8, 1–8. doi:10.1038/s41598-018-35471-8

Emaminejad, S., Gao, W., Wu, E., Davies, Z. A., Yin Yin Nyein, H., Challa, S., et al. (2017). Autonomous Sweat Extraction and Analysis Applied to Cystic Fibrosis and Glucose Monitoring Using a Fully Integrated Wearable Platform. *Proc. Natl. Acad. Sci. USA* 114, 4625–4630. doi:10.1073/pnas.1701740114

Farajikhah, S., Choi, J., Esrafilzadeh, D., Underwood, J., Innis, P. C., Paull, B., et al. (2020). 3D Textile Structures with Integrated Electroactive Electrodes for Wearable Electrochemical Sensors. *J. Textile Inst.* 111, 1587–1595. doi:10.1080/00405000.2020.1720968

Feng, Y., and Zhu, J. (2019). Copper Nanomaterials and Assemblies for Soft Electronics. *Sci. China Mater.* 62, 1679–1708. doi:10.1007/s40843-019-9468-5

Fraser, K. J., Curto, V. F., Coyle, S., Schazmann, B., Byrne, R., Benito-Lopez, F., et al. (2011). "Wearable Electrochemical Sensors for Monitoring Performance Athletes," in *Organic Semiconductors in Sensors and Bioelectronics IV* (Bellingham, WA: International Society for Optics and Photonics), 81180C.

Gangopadhyay, R., and De, A. (2000). Conducting Polymer Nanocomposites: a Brief Overview. *Chem. Mater.* 12, 608–622. doi:10.1021/cm990537f

Gao, W., Emaminejad, S., Nyein, H. Y. Y., Challa, S., Chen, K., Peck, A., et al. (2016a). Fully Integrated Wearable Sensor Arrays for Multiplexed *In Situ* Perspiration Analysis. *Nature* 529, 509–514. doi:10.1038/nature16521

Gao, W., Nyein, H. Y., Shahpar, Z., Tai, L.-C., Wu, E., Bariya, M., et al. (2016c). "Wearable Sweat Biosensors". 2016 IEEE International Electron Devices Meeting (IEDM). IEEE, 661–664. doi:10.1109/iedm.2016.7838363

Gao, W., Nyein, H. Y. Y., Shahpar, Z., Fahad, H. M., Chen, K., Emaminejad, S., et al. (2016b). Wearable Microsensor Array for Multiplexed Heavy Metal Monitoring of Body Fluids. *ACS Sens.* 1, 866–874. doi:10.1021/acssensors.6b00287

Gerard, M., Chaubey, A., and Malhotra, B. (2002). Application of Conducting Polymers to Biosensors. *Biosens. Bioelectron.* 17, 345–359. doi:10.1016/s0956-5663(01)00312-8

Gerard, M., and Malhotra, B. D. (2005). Application of Polyaniline as Enzyme Based Biosensor. *Curr. Appl. Phys.* 5, 174–177. doi:10.1016/j.cap.2004.06.016

Gonzalo-Ruiz, J., Mas, R., De Haro, C., Cabruja, E., Camero, R., Alonso-Lomillo, M. A., et al. (2009). Early Determination of Cystic Fibrosis by Electrochemical Chloride Quantification in Sweat. *Biosens. Bioelectron.* 24, 1788–1791. doi:10.1016/j.bios.2008.07.051

Gregory, R. V., Kimbrell, W. C., and Kuhn, H. H. (1989). Conductive Textiles. *Synth. Met.* 28, 823–835. doi:10.1016/0379-6779(89)90610-3

Guinovart, T., Parrilla, M., Crespo, G. A., Rius, F. X., and Andrade, F. J. (2013). Potentiometric Sensors Using Cotton Yarns, Carbon Nanotubes and Polymeric Membranes. *Analyst* 138, 5208–5215. doi:10.1039/c3an00710c

Guinovart, T., Valdés-Ramírez, G., Windmiller, J. R., Andrade, F. J., and Wang, J. (2014). Bandage-Based Wearable Potentiometric Sensor for Monitoring Wound pH. *Electroanalysis* 26, 1345–1353. doi:10.1002/elan.201300558

Guo, J., Peng, Q., Fu, H., Zou, G., and Zhang, Q. (2015). Heavy-metal Adsorption Behavior of Two-Dimensional Alkalization-Intercalated MXene by First-Principles Calculations. *J. Phys. Chem. C* 119, 20923–20930. doi:10.1021/acs.jpcc.5b05426

Guo, Y., Zhong, M., Fang, Z., Wan, P., and Yu, G. (2019). A Wearable Transient Pressure Sensor Made with MXene Nanosheets for Sensitive Broad-Range Human-Machine Interfacing. *Nano Lett.* 19, 1143–1150. doi:10.1021/acs.nanolett.8b04514

Haji-Hashemi, H., Safarnejad, M. R., Norouzi, P., Ebrahimi, M., Shahmirzaie, M., and Ganjali, M. R. (2019). Simple and Effective Label Free Electrochemical Immunosensor for Fig Mosaic Virus Detection. *Anal. Biochem.* 566, 102–106. doi:10.1016/j.ab.2018.11.017

Hamblin, M. R. (2016). Shining Light on the Head: Photobiomodulation for Brain Disorders. *BBA Clin.* 6, 113–124. doi:10.1016/j.bbacli.2016.09.002

Hatamie, A., Khan, A., Golabi, M., Turner, A. P. F., Beni, V., Mak, W. C., et al. (2015). Zinc Oxide Nanostructure-Modified Textile and its Application to Biosensing, Photocatalysis, and as Antibacterial Material. *Langmuir* 31, 10913–10921. doi:10.1021/acs.langmuir.5b02341

He, S., Zhu, Q., Soomro, R. A., and Xu, B. (2020). MXene Derivatives for Energy Storage Applications. *Sustainable Energ. Fuels* 4, 4988–5004. doi:10.1039/d0se00927j

Heikenfeld, J., Jajack, A., Rogers, J., Gutruf, P., Tian, L., Pan, T., et al. (2018). Wearable Sensors: Modalities, Challenges, and Prospects. *Lab. Chip* 18, 217–248. doi:10.1039/c7lc00914c

Hou, X., Zhou, Y., Liu, Y., Wang, L., and Wang, J. (2020). Coaxial Electrospun Flexible PANI//PU Fibers as Highly Sensitive pH Wearable Sensor. *J. Mater. Sci.* 55, 16033–16047. doi:10.1007/s10853-020-05110-7

Hou, Y., Duan, L., Gui, Z., and Hu, Y. (2017). An Infiltration Method to Synthesize Thermoplastic Polyurethane Composites Based on Size-Controlled Graphene Foams. *Composites A: Appl. Sci. Manufacturing* 97, 67–75. doi:10.1016/j.compositesa.2017.02.023

Huang, J., and Kaner, R. B. (2004). Nanofiber Formation in the Chemical Polymerization of Aniline: a Mechanistic Study. *Angew. Chem.* 116, 5941–5945. doi:10.1002/ange.200460616

Imamura, A., Zakashansky, J., Cho, K., Lin, L., Carrilho, E., and Khine, M. (2020). Stretchable Sensors for Nanomolar Glucose Detection. *Adv. Mater. Technol.* 5, 1900843. doi:10.1002/admt.201900843

Imani, S., Bandodkar, A. J., Mohan, A. M., Kumar, R., Yu, S., Wang, J., et al. (2016). A Wearable Chemical-Electrophysiological Hybrid Biosensing System for Real-Time Health and Fitness Monitoring. *Nat. Commun.* 7, 11650–11657. doi:10.1038/ncomms11650

Jang, J., and Han, J. I. (2017). High Performance Cylindrical Capacitor as a Relative Humidity Sensor for Wearable Computing Devices. *J. Electrochem. Soc.* 164, B136–B141. doi:10.1149/2.1121704jes

Jeerapan, I., Sempionatto, J. R., Pavinatto, A., You, J.-M., and Wang, J. (2016). Stretchable Biofuel Cells as Wearable Textile-Based Self-Powered Sensors. *J. Mater. Chem. A.* 4, 18342–18353. doi:10.1039/c6ta08358g

Jeerapan, I., Sonsa-Ard, T., and Nacapricha, D. (2020). Applying Nanomaterials to Modern Biomedical Electrochemical Detection of Metabolites, Electrolytes, and Pathogens. *Chemosensors* 8, 71. doi:10.3390/chemosensors8030071

Jia, X., Ge, Y., Shao, L., Wang, C., and Wallace, G. G. (2019). Tunable Conducting Polymers: toward Sustainable and Versatile Batteries. *ACS Sustainable Chem. Eng.* 7, 14321–14340. doi:10.1021/acssuschemeng.9b02315

Jiang, J., Wu, H., Su, Y., Liang, Y., Shu, B., and Zhang, C. (2020). Electrochemical Cloth-Based DNA Sensors (ECDSs): A New Class of Electrochemical Gene Sensors. *Anal. Chem.* 92, 7708–7716. doi:10.1021/acs.analchem.0c00669

Joung, H.-A., Ballard, Z. S., Ma, A., Tseng, D. K., Teshome, H., Burakowski, S., et al. (2019). Paper-based Multiplexed Vertical Flow Assay for point-of-care Testing. *Lab. Chip* 19, 1027–1034. doi:10.1039/c9lc00011a

Kaushik, A., Yndart, A., Kumar, S., Jayant, R. D., Vashist, A., Brown, A. N., et al. (2018). A Sensitive Electrochemical Immunosensor for Label-free Detection of Zika-Virus Protein. *Sci. Rep.* 8, 9700–9705. doi:10.1038/s41598-018-28035-3

Kim, D.-H., Lu, N., Ma, R., Kim, Y.-S., Kim, R.-H., Wang, S., et al. (2011). Epidermal Electronics. *Science* 333, 838–843. doi:10.1126/science.1206157

Kim, J., Kim, M., Lee, M. S., Kim, K., Ji, S., Kim, Y. T., et al. (2017). Wearable Smart Sensor Systems Integrated on Soft Contact Lenses for Wireless Ocular Diagnostics. *Nat. Commun.* 8, 14997–14998. doi:10.1038/ncomms14997

Kim, J., Campbell, A. S., de Ávila, B. E.-F., and Wang, J. (2019). Wearable Biosensors for Healthcare Monitoring. *Nat. Biotechnol.* 37, 389–406. doi:10.1038/s41587-019-0045-y

Kinnamon, D., Ghanta, R., Lin, K. C., Muthukumar, S., and Prasad, S. (2017). Portable Biosensor for Monitoring Cortisol in Low-Volume Perspired Human Sweat. *Sci. Rep.* 7, 13312–13313. doi:10.1038/s41598-017-13684-7

Kinnamon, D. S., Krishnan, S., Brosler, S., Sun, E., and Prasad, S. (2018). Screen Printed Graphene Oxide Textile Biosensor for Applications in Inexpensive and Wearable point-of-exposure Detection of Influenza for At-Risk Populations. *J. Electrochem. Soc.* 165, B3084–B3090. doi:10.1149/2.0131808jes

Lee, H.-B., Meeseepong, M., Trung, T. Q., Kim, B.-Y., and Lee, N.-E. (2020). A Wearable Lab-On-A-Patch Platform with Stretchable Nanostructured Biosensor for Non-invasive Immunodetection of Biomarker in Sweat. *Biosens. Bioelectron.* 156, 112133. doi:10.1016/j.bios.2020.112133

Lee, H., Choi, T. K., Lee, Y. B., Cho, H. R., Ghaffari, R., Wang, L., et al. (2016). A Graphene-Based Electrochemical Device with Thermoresponsive Microneedles for Diabetes Monitoring and Therapy. *Nat. Nanotech* 11, 566–572. doi:10.1038/nnano.2016.38

Lei, Y., Zhao, W., Zhang, Y., Jiang, Q., He, J. H., Baeumner, A. J., et al. (2019). A MXene-Based Wearable Biosensor System for High-Performance *In Vitro* Perspiration Analysis. *Small* 15, 1901190. doi:10.1002/smll.201901190

Li, G., and Wen, D. (2020). Wearable Biochemical Sensors for Human Health Monitoring: Sensing Materials and Manufacturing Technologies. *J. Mater. Chem. B* 8, 3423–3436. doi:10.1039/c9tb02474c

Li, M., Yuan, P., Chen, Q.-Q., Lin, L.-H., Radjenovic, P. M., He, Y.-L., et al. (2020). Shell-Isolated Nanoparticle-Enhanced Luminescence of Metallic Nanoclusters. *Anal. Chem.* 92, 7146–7153. doi:10.1021/acs.analchem.0c00600

Li, Y., Li, Y., Su, M., Li, W., Li, Y., Li, H., et al. (2017). Electronic Textile by Dyeing Method for Multiresolution Physical Kineses Monitoring. *Adv. Electron. Mater.* 3, 1700253. doi:10.1002/aelm.201700253

Li, Y., Young, D. J., and Loh, X. J. (2019). Fluorescent Gels: a Review of Synthesis, Properties, Applications and Challenges. *Mater. Chem. Front.* 3, 1489–1502. doi:10.1039/c9qm00127a

Lin, J., Zhu, Z., Cheung, C. F., Yan, F., and Li, G. (2020). Digital Manufacturing of Functional Materials for Wearable Electronics. *J. Mater. Chem. C* 8, 10587–10603. doi:10.1039/d0tc01112f

Liu, Y.-L., Jin, Z.-H., Liu, Y.-H., Hu, X.-B., Qin, Y., Xu, J.-Q., et al. (2016). Stretchable Electrochemical Sensor for Real-Time Monitoring of Cells and Tissues. *Angew. Chem. Int. Ed.* 55, 4537–4541. doi:10.1002/anie.201601276

Liu, Y.-L., Liu, R., Qin, Y., Qiu, Q.-F., Chen, Z., Cheng, S.-B., et al. (2018). Flexible Electrochemical Urea Sensor Based on Surface Molecularly Imprinted Nanotubes for Detection of Human Sweat. *Anal. Chem.* 90, 13081–13087. doi:10.1021/acs.analchem.8b04223

Liu, Y.-L., Qin, Y., Jin, Z.-H., Hu, X.-B., Chen, M.-M., Liu, R., et al. (2017). A Stretchable Electrochemical Sensor for Inducing and Monitoring Cell Mechanotransduction in Real Time. *Angew. Chem. Int. Ed.* 56, 9454–9458. doi:10.1002/anie.201705215

Liu, Y., Gorgutsa, S., Santato, C., and Skorobogatiy, M. (2012). Flexible, Solid Electrolyte-Based Lithium Battery Composed of LiFePO4Cathode and Li4Ti5O12Anode for Applications in Smart Textiles. *J. Electrochem. Soc.* 159, A349–A356. doi:10.1149/2.020204jes

Lu, Y., Jiang, K., Chen, D., and Shen, G. (2019). Wearable Sweat Monitoring System with Integrated Micro-supercapacitors. *Nano Energy* 58, 624–632. doi:10.1016/j.nanoen.2019.01.084

Mamalis, A. G., Vogtländer, L. O. G., and Markopoulos, A. (2004). Nanotechnology and Nanostructured Materials: Trends in Carbon Nanotubes. *Precision Eng.* 28, 16–30. doi:10.1016/j.precisioneng.2002.11.002

Manjakkal, L., Dang, W., Yogeswaran, N., and Dahiya, R. (2019). Textile-based Potentiometric Electrochemical pH Sensor for Wearable Applications. *Biosensors* 9, 14. doi:10.3390/bios9010014

Mannoor, M. S., Tao, H., Clayton, J. D., Sengupta, A., Kaplan, D. L., Naik, R. R., et al. (2012). Graphene-based Wireless Bacteria Detection on Tooth Enamel. *Nat. Commun.* 3, 763. doi:10.1038/ncomms1767

Mariani, F., Gualandi, I., Tonelli, D., Decataldo, F., Possanzini, L., Fraboni, B., et al. (2020). Design of an Electrochemically Gated Organic Semiconductor for pH Sensing. *Electrochemistry Commun.* 116, 106763. doi:10.1016/j.elecom.2020.106763

Meyyappan, M. (2004). *Carbon Nanotubes: Science and Applications*. Boca Raton, FL: CRC Press.

Mitsubayashi, K., Wakabayashi, Y., Murotomi, D., Yamada, T., Kawase, T., Iwagaki, S., et al. (2003). Wearable and Flexible Oxygen Sensor for Transcutaneous Oxygen Monitoring. *Sensors Actuators B: Chem.* 95, 373–377. doi:10.1016/s0925-4005(03)00441-6

Mpanza, T. E. (2016). Determination of Capsaicin Using Carbon Nanotube Based Electrochemical Biosensors (Doctoral dissertation).

Mpanza, T. E. (2016). *Determination of Capsaicin Using Carbon Nanotube Based Electrochemical Biosensors*. Durban, SA: Durban University of Technology.

Nah, J. S., Barman, S. C., Zahed, M. A., Sharifuzzaman, M., Yoon, H., Park, C., et al. (2021). A Wearable Microfluidics-Integrated Impedimetric Immunosensor Based on Ti3C2T MXene Incorporated Laser-Burned Graphene for Noninvasive Sweat Cortisol Detection. *Sensors Actuators B: Chem.* 329, 129206. doi:10.1016/j.snb.2020.129206

Nayak, P., Jiang, Q., Mohanraman, R., Anjum, D., Hedhili, M. N., and Alshareef, H. N. (2018). Inherent Electrochemistry and Charge Transfer Properties of Few-Layered Two-Dimensional Ti3C2TxMXene. *Nanoscale* 10, 17030–17037. doi:10.1039/c8nr01883a

Nyein, H. Y. Y., Gao, W., Shahpar, Z., Emaminejad, S., Challa, S., Chen, K., et al. (2016). A Wearable Electrochemical Platform for Noninvasive Simultaneous Monitoring of Ca2+ and pH. *ACS nano* 10, 7216–7224. doi:10.1021/acsnano.6b04005

Ogasawara, K., Tsuru, T., Mitsubayashi, K., and Karube, I. (1996). Electrical Conductivity of Tear Fluid in Healthy Persons and Keratoconjunctivitis Sicca Patients Measured by a Flexible Conductimetric Sensor. *Graefe's Arch. Clin. Exp. Ophthalmol.* 234, 542–546. doi:10.1007/bf00448797

Oh, S. Y., Hong, S. Y., Jeong, Y. R., Yun, J., Park, H., Jin, S. W., et al. (2018). Skin-attachable, Stretchable Electrochemical Sweat Sensor for Glucose and pH Detection. *ACS Appl. Mater. Inter.* 10, 13729–13740. doi:10.1021/acsami.8b03342

Park, S., Vosguerichian, M., and Bao, Z. (2013). A Review of Fabrication and Applications of Carbon Nanotube Film-Based Flexible Electronics. *Nanoscale* 5, 1727–1752. doi:10.1039/c3nr33560g

Parlak, O., Keene, S. T., Marais, A., Curto, V. F., and Salleo, A. (2018). Molecularly Selective Nanoporous Membrane-Based Wearable Organic Electrochemical Device for Noninvasive Cortisol Sensing. *Sci. Adv.* 4, eaar2904. doi:10.1126/sciadv.aar2904

Parrilla, M., Cánovas, R., Jeerapan, I., Andrade, F. J., and Wang, J. (2016). A Textile-Based Stretchable Multi-Ion Potentiometric Sensor. *Adv. Healthc. Mater.* 5, 996–1001. doi:10.1002/adhm.201600092

Parrilla, M., Ortiz-Gómez, I., Cánovas, R., Salinas-Castillo, A., Cuartero, M., and Crespo, G. A. (2019). Wearable Potentiometric Ion Patch for On-Body Electrolyte Monitoring in Sweat: toward a Validation Strategy to Ensure Physiological Relevance. *Anal. Chem.* 91, 8644–8651. doi:10.1021/acs.analchem.9b02126

Pérez López, B. (2009). *Carbon Nanotubes for Electrochemical (Bio) Sensing*. Barcelona, Spain: Universitat Autònoma de Barcelona.

Possanzini, L., Decataldo, F., Mariani, F., Gualandi, I., Tessarolo, M., Scavetta, E., et al. (2020). Textile Sensors Platform for the Selective and Simultaneous Detection of Chloride Ion and pH in Sweat. *Sci. Rep.* 10, 1–14. doi:10.1038/s41598-020-74337-w

Pungor, E. (2016). *Oscillometry and Conductometry: International Series of Monographs on Analytical Chemistry*. Elsevier.

Qu, H., Lu, X., and Skorobogatiy, M. (2018). All-solid Flexible Fiber-Shaped Lithium Ion Batteries. *J. Electrochem. Soc.* 165, A688–A695. doi:10.1149/2.1001803jes

Rahimi, R., Ochoa, M., Tamayol, A., Khalili, S., Khademhosseini, A., and Ziaie, B. (2017). Highly Stretchable Potentiometric pH Sensor Fabricated via Laser Carbonization and Machining of Carbon–Polyaniline Composite. *ACS Appl. Mater. Inter.* 9, 9015–9023. doi:10.1021/acsami.6b16228

Ramanavičius, A., Ramanavičienė, A., and Malinauskas, A. (2006). Electrochemical Sensors Based on Conducting Polymer—Polypyrrole. *Electrochimica acta* 51, 6025–6037.

Rebrin, K., Sheppard, N. F., Jr, and Steil, G. M. (2010). *Use of Subcutaneous Interstitial Fluid Glucose to Estimate Blood Glucose: Revisiting Delay and Sensor Offset*. Los Angeles, CA: SAGE Publications Sage CA.

Saberi, R.-S., Shahrokhian, S., and Marrazza, G. (2013). Amplified Electrochemical DNA Sensor Based on Polyaniline Film and Gold Nanoparticles. *Electroanalysis* 25, 1373–1380. doi:10.1002/elan.201200434

Salvo, P., Melai, B., Calisi, N., Paoletti, C., Bellagambi, F., Kirchhain, A., et al. (2018). Graphene-based Devices for Measuring pH. *Sensors Actuators B: Chem.* 256, 976–991. doi:10.1016/j.snb.2017.10.037

Schazmann, B., Morris, D., Slater, C., Beirne, S., Fay, C., Reuveny, R., et al. (2010). A Wearable Electrochemical Sensor for the Real-Time Measurement of Sweat Sodium Concentration. *Anal. Methods* 2, 342–348. doi:10.1039/b9ay00184k

Seesaard, T., Lorwongtragool, P., and Kerdcharoen, T. (2015). Development of Fabric-Based Chemical Gas Sensors for Use as Wearable Electronic Noses. *Sensors* 15, 1885–1902. doi:10.3390/s150101885

Semwal, V., and Gupta, B. D. (2019). Highly Sensitive Surface Plasmon Resonance Based Fiber Optic pH Sensor Utilizing rGO-Pani Nanocomposite Prepared by *In Situ* Method. *Sensors Actuators B: Chem.* 283, 632–642. doi:10.1016/j.snb.2018.12.070

Seshadri, D. R., Davies, E. V., Harlow, E. R., Hsu, J. J., Knighton, S. C., Walker, T. A., et al. (2020). Wearable Sensors for COVID-19: a Call to Action to Harness Our Digital Infrastructure for Remote Patient Monitoring and Virtual Assessments. *Front. Digit. Health* 2, 8. doi:10.3389/fdgth.2020.00008

Shahzad, A., Rasool, K., Miran, W., Nawaz, M., Jang, J., Mahmoud, K. A., et al. (2017). Two-Dimensional Ti3C2Tx MXene Nanosheets for Efficient Copper Removal from Water. *ACS Sustainable Chem. Eng.* 5, 11481–11488. doi:10.1021/acssuschemeng.7b02695

Shaikh, M. O., Zhu, P.-Y., Wang, C.-C., Du, Y.-C., and Chuang, C.-H. (2019). Electrochemical Immunosensor Utilizing Electrodeposited Au Nanocrystals and Dielectrophoretically Trapped PS/Ag/ab-HSA Nanoprobes for Detection of Microalbuminuria at point of Care. *Biosens. Bioelectron.* 126, 572–580. doi:10.1016/j.bios.2018.11.035

Shan, C., Yang, H., Song, J., Han, D., Ivaska, A., and Niu, L. (2009). Direct Electrochemistry of Glucose Oxidase and Biosensing for Glucose Based on Graphene. *Anal. Chem.* 81, 2378–2382. doi:10.1021/ac802193c

Shrivastava, S., Jadon, N., and Jain, R. (2016). Next-generation Polymer Nanocomposite-Based Electrochemical Sensors and Biosensors: A Review. *Trac Trends Anal. Chem.* 82, 55–67. doi:10.1016/j.trac.2016.04.005

Singh, K., Solanki, P. R., Basu, T., and Malhotra, B. D. (2012). Polypyrrole/multiwalled Carbon Nanotubes-Based Biosensor for Cholesterol Estimation. *Polym. Adv. Technol.* 23, 1084–1091. doi:10.1002/pat.2020

Smith, R. E., Totti, S., Velliou, E., Campagnolo, P., Hingley-Wilson, S. M., Ward, N. I., et al. (2019). Development of a Novel Highly Conductive and Flexible Cotton Yarn for Wearable pH Sensor Technology. *Sensors Actuators B: Chem.* 287, 338–345. doi:10.1016/j.snb.2019.01.088

Swift, R. M., Martin, C. S., Swette, L., Laconti, A., and Kackley, N. (1992). Studies on a Wearable, Electronic, Transdermal Alcohol Sensor. *Alcohol. Clin. Exp. Res.* 16, 721–725. doi:10.1111/j.1530-0277.1992.tb00668.x

Tan, C., Cao, X., Wu, X.-J., He, Q., Yang, J., Zhang, X., et al. (2017). Recent Advances in Ultrathin Two-Dimensional Nanomaterials. *Chem. Rev.* 117, 6225–6331. doi:10.1021/acs.chemrev.6b00558

Tao, X., Koncar, V., and Dufour, C. (2011). Geometry Pattern for the Wire Organic Electrochemical Textile Transistor. *J. Electrochem. Soc.* 158, H572. doi:10.1149/1.3562962

Teli, M., Dash, S., and Desai, P. (2014). Polyaniline Based Conductive Textiles. *J. Inst. Eng. India Ser. E* 95, 75–79. doi:10.1007/s40034-014-0037-x

Toi, P. T., Trung, T. Q., Dang, T. M. L., Bae, C. W., and Lee, N.-E. (2019). Highly Electrocatalytic, Durable, and Stretchable Nanohybrid Fiber for On-Body Sweat Glucose Detection. *ACS Appl. Mater. Inter.* 11, 10707–10717. doi:10.1021/acsami.8b20583

Tuteja, S. K., Ormsby, C., and Neethirajan, S. (2018). Noninvasive Label-free Detection of Cortisol and Lactate Using Graphene Embedded Screen-Printed Electrode. *Nanomicro Lett.* 10, 41–10. doi:10.1007/s40820-018-0193-5

Tzou, K., and Gregory, R. V. (1992). Kinetic Study of the Chemical Polymerization of Aniline in Aqueous Solutions. *Synth. met.* 47, 267–277. doi:10.1016/0379-6779(92)90367-r

Ugur, M., Schulz, O., Menon, M. B., Krueger, A., and Pabst, O. (2014). Resident CD4+ T Cells Accumulate in Lymphoid Organs after Prolonged Antigen Exposure. *Nat. Commun.* 5, 1–10. doi:10.1038/ncomms5821

Wang, L., Wang, L., Zhang, Y., Pan, J., Li, S., Sun, X., et al. (2018). Weaving Sensing Fibers into Electrochemical Fabric for Real-Time Health Monitoring. *Adv. Funct. Mater.* 28, 1804456. doi:10.1002/adfm.201804456

Wang, R., Zhai, Q., Zhao, Y., An, T., Gong, S., Guo, Z., et al. (2020). Stretchable Gold Fiber-Based Wearable Electrochemical Sensor toward pH Monitoring. *J. Mater. Chem. B* 8, 3655–3660. doi:10.1039/c9tb02477h

Wen, D., and Eychmüller, A. (2016). Enzymatic Biofuel Cells on Porous Nanostructures. *Small* 12, 4649–4661. doi:10.1002/smll.201600906

Wen, D., Herrmann, A.-K., Borchardt, L., Simon, F., Liu, W., Kaskel, S., et al. (2014). Controlling the Growth of Palladium Aerogels with High-Performance toward Bioelectrocatalytic Oxidation of Glucose. *J. Am. Chem. Soc.* 136, 2727–2730. doi:10.1021/ja412062e

Wen, D., Liu, W., Haubold, D., Zhu, C., Oschatz, M., Holzschuh, M., et al. (2016). Gold Aerogels: Three-Dimensional Assembly of Nanoparticles and Their Use as Electrocatalytic Interfaces. *ACS nano* 10, 2559–2567. doi:10.1021/acsnano.5b07505

Willner, I., Heleg-Shabtai, V., Blonder, R., Katz, E., Tao, G., Bückmann, A. F., et al. (1996). Electrical Wiring of Glucose Oxidase by Reconstitution of FAD-Modified Monolayers Assembled onto Au-Electrodes. *J. Am. Chem. Soc.* 118, 10321–10322. doi:10.1021/ja9608611

Windmiller, J. R., Bandodkar, A. J., Parkhomovsky, S., and Wang, J. (2012). Stamp Transfer Electrodes for Electrochemical Sensing on Non-planar and Oversized Surfaces. *Analyst* 137, 1570–1575. doi:10.1039/c2an35041f

Windmiller, J. R., and Wang, J. (2013). Wearable Electrochemical Sensors and Biosensors: a Review. *Electroanalysis* 25, 29–46. doi:10.1002/elan.201200349

Wu, L., Lu, X., Dhanjai, Z.-S., Wu, Z.-S., Dong, Y., Wang, X., et al. (2018). 2D Transition Metal Carbide MXene as a Robust Biosensing Platform for Enzyme Immobilization and Ultrasensitive Detection of Phenol. *Biosens. Bioelectron.* 107, 69–75. doi:10.1016/j.bios.2018.02.021

Xu, G., Cheng, C., Liu, Z., Yuan, W., Wu, X., Lu, Y., et al. (2019). Battery-Free and Wireless Epidermal Electrochemical System with All-Printed Stretchable Electrode Array for Multiplexed *In Situ* Sweat Analysis. *Adv. Mater. Technol.* 4, 1800658. doi:10.1002/admt.201800658

Xu, G., Jarjes, Z. A., Desprez, V., Kilmartin, P. A., and Travas-Sejdic, J. (2018). Sensitive, Selective, Disposable Electrochemical Dopamine Sensor Based on PEDOT-Modified Laser Scribed Graphene. *Biosens. Bioelectron.* 107, 184–191. doi:10.1016/j.bios.2018.02.031

Xu, G., Li, B., Wang, X., and Luo, X. (2014a). Electrochemical Sensor for Nitrobenzene Based on Carbon Paste Electrode Modified with a Poly(3,4-Ethylenedioxythiophene) and Carbon Nanotube Nanocomposite. *Microchim Acta* 181, 463–469. doi:10.1007/s00604-013-1136-y

Xu, M., Song, Y., Ye, Y., Gong, C., Shen, Y., Wang, L., et al. (2017). A Novel Flexible Electrochemical Glucose Sensor Based on Gold Nanoparticles/polyaniline Arrays/carbon Cloth Electrode. *Sensors Actuators B: Chem.* 252, 1187–1193. doi:10.1016/j.snb.2017.07.147

Xu, Q., Gu, S.-X., Jin, L., Zhou, Y.-E., Yang, Z., Wang, W., et al. (2014b). Graphene/polyaniline/gold Nanoparticles Nanocomposite for the Direct Electron Transfer of Glucose Oxidase and Glucose Biosensing. *Sensors Actuators B: Chem.* 190, 562–569. doi:10.1016/j.snb.2013.09.049

Xuan, X., Yoon, H. S., and Park, J. Y. (2018). A Wearable Electrochemical Glucose Sensor Based on Simple and Low-Cost Fabrication Supported Micro-patterned Reduced Graphene Oxide Nanocomposite Electrode on Flexible Substrate. *Biosens. Bioelectron.* 109, 75–82. doi:10.1016/j.bios.2018.02.054

Yang, Y.-L., Chuang, M.-C., Lou, S.-L., and Wang, J. (2010). Thick-film Textile-Based Amperometric Sensors and Biosensors. *Analyst* 135, 1230–1234. doi:10.1039/b926339j

Yang, Y., and Gao, W. (2019). Wearable and Flexible Electronics for Continuous Molecular Monitoring. *Chem. Soc. Rev.* 48, 1465–1491. doi:10.1039/c7cs00730b

Yoon, J. H., Kim, S.-M., Eom, Y., Koo, J. M., Cho, H.-W., Lee, T. J., et al. (2019). Extremely Fast Self-Healable Bio-Based Supramolecular Polymer for Wearable Real-Time Sweat-Monitoring Sensor. *ACS Appl. Mater. Inter.* 11, 46165–46175. doi:10.1021/acsami.9b16829

Yoon, J., Shin, M., Lim, J., Lee, J.-Y., and Choi, J.-W. (2020). Recent Advances in MXene Nanocomposite-Based Biosensors. *Biosensors* 10, 185. doi:10.3390/bios10110185

Zahed, M. A., Barman, S. C., Das, P. S., Sharifuzzaman, M., Yoon, H. S., Yoon, S. H., et al. (2020). Highly Flexible and Conductive Poly (3, 4-ethylene Dioxythiophene)-Poly (Styrene Sulfonate) Anchored 3-dimensional Porous Graphene Network-Based Electrochemical Biosensor for Glucose and pH Detection in Human Perspiration. *Biosens. Bioelectron.* 160, 112220. doi:10.1016/j.bios.2020.112220

Zamora, M. L., Domínguez, J. M., Trujillo, R. M., Goy, C. B., Sánchez, M. A., and Madrid, R. E. (2018). Potentiometric Textile-Based pH Sensor. *Sensors Actuators B: Chem.* 260, 601–608. doi:10.1016/j.snb.2018.01.002

Zdrachek, E., and Bakker, E. (2020). Potentiometric Sensing. *Anal. Chem.* 93, 72–102. doi:10.1021/acs.analchem.0c04249

Zeng, W., Shu, L., Li, Q., Chen, S., Wang, F., and Tao, X.-M. (2014). Fiber-Based Wearable Electronics: A Review of Materials, Fabrication, Devices, and Applications. *Adv. Mater.* 26, 5310–5336. doi:10.1002/adma.201400633

Zhang, C., Ning, J., Wang, B., Guo, H., Feng, X., Shen, X., et al. (2021). Hybridized 1T/2H-MoS2/graphene Fishnet Tube for High-Performance On-Chip Integrated Micro-systems Comprising Supercapacitors and Gas Sensors. *Nano Res.* 14, 114–121. doi:10.1007/s12274-020-3052-x

Zhang, L., Zhou, M., Wen, D., Bai, L., Lou, B., and Dong, S. (2012). Small-size Biofuel Cell on Paper. *Biosens. Bioelectron.* 35, 155–159. doi:10.1016/j.bios.2012.02.035

Zhao, J., Guo, H., Li, J., Bandodkar, A. J., and Rogers, J. A. (2019). Body-interfaced Chemical Sensors for Noninvasive Monitoring and Analysis of Biofluids. *Trends Chem.* 1, 559–571. doi:10.1016/j.trechm.2019.07.001

Zhao, X., Ding, J., Bai, W., Wang, Y., Yan, Y., Cheng, Y., et al. (2018). PEDOT:PSS/AuNPs/CA Modified Screen-Printed Carbon Based Disposable Electrochemical Sensor for Sensitive and Selective Determination of Carmine. *J. Electroanalytical Chem.* 824, 14–21. doi:10.1016/j.jelechem.2018.07.030

Zheng, J., Wang, B., Ding, A., Weng, B., and Chen, J. (2018). Synthesis of MXene/DNA/Pd/Pt Nanocomposite for Sensitive Detection of Dopamine. *J. Electroanalytical Chem.* 816, 189–194. doi:10.1016/j.jelechem.2018.03.056

Zhou, G., Byun, J.-H., Oh, Y., Jung, B.-M., Cha, H.-J., Seong, D.-G., et al. (2017). Highly Sensitive Wearable Textile-Based Humidity Sensor Made of High-Strength, Single-Walled Carbon Nanotube/Poly(vinyl Alcohol) Filaments. *ACS Appl. Mater. Inter.* 9, 4788–4797. doi:10.1021/acsami.6b12448

Zhou, G., Li, F., and Cheng, H.-M. (2014). Progress in Flexible Lithium Batteries and Future Prospects. *Energ. Environ. Sci.* 7, 1307–1338. doi:10.1039/c3ee43182g

Zhou, Q., and Shi, G. (2016). Conducting Polymer-Based Catalysts. *J. Am. Chem. Soc.* 138, 2868–2876. doi:10.1021/jacs.5b12474

Zhu, X., Liu, B., Hou, H., Huang, Z., Zeinu, K. M., Huang, L., et al. (2017). Alkaline Intercalation of Ti3C2 MXene for Simultaneous Electrochemical Detection of Cd(II), Pb(II), Cu(II) and Hg(II). *Electrochimica Acta* 248, 46–57. doi:10.1016/j.electacta.2017.07.084

Zhu, X., Yuan, S., Ju, Y., Yang, J., Zhao, C., and Liu, H. (2019). Water Splitting-Assisted Electrocatalytic Oxidation of Glucose with a Metal-Organic Framework for Wearable Nonenzymatic Perspiration Sensing. *Anal. Chem.* 91, 10764–10771. doi:10.1021/acs.analchem.9b02328

Conflict of Interest: The authors declare that the research was conducted in the absence of any commercial or financial relationships that could be construed as a potential conflict of interest.

Publisher's Note: All claims expressed in this article are solely those of the authors and do not necessarily represent those of their affiliated organizations, or those of the publisher, the editors and the reviewers. Any product that may be evaluated in this article, or claim that may be made by its manufacturer, is not guaranteed or endorsed by the publisher.

frontiers in Bioengineering and Biotechnology

ORIGINAL RESEARCH
published: 26 November 2021
doi: 10.3389/fbioe.2021.779632

Magnetic Microdimer as Mobile Meter for Measuring Plasma Glucose and Lipids

Shimin Yu[1,2], Zhongqi Sun[3], Zhanxiang Zhang[2,4], Haoran Sun[2], Lina Liu[2], Wuyi Wang[2], Mu Li[1], Qingsong Zhao[5]* and Tianlong Li[2]**

[1]Department of Pharmacy, The Second Affiliated Hospital of Harbin Medical University, Harbin, China, [2]State Key Laboratory of Robotics and System, Harbin Institute of Technology, Harbin, China, [3]Department of Radiology, The Second Affiliated Hospital of Harbin Medical University, Harbin, China, [4]Chongqing Research Institute of HIT, Harbin, China, [5]Department of Endocrinology, The Fourth Affiliated Hospital of Harbin Medical University, Harbin, China

With the development of designed materials and structures, a wide array of micro/nanomachines with versatile functionalities are employed for specific sensing applications. Here, we demonstrated a magnetic propelled microdimer-based point-of-care testing system, which can be used to provide the real-time data of plasma glucose and lipids relying on the motion feedback of mechanical properties. On-demand and programmable speed and direction of the microdimers can be achieved with the judicious adjustment of the external magnetic field, while their velocity and instantaneous postures provide estimation of glucose, cholesterol, and triglycerides concentrations with high temporal accuracy. Numerical simulations reveal the relationship between motility performance and surrounding liquid properties. Such technology presents a point-of-care testing (POCT) approach to adapt to biofluid measurement, which advances the development of microrobotic system in biomedical fields.

Keywords: magnetic microdimer, point-of-care testing, angle of procession, peak velocity, plasma glucose, plasma lipids

OPEN ACCESS

Edited by:
Tailin Xu,
Shenzhen University, China

Reviewed by:
Yunyun Li,
Tongji University, China
Changyong Gao,
Ningbo Institute of Materials Technology & Engineering (CAS), China

****Correspondence:***
Mu Li
limu@hrbmu.edu.cn
Qingsong Zhao
zqsjxw@126.com
Tianlong Li
tianlongli@hit.edu.cn

Specialty section:
This article was submitted to Biosensors and Biomolecular Electronics, a section of the journal Frontiers in Bioengineering and Biotechnology

Received: *19 September 2021*
Accepted: *08 October 2021*
Published: *26 November 2021*

Citation:
Yu S, Sun Z, Zhang Z, Sun H, Liu L, Wang W, Li M, Zhao Q and Li T (2021) Magnetic Microdimer as Mobile Meter for Measuring Plasma Glucose and Lipids. Front. Bioeng. Biotechnol. 9:779632. doi: 10.3389/fbioe.2021.779632

INTRODUCTION

Redundant glucose and lipids (cholesterol and triglycerides) in human blood can cause severe health problems such as diabetes mellitus, heart disease, arteriosclerosis, hypertension, hyperlipidemia, and cerebral thrombosis (Wang and Hu, 2020). Glucose, cholesterol, and triglycerides plasma levels have been important parameters for assessing risk factors of a population in disease diagnosis. With the growing demands for quick and convenient on-site diagnostic information, simple and fast blood glucose and blood lipid determination is essential and beneficial for early diagnosis. This goal can be pursued using point-of-care testing (POCT) (Sautter et al., 2018). Some POCT strategies and instruments that can measure glucose, cholesterol, and triglyceride levels in the blood have been developed (Rapi et al., 2009; Freckmann et al., 2014; Ning et al., 2021). These methods are quickly and highly reliable, but require extensive sample, advanced instruments, and qualified personnel operation. The past decade has witnessed a boom in the development of micro/nanomachines, which would open up an avenue and offer extensive opportunities for efficient sensing systems with excellent selectivity and sensitivity (Wang et al., 2012; Li J. et al., 2017).

Currently, plenty of micro/nanomachines get power from surrounding chemical fuel (Gao et al., 2011; Ma et al., 2016; Zhuang et al., 2017) or by harnessing external energy sources, such as magnetic (Li T. et al., 2017; Xie et al., 2019; Alapan et al., 2020; Fan et al., 2020; Wang et al., 2021), light (Dong

et al., 2016; Palagi et al., 2016; O'Neel-Judy et al., 2018; Wang et al., 2020), ultrasound (Wu et al., 2014; Xu et al., 2015; Ren et al., 2019), and electric (Demirörs et al., 2017; Alapan et al., 2019), and these combinations have been developed. Particularly, due to excellent maneuverability and high precision at the nano- and microscale, magnetically propelled micro and nanoswimmers provide great potential in targeted drug delivery (Felfoul et al., 2016; Gao et al., 2016; Xu H.et al., 2018), cell manipulation (Chang et al., 2019; Liao et al., 2019; Wang et al., 2020), minimally invasive surgery (Gao et al., 2015; Chen and Wang, 2020), guided imaging (Wu et al., 2014; Nothnagel et al., 2016; Medina-Sánchez et al., 2017), environmental remediation (Dekanovsky et al., 2020; Sun et al., 2020), and sensing (Moo et al., 2014; Ezhilan et al., 2015). More specifically, the enhanced physicochemical properties and motility of actively artificial nanomachine results in greater binding efficiency and synergic effect of micro/nanoscale dimensions and active motion, which can be useful in physical and chemical sensing (Yu et al., 2019; Ji et al., 2021). Three main applications of using magnetically driven micro/nanomotors for sensing and biosensing are investigated: 1) detection of the local microenvironment properties (e.g., fluid viscosity, ion strength) based on movement parameters (e.g., velocity, wobbling angle) of magnetic propelled microswimmers (Zhang et al., 2019), 2) acting as signal amplifier to enhance the detection sensitivity and efficiency for tagged signals (e.g., fluorescence) (Zhang et al., 2019), and 3) guiding and transporting payloads (i.e., biotin and avidin) to a user-defined site under the steering of external magnetic field (Park and Yossifon, 2020). To date, a mass of maneuvering micro/nanomachines with different morphologies, including tubular (Xu B. et al., 2018), Janus spherical (Li et al., 2018; Pourrahimi et al., 2018), wheel-like (Yang et al., 2019), body-deformable (Li et al., 2016), and helical shape (Ghosh et al., 2018; Wang et al., 2018), have been fabricated as mobile sensors capable of detecting analytical signals in real time directly or decorated with different receptors on their surface. The introduction of motion dimension further increases the accuracy of the various sensing abilities at local sites in 3D. However, there are no reports regarding microrobot-based microdevice for plasma glucose and lipid measurement. Hence, there is a current need in biomedical demands for new cost-effective, real-time, and easily integrated system for measuring plasma glucose and lipids.

In this work, a magnetically actuated microdimer was first used to estimate the concentration of plasma glucose and plasma lipid. The inconsistency in the length and width of geometric structure leads to changing posture with increase in frequency, presenting three motion modes of tumbling, wobbling, and rolling, while accompanying varying motion speeds. A similar tendency happens when the viscosity varies appreciably with the level of glucose and lipid of the plasma, which guides the detection of glucose, cholesterol, and triglycerides in plasma using the motility performances of velocity and posture. The method of manipulation with high spatial and temporal accuracy-based noninvasive magnetic actuation can be applied in the detection of most types of fluid samples.

MATERIALS AND METHODS

Synthesis of Magnetic Janus Microspheres

The silica microparticles with a diameter of 8 μm (Aladdin, China) was used as the base particles to prepare the magnetic Janus microspheres. Primarily, the silica microspheres were washed three times with deionized water and redispersed in ethyl alcohol. Then the sample was spread onto glass slides and dried uniformly to form microsphere monolayers. The microspheres were sputter coated with a 100-nm nickel layer using an ion-sputtering apparatus at 90° angle of incidence. After the fabrication, the sputtered microparticles were released from the substrate using a bath sonicator in ethanol and dispersed in ultrapure water. All magnetic microspheres were stored in ultrapure water at room temperature when not in use.

Magnetic Experiments

The controllable magnetically actuated locomotion of microdimer was driven by homogeneous rotating magnetic field generated by a vision-based magnetic navigation system. The external rotating uniform magnetic field consists of a three degrees of freedom Helmholtz coil system, a multifunction data acquisition, and a three single-channel output power amplifier. Various required rotating magnetic fields in any plane of 3D space were achieved by controlling the current and the voltage of Helmholtz coils.

Optical Observation and Tracking

In order to achieve real-time observation of swimmers, the external magnetic field setup was placed on the observation platform of an inverted microscope (IX73, Olympus, Japan) to achieve real-time observation of microdimers. Locomotion videos of Janus microdimers were captured by a digital CCD camera (DP74, Olympus, Japan) and analyzed by using ImageJ to obtain the trajectories, velocities, and postures of swimmers.

RESULTS AND DISCUSSION

Point-of-care-testing System for Clinical Index

As routine clinical parameters, glucose and lipid level detection have become the main approaches to prevent various human diseases such as diabetes, hypertension, and other cardiovascular diseases. To meet the demand of affordable and efficient clinical diagnostics, POCT has gained more and more attention and become in full swing for glucose, cholesterol, and triglyceride detection. **Figure 1** schematically shows the detection strategy using a microdimer under the external magnet. Whole blood was divided into three layers of red blood cells, translucid gel, and plasma. After centrifuging for 3 min at 3,000 rpm, the upper layer of the plasma was taken out and used for the experiments. The plasma containing Janus microspheres was placed into the center of a triaxial Helmholtz coil system (two x coils, two y coils, and two z coil) fixed on an inverted microscope. The microdimers were actuated using a rotating uniform magnetic field with

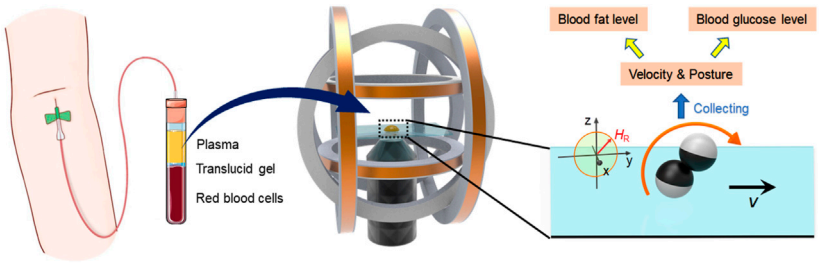

FIGURE 1 | Conceptual schematic illustration of the estimation of plasma glucose and lipids using magnetic propelled microdimers.

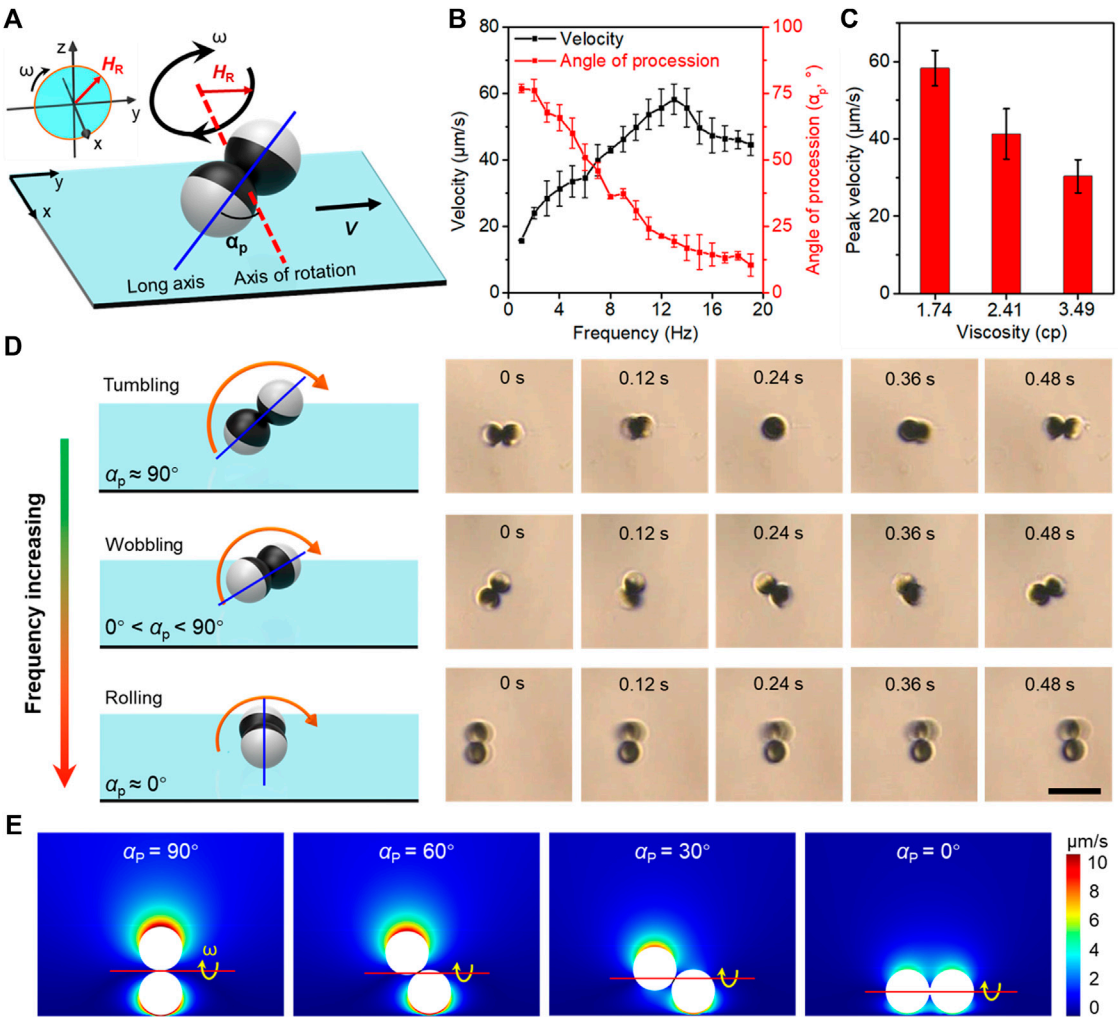

FIGURE 2 | Actuation mechanisms of magnetic-propelled microdimers. **(A)** Schematic of a microdimer with permanent magnetization. The applied field is of strength H_R rotating at angular velocity ω (frequency f = $\omega/2\pi$). **(B)** Velocity and angle of precession (α_p) varied with the driving frequency in 10% glycerol–water solution (1.74 cp). **(C)** The peak velocity of microdimers in glycerol–water solution of different viscosities. **(D)** Schemes of microdimers in tumbling, rolling, and wobbling modes at different α_p under a rotating magnetic field. Scale bar 20 μm. **(E)** Simulation of the section view from one side of the microdimer shows the fluid flow velocity near a microdimer on the substrate at different α_p.

strength of 5 mT and frequency of 1–30 Hz. The rolling direction of the microdimer was controlled by changing the orientation of applied magnetic field. Motion speed and posture in the plasma with different glucose, cholesterol, and triglyceride concentrations were captured and analyzed to seek the estimation approach for glucose and lipid levels.

Propulsion of Magnetic Microdimers on Flat Surfaces

In the method described here, artificially prepared plasma samples with different viscosities were prepared using different glucose (or cholesterol and triglyceride) concentration aqueous solutions. We could maneuver and position microdimers with a micrometer-scale resolution using externally applied magnetic fields, while simultaneously imaging its position and orientation to estimate the glucose, cholesterol, and triglyceride concentration in real time. The flat surface is critically important in converting the magnetically induced rotation to linear translation. The micro and nanorobots based on this "surface-assisted locomotion" mechanism is called "surface walkers." Such time-reversible reciprocal locomotion can still generate an effective propulsion in the blood (non-Newtonian fluids). In addition, propulsion using rotating magnetic fields is noninvasive, and the microdimers are stable in other types of biological fluids.

Based on the axial symmetry and "peanut-like" shape of microdimer, the estimation of the concentration of the local samples from the dynamics of the microdimer can be concentrated on the locomotion velocity and posture (Lin et al., 2018). When the coercivity is much higher than the applied magnetic field strength, the magnetization strength and direction are considered unchanged. **Figure 2A** schematically illustrates the magnetization of microdimers under a rotating magnetic field. H_R and ω were magnetic field strength and angular velocity (related to frequency), respectively. The angle of precession (α_p) is defined as the angle between the long axis and the axis of rotation. The long axis is defined as the connection between the centers of the two spheres of microdimers, and the axis of rotation is defined as the normal to the plane of rotating magnetic field. Excited by the stable input of the external magnetic field, the microdimer locomotes in a constant direction at a stable speed and posture in a homogeneous medium. The dynamics of the microdimer in 10% glycerol–water solution (~1.74 cp) was imaged and analyzed to estimate α_p, shown in **Figure 2B**. At a magnetic field strength of 5 mT, the velocity of microdimer increased linearly with the driving frequency and reached a maximum velocity of 55.8 μm s^{-1} (3.5 body length s^{-1}) at 14 Hz, further increasing the frequency, which reduced the velocity. Such a maximum synchronized frequency is called step-out frequency, which occurred from the increase in drag caused by the increasing speed. In brief, the frequency corresponding to the peak speed of the microdimer is defined as step-out frequency. Simultaneously, frequency-induced increasing drag also forced the microdimer to change motion posture to weaken the fluid impact, expressing a decrease in α_p. The α_p decreased from 76.8° to 4.2° upon increasing the driving frequency from 1 to 20 Hz. **Figure 2C** shows the peak velocity of microdimers in glycerol–water solutions of different viscosities. As can be seen, the peak velocity decreased with an increase in viscosity. Furthermore, the raised viscosity caused by the increasing glucose (or cholesterol and triglyceride) concentrations also enhances the resistance during locomotion, which further accelerated the occurrence of out-step frequency.

The microdimers exhibited three distributed locomotion modes, called tumbling, wobbling, and rolling (**Figure 2D**). When a uniform rotating magnetic field energizes them with increasing frequency, the essential details are as follows: 1) Under the excitation of the initial low-frequency magnetic field, the long axis of the microdimer was parallel to the rotation plane of the magnetic moment and perpendicular to the rotation axis, exhibiting a tumbling motion mode at $\alpha_p \approx 90^\circ$. 2) As the frequency increases, the raised fluid drag compelled the long axis to deviate from the rotation plane of the magnetic field. At this time, the microdimer wobbling at $0^\circ < \alpha_p < 90^\circ$ and can be divided into a rotation along its own axis and another homodromous rotation along an axis with an angle to the long axis. Step-out frequency also occurred during wobbling mode. 3) The wobbling mode gradually transformed into the rolling mode ($\alpha_p \approx 0^\circ$) as out-of-step phenomenon intensified. The long axis of the microdimer almost coincides with the axis of rotation in the rolling mode. Note that the velocity and angle of precession in rolling was more stable than the tumbling and wobbling modes. The continuous motion process of the three modes at a magnetic field strength of 5 mT was captured from **Supplementary Video S1** and is shown in **Figure 2D**.

The motion near the surface of the microdimer was impeded due to the hydrodynamic no-slip boundary, which created a mismatch of hydrodynamic interactions between the top and bottom and conversion of rotational motion to translational motion of microdimers. Microdimers will experience different drag forces in multimodes due to a discrepant fluidic interaction between them and the surrounding fluid. As shown in **Figure 2E**, the fluidic velocity field induced by a rotating microdimer at different precession angles (0°, 30°, 60°, and 90°) adjacent to the wall surface has been simulated and analyzed. All the simulations were performed within COMSOL Multiphysics 5.5 Simulation Software. For all motion mode groups, the total velocity acting on the microdimer increased with decreasing distance from the microdimer. Flow field strength at the same distance from the microdimer and the height of the rotation axis from the surface reduced with a decrease in the angle of precession.

Estimation of Glucose Concentration

Point-of-care testing of plasma glucose and plasma lipids has been used to quickly diagnose diabetes mellitus (fasting glucose >126 mg/dl or glucose after 75 g of glucose oral load >200 mg/dl) and hyperlipidemia [total cholesterol (T-chol) >250 mg/dl and/or triglycerides (TG) >250 mg/dl]. In terms of the impact on the motility of microdimers, the concentration of glucose, cholesterol, and triglyceride will change the plasma viscosity and further affect their motion behavior. To overcome this limitation, we separately

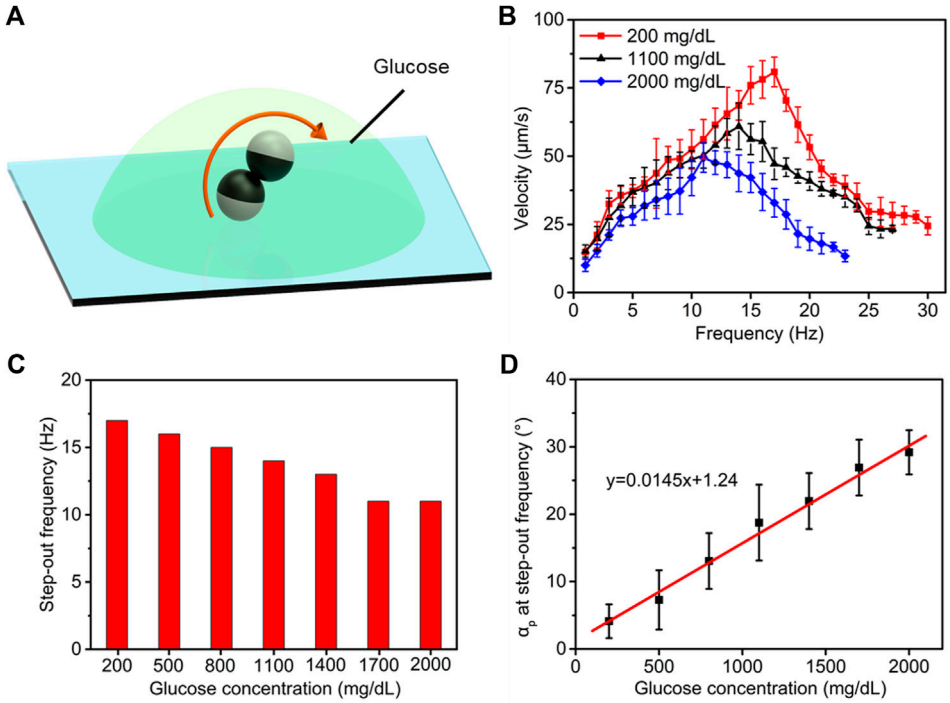

FIGURE 3 | Estimating the strategy of plasma glucose levels. **(A)** Controllable motion of the microdimers in plasma with different glucose concentrations. **(B)** Variation in the velocity of the microdimers upon changing magnetic frequency and glucose concentration. **(C)** The step-out frequency at different glucose concentrations. **(D)** Function of the α_p at step-out frequency as increasing glucose concentration.

investigated the influence rules of the concentration of glucose, cholesterol, and triglycerides on the motility of microdimers to seek respective customized methods for the characterization of the three variables. **Figure 3A** schematically presents the locomotion of microdimers in plasma with preprogrammed glucose concentration. We executed the linear motion of the microdimer in plasma with different glucose concentrations and analyzed the relationship of the velocity and posture of the microdimers with the frequency of the applied magnetic field and glucose concentration. **Figure 3B** shows that under a rotating magnetic field of 5 mT and glucose concentration of 200 mg/dl, the velocity of the microdimer first went up linearly as the frequency grows, reaching a maximum velocity of 80.9 μm s^{-1} at a step-out frequency of 17 Hz. It then went down reciprocally after the step-out frequency. Interestingly, the motion displayed a series of peak velocities and step-out frequencies at different glucose concentrations, which decreased upon an increase in glucose concentration and dropped to 49.4 μm s^{-1} and 11 Hz when the glucose concentration was 2,000 mg/dl. A more detailed explanation about the rule of step-out frequencies and glucose concentration is presented in **Figure 3C**. Large-scale increase in glucose concentration did not significantly bring the occurrence of synchrony losing forward, which means that the change in glucose concentration processed a small effect on plasma viscosity. In addition, the procession angle of microdimers, dependent on both plasma viscosity and spinning velocity, also changed with the variational frequency and glucose concentration. The increase in frequency and glucose concentration both reduced the precession angle. In order to accurately estimate the glucose concentration, we measured the precession angle α_p as a function of step-out frequency as the glucose concentration increased after comparing the corresponding relationship between various parameters and glucose concentration (**Figure 3D**). The α_p at step-out frequency increased from 4.1° to 29.2° upon increasing the glucose concentration from 200 to 2,000 mg/dl. The linear fitting (red line) of the experimental data further reveals that the α_p at step-out frequency and the glucose concentration show a good linear relationship, which confirms the quantitative accuracy estimation of the glucose concentration using α_p at step-out frequency.

Estimation of Cholesterol Level

Cholesterol and triglycerides, as the primary targets of plasma lipid routine examination, are the main components that induce hyperlipidemia. Therefore, we explored specific estimation schemes for the concentration of cholesterol and triglycerides, respectively. Similar to the detection of plasma glucose, we perform microrobot operations in plasma with constant plasma glucose concentration and different plasma lipid concentrations, capturing its locomotion performance (**Figure 4A**). Time-lapse optical microscopy images in **Figure 4B** illustrates that locomotion trajectories and posture of microdimers propelled by rotating a magnetic

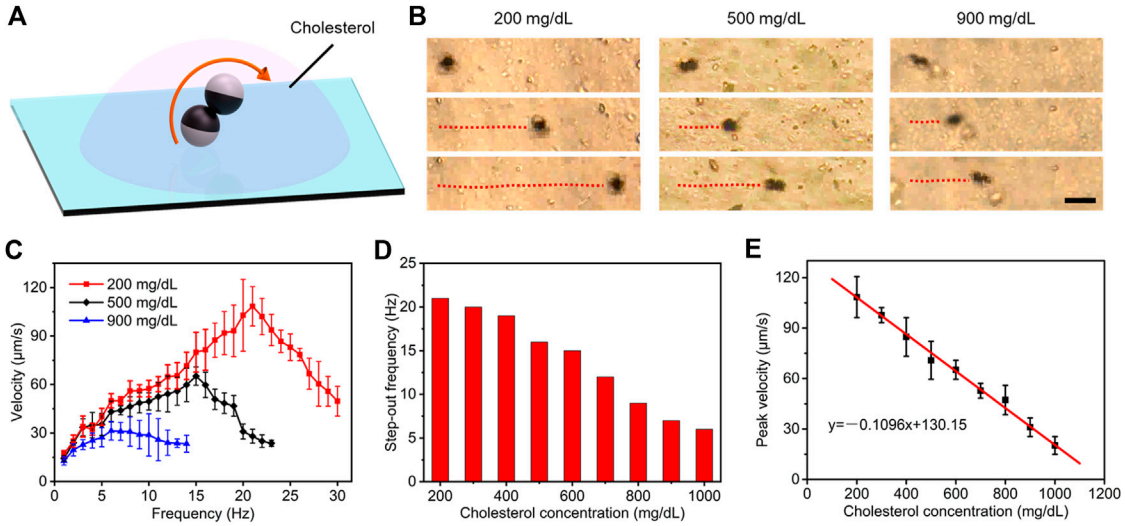

FIGURE 4 | Estimating strategy of plasma cholesterol level. **(A)** Controllable motion of the microdimers in plasma with different cholesterol concentrations. **(B)** Time-lapse optical microscopy images of locomotion trajectories of microdimers propelled by rotating magnetic field in cholesterol concentrations of 200, 500, and 900 mg/dl. Scale bar: 20 μm. **(C)** Dependence of the translational speed of microdimer on the frequency of the external rotating magnetic and cholesterol concentration. **(D)** The step-out frequency at different cholesterol concentrations. **(E)** The peak velocity of microdimer was dependent on cholesterol concentration.

field of 5 mT in cholesterol concentrations of 200, 500, and 900 mg/dl. Obviously, the velocity and procession angle of microdimers also were impacted evidently by the cholesterol concentration, and the former processed a stronger variation with the concentration. In view of this, we further analyzed the velocity of the microdimers changing with magnetic frequency under different cholesterol concentrations, as shown in **Figure 4C**. Compared with that in different glucose concentrations, the tendency of speed and the occurrence of step-out frequency were similar, but their decreasing amplitudes with an increase in cholesterol concentration were more significant. Particularly, when the concentration of cholesterol reached 900 mg/dl, the velocity increased from 12.8 μm s^{-1} at the minimum to only 31.4 μm s^{-1} at the maximum. This result indicates that increasing cholesterol concentration caused more apparent viscosity than glucose.

Next, we systematically investigated the step-out frequency and peak speed at different cholesterol concentrations. As described in **Figure 4D**, the step-out frequency decreased with an increase in concentration as nonlinear relationship, which limited the purpose of using step-out frequency to characterize cholesterol concentration. On the contrary, the peak velocity followed a linear relationship with the cholesterol concentration (**Figure 4E**). The linear fitting curve further illustrated that the estimation strategy based on peak velocity not only process a higher accuracy but also a large slope, which can be used to excellently estimate the concentration of cholesterol. A level of cholesterol over 250 mg/dl may indicate a greater risk for hyperlipidemia disease (Solá, et al., 2007). The experiments in this study cover the normal and abnormal cholesterol concentrations, so this strategy can be used to clinically estimate cholesterol level.

Estimation of Triglyceride Level

Triglyceride level, as another lipoid component similar to cholesterol in plasma, also directly affects the plasma lipid level. The same strategy was used to seek an estimation method of triglyceride level (**Figure 5A**). The velocity of microdimers was also dependent on driving frequency and concentration of triglycerides, as shown in **Figure 5B**. Similarly, step-out phenomena asynchronously occurred in plasma with different triglyceride concentrations, and the greater concentration caused the lower step-out frequency. It also can be seen from **Figure 5B** that step-out frequency and maximum speed varied nonlinearly with triglyceride concentration. As a consequence, we turned to study the change in precession angle of microdimers to estimate the triglyceride concentration. A rotating magnet with strength of 5 mT and frequency of 10 Hz has a precession angle of microdimers at triglyceride concentrations of 200, 400, 800, and 2,200 mg/dl, respectively. The captured images are shown in **Figure 5C**. The α_p was 79° at a triglyceride concentration of 200 mg/dl and decreased with rising triglyceride concentration, which dropped to 30° at 2,200 mg/dl. We next measured the changing process of α_p with the frequency variating from 1 to 30 Hz. As described in **Figure 5D**, the precession angle represented a decreasing trend of "Z" shape with increasing frequency, which was the precession angle decreasing slightly in the low- and high-frequency bands, while the cliff-like decline occurred at the middle-frequency band. Interestingly, similar to the phase transformation of electrical signals, the cliff-like decline emerged earlier as the triglyceride concentration increased. This difference made the precession angle in middle middle-frequency band vary greatly with concentration change, which provided a guideline for estimating triglyceride concentration

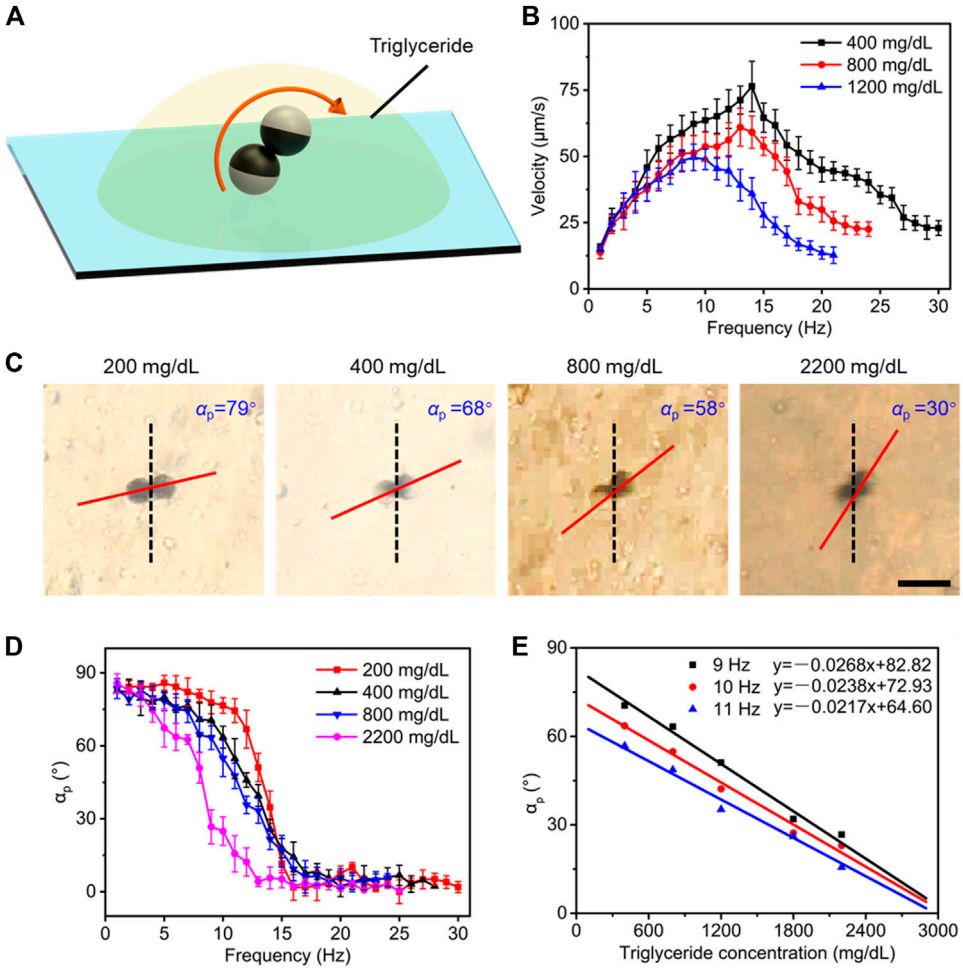

FIGURE 5 | Estimating strategy of plasma triglyceride level. **(A)** Controllable motion of the microdimer in plasma with different triglyceride concentrations. **(B)** The velocity of microdimers varied with the drive frequency and triglyceride concentrations. **(C)** Snapshots of the moving microdimer and corresponding measured α_p at different triglyceride concentrations. Scale bar: 20 μm. **(D)** "Z" decreasing trend of precession angle with the increase in driving frequency. **(E)** Linear relationship of the α_p at 9, 10, and 11 Hz with triglyceride concentration.

using α_p. Similar changing trends of the precession angle were not observed in the case of plasma glucose or plasma cholesterol. The precession angle in the middle middle-frequency of 9, 10, and 11 Hz as a function of triglyceride concentration was selected and exhibited in **Figure 5E**. The excellent linear fitting results demonstrated the feasibility of estimating the triglyceride concentration based on the precession angle at the middle-frequency band.

CONCLUSION

We first demonstrate that magnetic microdimer capable of dynamic motility performance with changing viscosity can be used to quantify the concentration of glucose, cholesterol, and triglyceride in plasma. The microdimers exhibited three locomotion modes of tumbling, wobbling and rolling with a change in resistance related to frequency and fluid viscosity, which were further supported by numerical studies. These results show the superiority of using precession angle α_p at step-out frequency and peak speed to estimate glucose and cholesterol levels, respectively. As for the measurement of triglyceride level, there is a linking synchronization in α_p changing the trend with variating frequency and triglyceride concentration. The dynamic ranges in concentration measurements of glucose, cholesterol, and triglyceride were almost 2,000, 1,000, and 3,000 mg/dl, respectively. This technique was envisaged to apply for detection in more scenarios that require fast mechanical changes.

DATA AVAILABILITY STATEMENT

The raw data supporting the conclusion of this article will be made available by the authors, without undue reservation.

AUTHOR CONTRIBUTIONS

SY, ZS, and ZZ contributed equally to this work. TL, ML, and QZ conceptualized the study. SY, ZS, and ZZ developed the methodology. HS and LL were in charge of the software. LL, YS, and ZS investigated the study. WW, HS, and LL performed the data analysis. SY, ZS, and ZZ wrote and prepared the original draft. TL, QZ, and ML wrote, reviewed, and edited the manuscript. TL and QZ acquired the funding.

FUNDING

This work was supported by the National Natural Science Foundation of China (No. 52175009), the Fundamental Research Funds for the Central Universities and Interdisciplinary Research Foundation of HIT, the Natural Science Foundation of Heilongjiang Province (No. LH2020H063), and the Excellent Youth Project of Fourth Affiliated Hospital of Harbin Medical University (No. HYDSYYXQN202008).

ACKNOWLEDGMENTS

TL acknowledges the support of State Key Laboratory of Robotics and System (Harbin Institute of Technology) and Key Lab for Microsystems and Microstructure Manufacturing (Harbin Institute of Technology).

SUPPLEMENTARY MATERIAL

The Supplementary Material for this article can be found online at: https://www.frontiersin.org/articles/10.3389/fbioe.2021.779632/full#supplementary-material

REFERENCES

Alapan, Y., Bozuyuk, U., Erkoc, P., Karacakol, A. C., and Sitti, M. (2020). Multifunctional Surface Microrollers for Targeted Cargo Delivery in Physiological Blood Flow. *Sci. Robot.* 5, eaba5726. doi:10.1126/scirobotics.aba5726

Alapan, Y., Yigit, B., Beker, O., Demirörs, A. F., and Sitti, M. (2019). Shape-encoded Dynamic Assembly of Mobile Micromachines. *Nat. Mater.* 18, 1244–1251. doi:10.1038/s41563-019-0407-3

Chang, X., Chen, C., Li, J., Lu, X., Liang, Y., Zhou, D., et al. (2019). Motile Micropump Based on Synthetic Micromotors for Dynamic Micropatterning. *ACS Appl. Mater. Inter.* 11, 28507–28514. doi:10.1021/acsami.9b08159

Chen, J., and Wang, Y. (2020). Personalized Dynamic Transport of Magnetic Nanorobots inside the Brain Vasculature. *Nanotechnology* 31, 495706. doi:10.1088/1361-6528/abb392

Dekanovsky, L., Khezri, B., Rottnerova, Z., Novotny, F., Plutnar, J., and Pumera, M. (2020). Chemically Programmable Microrobots Weaving a Web from Hormones. *Nat. Mach. Intell.* 2, 711–718. doi:10.1038/s42256-020-00248-0

Demirörs, A. F., Eichenseher, F., Loessner, M. J., and Studart, A. R. (2017). Colloidal Shuttles for Programmable Cargo Transport. *Nat. Commun.* 8, 1872. doi:10.1038/s41467-017-01956-9

Dong, R., Zhang, Q., Gao, W., Pei, A., and Ren, B. (2016). Highly Efficient Light-Driven TiO2-Au Janus Micromotors. *ACS Nano* 10, 839–844. doi:10.1021/acsnano.5b05940

Ezhilan, B., Gao, W., Pei, A., Rozen, I., Dong, R., Jurado-Sanchez, B., et al. (2015). Motion-based Threat Detection Using Microrods: Experiments and Numerical Simulations. *Nanoscale* 7, 7833–7840. doi:10.1039/c4nr06208f

Fan, X., Dong, X., Karacakol, A. C., Xie, H., and Sitti, M. (2020). Reconfigurable Multifunctional Ferrofluid Droplet Robots. *Proc. Natl. Acad. Sci. USA* 117, 27916–27926. doi:10.1073/pnas.2016388117

Felfoul, O., Mohammadi, M., Taherkhani, S., de Lanauze, D., Zhong Xu, Y., Loghin, D., et al. (2016). Magneto-Aerotactic Bacteria Deliver Drug-Containing Nanoliposomes to Tumour Hypoxic Regions. *Nat. Nanotech* 11, 941–947. doi:10.1038/nnano.2016.137

Freckmann, G., Schmid, C., Pleus, S., Baumstark, A., Link, M., Stolberg, E., et al. (2014). System Accuracy Evaluation of Systems for Point-of-care Testing of Blood Glucose: A Comparison of a Patient-Use System with Six Professional-Use Systems. *Clin. Chem. Lab. Med.* 52, 1079–1086. doi:10.1515/cclm-2013-0976

Gao, C., Lin, Z., Jurado-Sánchez, B., Lin, X., Wu, Z., and He, Q. (2016). Stem Cell Membrane-Coated Nanogels for Highly Efficient *In Vivo* Tumor Targeted Drug Delivery. *Small* 12, 4056–4062. doi:10.1002/smll.201600624

Gao, W., Dong, R., Thamphiwatana, S., Li, J., Gao, W., Zhang, L., et al. (2015). Artificial Micromotors in the Mouse's Stomach: A Step toward *In Vivo* Use of Synthetic Motors. *ACS Nano* 9, 117–123. doi:10.1021/nn507097k

Gao, W., Sattayasamitsathit, S., Orozco, J., and Wang, J. (2011). Highly Efficient Catalytic Microengines: Template Electrosynthesis of Polyaniline/Platinum Microtubes. *J. Am. Chem. Soc.* 133, 11862–11864. doi:10.1021/ja203773g

Ghosh, A., Dasgupta, D., Pal, M., Morozov, K. I., Leshansky, A. M., and Ghosh, A. (2018). Helical Nanomachines as Mobile Viscometers. *Adv. Funct. Mater.* 28, 1705687. doi:10.1002/adfm.201705687

Ji, F., Li, T., Yu, S., Wu, Z., and Zhang, L. (2021). Propulsion Gait Analysis and Fluidic Trapping of Swinging Flexible Nanomotors. *ACS Nano* 15, 5118–5128. doi:10.1021/acsnano.0c10269

Li, J., Esteban-Fernández de Ávila, B., Gao, W., Zhang, L., and Wang, J. (2017). Micro/Nanorobots for Biomedicine: Delivery, Surgery, Sensing, and Detoxification. *Sci. Robot.* 2, eaam6431. doi:10.1126/scirobotics.aam6431

Li, T., Li, J., Morozov, K. I., Wu, Z., Xu, T., Rozen, I., et al. (2017). Highly Efficient Freestyle Magnetic Nanoswimmer. *Nano Lett.* 17, 5092–5098. doi:10.1021/acs.nanolett.7b02383

Li, T., Li, J., Zhang, H., Chang, X., Song, W., Hu, Y., et al. (2016). Magnetically Propelled Fish-like Nanoswimmers. *Small* 12, 6098–6105. doi:10.1002/smll.201601846

Li, T., Zhang, A., Shao, G., Wei, M., Guo, B., Zhang, G., et al. (2018). Janus Microdimer Surface Walkers Propelled by Oscillating Magnetic Fields. *Adv. Funct. Mater.* 28, 1706066. doi:10.1002/adfm.201706066

Liao, P., Xing, L., Zhang, S., and Sun, D. (2019). Magnetically Driven Undulatory Microswimmers Integrating Multiple Rigid Segments. *Small* 15, 1901197. doi:10.1002/smll.201901197

Lin, Z., Fan, X., Sun, M., Gao, C., He, Q., and Xie, H. (2018). Magnetically Actuated Peanut Colloid Motors for Cell Manipulation and Patterning. *ACS Nano* 12, 2539–2545. doi:10.1021/acsnano.7b08344

Ma, X., Wang, X., Hahn, K., and Sánchez, S. (2016). Motion Control of Urea-Powered Biocompatible Hollow Microcapsules. *ACS. Nano* 10, 3597–3605. doi:10.1021/acsnano.5b08067

Medina-Sánchez, M., and Schmidt, O. G. (2017). Medical Microbots Need Better Imaging and Control. *Nature* 545, 406–408. doi:10.1038/545406a

Moo, J. G. S., Wang, H., Zhao, G., and Pumera, M. (2014). Biomimetic Artificial Inorganic Enzyme-free Self-Propelled Microfish Robot for Selective Detection of Pb2+in Water. *Chem. Eur. J.* 20, 4292–4296. doi:10.1002/chem.201304804

Ning, Y., Lu, F., Liu, Y., Yang, S., Wang, F., Ji, X., et al. (2021). Glow-type Chemiluminescent Hydrogels for Point-of-care Testing (POCT) of Cholesterol. *Analyst* 146, 4775–4780. doi:10.1039/d1an00676b

Nothnagel, N., Rahmer, J., Gleich, B., Halkola, A., Buzug, T. M., and Borgert, J. (2016). Steering of Magnetic Devices with a Magnetic Particle Imaging System. *IEEE Trans. Biomed. Eng.* 63, 2286–2293. doi:10.1109/tbme.2016.2524070

O'Neel-Judy, É., Nicholls, D., Castañeda, J., and Gibbs, J. G. (2018). Light-Activated, Multi-Semiconductor Hybrid Microswimmers. *Small* 14, e1801860. doi:10.1002/smll.201801860

Palagi, S., Mark, A. G., Reigh, S. Y., Melde, K., Qiu, T., Zeng, H., et al. (2016). Structured Light Enables Biomimetic Swimming and Versatile Locomotion of

Photoresponsive Soft Microrobots. *Nat. Mater* 15, 647–653. doi:10.1038/nmat4569

Park, S., and Yossifon, G. (2020). Micromotor-Based Biosensing Using Directed Transport of Functionalized Beads. *ACS Sens.* 5, 936–942. doi:10.1021/acssensors.9b02041

Pourrahimi, A. M., Villa, K., Ying, Y., Sofer, Z., and Pumera, M. (2018). ZnO/ZnO2/Pt Janus Micromotors Propulsion Mode Changes with Size and Interface Structure: Enhanced Nitroaromatic Explosives Degradation Under Visible Light. *ACS Appl. Mater. Inter.* 10, 42688–42697. doi:10.1021/acsami.8b16217

Rapi, S., Bazzini, C., Tozzetti, C., Sbolci, V., and Modesti, P. A. (2009). Point-of-Care Testing of Cholesterol and Triglycerides for Epidemiologic Studies: Evaluation of the Multicare-In System. *Transl. Res.* 153, 71–76. doi:10.1016/j.trsl.2008.11.010

Ren, L., Nama, N., McNeill, J. M., Soto, F., Yan, Z., Liu, W., et al. (2019). 3D Steerable, Acoustically Powered Microswimmers for Single-Particle Manipulation. *Sci. Adv.* 5, eaax3084. doi:10.1126/sciadv.aax3084

Sautter, R. L., Earnest, D. M., and Halstead, D. C. (2018). What's Old is New Again: Laboratory Oversight of Point of Care Testing-Guidelines, Challenges, and Practical Strategies. *Clin. Microbiol. Newsl.* 40, 191–198. doi:10.1016/j.clinmicnews.2018.11.001

Solá, E., Vayá, A., Simó, M., Hernández-Mijares, A., Morillas, C., España, F., et al. (2007). Fibrinogen, Plasma Viscosity and Blood Viscosity in Obesity. Relationship with Insulin Resistance. *Clin. Hemorheol. Micro.* 37, 309–318.

Sun, M., Chen, W., Fan, X., Tian, C., Sun, L., and Xie, H. (2020). Cooperative Recyclable Magnetic Microsubmarines for Oil and Microplastics Removal from Water. *Appl. Mater. Today* 20, 100682. doi:10.1016/j.apmt.2020.100682

Wang, B., Chan, K. F., Yuan, K., Wang, Q., Xia, X., Yang, L., et al. (2021). Endoscopy-Assisted Magnetic Navigation of Biohybrid Soft Microrobots with Rapid Endoluminal Delivery and Imaging. *Sci. Robot.* 6, eabd2813. doi:10.1126/scirobotics.abd2813

Wang, J., and Gao, W. (2012). Nano/microscale Motors: Biomedical Opportunities and Challenges. *ACS. Nano* 6, 5745–5751. doi:10.1021/nn3028997

Wang, J., Xiong, Z., Liu, M., Li, X.-m., Zheng, J., Zhan, X., et al. (2020a). Rational Design of Reversible Redox Shuttle for Highly Efficient Light-Driven Microswimmer. *ACS. Nano* 14, 3272–3280. doi:10.1021/acsnano.9b08799

Wang, W., Wu, Z., and He, Q. (2020b). Swimming Nanorobots for Opening a Cell Membrane Mechanically. *View* 1, 20200005. doi:10.1002/viw.20200005

Wang, X., Hu, C., Schurz, L., De Marco, C., Chen, X., Pané, S., et al. (2018). Surface-Chemistry-Mediated Control of Individual Magnetic Helical Microswimmers in a Swarm. *ACS Nano* 12, 6210–6217. doi:10.1021/acsnano.8b02907

Wang, X., and Hu, L. (2020). Review-Enzymatic Strips for Detection of Serum Total Cholesterol with Point-of-Care Testing (POCT) Devices: Current Status and Future Prospect. *J. Electrochem. Soc.* 167, 037535. doi:10.1149/1945-7111/ab64bb

Wu, Z., Li, T., Li, J., Gao, W., Xu, T., Christianson, C., et al. (2014). Turning Erythrocytes into Functional Micromotors. *ACS Nano* 8, 12041–12048. doi:10.1021/nn506200x

Xie, H., Sun, M., Fan, X., Lin, Z., Chen, W., Wang, L., et al. (2019). Reconfigurable Magnetic Microrobot Swarm: Multimode Transformation, Locomotion, and Manipulation. *Sci. Robot.* 4, eaav8006. doi:10.1126/scirobotics.aav8006

Xu, B., Zhang, B., Wang, L., Huang, G., and Mei, Y. (2018). Tubular Micro/Nanomachines: From the Basics to Recent Advances. *Adv. Funct. Mater.* 28, 1705872. doi:10.1002/adfm.201705872

Xu, H., Medina-Sánchez, M., Magdanz, V., Schwarz, L., Hebenstreit, F., and Schmidt, O. G. (2018). Sperm-Hybrid Micromotor for Targeted Drug Delivery. *ACS. Nano* 12, 327–337. doi:10.1021/acsnano.7b06398

Xu, T., Soto, F., Gao, W., Dong, R., Garcia-Gradilla, V., Magaña, E., et al. (2015). Reversible Swarming and Separation of Self-Propelled Chemically Powered Nanomotors under Acoustic Fields. *J. Am. Chem. Soc.* 137, 2163–2166. doi:10.1021/ja511012v

Yang, T., Tomaka, A., Tasci, T. O., Neeves, K. B., Wu, N., and Marr, D. W. M. (2019). Microwheels on Microroads: Enhanced Translation on Topographic Surfaces. *Sci. Robot.* 4, eaaw9525. doi:10.1126/scirobotics.aaw9525

Yu, S., Ma, N., Yu, H., Sun, H., Chang, X., Wu, Z., et al. (2019). Self-propelled Janus Microdimer Swimmers under a Rotating Magnetic Field. *Nanomaterials* 9, 1672. doi:10.3390/nano9121672

Zhang, Y., Zhang, L., Yang, L., Vong, C. I., Chan, K. F., Wu, W. K. K., et al. (2019b). Real-time Tracking of Fluorescent Magnetic Spore-Based Microrobots for Remote Detection of C. Diff Toxins. *Sci. Adv.* 5, eaau9650. doi:10.1126/sciadv.aau9650

Zhang, Y., Yuan, K., and Zhang, L. (2019a). Micro/Nanomachines: from Functionalization to Sensing and Removal. *Adv. Mater. Technol.* 4, 1800636. doi:10.1002/admt.201800636

Zhuang, J., Park, B.-W., and Sitti, M. (2017). Propulsion and Chemotaxis in Bacteria-Driven Microswimmers. *Adv. Sci.* 4, 1700109. doi:10.1002/advs.201700109

Conflict of Interest: The authors declare that the research was conducted in the absence of any commercial or financial relationships that could be construed as a potential conflict of interest.

Publisher's Note: All claims expressed in this article are solely those of the authors and do not necessarily represent those of their affiliated organizations, or those of the publisher, the editors. and the reviewers. Any product that may be evaluated in this article, or claim that may be made by its manufacturer, is not guaranteed or endorsed by the publisher.

frontiers in Bioengineering and Biotechnology

REVIEW
published: 29 November 2021
doi: 10.3389/fbioe.2021.773304

Paper-Based Point-of-Care Testing of SARS-CoV-2

Yuan Jia[1], Hao Sun[2]*, Jinpeng Tian[1], Qiuming Song[1] and Wenwei Zhang[3]**

[1]College of New Materials and New Energies, Shenzhen Technology University, Shenzhen, China, [2]School of Mechanical Engineering and Automation, Fuzhou University, Fuzhou, China, [3]Sino-German College of Intelligent Manufacturing, Shenzhen Technology University, Shenzhen, China

The COVID-19 pandemic has resulted in significant global social and economic disruption. The highly transmissive nature of the disease makes rapid and reliable detection critically important. Point-of-care (POC) tests involve performing diagnostic tests outside of a laboratory that produce a rapid and reliable result. It therefore allows the diagnostics of diseases at or near the patient site. Paper-based POC tests have been gaining interest in recent years as they allow rapid, low-cost detection without the need for external instruments. In this review, we focus on the development of paper-based POC devices for the detection of SARS-CoV-2. The review first introduces the principles of detection methods that are available to paper-based devices. It then summarizes the state-of-the-art paper devices and their analytical performances. The advantages and drawbacks among methods are also discussed. Finally, limitations of the existing devices are discussed, and prospects are given with the hope to identify research opportunities and directions in the field. We hope this review will be helpful for researchers to develop a clinically useful and economically efficient paper-based platform that can be used for rapid, accurate on-site diagnosis to aid in identifying acute infections and eventually contain the COVID-19 pandemic.

Keywords: paper-based, point-of-care, COVID-19 diagnostics, immunoassay, CRISPR

OPEN ACCESS

Edited by:
Yunlu Pan,
Harbin Institute of Technology, China

Reviewed by:
Xiaolin Huang,
Nanchang University, China
Sabarish Vellatheri Indran,
Sanofi Pasteur, United States

****Correspondence:***
Yuan Jia
jiayuan@sztu.edu.cn
Hao Sun
sh@fzu.edu.cn
Wenwei Zhang
zhangwenwei@sztu.edu.cn

Specialty section:
This article was submitted to Biosensors and Biomolecular Electronics, a section of the journal Frontiers in Bioengineering and Biotechnology

Received: *09 September 2021*
Accepted: *10 November 2021*
Published: *29 November 2021*

Citation:
Jia Y, Sun H, Tian J, Song Q and Zhang W (2021) Paper-Based Point-of-Care Testing of SARS-CoV-2. Front. Bioeng. Biotechnol. 9:773304. doi: 10.3389/fbioe.2021.773304

INTRODUCTION

The new coronavirus (SARS-CoV-2) caused pneumonia (COVID-19) outbreak has quickly spread the world and developed into a global pandemic. It has turned the lives of billions of people upside down and created chaos in healthcare, economic, and social domains (Mofijur et al., 2021). Looking back on history, although other infectious disease outbreaks have caused serious social and economic repercussions, such as the Middle East respiratory syndrome (MERS-CoV) and severe acute respiratory syndrome (SARS-CoV), none of them have posed the same level of threat to mankind as COVID-19 (Sohrabi et al., 2020; Wang et al., 2021).

SARS-CoV-2 is a positive-stranded non-segmented single-stranded RNA virus with a 29.9 kb genome length (Mousavizadeh and Ghasemi, 2021) (**Figure 1A**). Despite being a variant of a large group of viruses that cause the common cold, MERS-CoV, and SARS-CoV (Zhou et al., 2020), SARS-CoV-2 has four distinctively interconnected traits: high reproduction number, a large number of asymptomatic or mild symptom cases, relatively long incubation period, and survival of the virus in some environments (World Health Organization, 2020). In addition, it has been found that asymptomatic patients may have the same viral load as the symptomatic patients, thus making them both susceptible as a source of viral transmission, even in the early stages of the infection (Gao et al., 2021). Vaccines have been developed to prevent infection. However, SARS-CoV-2 mutations in

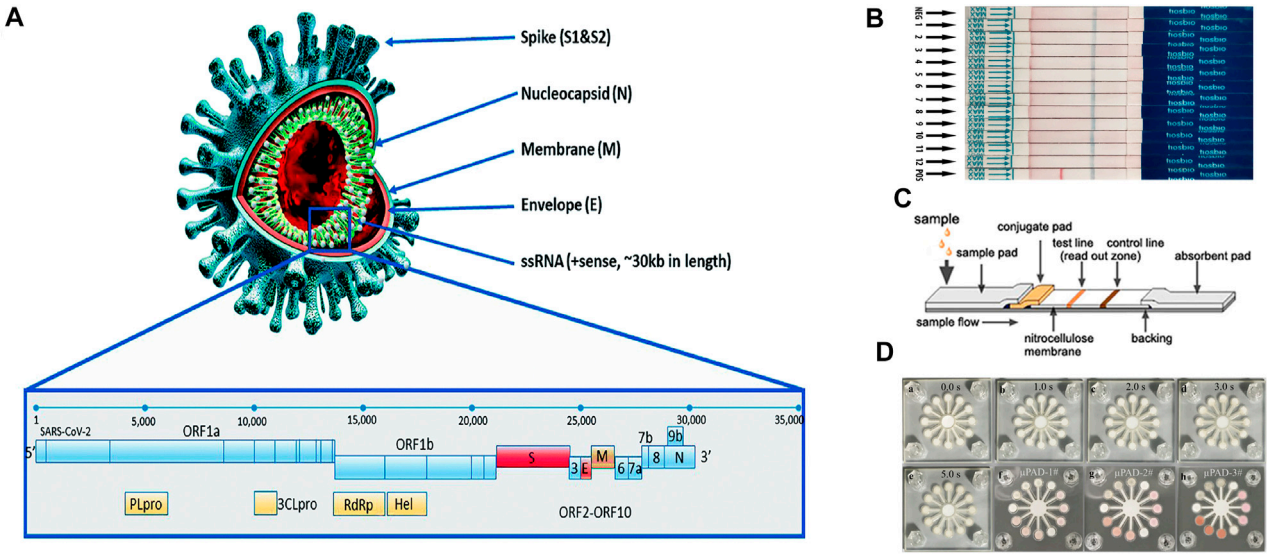

FIGURE 1 | (A) Structural proteins of SARS-CoV-2: envelope (E), membrane (M), spike (S), helicase (Hel), and nucleocapsid (N). Adapted with permission from (Kubina and Dziedzic, 2020) under Creative Commons license; **(B)** dipstick paper test. Adapted with permission from (Zheng Y.-Z. et al., 2021) under Creative Commons license; **(C)** lateral flow paper test. Adapted with permission from (He et al., 2016) under Creative Commons license; **(D)** microfluidic paper-based analytical devices. Adapted with permission from (Sun et al., 2019) under Creative Commons license.

the spreading of the disease pose a great challenge to the efficacy of vaccines (Dos Santos, 2021). Therefore, at the current stages of the pandemic, the development of diagnostic technologies is of critical importance as fast and accurate identification of early case clusters is still the key intervention measure to stop transmission. Nevertheless, because 51–67% of the world's population today lack equitable access to essential public health services (United Nations, 2020), the economically efficient and easy-to-use paper-based POC tests have been given serious consideration as a potential method for COVID-19 diagnostics.

Paper was first considered as a viable substrate material for enabling fluidic control for chromatography (Muller and Clegg, 1949). The first fully operable paper-based POC device was introduced by Whiteside's group in 2007 (Martinez et al., 2007; Sachdeva et al., 2021b). Since then, thanks to advantages including self-driven flow, a relatively high surface to volume ratio, ubiquity, and superb biocompatibility (Gong and Sinton, 2017), different types of paper devices such as dipstick tests (Yetisen et al., 2013), lateral flow devices (Huang et al., 2016; Zhou et al., 2019; Wu et al., 2020), and microfluidic paper-based analytical devices (μPADs) (Morbioli et al., 2017; Komatsu et al., 2018) have been extensively studied in academia and some of them have been successfully converted to commercial products (**Figures 1B–D**). They represent one of the promising technologies featuring cost-effectiveness, portability, and accessibility that are particularly useful in the field of POC medical diagnostics (Jia et al., 2018), environmental testing (Sun et al., 2019), and food quality assessment (Li et al., 2012). In the diagnostics of infectious diseases, paper-based POC devices have been demonstrated for the detections of human norovirus (Han et al., 2016), human papillomavirus (HPV) (Rodriguez et al., 2016), Hepatitis B (Li et al., 2015), West Nile virus (Channon et al., 2018), *etc*. Additionally, paper-based POC devices have shown comparable performances to conventional instruments in terms of both sensitivity and accuracy, while providing a faster turnaround time (Gong and Sinton, 2017). Therefore, this technology can be leveraged for detecting SARS-CoV-2 detection.

Given the urgency of the subject matter, several reviews on COVID-19 POC diagnostics methods have been published, which have provided valuable insights into the developmental progress and the outstanding issues for commercialization (Zhu H. et al., 2020; Choi, 2020; Wang et al., 2021). However, almost all of the reviews focused on the POC aspect, which applies to both paper-based platforms and conventional microfluidic platforms such as PDMS, PMMA, and others. This on one hand extends the scope of the existing reviews, but on the other hand, can only provide limited information on paper-based methods. Additionally, the few available reviews dedicated to paper-based methods are written in the early stage of the pandemic, and great progress has been made in paper-based POC devices since then (Antiochia, 2021). Therefore, a comprehensive review of paper-based COVID-19 diagnostics methods is still needed. In this review, we focus on the development of paper-based POC devices for the detection of SARS-CoV-2. The review first introduces the available paper-based SARS-CoV-2 detection methods that include immunoassay tests, nucleic acid amplification tests (NAAT), and Clustered Regularly Interspaced Short Palindromic Repeats/CRISPR associated proteins (CRISPR/Cas) systems. It then presents the state-of-the-art paper devices and their analytical performances, as well as the advantages and drawbacks. Finally, limitations of the paper devices are discussed, and prospects are given with the hope to identify research opportunities and directions in the field.

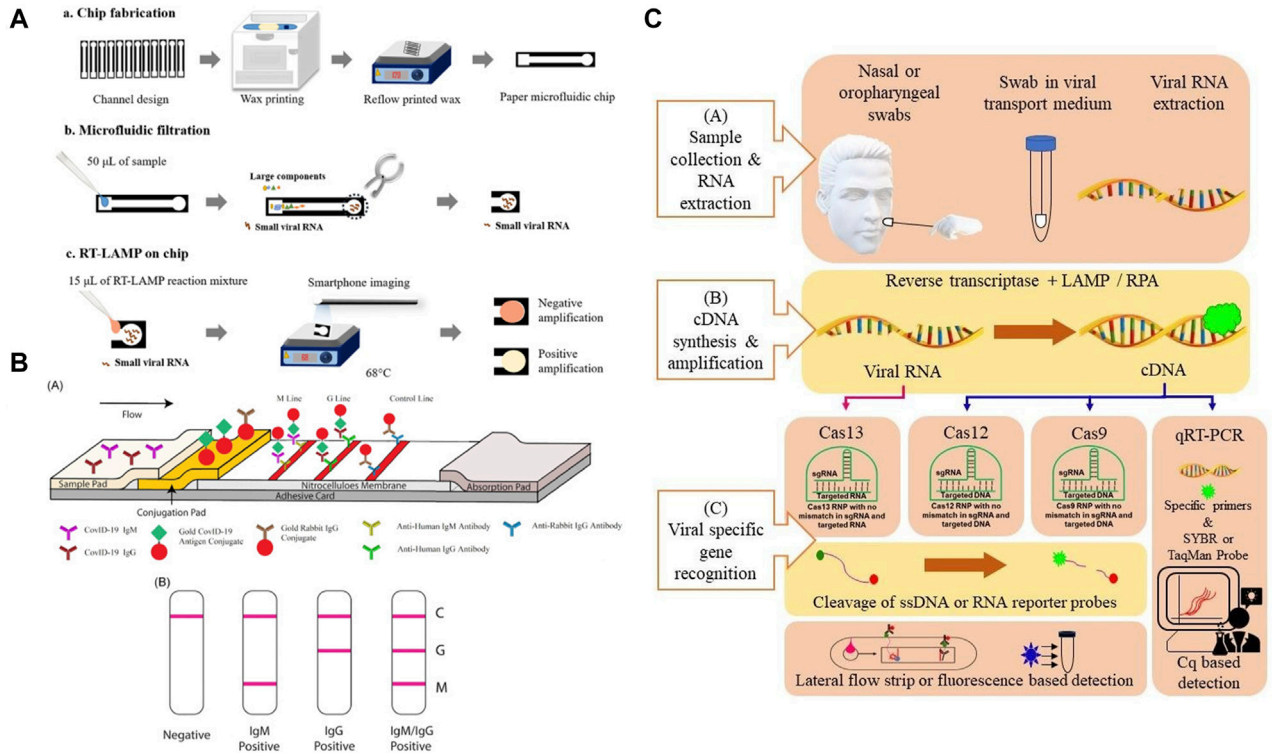

FIGURE 2 | (A) Principle of a typical Nucleic acid amplification test. Adapted with permission from (Kaarj et al., 2018) under Creative Commons license; **(B)** principle of a typical lateral flow test. Adapted with permission from (Li et al., 2020) under Creative Commons license; **(C)** principle of a CRISPR test. Adapted with permission from (Javalkote et al., 2020) under Creative Commons license.

PAPER-BASED SARS-COV-2 DIAGNOSTIC METHODS

According to the World Health Organization (WHO), because of its relatively high sensitivity and specificity, reverse transcription-polymerase chain reaction (RT-PCR)-based SARS-CoV-2 RNA detection from respiratory samples (e.g., nasopharynx) is the standard method for diagnosis. However, the conventional method still has the disadvantages of requiring expensive laboratory instruments and skilled laboratory personnel, which can be difficult to obtain in an underdeveloped area (Habibzadeh et al., 2021). Therefore, paper-based POC diagnostic methods have the potential to complement the conventional diagnostic method. The current paper-based diagnostic methods can be grouped based on the detection targets, including (a) detection of SARS-CoV-2 viral genes, (b) detection of viral antigens (c) detection of antibodies (serological test), each of them serves a different diagnostic need. The viral gene and antigen detection tests detect present viral infections, whereas serological tests determine prior infections (Antiochia, 2021). Of these, the immunoassay tests in particular lateral flow immunoassay tests (LFIA) are designed to target antibodies and antigens. The other methods including NAAT and CRISPR/Cas detect viral genes but rely on different detection approaches. In this section, we introduce the available paper-based SARS-CoV-2 diagnostic methods (**Figure 2**).

Lateral Flow Immunoassay

Relying on the natural wicking property of paper, LFIA is the most commercially successful paper-based POC diagnostic device to date. Although the most commonly known LFIA is the home pregnancy test, it has developed into the go-to method for the rapid detection of various biomarkers and substances (Liu and Rusling, 2021). The underlying principle of the LFIA is to utilize the specific binding between antibodies and antigens, proteins, or hormones. Unlike conventional PCR, LFIA is amplification-free, therefore much easier to operate. The typical device design of an LFIA consists of a sample pad, a conjugation pad, and an absorbent pad. Target analyte solution is first absorbed in the sample pad and moved toward the conjugation pad through cellulose membrane by capillary force. Here, a coloring agent labeled antibody or DNA/RNA oligonucleotide that is specific to the analyte forms a conjugate with the analyte and is transported along the membrane. Affinity ligands that are specific to the target analyte/conjugated antibody complex are immobilized in designated zones, which are called “test lines”. When the solution containing the complex reaches the test line, a signal in terms of a color change is generated as soon as the analyte is captured by the bioreceptor. The solution continues to flow across the membrane until it reaches the “control line”. The control line contains affinity ligands that will capture the conjugate with or without the presence of an analyte in solution to confirm that the assay is working properly. Finally, the excess solution reaches the

absorbent pad at the end of the strip and thus completing the assay (Yuce et al., 2021). For the case of SARS-CoV-2, its characteristic protein such as N protein and S protein can specifically bind to commonly used receptors IgG or IgM (Chen et al., 2020).

Nucleic Acid Amplification Tests

LFIAs primarily use antibodies as recognition elements and focus on detecting other antibodies, proteins, and hormones, etc (Koczula and Gallotta, 2016). However, because there is no possibility to enhance the response of LFIAs by enzyme reactions, the sensitivity of LFIAs is often limited (Mahmoudi et al., 2019). Additionally, nucleic acids are less prone to integrity loss. Therefore, nucleic acid detection is a more accurate approach when compared with immunoassays (Reid et al., 2020). The working principle of NAATs is to first generate copies of the target gene sequence through amplification and subsequently use a detection probe to produce a signal. The amount of signal produced is directly proportional to the nucleic acid concentration (Ballard and Ozcan, 2018). Therefore, similar to the conventional PCR-based testing, NAATs can be used to specifically identity target gene in a relatively low concentration and are regarded as one of the most sensitive of all available paper-based POC tests for infectious disease diagnosis (Kaur and Toley, 2018). Also similar to conventional PCR testing, there are three main steps in a NAAT assay: sample preparation (including extraction purification), amplification, and detection. Of these, the sample preparation step often involves the lysis of biological samples to release nucleic acids, which are then purified by separating from other lysed components and eluting (Magro et al., 2017). Nasopharyngeal swab or throat swab of sputum is frequently used for upper respiratory tract specimen collection, and subsequent centrifugation and filtration procedures may be required (Gao et al., 2021). During the amplification step, the nucleic acids are replicated from a template to obtain a large number of specific nucleic acid fragments for subsequent detection. Amplification in NAATs can be done either by on-chip PCR or isothermal amplification. Similar to the conventional method, the on-chip PCR requires thermocycling to mediate DNA melting, followed by primer annealing and extension (Niemz et al., 2011). Contrary to PCR, isothermal amplification is developed to replace the thermal cycling steps to simplify and lower the cost of NAATs. It copies target nucleic acids by using enzymes to denature the double strands of DNA and specially designed primer sets to amplify a target sequence (Gill and Ghaemi, 2008). Isothermal amplification techniques including loop-mediated isothermal amplification (LAMP), nucleic acid sequence-based amplification (NASBA), transcription-mediated amplification (TMA), rolling circle amplification (RCA), and recombinase polymerase amplification (RPA) have been used for developing COVID-19 diagnostic tests (Hosseini et al., 2020). the detection of NAATs is accomplished either by tagging the amplified nucleic acids with specific reporter molecules such as fluorescence-based dyes or measuring turbidity, which is a by-product (magnesium pyrophosphate) of DNA polymerization (Lee et al., 2008).

Combining the lateral flow technique and target gene amplification, NALF is the most commonly found paper-based NAAT device type. Currently, there are two primary methods for performing lateral flow nucleic acid tests, NALF and nucleic acid lateral flow immunoassay (NALFIA). Both NALF and NALFIA methods combine the power of enzymatic exponential amplification of the target gene sequence with the sensitivity and ease of use offered by the LFIA technique (Jauset-Rubio et al., 2016a). Although these methods detect target nucleic acids via hybridization to complementary sequences, their binding principles are different as NALF directly detects DNA exploiting capture and labeled reporter oligonucleotide probes, whereas NALFIA detects hapten-labeled DNA using capture and labeled reporter antibodies or streptavidin (Jauset-Rubio et al., 2016b). A typical workflow of lateral flow nucleic acid tests comprises nucleic acid extraction from biological samples, nucleic acid amplification, and the detection of an analyte through LFAs using labeled color-changing agents (Zheng C. et al., 2021).

Clustered Regularly Interspaced Short Palindromic

The CRISPR system is originally discovered in bacteria as a defense mechanism to fight against foreign nucleic acid invasions. When the guide RNA (gRNA) recognizes the genetic sequence of the foreign nucleic acids, it activates the Cas endonuclease to cut off the intruder's genetic sequence (Wright et al., 2016). CRISPR so far has discovered three major systems including Cas9, Cas13, and Cas12 (Li et al., 2019a). However, it is only discovered recently that it can be considered as a novel diagnostic tool for the detection of nucleic acids. For instance, Cas12a is one of the nucleases that possess collateral cleavage activities on single-stranded DNA (ssDNA) under the guidance of a gRNA. After recognizing its specific DNA targets, the Cas12a can be activated, cleave the collateral ssDNA reporter and generate a fluorescent signal (Gootenberg et al., 2018). It offers high sensitivity, specificity, simplicity and has been successfully applied to pathogen detection, cancer mutation detection, etc (Gootenberg et al., 2017). Recently, CRISPR has been combined with paper-based lateral flow techniques and used as a diagnostic tool for rapid detection of COVID-19. To obtain a sufficient amount of the target gene, an amplification step is usually included. To avoid the use of external a thermal cycler, isothermal amplification such as LAMP and RPA are also commonly used with the CRISPR/Cas systems.

APPLICATION OF PAPER-BASED POC TESTS FOR COVID-19

In this section, state-of-the-art paper-based POC devices are grouped by their detection methods and reviewed. Since both NAATs and lateral flow nucleic acid tests differ only in paper device design, they are categorized in the same group. The advantages and disadvantages of the tests are individually

discussed. In addition, tables are listed in the end to give a quick comparison between each work in each group.

Paper-Based Immunoassay Tests

According to the classification of detection targets, immunoassay tests are mainly used for antigen and antibody detection. Because of their advantages in operation simplicity, cost-effectiveness, and rapid detection time, paper-based immunoassay tests are usually used to complement SARS-CoV-2 nucleic acid detection. Based on different detection techniques, immunoassays mainly can be divided into LFIA, enzyme-linked immunosorbent assay (ELISA), and chemiluminescence.

Utilizing LFIA, Li and co-works developed a paper-based POC device for the detection of SARS-CoV-2 antibodies in human blood samples with a visual readout. SARS-CoV-2 Spike Glycoprotein (S1) recombinant antigen, which was conjugated to colloidal gold nanoparticles (AuNP), was chosen to bind to both SARS-CoV-2 immunoglobulin M (IgM) and immunoglobulin G (IgG) antibodies. When patient blood samples were introduced to the paper strip, anti-SARS-CoV-2 IgG and IgM antibodies, if present in the specimen, would specifically bind to the antigen on the conjugate pad, and the complex would subsequently bind to the antibodies on the test line. The detection sensitivity and specificity were obtained using whole blood samples collected from 397 PCR confirmed COVID-19 patients and 128 healthy individuals. The overall testing sensitivity was 88.66% and specificity was 90.63%, and the total test time was 15 min (Li et al., 2020). Using a direct antigen-antibody interactions principle, Wen and co-workers developed a LFIA by fixing SARS-CoV-2 nucleocapsid protein (N) to the surface of the strip and using anti-human IgG functionalized AuNPs to detect antibodies in serum. The IgG antibody will specifically bind to the anti-human IgG mAbs presented in the conjugation pad. The resulting complex subsequently binds to the N protein to induce a color change at the test line. The clinical test revealed a 69.1% sensitivity and a 100% specificity using samples collected from 55 clinically confirmed patients and 30 normal human sera (Wen et al., 2020). Despite their usefulness, reports have indicated that AuNP-LFIAs typically are limited by their relatively low sensitivity and high false-negative rates. To address these, Huang and co-workers carried out optimizations of the AuNP-LFIA include altering the pH value and the amount of antihuman IgM, the assay achieved higher sensitivity and specificity of 100 and 93.3%, respectively. However, the sample size in this work is relatively small, which consists of human serum samples collected from five confirmed patients and 14 healthy individuals (Huang et al., 2020). Zhou and co-workers first proposed the use of a polymer-type structure-directing agent polyethyleneimine to assist in copper *in-situ* growth (PEI-CISG) on the surface of AuNP probes. Because PEI-CISG can control the shape and size of the resultant Au-CuNP core-shell nanostructures, the detection signal of the conventional AuNP-LFIA can be amplified. The authors incorporated the PEI-CISG into a commercial AuNP-LFIA SARS-CoV-2 detection kit, and the PEI-CISG treated LIFA successfully detected all previous false-negative samples (Zhou et al., 2021b). In a later work, the same group developed an alternative fluorescent nanomaterial to replace the conventional AuNPs, the quantum dot nanobeads (QBs). Because of their high luminescent intensity and resistance to matrix interference, the QB-LFIA detected SARS-CoV-2 total antibodies in 69 human serum samples with a sensitivity of 97.1% and a specificity of 100% (Zhou et al., 2021a). In another study, lanthanide-doped polystyrene nanoparticles (LNPs) were used as a fluorescent reporter in a LFIA strip to detect anti-SARV-CoV-2 IgG in human serum. A recombinant N-phosphoprotein was used to specifically capture the target IgG. The test showed a 100% sensitivity and an 88% specificity using samples collected from seven confirmed patients and 51 normal human serum (Chen et al., 2020).

Instead of nitrocellulose based-LFA strips, Kim and co-workers developed a vertical flow paper device to detect SARS-CoV-2 antibodies. In this work, SARS-CoV-2 N protein was fused with a cellulose-binding domain (CBD) for the detection of target antibodies as cellulose-CBD interaction would allow rapid immobilization of SARS-CoV-2 antigens on cellulose paper strips. Also, leveraging the multivalency of target antibodies (both IgG and IgM), a double-antigen sandwich format was developed and the functionalized antigens were used as both capture and reporter reagents, replacing the anti-human antibodies. Specifically, the capture and reporter reagents are NP-CBD and biotinylated NP (NP-biotin), respectively. Biotin was used to conjugate NP with horseradish peroxidase (HRP) via a biotin−streptavidin (SA) interaction. Thus, HRP could be associated with CBD to form enzyme-antibody-CBD sandwich complexes as the presence of SARS-CoV-2 antibodies link the capture and reporter reagents. Samples were collected from three confirmed patients' serum and a 96.2 and 93.9% sensitivity was reported for IgG and IgM detection, respectively (Kim et al., 2021). Finally, instead of lateral flow strips, Kasetsirikul and co-workers developed a paper-based ELISA test for the detection of SARS-CoV-2 humanized antibodies. Circular paper reactions wells were fabricated by laser cutting and were then laminated for easy sample handling. Recombinant SARS-CoV-2 nucleocapsid antigen was coated on the reaction wells to capture the SARS-CoV-2 humanized antibody (Kasetsirikul et al., 2020).

Besides SARS-CoV-2 antibodies, paper-based devices for antigen detection have also been developed. Compared with antibodies, which usually do not appear in the early stage of infection, viral antigen has potential to become a viable target for early diagnosis of SARS-CoV-2 infection. Reports have indicated that the NP antigen is one of the best early diagnostic markers in SARS-CoV and can be detected up to 1 day before the appearance of clinical symptoms (Che et al., 2004). Based on this, Diao and coworkers proposed a lateral flow device based on fluorescence immunochromatographic principle to detect the SARS-CoV-2 NP antigen. Fluorescent microparticles-labeled mouse anti-NP antibody was immobilized on a nitrocellulose membrane for detecting NP antigen in nasopharyngeal swabs and urine samples within 10 min. By comparing with RT-PCR testing, a sensitivity of 68% and a specificity of 100% were achieved out of 251 patients (Diao et al., 2021). In another work, a dipstick test

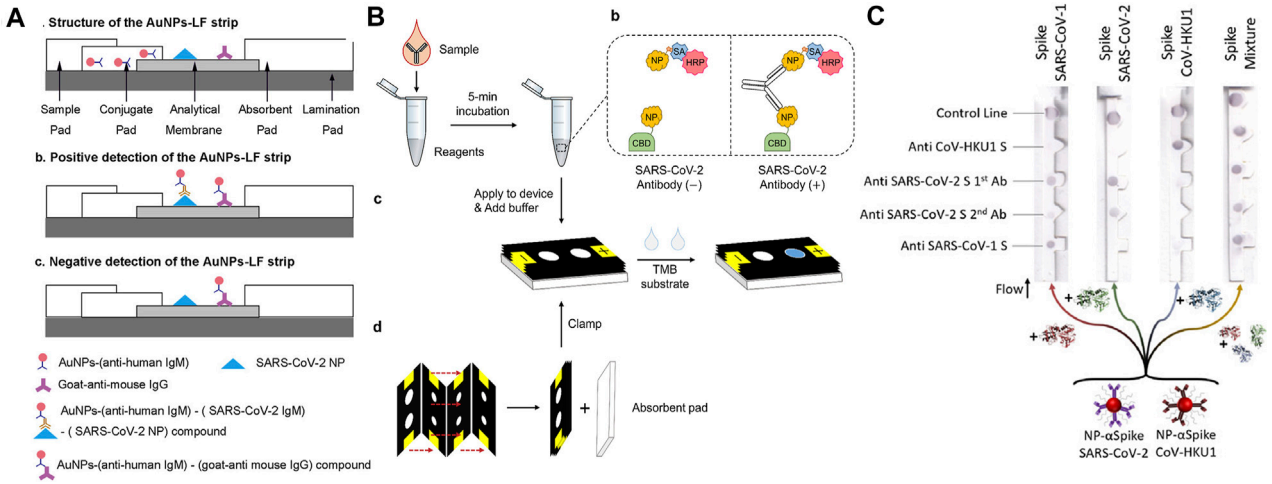

FIGURE 3 | (A) Lateral flow paper-based antibody test. Adapted with permission from (Huang et al., 2020), under ACS Author Choice License; **(B)** antibody test using a μPAD. Adapted with permission from (Kim et al., 2021), copyright American Chemical Society 2021; **(C)** lateral flow paper-based antigen test. Adapted with permission from (Hristov et al., 2021) copyright American Chemical Society 2021.

has been developed by Grant and co-workers for SARS-CoV-2 NP antigen detection. The dipstick test consists of a nitrocellulose membrane and a wicking pad, without sample and conjugate pads. Optical detection was achieved by conjugating red latex particles to commercially available polyclonal antibodies. However, no clinical samples were used in this study due to the specificity concern of the antibodies (Grant et al., 2020). Based on the chemiluminescence principle, Liu and co-workers developed a paper-based test for the detection of SARS-CoV-2 spike antigen (S antigen). Instead of using natural proteases such as HRP commonly used in paper-based enzymatic chemiluminescence assays, the authors developed a Co–Fe@ hemin-peroxidase nanozyme that can amplify immune reaction signals. Compared with HRP, the nanozyme is more stable and much suitable for POC testing. The assay achieved an ELISA comparable S antigen detection limit while reducing the operation time to approximately 15 min. However, no clinical samples were used in this study (Liu et al., 2021a). Hristov and co-workers developed a paper-based multiplexed antigen test that can differentiate S proteins from different coronaviruses including SARS-COV-1, SARS-COV-2, and CoV-HKU1 as well as spike protein variants from SARS-CoV-2. The test relied on a sandwich immunoassay and antibody cross-reactivity for antigen-specific test patterns. In their work, six antibodies were evaluated for antigen binding and sandwich immunoassay formation. By identifying specific binding patterns that are achieved by designating antibody-antigen reaction locations, fractions of the same spike protein can then be differentiated (Hristov et al., 2021). Finally, Yakoh and co-workers developed a paper-based electrochemical test for the detection of either SARS-CoV-2 anybody or antigen. Unlike previous LFIA tests, the electrochemical system is label-free, therefore does not require the use of reporter-labeled antibodies. Instead, the SARS-CoV-2 spike protein-containing receptor-binding domain is immobilized to capture incoming SARS-CoV-2 antibodies. The sensing scheme relies on the disruption of the redox conversion ([Fe (CN)6] 3-/4-) triggered by immunocomplex formation between the spike protein and target antibody. The test can also be extended for direct detection of the spike protein antigen of SARS-CoV-2 (Yakoh et al., 2021).

Representative paper-based antibody and antigen tests are illustrated in **Figure 3** and a summation table is given below (**Table I**). Generally, paper-based immunoassay tests completely satisfied the ASSURED criteria established by the World Health Organization (WHO). They have merits including low production cost, portability, ease of use, and long shelf life so that these tests are suitable for use in developing and low resource countries. However, when it comes to immunoassay tests, sensitivity and specificity have always been a concern. Other limitations also include the outcome of the tests are heavily dependent on the quality and preparation of the antibodies (Hu et al., 2017), it is difficult to obtain accurate quantitative information from immunoassay tests (Sachdeva et al., 2021a) and perform complex multiplexed assays due to a lack of fluidic control (Jia et al., 2020).

Paper-Based Nucleic Acid Tests

Paper-based nucleic acids tests combine the specificity of PCR and the portability of POC tests. They can be fully automated and have adequate sensitivity to identify clinical suspicious nucleic acid samples in relatively low concertations and are one of the most sensitive of all available POC tests for infectious disease diagnosis (Niemz et al., 2011). Garneret and co-workers developed a NAAT to detect SARS-CoV-2 by coupling isothermal amplification to paper-based microfluidic techniques. The device possessed capabilities including nucleic acids extraction, on-chip amplification using RT-LAMP, and naked-eye visualization for qualitative analysis. In this work, nasopharyngeal swabs were collected from suspected COVID-

TABLE 1 | Existing paper-based immunoassay tests.

Study	Receptor	Detection technique	Total time (excluding sample preparation)	R (min)eadout	LOD	Sensitivity/ specificity	Total clinical sample size
Li et al. (2020)	Antibody	LFIA	15	Colorimetric-AuNP	did not report	88.6%/90.63%	525
Wen et al. (2020)	Antibody	LFIA	15	Colorimetric-AuNP	did not report	69.1%/100%	85
Huang et al. (2020)	Antibody	LFIA	15	Colorimetric-AuNP	did not report	100%/93.3	19
Zhou et al. (2021a)	Antibody	LFIA	10	Colorimetric- PEI-CISG AuNP	did not report	100%/100%	10
Zhou et al. (2021b)	Antibody	LFIA	10	Fluorescent-QBs	did not report	97.1%/100%	69
Chen et al. (2020)	Antibody	LFIA	10	Fluorescent-LNP	did not report	100%/88%	58
Kim et al. (2021)	Antibody	Cellulose-binding domain	15	Colorimetric-TMB-HRP	5 nM	96.2%/93.9%	3
Kasetsirikul et al. (2020)	Antibody	ELISA	20	Colorimetric-TMB-HRP	9.00 ng μl^{-1}	N/A	N/A
Diao et al. (2021)	Antigen	LFIA	10	Fluorescent-FIC	did not report	75%/100%	251
Grant et al. (2020)	Antigen	LFIA	20	Colorimetric-Latex bead	0.65 ng/ml	N/A	N/A
Liu et al. (2021a, b)	Antigen	Chemiluminescence	15	Colorimetric-Nanozyme	0.1 ng/ml	N/A	N/A
Hristov et al. (2021)	Multiplexed antigen	30 min	30	Colorimetric-AuNP	0.1 nM	N/A	N/A
Yakoh et al. (2021)	Antibody or antigen	Electrochemical	30	Square voltammetry	0.14 nM	100%/90%	17

19 cases. Also, binder-free glass fiber was used as both extraction membrane and reaction membrane. The membranes were inserted into a 3D-printed disc to complete the POC device, which has a production cost of 2–4$. To prepare the sample, sample lysis and elution steps were performed manually using commercial buffers. Real-time RT-LAMP was used for the amplification of the Orf1ab gene. A DNA intercalating dye (SYTO-82) was used for measuring the fluorescence emission. The test took approximately 1 h to complete and a limit-of-detection (LOD) of 1 copy/μl was estimated (Garneret et al., 2021). However, the report indicated that the detection of only the ORF1ab gene cannot ensure reliable diagnostics of SARS-CoV-2 (Suo et al., 2020). Zhu and co-workers developed a multiplex RT-LAMP amplification method that used two LAMP primer sets in an isothermal reaction to simultaneously amplify SARS-CoV-2 target sequences (ORF1ab and the N gene) to improve the test accuracy. By labeling the amplicon products with FITC and biotin, Dig and biotin, respectively, the ORF1ab and N genes of SARS-CoV-2 were simultaneously detected by NALFIA through immunoreactions and biotin/streptavidin affinity binding. The test showed a LOD of 12 copies/reaction, a total run time of 1 h with a 15 min manual DNA extraction step, and a 100% test specificity as well as sensitivity was demonstrated by collecting and analyzing clinical oropharynx swab samples obtained from 33 patients infected with SARS-CoV-2 and 96 non-SARS-CoV-2 infected patients (Zhu X. et al., 2020). Also using the RT-LAMP amplification approach, Zhang and co-workers developed a one-pot direct RT-LAMP assay combined with lateral flow technology for the detection of SARS-CoV-2. Different from the previous works, NaOH solution was used to lyse the collected nasopharyngeal swab samples so that target nucleic acids (SARS-CoV-2 N gene and ORF1ab Gene) were directly released for isothermal amplification without nucleic acid extraction step, thereby shortening the tests time to ~40 min. NALFIA detection method through immunoreactions was also used in this work and the LOD was estimated to be 1 copy/μl (Zhang et al., 2021). Additionally, based on the NALF method, Yu and co-workers developed a paper device that is capable of simultaneous detection of three regions of the SARS-CoV-2 genome (RdRp, ORF3a, and the nucleocapsid (N)-protein gene) using RT-PCR amplification. The simultaneous detection of the three genes avoids cross-reactivity with other coronaviruses and possible false-negative results caused by mutations in the SARS-CoV-2 genome. The test allows the detection of SARS-CoV-2 in 30 min with a limit of detection (LOD) of 10 copies/test for each gene. However, a PCR instrument was necessary for the amplification of the genomic copies, thus limiting the possibility of the NALF assay to be developed into a POC test (Yu et al., 2020).

Other Isothermal amplification techniques have also been employed by the paper-based nucleic acid tests. Qian and co-workers developed a NALFIA test for the detection of SARS-CoV-2 N gene and S gene using a reverse-transcription recombinase polymerase amplification (RT-RPA) reaction. RPA is an isothermal amplification reaction optimally working between 37 and −42°C. It amplifies the target sequence using a recombinase, single-strand binding proteins, and a strand displacement polymerase (Magro et al., 2017). Compared with LAMP, RPA has the advantage of operating at a lower temperature. In this work, a forward and a FAM-labeled

reverse pair of primers specific to the target sequence were designed for amplification. By combining RT-RPA with lateral flow technology, after mixing the reaction components with running buffer, the mixture is delivered to the detection zone where dual FAM-labeled and biotin-labeled products are detected on a lateral flow strip. The test takes approximately ~45 min from sample collection to results and has a LOD of ~0.5 copy/μl (Qian et al., 2020). Xia and co-workers introduced a POC test for simultaneous detection of SARS-CoV-2 S gene and N gene by integrating reverse transcription–enzymatic recombinase amplification (RT–ERA), a modified version of RT-RPA. In their experiment, Mg^{2+} was used as the ERA activator and the authors designed a pair of nfo forward and reward primers to amplify an amplicon within both N and S genes. Nfo-affinity probes were also designed for the detection of the N and S gene. The approach demonstrated a detection limit of 0.05 copy/μl. The relatively high assay sensitivity allows target SARS-CoV-2 gene to be mixed directly with diluted throat swab without extra sample processing nor RNA purification, thereby simplifying the sample preparation step and reducing the overall analysis time to ~30 min (Xia and Chen, 2020). However, the amplification step for both works has to be completed off-chip. To address this, Liu and co-workers developed an integrated lateral flow RT-RPA assay for the detection of the SARS-CoV-2 N gene. During testing, the RT-RPA reaction components are introduced to the chip and then incubated. After incubation, amplification products and running buffer are mixed, then delivered to the lateral flow strips for easy qualitative results interpretations. This approach achieved a detection limit of 1 copy/μl and a total run time of ~30 min (Liu et al., 2021b).

Wu and co-workers instead used a barcoded isothermal nucleic acid sequence-based amplification technique (NASBA) to develop a two-stage test. After performing a rapid diagnosis on-chip using the NASBA reaction in stage one, the end product was sent to a central facility for pooled sequencing for improved detection accuracy and detailed analysis. Also, by introducing a FAM labeled and biotin-labeled RNA capture oligonucleotides into the NASBA reaction, both oligonucleotides can bind to different parts of the single-stranded RNA NASBA product. For target gene detection, neutravidin-conjugated carbon nanoparticles (NA-CNPs) were added to the lateral flow assay. The aggregation of NA-CNPs at the test line resulted in a color change. To achieve multiplexed sequencing, a sample-specific barcode pair was incorporated into the amplicon during the NASBA reaction to facilitate the selection in the sample pool in stage two. The second stage was then used to reconfirm the initial diagnosis and enabled centralized data processing. This approach allowed a quick decentralized readout within 2 h and achieved a detection limit of <50 copies of viral RNA per reaction (Wu et al., 2021). Additionally, methods for achieving detection signal amplification other PCR, LAMP, or other isothermal target amplification techniques have been developed. Wang and co-workers demonstrated a lateral flow nucleic acid immunoassay for rapid detection of SARS-CoV-2. The underlying principle of the assay relies on the affinity binding between the S9.6 monoclonal antibody with DNA–RNA hybrid molecules. In this work, the hybridized DNA-RNA double strands were formed by the specific SARS-CoV-2 DNA probes and the lysed virus genome (ORF1ab, envelope protein, and the N-protein gene). Upon introducing the target samples, the fluorescent-nanoparticle-labeled S9.6 antibody was used to bind to the double-stranded DNA–RNA hybrids. Unlike other nucleic acid detection techniques that use targe amplification, the sensitivity of this assay highly depends on the length of the DNA probe and the molar ratio of the antibody to the hybrid. The absence of nucleic acid amplification means that the assay does not suffer from contamination by amplicons. Also, the overall testing duration can be shortened and the process can be simplified. The assay demonstrated a PCR comparable LOD of 0.5 copies/μL. In addition, the assay also achieved a 100% sensitivity and 99% specificity, thus making the assay potentially viable for POC use (Wang D. et al., 2020).

Representative paper-based devices are illustrated in **Figure 4** and a summation table is also given below (**Table 2**). Although paper-based nucleic acids tests retained sensitivity and specificity of the conventional RT-PCR tests, and they represented a good solution for sample-in-answer-out testing in low-resource settings. However, like conventional PCR tests, paper-based nucleic acids tests also involve multiple physical and/or chemical steps, and existing works have not yet developed a fully integrated POC system, as one or more steps have to be completed off-chip. In this case, trained personnel are still required for administering these tests to avoid human mishandling. Therefore, designing paper-based nucleic acids tests that are fully integrated and usable by untrained users is the current goal and an unavoidable challenge that many POC tests face.

Paper-Based CRISPR/Cas Tests

CRISPR/Cas systems have been gaining tremendous attention in biotechnology since the modified CRISPR/Cas9 system was applied for gene editing in mammalian genomes (Cong et al., 2013). Recently, CRISPR-Cas systems, including CRISPR-Cas12 and CRISPR-Cas13, exhibit robust collateral activity against single-stranded DNA (ssDNA) and RNA targets, respectively. When combined with a FRET-based reporter, a fluorophore connected to a quencher via a short oligonucleotide sequence, the presence of the target can be thus confirmed. Such collateral activity provides the basis for highly specific, sensitive approaches for nucleic acid detection (Ali et al., 2020a).

Additionally, by exploiting the simplicity of isothermal amplification methods, such as LAMP and RPA, the detection of a few copies of the target nucleic acid can be readily achieved. In this regard, CRISPR-based diagnostic methods have been utilized in conjunction with paper-based platforms to achieve efficient POC testing of SARS-CoV-2 genes.

Broughton and co-workers developed a Cas12a-based DNA endonuclease Targeted CRISPR Trans Reporter (DETECTR) assay with a lateral flow platform for SARS-CoV-2 detection. In this assay, Cas12 gRNAs were designed to target the N and E genes of SARS-CoV-2. Upon performing simultaneous reverse transcription and isothermal amplification using loop-mediated amplification (RT-LAMP) for viral RNA extracted from patient nasopharyngeal or oropharyngeal swab samples and control RNA

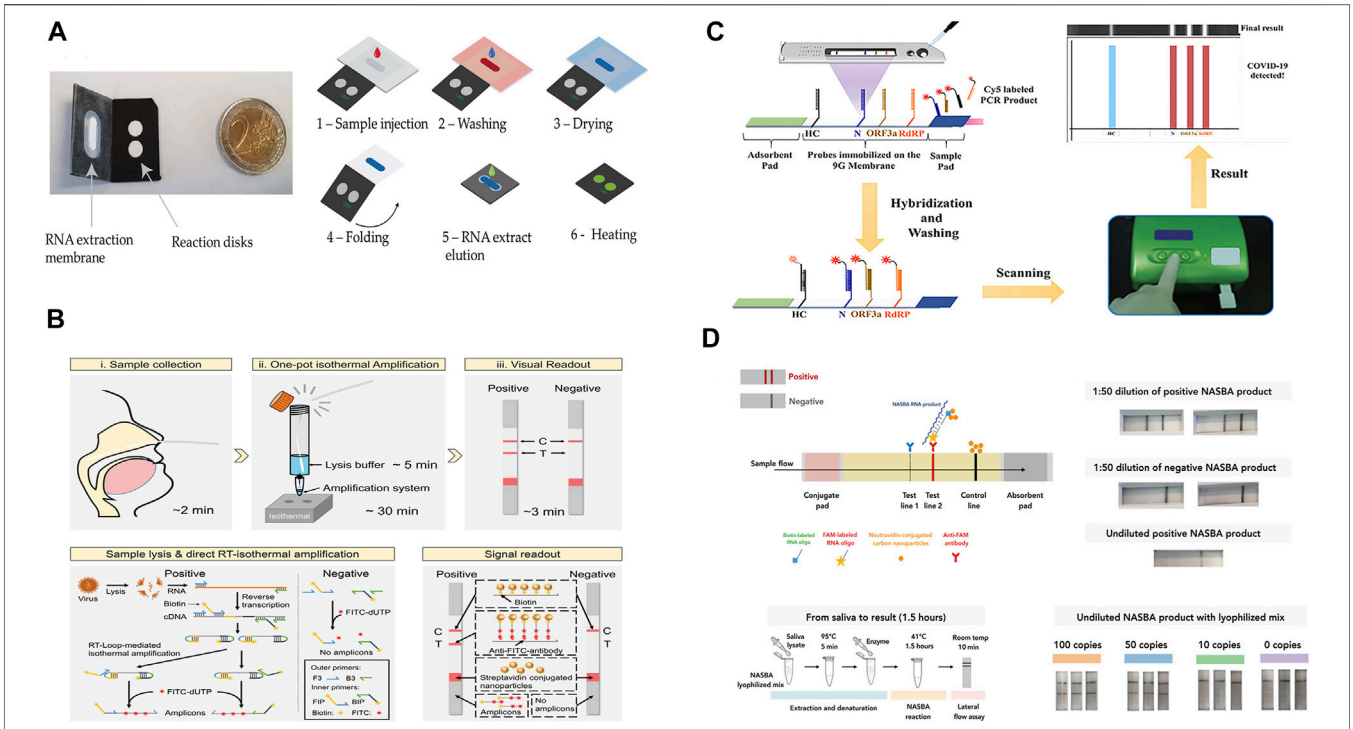

FIGURE 4 | (A) paper-based μPAD integrated with RT-LAMP amplification. Adapted with permission from (Garneret et al., 2021) under Creative Commons license; **(B)** lateral flow combined with one-pot RT-LAMP amplification. Adapted with permission from (Zhang et al., 2021), copyright American Chemical Society 2021; **(C)** multiplex detection of SARS-CoV-2 genome. Adapted with permission from (Yu et al., 2020) copyright American Chemical Society 2020; **(D)** two-stage detection and multiplexed sequencing technique. Adapted with permission from (Wu et al., 2021) under Creative Commons license.

TABLE 2 | Existing paper-based nucleic acid tests.

Study	Target gene	Amplification method	Total time (excluding sample preparation)	Extraction required	LOD	Sensitivity/ specificity	Total clinical sample size
Garnt et al. (2020)	ORF1ab	RT-LAMP	1 h	Off-chip	1 copy/μl	100%/100%	21
Zhu et al. (2020a, b)	ORF1ab, N	RT-LAMP	45 min	Off-chip	12 copies/ reaction	100%/100%	129
Zhang et al. (2021)	ORF1ab, N	One pot RT-LAMP	40 min (from sample collection to results)	No extraction	2 copy/μl	100%/100%	18
Yu et al. (2020)	RdRp, N, ORF3a	RT-PCR	30 min	Off-chip	10 copies/ reaction	100%/99%	162
Qian et al. (2020)	N, S	RT-RPA	45 min (from sample collection to results)	No extraction	0.5 copy/μl	86.7%/100%	51
Xia and Chen (2020)	N, S	One-pot RT-ERA	30 min	Off-chip	0.05 copy/μl	N/A	N/A
Liu et al. (2021a, b)	N	On-chip RT-RPA	30 min	Off-chip	1 copy/μl	97%/100%	54
Wu et al. (2021)	S	NASBA reaction	1–2 h	Off-chip	30 copy/μl	N/A	N/A
Wang et al. (2020a, b)	ORF1ab, N	No Amplification	40 min	No	0.5 copy/μl	100%/99%	734

targets, the Cas12a trans-cleavage activity allowed the detection of the target amplicons was achieved by cleaving the FAM-biotin reporter molecules at the test line of the lateral flow strip. Using a fluorescence-based readout, qualitative detection with a LOD of up to 10 copies/μL was achieved with an operating time of 45 min.

The assay was validated by testing 82 clinical respiratory swab samples collected from confirmed COVID-19 patients and others. After comparing with standard RT-PCR tests, 95% sensitivity and 100% specificity were achieved (Broughton et al., 2020). Nguyen and co-workers developed a modified

Cas12a-based assay by engineering guide RNA extensions to affect Cas12a trans-cleavage activity. The method was referred to as ENHANCE (enhanced analysis of nucleic acids with crRNA extensions) by the authors and was used for the detection of the SARS-CoV-2 N gene. The authors discovered that the extensions of guide RNA on the 3′ or 5′ end would increase the trans-cleavage activity, of which, the 3′ end with 7-mer extensions showed the highest activity. The authors contributed this improvement to the conformational changes of the LbCas12a effector induced by the engineered guide RNA. By combining with isothermal amplification of SARS-CoV-2 RNA using RT-LAMP, the modified Cas12a assay was incorporated in a lateral flow assay to detect SARS-CoV-2 viral. Similar to the previous work, the detection of the target amplicons was achieved by cleaving the FITC-ssDNA-Biotin reporter. The assay demonstrated a LOD of 3–300 RNA copies. However, no clinical samples were used for the assay validation (Nguyen et al., 2020). Ali and co-workers also developed a Cas12-based SARS-CoV-2 lateral flow detection method (iSCAN) incorporating RT-LAMP. Different from the DETECTR method, by replacing the Cas12a effector with Cas12b, the author achieved one-pot detection of SARS-CoV-2 viral, thereby further improving the assay accessibility. However, the author discovered simultaneous mixing of various components in one pot leads to a substantial reduction in detection performance and sensitivity. After optimizing the one-pot process flow by employing special tubes that allow sequential mixing of reaction components, a LOD of 100 copies per reaction was found. Also, a comparable detection sensitivity 86% and specificity was obtained by evaluating clinical samples from 21 SARS-CoV-2-positive patients and three healthy individuals (Ali et al., 2020a). Tsou and co-workers also developed a Cas12a-based SARS-CoV-2 detection method. Instead of RT-LAMP, the authors incorporated RT-RPA as the isothermal amplification technique, and the guide RNA was designed to target the S, M, and N genes of the virus. Similarly, the detection of target amplicons was achieved by cleaving the single-stranded DNA-FAM-quencher reporter at the lateral flow strip. The authors discovered that the guide RNA targeting M gene of the SARS-CoV-2 showed the highest efficiency and detection sensitivity with a LOD of 0.1 copy/μl. In addition, when cell lysate and supernatant of SARS-CoV-2 samples were directly added to the RT-RPA reaction without the RNA extraction step, a LOD of 10 copies/μl was found. The method was validated using 10 clinical nasopharyngeal swab samples of COVID-19 patients and 12 healthy individuals and an overall 100% sensitivity and 100% specificity were achieved. However, the validation experiments were performed in-tube instead of a lateral flow strip (Tsou et al., 2021). Moreover, to further improve the testing efficiency and facilitate the loss in the signal caused by viral mutations, Ooi and co-workers developed a Cas12-based method to detect wild-type and mutated SARS-CoV-2 viral. The authors discovered that the engineered effector enAsCas12a was more robust toward both the operating temperature and mismatch tolerance. Additionally, the use of modified guides improves reaction kinetics. Particularly, hybrid DNA-RNA guides would give higher collateral activities compared to regular gRNAs, thus enhancing the on-target signal while suppressing off-target background to negligible levels. The enhanced sensitivity and specificity allowed the assay to be completed without an RNA purification step. The authors first showed that the assay still worked when a S254F mutation was present in the viral template. The assay was then validated by testing nasopharyngeal swab samples obtained from 21 confirmed COVID-19 patients and 21 healthy individuals without a RNA purification step. A sensitivity of 80%, a specificity of 100%, and a LOD of 40 copies/μl (2 copies/μl for purified RNA samples) were determined with a total operating time of 30 min (Ooi et al., 2021). To resolve the current single gene detection limitation of the CRISPR-based lateral flow assay, Yin and co-workers developed a lab-on-paper platform for multiplex gene diagnosis of SARS-CoV-2. This method also combined RT-RPA and CRISPR-Cas12a detection. Paper-based CRISPR detection chambers and a 3D-printed RPA reactor were initially isolated through a normally closed sucrose valve. The detection reagents were pre-loaded in the detection chambers. After RPA amplification at a pre-set time, the sucrose valve automatically opened and amplicons migrated to the CRISPR-based detection chambers, reacting with the pre-loaded detection reagents with specific guide RNAs. The platform was capable of simultaneously detecting the N gene and S gene of the SARS-CoV-2 virus as well as a reference control in a single clinical sample with a total turnaround time of 1 h. The method was validated using RNA samples extracted from 21 nasopharyngeal swab clinical samples. A LOD of 100 copies per test was determined and 100% sensitivity and specificity were reported (Yin et al., 2021).

In addition to Cas12, Cas13a was discovered to possess the target RNA triggered trans-cleavage activity (Li et al., 2019b). Patchsung and co-workers used the specific high-sensitivity enzymatic reporter unlocking (SHERLOCK) technique for rapid detection of SARS-CoV-2. Similar to Cas12-based detection, SHERLOCK detection also relies on RT–RPA to amplify target gene segments, followed by CRISPR–Cas-mediated detection of the amplified genes. The authors designed a total of four RPA-primer pairs and the corresponding guide RNAs targeting S, N, and Orf1ab genes of SARS-CoV-2. Overall, the SHERLOCK detection system achieved 100% specificity and 88% sensitivity using SARS-CoV-2 RNA extracted from nasopharyngeal and throat swabs of infected patients with a LOD of 40 RNA copies per reaction. In addition, the technique was amenable to multiplexed detection in a single lateral-flow strip by incorporating an internal control for ribonuclease contamination (Patchsung et al., 2020). Additionally, based on the Cas 13 detection method, Li and co-workers developed a lateral flow test for targeting N genes of SARS-CoV-2. By incorporating reverse-transcription and recombinase-aided amplification (RT-RAA) with conventional colloidal gold test strip approach, this assay achieved a relatively high LOD of 1 copy/μl with a naked eye readout. However, the authors did not elaborate on the cause for this sensitivity enhancement. Additionally, to reduce the false-positive results commonly associated with the colloidal gold test strips, the authors adjusted the assay detection mode so that the cleaved FAM-biotinylated reporter molecules could

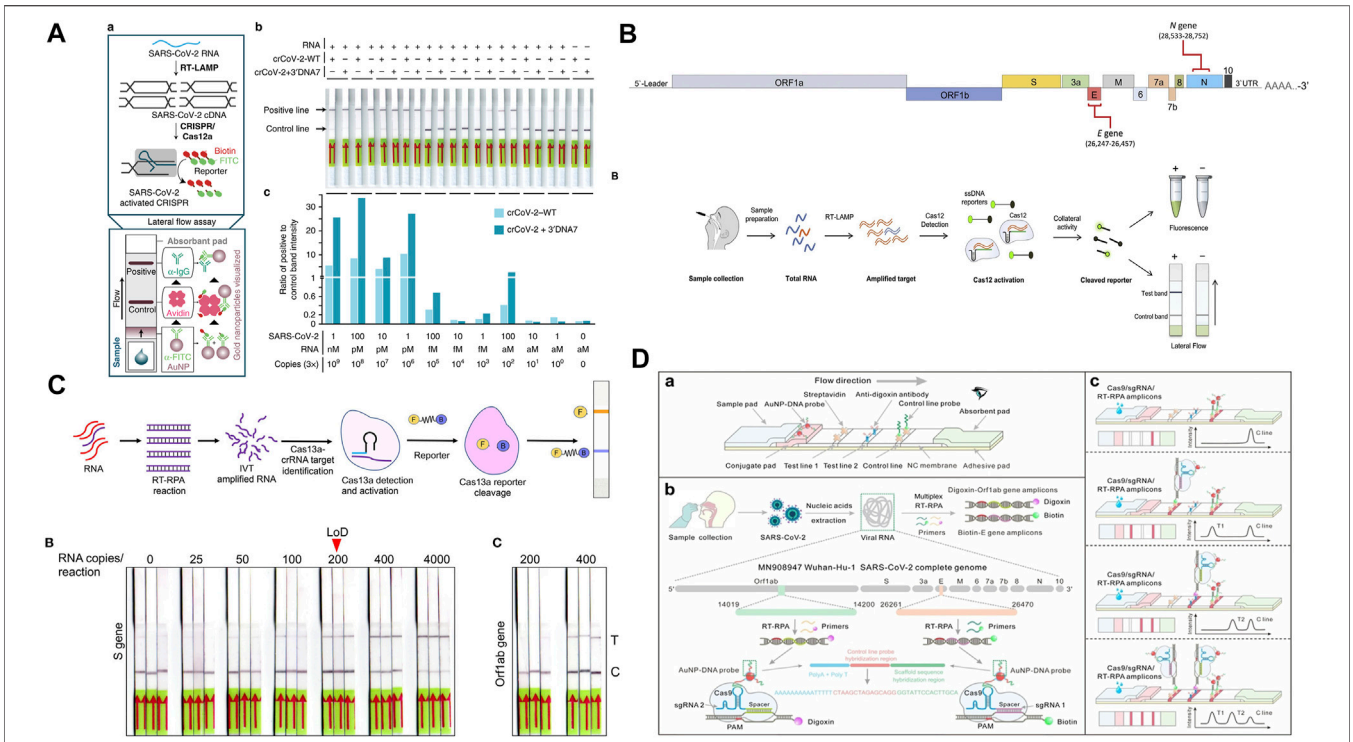

FIGURE 5 | (A) Cas12-based ENHANCE method with RT-LAMP amplification. Adapted with permission from (Nguyen et al., 2020) under Creative Commons license; **(B)** CRISPR–Cas12a-based iSCAN assay. Adapted with permission from (Ali et al., 2020a) under Creative Commons license; **(C)** Cas13a-based lateral-flow assay. Adapted with permission from (Azmi et al., 2021) under Creative Commons license; **(D)** CRISPR/Cas9-mediated lateral flow assay. Adapted with permission from (Xiong et al., 2021) copyright Wiley-VCH 2021.

only be captured at the control line but not at the test line. In this case, the authors considered the disappearance of the test band as positive, thus minimizing subjective readouts and improving the test accuracy. Validated with blind tests of 649 clinical samples, this assay achieved a test sensitivity of 90.67% and a specificity of 99.21% (Li et al., 2021). Moreover, Fozouni and co-workers developed another Cas13a-based lateral flow strip for the detection of SARS-CoV-2 viral. To make this assay applicable for POC testing, the authors did not include a nucleic acid amplification step. Instead, a combined guide RNA design targeting E and N genes was proposed to improve sensitivity and specificity. In addition, the authors used a mobile phone camera as a portable plate reader to eliminate the need for an external fluorescence plate reader. Nevertheless, the exclusion of the amplification step limited the LOD of the assay to 200 copies/μl (Fozouni et al., 2021). Azmi and co-workers on the other hand developed a Cas13a-based lateral-flow assay for the detection of SARS-CoV-2 viral in saliva. The authors used a combined method of chemical treatment and heat inactivation to release target RNA from saliva samples. RT-RPA and SHERLOCK assay was subsequently performed for the detection of the S gene. The method also incorporated a smartphone for semi-quantitative fluorescence signal on-site readout. This assay also achieved excellent sensitivity and specificity. However, a LOD of 100 copies/μl could potentially impact its utility (Azmi et al., 2021).

Cas12 and Cas13 based effectors are more frequently used in nucleic acids detection as Cas9 lacks trans-collateral activity. However, a few Cas9-based approaches have also been developed. Xiong and co-workers reported a CRISPR/Cas9-mediated lateral flow assay (CASLFA) combined with RT-RPA for multiplex detection of SARS-CoV-2 viral genes. In this case, various guide RNAs were designed for target genes recognition. Also, a scaffold sequence that contained a binding site for recruiting AuNP-DNA probes was incorporated in the guide RNA. After the biotinylated amplicons are specifically recognized by Cas9/gRNA complex, the AuNP-DNA probes will bind to the guide RNA via nucleic acid hybridization. The visible accumulation of AuNP-DNA probes at the lateral flow strip was used for naked-eye detection. Their design of the lateral flow strip included dual test lines for multiplex detection of the SARS-CoV-2 E gene and Orf1ab gene. Validated using nasopharyngeal swab clinical samples, a 97% assay sensitivity and a 100% specificity were achieved with a LOD of 4 copies/μl (Xiong et al., 2021). Additionally, previous works have shown that the Cas9 effector from the Gram-negative bacterium Francisella novicida (FnCas9) can be reprogrammed to target a specific RNA substrate (Price et al., 2015). Based on this, Azhar and co-workers developed another lateral flow test that utilized a direct FnCas9 based enzymatic readout for detecting SARS-CoV-2 viral gene sequences. Similar to an affinity-based method of detection, FnCas9 has a high specificity for mismatches. It can improve

TABLE 3 | Existing paper-based CRISPR/Cas tests.

Study	Target gene	Cas protein type/ Amplification method	Total time (excluding sample preparation)	Extraction required	LOD	Sensitivity/ specificity	Total clinical sample size
Broughton et al. (2020)	N, E	Cas12a/RT-LAMP	45 min	Off-chip	10 copies/μl	95%/100%	82
Nguyen et al. (2020)	N	LbCas12a/RT-LAMP	40–60 min	Off-chip	3–300 copies	N/A	N/A
Ali et al. (2020b)	E, N	Cas12b/RT-LAMP	1–2 h	Off-chip	10 copies/reaction	86%/100%	24
Tsou et al. (2021)	S, M, N	Cas12a/RT-RPA	1–2 h	Off-chip/or no extraction	0.1 copy/μl w extraction 10 copies/μl w/o extraction	100%/100%	22
Ooi et al. (2021)	S	enAsCas12a/RT-LAMP	30 min	Off-chip/or no extraction	2 copy/μl w extraction 40 copies/μL w/o extraction	80%/100%	42
Yin et al. (2021)	Multiplex N, S	Cas12a/on-chip RT-RPA	1 h	Off-chip	100 copies/reaction	100%/100%	21
Patchsung et al. (2020)	S, N Orf1ab	Cas13a/RT-RPA	1–2 h	Off-chip	40 copies/reaction	88%/100%	380
Li et al. (2021)	N	Cas13a/RT-RAA	1–2 h	Off-chip	1 copy/μl	90.67%/ 99.21%	649
Fozouni et al. (2021)	E, N	Cas13a/no amplification	40 min	Off-chip	200 copies/μl	did not report	5
Azmi et al. (2021)	S	Cas13a/RT-RPA	30 min	chemical treatment and heat inactivation	100 copies/μl	95.7%/100%	76 (saliva)
Xiong et al. (2021)	E, Orf1ab	Cas9/RT-RPA	45 min	Off-chip	4 copies/μl	97.14%/100%	64
Azhar et al. (2021)	N	FnCas9/RT-RPA	1 h	Off-chip	400 copies/reaction	100%/97%	46
Kumar et al. (2021)	S-N501Y	FnCas9/RT-RPA	1 h	Off-chip	400 copies/reaction	87%/97%	59
Marsic et al. (2021)	N	dCas9/RT-RPA	1 h	Off-chip	2.5 copies/μl	96.4%/100%	30

the assay's specificity while allowing a single-mismatch sensitivity. The same RT-RPA amplification and fluorescence detection methods were used for signal transduction and readout. As a result, for a total of 46 clinical samples, a 100% assay sensitivity and a 97% specificity were achieved with a LOD of 400 copies per reaction (Azhar et al., 2021). In another work, Kumar and co-workers also adapted the FnCas9-based method for the detection of SARS-CoV-2 S gene mutation N501Y using a lateral flow strip. Because Cas9 was highly sensitive to changes in its target sequence, a small mutation in the target nucleic acid led to the protein binding less strongly, thus allowing signal transduction. The results from clinical sample tests were also promising. A sensitivity of 87% and specificity of 97% were obtained with a LOD of 400 copies per reaction (Kumar et al., 2021). Marsic and co-workers also developed a Cas9-based detection technique, named Vigilant. The technique used a fusion of catalytically inactive Cas9 (dCas9) endonuclease and VirD2 relaxase to form Cas9-VirD2 fusions that have been demonstrated to be able to efficiently bind to DNA templates and cleave DNA targets (Ali et al., 2020b). In their work, VirD2-dCas9 specifically bound the target sequence via dCas9 and covalently bound to a FAM-tagged ssDNA reporter via VirD2. A guide RNA was designed to target the SARS-CoV-2 N gene. The complementarity of the guide RNA brought the VirD2-dCas9-ssDNA-FAM to the N gene sequence. Same as the others, off-chip RT-RPA coupled with fluorescent readout on a lateral flow strip was used for nucleic acid detection. Validated using clinical samples, the Vigilant technique also achieved excellent sensitivity and specificity of 96.4 and 100% with a LOD of 2.5 copies/μl, respectively (Marsic et al., 2021).

Representative paper-based CRISPR/Cas tests are illustrated in **Figure 5** and a comparison table is given below (**Table 3**). As an emerging biosensing technology, the current CRISPR/Cas systems have successfully demonstrated the potential to develop a highly sensitive, easy-to-use, and cost-effective paper-based detection platform. Also, it is easily adaptive to a variety of diagnostic tools such as LAMP and RPA to enhance sensitivity to a few copies of the targeted nucleic acid at a single temperature in a short time. Thus, CRISPR/Cas biosensing systems are well-suited for developing paper-based POCT devices. However, it is still a rather recent approach, the practicality of this approach remains a challenge as some of the Cas proteins are still only available in laboratories. Also, the long-time storage of the reagents, which is essential to paper-based POCT, needs further study.

Other Paper-Based Tests

Besides the most commonly used methods listed above, other paper-based tests also have been developed for the detection of SARS-CoV-2 (**Table 4**). Despite being unconventional, these methods may prove to be useful for testing under some specific conditions. De Silva and co-workers used paper spray mass spectrometry to detect the SARS-CoV-2 virus through analyzing lipid-related metabolomics. In this work, Teslin®

TABLE 4 | Other paper-based tests.

Study	Method	Amplification required	Total time (excluding sample preparation)	E (min) xtraction required	LOD	Sensitivity/ specificity	Total clinical sample size
De Silva et al. (2020)	paper spray mass spectrometry	No	1	Off-chip	did not report	93.3%/NA	30
Alafeef et al. (2020)	Graphene-based electrochemical	No	5	Off-chip	7 copies/μL	100%/100%	48

synthetic paper, which composed of micro-porous polyolefin-silica matrix was used as a substrate for depositing sample containing solution droplet. Compared with commonly used cellulose paper, previous work by the authors has indicated that Teslin® paper allowed the samples to have a larger active signal, resulting in a higher amount of ion formation, and with less interference of molecules from the substrate (De Silva et al., 2019). By comparing with standard RT-PCR tests, the mass spectrometry method achieved a 93.3% sensitivity with an analyzing time of 1 min. Although this method is not suitable as a POCT for virus detection since it requires the use of a complex instrument and lacks further clinical validation. However, the results are particularly meaningful for providing valuable insights into the immune response of the novel coronavirus (De Silva et al., 2020).

Finally, in recent years there have been many reports of using 2D nanomaterials for ultrasensitive diagnosis of diseases (Zhu et al., 2015). Due to its excellent intrinsic electrical and mechanical properties (Hao et al., 2018; Wang C. et al., 2020), graphene has emerged as the most promising functional material (Luo et al., 2021). To data, graphene-based biosensors have been reported to detect a wide range of biomolecules including nucleic acids (Wang et al., 2019a), proteins (Tang et al., 2018; Hao Z. et al., 2019), and small molecules (Wang et al., 2019b; Li et al., 2019c). Based on this, Alafeef and co-workers developed a paper-based electrochemical platform to enable the rapid detection of the SARS-CoV-2 viral gene. In this work, a graphene suspension was coated on filter paper. It played an important role in the sensing response as its high carrier mobility made it highly sensitive to the interaction and absorption of the charged target at its surface. The authors designed a specific oligonucleotide sequence that was mounted on the surface of gold nanoparticles to hybridize with its complementary viral RNA. In the presence of SARS-CoV-2 RNA, the specific RNA–DNA hybridization led to the change in charge and electron mobility on the graphene surface, which brought the change in sensor output voltage. The authors also developed a hand-held reader that potentially enabled on-site measurements of the sensor's voltage output. The platform achieved a LOD of 7 copies/μl while reducing the analysis time to 5 min because of the amplification-free detection process. The validity of the sensor platform was demonstrated with a 100% sensitivity and specificity using clinical samples gathered from COVID-19 positive patients and healthy individuals (Alafeef et al., 2020). The above methods all demonstrated feasibility in rapid, sensitive, low-cost SARS-CoV-2 detection and the potential for applying them for POC use. However, the study of these methods is still preliminary and more results in particular results for cross-interference and virus mutation detections are still needed.

CONCLUSION AND FUTURE RESEARCH PROSPECTS

It has been almost 2 years since the first reported case of COVID-19. Unfortunately, because of the highly transmissive nature of the virus and the frequent occurrence of new variant mutations, there is still no treatments available for the virus. Therefore, mass detection, timely diagnosis, and physical intervention methods such as social distancing remain as one of the effective methods to stop the virus from transmitting. However, mass detection and rapid diagnosis are difficult to achieve even in developed countries since the conventional methods for detecting viruses are extremely resource-consuming. Therefore, the development of rapid, robust, highly sensitive, and specific POC diagnostic tests is still in need. Based on such needs, this review summarized the recent developments of paper-based detection tools for the rapid diagnosis of SARS-CoV-2. Currently, the paper-based detection tools can be grouped into three major categories, nucleic acid tests, immunoassay tests, and CRISPR tests. These tests have the common advantages of being cost-effective, user-friendly, and time-efficient, thus holding a great potential to complement the conventional PCR methods. On other hand, the nucleic acids tests offer higher sensitivity and specificity, but they often are complex. CRISPR tests potentially represent the next-generation diagnostics methods. However, the method itself is still in the developmental stage, and how to integrate with paper-based platforms such as immobilizing CRISPR/Cas molecules onto paper substrate remains an outstanding issue. Finally, immunoassay tests are the simplest of them all, which is ideal for fast decision-making but lacks both sensitivity and specificity. Although novel research on paper-based tests has been making great progress to achieve reliable POC diagnostics, their applications in COVID-19 diagnosis are still hindered. In the article, we attempt to enlist and discuss some future research directions that apply to paper-based SARS-CoV-2 diagnostic tools in the hope to bring the technologies to practical use.

One of the research directions is reagent storage. In an ideal setting, reagents are stably stored within the paper devices and can be used at moment's notice. However, most biochemical reagents can regrade and lose their functionality within weeks or even days. Also, storage strategies for reagents can vary

substantially due to different degrees of reagent sensitivity to various environmental parameters such as storage temperature (Krauss et al., 2017). Although effective dry storage of specific enzymes and antibodies has been demonstrated successfully in porous materials (Wentland et al., 2021), research on the dry storage of PCR reagents and nucleic acids used in CRISPR/Cas systems are still scared. In addition, the rehydration of the stored reagents to their original functionality is equally important but is rarely discussed.

Another important research area is sample preparation. This is particularly important for nucleic acids and CRISPR tests as they often reply on amplification to enhance the detection sensitivity. However, amplification requires complex viral RNA extraction protocols that can only be done by professionals using dedicated instruments to avoid false results. This is one of the important reasons why there hasn't been a commercially available paper-based nucleic acids POC test yet. Although proof-of-concept paper tests discussed in this review have shown the ability to perform extraction-free amplification and subsequent viral gene detection, they are still in the early developmental stage and more studies on the extraction-free approaches must be done before a paper-based nucleic acids test can become practically useful.

Finally, Multiplex detection is a necessity in many medical diagnostic tests as many infectious diseases have almost identical symptoms such as SARS-COV-2 and the common cold. In addition, some diseases are caused by the co-existence of several pathogens and serotypes (Safenkova et al., 2019). Therefore, medical diagnoses will benefit much more from simultaneous and rapid detection of multiple targets as opposed to a single target. Also, autonomous multistep detection in a paper device is preferred, in particular for assays that require multiple manual processing steps such as in NAATs or CRISPR/Cas systems. Thus, it can eliminate most of the manually induced detection uncertainties and significantly reduce the complexity of the assays. Past research has demonstrated different types of paper-based valves through changing the wicking property of paper, varying geometric dimensions of the paper channels, and using manually, electrically, thermally, and electromagnetically actuated valves to adjust the connectivity of fluidic channels. These works have been thoroughly reviewed (Akyazi et al., 2018). Nevertheless, most of the valves still operate manually or can only operate on a single channel. As a result, a paper-based flow-control system that is applicable for performing fully autonomous multistep assays (e.g. NAATs) is still under development. Our group recently developed a paper-based valving technology that enabled multiplexed control of parallelized paper channels with a high degree of autonomy. We hope this technology can potentially pave the way for the development of fully automated paper-based NAATs.

Through the discussion of existing works and future research perspectives, we hope that this review identified what is needed, what has been done, and what are challenges still need to be addressed. We believe through close collaboration between academia and industries, a paper-based POC test with high sensitivity and specificity while fully satisfying the ASSURED criteria is on the horizon. Although it may not be here in time to stop the COVID-19 pandemic, it certainly will have a tremendous social and economic impact on our society for infectious diseases monitoring and prevention in the future.

AUTHOR CONTRIBUTIONS

YJ wrote the manuscript with support from HS and WZ, JT and QS contributed to the review process. All of the authors contributed to the final version of the manuscript.

FUNDING

The authors gratefully acknowledge financial supports from the National Natural Science Foundation of China (Award No. 62104160, 61604042, and 61901300); the Natural Science Foundation of Jiangsu Province (Award No. BK20180384); Natural Science Foundation of Top Talent of SZTU 20200204, Natural Science Foundation of Fujian Province (Award No. 2017J01501 and 2017J01692).

REFERENCES

Akyazi, T., Basabe-Desmonts, L., and Benito-Lopez, F. (2018). Review on Microfluidic Paper-Based Analytical Devices towards Commercialisation. *Analytica Chim. Acta* 1001, 1–17. doi:10.1016/j.aca.2017.11.010

Alafeef, M., Dighe, K., Moitra, P., and Pan, D. (2020). Rapid, Ultrasensitive, and Quantitative Detection of SARS-CoV-2 Using Antisense Oligonucleotides Directed Electrochemical Biosensor Chip. *ACS Nano* 14 (12), 17028–17045. doi:10.1021/acsnano.0c06392

Ali, Z., Aman, R., Mahas, A., Rao, G. S., Tehseen, M., Marsic, T., et al. (2020a). iSCAN: An RT-LAMP-Coupled CRISPR-Cas12 Module for Rapid, Sensitive Detection of SARS-CoV-2. *Virus. Res.* 288, 198129. doi:10.1016/j.virusres.2020.198129

Ali, Z., Shami, A., Sedeek, K., Kamel, R., Alhabsi, A., Tehseen, M., et al. (2020b). Fusion of the Cas9 Endonuclease and the VirD2 Relaxase Facilitates Homology-Directed Repair for Precise Genome Engineering in rice. *Commun. Biol.* 3 (1), 44. doi:10.1038/s42003-020-0768-9

Antiochia, R. (2021). Paper-Based Biosensors: Frontiers in Point-of-Care Detection of COVID-19 Disease. *Biosensors* 11 (4), 110. doi:10.3390/bios11040110

Azhar, M., Phutela, R., Kumar, M., Ansari, A. H., Rauthan, R., Gulati, S., et al. (2021). Rapid and Accurate Nucleobase Detection Using FnCas9 and its Application in COVID-19 Diagnosis. *Biosens. Bioelectron.* 183, 113207. doi:10.1016/j.bios.2021.113207

Azmi, I., Faizan, M. I., Kumar, R., Raj Yadav, S., Chaudhary, N., Kumar Singh, D., et al. (2021). A Saliva-Based RNA Extraction-free Workflow Integrated with Cas13a for SARS-CoV-2 Detection. *Front. Cel. Infect. Microbiol.* 11 (144). doi:10.3389/fcimb.2021.632646

Ballard, Z., and Ozcan, A. (2018). Nucleic Acid Quantification in the Field. *Nat. Biomed. Eng.* 2 (9), 629–630. doi:10.1038/s41551-018-0292-0

Broughton, J. P., Deng, X., Yu, G., Fasching, C. L., Servellita, V., Singh, J., et al. (2020). CRISPR-Cas12-based Detection of SARS-CoV-2. *Nat. Biotechnol.* 38 (7), 870–874. doi:10.1038/s41587-020-0513-4

Channon, R. B., Yang, Y., Feibelman, K. M., Geiss, B. J., Dandy, D. S., and Henry, C. S. (2018). Development of an Electrochemical Paper-Based Analytical Device for Trace Detection of Virus Particles. *Anal. Chem.* 90 (12), 7777–7783. doi:10.1021/acs.analchem.8b02042

Che, X.-Y., Hao, W., Wang, Y., Di, B., Yin, K., Xu, Y.-C., et al. (2004). Nucleocapsid Protein as Early Diagnostic Marker for SARS. *Emerg. Infect. Dis.* 10 (11), 1947–1949. doi:10.3201/eid1011.040516

Chen, Z., Zhang, Z., Zhai, X., Li, Y., Lin, L., Zhao, H., et al. (2020). Rapid and Sensitive Detection of Anti-SARS-CoV-2 IgG, Using Lanthanide-Doped Nanoparticles-Based Lateral Flow Immunoassay. *Anal. Chem.* 92 (10), 7226–7231. doi:10.1021/acs.analchem.0c00784

Choi, J. R. (2020). Development of Point-of-Care Biosensors for COVID-19. *Front. Chem.* 8 (517). doi:10.3389/fchem.2020.00517

Cong, L., Ran, F. A., Cox, D., Lin, S., Barretto, R., Habib, N., et al. (2013). Multiplex Genome Engineering Using CRISPR/Cas Systems. *Science* 339 (6121), 819–823. doi:10.1126/science.1231143

De Silva, I. W., Converse, D. T., Juel, L. A., Verbeck, G. F., and Verbeck, G. F. (2019). A Comparative Study of Microporous Polyolefin Silica-Based Paper and Cellulose Paper Substrates Utilizing Paper spray-mass Spectrometry in Drug Analysis. *Anal. Methods* 11 (24), 3066–3072. doi:10.1039/C9AY00641A

De Silva, I. W., Nayek, S., Singh, V., Reddy, J., Granger, J. K., and Verbeck, G. F. (2020). Paper spray Mass Spectrometry Utilizing Teslin Substrate for Rapid Detection of Lipid Metabolite Changes during COVID-19 Infection. *Analyst* 145 (17), 5725–5732. doi:10.1039/D0AN01074J

Diao, B., Wen, K., Zhang, J., Chen, J., Han, C., Chen, Y., et al. (2021). Accuracy of a Nucleocapsid Protein Antigen Rapid Test in the Diagnosis of SARS-CoV-2 Infection. *Clin. Microbiol. Infect.* 27 (2), e1–289. doi:10.1016/j.cmi.2020.09.057

Dos Santos, W. G. (2021). Impact of Virus Genetic Variability and Host Immunity for the success of COVID-19 Vaccines. *Biomed. Pharmacother.* 136, 111272. doi:10.1016/j.biopha.2021.111272

Fozouni, P., Son, S., Díaz de León Derby, M., Knott, G. J., Gray, C. N., D'Ambrosio, M. V., et al. (2021). Amplification-free Detection of SARS-CoV-2 with CRISPR-Cas13a and mobile Phone Microscopy. *Cell* 184 (2), 323–333. e329. doi:10.1016/j.cell.2020.12.001

Gao, Z., Xu, Y., Sun, C., Wang, X., Guo, Y., Qiu, S., et al. (2021). A Systematic Review of Asymptomatic Infections with COVID-19. *J. Microbiol. Immunol. Infect.* 54 (1), 12–16. doi:10.1016/j.jmii.2020.05.001

Garneret, P., Coz, E., Martin, E., Manuguerra, J.-C., Brient-Litzler, E., Enouf, V., et al. (2021). Performing point-of-care Molecular Testing for SARS-CoV-2 with RNA Extraction and Isothermal Amplification. *Plos One* 16 (1), e0243712. doi:10.1371/journal.pone.0243712

Gill, P., and Ghaemi, A. (2008). Nucleic Acid Isothermal Amplification Technologies-A Review. *Nucleosides, Nucleotides and Nucleic Acids* 27 (3), 224–243. doi:10.1080/15257770701845204

Gong, M. M., and Sinton, D. (2017). Turning the Page: Advancing Paper-Based Microfluidics for Broad Diagnostic Application. *Chem. Rev.* 117 (12), 8447–8480. doi:10.1021/acs.chemrev.7b00024

Gootenberg, J. S., Abudayyeh, O. O., Kellner, M. J., Joung, J., Collins, J. J., and Zhang, F. (2018). Multiplexed and Portable Nucleic Acid Detection Platform with Cas13, Cas12a, and Csm6. *Science* 360 (6387), 439–444. doi:10.1126/science.aaq0179

Gootenberg, J. S., Abudayyeh, O. O., Lee, J. W., Essletzbichler, P., Dy, A. J., Joung, J., et al. (2017). Nucleic Acid Detection with CRISPR-Cas13a/C2c2. *Science* 356 (6336), 438–442. doi:10.1126/science.aam9321

Grant, B. D., Anderson, C. E., Williford, J. R., Alonzo, L. F., Glukhova, V. A., Boyle, D. S., et al. (2020). SARS-CoV-2 Coronavirus Nucleocapsid Antigen-Detecting Half-Strip Lateral Flow Assay toward the Development of Point of Care Tests Using Commercially Available Reagents. *Anal. Chem.* 92 (16), 11305–11309. doi:10.1021/acs.analchem.0c01975

Habibzadeh, P., Mofatteh, M., Silawi, M., Ghavami, S., and Faghihi, M. A. (2021). Molecular Diagnostic Assays for COVID-19: an Overview. *Crit. Rev. Clin. Lab. Sci.* 58, 385–398. doi:10.1080/10408363.2021.1884640

Han, K. N., Choi, J.-S., and Kwon, J. (2016). Three-dimensional Paper-Based Slip Device for One-step point-of-care Testing. *Sci. Rep.* 6 (1), 25710. doi:10.1038/srep25710

Hao, Z., Pan, Y., Shao, W., Lin, Q., and Zhao, X. (2019b). Graphene-based Fully Integrated Portable Nanosensing System for On-Line Detection of Cytokine Biomarkers in Saliva. *Biosens. Bioelectron.* 134, 16–23. doi:10.1016/j.bios.2019.03.053

Hao, Z., Wang, Z., Li, Y., Zhu, Y., Wang, X., De Moraes, C. G., et al. (2018). Measurement of Cytokine Biomarkers Using an Aptamer-Based Affinity Graphene Nanosensor on a Flexible Substrate toward Wearable Applications. *Nanoscale* 10 (46), 21681–21688. doi:10.1039/C8NR04315A

He, Z.-X., Shi, L.-C., Ran, X.-Y., Li, W., Wang, X.-L., and Wang, F.-K. (2016). Development of a Lateral Flow Immunoassay for the Rapid Diagnosis of Invasive Candidiasis. *Front. Microbiol.* 7 (1451). doi:10.3389/fmicb.2016.01451

Hosseini, A., Pandey, R., Osman, E., Victorious, A., Li, F., Didar, T., et al. (2020). Roadmap to the Bioanalytical Testing of COVID-19: From Sample Collection to Disease Surveillance. *ACS Sens.* 5 (11), 3328–3345. doi:10.1021/acssensors.0c01377

Hristov, D., Rijal, H., Gomez-Marquez, J., and Hamad-Schifferli, K. (2021). Developing a Paper-Based Antigen Assay to Differentiate between Coronaviruses and SARS-CoV-2 Spike Variants. *Anal. Chem.* 93 (22), 7825–7832. doi:10.1021/acs.analchem.0c05438

Hu, J., Choi, J. R., Wang, S., Gong, Y., Feng, S., Pingguan-Murphy, B., et al. (2017). Multiple Test Zones for Improved Detection Performance in Lateral Flow Assays. *Sensors Actuators B: Chem.* 243, 484–488. doi:10.1016/j.snb.2016.12.008

Huang, C., Wen, T., Shi, F.-J., Zeng, X.-Y., and Jiao, Y.-J. (2020). Rapid Detection of IgM Antibodies against the SARS-CoV-2 Virus via Colloidal Gold Nanoparticle-Based Lateral-Flow Assay. *ACS Omega* 5 (21), 12550–12556. doi:10.1021/acsomega.0c01554

Huang, X., Aguilar, Z. P., Xu, H., Lai, W., and Xiong, Y. (2016). Membrane-based Lateral Flow Immunochromatographic Strip with Nanoparticles as Reporters for Detection: A Review. *Biosens. Bioelectron.* 75, 166–180. doi:10.1016/j.bios.2015.08.032

Jauset-Rubio, M., Svobodová, M., Mairal, T., McNeil, C., Keegan, N., El-Shahawi, M. S., et al. (2016a). Aptamer Lateral Flow Assays for Ultrasensitive Detection of β-Conglutin Combining Recombinase Polymerase Amplification and Tailed Primers. *Anal. Chem.* 88 (21), 10701–10709. doi:10.1021/acs.analchem.6b03256

Jauset-Rubio, M., Svobodová, M., Mairal, T., McNeil, C., Keegan, N., Saeed, A., et al. (2016b). Ultrasensitive, Rapid and Inexpensive Detection of DNA Using Paper Based Lateral Flow Assay. *Sci. Rep.* 6 (1), 37732. doi:10.1038/srep37732

Javalkote, V. S., Kancharla, N., Bhadra, B., Shukla, M., Soni, B., Sapre, A., et al. (2020). CRISPR-based Assays for Rapid Detection of SARS-CoV-2. *Methods.* S1046-2023, 30217. doi:10.20944/preprints202006.0025.v1

Jia, Y., Sun, H., Dong, H., Wang, C., Lin, X., and Dong, D. (2020). Scalable and Parallelized Biochemical Assays in Paper Devices Integrated with a Programmable Binary Valve Matrix. *Sensors Actuators B: Chem.* 321, 128466. doi:10.1016/j.snb.2020.128466

Jia, Y., Sun, H., Li, X., Sun, D., Hu, T., Xiang, N., et al. (2018). Paper-based Graphene Oxide Biosensor Coupled with Smartphone for the Quantification of Glucose in Oral Fluid. *Biomed. Microdevices* 20 (4), 89. doi:10.1007/s10544-018-0332-2

Kaarj, K., Akarapipad, P., and Yoon, J.-Y. (2018). Simpler, Faster, and Sensitive Zika Virus Assay Using Smartphone Detection of Loop-Mediated Isothermal Amplification on Paper Microfluidic Chips. *Sci. Rep.* 8 (1), 12438. doi:10.1038/s41598-018-30797-9

Kasetsirikul, S., Umer, M., Soda, N., Sreejith, K. R., Shiddiky, M. J. A., and Nguyen, N.-T. (2020). Detection of the SARS-CoV-2 Humanized Antibody with Paper-Based ELISA. *Analyst* 145 (23), 7680–7686. doi:10.1039/D0AN01609H

Kaur, N., and Toley, B. J. (2018). Paper-based Nucleic Acid Amplification Tests for point-of-care Diagnostics. *Analyst* 143 (10), 2213–2234. doi:10.1039/C7AN01943B

Kim, S., Hao, Y., Miller, E. A., Tay, D. M. Y., Yee, E., Kongsuphol, P., et al. (2021). Vertical Flow Cellulose-Based Assays for SARS-CoV-2 Antibody Detection in Human Serum. *ACS Sens.* 6 (5), 1891–1898. doi:10.1021/acssensors.1c00235

Koczula, K. M., and Gallotta, A. (2016). "Lateral Flow Assays," in *Biosensor Technologies for Detection of Biomolecules*. Editor P. Estrela, 60, 111–120. doi:10.1042/ebc20150012

Komatsu, T., Maeki, M., Ishida, A., Tani, H., and Tokeshi, M. (2018). Characteristics of Microfluidic Paper-Based Analytical Devices Fabricated by Four Different Methods. *Anal. Sci.* 34 (1), 39–44. doi:10.2116/analsci.34.39

Krauss, S. T., Holt, V. C., and Landers, J. P. (2017). Simple Reagent Storage in Polyester-Paper Hybrid Microdevices for Colorimetric Detection. *Sensors Actuators B: Chem.* 246, 740–747. doi:10.1016/j.snb.2017.02.018

Kubina, R., and Dziedzic, A. (2020). Molecular and Serological Tests for COVID-19. A Comparative Review of SARS-CoV-2 Coronavirus Laboratory and Point-of-Care Diagnostics. *Diagnostics* 10 (6), 434. doi:10.3390/diagnostics10060434

Kumar, M., Gulati, S., Ansari, A. H., Phutela, R., Acharya, S., Azhar, M., et al. (2021). FnCas9-based CRISPR Diagnostic for Rapid and Accurate Detection of Major SARS-CoV-2 Variants on a Paper Strip. *eLife* 10, e67130. doi:10.7554/eLife.67130

Lee, S.-Y., Huang, J.-G., Chuang, T.-L., Sheu, J.-C., Chuang, Y.-K., Holl, M., et al. (2008). Compact Optical Diagnostic Device for Isothermal Nucleic

Acids Amplification. *Sensors Actuators B: Chem.* 133 (2), 493–501. doi:10.1016/j.snb.2008.03.008

Li, H., Dong, X., Wang, Y., Yang, L., Cai, K., Zhang, X., et al. (2021). Sensitive and Easy-Read CRISPR Strip for COVID-19 Rapid Point-of-Care Testing. *CRISPR J.* 4 (3), 392–399. doi:10.1089/crispr.2020.0138

Li, X., Ballerini, D. R., and Shen, W. (2012). A Perspective on Paper-Based Microfluidics: Current Status and Future Trends. *Biomicrofluidics* 6 (1), 011301. doi:10.1063/1.3687398

Li, X., Scida, K., and Crooks, R. M. (2015). Detection of Hepatitis B Virus DNA with a Paper Electrochemical Sensor. *Anal. Chem.* 87 (17), 9009–9015. doi:10.1021/acs.analchem.5b02210

Li, Y., Li, S., Wang, J., and Liu, G. (2019a). CRISPR/Cas Systems towards Next-Generation Biosensing. *Trends Biotechnol.* 37 (7), 730–743. doi:10.1016/j.tibtech.2018.12.005

Li, Y., Li, S., Wang, J., and Liu, G. (2019b). CRISPR/Cas Systems towards Next-Generation Biosensing. *Trends Biotechnol.* 37 (7), 730–743. doi:10.1016/j.tibtech.2018.12.005

Li, Y., Zhu, Y., Wang, C., He, M., and Lin, Q. (2019c). Selective Detection of Water Pollutants Using a Differential Aptamer-Based Graphene Biosensor. *Biosens. Bioelectron.* 126, 59–67. doi:10.1016/j.bios.2018.10.047

Li, Z., Yi, Y., Luo, X., Xiong, N., Liu, Y., Li, S., et al. (2020). Development and Clinical Application of a Rapid IgM-IgG Combined Antibody Test for SARS-CoV-2 Infection Diagnosis. *J. Med. Virol.* 92 (9), 1518–1524. doi:10.1002/jmv.25727

Liu, D., Ju, C., Han, C., Shi, R., Chen, X., Duan, D., et al. (2021a). Nanozyme Chemiluminescence Paper Test for Rapid and Sensitive Detection of SARS-CoV-2 Antigen. *Biosens. Bioelectron.* 173, 112817. doi:10.1016/j.bios.2020.112817

Liu, D., Shen, H., Zhang, Y., Shen, D., Zhu, M., Song, Y., et al. (2021b). A Microfluidic-Integrated Lateral Flow Recombinase Polymerase Amplification (MI-IF-RPA) Assay for Rapid COVID-19 Detection. *Lab. Chip* 21 (10), 2019–2026. doi:10.1039/D0LC01222J

Liu, G., and Rusling, J. F. (2021). COVID-19 Antibody Tests and Their Limitations. *ACS Sens.* 6 (3), 593–612. doi:10.1021/acssensors.0c02621

Luo, B., Yuan, A., Yang, S., Han, L., Guan, R., Duan, J., et al. (2021). Synthesis of Diamond-like Carbon as a Dielectric Platform for Graphene Field Effect Transistors. *ACS Appl. Nano Mater.* 4 (2), 1385–1393. doi:10.1021/acsanm.0c02930

Magro, L., Escadafal, C., Garneret, P., Jacquelin, B., Kwasiborski, A., Manuguerra, J.-C., et al. (2017). Paper Microfluidics for Nucleic Acid Amplification Testing (NAAT) of Infectious Diseases. *Lab. Chip* 17 (14), 2347–2371. doi:10.1039/C7LC00013H

Mahmoudi, T., de la Guardia, M., Shirdel, B., Mokhtarzadeh, A., and Baradaran, B. (2019). Recent Advancements in Structural Improvements of Lateral Flow Assays towards point-of-care Testing. *Trac Trends Anal. Chem.* 116, 13–30. doi:10.1016/j.trac.2019.04.016

Marsic, T., Ali, Z., Tehseen, M., Mahas, A., Hamdan, S., and Mahfouz, M. (2021). Vigilant: An Engineered VirD2-Cas9 Complex for Lateral Flow Assay-Based Detection of SARS-CoV2. *Nano Lett.* 21 (8), 3596–3603. doi:10.1021/acs.nanolett.1c00612

Martinez, A. W., Phillips, S. T., Butte, M. J., and Whitesides, G. M. (2007). Patterned Paper as a Platform for Inexpensive, Low-Volume, Portable Bioassays. *Angew. Chem. Int. Ed.* 46 (8), 1318–1320. doi:10.1002/anie.200603817

Mofijur, M., Fattah, I. M. R., Alam, M. A., Islam, A. B. M. S., Ong, H. C., Rahman, S. M. A., et al. (2021). Impact of COVID-19 on the Social, Economic, Environmental and Energy Domains: Lessons Learnt from a Global Pandemic. *Sustainable Prod. consumption* 26, 343–359. doi:10.1016/j.spc.2020.10.016

Morbioli, G. G., Mazzu-Nascimento, T., Stockton, A. M., and Carrilho, E. (2017). Technical Aspects and Challenges of Colorimetric Detection with Microfluidic Paper-Based Analytical Devices (μPADs) - A Review. *Analytica Chim. Acta* 970, 1–22. doi:10.1016/j.aca.2017.03.037

Mousavizadeh, L., and Ghasemi, S. (2021). Genotype and Phenotype of COVID-19: Their Roles in Pathogenesis. *J. Microbiol. Immunol. Infect.* 54 (2), 159–163. doi:10.1016/j.jmii.2020.03.022

Müller, R. H., and Clegg, D. L. (1949). Automatic Paper Chromatography. *Anal. Chem.* 21 (9), 1123–1125. doi:10.1021/ac60033a032

Nguyen, L. T., Smith, B. M., and Jain, P. K. (2020). Enhancement of Trans-cleavage Activity of Cas12a with Engineered crRNA Enables Amplified Nucleic Acid Detection. *Nat. Commun.* 11 (1), 4906. doi:10.1038/s41467-020-18615-1

Niemz, A., Ferguson, T. M., and Boyle, D. S. (2011). Point-of-care Nucleic Acid Testing for Infectious Diseases. *Trends Biotechnol.* 29 (5), 240–250. doi:10.1016/j.tibtech.2011.01.007

Ooi, K. H., Liu, M. M., Tay, J. W. D., Teo, S. Y., Kaewsapsak, P., Jin, S., et al. (2021). An Engineered CRISPR-Cas12a Variant and DNA-RNA Hybrid Guides Enable Robust and Rapid COVID-19 Testing. *Nat. Commun.* 12 (1), 1739. doi:10.1038/s41467-021-21996-6

Patchsung, M., Jantarug, K., Pattama, A., Aphicho, K., Suraritdechachai, S., Meesawat, P., et al. (2020). Clinical Validation of a Cas13-Based Assay for the Detection of SARS-CoV-2 RNA. *Nat. Biomed. Eng.* 4 (12), 1140–1149. doi:10.1038/s41551-020-00603-x

Price, A. A., Sampson, T. R., Ratner, H. K., Grakoui, A., and Weiss, D. S. (2015). Cas9-mediated Targeting of Viral RNA in Eukaryotic Cells. *Proc. Natl. Acad. Sci. USA* 112 (19), 6164–6169. doi:10.1073/pnas.1422340112

Qian, J., Boswell, S. A., Chidley, C., Lu, Z.-x., Pettit, M. E., Gaudio, B. L., et al. (2020). An Enhanced Isothermal Amplification Assay for Viral Detection. *Nat. Commun.* 11 (1), 5920. doi:10.1038/s41467-020-19258-y

Reid, R., Chatterjee, B., Das, S. J., Ghosh, S., and Sharma, T. K. (2020). Application of Aptamers as Molecular Recognition Elements in Lateral Flow Assays. *Anal. Biochem.* 593, 113574. doi:10.1016/j.ab.2020.113574

Rodriguez, N. M., Wong, W. S., Liu, L., Dewar, R., and Klapperich, C. M. (2016). A Fully Integrated Paperfluidic Molecular Diagnostic Chip for the Extraction, Amplification, and Detection of Nucleic Acids from Clinical Samples. *Lab. Chip* 16 (4), 753–763. doi:10.1039/C5LC01392E

Sachdeva, S., Davis, R. W., and Saha, A. K. (2020b). Microfluidic Point-of-Care Testing: Commercial Landscape and Future Directions. *Front. Bioeng. Biotechnol.* 8, 602659. doi:10.3389/fbioe.2020.602659

Sachdeva, S., Davis, R. W., and Saha, A. K. (2021a). Microfluidic Point-of-Care Testing: Commercial Landscape and Future Directions. *Front. Bioeng. Biotechnol.* 8 (1537). doi:10.3389/fbioe.2020.602659

Safenkova, I. V., Panferov, V. G., Panferova, N. A., Varitsev, Y. A., Zherdev, A. V., and Dzantiev, B. B. (2019). Alarm Lateral Flow Immunoassay for Detection of the Total Infection Caused by the Five Viruses. *Talanta* 195, 739–744. doi:10.1016/j.talanta.2018.12.004

Sohrabi, C., Alsafi, Z., O'Neill, N., Khan, M., Kerwan, A., Al-Jabir, A., et al. (2020). World Health Organization Declares Global Emergency: A Review of the 2019 Novel Coronavirus (COVID-19). *Int. J. Surg.* 76, 71–76. doi:10.1016/j.ijsu.2020.02.034

Sun, H., Jia, Y., Dong, H., and Fan, L. (2019). Graphene Oxide Nanosheets Coupled with Paper Microfluidics for Enhanced On-Site Airborne Trace Metal Detection. *Microsyst Nanoeng* 5, 4. doi:10.1038/s41378-018-0044-z

Suo, T., Liu, X., Feng, J., Guo, M., Hu, W., Guo, D., et al. (2020). ddPCR: a More Accurate Tool for SARS-CoV-2 Detection in Low Viral Load Specimens. *Emerging Microbes & Infections* 9 (1), 1259–1268. doi:10.1080/22221751.2020.1772678

Tang, Y., Gu, C., Wang, C., Song, B., Zhou, X., Lou, X., et al. (2018). Evanescent Wave Aptasensor for Continuous and Online Aminoglycoside Antibiotics Detection Based on Target Binding Facilitated Fluorescence Quenching. *Biosens. Bioelectron.* 102, 646–651. doi:10.1016/j.bios.2017.12.006

Tsou, J.-H., Liu, H., Stass, S. A., and Jiang, F. (2021). Rapid and Sensitive Detection of SARS-CoV-2 Using Clustered Regularly Interspaced Short Palindromic Repeats. *Biomedicines* 9 (3), 239. doi:10.3390/biomedicines9030239

United Nations (2020). *The Sustainable Development Goals Report*. New York, NY, United States: United Nations Publications.

Wang, C., Liu, M., Wang, Z., Li, S., Deng, Y., and He, N. (2021). Point-of-care Diagnostics for Infectious Diseases: From Methods to Devices. *Nano Today* 37, 101092. doi:10.1016/j.nantod.2021.101092

Wang, C., Wu, J., He, Y., Song, Z., Shi, S., Zhu, Y., et al. (2019a). Fully Solid-State Graphene Transistors with Striking Homogeneity and Sensitivity for the Practicalization of Single-Device Electronic Bioassays. *Nano Lett.* 20 (1), 166–175. doi:10.1021/acs.nanolett.9b03528

Wang, C., Ye, W., Li, Y., Zhu, Y., Lin, Q., and He, M. (2019b). Exploiting Electrostatic Shielding-Effect of Metal Nanoparticles to Recognize Uncharged Small Molecule Affinity with Label-free Graphene Electronic Biosensor. *Biosens. Bioelectron.* 129, 93–99. doi:10.1016/j.bios.2018.12.051

Wang, C., Zhang, B., Li, Y., and Zhao, X. (2020a). Suspended Graphene Hydroacoustic Sensor for Broadband Underwater Wireless Communications. *IEEE Wireless Commun.* 27 (5), 44–52. doi:10.1109/mwc.001.2000056

Wang, D., He, S., Wang, X., Yan, Y., Liu, J., Wu, S., et al. (2020b). Rapid Lateral Flow Immunoassay for the Fluorescence Detection of SARS-CoV-2 RNA. *Nat. Biomed. Eng.* 4 (12), 1150–1158. doi:10.1038/s41551-020-00655-z

Wen, T., Huang, C., Shi, F.-J., Zeng, X.-Y., Lu, T., Ding, S.-N., et al. (2020). Development of a Lateral Flow Immunoassay Strip for Rapid Detection of IgG Antibody against SARS-CoV-2 Virus. *Analyst* 145 (15), 5345–5352. doi:10.1039/D0AN00629G

Wentland, L., Polaski, R., and Fu, E. (2021). Dry Storage of Multiple Reagent Types within a Paper Microfluidic Device for Phenylalanine Monitoring. *Anal. Methods* 13 (5), 660–671. doi:10.1039/D0AY02043E

World Health Organization (2020). *Maintaining Essential Health Services: Operational Guidance for the COVID-19 Context*.

Wright, A. V., Nuñez, J. K., and Doudna, J. A. (2016). Biology and Applications of CRISPR Systems: Harnessing Nature's Toolbox for Genome Engineering. *Cell* 164 (1-2), 29–44. doi:10.1016/j.cell.2015.12.035

Wu, Q., Suo, C., Brown, T., Wang, T., Teichmann, S. A., and Bassett, A. R. (2021). INSIGHT: A Population-Scale COVID-19 Testing Strategy Combining point-of-care Diagnosis with Centralized High-Throughput Sequencing. *Sci. Adv.* 7 (7), eabe5054. doi:10.1126/sciadv.abe5054

Wu, Y., Zhou, Y., Leng, Y., Lai, W., Huang, X., and Xiong, Y. (2020). Emerging Design Strategies for Constructing Multiplex Lateral Flow Test Strip Sensors. *Biosens. Bioelectron.* 157, 112168. doi:10.1016/j.bios.2020.112168

Xia, S., and Chen, X. (2020). Single-copy Sensitive, Field-Deployable, and Simultaneous Dual-Gene Detection of SARS-CoV-2 RNA via Modified RT-RPA. *Cell Discov* 6 (1), 37. doi:10.1038/s41421-020-0175-x

Xiong, E., Jiang, L., Tian, T., Hu, M., Yue, H., Huang, M., et al. (2021). Simultaneous Dual-Gene Diagnosis of SARS-CoV-2 Based on CRISPR/Cas9-Mediated Lateral Flow Assay. *Angew. Chem. Int. Ed.* 60 (10), 5307–5315. doi:10.1002/anie.202014506

Yakoh, A., Pimpitak, U., Rengpipat, S., Hirankarn, N., Chailapakul, O., and Chaiyo, S. (2021). Paper-based Electrochemical Biosensor for Diagnosing COVID-19: Detection of SARS-CoV-2 Antibodies and Antigen. *Biosens. Bioelectron.* 176, 112912. doi:10.1016/j.bios.2020.112912

Yetisen, A. K., Akram, M. S., and Lowe, C. R. (2013). Paper-based Microfluidic point-of-care Diagnostic Devices. *Lab. Chip* 13 (12), 2210–2251. doi:10.1039/C3LC50169H

Yin, K., Ding, X., Li, Z., Sfeir, M. M., Ballesteros, E., and Liu, C. (2021). Autonomous Lab-On-Paper for Multiplexed, CRISPR-Based Diagnostics of SARS-CoV-2. *Lab. Chip* 21 (14), 2730–2737. doi:10.1039/D1LC00293G

Yu, S., Nimse, S. B., Kim, J., Song, K.-S., and Kim, T. (2020). Development of a Lateral Flow Strip Membrane Assay for Rapid and Sensitive Detection of the SARS-CoV-2. *Anal. Chem.* 92 (20), 14139–14144. doi:10.1021/acs.analchem.0c03202

Yüce, M., Filiztekin, E., and Özkaya, K. G. (2021). COVID-19 Diagnosis -A Review of Current Methods. *Biosens. Bioelectron.* 172, 112752. doi:10.1016/j.bios.2020.112752

Zhang, C., Zheng, T., Wang, H., Chen, W., Huang, X., Liang, J., et al. (2021). Rapid One-Pot Detection of SARS-CoV-2 Based on a Lateral Flow Assay in Clinical Samples. *Anal. Chem.* 93 (7), 3325–3330. doi:10.1021/acs.analchem.0c05059

Zheng, C., Wang, K., Zheng, W., Cheng, Y., Li, T., Cao, B., et al. (2021a). Rapid Developments in Lateral Flow Immunoassay for Nucleic Acid Detection. *Analyst* 146 (5), 1514–1528. doi:10.1039/D0AN02150D

Zheng, Y.-Z., Chen, J.-T., Li, J., Wu, X.-J., Wen, J.-Z., Liu, X.-Z., et al. (2021b). Reverse Transcription Recombinase-Aided Amplification Assay with Lateral Flow Dipstick Assay for Rapid Detection of 2019 Novel Coronavirus. *Front. Cel. Infect. Microbiol.* 11 (24). doi:10.3389/fcimb.2021.613304

Zhou, P., Yang, X.-L., Wang, X.-G., Hu, B., Zhang, L., Zhang, W., et al. (2020). Addendum: A Pneumonia Outbreak Associated with a New Coronavirus of Probable Bat Origin. *Nature* 588 (7836), E6. doi:10.1038/s41586-020-2951-z

Zhou, Y., Chen, Y., Liu, W., Fang, H., Li, X., Hou, L., et al. (2021a). Development of a Rapid and Sensitive Quantum Dot Nanobead-Based Double-Antigen sandwich Lateral Flow Immunoassay and its Clinical Performance for the Detection of SARS-CoV-2 Total Antibodies. *Sensors Actuators B: Chem.* 343, 130139. doi:10.1016/j.snb.2021.130139

Zhou, Y., Chen, Y., Liu, Y., Fang, H., Huang, X., Leng, Y., et al. (2021b). Controlled Copper *In Situ* Growth-Amplified Lateral Flow Sensors for Sensitive, Reliable, and Field-Deployable Infectious Disease Diagnostics. *Biosens. Bioelectron.* 171, 112753. doi:10.1016/j.bios.2020.112753

Zhou, Y., Ding, L., Wu, Y., Huang, X., Lai, W., and Xiong, Y. (2019). Emerging Strategies to Develop Sensitive AuNP-Based ICTS Nanosensors. *Trac Trends Anal. Chem.* 112, 147–160. doi:10.1016/j.trac.2019.01.006

Zhu, H., Zhang, H., Ni, S., Korabečná, M., Yobas, L., and Neuzil, P. (2020a). The Vision of point-of-care PCR Tests for the COVID-19 Pandemic and beyond. *Trac Trends Anal. Chem.* 130, 115984. doi:10.1016/j.trac.2020.115984

Zhu, X., Wang, X., Han, L., Chen, T., Wang, L., Li, H., et al. (2020b). Multiplex Reverse Transcription Loop-Mediated Isothermal Amplification Combined with Nanoparticle-Based Lateral Flow Biosensor for the Diagnosis of COVID-19. *Biosens. Bioelectron.* 166, 112437. doi:10.1016/j.bios.2020.112437

Zhu, Y., Wang, C., Petrone, N., Yu, J., Nuckolls, C., Hone, J., et al. (2015). A Solid Dielectric Gated Graphene Nanosensor in Electrolyte Solutions. *Appl. Phys. Lett.* 106 (12), 123503. doi:10.1063/1.4916341

Conflict of Interest: The authors declare that the research was conducted in the absence of any commercial or financial relationships that could be construed as a potential conflict of interest.

Publisher's Note: All claims expressed in this article are solely those of the authors and do not necessarily represent those of their affiliated organizations, or those of the publisher, the editors and the reviewers. Any product that may be evaluated in this article, or claim that may be made by its manufacturer, is not guaranteed or endorsed by the publisher.

frontiers in Bioengineering and Biotechnology

ORIGINAL RESEARCH
published: 03 January 2022
doi: 10.3389/fbioe.2021.798079

Evaluation of Analytical Performances of Magnetic Force-Assisted Electrochemical Sandwich Immunoassay for the Quantification of Carcinoembryonic Antigen

Boo Young Hwang[1,2], *Eunsoo Kim*[1,2], *Seung-ha Kim*[1] *and Hyundoo Hwang*[3]*

[1]Department of Anesthesia and Pain Medicine, School of Medicine, Pusan National University, Yangsan, South Korea, [2]Department of Anesthesia and Pain Medicine, Biomedical Research Institute, Pusan National University Hospital, Busan, South Korea, [3]BBB Inc., Seoul, South Korea

Carcinoembryonic antigen (CEA) is a biomarker indicated in different cancers, targeted for quantitative analysis *via* immunoassay. Here we introduce a new technique called magnetic force-assisted electrochemical sandwich immunoassay (MESIA) for determination of CEA level in a drop of human serum using a fully automated point-of-care testing (POCT) device. The analytical performances of the assay are assessed based on precision, accuracy, limit of blank (LoB), limit of detection (LoD) and limit of quantitation (LoQ), linearity, Hook effect, interference, cross-reactivity, and method comparison following the guidelines of the Clinical Laboratory Standards Institute (CLSI). The LoD is 0.50 ng/ml. A linear relationship is shown in the range of 0.5–200 ng/ml. A high dose effect is not seen up to approximately 500,000 ng/ml. The recovery range is from 94.7 to 108.9%. The %CV of run-to-run and within-lab variations are less than 2.04 and 4.41% across the CEA concentrations, respectively, whereas reproducibility is 4.45–6.24%. Method comparison shows that the assay correlates well with the reference device (R^2 = 0.9884). The assay demonstrates acceptable precision, accuracy, LoB, LoD and LoQ, hook effect, linearity, interference, cross-reactivity, and high correlation with its reference device. Thus, the system is suitable for the quantification of CEA in clinical practices with a POCT manner.

Keywords: performance evaluation, immunoassay, CEA, MESIA, electrochemistry

OPEN ACCESS

Edited by:
Tailin Xu,
Shenzhen University, China

Reviewed by:
Tiancai Liu,
Southern Medical University, China
Miguel Ángel López Gil,
University of Alcalá, Spain

***Correspondence:**
Hyundoo Hwang
doo@bbbtech.com

Specialty section:
This article was submitted to Biosensors and Biomolecular Electronics, a section of the journal Frontiers in Bioengineering and Biotechnology

Received: *19 October 2021*
Accepted: *07 December 2021*
Published: *03 January 2022*

Citation:
Hwang BY, Kim E, Kim S-h and Hwang H (2022) Evaluation of Analytical Performances of Magnetic Force-Assisted Electrochemical Sandwich Immunoassay for the Quantification of Carcinoembryonic Antigen. Front. Bioeng. Biotechnol. 9:798079. doi: 10.3389/fbioe.2021.798079

1 INTRODUCTION

CEA is a polysaccharide-protein complex produced by the embryonic intestinal mucous membrane prior to birth. As the serum concentration of CEA can increase in the presence of several types of cancer, such as colorectal (Vernava et al., 1994), gastric (Takahashi et al., 2003), lung (Grunnet and Sorensen 2012), or breast (Park et al., 2008) cancers, CEA has been recognized as a broad-spectrum biomarker for cancer diagnosis and prognosis.

A variety of methods have been conducted for the quantitative detection of CEA, such as enzyme-linked immunosorbent assays (ELISA) (Tobi et al., 1992), fluorescence immunoassays (Wu et al., 2015; Yang et al., 2015), chemiluminescence immunoassays (Lin et al., 2004; Jiang et al., 2013),

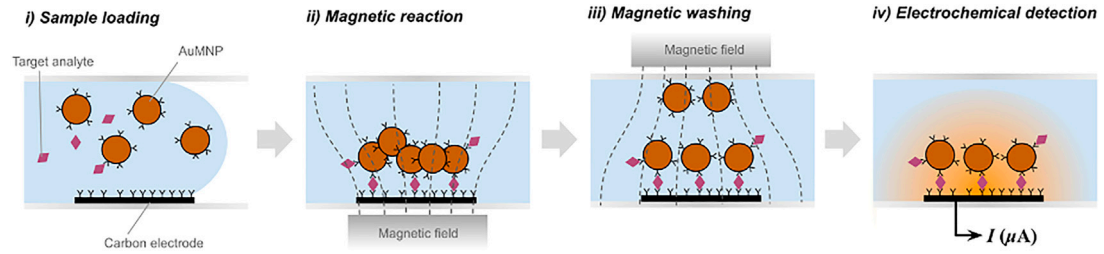

FIGURE 1 | Schematic diagram of magnetic force-assisted electrochemical sandwich immunoassays (MESIA).

electrochemiluminescence immunoassays (Wang et al., 2015) and amperometric immunoassays (Li et al., 2011). A common drawback of those methods is that they require multiple steps for washing with large amounts of buffer solution as well as sample preparation steps for isolating plasma or serum. These drawbacks can increase the complexity of assays and are the main reasons why the conventional assays could be conducted only by professionals at clinical laboratories. They also require complicated mechanical and optical systems for automation, which obstruct commercialization of miniaturized and portable quantitative immunoassay platforms.

Recently, a new immunoassay technique called magnetic force-assisted electrochemical sandwich immunoassay (MESIA) was demonstrated to be suitable for the quantitative detection of serological biomarkers (Hwang et al., 2019b). In MESIA, magnetic nanoparticles capture target analytes and form sandwich immuno-complexes on an electrode surface *via* antibody-antigen interactions (See **Figure 1**). The mixing and reaction processes are actively controlled by external magnetic fields. Unbound magnetic nanoparticles are removed from the electrode surface by a magnetic field, and the electrochemical signal from the nanoparticles is subsequently measured to determine the concentration of target analytes. This method requires neither a washing buffer nor optical components. Hence, it enables integration of all the assay processes into a single disposable chip and a portable electrochemical reader.

The MARK-B® (BBB Inc., Seoul, South Korea) is a point-of-care testing (POCT) immunoassay platform based on the MESIA (Hwang et al., 2019a). The MARK-B immunoassay system is composed of an analyzer, which is an electrochemical reader with a touch-screen mobile device, and a disposable test cartridge that contains gold-coated magnetic nanoparticles (AuMNPs), and screen-printed carbon electrodes (SPCE) in a microfluidic channel. Once a sample is loaded into the cartridge, the capillary force drives the sample into the channel. Subsequently, the pre-spotted AuMNPs are dissolved, and external magnetic fields are actively controlled by two external magnets to facilitate the reaction, in which the antibody-immobilized AuMNPs react with the target analytes to form sandwich immuno-complexes on the SPCE electrochemical sensor. After the reaction process is finalized, unbound AuMNPs are removed by the magnetic force. The amount of target analytes is quantitatively measured by analyzing signals induced by electrochemical oxidation and reduction of gold on the bound AuMNPs—more detailed information regarding the electrochemical measurement technique are described in the previous literature (Hwang et al., 2019b). This technology provides portable, highly sensitive, and fully automated system for quantification of proteins in a drop of liquid specimen without the requirement of any user intervention or additional reagents, thus is relevant for *in vitro* diagnostics based on POCT.

In this study, analytical performances of the MARK-B immunoassay system for the quantitative analysis of CEA are evaluated following the guidelines of the Clinical Laboratory Standards Institute (CLSI). The functional sensitivity, linearity, Hook effect, recovery, precision, and reproducibility of the assay were investigated. In addition, the accuracy was evaluated in comparison with a commercial immunoassay system for hospital uses.

2 MATERIALS AND METHODS

2.1 Materials and Reagents

Assay calibrators are traceable to Carcinoembryonic Antigen 1st International Reference Preparation provided by the National Institute of Biological Standards and Controls (NIBSC code: 73/601). Hemoglobin, bilirubin, albumin, gamma globulins, diethylstilbestrol, acetaminophen, acetylsalicylic acid, ampicillin, cyclosporine, goserelin, leuprolide, ibuprofen, ifosfamide, finasteride, flutamide, docetaxel, methotrexate, methyldopa, naproxen, urea, bleomycin, oxaliplatin, triglyceride, vinblastine, and warfarin were purchased from Sigma-Aldrich (Darmstadt, Germany). The beta subunit of human chorionic gonadotropin (Beta-hCG), Alpha-fetoprotein (AFP) and prostate-specific antigen (PSA) from NIBSC; Cancer antigen 19-9 (CA 19-9), cancer antigen 125 (CA-125), human anti-mouse antibody (HAMA) and rheumatoid arthritis (RF) plasma were purchased from Lee Biosolutions (Maryland Heights, MO, United States). Atorvastatin and paclitaxel were purchased from Chemscene (Monmouth Junction, NJ, United States). 5-Fluoro-1- (tetrahydro-2-furfuryl)uracil (Tegafur), doxorubicin, doxycycline, etoposide, furosemide, levodopa, lovastatin, N-acetyl-L-cysteine, prednisone, sodium 2-mercaptoethanesulfonate (Mesna), tamsulosin, theophylline, uric acid, cefoxitin, cisplatin, cyclophosphamide, phenylbutazone, and rifampicin were

purchased from TCI (Tokyo, Japan). 5-fluorouracil and L-ascorbic acid were purchased from Biosesang (Seongnam, South Korea).

2.2 Clinical Sample Preparation

From the November 28, 2019 to the December 13, 2019, 140 serum samples from colorectal cancer patients were collected from biorepositories. The serum samples were separated by centrifugation and stored at -70°C with complete storage records and were freeze-thawed prior to being used. All the information of the samples were anonymous until the end of detection.

2.3 Instruments

MARK-B (BBB Inc., Seoul, South Korea) and Unicel DxI 800 ACCESS Immunoassay System (Beckman Coulter, Indianapolis, IN, United States) as the reference device were applied for this study.

2.4 Functional Sensitivity: Limit of Blank, Limit of Detection, and Limit of Quantitation

The limit of blank (LoB) and the limit of detection (LoD) were determined according to the CLSI guideline EP-17-A2 (Clinical and Laboratory Standards Institute (CLSI) guidelines, 2012). The mean and standard deviation were calculated *via* 30 consecutive measurements of blank and low concentration specimens each. To assess the limit of quantitation (LoQ), the coefficients of variation (CVs) for specimens with various CEA concentrations were calculated. Each measurement was performed in 20 replicates. The lowest concentration measured with a CV ≤ 15% was defined as the estimated LoQ.

2.5 Linearity

Linearity was evaluated according to CLSI guideline EP-6-A (Clinical and Laboratory Standards Institute (CLSI)guidelines 2003). A sample with high analyte concentration (200 ng/ml) was diluted with one with low analyte concentration (0.5 ng/ml) into nine different fractional parts of each sample—0.50, 25.44, 50.38, 75.31, 100.25, 125.19, 150.13, 175.06, and 200.00 ng/ml. Five replicates were measured for each dilution fold using a single lot of cartridges. Linear regression analysis was conducted as recommended by Kroll and Emancipator (Kroll and Emancipator 1993).

2.6 Hook Effect

A specimen with CEA concentration of 500,000 ng/ml and its serial dilution samples each was used to assess the hook effect with the CEA assay. The specimen was diluted with a serum containing CEA below the assay detection limit, and each measurement was performed in four replicates.

2.7 Recovery

Four different CEA concentration samples - high (151.4 ng/ml), higher mid (75.2 ng/ml), and lower mid (15.5 ng/ml) and low (3.42 ng/ml)—were measured in four replicates. The percentage ratio between the measured and estimated concentrations was calculated. The acceptance criteria set for this study was a recovery range between 90–110%.

2.8 Single-Site Precision

Precision was evaluated according to CLSI guideline EP5-A (Clinical and Laboratory Standards Institute (CLSI) guidelines 2004). Human serum pools with five different levels of CEA concentration for each assay were obtained—Level 1 (0.5–2.00 ng/ml), Level 2 (2.00–10.0 ng/ml), Level 3 (10.0–50.0 ng/ml), Level 4 (50.0–100 ng/ml), and Level 5 (100.0–200.0 ng/ml). To determine and estimate repeatability, between-run, between-day and within-lab imprecisions, the five levels were measured in two replicates per run, two runs per day over 20 days using a single lot. Between-day imprecision was evaluated based on 40 runs over 20 separate days. The acceptance criteria were predetermined to be that repeatability, between-run, between-day and within-lab imprecisions are all less than 15%.

2.9 Multi-Site Precision

Human serum pools with five different levels of CEA concentration for each assay were obtained—Level 1 (0.5–2.00 ng/ml), Level 2 (2.00–10.0 ng/ml), Level 3 (10.0–50.0 ng/ml), Level 4 (50.0–100 ng/ml), and Level 5 (100.0–200.0 ng/ml). The five levels were measured in five replicates per day; 5 days per lot; two lots per site at three different sites. In the end, the data is statistically analyzed to determine and estimate the repeatability, between-day, between-lot, between-site and reproducibility imprecisions. The acceptance criteria were predetermined to be that repeatability, between-day and total variations are all less than 10%.

2.10 Interference Tests

Interference was evaluated according to CLSI guideline EP07-A2 (Clinical and Laboratory Standards Institute (CLSI) guidelines 2008), by testing drug free specimens at two CEA concentrations prepared in CEA-negative human sera (0.5–10.0 ng/ml and 100.0–200.0 ng/ml), spiked with potential interferents: hemoglobin (500 mg/dl), hemoglobin (1,000 mg/dl); bilirubin (20 μg/ml); bilirubin (60 mg/ml); total protein (5 g/dl); total protein (12 g/dl); triglyceride (3 g/dl); HAMA (52.5 ng/ml); RF (500 IU/ml), flutamide (10 μg/ml), diethylstilbestrol (5 μg/ml), goserelin (40 ng/ml); acetaminophen (250 ng/ml); acetysalicylic acid (600 μg/ml); leuprolide (275 ng/ml); ibuprofen (500 μg/ml); finasteride (250 ng/ml); docetaxel (10 μg/ml); urea (500 mg/dl); uric acid (20 mg/dl); 5-fluorouracil; ampicilin (1 mg/ml); ascorbic acid (300 μg/ml); astorvastatin (3,000 μg/ml); bleomycin (3 mg/dl); cefoxitin (2.5 mg/ml); cisplatin (8.8 mg/dl); cyclophosphamide (327.9 mg/dl); cyclosporine (10 μg/ml); diethylstilbestrol (5 μg/ml); docetaxel (10 μg/ml); doxorubicin (16.5 mg/dl); doxycycline (50 μg/ml); etoposide (22 mg/dl); finasteride (250 ng/ml); flutamide (10 μg/ml); furosemide (4 mg/ml); goserelin (40 ng/ml); ibuprofen (500 μg/ml); ifosfamide (261.8 mg/dl); leuprolide acetate (275 ng/ml); levodopa (20 μg/ml); lovastatin (2.5 μg/ml); Mesna (84 mg/dl); methotrexate (459.5 mg/dl); methyldopa (20 μg/ml); N-acetyl-L-cysteine (150 μg/ml); naproxen (500 μg/ml); oxaliplatin (100 μg/ml); paclitaxel (38.2 mg/dl); phenylbutazone (400 μg/ml); prednisone (5 μg/ml); rifampicin (60 μg/ml); tamsulosin (100 ng/ml);

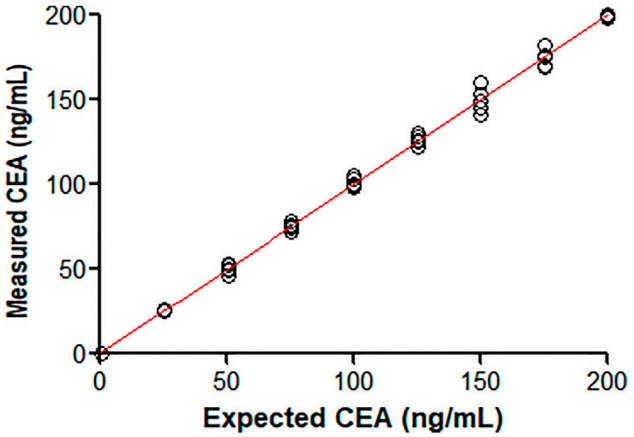

FIGURE 2 | Comparison of measured CEA values against known concentrations of nine different CEA-spiked samples.

tegafur (50 μg/ml); theophylline (50 μg/ml); vinblastine (4 mg/dl); vincristine (0.44 mg/dl); and warfarin (50 μg/ml). The potential interferents and CEA specimens were mixed at a ratio of one part to 19 parts, respectively (1-in-20 dilution) to prepare the test samples. Control sample was also prepared by diluting another aliquot of the same CEA specimen with pure solvent or a diluting solution without any suspected interferents. The percentage interference was calculated from the difference in mean CEA concentration between the test sample and the control sample. If the absolute value of percentage interference was less than 15%, then the assay is deemed to have 100 ± 15% recovery with no interference to the substances.

2.11 Cross-Reactivity Tests

Specimens spiked with beta-hCG (206 mIU/ml), CA125 (100 IU/ml), CA19-9 (423 U/mL), AFP (500 ng/ml), and PSA (50 ng/ml) were prepared to evaluate cross-reactivity. Specimens at two CEA concentrations (identical to the those indicated in **Section 2.10**) were tested for each potential cross-reacting compound in three replicates, and the percentage bias was calculated.

2.12 Method Comparison

The method comparison was conducted according to CLSI guideline EP09-A2 (Clinical and Laboratory Standards Institute (CLSI) guidelines 2013) at the EONE Laboratories (Incheon, South Korea). 140 human serum samples evenly distributed across the entire measuring range were collected from biorepositories, and stored at −70°C before analysis. The samples were analyzed using the Unicel DxI 800 Access Immunoassay System (Beckman Coulter) as the reference device. All specimens were also analyzed on a MARK-B immunoassay system for comparison. Deming regression analysis was conducted to define the Pearson correlation coefficient and the 95% confidence interval (CI) for both the proportional bias (slope) and constant bias (intercept) were determined to claim whether each is significantly different from 1.0 to 0, respectively.

3 RESULTS

3.1 Functional Sensitivity: Limit of Blank, Limit of Detection, and Limit of Quantitation

The claimed LoB was 0.47 ng/ml, where 28 out of 30 blank measurements (93%) were less than or equal to the LoB claim, which is higher than the lower bound (87%) for the sample size of 30. Therefore, the LoB claim was successfully verified. The claimed LoD was 0.50 ng/ml, where 27 out of 30 low level sample measurements (90%) were greater than or equal to the LoB claim. Therefore, the LoD claim was successfully verified. The claimed LoQ was 0.50 ng/ml, where 28 out of 30 measurements (93%) fell within the allowable error window. Therefore, the LoQ claim was successfully verified and was determined to be the same as the LoD.

3.2 Linearity

The measured CEA values of the diluted samples are shown in **Figure 2**. The line of best fit drawn in **Figure 1** produced the following equations as a first-order, second-order and third-order polynomial regression: the first order, $y = 0.9971x + 0.3256$; the second order, $y = -9.498e^{-5}x^2 + 1.016x - 0.2352$; the third order, $y = -6.52e^{-7}x^3 + 0.0001011x^2 + 1.001x - 0.05795$. The nonlinear coefficients of the second-order and the third-order models, b_2 and b_3, were not statistically significant; that is, the coefficients were not significantly different from 0. Therefore, the dataset was considered linear from 0.5 to 200 ng/ml.

3.3 Hook Effect

No clear high dose hook effect was observed up to approximately 500,000 ng/ml, as shown in **Figure 3**.

3.4 Recovery

As shown in **Table 1**, the %recovery ranged from 94.7 to 108.9% with a mean of 100.3%. The recovery range satisfied the predetermined acceptance criteria.

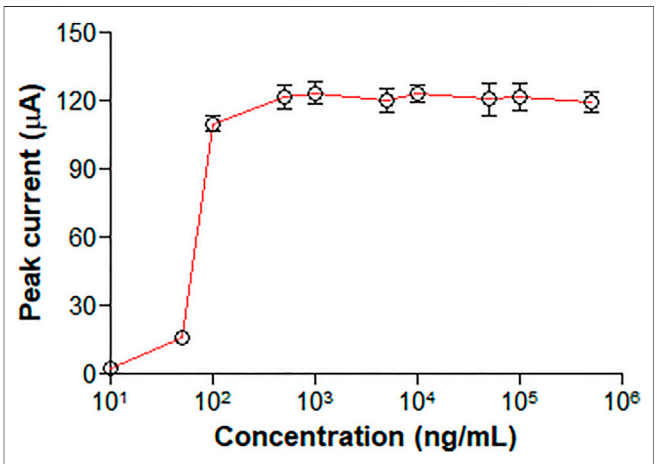

FIGURE 3 | Representation of peak current over a concentration range from 10 to 500,000 ng/ml CEA.

TABLE 1 | Mean % recoveries evaluated from four replicates for each level of concentration.

Sample	Expected concentration (ng/ml)	Measured concentration (ng/ml)	%Recovery	Mean %Recovery
Level 1	3.42	3.30	96.5	99.9
		3.61	105.6	
		3.24	94.7	
		3.51	102.6	
Level 2	15.50	14.90	96.1	99.7
		16.20	104.5	
		15.60	100.6	
		15.10	97.4	
Level 3	75.20	72.30	96.1	102.0
		78.50	104.4	
		81.90	108.9	
		74.20	98.7	
Level 4	151.40	151.20	99.9	99.6
		146.20	96.6	
		149.90	99.0	
		155.70	102.8	

TABLE 2 | Statistical analysis for single-site precision.

Sample	Mean (ng/ml)	N	Repeatability		Between-run		Between-day		Within-lab	
			SD	%CV	SD	%CV	SD	%CV	SD	%CV
1	1.30	80	0.058	4.45	0.000	0.00	0.000	0.00	0.053	4.06
2	3.35	80	0.138	4.11	0.000	0.00	0.038	1.13	0.137	4.10
3	15.3	80	0.539	3.52	0.312	2.04	0.263	1.71	0.676	4.41
4	74.7	80	2.478	3.32	1.228	1.64	0.750	1.00	2.866	3.84
5	154.9	80	5.372	3.47	2.698	1.74	0.604	0.39	4.606	2.97

TABLE 3 | Statistical analysis for multi-site precision.

Sample	Mean (ng/ml)	N	Repeatability		Between-day		Between-lot		Between-site		Reproducibility	
			SD	%CV	SD	%CV	SD	%CV	SD	%CV	SD	%CV
1	1.29	150	0.096	6.63	0.016	1.22	0.000	0.00	0.004	0.32	0.081	6.24
2	3.34	150	0.141	4.21	0.028	0.84	0.093	2.77	0.000	0.00	0.149	4.45
3	15.50	150	0.872	5.62	0.000	0.00	0.201	1.30	0.000	0.00	0.844	5.44
4	75.90	150	3.473	4.58	0.991	1.31	1.596	2.10	0.906	1.19	3.813	5.02
5	158.20	150	6.971	4.41	5.186	3.28	3.330	2.10	1.441	0.91	7.838	4.95

3.5 Single-Site Precision Study

The %CV for repeatability ranged from 3.32 to 4.45% (See **Table 2**). The %CV for run-to-run and day-to-day variations ranged from 0 to 2.04% and 0–1.71%, respectively, across the CEA concentrations from 1.3 ng/ml to 154.9 ng/ml. The within-lab variability across all samples ranged less than 4.41% across the CEA concentrations. Since all single-site precision %CV values were significantly less than 15%, the assay was deemed to satisfy the acceptance criteria.

3.6 Multisite Precision Study

The %CV for repeatability ranged from 4.21 to 6.63% (See **Table 3**). The %CV for between-day, between-lot and between-site variations were less than 3.28% across all the sites, lots, days and CEA concentrations. The %CV for reproducibility ranged from 4.45 to 6.24%. Since all %CV values for repeatability, between-day, between-lot, between-site and reproducibility were less than 10%, the assay was deemed to be acceptable.

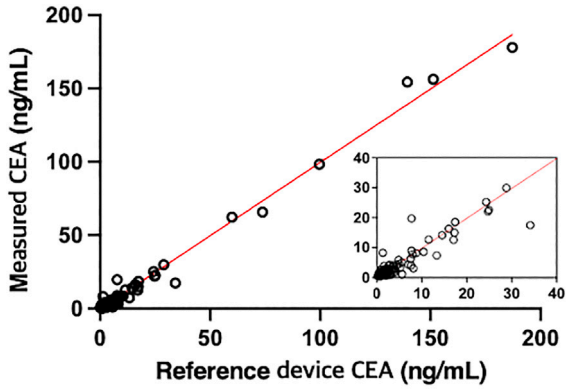

FIGURE 4 | Comparison of the CEA values of 131 samples derived from patients measured by the proposed method with those measured by a reference device, UniCel DxI 800 Access Immunoassay System (Beckman Coulter) (r = 0.9942, y = 0.9985x - 0.1924).

3.7 Interference Tests

The total interference (%) only ranged between −8.01 and 10.28% for both endogenous serum substances (See **Supplementary Table S1**) and drug substances (See **Supplementary Table S2**). Therefore, no significant interference was observed from neither the tested drugs nor the endogenous serum substances that would affect the interpretation of CEA results in this assay. No cross-reactivity with beta-hCG, CA 125, CA 19-9, AFP, and PSA was also observed as shown in **Supplementary Table S3**.

3.8 Method Comparison

140 samples were tested with the proposed and reference methods, nine of which were out of range (<0.5 or >200 ng/ml). Deming regression analysis of comparison gave a slope of 0.9985 (95% CI 0.9798–1.017) and an intercept of −0.1924 (95% CI −0.7154 to 0.3305) as shown in **Figure 4** and **Supplementary Table S4**. The slope was not significantly different from 1.0 (95% CI of slope includes 1.0) indicating the lack of proportional bias in assay results between the proposed and reference methods. The intercept was not significantly different from 0 (95% CI includes 0) indicating the lack of constant bias between the two methods. R (Takahashi et al., 2003) was 0.9884 indicating the differences between the proposed and reference methods are small enough.

4 DISCUSSION

Highly elevated concentrations of CEA in the blood have been known to be associated with a variety of different cancers including colon cancer, stomach cancer, large intestinal cancer (90%), non-small-cell lung carcinoma (70%) and breast cancer (50%) (Thompson et al., 1991). CEA is known to be produced on the cancer cell surface and distributed into the bloodstream, weakening immune responses and inducing cancer cell metastasis (Konstadoulakis et al., 1994; Thomas et al., 1995; Haidopoulos et al., 2000). Therefore, monitoring and managing blood CEA concentration are highly important in managing the conditions of cancer patients. Through a variety of studies, the importance of monitoring blood CEA concentration has been consolidated: it could be used as an indicator to predict whether the cancer would grow and spread again after surgery and make other prognostic assessments (Moertel et al., 1993); predict the survival and death rate (Ebeling et al., 2002). It has also been reported to have a sensitivity of 69% and a specificity of 68% in diagnosing lung cancer (Okamura et al., 2013).

Recently, the demand for not only within-laboratory, but also "in-the-field" (i.e., in a natural environment outside of hospitals and laboratories) diagnostic tests for better access to *in vitro* diagnostic instruments has been continuously expanding. As the *in vitro* diagnostic instruments being used in clinical laboratories and hospitals are too large and heavy to transport and complicated in their analyses requiring the assistance of an expert and other instruments to operate, diagnosis in the field is impossible. Hence, to be able to conduct diagnosis in the field, the instrument must not only be accurate and precise, but should also demonstrate portability and automation.

Currently, the most commonly adopted immunoassay techniques in POCT is lateral flow immunoassay (LFIA) (Liu et al., 2016; Lee and Lee 2020; Mahmoudi et al., 2021). In the case of LFIA, accurate quantification of protein concentration is very difficult, since the LFIA is based on a paper sheet, which is a random fiber network, to deliver the samples and reagents to the detection site. The flow through the paper sheet is also dependent on many physical parameters, such as the temperature, the gravity, the viscosity of samples, and so on. The antibody-antigen reactions in the LFIA are passive, thus its performances are not tunable once established. Due to the intrinsic limitations, most of the commercial rapid diagnostic testing kits based on LFIA could be applied only for the qualitative analysis of biomarkers, rather than the quantitative analysis.

The MESIA resolves all the issues mentioned prior. The antigen-antibody reactions are facilitated and actively controlled using AuMNPs and external magnetic fields (Hwang et al., 2019b). Therefore, the time for analysis is relatively short and the reaction scheme is programmable for the optimization of reaction conditions depending on the target biomarkers. The required volume of the sample is only a few microliters, which is fixed by the volume of the reaction chamber that is a fine plastic microchannel confined by a microvalve. The MESIA doesn't require any washing buffer, but utilizes the magnetic fields to remove unbound proteins and probes, thus all the required functions for immunoassay can be integrated into a tiny disposable chip. The detection is based on electrochemistry, so no optical components are required for a reader, which makes it portable and cost-effective, resulting in an *in vitro* diagnostic device relevant for POCT.

In this study, performance evaluation of the MARK-B immunoassay system, which is based on the MESIA, has been conducted according to the CLSI guidelines, where analytical parameters including linearity, hook effect, precision, recovery, interference, cross-reactivity, and accuracy compared to the reference device were assessed. The MARK-B immunoassay

system satisfied all the acceptance criteria for the analytical performances. Moreover, the method comparison results with Unicel DxI 800 Access Immunoassay System (Beckman Coulter) as the reference device revealed an *R* (Takahashi et al., 2003) value of 0.9985, showing that the CEA measurand values of the MESIA-incorporated instrument are almost equivalent to those of the large-scale instrument.

In the MARK-B immunoassay system, all the processes from sample preparation to electrochemical detection are fully integrated and automated, as like conventional automated instruments for hospital uses. Most of the automated instrument for CEA immunoassay utilize chemiluminescence immunoassay (Matsushita et al., 1996; Akbas et al., 2014; Zhang et al., 2016; Park et al., 2018), resulting in high sensitivity and high throughput, but they are too heavy and large to be mobile for the POCT applications. Although lots of research on the lab-on-a-chip technology that targets CEA for POCT have been reported in the past (e.g., glass capillaries (Hu et al., 2013), a combination of microfluidics and nanoimprint with plasmonic biochips (Zhou et al., 2019), and electrochemical microfluidic chip (Xie et al., 2015)), most of the currently being researched lab-on-a-chip techniques do not address the issues regarding mass production and reproducibility. The MARK-B immunoassay system has already been successfully validated and commercialized for both qualitative and quantitative determination of various biomarkers by applying different types of antibodies, proving that the platform could be useful for the diagnostics of a variety of diseases including infectious diseases and cancers (Hwang et al., 2019a; Jo et al., 2021).

In conclusion, the MARK-B immunoassay system, which is based on MESIA, satisfied the acceptable criteria for precision, accuracy, functional sensitivity, Hook effect, linearity, interference, cross-reactivity, and method comparison with a commercial instrument for hospital uses. Therefore, the MARK-B immunoassay system has been shown to be useful in clinical practices as a rapid, accurate, and convenient way for the quantification of CEA.

DATA AVAILABILITY STATEMENT

The original contributions presented in the study are included in the article/**Supplementary Material**, further inquiries can be directed to the corresponding author.

ETHICS STATEMENT

The studies involving human participants were reviewed and approved by Advarra IRB. The patients/participants provided their written informed consent to participate in this study.

AUTHOR CONTRIBUTIONS

HH designed and directed the study. BH performed the experiments and wrote the manuscript. EK and S-hK contributed to sample preparation and interpretation of the results.

FUNDING

This research was supported by the Korea Health Technology R & D Project through the Korea Health Industry Development Institute (KHIDI) and Korea Dementia Research Center (KDRC), funded by the Ministry of Health & Welfare and Ministry of Science and ICT, Republic of Korea (grant number: HU21C0007).

SUPPLEMENTARY MATERIAL

The Supplementary Material for this article can be found online at: https://www.frontiersin.org/articles/10.3389/fbioe.2021.798079/full#supplementary-material

REFERENCES

Akbas, N., Schryver, P. G., Algeciras-Schimnich, A., Baumann, N. A., Block, D. R., Budd, J. R., et al. (2014). Evaluation of Beckman Coulter DxI 800 Immunoassay System Using Clinically Oriented Performance Goals. *Clin. Biochem.* 47, 158–163. doi:10.1016/j.clinbiochem.2014.08.005

Clinical and Laboratory Standards Institute (CLSI) guidelines (2012). *EP-17-A2 Evaluation of Detection Capability for Clinical Laboratory Measurement Procedures; Approved Guidelines*. 2nd Edition. Malvern: CLSI.

Clinical and Laboratory Standards Institute (CLSI) guidelines (2003). *EP-6-A Evaluation of Quantitative Measurement Procedures: Statistical Approach; Approved Guidelines*. Malvern: CLSI.

Clinical and Laboratory Standards Institute (CLSI) guidelines (2013). *EP09-A3 Method Comparison and Bias Estimation Using Patient Samples; Approved Guidelines*. Malvern: CLSI.

Clinical and Laboratory Standards Institute (CLSI) guidelines (2004). *EP5-A2 Evaluation of Precision Performance of Quantitative Measurement Methods; Approved Guideline*. Second Edition. Malvern: CLSI.

Clinical and Laboratory Standards Institute (CLSI) guidelines (2008). *EP7-A Interference Testing in Clinical Chemistry*. Malvern: CLSI.

Ebeling, F. G., Stieber, P., Untch, M., Nagel, D., Konecny, G. E., Schmitt, U. M., et al. (2002). Serum CEA and CA 15-3 as Prognostic Factors in Primary Breast Cancer. *Br. J. Cancer* 86, 1217–1222. doi:10.1038/sj.bjc.6600248

Grunnet, M., and Sorensen, J. B. (2012). Carcinoembryonic Antigen (CEA) as Tumor Marker in Lung Cancer. *Lung Cancer* 76, 138–143. doi:10.1016/j.lungcan.2011.11.012

Haidopoulos, D., Konstadoulakis, M. M., Antonakis, P. T., Alexiou, D. G., Manouras, A. M., Katsaragakis, S. M., et al. (2000). Circulating Anti-CEA Antibodies in the Sera of Patientswith Breast Cancer. *Eur. J. Surg. Oncol. (Ejso)* 26 (8), 742–746. doi:10.1053/ejso.2000.0996

Hu, W., Lu, Z., Liu, Y., Chen, T., Zhou, X., and Li, C. M. (2013). A Portable Flow-Through Fluorescent Immunoassay Lab-On-A-Chip Device Using ZnO Nanorod-Decorated Glass Capillaries. *Lab. Chip* 13, 1797–1802. doi:10.1039/c3lc41382a

Hwang, H., Kim, J., Choi, J., Kim, K. H., and Han, H. S. (2019a). Evaluation of MARK BTM for Quantitative Measurement of Three Tumor Markers: Prostate Specific Antigen, Alpha Fetoprotein, and Carcinoembryonic Antigen. *Clin. Lab.* 65 (8), 1567–1570. doi:10.7754/Clin.Lab.2019.190130

Hwang, H., Choi, E., Han, S., Lee, Y., Choi, T., Kim, M., et al. (2019b). MESIA: Magnetic Force-Assisted Electrochemical sandwich Immunoassays for Quantification of Prostate-specific Antigen in Human Serum. *Analytica Chim. Acta* 1061, 92–100. doi:10.1016/j.aca.2019.02.018

Jiang, J., Zhao, S., Huang, Y., Qin, G., and Ye, F. (2013). Highly Sensitive Immunoassay of Carcinoembryonic Antigen by Capillary Electrophoresis with Gold Nanoparticles Amplified Chemiluminescence Detection. *J. Chromatogr. A* 1282, 161–166. doi:10.1016/j.chroma.2013.01.066

Jo, S. J., Shin, S.-h., Kim, J., Lee, S., and Lee, J. (2021). Evaluation of the Clinical Performance of a Magnetic Force-Assisted Electrochemical Immunoassay for the Detection of SARS-CoV-2 Antigens. *PLoS One* 16 (10), e0258394. doi:10.1371/journal.pone.0258394

Konstadoulakis, M. M., Syrigos, K. N., Albanopoulos, C., Mayers, G., and Golematis, B. (1994). The Presence of Anti-carcinoembryonic Antigen (CEA) Antibodies in the Sera of Patients with Gastrointestinal Malignancies. *J. Clin. Immunol.* 14 (5), 310–313. doi:10.1007/bf01540984

Kroll, M. H., and Emancipator, K. (1993). A Theoretical Evaluation of Linearity. *Clin. Chem.* 39 (3), 405–413. doi:10.1093/clinchem/39.3.405

Lee, S., and Lee, H. J. (2020). Recent Research Trend in Lateral Flow Immunoassay Strip (LFIA) with Colorimetric Method for Detection of Cancer Biomarkers. *Appl. Chem. Eng.* 31 (6), 585–590.

Li, Y., Yang, W.-K., Fan, M.-Q., and Liu, A. (2011). A Sensitive Label-free Amperometric CEA Immunosensor Based on Graphene-Nafion Nanocomposite Film as an Enhanced Sensing Platform. *Anal. Sci.* 27 (7), 727. doi:10.2116/analsci.27.727

Lin, J., Yan, F., and Ju, H. (2004). Noncompetitive Enzyme Immunoassay for Carcinoembryonic Antigen by Flow Injection Chemiluminescence. *Clinica Chim. Acta* 341, 109–115. doi:10.1016/j.cccn.2003.11.014

Liu, F., Zhang, H., Wu, Z., Dong, H., Zhou, L., Yang, D., et al. (2016). Highly Sensitive and Selective Lateral Flow Immunoassay Based on Magnetic Nanoparticles for Quantitative Detection of Carcinoembryonic Antigen. *Talanta* 161, 205–210. doi:10.1016/j.talanta.2016.08.048

Mahmoudi, T., Pourhassan-Moghaddam, M., Shirdel, B., Baradaran, B., Morales-Narváez, E., and Golmohammadi, H. (2021). On-site Detection of Carcinoembryonic Antigen in Human Serum. *Biosensors* 11, 392. doi:10.3390/bios11100392

Matsushita, H., Jingzhi, X., Kuroki, M., Kondo, A., Inoue, E., Teramura, Y., et al. (1996). Establishment and Evaluation of a New Chemiluminescent Enzyme Immunoassay for Carcinoembryonic Antigen Adapted to the Fully Automated ACCESS System. *Eur. J. Clin. Chem. Clin. Biochem.* 34, 829–835. doi:10.1515/cclm.1996.34.10.829

Moertel, C. G., Fleming, T. R., Tangen, C., Haller, D. G., Laurie, J. A., and Macdonald, J. S. (1993). An Evaluation of the Carcinoembryonic Antigen (CEA) Test for Monitoring Patients with Resected colon Cancer. *JAMA* 270 (8), 943–947. doi:10.1001/jama.270.8.943

Okamura, K., Takayama, K., Izumi, M., Harada, T., Furuyama, K., and Nakanishi, Y. (2013). Diagnostic Value of CEA and CYFRA 21-1 Tumor Markers in Primary Lung Cancer. *Lung Cancer* 80 (1), 45–49. doi:10.1016/j.lungcan.2013.01.002

Park, B.-W., Oh, J.-W., Kim, J.-H., Park, S. H., Kim, K.-S., Kim, J. H., et al. (2008). Preoperative CA 15-3 and CEA Serum Levels as Predictor for Breast Cancer Outcomes. *Ann. Oncol.* 19, 675–681. doi:10.1093/annonc/mdm538

Park, J., Lee, S., Kim, Y., Choi, A., Lee, H., Lim, J., et al. (2018). Comparison of Four Automated Carcinoembryonic Antigen Immunoassays: ADVIA Centaur XP, ARCHITECT I2000sr, Elecsys E170, and Unicel Dxi800. *Ann. Lab. Med.* 38 (4), 355–361. doi:10.3343/alm.2018.38.4.355

Takahashi, Y., Takeuchi, T., Sakamoto, J., Touge, T., Mai, M., Ohkura, H., et al. (2003). The Usefulness of CEA And/or CA19-9 in Monitoring for Recurrence in Gastric Cancer Patients: a Prospective Clinical Study. *Gastric Cancer* 6, 142–145. doi:10.1007/s10120-003-0240-9

Thomas, P., Gangopadhyay, A., Steele, G., Andrews, C., Nakazato, H., Oikawa, S., et al. (1995). The Effect of Transfection of the CEA Gene on the Metastatic Behavior of the Human Colorectal Cancer Cell Line MIP-101. *Cancer Lett.* 92 (1), 59–66. doi:10.1016/0304-3835(95)03764-n

Thompson, J. A., Grunert, F., and Zimmermann, W. (1991). Carcinoembryonic Antigen Gene Family: Molecular Biology and Clinical Perspectives. *J. Clin. Lab. Anal.* 5 (5), 344–366. doi:10.1002/jcla.1860050510

Tobi, M., O'Kieffe, D., Trujillo, N., Nochomovitz, L. E., and Steinberg, W. M. (1992). Detection of Carcinoembryonic Antigen in Colonic Effluent by Specific Anti-CEA Monoclonal Antibodies. *Cancer Lett.* 67, 47–54. doi:10.1016/0304-3835(92)90007-i

Vernava, A. M., III, Longo, W. E., Virgo, K. S., Coplin, M. A., Wade, T. P., and Johnson, F. E. (1994). Current Follow-Up Strategies after Resection of colon Cancer. *Dis. Colon Rectum* 37, 573–583. doi:10.1007/bf02050993

Wang, D., Li, Y., Lin, Z., Qiu, B., and Guo, L. (2015). Surface-enhanced Electrochemiluminescence of Ru@SiO2 for Ultrasensitive Detection of Carcinoembryonic Antigen. *Anal. Chem.* 87 (12), 5966–5972. doi:10.1021/acs.analchem.5b01038

Wu, K., Chu, C., Ma, C., Yang, H., Yan, M., Ge, S., et al. (2015). Immunoassay for Carcinoembryonic Antigen Based on the Zn2+-Enhanced Fluorescence of Magnetic-Fluorescent Nanocomposites. *Sensors Actuators B: Chem.* 206, 43–49. doi:10.1016/j.snb.2014.09.041

Xie, Y., Zhi, X., Su, H., Wang, K., Yan, Z., He, N., et al. (2015). A Novel Electrochemical Microfluidic Chip Combined with Multiple Biomarkers for Early Diagnosis of Gastric Cancer. *Nanoscale Res. Lett.* 10, 477. doi:10.1186/s11671-015-1153-3

Yang, X., Zhuo, Y., Zhu, S., Luo, Y., Feng, Y., and Xu, Y. (2015). Selectively Assaying CEA Based on a Creative Strategy of Gold Nanoparticles Enhancing Silver Nanoclusters' Fluorescence. *Biosens. Bioelectron.* 64, 345–351. doi:10.1016/j.bios.2014.09.029

Zhang, G.-M., Guo, X. X., Ma, X.B., and Zhang, G. M. (2016). Reference Intervals of Alpha-Fetoprotein and Carcinoembryonic Antigen in the Apparently Healthy Population. *Med. Sci. Monit.* 22, 4875–4880. doi:10.12659/msm.901861

Zhou, J., Tao, F., Zhu, J., Lin, S., Wang, Z., Wang, X., et al. (2019). Portable Tumor Biosensing of Serum by Plasmonic Biochips in Combination with Nanoimprint and Microfluidics. *Nanophotonics* 8 (2), 307–316. doi:10.1515/nanoph-2018-0173

Conflict of Interest: Author HH is employed by the company BBB Inc.

The remaining authors declare that the research was conducted in the absence of any commercial or financial relationships that could be construed as a potential conflict of interest.

Publisher's Note: All claims expressed in this article are solely those of the authors and do not necessarily represent those of their affiliated organizations, or those of the publisher, the editors, and the reviewers. Any product that may be evaluated in this article, or claim that may be made by its manufacturer, is not guaranteed or endorsed by the publisher.

frontiers in Bioengineering and Biotechnology

METHODS
published: 08 February 2022
doi: 10.3389/fbioe.2021.797957

Loop-Mediated Isothermal Amplification Coupled With Nanoparticle-Based Lateral Biosensor for Rapid, Sensitive, and Specific Detection of *Bordetella pertussis*

Chunrong Sun, Fei Xiao, Jin Fu, Xiaolan Huang, Nan Jia, Zheng Xu, Yi Wang * and Xiaodai Cui *

Experiment Center, Captital Institute of Pediatrics, Beijing, China

OPEN ACCESS

Edited by:
Tailin Xu,
Shenzhen University, China

Reviewed by:
Junjie Yue,
Institute of Biotechnology (CAAS), China
Yan Huang,
University of Science and Technology Beijing, China

***Correspondence:**
Xiaodai Cui
xdcui61@163.com
Yi Wang
wildwolf0101@163.com

Specialty section:
This article was submitted to Biosensors and Biomolecular Electronics, a section of the journal Frontiers in Bioengineering and Biotechnology

Received: *19 October 2021*
Accepted: *23 December 2021*
Published: *08 February 2022*

Citation:
Sun C, Xiao F, Fu J, Huang X, Jia N, Xu Z, Wang Y and Cui X (2022) Loop-Mediated Isothermal Amplification Coupled With Nanoparticle-Based Lateral Biosensor for Rapid, Sensitive, and Specific Detection of Bordetella pertussis. *Front. Bioeng. Biotechnol. 9:797957. doi: 10.3389/fbioe.2021.797957*

Bordetella pertussis is the most frequent causative agent for pertussis, which is a highly contagious disease. Here, we developed a method based on loop-mediated isothermal amplification (LAMP) and nanoparticle-based lateral flow biosensor (LFB) for the timely diagnosis of *B. pertussis* infections. A set of six primers was designed for LAMP reactions, and the LAMP results were rapidly and visually indicated using LFB. The recommended condition for the *B. pertussis* LAMP reactions is 40 min at 66°C. Our results confirmed that the LAMP-LFB assay could specifically detect *B. pertussis* and did not cross-react with non-*B. pertussis* isolates. The sensitivity of the *B. pertussis* LAMP-LFB assay was 50 fg per reaction. In particular, 108 nasopharyngeal swab (NPS) samples were collected to evaluate the *B. pertussis* LAMP-LFB assay, and the results were compared with those of the quantitative PCR (qPCR) method. The positive rates of *B. pertussis* LAMP-LFB and qPCR were 40.7% and 38.8%, respectively, and the agreement between the LAMP-LFB and qPCR results was 98%, with a kappa value of 0.96. The whole process of LAMP-LFB can be completed within 1 h, which is much shorter than that of qPCR, including about 15 min of rapid DNA extraction, 40 min of LAMP reaction, and within 2 min of the LFB test. Collectively, the *B. pertussis* LAMP-LFB assay developed in this report offers a new option for the rapid, reliable, and simple diagnosis of *B. pertussis* infections.

Keywords: Bordetella pertussis, LAMP, lateral flow biosensor, rapid diagnosis, qPCR

INTRODUCTION

*B*ordetella *pertussis* mainly causes pertussis, a highly infectious, even fatal illness in children. In the past few years, the resurgence of pertussis has become a global public health issue in spite of high vaccination rates (Wood and McIntyre, 2008; Cherry, 2013; Mooi et al., 2014; Yeung et al., 2017; Del Valle-Mendoza et al., 2021; Pandolfi et al., 2021). In China, *B. pertussis* infections are becoming more and more prevalent even with over 99% vaccination coverage in children during the last 20 years (Liu et al., 2018; Fu et al., 2019; Zhang et al., 2019; Kang et al., 2022). Consequently, a rapid and reliable laboratory diagnosis of *B. pertussis* is particularly important (Cherry et al., 2005; de Greeff et al., 2010; Tao et al., 2019; Wu et al., 2019; Macina and Evans, 2021).

The current approaches to the diagnosis of pertussis include direct fluorescent antibody (DFA) assay, culture-based approaches, serodiagnosis, and PCR assays (van der Zee et al., 2015). DFA is a simple

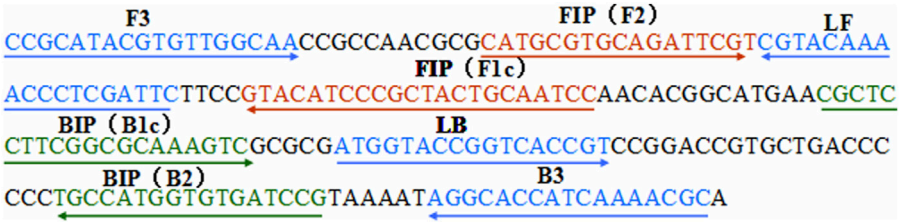

FIGURE 1 | Locations of the primer sequences used in this study for targeting the pertussis toxin (PT) promoter region of *Bordetella pertussis*. *Right* and *left arrows* show the sense and complementary sequences, respectively. The *colored text* indicates the positions of the primers, including two outer primers (F3 and B3), two inner primers (FIP and BIP), and two loop primers (LF* and LB).

fluorescent antibody examination done through microscopic observation directed to the pathogen, but lacks both specificity and sensitivity (Chia et al., 2004; van der Zee et al., 2015). Culture is the gold standard diagnostic test, but with very low sensitivity. Meanwhile, the process of culture is laborious and time-consuming, which do not help with timely treatment, especially for infants too young to be vaccinated. Serodiagnosis is another technique earlier used for confirmation of the clinical diagnosis of pertussis, but it suffers persistent problems, including cross-reactivity with other bacteria, not only with *Bordetella* species, and the interference of previous vaccination or previous infections (Chia et al., 2004; Mertens et al., 2007; Bock et al., 2012). At present, PCR-based assays [e.g., conventional PCR, real-time PCR (RT-PCR), and quantitative PCR (qPCR)] have been established for the detection of *B. pertussis* (Roorda et al., 2011; Tatti et al., 2011; Abu Raya et al., 2012; Gao et al., 2014; Pittet et al., 2014). In particular, RT-PCR and qPCR use labeled probes to release a reporter or high-resolution melt (HRM) analysis to the amplicon, thus allowing the real-time monitoring of the amplification results. However, RT-PCR and qPCR examination is rarely available in primary medical institutions or in underdeveloped areas due to the high requirements of equipment and skilled professionals for a PCR laboratory.

Loop-mediated isothermal amplification (LAMP) is a newly developed amplification technique amplifying DNA at an isothermal condition, which can be satisfied merely by a water bath or a heater. By using six primers directing the different regions of the target sequence, this method showed high specificity, sensitivity, and efficiency (Notomi et al., 2000; Kamachi et al., 2006; Fujino et al., 2015; Notomi et al., 2015). In this report, we employed LAMP to amplify the target sequence of the pertussis toxin (PT) promoter, *ptxA* (pertussis toxin subunit 1), assumed to be specific for *B. pertussis* (Grimprel et al., 1993; Nygren et al., 2000). The LAMP products were judged using nanoparticle-based lateral flow biosensor (LFB), a method for the detection of nucleic acid and protein molecules (Huang et al., 2021; Huang et al., 2020; Huang et al., 2019), which can visually, rapidly and objectively indicate the results without the need for any extra instrument. The *B. pertussis* LAMP-LFB assay was further evaluated by applying it to clinical nasopharyngeal swab (NPS) samples.

MATERIALS AND METHODS

Reagents and Instruments

The DNA isothermal amplification kit, visual detection reagent (VDR), and the nanoparticle-based LFB were obtained from Huidexin Biotech Co., Ltd. (Tianjin, China). The primers and labeled primers used in this study were synthesized by AoKe Biotech (Beijing) Co., Ltd. (Beijing, China). The *B. pertussis* isolate and qPCR kits were purchased from Beijing Transgen Biotech Co., Ltd. (Beijing, China) and Shanghai ZJ Bio-Tech Co., Ltd. (Shanghai, China). Real-time turbidimeter LA-320C was purchased from Eiken Chemical Co., Ltd. (Tokyo, Japan).

Primer Design

A set of six primers, including two outer primers (F3 and B3), two inner primers (FIP and BIP), and two loop primers (LF* and LB), was designed based on the specific pertussis toxin (PT) promoter gene of *Bordetella pertussis* (genome positions 159549–159755; GeneBank: BX640422) using Primer Premier 5.0. The sequences, locations, and modifications of the primers used in this report are shown in **Figure 1** and **Table 1**.

TABLE 1 | Sequences of the primers used in this study

Assay	Primers	Sequence (5'–3')
LAMP	BT-F3	CCGCATACGTGTTGGCA
	BT-B3	GCGTTTTGATGGTGCCT
	BT-FIP	GGATTGCAGTAGCGGGATGTAC-CATGCGTGCAGATTCGT
	BT-BIP	CGCTCCTTCGGCGCAAAGTC-CGGATCACACCATGGCA
	BT-LF	GAATCGAGGGTTTTGTACG
	BT-LB	ATGGTACCGGTCACCGT
Labeled primer[a]	BT-LF*	5'-Fam-GAATCGAGGGTTTTGTACG-3'

[a]*Fam, carboxyfluorescein. BT-LF*, 5' labeled with Fam used in the loop-mediated isothermal amplification/nanoparticle-based lateral flow biosensor (LAMP-LFB) assay*

TABLE 2 | Bacterial strains used to determine the specificity of loop-mediated isothermal amplification (LAMP)

Bacteria	Strain no. (source of strains)	No. of strains	*B. pertussis* LAMP-LFB
Bordetella pertussis	Isolated strains (CIP)	3	P
Enteroinvasive *Escherichia coli*	Isolated strains (CDC)	1	N
Enteroadherent *Escherichia coli*	Isolated strains (CDC)	1	N
Enterotoxic *Escherichia coli*	Isolated strains (CDC)	1	N
Enteropathogenic *Escherichia coli*	Isolated strains (CDC)	1	N
Shiga toxin-producing *Escherichia coli*	Isolated strains (CDC)	1	N
Streptococcus suis	Isolated strains (CDC)	2	N
Citrobacter	Isolated strains (CDC)	2	N
Listeria innocua	Isolated strains (CDC)	1	N
Listeria monocytogenes	Isolated strains (CDC)	1	N
Listeria ivanovii	Isolated strains (CDC)	1	N
Klebsiella pneumoniae	Isolated strains (CDC)	3	N
Streptococcus salivarius	Isolated strains (CDC)	1	N
Mycobacterium tuberculosis	Isolated strains (CDC)	1	N
Corynebacterium striatum	Isolated strains (CDC)	1	N
Nocardia asteroides	Isolated strains (CDC)	1	N
Moraxella catarrhalis	Isolated strains (CDC)	1	N
Stenotrophomonas maltophilia	Isolated strains (CDC)	1	N
Staphylococcus epidermidis	Isolated strains (CDC)	1	N
Staphylococcus amber	Isolated strains (CDC)	1	N
Staphylococcus haemolyticus	Isolated strains (CDC)	1	N
N.Lac	Isolated strains (CDC)	1	N
Neisseria meningitidis	Isolated strains (CDC)	1	N
Streptococcus pneumoniae	Isolated strains (CDC)	1	N
Streptococcus pyogenes	Isolated strains (CDC)	1	N
Pseudomonas aeruginosa	Isolated strains (CDC)	4	N
Monilia albicans	Isolated strains (CDC)	2	N
Bacillus cereus	Isolated strains (CDC)	1	N
Streptococcus aureus	Isolated strains (CDC)	1	N
Salmonella	Isolated strains (CDC)	2	N
Shigella sonnei	Isolated strains (CDC)	1	N
Shigella baumannii	Isolated strains (CDC)	1	N
Enterococcus faecalis	Isolated strains (CDC)	2	N

Only Bordetella pertussis *strains were detected as positive, indicating the high specificity of the* B. pertussis *loop-mediated isothermal amplification/nanoparticle-based lateral flow biosensor (LAMP-LFB) assay.*

CIP, *Capital Institute of Pediatrics;* CDC, *Chinese Center for Disease Control and Prevention.;* P, *positive;* N, *negative*

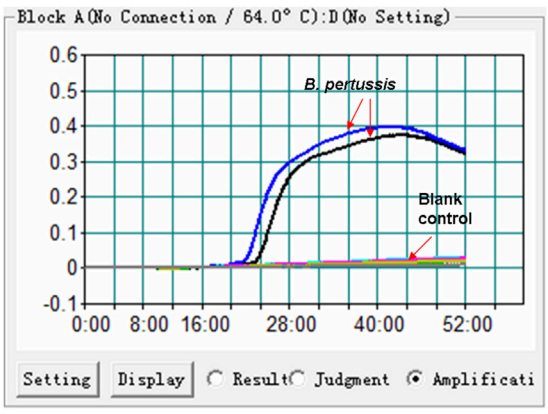

FIGURE 2 | Effectiveness of the primer set for the *Bordetella pertussis* loop-mediated isothermal amplification (LAMP) reaction. The DNA templates extracted from *B. pertussis* strains were effectively amplified with LAMP reaction at 64°C, while there was no reaction for the blank controls (distilled water, DW).

LAMP Reaction

LAMP reactions were performed as a one-step reaction in a 25-μl mixture containing 12.5 μl reaction buffer, 0.1 μmol L^{-1} each of the displacement primers (F3 and B3), 0.4 μmol L^{-1} each of the inner primers (FIP and BIP), 0.2 μmol L^{-1} each of the loop primers (LF* and LB), 1.0 μl *Bst* DNA polymerase (8 U), 0.5 μl biotin-14-dCTP (Huidexin Biotech Co., Ltd., Tianjin, China), 1.0 μl VDR, and 1.0 μl template for pure culture (5 μl for clinical sample).

Lateral Flow Biosensor (LFB) Test

LFB was constructed according to the previous report (Li et al., 2020). Briefly, LFB contained a sample pad, a conjugate pad, a nitrocellulose(NC)membrane (#Whatma99; Jie-Yi biotech Co., Ltd, Shanghai, China) and a absorbent pad (Huidexin Biotech Co., Ltd, Tianjin, China). On the conjugated pad, the detector reagents (dye streptavidin-coated gold nanoparticles (streptavidin-GNPs)) were laminated. As for the control line (CL) and test line (TL),

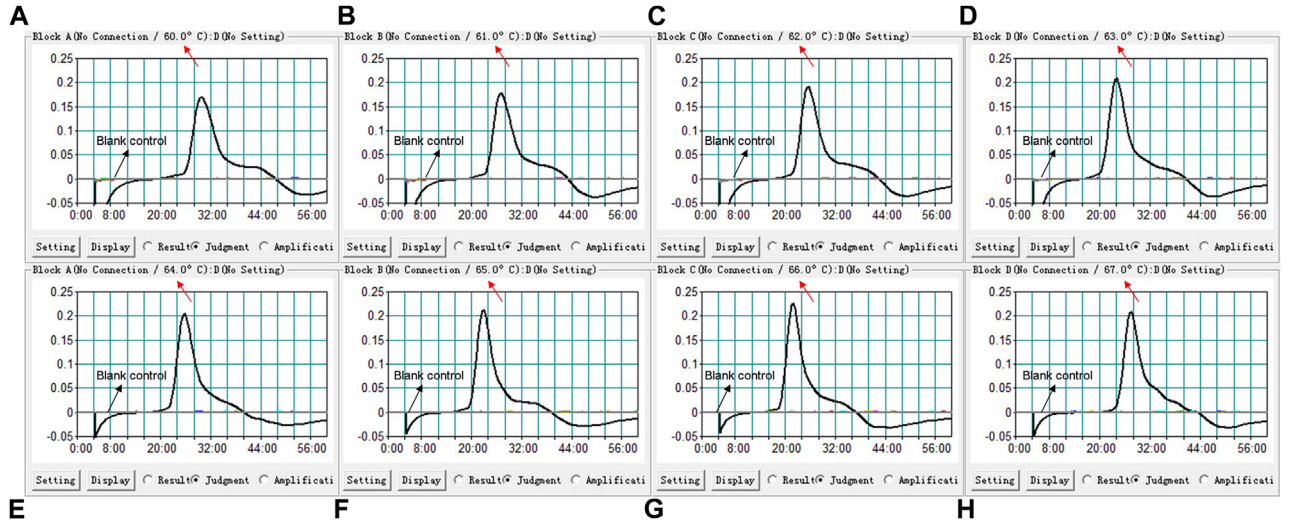

FIGURE 3 | Temperature optimization for the loop-mediated isothermal amplification (LAMP) assay. LAMP reactions detecting *Bordetella pertussis* were conducted using real-time turbidimetry and kinetic curves **(A–H)** at different temperatures ranging from 60°C to 67°C were acquired, showing that 66°C was optimal for the *B. pertussis* LAMP reaction.

Biotin-BSA and anti-FAM were immobilized on the NC membrane, respectively. The finally assembled biosensors were packaged in plastic box and conserved with silica gel desiccant at room temperature. For indicating the LAMP results, a 5 µl aliquot of LAMP reaction products was added to the sample pad, followed with 100 µl running buffer (10 mM PBS, PH 7.4 with 1% Tween 20), The results was indicated within 2 min, two red lines at TL and CL represent positive and one red line at CL means negative.

Optimal Temperature for the *B. pertussis* LAMP Assay

The amplification temperatures were optimized from 60°C to 67°C with 1°C intervals for the optimal temperature of the LAMP reaction. The DNA template of *B. pertussis* was used as a positive control and distilled water (DW) was used as the blank control. The LAMP reactions were monitored using real-time turbidity measurements.

Specificity of the *B. pertussis* LAMP-LFB Assay

To evaluate the specificity of the *B. pertussis* LAMP-LFB assay, the DNA templates from *B. pertussis* and non-*B. pertussis* strains (**Table 2**) were tested at least twice with the assay.

Sensitivity of the *B. pertussis* LAMP-LFB Assay

To verify the limit of detection (LoD), the DNA templates of *B. pertussis* were serially diluted (5 ng ml^{-1}; 500, 50, and 5 pg ml^{-1}; and 500, 50, and 5 fg ml^{-1}) for the LAMP assay, and 1 µl of each serial dilution or DW was added to the reaction mixtures. The LoD of the *B. pertussis* LAMP assay was determined using real-time turbidity measurement, VDR, and the LFB test. All tests were repeated at least twice.

Optimal Amplification Time for the *B. pertussis* LAMP Assay

Serially diluted templates were applied to obtain the optimal amplification time. LAMP reactions were conducted at 66°C with reaction times ranging from 10 to 40 min, with 10-min intervals. Each reaction time was verified twice.

Application of the *B. pertussis* LAMP-LFB Assay in Clinical Specimens

A total of 108 NPS samples collected from patients suspected of pertussis in the clinics of the Children's Hospital affiliated with the Capital Institute of Pediatrics from January 1, 2019 to December 30, 2020 were retrospectively used. All samples were obtained with informed consent signed by the guardians of the participants. Nucleic extractions from these samples were firstly used for clinical and laboratory diagnosis. A volume of 5 µl DNA template was collected from the remaining samples for the *B. pertussis* LAMP-LFB assay. The results of the *B. pertussis* LAMP-LFB assay were compared with those of the qPCR assay for identical samples. All procedures were reviewed and approved by the Ethics Committee of the Capital Institute of Pediatrics.

Statistical Analysis

A comparison between two methods, qPCR and LAMP-LFB assay, was analyzed using the χ^2 test with SPSS software

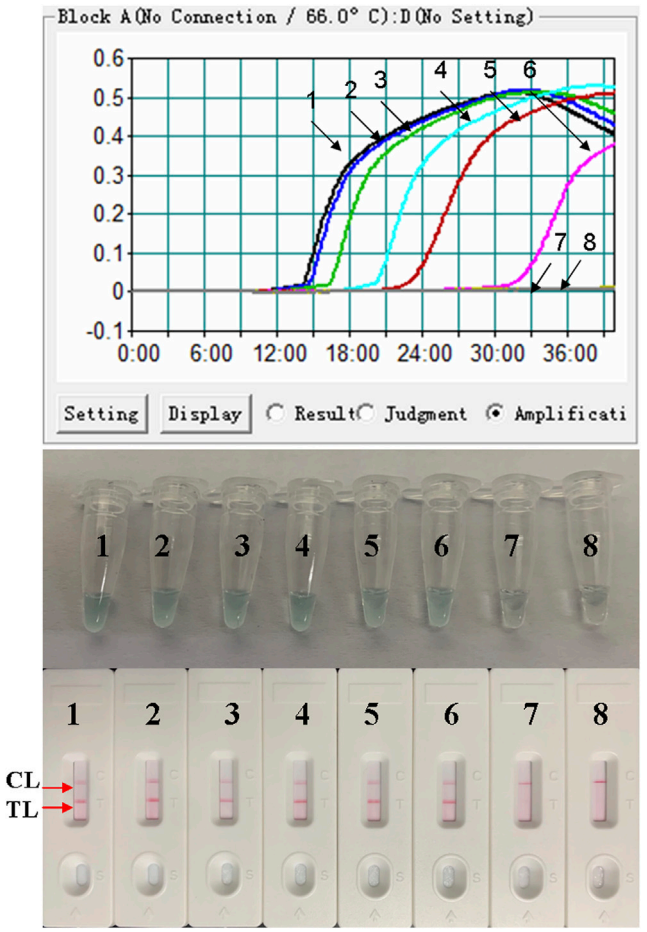

FIGURE 4 | Sensitivity confirmation of the *Bordetella pertussis* loop-mediated isothermal amplification (LAMP) assay. The sensitivity of the assay was analyzed using 10-fold serial dilutions from 5 ng to 5 fg per reaction. The LAMP reactions with various levels of DNA templates were recorded with turbidity curves, and the products were indicated by a visual detection reagent (VDR) and a nanoparticle-based lateral flow biosensor (LFB). Turbidity curves/tubes/strips *1–7* represent different concentrations of DNA: 5 ng; 500, 50, and 5 pg; and 500, 50, and 5 fg per reaction. Turbidity curve/tube/strip *8* represents the blank control. *TL*, test line; *CL*, control line.

(version 11.5). A $p < 0.05$ was considered statistically significant.

RESULTS

Confirming the Feasibility of the *B. pertussis* LAMP Reaction

The feasibility of the *B. pertussis* LAMP primer set (**Figure 1** and **Table. 1**) was confirmed using DNA templates extracted from *B. pertussis* strains. The LAMP reaction was conducted at 64°C for ~60°min. The results showed that the templates were effectively amplified, and no amplifications were observed for DW (blank control) (**Figure 2**). Thus, the primer set designed in our report was used as the candidate to establish the *B. pertussis* LAMP-LFB assay.

Optimal Temperature for the *B. pertussis* LAMP Reaction

We used eight different temperatures ranging from 60°C to 67°C at 1°C intervals for 40°min to conduct the *B. pertussis* LAMP reaction for the optimal temperature. As shown in **Figure 3**, faster amplification was observed at 66°C, which was subsequently used for the *B. pertussis* LAMP-LFB reaction as the optimal temperature in this report.

Sensitivity of the LAMP-LFB Assay for the Detection of *B. pertussis*

The DNA templates of *B. pertussis* were serially diluted to examine the LoD of the *B. pertussis* LAMP-LFB assay. The results were indicated by LFB and further confirmed by turbidity and VDR. As shown in **Figure 4**, the LoD of the *B. pertussis* LAMP-LFB assay was as low as 50 fg (~12 copies) per reaction.

Optimal Time for the *B. pertussis* LAMP Reaction

We examined a total of four reaction times, 10–40 min with 10-min intervals, for the optimal amplification time of the *B. pertussis* LAMP assay. As shown in **Figure 5**, at 40 min, the amplicon of the diluted template at the LoD level was successfully detected by LFB, in which two red lines appeared respectively at the location of the test line (TL) and the control line (CL) on the strips. Therefore, 40 min was subsequently used as the optimal time for the *B. pertussis* LAMP assay. Hence, the whole procedure, which included rapid DNA extraction (15 min), LAMP reaction (40 min), and LFB indication (2 min), takes approximately 60 min, which is only half of that of qPCR.

Specificity of the *B. pertussis* LAMP-LFB Assay

The specificity of the *B. pertussis* LAMP-LFB assay was examined using *B. pertussis* and non-*B. pertussis* strains (**Table 2**). As in the results shown in **Figure 6**, only CL lines appeared on the LFB strips of the non-*B. pertussis* strains and blank controls, while two red lines appeared at the CL and TL locations on the strips of the *B. pertussis* strains, suggesting the specificity of the primers in that only DNA isolates from *B. pertussis* strains could be amplified.

Application of the *B. pertussis* LAMP-LFB Assay in Clinical Specimens

In order to confirm its clinical application value, the optimized *B. pertussis* LAMP-LFB assay was used to detect 108 NPS samples, which were also detected using qPCR. The results (**Figure 7**) showed that 44 samples (40.7%) tested positive

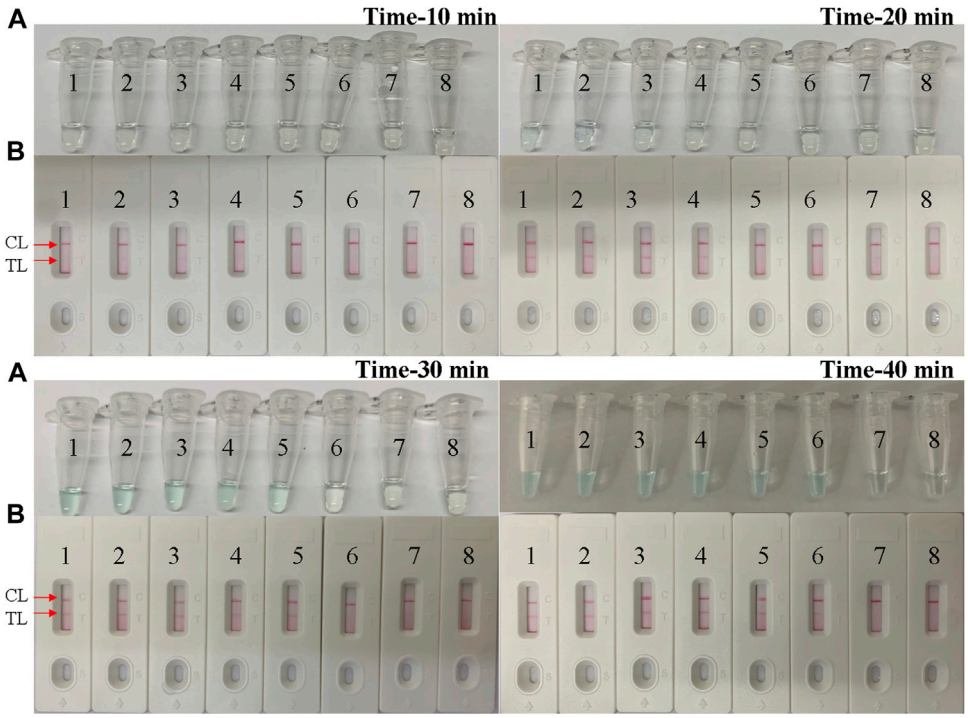

FIGURE 5 | Optimal time for the *Bordetella pertussis* loop-mediated isothermal amplification (LAMP) assay. Tenfold serial dilutions of the *B. pertussis* templates were used for the optimization of time. The LAMP reactions were conducted at different times from 10 to 40 min, with 10-min intervals. The products were indicated by the visual detection reagent **(A)** and a nanoparticle-based lateral flow biosensor (LFB) test **(B)**. Tubes/strips *1–7* represent serial dilutions of DNA: 5 ng; 500, 50, and 5 pg; and 500, 50, and 5 fg per reaction. Tube/strip *8* represents the blank control. *TL*, test line; *CL*, control line.

with the LAMP-LFB assay, while 42 samples (38.8%) tested positive with the qPCR. The agreement in the results between the qPCR and the LAMP-LFB assay was 98%, with a kappa value of 0.96.

DISCUSSION

As a previous major cause of infant death, the morbidity and mortality of *B. pertussis* infections have significantly declined, benefitting from general vaccinations in childhood since 1950s. However, in the last 20 years, global resurgence was found in several highly vaccinated populations (Mooi et al., 2014; Yeung et al., 2017; Liu et al., 2018; Fu et al., 2019; Tao et al., 2019; Wu et al., 2019; Zhang et al., 2019; Kang et al., 2022). An estimation of the infection frequency derived from seroprevalence studies among adolescents and adults revealed a high circulation rate (1%–9% annually) in vaccinated populations (Wood and McIntyre, 2008; Cherry, 2013). Thus, the early detection of *B. pertussis* enables not only timely treatment, especially for infants much more fragile to the infection, but also the prevention of transmission and unnecessary diagnostic procedure, especially during an outbreak.

In this report, a simple LAMP-LFB assay for the detection of *B. pertussis* was designed and validated by its application in clinical samples. The assay takes less time, ~60 min, with 15 min for rapid DNA extraction, 40 min for LAMP reaction, and 2 min for LFB detection, which was more rapid than that of traditional molecule-based diagnosis (e.g., PCR-based assay). Moreover, the significant advantage of the LAMP reaction is the isothermal condition, so the assay can be easily carried out under any experiment conditions with just a thermostatic water bath or a heater. The LFB test can subjectively indicate the results of the amplicons within 2 min.

As a molecular technique, the efficiency of the LAMP reaction is mostly decided by the primers and its targeting sequence. In previous studies, the sequence of the PT promoter has been considered as the very specific region for the diagnosis of *B. pertussis*. Comparison with previously used popular targeting sequences, such as insert sequence (IS) 1002 or IS481, demonstrated that primers targeting the PT gene showed marked reliability, selectivity, and sensitivity (van der Zee et al., 2015; Kilgore et al., 2016; Wu et al., 2019). We designed six primers targeting the PT sequence for the LAMP assay. The efficiency was conformed, as shown in **Figure 3G**, with the amplification peaking at 20–24 min under the condition of 66°C by turbidimetry. The specificity was confirmed by using the genomic templates of other bacterial strains, shown in **Table 2**. The high specificity (100%) indicated that the LAMP-LFB assay we investigated was reliable for the detection of *B. pertussis*.

In addition to the specificity, sensitivity was confirmed by using serial dilutions of genomic DNA. As shown in **Figure 4**, the

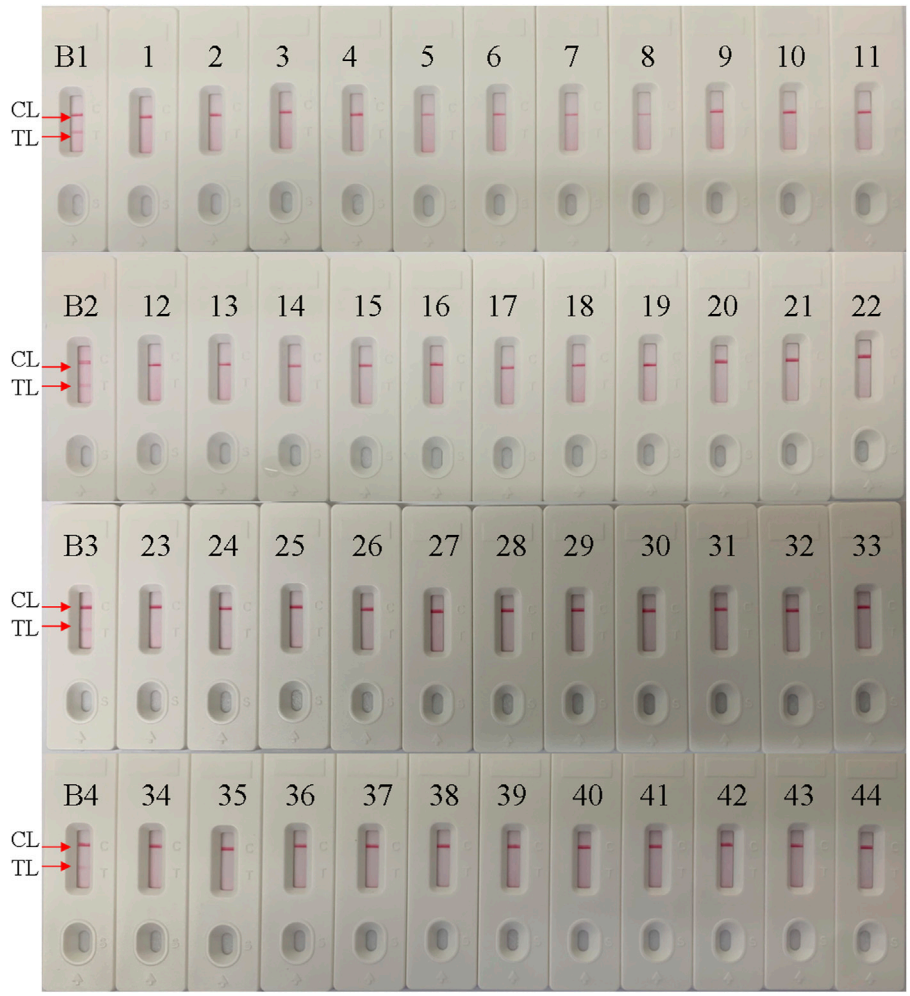

FIGURE 6 | Specificity conformation for the *Bordetella pertussis* loop-mediated isothermal amplification (LAMP) assay. A lateral flow biosensor was applied for the LAMP products. Strips *B1–B4* represent DNA isolation of the *B. pertussis*-positive clinical samples; strips *1–44* represent the other bacterial strains, shown in **Table 2**. *TL*, test line; *CL*, control line.

lowest detection level of the LAMP-LFB assay was 50 fg of the DNA templates isolated from pure culture of *B. pertussis*. Since the LF primers were labeled with Fam at the 5' end and biotin-14-dCTP was used in the reaction system, the amplicons positive in LAMP were simultaneously labeled with Fam and biotin, which can be detected by LFB. Thus, the positive LAMP amplicons displayed two red lines (CL and TL), while the negative reactions and the blank control displayed only the CL line when the reaction products were tested using LFB. The use of biotin-14-dCTP in the LAMP reaction instead of a biotin-labeled primer such as FIP absolutely avoided the interference of primer dimers containing Fam-labeled LF and biotin-labeled FIP.

For evaluation of the feasibility of the LAMP-LFB assay in the clinical diagnosis of *B. pertussis* infections, we compared the test with qPCR, the established method for *B. pertussis* diagnosis. Of the 108 clinical samples tested, 42 (38.8%) were positive by qPCR and 44 (40.7%) were positive by the LAMP-LFB assay. According to manual in the kit, the LoD of the qPCR assay used in this report is 250 copies, which is equal to about 1 pg DNA template, while the *B. pertussis* LAMP-LFB assay we conducted displayed better sensitivity with an LoD of 50 fg DNA template. For this reason, the LAMP-LFB assay yielded a higher positive rate than that of the qPCR assay in the clinical samples. Besides the lower LoD of the qPCR kit, the presence of some inhibitors specific to qPCR may have also contributed to the lower positive rates of detections. Therefore the application of the *B. pertussis* LAMP-LFB assay was verified to be sensitive and specific for the clinical diagnosis of *B. pertussis* infections. Moreover, the lower cost of the LAMP-LFB assay could also benefit its extensive application prospects in resource-limited laboratories.

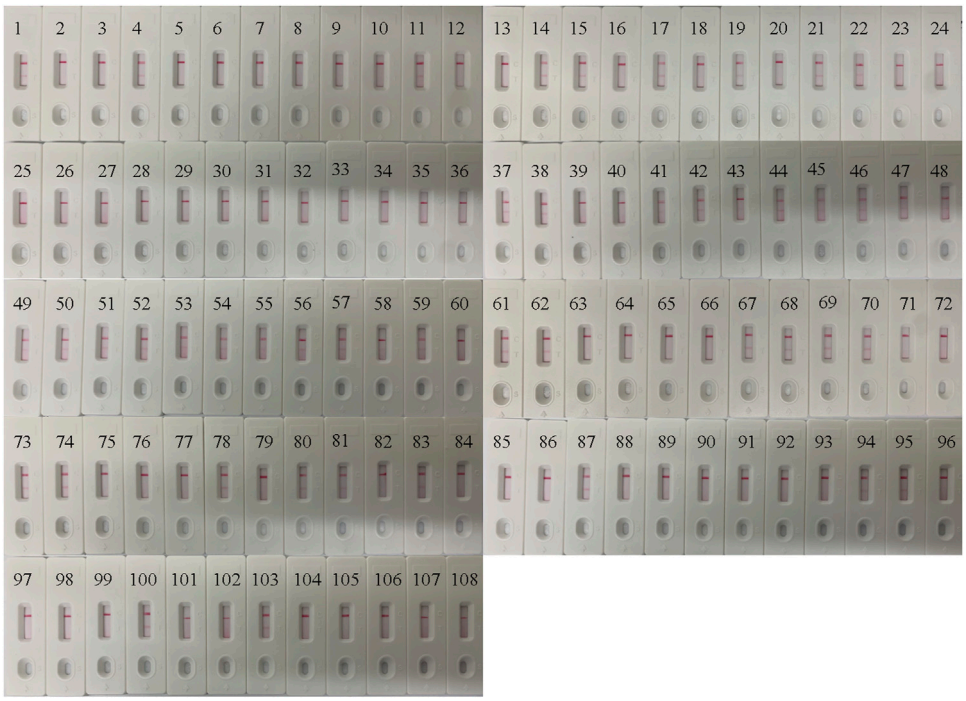

FIGURE 7 | Application of the *Bordetella pertussis* loop-mediated isothermal amplification/nanoparticle-based lateral flow biosensor (LAMP-LFB) assay in clinical specimens. A total of 108 nasopharyngeal swab (NPS) samples were detected by the LAMP-LFB assay, with the results showing 44 samples testing positive.

DATA AVAILABILITY STATEMENT

The datasets presented in this study can be found in online repositories. The names of the repository/repositories and accession number(s) can be found in the article/supplementary material.

ETHICS STATEMENT

The studies involving human participants were reviewed and approved by the Ethics Committee of the Capital Institute of Pediatrics (ethical approval no. SHERLL2021031). The patients/participants legal guardian/next of kin provided written informed consent to participate in this study.

AUTHOR CONTRIBUTIONS

YW and XC designed this study and revised the manuscript. CS, FX, and JF performed the experiments. CS analyzed the data and drafted the manuscript. CS, FX, JF, XH, NJ, and ZX contributed to the reagents and materials. YW conducted the software. All authors contributed to the article and approved the submitted version.

FUNDING

This study was funded by National Key Research and Development Program of China (Grant Nos. 2021YFC2301101 (YW), 2021YFC2301102 (YW)) and the Research Foundation of Capital Institute of Pediatrics (Grant No. PY-2019-07).

ACKNOWLEDGMENTS

We thank Prof. Rong Mi (Neonates Department, Children's Hospital Affiliated to Capital Institute of Pediatrics) and Prof. Linqing Zhao (Virus Laboratory of Capital Institute of Pediatrics) for their kind help.

REFERENCES

Abu Raya, B., Bamberger, E., Gershtein, R., Peterman, M., and Srugo, I. (2012). The Laboratory Diagnosis of Bordetella Pertussis Infection: a Comparison of Semi-nested PCR and Real-Time PCR with Culture. *Eur. J. Clin. Microbiol. Infect. Dis.* 31, 619–622. doi:10.1007/s10096-011-1327-6

Bock, J. M., Burtis, C. C., Poetker, D. M., Blumin, J. H., and Frank, M. O. (2012). Serum Immunoglobulin G Analysis to Establish a Delayed Diagnosis of Chronic Cough Due to Bordetella Pertussis. *Otolaryngol. Head Neck Surg.* 146 (1), 63–67. doi:10.1177/0194599811425145

Cherry, J. D. (2013). Pertussis: Challenges Today and for the Future. *Plos Pathog.* 9 (7), e1003418. doi:10.1371/journal.ppat.1003418

Cherry, J. D., Grimprel, E., Guiso, N., Heininger, U., and Mertsola, J. (2005). Defining Pertussis Epidemiology. *Pediatr. Infect. Dis. J.* 24 (Suppl. 5), S25–S34. doi:10.1097/01.inf.0000160926.89577.3b

Chia, J. H., Su, L. H., Lin, P. Y., Chiu, C. H., Kuo, A. J., Sun, C. F., et al. (2004). Comparison of Multiplex Polymerase Chain Reaction, Culture, and Serology

for the Diagnosis of Bordetella Pertussis Infection. *Chang Gung Med. J.* 27, 408–415.

de Greeff, S. C., de Melker, H. E., van Gageldonk, P. G. M., Schellekens, J. F. P., van der Klis, F. R. M., Mollema, L., et al. (2010). Seroprevalence of Pertussis in the Netherlands: Evidence for Increased Circulation of Bordetella Pertussis. *PLoS One* 5, e14183. doi:10.1371/journal.pone.0014183

Del Valle-Mendoza, J., Del Valle-Vargas, C., Aquino-Ortega, R., Del Valle, L. J., Cieza-Mora, E., Silva-Caso, W., et al. (2021). Clinical Characteristics and Molecular Detection of Bordetella Pertussis in Hospitalized Children with a Clinical Diagnosis of Whooping Cough in Peru. *Iran J. Microbiol.* 13 (1), 23–30. doi:10.18502/ijm.v13i1.5488

Fu, P., Wang, C., Tian, H., Kang, Z., and Zeng, M. (2019). Bordetella Pertussis Infection in Infants and Young Children in Shanghai, China, 2016-2017: Clinical Features, Genotype Variations of Antigenic Genes and Macrolides Resistance. *Pediatr. Infect. Dis. J.* 38 (4), 370–376. doi:10.1097/INF.0000000000002160

Fujino, M., Suzuki, E., Watanabe, M., and Nakayama, T. (2015). Loop-Mediated Isothermal Amplification (LAMP) Aids the Clinical Diagnosis of Pertussis. *Jpn. J. Infect. Dis.* 68 (6), 532–533. doi:10.7883/yoken.JJID.2015.125

Gao, F., Mahoney, J. C., Daly, E. R., Lamothe, W., Tullo, D., and Bean, C. (2014). Evaluation of a Multitarget Real-Time PCR Assay for Detection of Bordetella Species during a Pertussis Outbreak in New Hampshire in 2011. *J. Clin. Microbiol.* 52, 302–306. doi:10.1128/JCM.01656-13

Grimprel, E., Bégué, P., Anjak, I., Betsou, F., and Guiso, N. (1993). Comparison of Polymerase Chain Reaction, Culture, and Western Immunoblot Serology for Diagnosis of Bordetella Pertussis Infection. *J. Clin. Microbiol.* 31 (10), 2745–2750. doi:10.1128/jcm.31.10.2745-2750.1993

Huang, Y., Cheng, Z., Han, R., Gao, X., Qian, L., Wen, Y., et al. (2020). Target-Induced Molecular-Switch On Triple-Helix DNA-Functionalized Carbon Nanotubes For Simultaneous Visual Detection Of Nucleic Acids And Proteins. *Chem. Commun. (Camb)* 56 (88), 13657–13660. doi:10.1039/d0cc05986b

Huang, Y., Xu, T., Luo, Y., Liu, C., Gao, X., Cheng, Z., et al. (2021). Ultra-Trace Protein Detection by Integrating Lateral Flow Biosensor with Ultrasound Enrichment. *Anal. Chem.* 93 (5), 2996–3001. doi:10.1021/acs.analchem.0c05032

Huang, Y., Xu, T., Wang, W., Wen, Y., Li, K., Qian, L., et al. (2019). Lateral Flow Biosensors Based On The Use Of Micro- And Nanomaterials: A Review On Recent Developments. *Mikrochim Acta.* 187 (1), 70. doi:10.1007/s00604-019-3822-x

Kang, L., Cui, X., Fu, J., Wang, W., Li, L., Li, T., et al. (2022). Clinical Characteristics of 967 Children with Pertussis: a Single-center Analysis over an 8-year Period in Beijing, China. *Eur. J. Clin. Microbiol. Infect. Dis.* 41 (1), 9–20. doi:10.1007/s10096-021-04336-w

Kamachi, K., Toyoizumi-Ajisaka, H., Toda, K., Soeung, S. C., Sarath, S., Nareth, Y., et al. (2006). Development and Evaluation of a Loop-Mediated Isothermal Amplification Method for Rapid Diagnosis of Bordetella Pertussis Infection. *J. Clin. Microbiol.* 44 (5), 1899–1902. doi:10.1128/JCM.44.5.1899-1902.2006

Kilgore, P. E., Salim, A. M., Zervos, M. J., and Schmitt, H-J. (2016). Pertussis: Microbiology, Disease, Treatment, and Prevention. *Clin. Microbiol. Rev.* 29 (3), 449–486. doi:10.1128/CMR.00083-15

Li, S., Jiang, W., Huang, J., Liu, Y., Ren, L., Zhuang, L., et al. (2020). Highly Sensitive And Specific Diagnosis Of COVID-19 By Reverse Transcription Multiple Cross-Displacement Amplification-Labelled Nanoparticles Biosensor. *Eur. Respir. J.* 56 (6), 2002060. doi:10.1183/13993003.02060-2020

Liu, X., Wang, Z., Zhang, J., Li, F., Luan, Y., Li, H., et al. (2018). Pertussis Outbreak in a Primary School in China. *Pediatr. Infect. Dis. J.* 37 (6), e145–e148. doi:10.1097/INF.0000000000001814

Macina, D., and Evans, K. E. (2021). Bordetella Pertussis in School-Age Children, Adolescents and Adults: A Systematic Review of Epidemiology and Mortality in Europe. *Infect. Dis. Ther.* 10, 2071–2118. doi:10.1007/s40121-021-00520-9

Mertens, P. L., Stals, F. S., Steyerberg, E. W., and Richardus, J. H. (2007). Sensitivity and Specificity of Single IgA and IgG Antibody Concentrations for Early Diagnosis of Pertussis in Adults: an Evaluation for Outbreak Management in Public Health Practice. *BMC Infect. Dis.* 7, 53. doi:10.1186/1471-2334-7-53

Mooi, F. R., Van Der Maas, N. A. T., and De Melker, H. E. (2014). Pertussis Resurgence: Waning Immunity and Pathogen Adaptation - Two Sides of the Same coin. *Epidemiol. Infect.* 142, 685–694. doi:10.1017/S0950268813000071

Notomi, T., Mori, Y., Tomita, N., and Kanda, H. (2015). Loop-mediated Isothermal Amplification (LAMP): Principle, Features, and Future Prospects. *J. Microbiol.* 53, 1–5. doi:10.1007/s12275-015-4656-9

Notomi, T., Okayama, H., Masubuchi, H., Yonekawa, T., Watanabe, K., Amino, N., et al. (2000). Loop-mediated Isothermal Amplification of DNA. *Nucleic Acids Res.* 28, 63e. doi:10.1093/nar/28.12.e63

Nygren, M., Reizenstein, E., Ronaghi, M., and Lundeberg, J. (2000). Polymorphism in the Pertussis Toxin Promoter Region Affecting the DNA-Based Diagnosis of Bordetella Infection. *J. Clin. Microbiol.* 38 (1), 55–60. doi:10.1128/JCM.38.1.55-60.2000

Pandolfi, E., Gesualdo, F., Rizzo, C., Russo, L., Campagna, I., Carloni, E., et al. (2021). The Impact of Pertussis in Infants: Insights from a Hospital-Based Enhanced Surveillance System, Lazio Region, Italy, 2016 to 2019. *Euro Surveill.* 26 (24), 2000562. doi:10.2807/1560-7917.ES.2021.26.24.2000562

Pittet, L. F., Emonet, S., François, P., Bonetti, E.-J., Schrenzel, J., Hug, M., et al. (2014). Diagnosis of Whooping Cough in Switzerland: Differentiating Bordetella Pertussis from Bordetella Holmesii by Polymerase Chain Reaction. *PLoS One* 9 (2), e88936. doi:10.1371/journal.pone.0088936

Roorda, L., Buitenwerf, J., Ossewaarde, J. M., and van der Zee, A. (2011). A Real-Time PCR Assay with Improved Specificity for Detection and Discrimination of All Clinically Relevant Bordetella Species by the Presence and Distribution of Three Insertion Sequence Elements. *BMC Res. Notes* 4, 11. doi:10.1186/1756-0500-4-11

Tao, Y., Tang, M., Luo, L., Xiang, L., Xia, Y., Li, B., et al. (2019). Identification of Etiologic Agents and Clinical Characteristics for Patients Suspected of Having Pertussis in a Large Children's Hospital in China. *Ann. Transl. Med.* 7 (18), 443. doi:10.21037/atm.2019.08.85

Tatti, K. M., Sparks, K. N., Boney, K. O., and Tondella, M. L. (2011). Novel Multitarget Real-Time PCR Assay for Rapid Detection of Bordetella Species in Clinical Specimens. *J. Clin. Microbiol.* 49, 4059–4066. doi:10.1128/JCM.00601-11

van der Zee, A., Schellekens, J. F. P., and Mooi, F. R. (2015). Laboratory Diagnosis of Pertussis. *Clin. Microbiol. Rev.* 28, 1005–1026. doi:10.1128/cmr.00031-15

Wood, N., and McIntyre, P. (2008). Pertussis: Review of Epidemiology, Diagnosis, Management and Prevention. *Paediatric Respir. Rev.* 9 (3), 201–212. doi:10.1016/j.prrv.2008.05.010

Wu, D.-X., Chen, Q., Yao, K.-H., Li, L., Shi, W., Ke, J.-W., et al. (2019). Pertussis Detection in Children with Cough of Any Duration. *BMC Pediatr.* 19 (1), 236. doi:10.1186/s12887-019-1615-3

Yeung, K. H. T., Duclos, P., Nelson, E. A. S., Hutubessy, R. C. W., and Hutubessy Rcw Lancet Infect Dis (2017). An Update of the Global burden of Pertussis in Children Younger Than 5 years: a Modelling Study. *Lancet Infect. Dis.* 17 (9), 974–980. doi:10.1016/s1473-3099(17)30390-0

Zhang, Y., Bambrick, H., Mengersen, K., Tong, S., Feng, L., Zhang, L., et al. (2019). Resurgence of Pertussis Infections in Shandong, China: Space-Time Cluster and Trend Analysis. *Am. J. Trop. Med. Hyg.* 100 (6), 1342–1354. doi:10.4269/ajtmh.19-0013

Conflict of Interest: The authors declare that the research was conducted in the absence of any commercial or financial relationships that could be construed as a potential conflict of interest.

Publisher's Note: All claims expressed in this article are solely those of the authors and do not necessarily represent those of their affiliated organizations, or those of the publisher, the editors and the reviewers. Any product that may be evaluated in this article, or claim that may be made by its manufacturer, is not guaranteed or endorsed by the publisher.

Advantages of publishing in Frontiers

OPEN ACCESS
Articles are free to read for greatest visibility and readership

FAST PUBLICATION
Around 90 days from submission to decision

HIGH QUALITY PEER-REVIEW
Rigorous, collaborative, and constructive peer-review

TRANSPARENT PEER-REVIEW
Editors and reviewers acknowledged by name on published articles

Frontiers
Avenue du Tribunal-Fédéral 34
1005 Lausanne | Switzerland

Visit us: www.frontiersin.org
Contact us: frontiersin.org/about/contact

REPRODUCIBILITY OF RESEARCH
Support open data and methods to enhance research reproducibility

DIGITAL PUBLISHING
Articles designed for optimal readership across devices

FOLLOW US
@frontiersin

IMPACT METRICS
Advanced article metrics track visibility across digital media

EXTENSIVE PROMOTION
Marketing and promotion of impactful research

LOOP RESEARCH NETWORK
Our network increases your article's readership